Published in Journals: Biomolecules, International Journal of Molecular Sciences, Journal of Clinical Medicine, Molecules and Separations

Topic Reprint

Chromatography–Mass Spectrometry Analysis in Biomedical Research and Clinical Laboratory

Edited by
Constantinos K. Zacharis and Andreas Tsakalof

mdpi.com/topics

MDPI

Chromatography–Mass Spectrometry Analysis in Biomedical Research and Clinical Laboratory

Chromatography–Mass Spectrometry Analysis in Biomedical Research and Clinical Laboratory

Topic Editors

Constantinos K. Zacharis
Andreas Tsakalof

MDPI

Basel • Beijing • Wuhan • Barcelona • Belgrade • Novi Sad • Cluj • Manchester

Topic Editors
Constantinos K. Zacharis
Department of Pharmaceutical Technology
Aristotle University of Thessaloniki
Thessaloniki
Greece

Andreas Tsakalof
School of Health Sciences
University of Thessaly
Larissa
Greece

Editorial Office
MDPI AG
Grosspeteranlage 5
4052 Basel, Switzerland

This is a reprint of the Topic, published open access by the journals *Biomolecules* (ISSN 2218-273X), *International Journal of Molecular Sciences* (ISSN 1422-0067), *Journal of Clinical Medicine* (ISSN 2077-0383), *Molecules* (ISSN 1420-3049) and *Separations* (ISSN 2297-8739), freely accessible at: https://www.mdpi.com/topics/FQGV30XQON.

For citation purposes, cite each article independently as indicated on the article page online and as indicated below:

Lastname, A.A.; Lastname, B.B. Article Title. *Journal Name* **Year**, *Volume Number*, Page Range.

ISBN 978-3-7258-7775-1 (Hbk)
ISBN 978-3-7258-7776-8 (PDF)
https://doi.org/10.3390/books978-3-7258-7776-8

© 2026 by the authors. Articles in this reprint are Open Access and distributed under the Creative Commons Attribution (CC BY) license. The reprint as a whole is distributed by MDPI under the terms and conditions of the Creative Commons Attribution-NonCommercial-NoDerivs (CC BY-NC-ND) license (https://creativecommons.org/licenses/by-nc-nd/4.0/).

Contents

About the Editors . . . . . **ix**

Preface . . . . . **xi**

Andreas Tsakalof and Constantinos K. Zacharis
Editorial of Topic Issue "Chromatography–Mass Spectrometry Analysis in Biomedical Research and Clinical Laboratory"
Reprinted from: *Molecules* **2026**, *31*, 481, https://doi.org/10.3390/molecules31030481 . . . . . **1**

Kyung-Geun Ahn, Ryuho Choi, Soonchul Gwak, Inyoung Choi, Giup Jang, Jin-Wook Kim and Geon A Kim
A Novel Sample Preparation Method for GC-MS Analysis of Volatile Organic Compounds in Whole Blood for Veterinary Use
Reprinted from: *Int. J. Mol. Sci.* **2025**, *26*, 4667, https://doi.org/10.3390/ijms26104667 . . . . . **6**

Anna Błażewicz, Michał Kiełbus, Katarzyna Skórzyńska-Dziduszko, Andreas M. Grabrucker, Jacqueline Jonklaas, Piotr Sosnowski, et al.
Application of Human Plasma Targeted Lipidomics and Analysis of Toxic Elements to Capture the Metabolic Complexities of Hypothyroidism
Reprinted from: *Molecules* **2024**, *29*, 5169, https://doi.org/10.3390/molecules29215169 . . . . . **16**

Gregori Casals, María Antonieta Ballesteros, Angielys Zamora, Irene Martínez, Guillermo Fernández-Varo, Mireia Mora, et al.
LC-HRMS and GC-MS Profiling of Urine Free Cortisol, Cortisone, 6B-, and 18-Hydroxycortisol for the Evaluation of Glucocorticoid and Mineralocorticoid Disorders
Reprinted from: *Biomolecules* **2024**, *14*, 558, https://doi.org/10.3390/biom14050558 . . . . . **45**

Kevin P. Gillespie, Ross Pirnie, Clementina Mesaros and Ian A. Blair
Cisplatin Dependent Secretion of Immunomodulatory High Mobility Group Box 1 (HMGB1) Protein from Lung Cancer Cells
Reprinted from: *Biomolecules* **2023**, *13*, 1335, https://doi.org/10.3390/biom13091335 . . . . . **61**

Honghui Guo, Guang Wang, Wei Huang, Lingrui Li, Yang Bai, Haifeng Wang and Lina Gao
The Mechanism of Hepatic Encephalopathy Induced by Thioacetamide Based on Metabolomics and Proteomics: A Preliminary Study
Reprinted from: *Int. J. Mol. Sci.* **2024**, *25*, 284, https://doi.org/10.3390/ijms25010284 . . . . . **87**

Mohammed E. Hefni and Cornelia M. Witthöft
Development and Application of a UPLC–MRM–MS Method for Quantifying Trimethylamine, Trimethylamine-N-Oxide, and Related Metabolites in Individuals with and Without Metabolic Syndrome
Reprinted from: *Separations* **2025**, *12*, 53, https://doi.org/10.3390/separations12020053 . . . . . **109**

Hee-Jung Kim, Seo-Hyeon Jung, Shokhid Gulyamov, Hyun-Gy Lee, Oybek Boyjigitov and Yong-Moon Lee
HPLC-MS/MS Analysis for Sphingosine 1-Phosphate after the Dephosphorylation by Hydrogen Fluoride
Reprinted from: *Separations* **2024**, *11*, 34, https://doi.org/10.3390/separations11010034 . . . . . **122**

Piotr Kośliński, Łukasz Rzepiński, Marcin Koba, Zdzisław Maciejek, Mariusz Kowalewski and Emilia Daghir-Wojtkowiak
Comparative Analysis of Serum Amino Acid Profiles in Patients with Myasthenia Gravis and Multiple Sclerosis
Reprinted from: *J. Clin. Med.* **2024**, *13*, 4083, https://doi.org/10.3390/jcm13144083 . . . . . **134**

Peter Meinarovich, Alisa Pautova, Evgenii Zuev, Ekaterina Sorokina, Ekaterina Chernevskaya and Natalia Beloborodova
An Integrated Approach Based on Clinical Data Combined with Metabolites and Biomarkers for the Assessment of Post-Operative Complications after Cardiac Surgery
Reprinted from: *J. Clin. Med.* **2024**, *13*, 5054, https://doi.org/10.3390/jcm13175054 . . . . . **150**

Linda Molteni, Bruno Charlier, Albino Coglianese, Viviana Izzo, Giovanni Assenza, Pierantonio Menna, et al.
Quantitative Analysis of Cenobamate and Concomitant Anti-Seizure Medications in Human Plasma via Ultra-High Performance Liquid Chromatography–Tandem Mass Spectrometry
Reprinted from: *Molecules* **2024**, *29*, 884, https://doi.org/10.3390/molecules29040884 . . . . . **165**

Linda Molteni, Bruno Charlier, Viviana Izzo, Albino Coglianese, Valeria Conti, Roberto Eleopra, et al.
Development and Validation of a New LC-MS/MS Bioanalytical Method for the Simultaneous Determination of Levodopa, Levodopa Methyl Ester, and Carbidopa in Human Plasma Samples
Reprinted from: *Molecules* **2023**, *28*, 4264, https://doi.org/10.3390/molecules28114264 . . . . . **182**

Sherifdeen Onigbinde, Cristian D. Gutierrez Reyes, Mojibola Fowowe, Oluwatosin Daramola, Mojgan Atashi, Andrew I. Bennett and Yehia Mechref
Variations in *O*-Glycosylation Patterns Influence Viral Pathogenicity, Infectivity, and Transmissibility in SARS-CoV-2 Variants
Reprinted from: *Biomolecules* **2023**, *13*, 1467, https://doi.org/10.3390/biom13101467 . . . . . **195**

Mustafa Ozgul, Anthony B. Nesburn, Nader Nasralla, Benjamin Katz, Enes Taylan, Baruch D. Kuppermann and Maria Cristina Kenney
Stability Determination of Intact Humanin-G with Characterizations of Oxidation and Dimerization Patterns
Reprinted from: *Biomolecules* **2023**, *13*, 515, https://doi.org/10.3390/biom13030515 . . . . . **216**

Rene A. Posma, Stephan J. L. Bakker, Maarten W. Nijsten, Daan J. Touw and Dimitrios Tsikas
Comprehensive GC-MS Measurement of Amino Acids, Metabolites, and Malondialdehyde in Metformin-Associated Lactic Acidosis at Admission and during Renal Replacement Treatment
Reprinted from: *J. Clin. Med.* **2024**, *13*, 3692, https://doi.org/10.3390/jcm13133692 . . . . . **237**

Yuki Taya, Mari Mizunaga, Shunsuke Nakao, Mirinthorn Jutanom, Naoki Shimizu, Yukihiro Nomura and Kiyotaka Nakagawa
Clinical Evaluation Based on a New Approach to Improve the Accuracy of 4β-Hydroxycholesterol Measurement as a Biomarker of CYP3A4 Activity
Reprinted from: *Molecules* **2023**, *28*, 1576, https://doi.org/10.3390/molecules28041576 . . . . . **249**

Andreas Tsakalof, Alexey A. Sysoev, Kira V. Vyatkina, Alexander A. Eganov, Nikolay N. Eroshchenko, Alexey N. Kiryushin, et al.
Current Role and Potential of Triple Quadrupole Mass Spectrometry in Biomedical Research and Clinical Applications
Reprinted from: *Molecules* **2024**, *29*, 5808, https://doi.org/10.3390/molecules29235808 . . . . . **263**

Dong Wei, Kristin L. Horton, John Chen, Linlin Dong, Susan Chen, Kojo Abdul-Hadi, et al.
Development of a Highly Sensitive Hybrid LC/MS Assay for the Quantitative Measurement of CTLA-4 in Human T Cells
Reprinted from: *Molecules* **2023**, *28*, 3311, https://doi.org/10.3390/molecules28083311 . . . . . **280**

About the Editors

Constantinos K. Zacharis

Constantinos K. Zacharis is an Associate Professor of Pharmaceutical Analysis at the Department of Pharmacy, Aristotle University of Thessaloniki. He received his Ph.D. in Analytical Chemistry in 2006 from the Department of Chemistry at the same institution. He served as Editor of the Analytical Chemistry section of *Open Chemistry Journal* (2010–2020) and currently serves on the editorial boards of *Microchemical Journal*, *Instrumentation Science and Technology*, *Molecules*, and *Analytica*. Dr. Zacharis is the supervisor of three ongoing Ph.D. theses, has supervised one postdoctoral researcher, 28 master's theses, and more than 40 undergraduate research projects. His scientific work focuses on two main areas: (i) the development of analytical methods for pharmaceutical quality control using chemometrics, and (ii) the development of novel microextraction techniques for bioanalytical applications. He also collaborates in related fields such as food and environmental analysis. Dr. Zacharis has authored nearly 125 publications, which have received over 2280 citations (h-index: 27). He has co-authored more than 6 book chapters and has guest-edited over 15 special issues published in *Microchemical Journal*, *Journal of Chromatography B*, *Molecules*, etc. In addition, he has served as a reviewer for more than 50 scientific journals, reviewing over 1100 manuscripts. In recognition of his scientific contributions, he received the Excellence in Research Award from the Faculty of Health Sciences, Aristotle University of Thessaloniki, in both 2022 and 2023.

Andreas Tsakalof

Andreas Tsakalof, PhD, Professor (retired) of Medical Chemistry (University of Thessaly, Greece), has long-term experience in teaching medical chemistry, environmental chemistry and toxicology, instrumental analysis, and biochemistry at the undergraduate and postgraduate levels, as well as in the supervision of postgraduate and PhD theses and postdoctoral research. He is the author of manuals and textbooks on these subjects. His research experiences and interests comprise the application of chromatography and chromatography–mass spectrometry in clinical chemistry, toxicology, and human biomonitoring, GC-MS analysis of VOC in exhaled air for clinical diagnosis, Vitamin D in human health and disease, and the fabrication of molecularly imprinted polymers and their application for the identification and isolation of bioactive molecules. Professor Tsakalof has published 72 peer reviewed articles, accumulating over 3,145 citations and an h index of 31 (Scopus, 02 02 2026; Author ID: 6602277700). Professor Andreas Tsakalof is a member of editorial boards and a reviewer at more than 14 journals and has been recognized as a Top reviewer (*Toxicology Letters*) and for Outstanding contribution in Reviewing (*Food and Chemical Toxicology*). He has also acted as a Guest Editor for two special issues and two topical collections at MDPI.

Preface

Throughout the 21st century, chromatography–mass spectrometry (CMS) has evolved from a highly specialized analytical technique into a cornerstone technology in biomedical and clinical research. Its increasing accessibility, robustness, and analytical power have driven widespread adoption across research laboratories and clinical settings, fundamentally transforming approaches to disease diagnosis, biomarker discovery, and therapeutic development. Today, CMS underpins a broad range of cutting-edge applications, including omics sciences, metabolic pathway analysis, personalized medicine, drug discovery, and routine clinical diagnostics.

The scope of this scientific work reflects the inherently multidisciplinary nature of CMS-based research. It encompasses methodological advances, innovative applications, and translational studies that bridge fundamental research and clinical practice. The primary aim of this work is to highlight the versatility and unifying role of the CMS instrumental platform across diverse scientific domains, while showcasing recent developments that advance our understanding of biological systems and disease mechanisms. By bringing together contributions from different research areas, this work seeks to foster cross-disciplinary dialogue and knowledge exchange, enabling researchers to gain insight into CMS applications beyond their immediate area of expertise.

The motivation for compiling this work arises from the rapid expansion of CMS technologies and their growing impact on both research and clinical decision-making applications. As the field continues to evolve, there is a clear need for a dedicated forum that captures current trends, shares best practices, and presents emerging discoveries in a coherent and accessible manner. This work is addressed to a broad audience, including analytical chemists, biomedical researchers, clinicians, and industry scientists, as well as graduate students and early-career researchers seeking a comprehensive perspective on contemporary CMS applications. Ultimately, it aims to serve as both a reference and an inspiration for future research at the intersection of analytical technology and biomedical science.

Constantinos K. Zacharis and Andreas Tsakalof
Topic Editors

molecules

MDPI

Editorial

Editorial of Topic Issue "Chromatography–Mass Spectrometry Analysis in Biomedical Research and Clinical Laboratory"

Andreas Tsakalof [1,*] and Constantinos K. Zacharis [2,*]

[1] School of Medicine, University of Thessaly, GR-41500 Larissa, Greece
[2] Department of Pharmacy, Aristotle University of Thessaloniki, GR-54124 Thessaloniki, Greece
* Correspondence: atsakal@med.uth.gr (A.T.); czacharis@pharm.auth.gr (C.K.Z.)

Throughout the 21st century, chromatography–mass spectrometry (CMS) evolved from a specialized, expert-level analytical technique to a central instrumental platform in biomedical research, and its adoption by clinical laboratories has brought about a revolution in disease diagnosis. Nowadays, CMS plays a pivotal role in cutting-edge omics research, disease biomarkers discovery and validation, metabolic pathway elucidation, personalized medicine, drug development, and clinical disease diagnosis. These research areas are unified by their use of the CMS instrumental platform, and the aim of this issue was to highlight the multidisciplinary nature of the field and to provide a forum in which researchers can present their latest findings while becoming acquainted with CMS applications across diverse scientific domains. Six MDPI journals participated, giving the authors the opportunity to select the journal that best matches the subject of their research (Figure 1). Fifty-five (55) manuscripts were submitted, and seventeen (17) were ultimately accepted for publication.

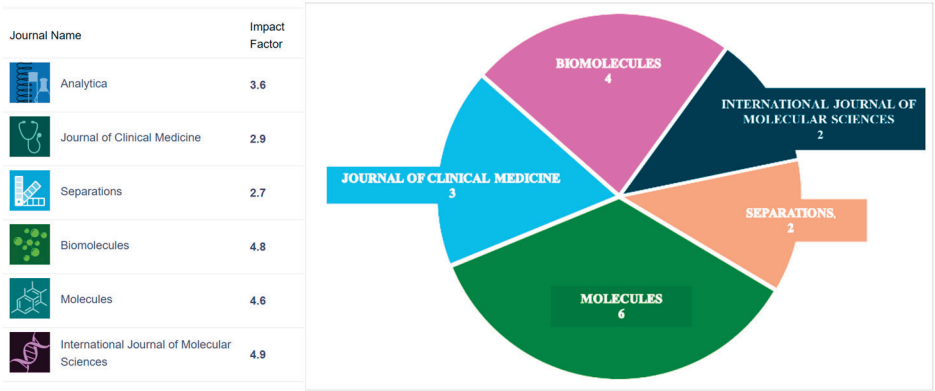


Figure 1. Participating journals and the distribution of the published manuscripts.

The largest number of manuscripts (six) was published in *Molecules*, which focuses on chemistry and related scientific disciplines. The published articles encompassed a wide range of biomedical applications. The study of A. Blazewicz et al. [1] combines targeted lipidomics via flow injection electrospray–tandem mass spectrometry (FI-ESI–MS/MS) with inductively coupled plasma–mass spectrometry (ICP-MS) trace element analy-sis to uncover metabolic signatures of hypothyroidism and lipidome relationship with non-occupational exposure to toxic elements. Using the multiple reaction monitoring (MRM) mode, the authors achieved sensitive and selective quantification of 145 plasma lipid species, enabling the precise characterization of alterations in lysophosphatidylcholines and phosphatidylcholines. The integration of lipidome analysis with measurements of

toxic elements revealed how subtle environmental exposures and disease subtypes shape lipid metabolism in autoimmune and non-autoimmune hypothyroidism. The research of L. Molteni et al. presents a robust ultra-high-pressure liquid chromatography–tandem mass spectrometry (UHPLC–MS/MS) method for the simultaneous quantification of L-DOPA, levodopa methyl ester, and carbidopa in human plasma, providing a powerful analytical tool for therapeutic drug monitoring in Parkinson's disease [2]. By coupling UHPLC with triple quadrupole mass spectrometer (QqQ) mass spectrometry, the method ensures high selectivity, sensitivity, and reproducibility, enabling the accurate assessment of L-DOPA pharmacokinetics under different therapeutic regimens. Its successful application to a clinical case highlights the potential of LC–MS/MS-based approaches to support personalized treatment strategies and optimize the efficacy and safety of L-DOPA therapy. A year later, a fully validated UHPLC–MS/MS method for the simultaneous quantification of cenobamate and concomitant anti-seizure medications in human plasma has been developed and validated in the same laboratory [3]. This method offers a powerful analytical tool for therapeutic drug monitoring. It ensures high sensitivity, selectivity, and robustness across a clinically relevant concentration range, in compliance with ICH M10 guidelines. This approach supports precision medicine in epilepsy by enabling accurate monitoring of drug levels during combination therapy, thereby improving the clinical management of patients with refractory and drug-resistant epilepsies. This Editorial highlights the development of a highly sensitive LC–MS/MS-based assay for the quantification of cytotoxic T-lymphocyte-associated protein 4 (CTLA-4) in human T cells, addressing a major analytical gap in immuno-oncology research [4]. By leveraging the specificity and sensitivity of liquid chromatography–mass spectrometry, the method enables the absolute quantification of CTLA-4 down to a few copies per cell, providing a powerful tool to support pharmacodynamic, efficacy, and safety assessments of CTLA-4–targeted cancer therapies across preclinical and clinical studies. The study of Y. Taya et al. [5] underscores the value of LC–MS/MS-based analysis of 4β-hydroxycholesterol as a sensitive biomarker for detecting even weak cytochrome P450 family 3 subfamily A member 4 (CYP3A4) induction in clinical drug development. By optimizing plasma collection and storage conditions and introducing the monitoring of a cholesterol oxidation product as a quality marker, the authors ensure accurate and reliable quantification of 4β-HC using liquid chromatography–mass spectrometry. This refined LC–MS approach enables robust evaluation of CYP3A4 induction by new chemical entities without the need for probe substrates, strengthening the role of lipid biomarkers in clinical DDI studies. Notably, all studies published in *Molecules* utilized QqQ from different vendors, reaffirming the status of QqQ as the instrument of choice in biomedical research, a point further emphasized by Tsakalof et al. in their review of QqQ applications in biomedicine [6]. By analyzing publication trends, the review shows a marked increase in QqQ use over the past decade, particularly in endocrine research, therapeutic drug monitoring, and forensic toxicology, where it is progressively replacing traditional immunoassays. The paper also discusses recent technological advances in QqQ platforms that have strengthened their clinical applicability, while positioning high-resolution accurate mass (HRAM) instruments as complementary tools driving innovation in untargeted biomarker discovery.

Four manuscripts were published in *Biomolecules*, a journal dedicated to multidisciplinary research in "chemistry, biology, molecular medicine and material sciences." The clinical impact of LC–HRMS as a superior alternative to immunoassays for urinary free cortisol analysis has been highlighted by G. Casals et al. [7]. By exploiting the high specificity of liquid chromatography coupled with high-resolution accurate mass detection, the validated method enables the simultaneous and reliable quantification of cortisol, cortisone, 6β-hydroxycortisol, and 18-hydroxycortisol, while also allowing for untargeted

https://doi.org/10.3390/molecules31030481

compound identification. This LC–HRMS approach overcomes the major limitations of immunoassays caused by metabolite cross-reactivity, providing a more accurate and comprehensive tool for the diagnosis and follow-up of hypercortisolism and disorders of adrenal steroid metabolism. The research group of Y. Mechref showcases the power of advanced LC–MS/MS glycoproteomics to unravel variant-specific *O*-glycosylation patterns of the SARS-CoV-2 spike S1 protein [8]. By combining a double-digestion strategy with a highly sensitive LC-MS/MS workflow, the authors achieved in-depth and site-specific characterization of *O*-glycans across eleven viral variants. The approach reveals both conserved and variant-dependent glycosylation features, highlighting the exceptional O-glycosylation density and sialylation of the Omicron variant, and provides critical molecular insight into how glycan remodelling may influence immune evasion, infectivity, and vaccine design. The unique ability of advanced nano-LC-PRM/HRMS to decipher the secretion mechanisms and redox states of immunomodulatory high mobility group box 1 (HMGB)1 in response to anticancer drugs has been proven [9]. By combining immunoprecipitation, stable isotope dilution, and differential alkylation with high-resolution mass spectrometry, the authors achieved sensitive and selective quantification of HMGB1 and its post-translational modifications. The LC-MS-based approach revealed that cisplatin, unlike carboplatin, induces HMGB1 secretion through an XPO1-dependent pathway and predominantly releases the fully reduced, immunologically active form of the protein. These findings demonstrate how high-resolution targeted mass spectrometry can uncover drug-specific molecular mechanisms with direct implications for tumour biology, immune modulation, and the optimization of combined chemo-immunotherapy strategies. The combination of HPLC and LC-HRMS provides a powerful platform to assess the stability and structural integrity of mitochondrial-derived peptides such as Humanin-G [10]. By using LC-HRMS, the authors achieved precise identification and characterization of HNG degradation products, including site-specific oxidation and dimerization species, which cannot be resolved by conventional analytical techniques alone. The work highlights the essential role of high-resolution LC–MS in monitoring peptide stability, elucidating degradation pathways, and guiding optimal formulation and storage conditions for biologically active therapeutic peptides.

The *Journal of Clinical Medicine*, dedicated to clinical and preclinical research, accepted three submitted studies related to the scope and aims of the journal. Meinarovich et al. propose a multimodal risk assessment algorithm for post-cardiac surgery complications, combining clinical data with metabolomic profiles and sepsis-related biomarkers and using gas chromatography coupled with a single quadrupole mass analyser (ISQ, Thermo Electron Corporation, Santa Clara, CA, USA) for microbiome metabolite quantification in patients' blood [11]. The second study by Kośliński et al. reveal the significant differences in amino acids metabolic profiles in serum between patients with multiple sclerosis and myasthenia gravis and healthy controls, thus forming the groundwork for the development of a clinical assay for the differential diagnosis of these autoimmune neurological diseases [12]. The target amino acids were quantified by liquid chromatography coupled with a triple quadrupole mass spectrometer LCMS-8045 (Shimadzu, Kyoto, Japan). Amino acids homeostasis was also investigated by Posma et al. in patient with metformin intoxication to clarify the biochemical basis of intoxication [13]. In this study, the amino acids and other metabolites were quantified in plasma, urine, and dialysate samples by gas chromatography coupled to a single quadrupole ISQ mass analyser (ThermoFisher, Dreieich, Germany).

Two studies were published in the *International Journal of Molecular Sciences*, which provides a forum for research in molecular medicine, molecular and cellular biology, and biochemistry. The biochemical pathways involved in hepatic encephalopathy (HE), a

https://doi.org/10.3390/molecules31030481

central nervous dysfunction syndrome, were investigated on animal models (mice) by Guo et al. using combined metabolomic and proteomic profiling in serum samples [14]. High-resolution hybrid Orbitrap mass analysers (Q Exactive™ HF and Q Exactive™ HF-X, Thermo Fisher Scientific, Waltham, MA, United States) with UHPLC liquid chromatography systems were used in this study for the quantification of 50 metabolites and 226 proteins. The acquired analytical data enabled the identification of altered metabolic pathways in HE. The study underscores the capacity of multi-omics approaches to reveal the complex biochemical mechanisms that drive disease pathophysiology, as well as their potential in disease biomarkers discovery. The second study, by Ahn et al., focuses on optimizing sample pre-treatment for the subsequent headspace GC-MS quantification of volatile organic compounds (VOCs) in whole canine blood [15]. With the overarching aim of minimizing matrix effects and enhancing analytical sensitivity, the authors developed an optimized protocol that improves VOC recovery and measurement reliability. The analytical setup employed in this study consisted of a Trace 1610 gas chromatograph coupled with an ISQ 7610 single-quadrupole mass spectrometer and a TriPlus 500 headspace autosampler (Thermo Fisher Scientific, Waltham, MA, USA).

The journal *Separations* accepted two publications dedicated to development of new approaches for the analysis of biologically important compounds and metabolites in biological fluids. In the study of Hefni et al., the UPLC-MS/MS method was developed for the simultaneous quantification of nutritional quaternary ammonium compounds (betaine, L-carnitine, acetyl-L-carnitine, and propionyl-L-carnitine) and their downstream metabolites (trimethylamine, trimethylamine-N-oxide) in plasma [16]. The terminal metabolite of this pathway, trimethylamine-N-oxide, is associated with various chronic diseases that mainly are consequences of metabolic syndrome. The developed assay is intended to have clinical value in the monitoring of this pathway in patients with metabolic syndrome. The study by Kim et al. presents a new LC-MS/MS method for the indirect, after-dephosphorylation quantification of signalling lipid sphingosine-1-phosphate (S1P) in plasma and kidney tissues obtained from a chronic kidney disease (CKD) mouse model [17]. The liquid chromatography-AB Sciex QTRAP 3200 mass spectrometer (SCIEX, Toronto, Canada) was used for analyte quantification.

In conclusion, we would like to underline that the papers presented above originate from different scientific domains, but they are unified by their common use of the chromatography–mass spectrometry (CMS) platform. Grouping them within a single thematic topic highlights the multifaceted potential of CMS and demonstrates its broad applicability across both biomedical research and clinical practice. Additionally, presenting them as a unified topic allows the readership of each contributing journal to gain exposure to related studies published in the other journals represented in this collection, thereby enhancing cross-disciplinary visibility.

We wish to sincerely thank all the authors for their outstanding contributions to this topical issue. Their high-quality studies demonstrate the depth and continuous innovation of CMS applications in biomedical and clinical research, ranging from therapeutic drug monitoring and biomarker discovery to proteomics, lipidomics, steroid analysis, and glycoproteomics. Through the development and validation of robust LC/GC–MS- and HRMS-based methodologies, the authors have highlighted the essential role of advanced analytical platforms in improving diagnostic accuracy, understanding disease mechanisms, and supporting precision medicine. Their collective efforts not only advance the state of the art in analytical and clinical mass spectrometry but also provide valuable reference frameworks for future research and clinical implementation.

Data Availability Statement: No new data were created or analyzed in this study. Data sharing is not applicable to this article.

https://doi.org/10.3390/molecules31030481

Conflicts of Interest: The authors declare no conflict of interest.

References

1. Błażewicz, A.; Kiełbus, M.; Skórzyńska-Dziduszko, K.; Grabrucker, A.M.; Jonklaas, J.; Sosnowski, P.; Trzpil, A.; Kozub-Pędrak, A.; Szmagara, A.; Wojnicka, J.; et al. Application of Human Plasma Targeted Lipidomics and Analysis of Toxic Elements to Capture the Metabolic Complexities of Hypothyroidism. *Molecules* **2024**, *29*, 5169. [CrossRef] [PubMed]
2. Molteni, L.; Charlier, B.; Izzo, V.; Coglianese, A.; Conti, V.; Eleopra, R.; Cilia, R.; Capelli, C.; D'Urso, A.; de Grazia, U. Development and Validation of a New LC-MS/MS Bioanalytical Method for the Simultaneous Determination of Levodopa, Levodopa Methyl Ester, and Carbidopa in Human Plasma Samples. *Molecules* **2023**, *28*, 4264. [CrossRef] [PubMed]
3. Molteni, L.; Charlier, B.; Coglianese, A.; Izzo, V.; Assenza, G.; Menna, P.; de Grazia, U.; D'Urso, A. Quantitative Analysis of Cenobamate and Concomitant Anti-Seizure Medications in Human Plasma via Ultra-High Performance Liquid Chromatography–Tandem Mass Spectrometry. *Molecules* **2024**, *29*, 884. [CrossRef] [PubMed]
4. Wei, D.; Horton, K.L.; Chen, J.; Dong, L.; Chen, S.; Abdul-Hadi, K.; Zhang, T.T.; Casson, C.N.; Shaw, M.; Shiraishi, T.; et al. Development of a Highly Sensitive Hybrid LC/MS Assay for the Quantitative Measurement of CTLA-4 in Human T Cells. *Molecules* **2023**, *28*, 3311. [CrossRef] [PubMed]
5. Taya, Y.; Mizunaga, M.; Nakao, S.; Jutanom, M.; Shimizu, N.; Nomura, Y.; Nakagawa, K. Clinical Evaluation Based on a New Approach to Improve the Accuracy of 4β-Hydroxycholesterol Measurement as a Biomarker of CYP3A4 Activity. *Molecules* **2023**, *28*, 1576. [CrossRef] [PubMed]
6. Tsakalof, A.; Sysoev, A.A.; Vyatkina, K.V.; Eganov, A.A.; Eroshchenko, N.N.; Kiryushin, A.N.; Adamov, A.Y.; Danilova, E.Y.; Nosyrev, A.E. Current Role and Potential of Triple Quadrupole Mass Spectrometry in Biomedical Research and Clinical Applications. *Molecules* **2024**, *29*, 5808. [CrossRef] [PubMed]
7. Casals, G.; Ballesteros, M.A.; Zamora, A.; Martínez, I.; Fernández-Varo, G.; Mora, M.; Hanzu, F.A.; Morales-Ruiz, M. LC-HRMS and GC-MS Profiling of Urine Free Cortisol, Cortisone, 6B-, and 18-Hydroxycortisol for the Evaluation of Glucocorticoid and Mineralocorticoid Disorders. *Biomolecules* **2024**, *14*, 558. [CrossRef]
8. Onigbinde, S.; Reyes, C.D.G.; Fowowe, M.; Daramola, O.; Atashi, M.; Bennett, A.I.; Mechref, Y. Variations in O-Glycosylation Patterns Influence Viral Pathogenicity, Infectivity, and Transmissibility in SARS-CoV-2 Variants. *Biomolecules* **2023**, *13*, 1467. [CrossRef] [PubMed]
9. Gillespie, K.P.; Pirnie, R.; Mesaros, C.; Blair, I.A. Cisplatin Dependent Secretion of Immunomodulatory High Mobility Group Box 1 (HMGB1) Protein from Lung Cancer Cells. *Biomolecules* **2023**, *13*, 1335. [CrossRef]
10. Ozgul, M.; Nesburn, A.B.; Nasralla, N.; Katz, B.; Taylan, E.; Kuppermann, B.D.; Kenney, M.C. Stability Determination of Intact Humanin-G with Characterizations of Oxidation and Dimerization Patterns. *Biomolecules* **2023**, *13*, 515. [CrossRef] [PubMed]
11. Meinarovich, P.; Pautova, A.; Zuev, E.; Sorokina, E.; Chernevskaya, E.; Beloborodova, N. An Integrated Approach Based on Clinical Data Combined with Metabolites and Biomarkers for the Assessment of Post-Operative Complications after Cardiac Surgery. *J. Clin. Med.* **2024**, *13*, 5054. [CrossRef] [PubMed]
12. Kośliński, P.; Rzepiński, Ł.; Koba, M.; Maciejek, Z.; Kowalewski, M.; Daghir-Wojtkowiak, E. Comparative Analysis of Serum Amino Acid Profiles in Patients with Myasthenia Gravis and Multiple Sclerosis. *J. Clin. Med.* **2024**, *13*, 4083. [CrossRef] [PubMed]
13. Posma, R.A.; Bakker, S.J.L.; Nijsten, M.W.; Touw, D.J.; Tsikas, D. Comprehensive GC-MS Measurement of Amino Acids, Metabolites, and Malondialdehyde in Metformin-Associated Lactic Acidosis at Admission and during Renal Replacement Treatment. *J. Clin. Med.* **2024**, *13*, 3692. [CrossRef] [PubMed]
14. Guo, H.; Wang, G.; Huang, W.; Li, L.; Bai, Y.; Wang, H.; Gao, L. The Mechanism of Hepatic Encephalopathy Induced by Thioacetamide Based on Metabolomics and Proteomics: A Preliminary Study. *Int. J. Mol. Sci.* **2024**, *25*, 284. [CrossRef] [PubMed]
15. Ahn, K.G.; Choi, R.; Gwak, S.; Choi, I.; Jang, G.; Kim, J.W.; Kim, G.A. A Novel Sample Preparation Method for GC-MS Analysis of Volatile Organic Compounds in Whole Blood for Veterinary Use. *Int. J. Mol. Sci.* **2025**, *26*, 4667. [CrossRef] [PubMed]
16. Hefni, M.E.; Witthöft, C.M. Development and Application of a UPLC–MRM–MS Method for Quantifying Trimethylamine, Trimethylamine-N-Oxide, and Related Metabolites in Individuals with and Without Metabolic Syndrome. *Separations* **2025**, *12*, 53. [CrossRef]
17. Kim, H.-J.; Jung, S.-H.; Gulyamov, S.; Lee, H.-G.; Boyjigitov, O.; Lee, Y.-M. HPLC-MS/MS Analysis for Sphingosine 1-Phosphate after the Dephosphorylation by Hydrogen Fluoride. *Separations* **2024**, *11*, 34. [CrossRef]

Disclaimer/Publisher's Note: The statements, opinions and data contained in all publications are solely those of the individual author(s) and contributor(s) and not of MDPI and/or the editor(s). MDPI and/or the editor(s) disclaim responsibility for any injury to people or property resulting from any ideas, methods, instructions or products referred to in the content.

https://doi.org/10.3390/molecules31030481

International Journal of
Molecular Sciences

MDPI

Communication

A Novel Sample Preparation Method for GC-MS Analysis of Volatile Organic Compounds in Whole Blood for Veterinary Use

Kyung-Geun Ahn [1,2], Ryuho Choi [2], Soonchul Gwak [2], Inyoung Choi [2], Giup Jang [2], Jin-Wook Kim [2,*] and Geon A Kim [1,*]

[1] Department of Biomedical Laboratory Science, University of Health Science, Eulji University, Uijeongbu 11759, Republic of Korea; akg@metadxlab.com
[2] Center for Veterinary Bioinformatics Research and Development, MetaDx Inc., Seoul 04799, Republic of Korea; ryuho@metadxlab.com (R.C.); gsc@metadxlab.com (S.G.); inyoungvet@hanmail.net (I.C.); cto@metadxlab.com (G.J.)
* Correspondence: chris@metadxlab.com (J.-W.K.); 20201034@eulji.ac.kr (G.A.K.)

Abstract: Volatile organic compounds (VOCs) in biological samples originate both from exogenous and endogenous sources. Recent studies have highlighted their potential as cancer biomarkers, emphasizing the need for accurate detection methods in clinical settings. However, analysis of VOCs in whole blood (WB) samples remains challenging due to the complex matrix effects caused by the protein−VOC binding phenomenon and lack of standardized sample preparation protocols. Therefore, this study suggests a standardized method for advanced VOC analysis in WB samples specifically for veterinary applications. We compared 12 combinations of reagents composed of protein denaturing reagents and salts, particularly urea mixtures, to enhance VOC decoupling from proteins and improve matrix effect uniformity in gas chromatography−mass spectrometry (GC-MS) analysis. Among all combinations, urea with NaCl showed an optimal performance, demonstrating an advancement in the detection sensitivity of up to 151.3% and a significantly reduced matrix effect variation (−35.5% to 25%) compared with the water-only control. This novel approach eliminates complex procedures while maintaining accuracy, making it particularly suitable for veterinary uses. The method's standardization and improved performance characteristics offer a practical solution for efficient VOC detection in veterinary diagnostics, potentially advancing tumor biomarker research.

Keywords: veterinary cancer; sample preparation; VOCs; mass spectrometry; dog

1. Introduction

Volatile organic compounds (VOCs) are environmental pollutants originating from various industries, vehicle emissions, and other anthropogenic sources [1,2]. Recently, specific VOCs have been identified as potential cancer biomarkers due to their association with altered cancer metabolism, emphasizing the need for accurate detection methods for novel diagnostic solutions. Some studies have suggested multiple VOC biomarkers from breath samples for detecting colorectal cancer [3] and from urine samples for detecting prostate cancer [4,5]. However, in veterinary medicine, these biological samples are difficult to use for quantitative analysis due to the sample quality [6]. Therefore, studies have been conducted to find biomarkers from blood samples for cancer diagnosis in dogs, yet the analysis of VOCs in blood samples remains challenging due to complex matrix effects [7,8].

The matrix effect (ME) refers to the phenomenon in which the sensitivity of an analysis is either increased or decreased due to the matrix contained within the sample [9,10].

To enhance analytical reliability, these MEs are generally corrected or eliminated during the instrumental analysis stage using methods such as standard addition (SA) or matrix matched calibration (MMC) [11,12]. However, as blood exhibits significant variations in concentration and composition among individual samples, the corresponding ME also varies greatly, making it impractical to apply MMC to a representative sample. In other words, to correct for the differing ME in each sample, SA or MMC must be applied to every individual specimen—a process that is extremely cumbersome. Moreover, in cases where the suppression of sensitivity is severe, even correction via SA or MMC may result in analytes being evaluated as undetectable, thereby necessitating the development of approaches to reduce the ME itself during either the pre-treatment or analytical stages.

To minimize ME in blood samples, we selected headspace−gas chromatography−mass spectrometry (HS-GC/MS) as the analytical instrument. This technique analyzes components that have been transferred into the gas phase by heating the sample in a sealed vial [13]. Based on the analytical principle of HS-GC/MS, it was expected that ME would be extremely low during the analysis of VOCs; however, analyses using blood or biological samples still have to confirm the presence of ME [14]. Noting that the target analytes are VOCs and that the sample is blood, we hypothesized that the ME observed during HS-GC/MS analysis of blood is due to VOCs being captured by the abundant proteins in blood through specific interactions.

A study demonstrated that benzene binds stably to hemoglobin (Hb)'s heme pocket, significantly reducing the oxygen binding capacity even at high temperatures (70–80 °C) [15]. In addition, protein aromatic residues and cationic sites have been shown to form strong π−π interactions [16] and cation−π interactions [17]. Also, the influence of ionic strength on aromatic compound solubility suggests that protein−VOC interactions can be modulated by chemical conditions [18]. These studies collectively indicate that VOCs can form specific, stable interactions with blood proteins, which can be disrupted by altering the biochemical conditions, thus providing a theoretical framework for developing improved analytical methods for VOC detection in blood samples.

Generally, when VOC analysis in an aqueous solution is challenging, salts like NaCl are added during the preparation step to decrease the VOC solubility and increase the sensitivity [19,20]. However, to our knowledge, in cases of body fluid samples (serum, plasma, urine, and whole blood), there have been no studies that induce protein denaturation using chemicals to facilitate the release of protein-bound VOCs. Therefore, in this study, we propose a unique method during the sample pretreatment stage that not only enhances sensitivity, but also minimizes the highly variable matrix effects across different matrices, all while being simple, rapid, and highly reproducible.

2. Results

2.1. Sensitivity Comparison Across Sample Preparation Reagent Combinations

The sensitivity alteration effects among each combination were evaluated by comparing the relative responses to a control containing no additives (Formula (1)). Protein denaturing reagents, urea(U) and SDS(S), were used as additives, while NaCl(NC), K_2SO_4(KS), and Na_2SO_4(NS) were employed as salts. The specific combinations of protein denaturing reagents (PDR; urea and SDS) and salts that were tested are summarized in Table 1.

Table 1. Combination of PDRs and salts used in this study.

Combination(s)	PDR	Salt
Cont.	H_2O	H_2O
Comb 1	Urea	NaCl
Comb 2	Urea	K_2SO_4
Comb 3	Urea	Na_2SO_4
Comb 4	SDS	NaCl
Comb 5	SDS	K_2SO_4
Comb 6	SDS	Na_2SO_4
Comb 7	H_2O	NaCl
Comb 8	H_2O	K_2SO_4
Comb 9	H_2O	Na_2SO_4
Comb 10	Urea	H_2O
Comb 11	SDS	H_2O

Among all of the components, Comb 1(U+NC), 7(NC), and 9(NS) exhibited the most outstanding sensitivity enhancement effect (Table 2). In the case of Comb 7(NC), which showed the most pronounced sensitivity improvement, the enhancement relative to the control group ranged from 196.8% for ethylbenzene to 241.2% for styrene. For Comb 1(U+NC), the sensitivity enhancement for all components ranged from 136.8% to 151.3%, and for Comb 9(NS), it ranged from 126.4% to 169.9%. When comparing Comb 1(U+NC) and 9(NS), benzene, toluene, and styrene in Comb 9(NS) showed sensitivity values of 169.9%, 155.2%, and 154.5%, respectively, which were higher or similar to the values of 143.4%, 147.3%, and 151.3% observed in Comb 1(U+NC). Conversely, in Comb 1(U+NC), ethylbenzene, m-/p-xylene, and o-xylene exhibited sensitivity values of 136.8%, 140.1%, and 147.1%, respectively, which were higher or similar to the 126.4%, 128.7%, and 145.5% observed in Comb 9(NS). Additionally, when evaluating reproducibility through the coefficient of variation(CV) for each combination, Comb 7(NC) showed a distribution ranging from 5.2% to 6.6% for all components, whereas combinations 1(U+NC) and 9(NS) demonstrated superior reproducibility with distributions ranging from 0.8% to 1.1% and 0.5% to 1.0%, respectively.

Table 2. The sensitivity comparison results across the 12 combinations.

Combination	Benzene		Toluene		Ethylbenzene		m-/p-Xylene		o-Xylene		Styrene	
	Mean [(1)]	CV [(2)]	Mean	CV	Mean	CV	Mean	CV	Mean	CV	Mean	CV
Cont.	100.0	3.4	100.0	3.8	100.0	4.1	100.0	4.1	100.0	4.0	100.0	3.7
Comb 1(U+NC)	**143.4**	**0.8**	**147.3**	**1.0**	**136.8**	**1.0**	**140.1**	**1.1**	**147.1**	**0.9**	**151.3**	**1.0**
Comb 2(U+KS)	97.3	1.0	102.8	0.9	103.8	1.4	105.3	1.3	104.2	1.3	105.4	1.0
Comb 3(U+NS)	137.5	2.2	140.8	1.3	116.5	0.8	117.1	1.1	130.9	0.8	150.5	0.6
Comb 4(S+NC)	138.3	6.4	115.5	8.3	72.9	8.8	69.9	8.7	79.2	7.8	82.4	6.8
Comb 5(S+KS)	130.2	3.9	123.3	2.3	102.3	2.3	99.7	2.5	101.3	2.8	119.0	2.6
Comb 6(S+NS)	207.1	10.1	148.2	7.3	90.0	10.2	86.8	10.8	101.0	9.1	111.2	10.9
Comb 7(NC)	**222.3**	**5.3**	**235.9**	**6.0**	**196.8**	**6.2**	**197.3**	**6.6**	**215.0**	**6.2**	**241.2**	**5.2**
Comb 8(KS)	126.6	2.0	124.5	1.7	122.9	1.9	123.4	2.0	126.4	1.7	119.8	4.6
Comb 9(NS)	**169.9**	**0.8**	**155.2**	**1.0**	**126.4**	**0.6**	**128.7**	**0.8**	**145.5**	**1.0**	**154.5**	**0.5**
Comb 10(U)	82.2	2.3	84.5	2.8	85.3	3.0	86.1	2.9	84.0	3.2	89.6	2.9
Comb 11(S)	93.6	9.1	94.9	11.0	85.6	11.0	84.4	10.7	84.5	10.8	53.0	12.8

[(1)] Mean(%) of triplicate measurements. [(2)] Coefficient of variation (%).

2.2. Sensitivity Alterations According to Sample Volume

The stability of the analytical performance across different sample volumes was assessed by comparing the variability in sensitivity between 0.5 mL and 1.5 mL blood samples, both spiked with 100 ng/mL of the analyte (Formula (2)). This comparison aimed to evaluate the consistency of sensitivity across samples with different matrix levels but identical analyte concentrations (Table 3). Consequently, among the initially selected combinations 1(U+NC), 7(NC), and 9(NS) based on sensitivity comparisons, Comb 9(NS) exhibited high variability exceeding 40% for ethylbenzene (42.8%), m,p-xylene (44.0%), o-xylene (42.9%), and styrene (50.9%). In addition, it showed high standard deviation (SD) values ranging from 16.3 to 21.1 across all components, indicating the lowest reproducibility; hence, Comb 9(NS) was excluded from the list of optimal condition candidates. Conversely, although Comb 2 (U+KS, 10.3–26.5%), 5 (S+KS, 6.3–23.9%), and 10 (U, 4.9–29.2%) exhibited relatively low variability, they were not considered optimal candidates due to their minimal sensitivity enhancement effects compared to the control group.

Table 3. Comparison of sensitivity variations across sample volumes for 12 combinations.

Combination	Mean (%) ± SD [1]					
	Benzene	**Toluene**	**Ethylbenzene**	**m,p-Xylene**	**o-Xylene**	**Styrene**
Cont.	12.8 ± 0.7	19.5 ± 0.9	22.8 ± 0.5	23.2 ± 0.5	23.3 ± 0.6	35.0 ± 0.3
Comb 1(U+NC)	**16.7 ± 2.2**	**15.6 ± 3.0**	**26.6 ± 2.7**	**28.2 ± 2.6**	**28.5 ± 2.8**	**31.7 ± 1.8**
Comb 2(U+KS)	10.3 ± 0.9	26.5 ± 0.9	14.6 ± 1.0	15.9 ± 0.8	16.6 ± 0.4	24.6 ± 1.6
Comb 3(U+NS)	16.6 ± 5.2	4.3 ± 7.0	43.5 ± 4.7	45.5 ± 4.7	47.7 ± 4.8	44.9 ± 4.7
Comb 4(S+NC)	31.8 ± 6.3	8.4 ± 7.4	39.9 ± 2.8	39.6 ± 2.8	41.3 ± 3.1	39.1 ± 3.9
Comb 5(S+KS)	6.3 ± 1.1	31.2 ± 7.6	13.3 ± 5.0	13.9 ± 5.3	14.4 ± 5.3	23.9 ± 3.8
Comb 6(S+NS)	39.1 ± 3.0	28.1 ± 3.8	48.7 ± 2.3	49.1 ± 2.1	51.2 ± 3.1	47.1 ± 3.0
Comb 7(NC)	**19.2 ± 0.8**	**2.7 ± 2.3**	**30.8 ± 1.0**	**31.5 ± 1.0**	**32.6 ± 0.8**	**35.5 ± 1.8**
Comb 8(KS)	18.9 ± 6.7	14.2 ± 4.9	26.2 ± 4.3	27.1 ± 4.4	27.3 ± 3.6	37.8 ± 1.7
Comb 9(NS)	25.4 ± 16.5	17.9 ± 16.3	42.8 ± 20.6	44.0 ± 21.1	42.9 ± 19.1	50.9 ± 18.5
Comb 10(U)	4.9 ± 0.3	34.5 ± 0.7	8.2 ± 0.4	9.4 ± 0.3	10.4 ± 0.2	29.2 ± 0.4
Comb 11(S)	12.8 ± 7.3	54.7 ± 6.0	3.5 ± 1.1	3.9 ± 1.5	4.7 ± 3.1	42.0 ± 5.6

[1] Standard deviation of triplicate measurements.

2.3. Comparison of Matrix Effect Uniformity Across Combinations

After confirming the sensitivity advancement and variation, we examined the uniformity of matrix effects according to Comb 1(U+NC) and 7(NC). We aimed to experimentally implement various matrices by using different sample volumes and verified the degree of matrix effects when applying and analyzing each combination across various matrices. Matrix effects were evaluated by measuring the sensitivity changes in samples, calculated by dividing the area values from samples with different blood weights by the area values from samples using water instead of blood (Formula (3)).

First, when analyzing 63 blood samples obtained from Naeun Animal Hospital using 1 mL of blood without urea, fluorobenzene's matrix effects showed a wide distribution ranging from −81.6% to 44% (Figure 1a). Next, the matrix effects were examined for samples of 0.5 mL and 1.5 mL in Comb 1(U+NC) and 7(NC). In Comb 1(U+NC), suppression was observed at 25.7% and 36.8%, respectively, while Comb 7(NC) showed suppression values of 24.4% and 39.3%. Both combinations demonstrated an improved, narrower range of matrix effects compared to the condition without reagent application. Notably, Comb 1(U+NC) exhibited an 11.1% difference between the matrix effects of 0.5 mL and 1.5 mL samples, which is less pronounced than the 14.9% difference observed in Comb 7(NC).

Additionally, the variability in repeated analyses across different sample volumes was extremely low for Comb 1(U+NC), experimentally confirming that it allows for a more stable analysis under various matrix conditions (Figure 2).

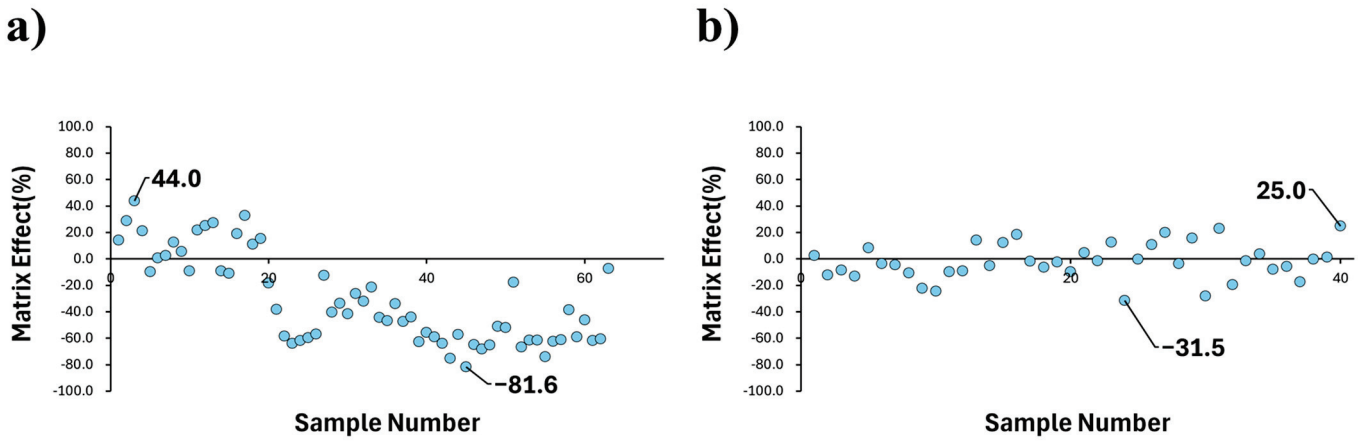


Figure 1. Distribution of fluorobenzene matrix effects with or without the application of Comb 1(U+NC). Matrix effects range from −31.5% to 25%, indicating enhanced uniformity and reduced variability (**b**) compared to the control (**a**).

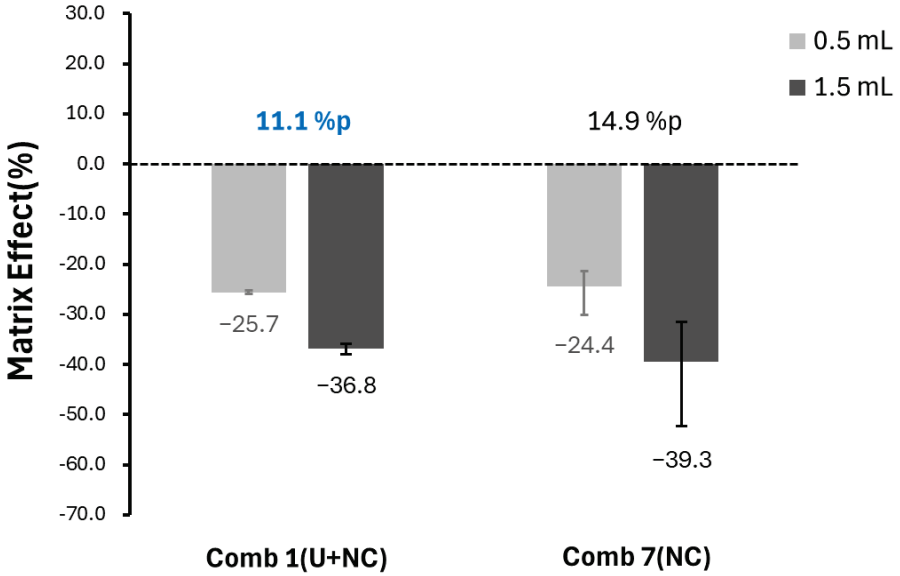


Figure 2. Variance in matrix effects depending on the sample volume according to the combinations.

Subsequently, urea and NaCl from Comb 1—chosen for its minimal matrix effect along with its sensitivity enhancement benefit—were applied to 1 mL samples of various blood matrices. These samples were then analyzed by HS-GC-MS to evaluate the level of matrix effect variability. When analyzing 40 samples, the matrix effects showed a distribution from −31.5% to 25% confirming reduced matrix effects compared to the control (Figure 1b). In short, cases with urea mixtures showed matrix effects more uniformly compared to cases without urea.

3. Discussion

Our study demonstrates that protein denaturation combined with salt addition significantly improves the sensitivity and reproducibility of VOC detection in canine blood samples. The wide distribution of matrix effects (−81.6% to 44%) observed in untreated blood samples indicates strong protein−VOC interactions, consistent with previous studies showing stable binding of benzene to the heme pocket [9]. The dramatic reduction in

matrix effect variation (−31.5% to 25%) achieved with Comb 1(U+NC) suggests partial disruption of these protein−VOC interactions through the combined action of urea and NaCl. The optimal performance of Comb 1(U+NC) can be attributed to two complementary mechanisms. First, urea's protein denaturing effect likely disrupts the structural integrity of blood proteins, particularly hemoglobin, releasing trapped VOCs. Second, the addition of NaCl creates a salting-out effect, reducing VOC solubility in the aqueous phase and enhancing their partitioning into the headspace. This dual mechanism not only improves sensitivity, but also provides consistent results across varying sample volumes, a crucial feature for clinical diagnostic applications in veterinary medicine.

While our study demonstrates the significance of protein−VOC interactions in blood analysis, several important aspects remain to be investigated. Although we observed clear effects of protein denaturation on VOC detection, the quantitative relationship between the protein concentration and internal standard response has not been established. Future studies should investigate this correlation to better understand the impact of protein levels on VOC analysis. Additionally, while our focus was on protein interactions, other biomolecules such as DNA and lipids are known to interact with aromatic compounds through various mechanisms. Further research examining the relationships between different biomolecule concentrations and VOC detection would provide a more comprehensive understanding of matrix effects in biological samples.

Nevertheless, the enhanced sensitivity and improved matrix effect uniformity achieved with Comb 1(U+NC) address key challenges in blood VOC analysis. The method's stability across different sample volumes makes it particularly suitable for veterinary medicine where sample quantities may be limited or varied. Furthermore, the simplified sample preparation procedure, requiring only the addition of urea and NaCl, makes this method both practical and easily implementable in routine laboratory analysis.

4. Materials and Methods

4.1. Standards and Chemicals

All standard reference materials including benzene, toluene, ethylbenzene, m-/p-xylene, o-xylene, styrene, and fluorobenzene were purchased from Accustandard (New Haven, CT, USA). Stock solutions dissolved in methanol were stored at −20 °C and diluted with methanol as needed. Methanol and HPLC-grade deionized water used for standard dilution were purchased from J.T. Baker (Avantor, Radnor, PA, USA). Urea and SDS (sodium dodecyl sulfate), used to induce protein denaturation, were obtained from JUNSEI (Kosigaya, Saitama, Japan) and Daejung Chemicals (Siheung, Gyeonggi, Republic of Korea), respectively. Among the salts added to facilitate VOC release from blood, NaCl was purchased from Daejung Chemicals (Siheung, Gyeonggi, Republic of Korea), while Na_2SO_4 and K_2SO_4 were obtained from Junsei (Kosigaya, Saitama, Japan).

4.2. Sample Collection

Here, 350 mL canine whole blood packs preserved in a CPDA (citrate−phosphate−dextrose−adenine) bag were purchased from Korea Animal Blood Bank (Goseong, Gangwon, Republic of Korea) and 103 samples were provided by Naeun Animal Hospital located in Euijeongbu, Gyeonggi, Repubilc of Korea, with consent from the owners for research uses. Citric acid or EDTA (ethylene−diamine−tetra acetic acid) were supplemented as anti-coagulants and the samples were preserved at 4 °C until use.

4.3. Sample Preparation

PDR along with salts that increase the release intensity of VOCs from samples, as well as water, were added in multiple combinations to a 20 mL headspace (H/S) vial containing

the blood sample. For samples treated solely with NaCl, K_2SO_4, or Na_2SO_4 without PDR, 12 mL of their respective saturated solutions were added. For samples containing urea and SDS, 12 mL of NaCl, K_2SO_4, or Na_2SO_4 saturated solutions formulated to contain 2.5 M urea and 0.5% SDS, respectively, were added to each sample. The addition of salts induced a salt-out effect, reducing VOC solubility in the aqueous phase and thereby enhancing analytical sensitivity. PDR was formulated by selecting urea and SDS—agents commonly added during protein fragmentation to denature the tertiary structure [21]. These reagents were incorporated to further release VOCs that interact with (or are bound to) proteins in blood, in addition to the free VOCs, through protein denaturation. By transferring VOCs from the aqueous sample phase to the headspace gas in the vial for analysis, the advantages of HS-GC/MS—which eliminates the need for additional processes such as filtration or centrifugation—were fully maximized. This approach greatly simplifies the pretreatment process for practical, routine analyses by merely mixing the blood samples with the reagents.

4.4. Gas Chromatography-Mass Spectrometry Analysis

VOCs in canine blood were analyzed using a HS-GC/MS (system equipped with a TriPlus 500 (headspace autosampler) and ISQ 7610 (single quadrupole mass spectrometry) from Thermo Fisher Scientific (Waltham, MA, USA). Sample analysis was performed using 20 mL amber screw cap vials (Thermo Fisher Scientific, Waltham, MA, USA), and the separation of target compounds was achieved using a TG-624SilMS capillary column (30 m, 0.32 mm I.D., 1.8 μm film thickness). The detailed specifications of HS-GC/MS are summarized in Table S1.

4.5. Selection of Quantification and Qualification Ions for GC-MS Analysis

Quantification ions were selected from fragment ions showing the highest sensitivity in MS spectra obtained by analyzing standard solutions in positive scan mode. Qualification ions were chosen from ions that showed sufficient sensitivity for compound confirmation and ion ratio verification without interference from other compounds. These ions were analyzed in SIM (selected ion monitoring) mode for quantification, and the detailed mass to charge (m/z) values are presented in Table 4.

Table 4. The retention time and targeted ions analyzed in this study.

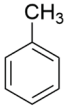
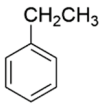
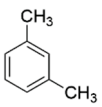
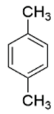
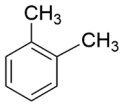
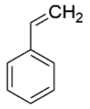
Compound	Structure	Molecular Formula	Molecular Weight	Retention Times	Quantification Ion (m/z)	Qualification Ion (m/z)
Benzene		C_6H_6	78.11	4.78	78	77
Toluene		$C_5H_5CH_3$	92.14	8.08	91	92
Ethylbenzene		$C_6H_5CH_2CH_3$	106.17	10.48	91	106
m-xylene		$C_6H_4(CH_3)_2$	106.16	10.68	106	105

Table 4. *Cont.*

Compound	Structure	Molecular Formula	Molecular Weight	Retention Times	Quantification Ion (*m*/*z*)	Qualification Ion (*m*/*z*)
p-xylene		$C_6H_4(CH_3)_2$	106.16	10.68	106	105
o-xylene		$C_6H_4(CH_3)_2$	106.16	11.16	91	106
Styrene		$C_6H_5CH{=}CH_2$	104.15	11.24	104	78
Fluorobenzene		C_6H_5F	96.10	5.47	96	70

4.6. GC-MS Analysis

The prepared samples were heated at 99 °C for 40 min in the instrument's incubator, after which 1 mL of each headspace gas was injected into the GC-MS. For the separation of VOCs loaded onto the capillary column, the column oven temperature was held at 50 °C for 5 min, then increased to 100 °C at a rate of 10 °C per min and further raised to 120 °C at a rate of 20 °C per min. Subsequently, the temperature was increased from 120 °C to 260 °C at a rate of 30 °C per min and held for 4.33 min, resulting in a total temperature program time of 20 min. Peak integration and quantification of the analyzed data were performed using Trace Finder 5.1 software (Thermo Fisher Scientific, Walthan, MA, USA).

4.7. Comparison of Sensitivity and Matrix Effects Among Combinations

Samples purchased from the Korean Animal Blood Bank were analyzed using 0.5 mL for each combination summarized in Table 1 to compare their relative sensitivities. The sensitivity comparison for each combination was performed as a ratio relative to control, which contained no salt or reagent (Formula (1)). Additionally, to indirectly evaluate whether similar sensitivities could be achieved across samples with various matrices, sensitivity changes were measured using blood sample volumes of 0.5 mL and 1.5 mL for each combination in Table 3, with standard solutions added at the same concentration of 100 ng/mL (Formula (2)). Subsequently, after comprehensively reviewing the sensitivity, reproducibility, and sensitivity variations according to sample volume, the two best reagent combinations were selected. The matrix effect was then evaluated by comparing samples without blood to those containing 0.5 mL and 1.5 mL of blood, using fluorobenzene—a commonly used internal standard (Formula (3)). Finally, for the optimal combination, matrix effects on fluorobenzene were assessed using 1 mL of actual samples received from Naeun Animal Hospital.

$$\text{Recovery}(\%) = \frac{\text{Each Combination}}{\text{Control}} \times 100 \quad (1)$$

$$\text{Degree of Sensitivity Change}(\%) = \frac{\text{Sensitivity in 1.5 mL} - \text{Sensitivity in 0.5 mL}}{\text{Sensitivity in 0.5 mL}} \times 100 \quad (2)$$

$$\text{Matrix Effect}(\%) = \frac{\text{Blood Sample} - \text{Control Sample}}{\text{Control Sample}} \times 100 \quad (3)$$

5. Conclusions

In this study, we developed a standardized sample preparation method for VOC analysis in WB samples using a combination of urea and NaCl. This optimized method demonstrated significant improvements in both sensitivity and matrix effect uniformity, while maintaining a consistent performance across varying sample volumes. This novel method's simplified procedure and enhanced analytical performance make it particularly suitable for VOC analysis in veterinary medicine.

Supplementary Materials: The following supporting information can be downloaded at: https://www.mdpi.com/article/10.3390/ijms26104667/s1.

Author Contributions: Conceptualization, J.-W.K. and G.J.; investigation, K.-G.A. and R.C.; resources, K.-G.A. and I.C.; writing—original draft preparation, K.-G.A. and J.-W.K.; writing—review and editing, J.-W.K. and S.G.; visualization, J.-W.K.; supervision, G.A.K.; project administration, G.A.K.; funding acquisition, J.-W.K. and G.J. All authors have read and agreed to the published version of the manuscript.

Funding: This research was supported by Technology Incubator Program for Startups (TIPS) funded by the ministry of SMEs (RS-2024-00441828) and Startups (MSS, Korea) and Korea Institute of Startup and Entrepreneurship Development.

Institutional Review Board Statement: Not applicable.

Informed Consent Statement: Not applicable.

Data Availability Statement: Data is contained within the article and Supplementary Materials.

Acknowledgments: We thank all partner veterinary clinics and veterinarians for collecting our data.

Conflicts of Interest: K.-G.A., R.C., S.G., I.C., G.J. and J.-W.K. are employees of MetaDx Inc. and conducted this study as part of the company's research and development activities. This financial affiliation represents a potential conflict of interest. All experimental procedures, data collection, and analyses were carried out objectively, and the results are reported without bias.

Abbreviations

CPDA	Citrate−phosphate−dextrose−adenine
SDS	Sodium dodecyl sulfate
VOC	Volatile organic compound
NaCl	Sodium chloride
K_2SO_4	Potassium sulfate
Na_2SO_4	Sodium sulfate
GC-MS	Gas chromatography−mass spectrometry
H/S	Headspace
SIM	Selective ion monitoring

References

1. Tan, T.; Xu, X.; Gu, H.; Cao, L.; Liu, T.; Zhang, Y.; Wang, J.; Chen, M.; Li, H.; Ge, X. The Characteristics, Sources, and Health Risks of Volatile Organic Compounds in an Industrial Area of Nanjing. *Toxics* **2024**, *12*, 868. [CrossRef]
2. Chen, J.J.; Wang, T.B.; Chang, L.-T.; Chuang, K.-J.; Chuang, H.-C.; Chang, T.-Y. Exposure and health risk assessment of volatile organic compounds among drivers and passengers in long-distance buses. *Environ. Res.* **2024**, *252 Pt 3*, 118959. [CrossRef]
3. Alsaadi, D.; Clements, N.; Gabuniya, N.; Francis, N.; Chand, M. Exhaled volatile organic compounds in the detection of colorectal cancer: A systematic review and meta-analysis. *Excli. J.* **2024**, *23*, 795–810. [PubMed]
4. Dawson, J.; Green, K.; Lazarowicz, H.; Cornford, P.; Probert, C. Analysis of urinary volatile organic compounds for prostate cancer diagnosis: A systematic review. *BJUI Compass* **2024**, *5*, 822–833. [CrossRef]
5. Khalid, T.; Aggio, R.; White, P.; De Lacy Costello, B.; Persad, R.; Alkateb, H.; Jones, P.; Probert, C.S.; Ratcliffe, N. Urinary Volatile Organic Compounds for the Detection of Prostate Cancer. *PLoS ONE* **2015**, *10*, e0143283. [CrossRef] [PubMed]

6. Perera, T.R.W.; Skerrett-Byrne, D.A.; Gibb, Z.; Nixon, B.; Swegen, A. The Future of Biomarkers in Veterinary Medicine: Emerging Approaches and Associated Challenges. *Animals* **2022**, *12*, 2194. [CrossRef] [PubMed]
7. Einoch Amor, R.; Levy, J.; Broza, Y.Y.; Vangravs, R.; Rapoport, S.; Zhang, M.; Wu, W.; Leja, M.; Behar, J.A.; Haick, H. Liquid Biopsy-Based Volatile Organic Compounds from Blood and Urine and Their Combined Data Sets for Highly Accurate Detection of Cancer. *ACS Sens.* **2023**, *8*, 1450–1461. [CrossRef]
8. Williams, M.L.; Olomukoro, A.A.; Emmons, R.V.; Godage, N.H.; Gionfriddo, E. Matrix effects demystified: Strategies for resolving challenges in analytical separations of complex samples. *J. Sep. Sci.* **2023**, *46*, e2300571. [CrossRef]
9. Tarakhovskaya, E.; Marcillo, A.; Davis, C.; Milkovska-Stamenova, S.; Hutschenreuther, A.; Birkemeyer, C. Matrix Effects in GC-MS Profiling of Common Metabolites after Trimethylsilyl Derivatization. *Molecules* **2023**, *28*, 2653. [CrossRef]
10. Gosetti, F.; Mazzucco, E.; Zampieri, D.; Gennaro, M.C. Signal suppression/enhancement in high-performance liquid chromatography tandem mass spectrometry. *J. Chromatogr. A.* **2010**, *1217*, 3929–3937. [CrossRef]
11. Kandaswamy, C.; Presley, D.; Ahammed, T.P.S.; Anadaram, S. Improved chromatographic performance in red chilli powder pesticide residue quantitation by retention gap introduction in gas chromatography tandem mass spectrometry. *J. Food Sci. Technol.* **2022**, *59*, 1692–1703. [CrossRef] [PubMed]
12. Huertas-Perez, J.F.; Baslé, Q.; Dubois, M.; Theurillat, X. Multi-residue pesticides determination in complex food matrices by gas chromatography tandem mass spectrometry. *Food Chem.* **2024**, *436*, 137687. [CrossRef]
13. Kim, Y.K.; Kwon, S.-Y.; Seo, Y.-S.; Lee, Y.-B.; Mok, J.H. Application of static headspace GC-MS for detection of residual trichloroethylene and toluene solvents in beta-cyclodextrin. *Food Res. Int.* **2024**, *197 Pt 2*, 115292. [CrossRef] [PubMed]
14. Wei, Y.; Wang, M.; Liu, H.; Niu, Y.; Wang, S.; Zhang, F.; Liu, H. Simultaneous determination of seven endogenous aldehydes in human blood by headspace gas chromatography-mass spectrometry. *J. Chromatogr. B. Analyt. Technol. Biomed. Life Sci.* **2019**, *1118–1119*, 85–92. [CrossRef]
15. Hosseinzadeh, R.; Moosavi-Movahedi, A.A. Human hemoglobin structural and functional alterations and heme degradation upon interaction with benzene: A spectroscopic study. *Spectrochim. Acta A Mol. Biomol. Spectrosc.* **2016**, *157*, 41–49. [CrossRef] [PubMed]
16. Shao, J.; Kuiper, B.P.; Thunnissen, A.-M.W.H.; Cool, R.H.; Zhou, L.; Huang, C.; Dijkstra, B.W.; Broos, J. The Role of Tryptophan in pi Interactions in Proteins: An Experimental Approach. *J. Am. Chem. Soc.* **2022**, *144*, 13815–13822. [CrossRef]
17. Crowley, P.B.; Golovin, A. Cation-pi interactions in protein-protein interfaces. *Proteins* **2005**, *59*, 231–239. [CrossRef]
18. Poulson, S.; Harrington, R.; Drever, J. The solubility of toluene in aqueous salt solutions. *Talanta* **1999**, *48*, 633–641. [CrossRef]
19. Yang, X.; Wang, C.; Shao, H.; Zheng, Q. Non-targeted screening and analysis of volatile organic compounds in drinking water by DLLME with GC-MS. *Sci. Total Environ.* **2019**, *694*, 133494. [CrossRef]
20. Cervera, M.I.; Beltran, J.; Lopez, F.; Hernandez, F. Determination of volatile organic compounds in water by headspace solid-phase microextraction gas chromatography coupled to tandem mass spectrometry with triple quadrupole analyzer. *Anal. Chim. Acta* **2011**, *704*, 87–97. [CrossRef]
21. Dupree, E.J.; Jayathirtha, M.; Yorkey, H.; Mihasan, M.; Petre, B.A.; Darie, C.C. A Critical Review of Bottom-Up Proteomics: The Good, the Bad, and the Future of this Field. *Proteomes* **2020**, *8*, 14. [CrossRef] [PubMed]

Disclaimer/Publisher's Note: The statements, opinions and data contained in all publications are solely those of the individual author(s) and contributor(s) and not of MDPI and/or the editor(s). MDPI and/or the editor(s) disclaim responsibility for any injury to people or property resulting from any ideas, methods, instructions or products referred to in the content.

molecules

MDPI

Article

Application of Human Plasma Targeted Lipidomics and Analysis of Toxic Elements to Capture the Metabolic Complexities of Hypothyroidism

Anna Błażewicz [1,2,*], Michał Kiełbus [3,4], Katarzyna Skórzyńska-Dziduszko [5], Andreas M. Grabrucker [2,6,7], Jacqueline Jonklaas [8], Piotr Sosnowski [9], Alicja Trzpil [9], Anna Kozub-Pędrak [9], Agnieszka Szmagara [10], Julia Wojnicka [1], Ewelina Grywalska [11] and Agostinho Almeida [12,*]

1 Department of Pathobiochemistry and Interdisciplinary Applications of Ion Chromatography, Chair of Biomedical Sciences, Medical University of Lublin, 1 Chodźki Street, 20-093 Lublin, Poland; julia.wojnicka@umlub.pl
2 Department of Biological Sciences, University of Limerick, V94 T9PX Limerick, Ireland; andreas.grabrucker@ul.ie
3 Department of Experimental Hematooncology, Medical University of Lublin, Chodzki 1, 20-093 Lublin, Poland; michal.kielbus@umlub.pl
4 Chair and Department of Biochemistry and Molecular Biology, Medical University of Lublin, Chodzki 1, 20-093 Lublin, Poland
5 Department of Human Physiology, Medical University of Lublin, Radziwillowska 11 Str., 20-080 Lublin, Poland; katarzyna.skorzynska-dziduszko@umlub.pl
6 Bernal Institute, University of Limerick, V94 T9PX Limerick, Ireland
7 Health Research Institute (HRI), University of Limerick, V94 T9PX Limerick, Ireland
8 Division of Endocrinology, Georgetown University, Washington, DC 20007, USA; jonklaaj@georgetown.edu
9 Department of Bioanalytics, Medical University of Lublin, ul. Jaczewskiego 8b, 20-090 Lublin, Poland; piotr.sosnowski.phd@gmail.com (P.S.); alicja.trzpil@umlub.pl (A.T.); annakozub2810@gmail.com (A.K.-P.)
10 Department of Chemistry, Faculty of Medicine, Institute of Biological Sciences, The John Paul II Catholic University of Lublin, Konstantynow 1J, 20-708 Lublin, Poland; agnieszka.szmagara@kul.pl
11 Department of Experimental Immunology, Medical University of Lublin, Chodźki 4a St., 20-093 Lublin, Poland; ewelina.grywalska@umlub.pl
12 Associated Laboratory for Green Chemistry (LAQV) of the Network of Chemistry and Technology (REQUIMTE), Department of Chemical Sciences, Laboratory of Applied Chemistry, Faculty of Pharmacy, University of Porto, 50-313 Porto, Portugal
* Correspondence: anna.blazewicz@umlub.pl (A.B.); aalmeida@ff.up.pt (A.A.)

Abstract: Background: Hypothyroidism (HT) affects millions worldwide and can lead to various lipid disorders. The metabolic complexity and the influence of toxic elements in autoimmune and non-autoimmune HT subtypes are not fully understood. This study aimed to investigate the relationships between plasma lipidome, toxic elements, and clinical classifications of HT in unexposed individuals. Methods: Samples were collected from 120 adults assigned to a study group with Hashimoto's disease and non-autoimmune HT, and a healthy control group. Quantification of 145 pre-defined lipids was performed by using triple quadrupole tandem mass spectrometry (TQ MS/MS) in multiple reactions monitoring (MRM) mode via positive electrospray ionization (ESI). Levels of toxic elements were determined using inductively coupled plasma mass spectrometry (ICP-MS). Results: Significant associations between altered levels of several components of the plasma lipidome and Al, Cd, Ni, As, and Pb with HT were found. We show metabolic differences in lysophosphatidylcholines (LPC) and phosphatidylcholines (PC) between HT and controls, with distinct predicted activation patterns for lysolecithin acyltransferase and phospholipase A2. Conclusions: There are significant changes in the lipidome profiles of healthy subjects compared to euthyroid HT patients treated with L-thyroxine, which are related to the type of hypothyroidism and non-occupational exposure to toxic elements.

Keywords: human plasma lipidome; targeted lipidomics; toxic elements; hypothyroidism; Hashimoto disease

1. Introduction

Thyroid diseases are complex and often multifactorial, involving factors such as genetics, immune responses, hormonal imbalances, and environmental factors [1]. Hypothyroidism (HT) is a chronic condition characterized by a deficiency of thyroid hormones [2] and is associated with an increased risk of developing components of metabolic syndrome, such as obesity and insulin resistance [3]. Absent or inadequate treatment of HT results in harmful consequences for the human body [4]. Symptoms of HT are nonspecific and include mild to moderate weight gain, fatigue, lack of concentration, and depression.

Currently, HT affects up to 5% of the general population, while it is estimated that 5% of cases remain undiagnosed [5]. In iodine-sufficient areas, the most common cause of primary HT is autoimmune thyroiditis (Hashimoto's disease) [6]. Thyroid hormones stimulate fatty acid synthesis (lipogenesis), triglyceride breakdown (lipolysis), fatty acid oxidation, cholesterol synthesis, and low-density lipoprotein (LDL) receptors. They modulate all pathways of lipoprotein metabolism, influence the expression of lipoprotein receptors, the production of apolipoproteins, the activity of plasma lipoprotein-modifying enzymes, and the blood concentrations of substrates for the synthesis of triglycerides (TG), such as fatty acids and glucose. Therefore, it is reasonable to evaluate the lipid profile in patients with HT, as it may be affected by altered levels of thyroid hormones [7].

Lipids, which play vital roles in building cell membrane structure, cell signaling, and energy storage, are sensitive indicators of metabolic changes in health and disease [8,9]. Much attention has been directed to total cholesterol (TC) and lipoprotein particles (low-density lipoproteins—LDL, high-density lipoproteins—HDL) as risk factors for serious health disorders. However, the knowledge gap regarding lipid disorders in endocrine diseases is widely recognized. In recent years, there has been increasing interest in the diagnostic potential of lipidomics [10], as it has been realized that lipidome analysis can help identify pathogenic mechanisms that contribute to the development or progression of various diseases and identify affected metabolic pathways, thus providing useful information in specifying potential drug targets [11]. Disturbed lipid metabolism plays a significant role in metabolic disorders that occur in various diseases, including obesity, diabetes, non-alcoholic fatty liver disease (NAFLD), non-alcoholic steatohepatitis (NASH), and neurodegenerative diseases [12]. Deteriorated thyroid status can lead to an unfavorable lipid profile, which can consequently increase the risk of serious conditions, particularly cardiovascular diseases [13].

Patients with hypothyroidism often suffer disproportionately from lipid disorders. And this has huge health and economic implications. To the best of our knowledge, human lipidome alterations have not been studied in patients with well-controlled hypothyroidism (i.e., with thyroid-stimulating hormone (TSH) levels within the normal range under the appropriate dose of levothyroxine (LT4) replacement therapy). Research shows that LT4 treatment can reduce TC and LDL-C levels in patients with subclinical HT, including those with mild impairment [14]. According to the Endocrine Society clinical practice guidelines, the lipid profile should be reassessed when the patient's thyroid hormones are in the normal range after treatment stabilization [7]. Knowing that thyroid hormones modulate all pathways involved in lipid metabolism and that an increasing number of studies are reporting the role of specific lipid classes in endocrine pathologies, it seems reasonable and advisable to expand research and explore beyond routine cholesterol and triglyceride testing in patients with HT. There is published evidence for the rapid identification and quantification of numerous lipid compounds in plasma using commercially available metabolomic kits. Previously published studies indicating the role of lipid species involved in thyroid metabolism include a broad group of lipid molecules that can be analyzed using a targeted lipidomic approach. The targeted lipidomics focuses on the absolute quantification of pre-defined lipids. The targeted approach, although limited to the measurement of known substances of great (known) biological importance, is high-throughput because data generation and analysis are fast, straightforward, and quantitative. The number of analytical targets is often limited due to the lack of commercially available standards [15].

A study by Jiang et al. [16] found that phospholipids, such as sphingomyelins (SM), lysophosphatidylcholines (LPC), phosphatidylcholines (PC), influence the pathogenesis of Hashimoto's thyroiditis. Zheng et al. [17] suggest that both CD3 antigen and sphingomyelin (d18:1/20:0, d16:1/22:0) could be identified as risk factors for hypothyroidism, and found the 1-(1-enyl-palmitoyl)-2-oleoyl-GPE (p-16:0/18:1), a derivative of glycerophospholipids (GPL), to be associated with decreased hypothyroidism risk. An increase in the percentage of CD3+ cells (T lymphocytes) can be observed in cases of excessive immune system activity, and as it is known, mechanistically, Hashimoto thyroiditis is characterized by a direct T-cell attack on the thyroid gland [18,19].

Although many chemical elements have the potential to disrupt the endocrine system of humans at ecologically relevant concentrations [20], it is still unknown to what extent such exposures to environmental chemical contaminants impact lipid levels in the human body. Numerous research articles highlight the pathophysiological significance of chemical elements such as Cd, As, Pb, Al, and Ni. They can bioaccumulate in living organisms, severely damaging various cells, tissues, and vital organs [21]. However, it is still unknown how individual lipid species are quantitatively altered in the presence of such toxic elements in the human body.

In this context, we decided to test the hypothesis that changes in plasma lipidome related to HT occur, even in well-controlled patients on LT4 therapy and who present normal lipid profiles on routine tests (i.e., LDL-C, HDL-C, TC, and TG) [22]. Additionally, we evaluated the association of HT with altered levels of Al, As, Ni, Cd, and Pb. The aim was also to verify which specific lipid compounds differ quantitatively between healthy adults and hypothyroid individuals and whether toxic trace element levels allow differentiation between autoimmune and non-autoimmune HT subtypes. To the best of our knowledge, there are no detailed lipidome studies in patients with hypothyroidism. Likewise, there is a lack of current human biomonitoring data regarding toxic elements in relation to the Polish population. We decided to test whether, with compensated thyroid hormone levels, the lipid profile of patients differs compared to healthy subjects, and whether environmental exposure to toxic elements affects the potential differences reflected in the plasma lipidome. To this end, a modern targeted metabolomics approach aimed at the quantification of 40 acylcarnitines, 90 glycerophospholipids, and 15 sphingomyelins was combined with inductively coupled plasma mass spectrometry (ICP-MS) as the analytical technique used to determine the toxic elements at trace levels in biological samples. To analyze the dataset, Principal Component Analysis (PCA) was used combined with the Monte Carlo Feature Selection and Interdependency Discovery (MCFS-ID) method in order not to overlook potentially valuable information contained in the collected data. Focusing on selected 145 lipid species with important biological roles, we used the most widely used platforms for targeted analysis that provide high sensitivity, selectivity, and a wide dynamic range (i.e., triple quadrupole tandem mass spectrometry (TQ MS/MS) in multiple reactions monitoring (MRM) mode via positive electrospray ionization (ESI)).

2. Results

Detailed characteristics of patients with Hashimoto's disease or non-autoimmune hypothyroidism (Hypo-non-Hashimoto) and the control group are presented in Table 1. The Cohort was defined as comprising the control group (Controls) and the entire HT group (see Table 1). The disease group was characterized as including the control group (Controls), along with both the autoimmune HT subgroup and the non-autoimmune HT subgroup (as detailed in Table 1). The groups were matched by age, sex, and BMI. There were no significant differences in TSH and free thyroid hormones (fT4 and fT3) levels between the two HT subgroups (which consisted of patients adequately treated with levothyroxine to maintain euthyroidism, as highlighted above) and healthy controls.

Table 1. Summary table of demographic, clinical, and biochemical data of all study subjects (patients and controls) *.

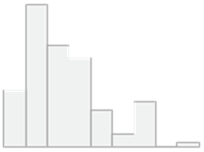
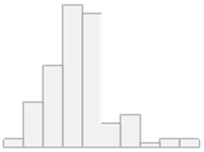
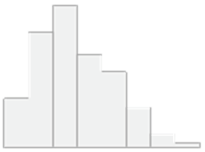
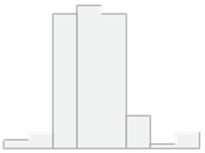
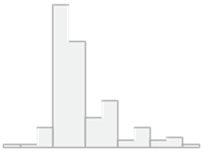
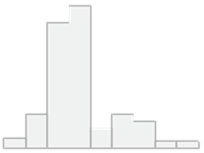
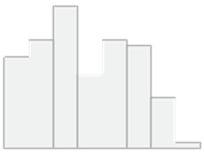
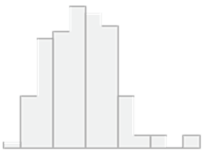
No	Variable	Stats/Values	Freqs (% of Valid)	Graph	Valid	Missing
1	Gender [character]	1. F	104 (86.7%)		120 (100.0%)	0 (0.0%)
		2. M	16 (13.3%)			
2	Age [numeric]	Mean (sd): 29.6 (9.1)	30 distinct values		120 (100.0%)	0 (0.0%)
		min ≤ med ≤ max:				
		18 ≤ 28 ≤ 59				
		IQR (CV): 11.2 (0.3)				
3	BMI [numeric]	Mean (sd): 23.7 (3.3)	103 distinct values		120 (100.0%)	0 (0.0%)
		min ≤ med ≤ max:				
		17.7 ≤ 23.7 ≤ 35.3				
		IQR (CV): 3.7 (0.1)				
4	LDL [numeric]	Mean (sd): 98.7 (30.4)	93 distinct values		120 (100.0%)	0 (0.0%)
		min ≤ med ≤ max:				
		47 ≤ 94.2 ≤ 186.2				
		IQR (CV): 42.3 (0.3)				
5	HDL [numeric]	Mean (sd): 57.2 (12.9)	73 distinct values		120 (100.0%)	0 (0.0%)
		min ≤ med ≤ max:				
		23.3 ≤ 56 ≤ 98				
		IQR (CV): 16.5 (0.2)				
6	TC [numeric]	Mean (sd): 177.7 (38.9)	84 distinct values		120 (100.0%)	0 (0.0%)
		min ≤ med ≤ max:				
		98 ≤ 165.2 ≤ 301.2				
		IQR (CV): 44 (0.2)				
7	TG [numeric]	Mean (sd): 90.1 (30.4)	88 distinct values		120 (100.0%)	0 (0.0%)
		min ≤ med ≤ max:				
		36 ≤ 83.7 ≤ 182				
		IQR (CV): 27.2 (0.3)				
8	TSH [numeric]	Mean (sd): 2.2 (0.9)	94 distinct values		120 (100.0%)	0 (0.0%)
		min ≤ med ≤ max:				
		0.7 ≤ 2 ≤ 4.3				
		IQR (CV): 1.6 (0.4)				
9	fT4 [numeric]	Mean (sd): 1.5 (1.2)	62 distinct values		120 (100.0%)	0 (0.0%)
		min ≤ med ≤ max:				
		0.8 ≤ 1.5 ≤ 10.2				
		IQR (CV): 0.5 (0.8)				
10	fT3 [numeric]	Mean (sd): 2.9 (1)	90 distinct values		120 (100.0%)	0 (0.0%)
		min ≤ med ≤ max:				
		0.8 ≤ 2.9 ≤ 6.1				
		IQR (CV): 1.4 (0.3)				

Table 1. *Cont.*

No	Variable	Stats/Values	Freqs (% of Valid)	Graph	Valid	Missing
11	Cohort [character]	1. Controls	61 (50.8%)		120 (100.0%)	0 (0.0%)
		2. HT patients	59 (49.2%)			
12	Disease [character]	1. Autoimmune_HT	32 (26.7%)		120 (100.0%)	0 (0.0%)
		2. Controls	61 (50.8%)			
		3. Non_autoimmune_HT	27 (22.5%)			
13	TSH_level [character]	1. high	1 (0.8%)		120 (100.0%)	0 (0.0%)
		2. normal	119 (99.2%)			
14	fT3_level [character]	1. high	14 (11.7%)		120 (100.0%)	0 (0.0%)
		2. low	9 (7.5%)			
		3. normal	97 (80.8%)			
15	fT4_level [character]	1. high	11 (9.2%)		120 (100.0%)	0 (0.0%)
		2. low	1 (0.8%)			
		3. normal	108 (90.0%)			
16	TC_level [character]	1. normal	78 (65.0%)		120 (100.0%)	0 (0.0%)
		2. primary_prevention	32 (26.7%)			
		3. secondary_prevention	10 (8.3%)			
17	LDL_level [character]	1. normal	69 (57.5%)		120 (100.0%)	0 (0.0%)
		2. primary_prevention	34 (28.3%)			
		3. secondary_prevention	17 (14.2%)			
18	HDL_level [character]	1. low	19 (15.8%)		120 (100.0%)	0 (0.0%)
		2. normal	101 (84.2%)			
19	TG_level [character]	1. high	11 (9.2%)		120 (100.0%)	0 (0.0%)
		2. low	1 (0.8%)			
		3. normal	108 (90.0%)			
20	Weight_status [factor]	1. Underweight	5 (4.2%)		120 (100.0%)	0 (0.0%)
		2. Healthy_weight	78 (65.0%)			
		3. Overweight	32 (26.7%)			
		4. Obesity	5 (4.2%)			
21	Weight_groups [factor]	1. Underweight_or_Healthy	83 (69.2%)		120 (100.0%)	0 (0.0%)
		2. Overweight_or_Obesity	37 (30.8%)			

* Abbreviations: BMI—body mass index; LDL—low-density lipoprotein; HDL—high-density lipoprotein; TC—total cholesterol; TG—triglycerides; TSH—thyroid-stimulating hormone; fT3—free triiodothyronine; fT4—free thyroxine.

Table S1 Nomenclature of lipids used in the study and lipid abbreviations conformed to LipidMaps standards.

Based on the analysis of each lipid group or trace element content, each highlighted in separate figures, PCA correctly classified all participants into the respective group: HT patients or controls.

PCA revealed the clusters representing groups of data points (individuals) that are closely positioned in the reduced-dimensional space, indicating similar underlying characteristics or patterns. The clusters for acylcarnitines are shown in Supplementary Figure S1A, with the key compounds for patient stratification depicted in Supplementary Figure S1B–D.

The variance explained by the first two principal components (PC1, PC2), used for visualization, reached 66.1%, as shown in Supplementary Figure S1E. Similarly, for glycerophospholipids, patient subgroups are shown in Supplementary Figure S2A. The essential compounds for stratification are shown in Supplementary Figure S2B–D, with PC1 and PC2 accounting for 81.4% of the variance, as shown in Supplementary Figure S2E. Sphingolipids also contributed to patient stratification, as shown in Supplementary Figure S3A. The key compounds and their impact on variance are shown in Supplementary Figure S3B–D and summarized in Supplementary Figure S3E, reaching 86.3% of the variance for the first two components. Lastly, toxic trace elements data led to comparable subgroup distinctions, depicted in Supplementary Figure S4A. The influential compounds and variance explained by the principal components are shown in Supplementary Figures S4B–D and S4E, with 89.2% of variance explained by PC1 and PC2. All lipid groups analyzed, i.e., acylcarnitines, glycerophospholipids, sphingolipids, as well as toxic trace elements played a pivotal role in stratifying participants (controls together with HT patients), showing the ability of PCA to highlight critical biomarkers across diverse biochemical domains.

In a subsequent statistical analysis step, the relationships between the distribution of clinical variables and the clustering of all individuals resulting from PCA for different groups of lipid compounds or trace elements were determined (Table 2).

Table 2. Adjusted *p* values for enrichment of clinical categories within PCA of all individuals clustering based on statistical association tests. Calculations used the asymptotic chi-square or Fisher's exact tests with BH *p*-value correction on all the analyzed participants.

	Acylcarnitines	**Glycerophospholipids**	**Sphingolipids**	**Toxic Trace Elements**
Variable	**padj**	**padj**	**padj**	**padj**
Gender	0.478351867	0.565579025	0.565579025	0.090293429
Cohort (Controls vs. HT patients)	2.36664×10^{-5}	8.6635×10^{-8}	8.6635×10^{-8}	3.02895×10^{-6}
Disease (Controls vs. autoimmune HT vs. non-autoimmune HT)	3.7519×10^{-5}	1.12254×10^{-7}	1.12254×10^{-7}	1.6082×10^{-11}
fT3_level	0.223051666	0.769335436	0.769335436	1
fT4_level	0.665371092	0.916228719	0.916228719	0.818701672
TC_level	0.373032061	0.086842311	0.086842311	0.00382032
LDL_level	0.478351867	0.769335436	0.769335436	0.58095462
HDL_level	0.223051666	0.769335436	0.769335436	0.00382032
TG_level	0.11759458	0.250574397	0.250574397	0.114958437
Weight_status	0.478351867	0.769335436	0.769335436	0.220153881
Weight_groups	0.665371092	1	1	0.198591583

Statistically significant associations (padj < 0.05) were found between the Cohort groups (Controls vs. HT patients) and all studied chemical compounds groups. Likewise, there were statistically significant associations between the disease group (Controls vs. Autoimmune HT vs. Non-autoimmune HT) and all chemical compound groups. Moreover, a significant association was observed between both TC and HDL with toxic trace element levels. These results suggest that specific clinical grouping of all examined individuals, such as (1) Controls vs. HT patients and more detailed (2) Controls vs. autoimmune HT vs. non-autoimmune HT, significantly impacts the chemical compound profiles measured across different substance groups. Particularly, strong associations with every analyzed lipid group and trace elements were observed for the Disease variable, which may indicate significant biological differences between disease groups in cellular metabolism. Additionally, HDL and total cholesterol levels showed significant associations with toxic trace elements, indicating a potential impact on individuals' lipid profiles.

Detailed plots showing the relationship between the distribution of demographic, clinical, and biochemical variables, and the clustering of participants derived from the PCA, including PCA clustering and percentage contingency of each analyzed demographic, clinical, and biochemical variable, are shown in Supplementary Materials (Figures S5–S8).

PCA successfully segregated HT patients into two clear subgroups based on each lipid group or trace element content, each shown in separate figures. As shown in Supplementary Figure S9A, patients were clearly grouped based on the pattern of acylcarnitines, while the key compounds for stratifying these patients are illustrated in Supplementary Figure S9B–D.

The variance captured by PC1 and PC2 totaled 73.5%, as indicated in Supplementary Figure S9E. Similarly, glycerophospholipids distinguished patient subgroups, depicted in Supplementary Figure S10A, with key compounds for stratification shown in Supplementary Figure S10B–D. In this case, the principal components explained 90.8% of the variance, as detailed in Supplementary Figure S10E. Sphingolipids also played a significant role in clearly patients stratifying into separate clusters as shown in Supplementary Figure S11A, with key compounds and their contribution to variance illustrated in Supplementary Figure S11B–D. They accounted for 85.2% of the variance captured by the first two components. Furthermore, the concentration patterns of toxic trace elements allow patients to be separated into similar subgroups, outlined in Supplementary Figure S12A. The significant compounds and the variance explained by the principal components are shown in Supplementary Figure S12B–D, with a total of 86.9% of the variance captured by PC1 and PC2, as shown in Supplementary Figure S12E. Each group of lipids and toxic trace elements played a key role in stratifying patients, demonstrating the effectiveness of PCA in identifying crucial chemicals that allow us to separate the patients into distinct clusters (Table 3).

Table 3. Table of adjusted *p* values for enrichment of clinical subgroups within PCA participants clustering based on statistical association tests. The calculations were performed using asymptotic Chi-square or Fisher's test with BH *p*-value correction on the HT patients' cohort.

Variable	Acylcarnitines padj	Glycerophospholipids padj	Sphingolipids padj	Toxic Trace Elements padj
Gender	1	0.970383293	0.970383293	0.265454073
Disease (autoimmune HT vs. non-autoimmune HT)	0.851078962	0.970383293	0.970383293	1.41723×10^{-5}
fT3_level	1	0.698006698	0.698006698	1
fT4_level	0.851078962	1	1	1
TC_level	0.851078962	0.955552885	0.955552885	1
LDL_level	0.851078962	0.970383293	0.970383293	0.688602232
HDL_level	1	1	1	0.037488777
TG_level	0.851078962	1	1	1
Weight_status	0.087940642	0.955552885	0.955552885	0.369851258
Weight_groups	0.159298729	0.955552885	0.955552885	1

The detailed plots illustrating the correlation between the distribution of clinical variables and the clustering of all participants as determined by PCA, including PCA clustering and the percentage contingency of each analyzed clinical variable are presented in the supplementary data (Figures S13–S16).

PCA is widely used for dimensionality reduction in biological datasets that include multiple variables, such as chemical substances and their concentrations in participants, along with demographic, clinical, and biochemical features. Its primary function is to transform original variables into a new set of uncorrelated variables—principal components—that maximize variance. However, PCA has inherent limitations, especially when applied to complex and heterogeneous data. The effectiveness of PCA may be compromised on datasets with complex structures or nonlinear relationships between variables.

To overcome the limitations of PCA, we used the MCFS-ID algorithm. Unlike PCA, which focuses on variance, MCFS-ID evaluates features based on their predictive power and interdependencies without assuming linear relationships. This enables MCFS-ID to identify the most relevant features and reveal complex interactions, offering a more robust approach for analyzing complex datasets and understanding clinical outcomes.

Therefore, we used the MCFS-ID method to explore potential associations within the dataset, including between concentrations of analyzed chemical species together with trace elements and demographic, clinical, and biochemical variables. This data analysis produced a ranked list of features, highlighting those most effective for distinguishing between classes based on specific clinical characteristics.

Figure 1 shows the 23 critical features that are crucial for distinguishing controls from HT patients. These include the following: Al, PC.aa.C40.1, PC.ae.C40.3, Cd, Ni, PC.ae.C38.1, As, PC.ae.C38.3, C7.DC, PC.ae.C42.0, PC.aa.C26.0, SM.C18.0, PC.aa.C28.1, C12.DC, SM.C16.1, SM.C24.0, PC.aa.C34.2, Pb, PC.aa.C40.6, PC.aa.C38.6, SM..OH..C22.2, PC.aa.C30.2, and PC.aa.C36.3.

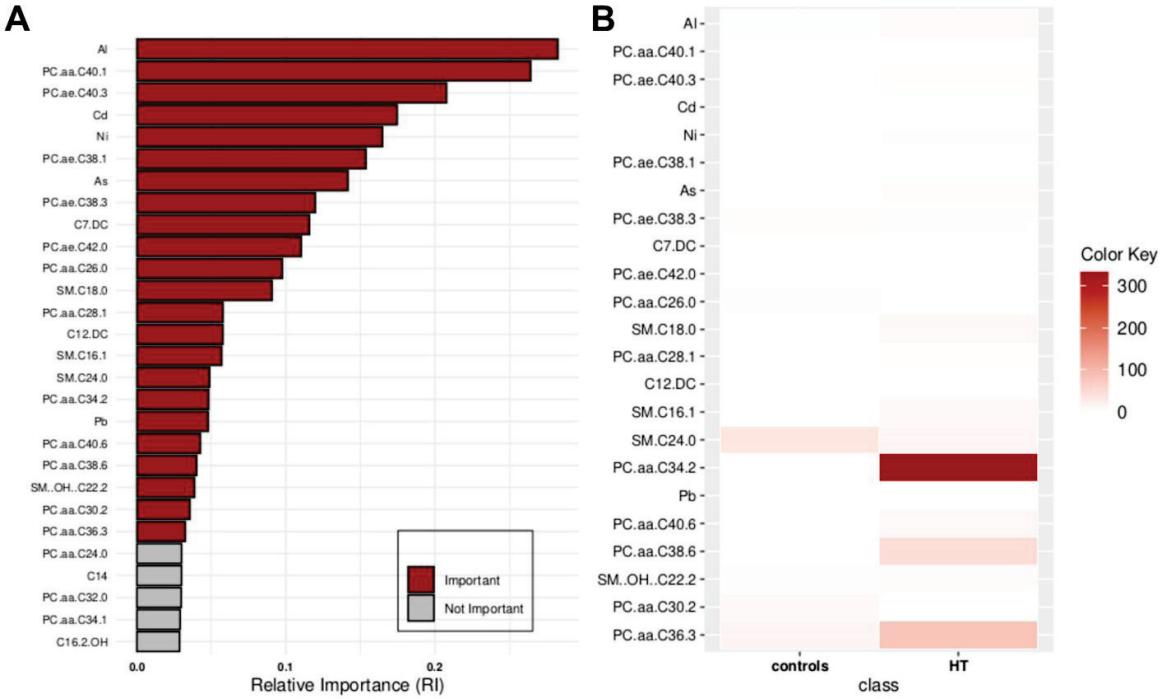


Figure 1. Key features identified at the top of the MCFS-ID prioritization analysis of all participants across controls vs. HT patients. (**A**) The Relative Importance (RI) of ranked features, with red color indicating significant features and gray denoting those below the cutoff (see Section 4). (**B**) The mean values of the significant features in each decision class correspond to the analyzed grouping variable.

Figure 2 illustrates another set of 17 compounds found essential for distinguishing participants into controls, autoimmune HT, and non-autoimmune HT types, which were as follows: Al, Cd, PC.aa.C40.1, Ni, As, Pb, PC.ae.C40.3, PC.ae.C42.0, SM.C18.0, PC.ae.C38.1, C7.DC, PC.ae.C38.3, PC.aa.C26.0, SM.C16.1, PC.aa.C28.1, C12.DC, and C16.

Focusing specifically on HT patients, the data analysis identified Al, Cd, As, Ni, and Pb as significant features for classifying the autoimmune versus non-autoimmune types of HT, as detailed in Figure 3.

To strengthen the Monte Carlo Feature Selection and Interdependency Discovery (MCFS-ID) results, a canonical statistical analysis using multiple comparisons with the Mann–Whitney–Wilcoxon test was performed. This traditional statistical analysis complements the MCFS-ID by validating differences between study groups. By using both statistical tools, we aimed to examine the data in a comprehensive way, highlighting sta-

tistically significant differences. This dual approach increases the robustness of the data analysis, increasing the credibility of the conclusions drawn.

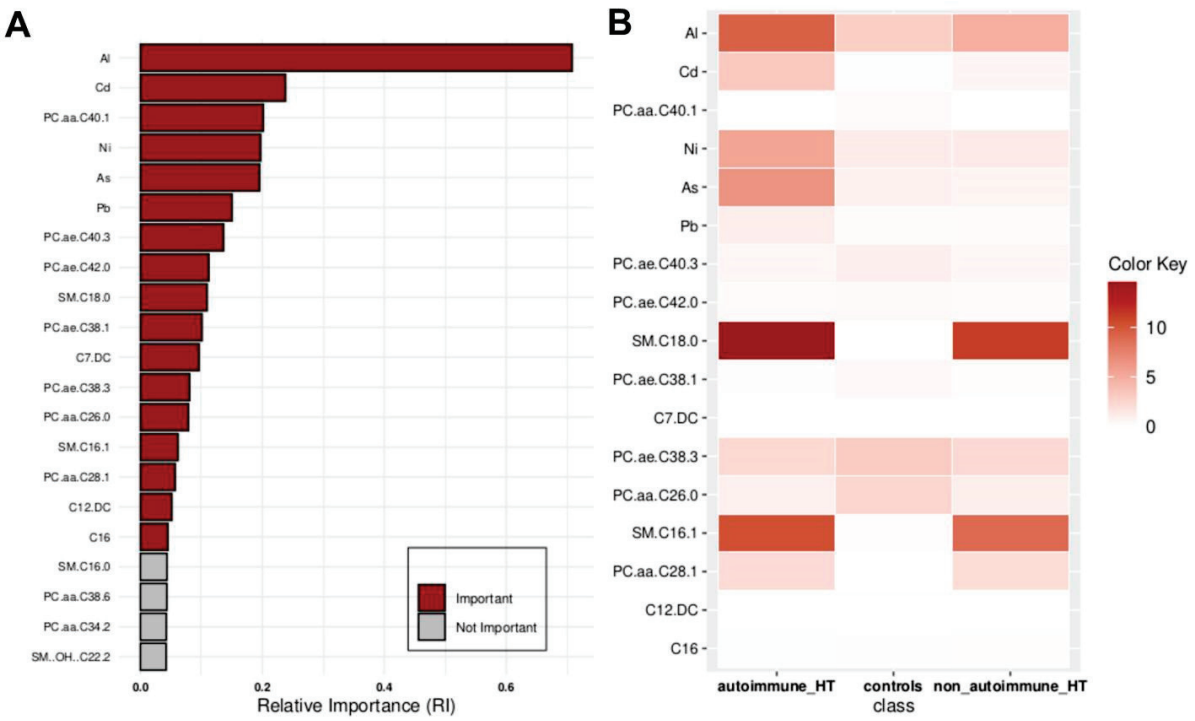


Figure 2. Key features identified at the top of the MCFS-ID prioritization analysis of all participants across autoimmune HT, non-autoimmune HT, and Controls. (**A**) The Relative Importance (RI) of ranked features, with red indicating significant features and gray denoting those below the cut-off point (refer to Section 4). (**B**) The average values of significant features across each decision class correspond to the analyzed grouping variable.

The results of this statistical analysis are detailed in Figures 4–6, which illustrate significant differences in the concentrations of chemical compounds and trace elements between participant groups, grouped by demographic, clinical, and biochemical variables. Figure 4 compares control subjects and HT patients, highlighting the differences in the biochemical profile between analyzed subgroups. Figure 5 displays these comparisons, providing insight into how compound concentrations differ by disease classification. Figure 6 focuses on HT patients only, comparing the concentrations of trace elements between autoimmune HT and non-autoimmune HT patients. These figures present a clear view of significant statistical findings, showing how the concentration of chemical compounds analyzed varies across different clinical categories. The results presented in Figures 4–6 are also summarized in Tables 4–6, which highlight the most significantly altered lipids and toxic elements that differentiate between controls, autoimmune HT, and non-autoimmune HT.

The completed statistical analysis results corresponding to Figures 4–6 are also attached in Supplementary Tables S2–S4 (ST2–ST4).

The Manhattan plot illustrates the −log10 adjusted *p*-values of the Mann–Whitney–Wilcoxon tests. The red and blue dashed lines depict the thresholds for adjusted *p*-values, set at 0.05 and 0.01, respectively. Only those points representing statistically significant comparisons have been marked with labels on the plot.

The Manhattan plot illustrates the −log10 adjusted *p*-values from the Mann–Whitney–Wilcoxon test to compare the concentrations of analyzed chemical compounds between the participant groups studied. The dashed red and blue lines delineate the thresholds for adjusted *p*-values at 0.05 and 0.01, respectively. Additionally, only those points representing statistically significant comparisons have been annotated with labels on the plot.

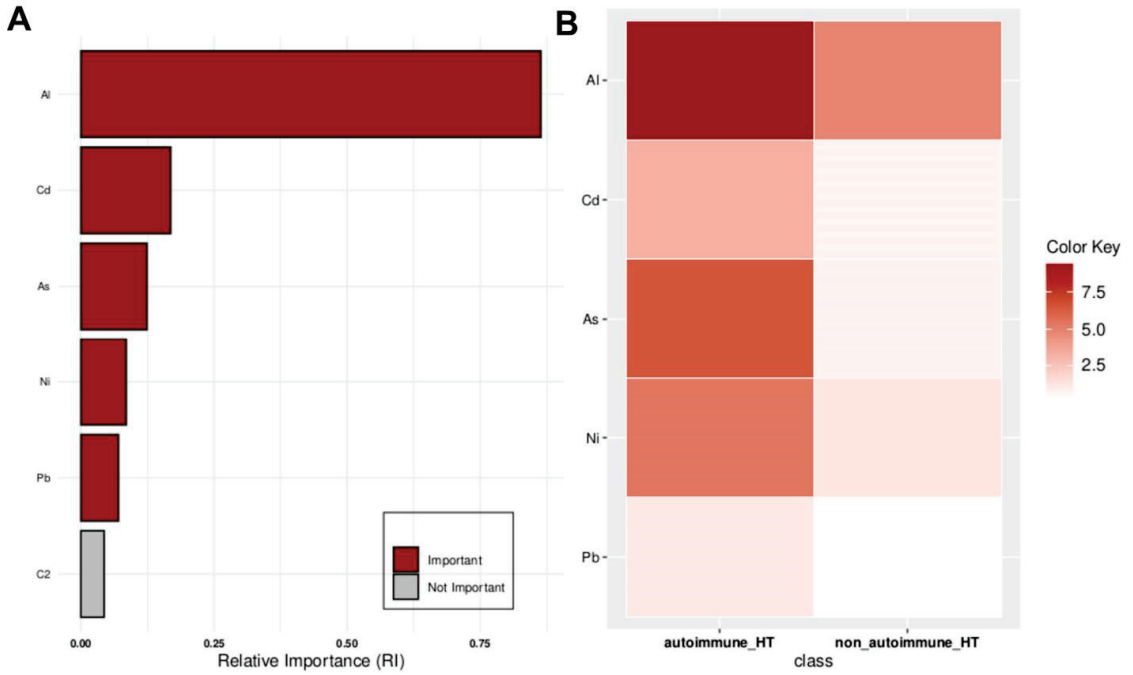


Figure 3. Key features identified at the top of the MCFS-ID ranking analysis of the HT patients across autoimmune HT and non-autoimmune HT. (**A**) The Relative Importance (RI) of ranked features, with red indicating significant features and gray denoting those below the cut-off point (refer to Section 4). (**B**) The average values of significant features across each decision class correspond to the analyzed grouping variable.

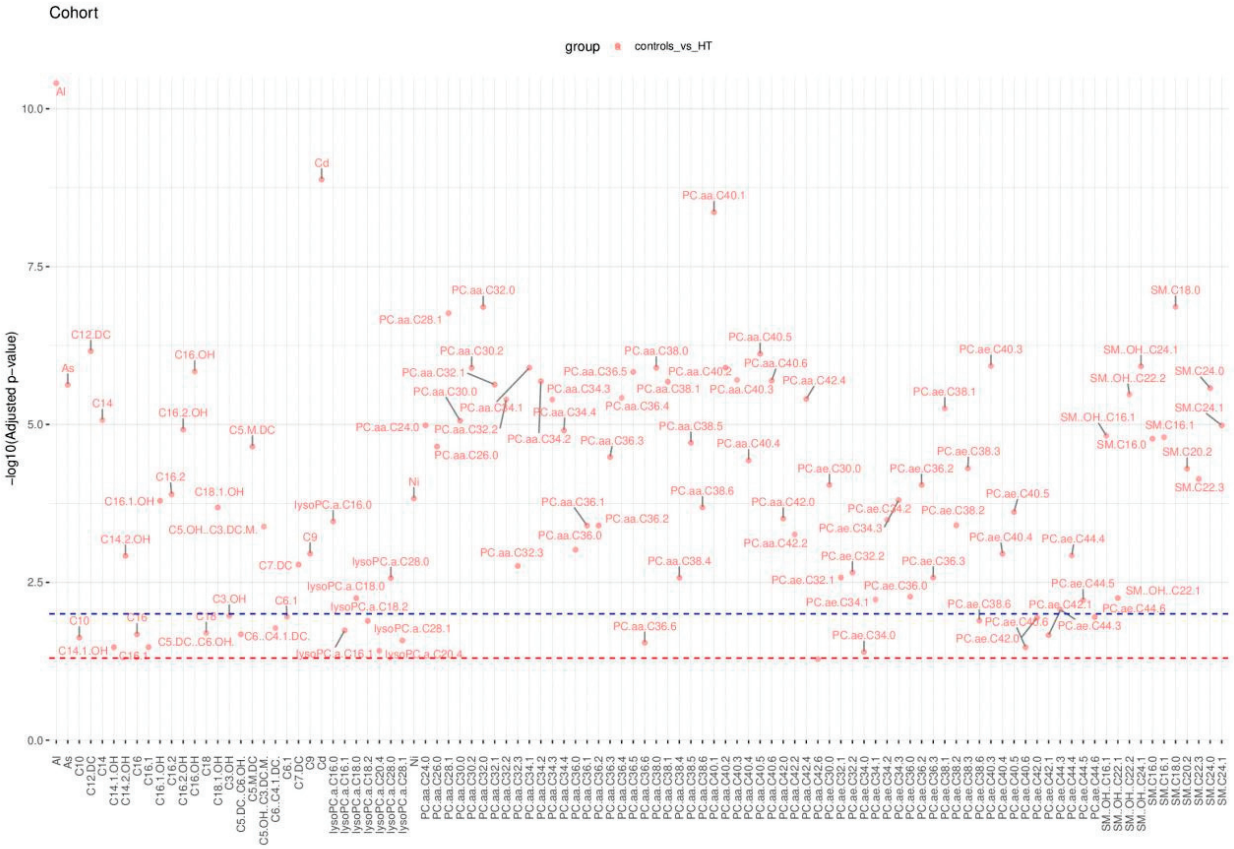


Figure 4. Significant comparisons of analyzed chemical substance concentrations in controls and HT patients across the controls and HT patients.

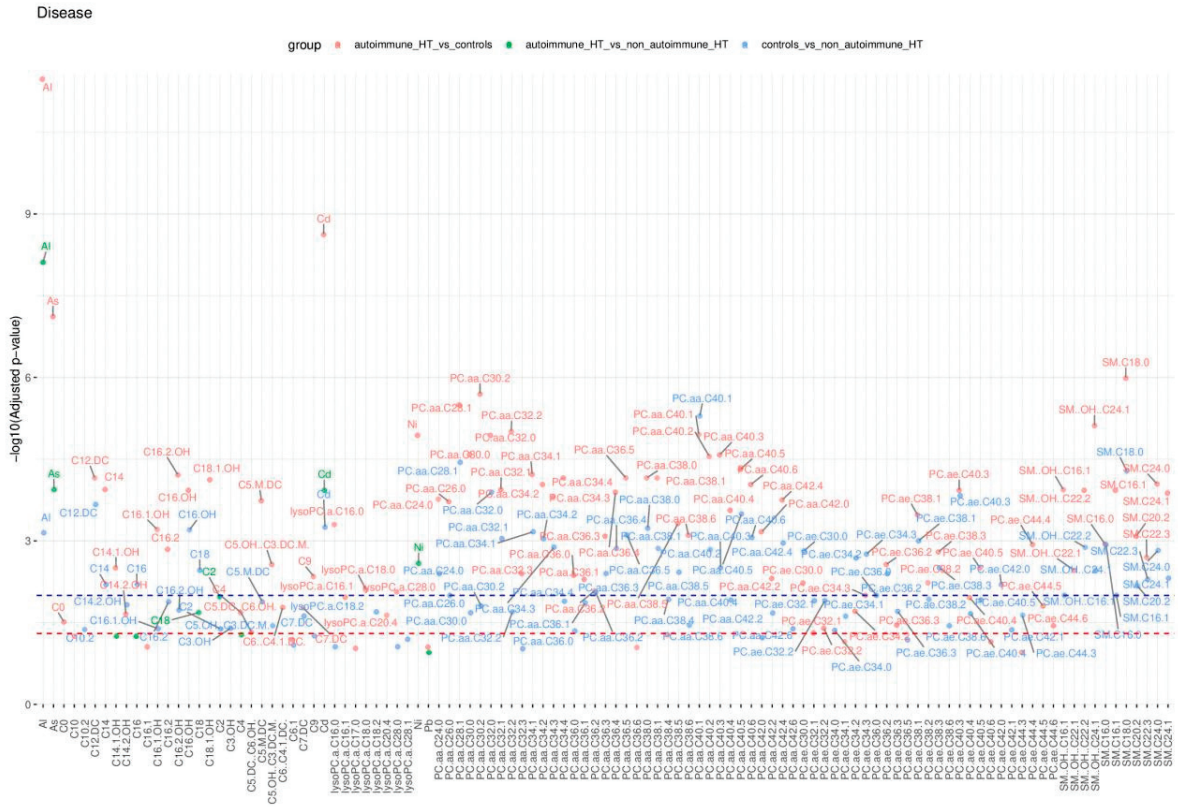


Figure 5. Significant comparisons of analyzed chemical substance concentrations in controls and HT patients across autoimmune HT and non-autoimmune HT patients.

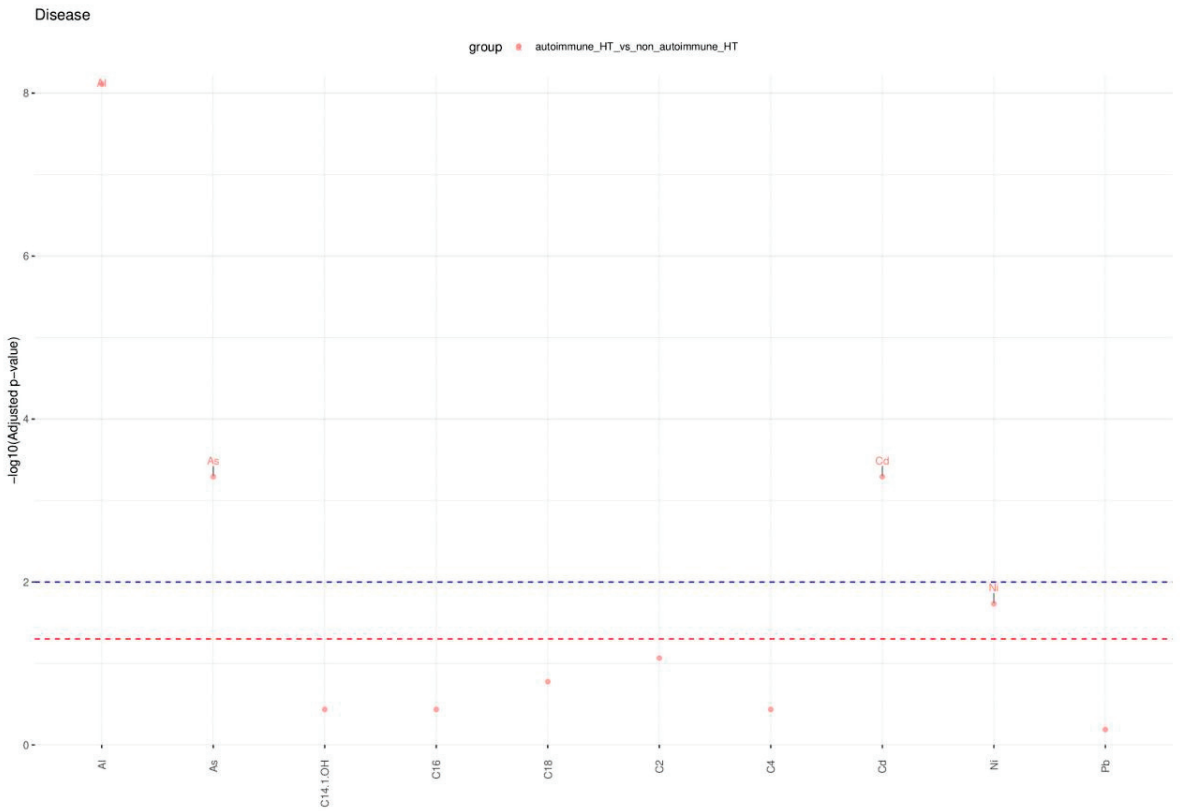


Figure 6. Significant comparisons of analyzed chemical substance concentrations in HT patients across disease variables.

Table 4. Summary of lipids and toxic elements distinguishing controls from HT. The table presents the top 20 lipids and toxic elements ranked by absolute log fold change (logFC) between controls and HT.

Chemicals	Comparisons		logFC	padj
PC.aa.C36.4	controls	HT	2.712505038	3.78063×10^{-6}
PC.aa.C38.6	controls	HT	2.6773185	0.000205764
PC.aa.C34.2	controls	HT	2.673914809	2.06004×10^{-6}
PC.aa.C38.5	controls	HT	2.330352069	1.94959×10^{-5}
SM.C24.1	controls	HT	2.286497476	1.03295×10^{-5}
SM.C18.0	controls	HT	2.254098795	1.37211×10^{-7}
PC.aa.C40.6	controls	HT	2.235902323	2.02544×10^{-6}
PC.aa.C34.1	controls	HT	2.162178595	1.26346×10^{-6}
SM.C16.1	controls	HT	1.939967921	1.59859×10^{-5}
SM.C16.0	controls	HT	1.929180292	1.67982×10^{-5}
PC.aa.C32.1	controls	HT	1.893584951	2.32902×10^{-6}
PC.aa.C34.3	controls	HT	1.621706394	4.01834×10^{-6}
PC.aa.C36.5	controls	HT	1.561174879	1.47071×10^{-6}
PC.aa.C36.3	controls	HT	1.466726329	3.27657×10^{-5}
As	controls	HT	1.354226923	2.34859×10^{-6}
PC.aa.C32.0	controls	HT	1.321623991	1.37967×10^{-7}
PC.aa.C40.5	controls	HT	1.292471945	7.61078×10^{-7}
PC.aa.C38.1	controls	HT	−1.265456573	2.0985×10^{-6}
Cd	controls	HT	1.234674307	1.31768×10^{-9}
PC.aa.C32.2	controls	HT	−1.199293026	4.01834×10^{-6}

The Manhattan plot illustrates the −log10 adjusted *p*-values from the Mann–Whitney–Wilcoxon test to compare the concentrations of analyzed chemical compounds between the patient groups studied. The dashed red and blue lines delineate the thresholds for adjusted *p*-values at 0.05 and 0.01, respectively. Additionally, only those points representing statistically significant comparisons have been annotated with labels on the plot.

The pathway activity network analysis highlights several key lipid metabolic reactions that differentiate HT patients from healthy controls (Figure 7). The conversion of lysophosphatidylcholine (LPC) to phosphatidylcholine (PC), with a pathway score of 4.035, is mediated by the genes LPCAT1, LPCAT2, LPCAT3, LPCAT4, MBOAT1, and MBOAT2, indicating increased activity in HT. The conversion of sphingomyelin (SM) to PC, with a score of 2.297, involves SGMS1 and SGMS2, showing activation in HT. Conversely, the conversion of PC to SM, with a negative pathway score of −2.782, also involves SGMS1 and SGMS2, indicating inhibition. The reaction from PC to LPC, with the most negative score of −4.596, involves a large array of genes, including ABHD3, JMJD7-PLA2G4B, PLA2G10, PLA2G12A, PLA2G12B, PLA2G15, PLA2G1B, PLA2G2A, PLA2G2C, PLA2G2D, PLA2G2E, PLA2G2F, PLA2G3, PLA2G4A, PLA2G4B, PLA2G4C, PLA2G4D, PLA2G4E, PLA2G4F, PLA2G5, PLA2G6, PLAAT1, PLAAT2, PLAAT3, PLAAT4, PLB1, PNPLA2, PNPLA3, PNPLA4, and PNPLA8, showing significant inhibition of this pathway in HT. These findings suggest specific disruptions in lipid metabolism that are distinct in HT.

Table 5. Summary of lipids and toxic elements distinguishing autoimmune and non-autoimmune HT from controls. The table displays the top 20 lipids and toxic elements, ranked by absolute log fold change (logFC), comparing controls with autoimmune and non-autoimmune HT.

Chemicals	Comparisons		logFC	padj
PC.aa.C38.6	autoimmune_HT	controls	−2.801529125	0.000783075
PC.aa.C36.4	autoimmune_HT	controls	−2.76501264	0.000128351
PC.aa.C34.2	autoimmune_HT	controls	−2.71255371	9.24707×10^{-5}
PC.aa.C36.4	controls	non_autoimmune_HT	2.647693225	0.001373544
PC.aa.C34.2	controls	non_autoimmune_HT	2.626738818	0.000905786
PC.aa.C38.6	controls	non_autoimmune_HT	2.514758915	0.035409203
PC.aa.C38.5	autoimmune_HT	controls	−2.421935645	0.0004787
SM.C18.0	autoimmune_HT	controls	−2.421344404	1.02889×10^{-6}
SM.C24.1	autoimmune_HT	controls	−2.36087846	0.000132443
PC.aa.C40.6	autoimmune_HT	controls	−2.355839891	9.24707×10^{-5}
PC.aa.C34.1	autoimmune_HT	controls	−2.269229324	6.00058×10^{-5}
PC.aa.C38.5	controls	non_autoimmune_HT	2.213697601	0.003754317
SM.C24.1	controls	non_autoimmune_HT	2.193069239	0.004835913
SM.C16.1	autoimmune_HT	controls	−2.092035671	0.000117817
SM.C16.0	autoimmune_HT	controls	−2.086614683	0.00114639
PC.aa.C40.6	controls	non_autoimmune_HT	2.079498496	0.000866283
SM.C18.0	controls	non_autoimmune_HT	2.026957117	5.23654×10^{-5}
PC.aa.C34.1	controls	non_autoimmune_HT	2.024073637	0.000680065
PC.aa.C32.1	autoimmune_HT	controls	−2.017971279	0.000113843
As	autoimmune_HT	controls	−1.80228527	7.65009×10^{-8}

Table 6. Summary of top toxic elements distinguishing autoimmune from non-autoimmune. The chemicals were ranked by absolute log fold change (logFC) concentration in both analyzed sub-groups.

Chemicals	Comparisons		logFC	padj
As	autoimmune_HT	non_autoimmune_HT	−1.263201744	0.000510539
Cd	autoimmune_HT	non_autoimmune_HT	−1.073686488	0.000510539
Ni	autoimmune_HT	non_autoimmune_HT	−1.044931292	0.018508604
Al	autoimmune_HT	non_autoimmune_HT	−0.972513698	7.7266×10^{-9}

The Lipid Reaction Network analysis, applied to lipidomics data to compare metabolic differences between hypothyroidism (HT) and controls, reveals that the critical metabolic reactions between lysophosphatidylcholine (LPC) and phosphatidylcholine (PC) are regulated differently in these groups, with certain pathways being activated in HT and inhibited in controls, and vice versa. The conversion of LPC to PC is catalyzed by lysolecithin acyltransferase (enzyme 2.3.1.23, 1-acylglycerophosphocholine O-acyltransferase), with involvement from the six genes listed above. The reverse reaction, from PC to LPC, is catalyzed by phospholipase A2 (enzyme 3.1.1.4), with 32 genes involved and listed above. These pathways play a crucial role in lipid metabolism, regulating the dynamic balance between LPC and PC. The Lipid Reaction Network analysis did not identify any additional enzymes that might be differentially affected between the analyzed groups. Additionally, we used the KEGG database to annotate genes that were estimated, based on pathway activity network analysis, to be involved in the metabolism of lipids showing differential concentrations between HT and controls (Supplementary Table S5, ST5).

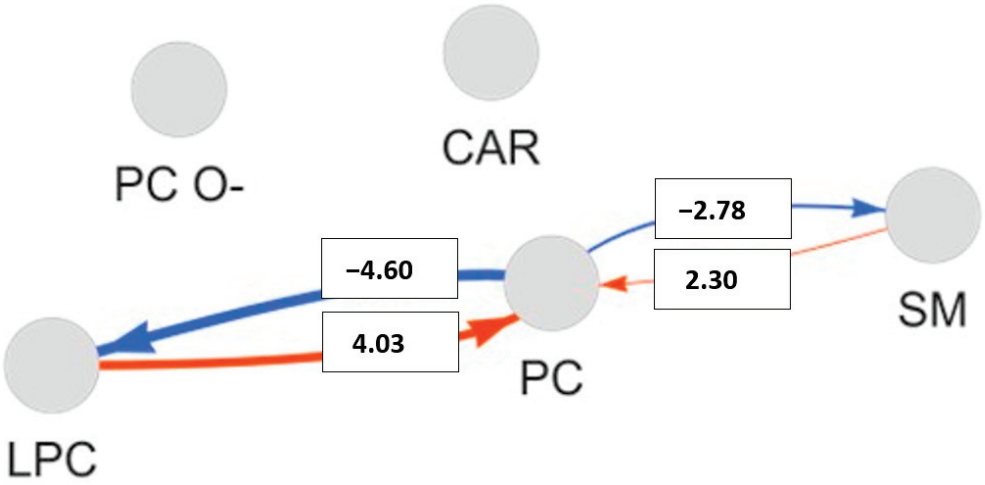


Figure 7. Pathway activity network of lipid classes comparing controls and HT. The figure depicts a pathway activity network connecting lipid classes, with nodes representing phosphatidylcholine (PC), acylcarnitines (CAR), lysophosphatidylcholine (LPC), and sphingomyelins (SM). Pathways between these lipid classes are illustrated by lines, with color-coding: red for pathways with positive activity values and blue for negative ones. The thickness and color intensity of the lines represent the frequency and strength of each pathway's activity, which is quantified by a pathway activity score.

3. Discussion

Our study demonstrates the potential of targeted lipidomics, as well as biomonitoring studies in humans, to provide valuable information on the plasma lipidomic profiles and non-occupational exposure to toxic elements of the adult hypothyroid and healthy population. In addition, we present the interrelationships between individual metabolites and toxic element content depending on the type of hypothyroidism.

Lipidomics follows the tenets of translational medicine, whose overarching goal is to transfer knowledge gained in the laboratory to everyday clinical practice. Since our aim was to focus on lipid compounds with already defined structures and important biological roles (using targeted lipidomics), we did not look for new biomarkers of hypothyroidism. Patients with both types of hypothyroidism described here manifest similar symptoms, and lipid abnormalities usually worsen during the course of the disease, regardless of the origins, although not in everyone, and not equally. Hypothyroidism is a condition that requires treatment and threatens serious health complications, including those associated with lipid disorders. This condition, as is well known, increases the risk of various cardiovascular-related diseases. Examining lipid profiles significantly accelerates the diagnosis of hypothyroidism. Normalization of thyroid hormones often also restores normal levels of plasma lipids.

Studies report that when the concentration of thyroid hormones decreases, the processes of lipolysis are impaired, and total cholesterol, LDL fraction cholesterol, triglycerides, and lipoproteins A and B often increase. On the other hand, the concentration of HDL fraction cholesterol can be both normal and reduced or increased [23]. An interesting study by Jung et al. [24] on a group of patients with differentiated thyroid cancer who underwent total thyroidectomy and radioactive iodine (RAI) treatment showed that total cholesterol, triglycerides, low-density lipoprotein cholesterol, apoB, and the apoA-I/II ratio were significantly elevated in RAI-treated patients and returned to baseline values after levothyroxine replacement. HDL-C and apoE levels were consistently elevated despite levothyroxine substitution. Paraoxonase-1 activity, adjusted for apoA-I, decreased in the overt hypothyroid state, but returned to baseline values after levothyroxine substitution. Cholesterol efflux also decreased significantly in the overt hypothyroid state, but remained low despite restoration of thyroid function. The cited study, although included only 27 patients and described acute dynamic changes in thyroid function, confirmed that changes in thyroid function are associated with changes in the concentrations of various plasma lipid

components. The current literature suggests that complex lipid metabolism abnormalities associated with hypothyroidism may involve lipid metabolism-related enzymes, receptors, and transport proteins [25].

Our study confirms that hypothyroidism is associated with important changes in the plasma lipid profile of patients beyond those already reported by other researchers regarding TSH [26], LDL-cholesterol, and TG levels [27]. Studies suggest that overt HT is a secondary cause of hyperlipidemia [28], so further insights into the human lipidome in HT patients are necessary. The use of lipidomics, and thus insights into the world of molecules such as acylcarnitines, glycerophospholipids, and sphingomyelins (overlooked in routine testing) in patients with pharmacologically balanced thyroid hormone levels, may not only help in drug selection, but may also predict some health complications. This includes also patients with Hashimoto's thyroiditis, in which thyroid autoimmune processes affect lipid metabolism by altering thyroid hormone levels [29].

Most of the effects of the thyroid hormones result from their interaction with thyroid hormone receptors (THR). A recent study by Zhang et al. highlighted the role of THR in lipid metabolism [30]. The role of THR and subsequent pathways in lipid metabolism appears complex and is still under investigation. Referring to animal studies, the authors emphasize that thyroid hormones not only directly regulate lipogenic gene expression, but also influence the activity of other transcription factors, such as sterol regulatory element binding protein-1c (SREBP1c) and carbohydrate-responsive element binding protein (ChREBP), which indirectly affect hepatic lipogenesis [31].

In addition, thyroid hormones promote lipolysis of white adipose tissue, which is a source of circulating free fatty acids (FFAs), induce the expression of protein transporters such as fatty acid transporter protein (FATP), liver fatty acid binding protein (L-FABP) and fatty acid translocase [32]. Thyroxine (T4) and triiodothyronine (T3) exert their effects by binding to specific nuclear receptors that modulate gene expression [33]. Glycerophospholipids provide the normal cell membrane structure necessary for the function of these receptors [34]. Abnormalities in glycerophospholipid levels and structure may play a role in immune recognition and response, as changes in membrane composition can potentially affect antigen presentation and immune responses [35,36]. Importantly, oxidative damage affecting, among others, glycerophospholipids leads to lipid peroxidation and the release of inflammatory molecules, which exacerbates thyroid dysfunction [37].

It should be emphasized that the prevalence of HT in patients with hyperlipidemia reaches almost 13% [38]. In many patients, worrying signs of metabolic and hormonal imbalances can go unnoticed for a long time. Recent advances in omics techniques and methodologies make it increasingly possible to link specific lipid species and metabolic pathways to disease onset and progression [39–41]. Many quantitative and qualitative changes in plasma lipid species remain undetected when simply resorting to enzymatic assays routinely performed in clinical laboratories. The quantitative determination of other important lipid compounds, such as acylcarnitines, glycerophospholipids, and sphingomyelins, can provide important information about the dyslipidemia that affects patients with HT. The carnitine system allows metabolically active fatty acids to be transported across the mitochondrial membrane and thus forms an integral part of the cell energy-producing system. More specifically, the plasma acylcarnitine profile can aid in the diagnosis of fatty acid oxidation disorders [42]. Glycerophospholipids are structural components of biological membranes, essential constituents of lipoproteins, and play key roles in several cellular processes, such as signal induction and transport [43]. Sphingomyelins have important structural and functional roles in the cell, both as components of the plasma membrane and as participants in many signaling pathways [44].

Our results suggest that many lipid species correlate with either Hashimoto's (autoimmune) or non-Hashimoto's (non-autoimmune) HT. Glycerophospholipids are present in cell membranes, influencing many cellular functions [9]. Disturbed homeostasis affects ion transport. To our knowledge, no study has described a significant association of glycerophospholipids such as phosphatidylcholines: PC ae C30:1, PC ae C36:5, or PC ae C42:0

(PC O-30:1, PC O-36:5, or PC O-42:0, respectively, in accordance with abbreviations conformed to LipidMaps standards; please see Table S1) with any disease. Recently, Dong et al. reported an association of acylcarnitines, lysophospholipids, and phosphatidylcholines with BMI and type 2 diabetes (T2D) [45]. However, there is no conclusive data that glycerophospholipids directly affect the onset and development of thyroid diseases, including non-Hashimoto's and Hashimoto's HT. Glycerolipids are key molecules for membrane formation, energy storage, and crucial intracellular signaling processes. Triacylglycerol species, essential for normal physiology, are markers of lipotoxicity. It is reported that their excessive accumulation in adipose tissue and other organs can result in obesity, insulin resistance, steatohepatitis, and cardiomyopathy [46].

Sphingolipids, including sphingomyelins, are known to be involved in cell signaling and membrane functions, and cholesterol contributes to membrane stability, fluidity, and lipid raft formation [47]. Sphingolipids contain long-chain sphingoid bases. Sphingosine, which can be formed from palmitoyl-CoA and serine, is used by cells to form ceramides, so their quantitative measurement is crucial for understanding sphingolipid metabolism [9]. Their specific involvement in thyroid diseases such as hypothyroidism, including Hashimoto's thyroiditis, has not yet been established. Available studies on the de novo synthesis of sphingolipids and the sphingomyelinase pathway concern, among other diseases, autoimmune encephalomyelitis [48] and arthritis [49]. To our knowledge, no research into the relationship between sphingomyelins and Hashimoto's disease in patients undergoing treatment with levothyroxine and in euthyroid status has been published.

Wong et al. presented the first studies to evaluate acylcarnitine species in individuals with hypo- or hyperthyroidism [50]. The authors suggested that a serum acylcarnitine profile, used as a diagnostic test for metabolic myopathies, would have similar sensitivity and specificity in patients with treated or untreated thyroid disorders. However, the power of the study was very low due to the evaluation of only 12 patients (6 with hypothyroidism) and the lack of a control group. The authors acknowledged that larger-scale studies are needed to test whether differences in the profiles of these molecules truly represent reproducible pathophysiological changes associated with a given form and/or severity of thyroid disease. As acylcarnitine is responsible for carrying out the beta-oxidation of fatty acids, one of the most important pathways for metabolic energy production [51], studies in populations with metabolic and endocrine diseases should be carried out in order to make explicit the changes identified in acylcarnitine profiles.

It is unknown whether the levels of the specific molecules such as those described above, as a result of compensating for hormonal deficiencies with a dose of synthetic hormone, also return to normal in hypothyroid patients. Future research directions that stand out in the area of hypothyroidism today focus, among other things, on understanding the detailed mechanisms of TSH involvement in lipid metabolism and its broader implications for various disorders (including, for example, neuropsychiatric) [52]. Our lipidomic study, based on a selected group of patients with normal (stabilized) TSH levels, will help other researchers widen the search for solutions to these complex mechanisms. Taking into consideration that blood plasma contains plenty of distinct lipid molecular species, searching for an explanation by conducting only partial lipid analysis (such as these tested during routine analyses) may not be sufficient. The role of individual lipid metabolites belonging to various lipid classes and how their levels change in response to hormonal therapy remain largely unknown. We consider that it would be beneficial to supplement our studies with research into other thyroid diseases and various treatments for their pathologies, which could provide in-depth insights into thyroid metabolism and pathogenesis.

Both the synthesis, transport, and metabolism of thyroid hormones can be modified by various toxic substances, which can disrupt the functioning of hormone receptors and contribute to the development of autoimmunity [53]. It is shown that some toxic elements (including Al, Pb, As, Cd, and Ni determined in our study) are capable of interfering with

hormone action and have been recognized to impact thyroid function and health a long time ago [54].

Our study shows the content of toxic elements in people with normal levels of fT3, fT4, and TSH in relation to health and disease state, suggesting the great importance of small trace levels of the toxins analyzed. As we have shown the hormonal changes are not out of the norm at the plasma concentrations of Al, As, Cd, Pb, and Ni we detected, but the effects of these toxic elements on the lipidome are revealed even at such low concentrations. To our knowledge, the present study is the first to demonstrate a significant association between multiple components of the human lipidome and toxic substances in both non-autoimmune and autoimmune HT. Exposure to toxic trace elements, such as Cd, As, Al, Pb, and Ni, is a public health problem worldwide, so they were determined in samples collected from all participants in our study. A considerable body of evidence documents the deleterious human health effects of toxic trace elements and although high levels of several metals have been linked to different disease processes, the exact mechanisms underlying many of these conditions are not completely understood [55–57]. It is known that toxic trace elements can substitute essential elements in the body (e.g., Ca may be substituted by Pb or Al, Zn by Cd, etc.) [58], inhibit the activity of various enzymes, and induce the production of oxidative stress through increased formation of free radicals and other reactive species [59]. Thus, toxic trace elements can affect all organs, mainly the heart, kidneys, liver, lungs, and nervous system, through DNA damage, lipid peroxidation, and protein sulfhydryl depletion [60]. Membrane phospholipids, containing high levels of polyunsaturated fatty acids, are predominantly susceptible to peroxidation damage [61]. It should be noted that chronic low-level exposure to many toxic metals has been associated with an increased risk for the same health problems found in individuals occupationally exposed to much higher levels [62]. Some epidemiological data highlight the association of exposure to toxic metals with dyslipidemia and a particularly increased risk of cardiovascular diseases [59]. Research on blood lipid profile abnormalities in Cd-exposed workers in China revealed that high concentrations were associated with an increased prevalence of dyslipidemia [63]. The accumulation of Cd in hepatocytes can inhibit the activity of gluconeogenesis enzymes, which affects lipid synthesis pathways and consequently blood lipid profiles [64]. Excessive hepatic gluconeogenesis promotes excessive lipid synthesis in insulin-resistant hepatocytes and is an important factor in the development of dyslipidemia [65]. Rats exposed to Cd exhibited progressive dyslipidemia characterized by increased serum levels of FFA, TC, VLDL and LDL fractions, and decreased HDL fraction. The reported results have shown features similar to human metabolic syndrome [66].

The effects of As exposure were also studied in rats, and a decrease in HDL-C and HDL-C/LDL-C ratio was observed, with an increase in TG, TC, and LDL-C [67]. Arsenic is known to generate reactive oxygen species (ROS), resulting in oxidative stress, which causes DNA damage, alters ion channel function, and increases lipid peroxidation. In addition, As affects the lipolysis process through G-protein-coupled receptors by activating hormone-sensitive lipase, decreasing lipid storage, and increasing plasma lipids, further promoting atherosclerosis and cardiovascular disease [68]. Results from animal studies have shown significant effects of arsenic on cholesterol and lipid metabolism, while suggesting that arsenic-induced health effects may be attenuated by modulation of the gut microflora [69]. Interestingly, the composition of the gut microbiota affects the availability of essential micronutrients such as iodine, selenium, and iron for the thyroid gland. Moreover, gut microbial imbalance (dysbiosis) may promote autoimmune diseases such as autoimmune thyroid disease [69]. Unfortunately, so far we have not found human studies supporting a link between arsenic exposure and dysbiosis in people with thyroid diseases.

Lead can induce the synthesis of ROS, which results in oxidative stress in the cell, decreasing the levels of antioxidants and cytosolic calcium. Pb exposure upregulates lipid peroxidation, which is directly related to membrane tissue damage [70]. Rehman studied the potential of Pb to induce lipid peroxidation in erythrocytes, which are highly vulnerable to this damage [61]. It was found that the phospholipids composition of erythrocyte

membranes was highly affected by Pb exposure. It has been reported that, in battery manufacturing workers, increased TC/HDL-C and LDL-C/HDL-C ratios were associated with Pb exposure, which in turn led to an increased risk of cardiovascular diseases in that population [9].

Aluminum interference with iron-dependent enzymatic activities in the tricarboxylic acid cycle and electron transport chain results in decreased mitochondrial ATP production, contributing to iron-mediated oxidative stress and lipid peroxidation. This and the modulation of α-ketoglutarate and L-carnitine disrupt lipid metabolism, leading to dyslipidemia. The effect of Al exposure on glycolysis causes, among other effects, fat accumulation and an increase in the pro-inflammatory response. Metalloestrogenic properties have been attributed to Al, as it can modulate estrogen receptors [71]. Studies suggest that Al increases lipid biosynthesis and secretion. Furthermore, it hinders the normal physiological estrogen pathway, leading to severe dyslipidemia [72].

Nickel exposure can induce oxidative stress by inducing ROS production in cells, and ROS causes lipid peroxidation. This process damages cell membranes and alters lipid composition, disrupting lipid metabolism. Lipid peroxidation products can further exacerbate oxidative stress and inflammation, further contributing to lipid dysregulation [73]. Polyunsaturated fatty acids are especially susceptible to this damage [74]. The association between Ni exposure and blood lipids in humans remains largely unclear, and studies on the effect of Ni on human blood lipids are still scarce [75]. According to Wang et al., who identified BMI as an important indicator of the relationship between exposure to Ni and serum lipid profiles (TC, non-HDL-C, and TC/HDL-C ratio) in humans, Ni can block key sulfhydryl groups of enzymes involved in fatty acid synthesis, thus inhibiting their activity [76]. Recent studies in the NHANES general population have indicated a linear association of Ni exposure with serum TC and LDL-C, and a nonlinear association with HDL-C [77]. Nickel exposure can trigger an inflammatory response in the cells and tissues. It can activate signaling pathways involved in inflammation, such as nuclear factor kappa B (NF-κB) and mitogen-activated protein kinase (MAPK) [78]. These molecules, released in response to Ni exposure, may interfere with cellular processes, including those related to lipid metabolism, by inhibiting insulin signaling, promoting lipogenesis, and impairing lipid oxidation, but no data are available at present. Ni exposure can also interfere with lipid-derived signaling molecules, such as prostaglandins and leukotrienes, and induce inflammation [79].

Considering all the available toxicological evidence and the ubiquity of toxic metals in the human environment, future directions of research on toxic metals and other toxins affecting the thyroid gland are aimed at identifying their harmful effects, developing risk assessment methods, and explaining the mechanisms of action in populations exposed to the frequent complications of comorbidities. Our study contributes to the understanding of lipid disorders in hypothyroid patients and should be replicated on a larger number of patients also with other thyroid pathologies, preferably at different time points.

Strengths and Limitations of the Study

This study represents a valuable approach to clarify possible links between lipid metabolism, toxic trace elements exposure, and hypothyroidism. In addition to the compounds currently analyzed for the purposes of clinical diagnosis and monitoring of dyslipidemias (i.e., triglycerides, cholesterol), human plasma contains thousands of other lipid molecular species, such as acylcarnitines, glycerophospholipids, sphingolipids, etc. Lipidomics studies, such as the one presented here, will contribute to deepening the understanding of the functions of different lipids in normal physiological conditions as well as their association with specific diseases. We have identified significant differences in both plasma lipidome and toxic element content in HT patients compared with healthy subjects, as well as in different subtypes of autoimmune and non-autoimmune HT. Our results demonstrate that plasma lipidomic studies can further contribute to the understanding of complex metabolism in HT.

A strength of the work was the fulfillment of strict criteria for the qualification of participants. The patient group and control group were well matched regarding age and BMI and there were also no statistically significant differences between groups in the serum levels of TC, LDL-C, HDL-C, and TG. Furthermore, common comorbidities most often associated with hypothyroidism, such as insulin resistance, diabetes, and cardiovascular disease, were excluded and it was also ensured that there were well-controlled levels of thyroid hormones in the patient group, thus allowing us to assume that lipidome changes observed are typical of hypothyroidism itself, even when therapeutically compensated.

We also addressed the issue of important metabolic pathways in the context of hypothyroidism. The key pathways include those related to lipid metabolism (e.g., glycerophospholipids, linoleic acid, and ether lipid metabolism), as thyroid hormones regulate lipid synthesis and degradation [80]. Hormonal pathways, such as ovarian steroidogenesis, GnRH, and oxytocin signaling, are also important due to the hormonal imbalances often observed in thyroid dysfunction [81]. In addition, pathways such as MAPK and Ras signaling are important because they are involved in metabolism and cell growth, which can be influenced by thyroid hormone levels in certain cell types [82]. Pathways related to the immune system (e.g., Fc gamma R-dependent phagocytosis) may be important, especially in the context of autoimmune thyroid diseases [83–85]. Moreover, processes such as mitochondrial biogenesis, membrane transport, and lipid biosynthesis are crucial, as thyroid hormones play a significant role in regulating cellular energy production, membrane integrity, and the synthesis of essential lipids [80,86,87]. Pathways related to acylglycerol degradation and triacylglycerol biosynthesis are critical for lipid homeostasis, as thyroid hormones regulate the breakdown and synthesis of fats [80]. Ferroptosis, a form of cell death caused by iron-dependent lipid peroxidation, is not directly related to hypothyroidism; however, thyroid cancer, lipid, and iron metabolism disorders may sensitize cells to this process, especially under conditions of oxidative stress associated with thyroid dysfunction [88].

When it comes to the relationship between toxic trace elements and hypothyroidism it is an area of growing research interest. Exposure to these elements has been associated with various adverse health effects, including potential impacts on thyroid function. The present study is the first to demonstrate a significant association of toxic trace elements with the human lipidome profile in patients with hypothyroidism (both non-autoimmune and autoimmune forms).

Some limitations of the study are also acknowledged. First, we cannot rule out reverse causality in this cross-sectional study. Thus, whether differences in toxic trace element levels are a cause or consequence of hypothyroidism and changes in the lipidome is an open question. Second, we collected data at a single time point. Thus, the data (level of toxic trace elements and lipid profile) reflect the current patient's status while hypothyroidism generally develops slowly, often with an evolution of several years. Third, potential confounders, such as other chemicals, may have influenced the observed associations. Future research should address the identified limitations.

In our study, we determined lipid molecules in human plasma and also used this biological specimen to determine selected toxic trace elements. We are aware that most of the elements analyzed are usually measured in whole blood samples (not plasma). However, for example, for Pb, some studies suggest that plasma levels may better reflect the toxicologically labile fraction of circulating Pb, which will be more available for exchange with target tissues, than Pb levels in whole blood [89].

In most cases, human biomonitoring does not distinguish between natural and human-caused sources, but it is a reliable tool for assessing human exposure to chemicals from different sources, through different pathways, and at specific times in life [90]. Current data on biomonitoring of the general population in Poland, aimed at establishing baseline concentrations of the chemical elements in the Polish population and tracking trends in concentrations over time, are not available. Our measurements do not indicate the source or route of exposure to a given chemical element. The content we measured represents

the amount that entered the body through any or all routes of exposure (such as ingestion, inhalation, or skin contact) and from any or all sources (such as water, air, soil, food, and consumer products). It should be emphasized that the presence of Al, As, Ni, Cd, and Pb in the human body may result from exposure to a single source or multiple sources. Any exposure assessment in future studies should include consideration of the size and nature of exposed populations, as well as the magnitude, frequency, duration, and routes of exposure.

4. Materials and Methods

4.1. Patients and Control Group

The study protocol received ethical approval from the Bioethics Committee of the Medical University of Lublin (KE-0254/7/2021). Written informed consent was obtained from each participant. The study was conducted in accordance with the principles of the Declaration of Helsinki. Study participants were recruited for the project entitled "Study of endocrine disrupting substances, elemental and lipid profiles in biological fluids and tissues in people with endocrine disorders") in the period 2021–2023 at the Medical University of Lublin. One hundred and twenty participants without occupational exposure to metals were selected and assigned to two groups: the study group (n = 59), individuals diagnosed with either Hashimoto's disease (n = 32) or non-autoimmune hypothyroidism (hypo-non-Hashimoto, n = 27) according to endocrinological assessment; and the control group, consisting of 61 healthy volunteers with normal thyroid function. Participant characteristics are presented in Table 1.

Study subjects were recruited from a specialized thyroid outpatient unit observing higher frequencies of thyroid disorders than the general population. Thyroid-stimulating hormone (TSH), free T4 (fT4), free T3 (fT3), lipid profile, thyroid peroxidase antibody (TPOAb), and antithyroglobulin antibody (TgAb) were assessed to confirm autoimmune thyroiditis in patients with Hashimoto's disease. All patients, whether with Hashimoto's disease or non-autoimmune HT, were receiving thyroid hormone replacement therapy with levothyroxine tablets (Euthyrox®) at a stable dose of at least 75 μg/day for at least 1 year. A stable euthyroid state was defined as a stable serum TSH level within the reference range of 0.4–4.0 μIU/mL. LT4 doses were carefully selected (based on information such as the patient's weight, age, and other medical conditions) to maintain euthyroidism. There were no differences in TSH, fT4, and fT3 levels between the patient group and healthy controls (see Table 1 in Section 2).

Study participants were not receiving any other medical treatment. Aware that comorbidities can significantly modify the individual metabolic profile, patients with common diseases such as diabetes, insulin resistance, liver disease, and hypertension were excluded. Participants had not taken mineral or vitamin supplements for at least three months before collecting the samples for analysis, nor did they follow any special diet beforehand. Importantly in the context of toxic metal exposure studies, none of the participants were active smokers in the six months prior to the study.

All participants (study group and control group) were residents of the same geographic area (central and south-eastern Poland, a predominantly agricultural region). None of the study participants had occupational exposure to toxic metals.

Participants were categorized by body mass index (BMI) values according to US Centres for Disease Control and Prevention (CDC) criteria for adults as "underweight", "healthy_weight", "overweight", and "obesity" [91]. Two weight groups were considered: "underweight_or_healthy weight" and "overweight_or_obesity".

4.2. Sample Collection

Blood samples (about 4 mL) were collected after overnight fasting into commercially available collection tubes (BD Vacutainer™ plastic blood collection tubes for trace element testing with K_2EDTA, Thermo Fisher Scientific, Waltham, MA, USA). Plasma was separated from cells by centrifugation for 10 min at 1800× g using a refrigerated centrifuge. Samples

were stored in plastic vials at a temperature below −80 °C. Plasma samples were used for metabolomic analysis and quantitative measurements of toxic trace elements. None of the samples showed signs of hemolysis, which could affect the measurement results.

TC and TG levels were determined with commercial enzymatic kits and HDL-C was measured by immunoassay in serum samples from routine analysis. LDL-C was calculated using the Friedewald formula: LDL-C = TC − HDL-C − TG/5 [92]. Thyroid function parameters, including free T3 (fT3; normal range: 1.5–4.0 ng/L), free T4 (fT4; normal range: 0.8–1.8 ng/dL), and TSH (normal range: 0.4–4.0 μIU/mL), were measured using an Immunoassay Analyser Alinity I (Abbott Laboratories, Abbott Park, IL, USA).

Samples from patients and controls were collected and analyzed under exactly the same conditions.

4.3. Targeted Metabolomic Analysis

Targeted Metabolomic Analysis (TMA) was used because it is an analytical approach with better quantitative analytical capabilities than untargeted approaches, where the metabolites, namely the lipid species of interest, are not predefined [93]. Quantification of a broad panel of metabolites, such as 40 acylcarnitines, 90 glycerophospholipids (phosphatidylcholines—PC, lysophosphatidylcholines—lysoPC), and 15 sphingomyelins (SM), was performed using an AbsoluteIDQ® p180 kit (Biocrates Life Sciences AG, Innsbruck, Austria). The purchased kits were stored at –80 °C and were prepared within one working day. Sample preparation was performed, following the manufacturer's recommended protocol. Blood plasma (10 μL) was pipetted onto the kit filter plate. Then, 10 μL internal standards were added and the plate was dried under a nitrogen stream. Phenylisothiocyanate was used as a derivatization reagent and the samples were then dried again under a nitrogen stream. Metabolites were extracted using 5 mM ammonium acetate in methanol. After dilution, the samples were introduced by direct flow injection analysis (FIA, injection volume: 20 μL) and analyzed using a triple quadrupole mass spectrometer (6470 QQQ triple quadrupole, Agilent Technologies, Santa Clara, CA, USA). FIA-ESI-MS/MS (QQQ) was performed in positive ion mode. The automation of the flow injection was realized with HPLC equipment (Agilent 1290 Infinity II LC system).

Acquisition methods were set as recommended by the AbsoluteIDQ® p180 kit. Data acquisition was performed by MassHunter Data Acquisition for LC/TQ B.10.0 (Agilent Technologies) and data analysis was performed using MetIDQ™ (Biocrates) and Mass Hunter Quantitative Analysis v.10.2 software (Agilent Technologies). Metabolite concentrations were calculated using internal standards and reported in μM/L. Analytical specifications of AbsoluteIDQ® p180, including analytical performance characteristics, were provided by the manufacturer [94]. Table S6 lists the limits of detection (LODs) of all the lipid species determined in our study.

4.4. Determination of Toxic Elements

For trace element analysis, plasma samples were subjected to acid mineralization in an ETHOS™ UP high-performance microwave digestion system (Milestone, Sorisole, Italy) equipped with the SK-15 easyTEMP high-pressure rotor (PTFE-TFM vessels). After thawing, the samples were homogenized by sonification (15 min) and vortexing (30 s). Then, 0.5 mL of plasma sample were mineralized with 3.5 mL of nitric acid 65% (Suprapur® grade, Supelco®, Merck, Darmstadt, Germany) and 1.5 mL of deionized water (DI water, conductivity <0.08 μS/cm, obtained with an HLP10 system, Hydrolab, Poland). After mineralization, samples were diluted to a final volume of 7 mL with DI water. Solutions were stored at 4 °C until analysis by ICP-MS. Calibration standard solutions were prepared from individual single element standards (1.000 mg/L, TraceCERT®, Sigma-Aldrich Production GmbH, Buchs, Switzerland), and calibration curves were obtained in the range of 0.2–50 μg/L. All solutions were prepared in freshly decontaminated plastic tubes (nitric acid and DI 1:1 at least three times). The concentration of Al, Ni, As, Cd, and Pb was determined with an XSeries 2 ICP-MS instrument (Thermo Fisher Scientific, Bremen,

Germany) equipped with a collision/reaction cell operated using 7% H_2/He gas mixture (Linde Gaz Polska, Kraków, Poland), an ASX-510 autosampler (CETAC, Omaha, NE, USA) and the PlasmaLab software version 2.6.1.335 (Thermo Fisher Scientific, Waltham, MA, USA). Each sample was analyzed in triplicate. The confirmation of linearity was performed based on the lack-of-fit test and regression model test using ANOVA. The limit of detection (LOD) of the method was calculated based on a 3 × standard deviation of 100 analytical blanks. Analytical accuracy was checked using certified reference material (CRM) with the serum matrix (Seronorm Trace Elements serum L2, Sero, Billingstad, Norway) with certified concentrations of analyzed elements. Additional non-matrix matched CRMs—EP-H-2 (EnviroMAT Drinking Water), and EU-H-3 (EnviroMAT Waste Water) (SCP Science, Quebec, ON, Canada)—were applied for validation of the analytical procedure. The concentrations found were in good agreement with the certified values. Recoveries were in the range of 95–110%. Table S7 lists the limits of detection (LODs) of all the toxic elements determined in our study.

4.5. Data Analysis and Statistical Methods

For the imputation of values below the LOQ, the following approach was adopted: values below the LOD were set to 0, acknowledging that such values fall below the detection capability of the measurement method. For values that fell between the LOD and LLOQ, the mean of the values within this range (greater than LOD but less than LLOQ) was computed and used for imputation. This mean value replaces missing values or those within the specified range, ensuring that the imputed data reflect a conservative estimate of concentration, grounded in the observed data distribution. This methodological choice aims to maintain the integrity of the dataset while addressing the challenges posed by values that are not quantifiable within the established analytical range.

4.5.1. Principal Component Analysis

The prcomp function in the R stats package v. 3.6.2 (with centered data and "scale". set as TRUE, so that data are standardized) was used to conduct PCA. Visualization of PCA results was performed using the factoextra R package. Loading scores, correlating the analyzed variables with principal components, were calculated and their absolute values were assessed to gauge each variable's contribution. Variables exceeding a predefined threshold (the cut-off value for the absolute loading scores was 0.15 for glycerophospholipids and 0.25 for the other groups of lipids and analyzed trace elements) for the first two components (PC1 and PC2) were selected as having significant contribution. The goal was to focus on the features that most explain the variance captured by these components, as they typically contain the bulk of the information in the dataset. This approach improves the interpretability and efficiency of PCA by analyzing a reduced set of pertinent variables. The approach to determining the number of clusters, defined as the groups of data points that are close to each other in the reduced-dimensional space, in the dataset combined scree plot and K-means clustering analysis. Scree plots visually determined the variance explained for different numbers of clusters, pinpointing the "elbow" where more clusters do not noticeably improve variance explanation. This indicated that the two clusters were optimally balanced, minimizing within-cluster variance across all groups analyzed and maximizing between-cluster distinction.

The relationship between the analytical parameters evaluated (lipid compounds and toxic trace elements) and the patients' clinicopathological data was investigated. Continuous variables were analyzed using the Mann–Whitney–Wilcoxon test. Log fold change (logFC) was calculated as log((mean2+1)/(mean1+1)), with a pseudo count of 1 added to prevent division by zero. Power analysis for the Wilcoxon test was conducted using the wmwpow package, based on Shieh's method [95]. The power for a two-sided test with a 0.05 significance level was estimated via the shiehpow() function. Effect sizes were calculated using the wilcox_effsize() function from the rstatix package. Categorical variables were evaluated using the asymptotic chi-square or Fisher's exact tests, depending

on the count of observed subgroups, as described in the statistical package documentation. Enrichment, in this context, refers to the overrepresentation of certain subgroups based on demographic, clinical, and biochemical data within PCA-derived clusters. The Benjamini–Hochberg (BH) *p*-value adjustment method was employed to manage the false discovery rate for multiple comparisons. The results were considered statistically significant for adjusted *p*-values (padj) < 0.05. Data visualization and statistical analyses were performed using the ggpubr and ggplot2 R packages, version 4.1.3.

4.5.2. Monte Carlo Feature Selection and Interdependency Discovery

Data simplification with simultaneous preservation of informative features was achieved by applying feature selection through the MCFS-ID method, using the rmcfs package [96]. Default parameters with 100 permutations were set to run MCFS-ID. The algorithm identifies features that collaborate to classify objects into subclasses, exploring multidimensional dependencies between classes and features. It creates a classifier to accurately categorize objects, each described by a feature vector. The MCFS-ID algorithm ranks features based on their relevance for classification, revealing both linear and nonlinear interdependencies regardless of the classifier used. This is achieved by building decision trees from randomly selected subsets of features and objects. The relative importance of features for classification is evaluated through decision tree analysis. With enough iterations for the algorithm to converge, the most effective classification features rise to the top of the ranking, allowing the algorithm to uncover collaborative feature effects on class assignments through multidimensional analysis.

4.5.3. Pathway Analysis on the Significantly Affected Lipids

Pathway Activity Network of Lipid Classes and The Lipid Reaction Network analyses were conducted using the LipidSig 2.0 platform [97]. Initially, the Differential Expression (DE) module was employed on percentage normalized and log10 transformed data. The genes identified from the initial analysis were imputed into KEGG Mapper [98] to annotate metabolic pathways, signaling pathways, and biological processes.

5. Conclusions

Our study makes a significant contribution to deciphering the plasma lipidome precisely in people with hypothyroidism, as these are the patients who will potentially develop different manifestations of lipid disorders. A significant association between altered levels of several components of the plasma lipidome and several toxic trace elements with hypothyroidism was found. A set of 23 chemical substances have been identified that are fundamental in differentiating between healthy individuals and patients suffering from hypothyroidism. These include Al, Cd, Ni, As, and Pb, along with a large set of lipid compounds. We also identified a set of 17 different compounds and elements that were significantly different in patients depending on the type of disease: autoimmune or non-autoimmune hypothyroidism.

For several reasons, in-depth knowledge of the lipid profile of patients with hypothyroidism can be important. First, it is important for developing personalized treatment strategies that can effectively address each patient's unique needs, thereby improving overall management and outcomes in treating patients. Hypothyroidism has a significant impact on metabolic rate, which can lead to profound changes in energy expenditure and nutrient utilization. Slow metabolism in HT patients can result in rapid weight gain. Understanding the specific metabolic changes associated with hypothyroidism can help tailor dietary treatments more effectively. Second, knowledge of the lipidome profile can provide information about risk factors and potential complications associated with HT. In particular, it is well known that altered lipid metabolism can increase the risk of cardiovascular diseases, which are a common comorbidity in HT patients. Profiling metabolic changes makes it possible to pre-emptively address these risks with appropriate interventions. Finally, metabolic profiling can also be a tool to monitor treatment effective-

ness. Changes in specific metabolites can help assess the organism's response to thyroid hormone replacement therapy or other treatments, allowing for timely adjustments in management strategies.

This work also highlights the great scientific potential of modern analytical techniques such as FIA-ESI-MS/MS and ICP-MS, capable of quickly generating a huge amount of data about a biological sample, as well as the application of novel statistical approaches in the analysis of bioanalytical and clinical data. In fact, when dealing with large datasets, it is crucial to choose the appropriate statistical analysis tools to extract the most information from them. The approach we used, based on MCFS-ID, has proven to be a powerful tool for dealing with biochemical data, increasing our understanding of the mechanisms underlying diseases. Our findings should be extended and complemented with other omics data such as proteomics and genomics, which could provide a much greater understanding of thyroid dysfunction and associated lipid imbalances.

Supplementary Materials: The following supporting information can be downloaded at https://www.mdpi.com/article/10.3390/molecules29215169/s1. The article has accompanying supplementary files: Figures S1–S16 and Tables S1–S7. Supplementary Figure S1. Identification of key acylcarnitines for patient classification using PCA; Supplementary Figure S2. Identification of key glycerophospholipids for patient classification using PCA; Supplementary Figure S3. Identification of key sphingolipids for patient classification using PCA; Supplementary Figure S4. Identification of key toxic trace elements for patient classification using PCA; Supplementary Figure S5. Detailed analysis of PCA clustering of acylcarnitines for all patients; Supplementary Figure S6. Detailed analysis of PCA clustering of glycerophospholipids for all patients; Supplementary Figure S7. Detailed analysis of PCA clustering of sphingolipids for all patients; Supplementary Figure S8. Detailed analysis of PCA clustering of lipids and toxic elements for all patients; Supplementary Figure S9. Identification of key acylcarnitines for HT patient stratification using PCA; Supplementary Figure S10. Identification of key glycerophospholipids for all HT patient stratification using PCA; Supplementary Figure S11. Identification of key sphingolipids for HT patient stratification using PCA; Supplementary Figure S12. Identification of key toxic elements for HT patient stratification using PCA; Supplementary Figure S13. Detailed analysis of PCA clustering of acylcarnitines for disease-only patients; Supplementary Figure S14. Detailed analysis of PCA clustering of glycerophospholipids for disease-only; Supplementary Figure S15. Detailed analysis of PCA clustering of sphingolipids for disease-only patients; Supplementary Figure S16. Detailed analysis of PCA clustering of toxic elements for disease-only patients. Description for S1–S4 and S9–S12 figures: (A) PCA plots showing cluster analysis results. The figure presents a PCA dot plot, showing the distribution of data points along the first two principal components, PC1 and PC2. Dots are color-coded according to two distinct clusters, providing visual differentiation of the data groups based on their PCA scores. (B) PCA features. The arrow length corresponds to the square of the cosine (cos^2) values for each variable, with higher values suggesting a stronger association with the respective principal components. (C) and (D) feature bar plots of PC1 and PC2, respectively. Bar plots detailing the contribution of variables to PC1 and PC2, respectively. Viewing the dataset's structure allows the identification of compounds that most significantly influence the variance explained by PC1 and PC2. (E) PCA scree plot. The plot displays the proportion of variance explained by each principal component (Dimension), effectively mapping the contribution of each dimension. Description for S5–S8 and S13–S16 figures: Each panel consists of a PCA clustering scatter plot (on the left) alongside a normalized bar plot of a contingency table for each analyzed grouping feature, as indicated in the legend. The PCA clustering displays the first two principal components (PC1 and PC2), with events colored according to the grouping feature. The bar plot of a contingency table shows the relationship of patients grouped by PCA clusters (labeled as "Cluster") across the grouping feature. The *p*-value from Fisher's test is also displayed, allowing for the assessment of statistical significance between the groups. Supplementary Tables: Table S1. Nomenclature of lipids; Table S2. Comparative analysis of chemical compound concentrations in all patients grouped by Cohort variable using Mann–Whitney–Wilcoxon Test with *p*-value adjustment and descriptive statistics; Table S3. Comparative analysis of chemical compound concentrations in all patients grouped by Disease variable using Mann–Whitney–Wilcoxon Test with *p*-value adjustment and descriptive statistics; Table S4. Comparative analysis of chemical compound concentrations in HT patients grouped by Disease variable using Mann–Whitney–Wilcoxon Test with *p*-value adjustment and descriptive statis-

tics; Table S5. KEGG Annotated Metabolic Pathways, Signaling Pathways, and Biological Processes Differentiating Between Controls and HT; Table S6. Chemical Species Concentrations. The table presents the concentrations of the analyzed chemicals along with metadata annotations; Table S7. Limits of detection of toxic elements in plasma of the study population (N = 120); Table S8. Limits of detection of studied lipid species in plasma of the study population (N = 120). Supplementary Tables S2–S4 Description: the Mann–Whitney–Wilcoxon analysis of differences in lipids and trace elements concentration among analyzed subgroups. The *p*-values of the Mann–Whitney–Wilcoxon test (p_value) and padj (adj_p_value) are shown. The column 'Continuous_Variable' represents analyzed chemicals under analysis, while 'Subgroup_Variable' defines the subgroups being compared. 'Group1' and 'Group2' correspond to the compared subgroups, with their respective sample sizes (N1 and N2). Descriptive statistics such as median (Median_Group1, Median_Group2), mean (Mean_Group1, Mean_Group2), and standard deviation (SD_Group1, SD_Group2) are provided for both subgroups. The log fold change (logFC), Mann–Whitney statistic (Statistic), effect size (Effect_Size), and power of the test (Power) are also included. Each row corresponds to a single statistical comparison.

Author Contributions: Conceptualization, A.B.; data curation, A.B. and M.K.; formal analysis, P.S., A.T., A.K.-P. and A.S.; funding acquisition, A.B. and E.G.; investigation, A.B. and M.K.; methodology, A.B., M.K., P.S., A.T., A.K.-P. and A.S.; project administration, A.B.; resources, A.B., A.M.G., J.W. and E.G.; software, M.K., P.S., A.T. and A.K.-P.; supervision, K.S.-D.; validation, A.B., P.S., A.T. and A.K.-P.; biostatistics and data visualization, M.K.; writing—original draft, A.B., M.K. and A.M.G.; writing—review and editing, A.B., J.J. and A.A. All authors have read and agreed to the published version of the manuscript.

Funding: This study was financially supported by the Medical University of Lublin (MUL), PL (grant: DS 53/ 2021–2023/Anna Błażewicz: "Investigation of endocrine disruptors, elemental and lipid profiles in biological fluids and tissues in people with endocrine disorders"). MUL financed the purchase of chemical reagents and research materials and provided scientific equipment.

Institutional Review Board Statement: The study protocol received ethical approval from the Bioethics Committee of the Medical University of Lublin (KE-0254/7/2021). The study was conducted in accordance with the principles of the Declaration of Helsinki.

Informed Consent Statement: Informed consent was obtained from all subjects involved in the study.

Data Availability Statement: The original contributions presented in the study are included in the article/supplementary material, further inquiries can be directed to the corresponding author.

Acknowledgments: We would like to express our gratitude to all the volunteers who participated in this study and to the Directorate of the Institute of Rural Health in Lublin, Poland. We acknowledge the use of the services and facilities of the Interdisciplinary Research Center of the John Paul II Catholic University of Lublin, co-funded by the European Union from the European Regional Development Fund under the Operational Programme "Development of Eastern Poland", 2007–2013 (POPW.01.03.00-06-003/09-00).

Conflicts of Interest: The authors declare no conflicts of interest.

References

1. Franco, J.-S.; Amaya-Amaya, J.; Anaya, J.-M. Thyroid disease and autoimmune diseases. In *Autoimmunity: From Bench to Bedside [Internet]*; El Rosario University Press: Bogotá, Colombia, 2013.
2. Chaker, L.; Razvi, S.; Bensenor, I.M.; Azizi, F.; Pearce, E.N.; Peeters, R.P. Hypothyroidism. *Nat. Rev. Dis. Primers* **2022**, *8*, 30. [CrossRef] [PubMed]
3. Mavromati, M.; Jornayvaz, F.R. Hypothyroidism-Associated Dyslipidemia: Potential Molecular Mechanisms Leading to NAFLD. *Int. J. Mol. Sci.* **2021**, *22*, 12797. [CrossRef] [PubMed]
4. Feldt-Rasmussen, U.; Effraimidis, G.; Bliddal, S.; Klose, M. Consequences of Undertreatment of Hypothyroidism. *Endocrine* **2024**, *84*, 301–308. [CrossRef] [PubMed]
5. Chiovato, L.; Magri, F.; Carlé, A. Hypothyroidism in Context: Where We've Been and Where We're Going. *Adv. Ther.* **2019**, *36*, 47–58. [CrossRef] [PubMed]
6. Mincer, D.L.; Jialal, I. Hashimoto Thyroiditis. In *StatPearls [Internet]*; StatPearls Publishing: Treasure Island, FL, USA, 2023.

7. Newman, C.B.; Blaha, M.J.; Boord, J.B.; Cariou, B.; Chait, A.; Fein, H.G.; Ginsberg, H.N.; Goldberg, I.J.; Murad, M.H.; Subramanian, S.; et al. Lipid Management in Patients with Endocrine Disorders: An Endocrine Society Clinical Practice Guideline. *J. Clin. Endocrinol. Metab.* **2020**, *105*, dgaa674. [CrossRef]
8. Wu, J.H.Y.; Micha, R.; Mozaffarian, D. Dietary Fats and Cardiometabolic Disease: Mechanisms and Effects on Risk Factors and Outcomes. *Nat. Rev. Cardiol.* **2019**, *16*, 581–601. [CrossRef]
9. Han, X. Lipidomics for Studying Metabolism. *Nat. Rev. Endocrinol.* **2016**, *12*, 668–679. [CrossRef]
10. Buszewska-Forajta, M.; Pomastowski, P.; Monedeiro, F.; Walczak-Skierska, J.; Markuszewski, M.; Matuszewski, M.; Markuszewski, M.J.; Buszewski, B. Lipidomics as a Diagnostic Tool for Prostate Cancer. *Cancers* **2021**, *13*, 2000. [CrossRef]
11. Kim, E.J.; Ramachandran, R.; Wierzbicki, A.S. Lipidomics in Diabetes. *Curr. Opin. Endocrinol. Diabetes Obes.* **2022**, *29*, 124–130. [CrossRef]
12. Chew, H.; Solomon, V.A.; Fonteh, A.N. Involvement of Lipids in Alzheimer's Disease Pathology and Potential Therapies. *Front. Physiol.* **2020**, *11*, 598. [CrossRef]
13. van Vliet, N.A.; Bos, M.M.; Thesing, C.S.; Chaker, L.; Pietzner, M.; Houtman, E.; Neville, M.J.; Li-Gao, R.; Trompet, S.; Mustafa, R.; et al. Higher Thyrotropin Leads to Unfavorable Lipid Profile and Somewhat Higher Cardiovascular Disease Risk: Evidence from Multi-Cohort Mendelian Randomization and Metabolomic Profiling. *BMC Med.* **2021**, *19*, 266. [CrossRef] [PubMed]
14. Li, X.; Wang, Y.; Guan, Q.; Zhao, J.; Gao, L. The Lipid-Lowering Effect of Levothyroxine in Patients with Subclinical Hypothyroidism: A Systematic Review and Meta-Analysis of Randomized Controlled Trials. *Clin. Endocrinol.* **2017**, *87*, 1–9. [CrossRef] [PubMed]
15. Lee, H.-C.; Yokomizo, T. Applications of Mass Spectrometry-Based Targeted and Non-Targeted Lipidomics. *Biochem. Biophys. Res. Commun.* **2018**, *504*, 576–581. [CrossRef] [PubMed]
16. Jiang, X.; Zhao, X.; Gu, X.; Luo, T.; Li, P.; Wan, C.; Liu, H. Serum metabolomic analysis in patients with Hashimoto's thyroiditis. *Front. Endocrinol.* **2022**, *13*, 1046159. [CrossRef] [PubMed]
17. Zheng, S.; Liu, L.; Liang, K.; Yan, J.; Meng, D.; Liu, Z.; Tian, S.; Shan, Y. Multi-omics insight into the metabolic and cellular characteristics in the pathogenesis of hypothyroidism. *Commun. Biol.* **2024**, *7*, 990. [CrossRef]
18. Chaker, L.; Bianco, A.C.; Jonklaas, J.; Peeters, R.P. Hypothyroidism. *Lancet* **2017**, *390*, 1550–1562. [CrossRef]
19. Klubo-Gwiezdzinska, J.; Wartofsky, L. Hashimoto thyroiditis: An evidence-based guide to etiology, diagnosis and treatment. *Pol. Arch. Intern. Med.* **2022**, *132*, 16222. [CrossRef]
20. Bimonte, V.M.; Besharat, Z.M.; Antonioni, A.; Cella, V.; Lenzi, A.; Ferretti, E.; Migliaccio, S. The Endocrine Disruptor Cadmium: A New Player in the Pathophysiology of Metabolic Diseases. *J. Endocrinol. Investig.* **2021**, *44*, 1363–1377. [CrossRef]
21. Abd Elnabi, M.K.; Elkaliny, N.E.; Elyazied, M.M.; Azab, S.H.; Elkhalifa, S.A.; Elmasry, S.; Mouhamed, M.S.; Shalamesh, E.M.; Alhorieny, N.A.; Abd Elaty, A.E.; et al. Toxicity of Heavy Metals and Recent Advances in Their Removal: A Review. *Toxics* **2023**, *11*, 580. [CrossRef]
22. Solnica, B.; Sygitowicz, G.; Sitkiewicz, D.; Cybulska, B.; Jóźwiak, J.; Odrowąż-Sypniewska, G.; Banach, M. 2020 Guidelines of the Polish Society of Laboratory Diagnostics (PSLD) and the Polish Lipid Association (PoLA) on Laboratory Diagnostics of Lipid Metabolism Disorders. *Arch. Med. Sci.* **2020**, *16*, 237–252. [CrossRef]
23. Duntas, L.H.; Brenta, G. A Renewed Focus on the Association Between Thyroid Hormones and Lipid Metabolism. *Front. Endocrinol.* **2018**, *9*, 511. [CrossRef]
24. Jung, K.Y.; Ahn, H.Y.; Han, S.K.; Park, Y.J.; Cho, B.Y.; Moon, M.K. Association between Thyroid Function and Lipid Profiles, Apolipoproteins, and High-Density Lipoprotein Function. *J. Clin. Lipidol.* **2017**, *11*, 1347–1353. [CrossRef]
25. Wang, X.; Wu, Z.; Liu, Y.; Wu, C.; Jiang, J.; Hashimoto, K.; Zhou, X. The Role of Thyroid-Stimulating Hormone in Regulating Lipid Metabolism: Implications for Body–Brain Communication. *Neurobiol. Dis.* **2024**, *201*, 106658. [CrossRef]
26. Delitala, A.P.; Fanciulli, G.; Maioli, M.; Delitala, G. Subclinical Hypothyroidism, Lipid Metabolism and Cardiovascular Disease. *Eur. J. Intern. Med.* **2017**, *38*, 17–24. [CrossRef]
27. Duntas, L.H. Thyroid Disease and Lipids. *Thyroid* **2002**, *12*, 287–293. [CrossRef]
28. Willard, D.L.; Leung, A.M.; Pearce, E.N. Thyroid Function Testing in Patients with Newly Diagnosed Hyperlipidemia. *JAMA Intern. Med.* **2014**, *174*, 289. [CrossRef]
29. Ralli, M.; Angeletti, D.; Fiore, M.; D'Aguanno, V.; Lambiase, A.; Artico, M.; de Vincentiis, M.; Greco, A. Hashimoto's Thyroiditis: An Update on Pathogenic Mechanisms, Diagnostic Protocols, Therapeutic Strategies, and Potential Malignant Transformation. *Autoimmun. Rev.* **2020**, *19*, 102649. [CrossRef]
30. Zhang, D.; Wei, Y.; Huang, Q.; Chen, Y.; Zeng, K.; Yang, W.; Chen, J.; Chen, J. Important Hormones Regulating Lipid Metabolism. *Molecules* **2022**, *27*, 7052. [CrossRef]
31. Wang, Y.; Viscarra, J.; Kim, S.-J.; Sul, H.S. Transcriptional Regulation of Hepatic Lipogenesis. *Nat. Rev. Mol. Cell Biol.* **2015**, *16*, 678–689. [CrossRef]
32. Santana-Farré, R.; Mirecki-Garrido, M.; Bocos, C.; Henríquez-Hernández, L.A.; Kahlon, N.; Herrera, E.; Norstedt, G.; Parini, P.; Flores-Morales, A.; Fernández-Pérez, L. Influence of Neonatal Hypothyroidism on Hepatic Gene Expression and Lipid Metabolism in Adulthood. *PLoS ONE* **2012**, *7*, e37386. [CrossRef]
33. Sinha, R.; Yen, P.M. Cellular Action of Thyroid Hormone. In *Endotext [Internet]*; MDText.com, Inc.: South Dartmouth, MA, USA, 2018.

34. Johnson, J.L.; Johnson, L.A. Homeostasis of Lipid Metabolism in Disorders of the Brain. In *Encyclopedia of Behavioral Neuroscience*, 2nd ed.; Della Sala, S., Ed.; Elsevier: Oxford, UK, 2022; pp. 372–382, ISBN 978-0-12-821636-1.
35. Sorrenti, S.; Baldini, E.; Pironi, D.; Lauro, A.; D'Orazi, V.; Tartaglia, F.; Tripodi, D.; Lori, E.; Gagliardi, F.; Praticò, M.; et al. Iodine: Its Role in Thyroid Hormone Biosynthesis and Beyond. *Nutrients* **2021**, *13*, 4469. [CrossRef]
36. Hubler, M.J.; Kennedy, A.J. Role of Lipids in the Metabolism and Activation of Immune Cells. *J. Nutr. Biochem.* **2016**, *34*, 1–7. [CrossRef]
37. Cengiz, H.; Demirci, T.; Varim, C.; Tamer, A. The Effect of Thyroid Autoimmunity on Dyslipidemia in Patients with Euthyroid Hashimoto Thyroiditis. *Pak. J. Med Sci.* **2021**, *37*, 1365–1370. [CrossRef]
38. Tagami, T.; Kimura, H.; Ohtani, S.; Tanaka, T.; Tanaka, T.; Hata, S.; Saito, M.; Miyazaki, Y.; Araki, R.; Tanaka, M.; et al. Multi-Center Study on the Prevalence of Hypothyroidism in Patients with Hypercholesterolemia. *Endocr. J.* **2011**, *58*, 449–457. [CrossRef]
39. Meikle, T.G.; Huynh, K.; Giles, C.; Meikle, P.J. Clinical Lipidomics: Realizing the Potential of Lipid Profiling. *J. Lipid Res.* **2021**, *62*, 100127. [CrossRef]
40. Munir, R.; Lisec, J.; Swinnen, J.V.; Zaidi, N. Lipid Metabolism in Cancer Cells under Metabolic Stress. *Br. J. Cancer* **2019**, *120*, 1090–1098. [CrossRef]
41. Zandl-Lang, M.; Plecko, B.; Köfeler, H. Lipidomics—Paving the Road towards Better Insight and Precision Medicine in Rare Metabolic Diseases. *Int. J. Mol. Sci.* **2023**, *24*, 1709. [CrossRef]
42. Rinaldo, P.; Cowan, T.M.; Matern, D. Acylcarnitine Profile Analysis. *Genet. Med.* **2008**, *10*, 151–156. [CrossRef]
43. Castro-Gómez, P.; Garcia-Serrano, A.; Visioli, F.; Fontecha, J. Relevance of Dietary Glycerophospholipids and Sphingolipids to Human Health. *Prostag. Leukot. Ess. Fat. Acids* **2015**, *101*, 41–51. [CrossRef]
44. Chakraborty, M.; Jiang, X.-C. Sphingomyelin and Its Role in Cellular Signaling. In *Lipid-Mediated Protein Signaling*; Advances in Experimental Medicine and Biology; Springer: Dordrecht, The Netherlands, 2013; Volume 991, pp. 1–14. [CrossRef]
45. Dong, Q.; Sidra, S.; Gieger, C.; Wang-Sattler, R.; Rathmann, W.; Prehn, C.; Adamski, J.; Koenig, W.; Peters, A.; Grallert, H.; et al. Metabolic Signatures Elucidate the Effect of Body Mass Index on Type 2 Diabetes. *Metabolites* **2023**, *13*, 227. [CrossRef]
46. Christie, W.W. Triacylglycerols: 2. Biosynthesis and Metabolism. *The LipidWeb.* 2024. Available online: https://www.lipidmaps.org/resources/lipidweb/lipidweb_html/lipids/simple/tag2/index.htm (accessed on 1 September 2022).
47. Olsen, A.S.B.; Færgeman, N.J. Sphingolipids: Membrane Microdomains in Brain Development, Function and Neurological Diseases. *Open Biol.* **2017**, *7*, 170069. [CrossRef]
48. Lee, M.; Lee, S.Y.; Bae, Y.-S. Functional Roles of Sphingolipids in Immunity and Their Implication in Disease. *Exp. Mol. Med.* **2023**, *55*, 1110–1130. [CrossRef]
49. Walter, S.; Gulbins, E.; Halmer, R.; Jahromi, N.H.; Becker, K.A.; Schottek, A.; Blatti, C.; Davies, L.; Schnoeder, L.; Bertsch, T.; et al. Pharmacological Inhibition of Acid Sphingomyelinase Ameliorates Experimental Autoimmune Encephalomyelitis. *Neurosignals* **2019**, *27*, 20–31. [CrossRef]
50. Wong, S.; Hannah-Shmouni, F.; Sinclair, G.; Sirrs, S.; Dahl, M.; Mattman, A. Acylcarnitine Profile in Thyroid Disease. *Clin. Biochem.* **2013**, *46*, 180–183. [CrossRef]
51. Indiveri, C.; Iacobazzi, V.; Tonazzi, A.; Giangregorio, N.; Infantino, V.; Convertini, P.; Console, L.; Palmieri, F. The Mitochondrial Carnitine/Acylcarnitine Carrier: Function, Structure and Physiopathology. *Mol. Asp. Med.* **2011**, *32*, 223–233. [CrossRef]
52. Lekurwale, V.; Acharya, S.; Shukla, S.; Kumar, S. Neuropsychiatric Manifestations of Thyroid Diseases. *Cureus* **2023**, *15*, e33987. [CrossRef]
53. Street, M.E.; Shulhai, A.-M.; Petraroli, M.; Patianna, V.; Donini, V.; Giudice, A.; Gnocchi, M.; Masetti, M.; Montani, A.G.; Rotondo, R.; et al. The Impact of Environmental Factors and Contaminants on Thyroid Function and Disease from Fetal to Adult Life: Current Evidence and Future Directions. *Front. Endocrinol.* **2024**, *15*, 1429884. [CrossRef]
54. Li, A.; Zhou, Q.; Mei, Y.; Zhao, J.; Zhao, M.; Xu, J.; Ge, X.; Li, Y.; Li, K.; Yang, M.; et al. Thyroid Disrupting Effects of Multiple Metals Exposure: Comprehensive Investigation from the Thyroid Parenchyma to Hormonal Function in a Prospective Cohort Study. *J. Hazard. Mater.* **2023**, *459*, 132115. [CrossRef]
55. Błażewicz, A.; Wiśniewska, P.; Skórzyńska-Dziduszko, K. Selected Essential and Toxic Chemical Elements in Hypothyroidism—A Literature Review (2001–2021). *Int. J. Mol. Sci.* **2021**, *22*, 10147. [CrossRef]
56. Błażewicz, A.; Grywalska, E.; Macek, P.; Mertowska, P.; Mertowski, S.; Wojnicka, J.; Durante, N.; Makarewicz, A. Research into the Association of Cadmium and Manganese Excretion with Thyroid Function and Behavioral Areas in Adolescents with Autism Spectrum Disorders. *J. Clin. Med.* **2022**, *11*, 579. [CrossRef]
57. Błażewicz, A.; Dolliver, W.; Sivsammye, S.; Deol, A.; Randhawa, R.; Orlicz-Szczęsna, G.; Błażewicz, R. Determination of Cadmium, Cobalt, Copper, Iron, Manganese, and Zinc in Thyroid Glands of Patients with Diagnosed Nodular Goitre Using Ion Chromatography. *J. Chromatogr. B* **2010**, *878*, 34–38. [CrossRef] [PubMed]
58. Rehman, K.; Fatima, F.; Waheed, I.; Akash, M.S.H. Prevalence of Exposure of Heavy Metals and Their Impact on Health Consequences. *J. Cell. Biochem.* **2018**, *119*, 157–184. [CrossRef] [PubMed]
59. Jan, A.T.; Azam, M.; Siddiqui, K.; Ali, A.; Choi, I.; Haq, Q.M.R. Heavy Metals and Human Health: Mechanistic Insight into Toxicity and Counter Defense System of Antioxidants. *Int. J. Mol. Sci.* **2015**, *16*, 29592–29630. [CrossRef] [PubMed]
60. Renu, K.; Mukherjee, A.G.; Wanjari, U.R.; Vinayagam, S.; Veeraraghavan, V.P.; Vellingiri, B.; George, A.; Lagoa, R.; Sattu, K.; Dey, A.; et al. Misuse of Cardiac Lipid upon Exposure to Toxic Trace Elements—A Focused Review. *Molecules* **2022**, *27*, 5657. [CrossRef]

61. Rehman, S.U. Effect of Lead on Lipid Peroxidation, Phospholipids Composition, and Methylation in Erythrocyte of Human. *Biol. Trace Elem. Res.* **2013**, *154*, 433–439. [CrossRef]
62. Crinnion, W.J.; Pizzorno, J.E. *Clinical Environmental Medicine*; Elsevier: Amsterdam, The Netherlands, 2019; ISBN 978-0-323-48086-4.
63. Zhou, Z.; Lu, Y.-H.; Pi, H.-F.; Gao, P.; Li, M.; Zhang, L.; Pei, L.-P.; Mei, X.; Liu, L.; Zhao, Q.; et al. Cadmium Exposure Is Associated with the Prevalence of Dyslipidemia. *Cell. Physiol. Biochem.* **2016**, *40*, 633–643. [CrossRef]
64. Larregle, E.V.; Varas, S.M.; Oliveros, L.B.; Martinez, L.D.; Antón, R.; Marchevsky, E.; Giménez, M.S. Lipid Metabolism in Liver of Rat Exposed to Cadmium. *Food Chem. Toxicol.* **2008**, *46*, 1786–1792. [CrossRef]
65. Onyango, A.N. Excessive Gluconeogenesis Causes the Hepatic Insulin Resistance Paradox and Its Sequelae. *Heliyon* **2022**, *8*, e12294. [CrossRef]
66. Sarmiento-Ortega, V.E.; Treviño, S.; Flores-Hernández, J.Á.; Aguilar-Alonso, P.; Moroni-González, D.; Aburto-Luna, V.; Diaz, A.; Brambila, E. Changes on Serum and Hepatic Lipidome after a Chronic Cadmium Exposure in Wistar Rats. *Arch. Biochem. Biophys.* **2017**, *635*, 52–59. [CrossRef]
67. Waghe, P.; Sarkar, S.N.; Sarath, T.S.; Kandasamy, K.; Choudhury, S.; Gupta, P.; Harikumar, S.; Mishra, S.K. Subchronic Arsenic Exposure Through Drinking Water Alters Lipid Profile and Electrolyte Status in Rats. *Biol. Trace Elem. Res.* **2017**, *176*, 350–354. [CrossRef]
68. Chi, L.; Lai, Y.; Tu, P.; Liu, C.-W.; Xue, J.; Ru, H.; Lu, K. Lipid and Cholesterol Homeostasis after Arsenic Exposure and Antibiotic Treatment in Mice: Potential Role of the Microbiota. *Environ. Health Perspect.* **2019**, *127*, 97002. [CrossRef] [PubMed]
69. Fröhlich, E.; Wahl, R. Microbiota and Thyroid Interaction in Health and Disease. *Trends Endocrinol. Metab.* **2019**, *30*, 479–490. [CrossRef] [PubMed]
70. Ademuyiwa, O.; Ugbaja, R.N.; Idumebor, F.; Adebawo, O. Plasma Lipid Profiles and Risk of Cardiovascular Disease in Occupational Lead Exposure in Abeokuta, Nigeria. *Lipids Health Dis.* **2005**, *4*, 19. [CrossRef] [PubMed]
71. Gaur, A.; Nayak, P.; Ghosh, S.; Sengupta, T.; Sakthivadivel, V. Aluminum as a Possible Cause Toward Dyslipidemia. *Indian J. Occup. Environ. Med.* **2023**, *27*, 112–119. [CrossRef]
72. Mailloux, R.; Lemire, J.; Appanna, V. Aluminum-Induced Mitochondrial Dysfunction Leads to Lipid Accumulation in Human Hepatocytes: A Link to Obesity. *Cell. Physiol. Biochem.* **2007**, *20*, 627–638. [CrossRef]
73. Das, S.; Reddy, R.C.; Chadchan, K.S.; Patil, A.J.; Biradar, M.S.; Das, K.K. Nickel and Oxidative Stress: Cell Signaling Mechanisms and Protective Role of Vitamin C. *Endocr. Metab. Immune Disord. Drug Targets* **2020**, *20*, 1024–1031. [CrossRef]
74. Endale, H.T.; Tesfaye, W.; Mengstie, T.A. ROS Induced Lipid Peroxidation and Their Role in Ferroptosis. *Front. Cell Dev. Biol.* **2023**, *11*, 1226044. [CrossRef]
75. Zambelli, B.; Ciurli, S. Nickel and Human Health. In *Interrelations Between Essential Metal Ions and Human Diseases*; Metal Ions in Life Sciences; Springer: Dordrecht, The Netherlands, 2013; Volume 13, pp. 321–357. [CrossRef]
76. Wang, S.; Shan, T.; Zhu, J.; Jiang, Q.; Gu, L.; Sun, J.; Bao, Y.; Deng, B.; Wang, H.; Wang, L. Mediation Effect of Body Mass Index on the Association of Urinary Nickel Exposure with Serum Lipid Profiles. *Biol. Trace Elem. Res.* **2023**, *201*, 2733–2743. [CrossRef]
77. Chen, Z.; He, J.; Chen, L.; Wu, X.; Yu, X. Association between the Nickel Exposure and Lipid Profiles in General Population from NHANES. *Environ. Sci. Pollut. Res. Int.* **2022**, *29*, 66383–66388. [CrossRef]
78. Saito, R.; Hirakawa, S.; Ohara, H.; Yasuda, M.; Yamazaki, T.; Nishii, S.; Aiba, S. Nickel Differentially Regulates NFAT and NF-κB Activation in T Cell Signaling. *Toxicol. Appl. Pharmacol.* **2011**, *254*, 245–255. [CrossRef]
79. Hirasawa, N.; Goi, Y.; Tanaka, R.; Ishihara, K.; Ohtsu, H.; Ohuchi, K. Involvement of Prostaglandins and Histamine in Nickel Wire-Induced Acute Inflammation in Mice. *J. Biomed. Mater. Res. A* **2010**, *93*, 1306–1311. [CrossRef]
80. Jonklaas, J. Hypothyroidism, lipids, and lipidomics. *Endocrine* **2024**, *84*, 293–300. [CrossRef]
81. Brown, E.D.L.; Obeng-Gyasi, B.; Hall, J.E.; Shekhar, S. The Thyroid Hormone Axis and Female Reproduction. *Int. J. Mol. Sci.* **2023**, *24*, 9815. [CrossRef]
82. Tang, H.-Y.; Lin, H.-Y.; Zhang, S.; Davis, F.B.; Davis, P.J. Thyroid Hormone Causes Mitogen-Activated Protein Kinase-Dependent Phosphorylation of the Nuclear Estrogen Receptor. *Endocrinology* **2004**, *145*, 3265–3272. [CrossRef]
83. Perrotta, C.; Buldorini, M.; Assi, E.; Cazzato, D.; De Palma, C.; Clementi, E.; Cervia, D. The Thyroid Hormone Triiodothyronine Controls Macrophage Maturation and Functions: Protective Role during Inflammation. *Am. J. Pathol.* **2014**, *184*, 230–247. [CrossRef]
84. Montesinos, M.M.; Pellizas, C.G. Thyroid Hormone Action on Innate Immunity. *Front. Endocrinol.* **2019**, *10*, 350. [CrossRef]
85. Vargas-Uricoechea, H. Molecular Mechanisms in Autoimmune Thyroid Disease. *Cells* **2023**, *12*, 918. [CrossRef]
86. Cioffi, F.; Giacco, A.; Goglia, F.; Silvestri, E. Bioenergetic Aspects of Mitochondrial Actions of Thyroid Hormones. *Cells* **2022**, *11*, 997. [CrossRef]
87. Davis, P.J.; Davis, F.B.; Mousa, S.A.; Luidens, M.K.; Lin, H.-Y. Membrane receptor for thyroid hormone: Physiologic and pharmacologic implications. *Annu. Rev. Pharmacol. Toxicol.* **2011**, *51*, 99–115. [CrossRef]
88. Chen, S.; Diao, J.; Yue, Z.; Wei, R. Identification and validation of ferroptosis-related genes and immune cell infiltration in thyroid associated ophthalmopathy. *Front. Genet.* **2023**, *14*, 1118391. [CrossRef]
89. Smith, D.; Hernandez-Avila, M.; Téllez-Rojo, M.M.; Mercado, A.; Hu, H. The Relationship between Lead in Plasma and Whole Blood in Women. *Environ. Health Perspect.* **2002**, *110*, 263–268. [CrossRef] [PubMed]

90. WHO/EURO:2023-7574-47341-69480, Human Biomonitoring: Assessment of Exposure to Chemicals and Their Health Risks. Summary for Decision Makers. Available online: https://iris.who.int/bitstream/handle/10665/368106/WHO-EURO-2023-7574-47341-69480-eng.pdf?sequence=3 (accessed on 10 September 2024).
91. CDC Adult BMI Categories. Available online: https://www.cdc.gov/bmi/adult-calculator/bmi-categories.html (accessed on 15 July 2024).
92. Friedewald, W.T.; Levy, R.I.; Fredrickson, D.S. Estimation of the Concentration of Low-Density Lipoprotein Cholesterol in Plasma, without Use of the Preparative Ultracentrifuge. *Clin. Chem.* **1972**, *18*, 499–502. [CrossRef] [PubMed]
93. Swinnen, J.; Dehairs, J. A Beginner's Guide to Lipidomics. *Biochem.* **2022**, *44*, 20–24. [CrossRef]
94. Analytical Specifications AbsoluteIDQ® p180, AS-p180 (v10-2024) l Last Modified on 2024-07-23. Available online: www.biocrates.com (accessed on 15 July 2024).
95. Shieh, G.; Jan, S.-L.; Randles, R.H. On power and sample size determinations for the Wilcoxon–Mann–Whitney test. *J. Nonparametric Stat.* **2006**, *18*, 33–43. [CrossRef]
96. Dramiński, M.; Koronacki, J. Rmcfs: An R Package for Monte Carlo Feature Selection and Interdependency Discovery. *J. Stat. Softw.* **2018**, *85*, 1–28. [CrossRef]
97. Available online: https://lipidsig.bioinfomics.org/ (accessed on 15 October 2024).
98. Available online: https://www.genome.jp/kegg/mapper/ (accessed on 22 October 2024).

Disclaimer/Publisher's Note: The statements, opinions and data contained in all publications are solely those of the individual author(s) and contributor(s) and not of MDPI and/or the editor(s). MDPI and/or the editor(s) disclaim responsibility for any injury to people or property resulting from any ideas, methods, instructions or products referred to in the content.

biomolecules

MDPI

Article

LC-HRMS and GC-MS Profiling of Urine Free Cortisol, Cortisone, 6B-, and 18-Hydroxycortisol for the Evaluation of Glucocorticoid and Mineralocorticoid Disorders

Gregori Casals [1,2,*], María Antonieta Ballesteros [3], Angielys Zamora [4], Irene Martínez [1], Guillermo Fernández-Varo [1], Mireia Mora [5,6], Felicia A. Hanzu [5,6,*] and Manuel Morales-Ruiz [1,7]

[1] Biochemistry and Molecular Genetics Department, Hospital Clínic of Barcelona, Institut d'Investigacions Biomèdiques August Pi i Sunyer (IDIBAPS), Centro de Investigación Biomédica en Red de Enfermedades Hepáticas y Digestivas (CIBERehd), 08036 Barcelona, Spain; imartin1@clinic.cat (I.M.); gfvaro@recerca.clinic.cat (G.F.-V.); morales@clinic.cat (M.M.-R.)
[2] Department of Fundamental and Clinical Nursing, Faculty of Nursing, University of Barcelona, 08036 Barcelona, Spain
[3] Service of Clinical Analysis, Hospital Universitario Son Espases, 07210 Palma de Mallorca, Spain; antonietabv@hotmail.com
[4] Department of Clinical Biochemistry, Hospital General Universitario Gregorio Marañón, 28007 Madrid, Spain; angielys.zamora@salud.madrid.org
[5] Department of Endocrinology and Nutrition, Hospital Clinic, Institut d'Investigacions Biomèdiques August Pi i Sunyer (IDIBAPS), 08036 Barcelona, Spain; mporta@clinic.cat
[6] Department of Medicine, Faculty of Medicine and Health Science, University of Barcelona, 08036 Barcelona, Spain
[7] Department of Biomedicine, Faculty of Medicine and Health Science, University of Barcelona, 08036 Barcelona, Spain
* Correspondence: casals@clinic.cat (G.C.); fhanzu@clinic.cat (F.A.H.)

Abstract: Introduction: Urine free cortisol measurements are routinely performed to evaluate hypercortisolism. Despite their analytical inaccuracy, immunoassay-based methods are frequently used. Advances in liquid chromatography–high-resolution mass spectrometry (LC-HRMS) facilitate the incorporation of powerful diagnostic tools into clinical laboratories. In addition to its high analytical specificity and simultaneous analysis of different metabolites, accurate mass measurement allows for untargeted compound identification, which may help to identify clinically relevant metabolites or drugs. Methods: The present study aimed to validate a simple routine LC–HRMS method to quantify cortisol, cortisone, 6β-hydroxycortisol, and 18-hydroxycortisol simultaneously in human urine. Additionally, the study also validated a GC-MS method for the same steroids, evaluated their cross-reactivity with commercial cortisol immunoassays, and quantified the 24 h urine excretion in patients under clinical suspicion or follow-up for hypercortisolism. Results: The LC-HRMS method involved liquid–liquid extraction using dichloromethane, micro-LC for chromatographic separation and detection using the accurate masses of the steroids, and simultaneous high-resolution full scan acquisition. The method presented acceptable linearity, precision, and accuracy. Significant interference from 6β-hydroxycortisol and cortisone was demonstrated in the cortisol immunoassays, which impacted their reliability in the follow-up of patients with hypercortisolism and significant changes in these cortisol metabolites (i.e., due to drug-induced changes in CYP3A4 activity). Conclusion: A rapid and accurate routine LC-HRMS method was validated, which is useful for the evaluation of hypercortisolism and other disorders of glucocorticoid and mineralocorticoid metabolism.

Keywords: urine free cortisol; micro-liquid chromatography; high-resolution mass spectrometry; Cushing's syndrome; cortisone

1. Introduction

Urine free (unconjugated) cortisol measurements are fundamental in the screening and follow-up of Cushing's syndrome (CS). Despite their high analytical inaccuracy [1,2], these measurements are widely performed using immunoassay [3,4]. Recent advances in liquid chromatography–mass spectrometry (LC-MS) allow for a considerable reduction in the complexity of the analytical methods, which facilitates the incorporation of powerful diagnostic tools into routine clinical laboratories. In addition to the high analytical specificity that makes them the state-of-the-art techniques for the quantification of steroid hormones, LC-MS allows for the simultaneous analysis of different metabolites, thus providing additional information that may be clinically helpful.

Liquid chromatography–high-resolution mass spectrometry (LC-HRMS) has been associated with qualitative analysis and research, whereas liquid chromatography with tandem mass spectrometry (LC-MS/MS) has been associated with quantitative and routine analysis. However, the currently available LC-HRMS instruments have shown sensitivity and quantitative performance comparable to those of LC-MS/MS for small molecules, including steroids [5,6]. In addition, HRMS provides more accurate masses than triple-quadrupole instruments with a lower resolution. Moreover, current LC-HRMS allows for simultaneous sensitive quantitative and qualitative analyses [5–9]. Thus, high-resolution full scan acquisitions allow for untargeted compound identification, which may be helpful to identify clinically relevant metabolites or drugs. Also, metabolic phenotyping, data mining for biomarker discovery, and retrospective data analysis are advantages for clinical research. These factors, together with good versatility and increasing affordability, explain the increasing interest of clinical and research laboratories in developing analysis methods using LC-HRMS.

The aim of the present study was to validate a simple routine LC–HRMS method to quantify simultaneously the urine concentrations of cortisol, cortisone, 6β-hydroxycortisol, and 18-hydroxycortisol. In addition to the key role of urine cortisol measurements in CS, the cortisol/cortisone ratio (11β-hydroxysteroid dehydrogenase 2 (11βHSD2) activity) is a sensitive marker for the apparent mineralocorticoid excess syndrome [10] and may help to differentiate between Cushing's disease and ectopic ACTH production [11]. The 6β-hydroxycortisol/cortisol ratio is a widely used endogenous marker for CYP3A activity [12–15], and 18-hydroxycortisol levels are useful in the evaluation of primary hyperaldosteronism, especially in the diagnosis of its familial forms [10,16].

There are previously validated LC-MS/MS methods for the measurement of urine cortisol and cortisone [17–26], cortisol and 6β-hydroxycortisol [12–15,19], and 18-hydroxycortisol [27,28]. Recently, two LC-HRMS urine profiling methods included cortisol, cortisone, and 6β-hydroxycortisol [29,30]. However, to the best of our knowledge, the GC-MS method developed by Shackleton et al. [31] remains the only validated method including cortisol, cortisone, 6β-hydroxycortisol, and 18-hydroxycortisol. Therefore, our study also validated in parallel a GC-MS method based on the one developed by Shackleton et al., which was compared with the LC-HRMS method. In addition, we evaluated the cross-reactivity of the measured cortisol metabolites with commercial cortisol immunoassays and quantified the 24 h urine excretion of the four steroids using LC-HRMS in patients with clinical suspicion of hypercortisolism or in follow-up for CS.

2. Materials and Methods

2.1. Chemicals Reagents

Cortisol, cortisone, 6β-hydroxycortisol, cortisol-d4, and cortisone-d8 were purchased from Merck (Darmstadt, Germany); the 18-hydroxycortisol was from Steraloids (Newport, RI, USA); the 6β-hydroxycortisol-d4 was from Toronto Research Chemicals (North York, ON, Canada), the 18-hydroxycortisol-d4 was obtained from Cambridge Isotopes Laboratories Inc. (Andover, MA, USA). Methoxyamine hydrochloride, *N*-trimethylsilylimidazole, cyclohexane, dichloromethane, pyridine, and the certified reference material ERM-DA192 were from Merck (Darmstadt, Germany). Mobile phases A and B were obtained from

Chromsystems (reference numbers 72011 and 72002, respectively). Ultrapure water was obtained using a Millipore Milli-Q purification system.

2.2. Preparation of Stock Solutions, Working Solutions, Calibrators, and Quality Control Samples

Calibration curves were prepared in methanol as a free surrogate matrix. The analytical response differences between urine and methanol were evaluated according to a recovery assessment (Section 2.5.1). Stock solutions of each steroid were prepared at 1 g/L in methanol. Working solution was prepared by mixing and diluting the four metabolites in methanol to a final concentration of each metabolite of 1.25 mg/L. Six-point calibration curves were prepared for the calibration of both the GC-MS and the LC-HRMS methods (12.5, 50, 100, 250, 500, and 1000 µg/L). For the quality controls (QCs), two levels were prepared for both the GC-MS method (25 and 125 µg/L) and the LC-HRMS method (80 and 160 µg/L). The internal standard (IS) stock solutions of cortisol-d4, cortisone-d8, 6β-hydroxycortisol-d4, and 18-hydroxycortisol-d4 were prepared at a concentration of 0.1 g/L in methanol and stored at −20 °C. A combined IS working solution was prepared at a final concentration of 0.010 g/L for each steroid.

2.3. GC-MS

2.3.1. Sample Preparation

Prior to the GC-MS analysis, the samples were stored at −20 °C for up to 2 months. The urine samples were centrifuged (3000× *g*, 10 min), and 2 mL was extracted with 5 mL of dichloromethane already containing the combined IS (0.1 µg). After liquid–liquid extraction, the organic phase was evaporated to dryness under nitrogen, and the methyloxime–trimethylsilyl ether derivatives were formed according to two-step derivatization. First, methyloxime formation was achieved by adding 100 µL of a solution of methoxyamine hydrochloride (2% in pyridine) to them and heating them at 55 °C in a thermoblock for 60 min. Second, trimethylsilyl ethers were formed by adding 50 µL of *N*-trimethylsilylimidazole to the oximated substances and irradiating them for 2 min at 600 W in a domestic microwave (SpeedyGrill, Taurus, Oliana, Spain). After derivatization, two microliters were injected into the GC-MS instrument. The same procedure was followed with the calibrators and the QC samples.

2.3.2. Instrumentation

GC-MS analyses were performed using a Shimadzu GCMS-QP2010 Ultra instrument. The final extracts were injected in splitless mode (valve opened at 2 min) into the gas chromatograph interfaced with a mass selective detector. A total of 2 µL was injected into the chromatographic system, and three pre- and post-injection washes (in cyclohexane) were performed between injections. Chromatographic separation was achieved using a Sapiens-5MS+ capillary column (30 m × 0.25 mm internal diameter × 0.25 µm film thickness) from Teknokroma (Barcelona, Spain) with helium as the carrier gas at a constant velocity of 50 cm/s. The temperature program was set to begin at 50 °C, maintained at this temperature for 3 min, elevated at 80 °C min^{-1} to 240 °C, then increased at 2 °C min^{-1} until 290 °C, and finally maintained for 5 min at 290 °C. The total run time was 35 min. The ion source and transfer line temperatures were set to 240 °C and 280 °C, respectively. Following a 22 min solvent delay, the mass detector was operated in synchronous selected ion monitoring (SIM) mode (*m*/*z* 531, 539, 605, 608, 513, 517, 385, 389) using a dwell time of 150 ms. Identification of the analytes in the sample extracts was achieved according to the GC retention time and comparison with the reference standards. Data acquisition and processing were performed using the GCMSsolution workstation software version 4 (Shimadzu, Kyoto, Japan). Figure S1A shows a chromatogram of a urine sample. The retention times were cortisone 25.0 min, cortisol 26.1 min, 6β-hydroxycortisol 26.4 min, and 18-hydroxycortisol 30.7 min.

2.4. LC-HRMS

2.4.1. Sample Preparation

Prior to the LC-HRMS analysis, the samples were stored at −20 °C for up to 2 months. After centrifugation, the urine samples (0.5 mL) were extracted with 5 mL of dichloromethane already containing the combined IS (0.03 µg). After liquid–liquid extraction, the organic phase was evaporated to dryness under nitrogen, and the residue was reconstituted in 100 µL of the mobile phases (83% of mobile phase A, 17% mobile phase B) and transferred into an autosampler glass vial. One microliter was injected into the LC-HRMS instrument. The same procedure was followed with the calibrators and the QC samples.

2.4.2. Instrumentation

Micro-flow LC-HRMS analyses were carried out using a Dionex UltiMate 3000 RSLC-nano system coupled to a hybrid quadrupole-Orbitrap mass spectrometer, Orbitrap Exploris 120 (Thermo Fisher Scientific, Bremen, Germany), equipped with a heated electrospray ionization (ESI) source. The analytical column was a HALO 90 Å C18, 2.7 µm, 0.3 × 100 mm (Advanced Materials Technology, Wilmington, DE, USA), connected to a Thermo Scientific Pep Map Neo Trap Cartridge Holder. The heated column compartment was at 35 °C. The mobile phase for the chromatographic separation was mixed from mobile phase A (Chromsystems, reference number 72011) and mobile phase B (Chromsystems, reference number 72002). Gradient elution of the NC pump started at 83% A with a flow rate of 10 µL/min. The flow was linearly decreased from 10 µL/min to 5 µL/min in 2 min. Then, 67% A was programmed from minute 2.0 to 4.7, followed by 63% A until minute 12. From minutes 12 to 14, 100% A was programmed. Finally, from minutes 14 to 16, the initial conditions were set (83% A, 10 µL/min). A loading pump was connected to the LC column flow with a flow rate of 100 µL/min from minute 0 to 0.25 and from minute 15 to 16. From minutes 0.25 to 15, the loading pump was not connected to the LC column, and the flow rate was 10 µL/min. The ion source was operated in both positive and negative ion mode, and the following settings were used: positive ion 3400 V, negative ion 2000 V, sheath gas 8, aux gas 2, ion transfer tube temperature 320 °C. The data were collected both in the full scan and targeted MS2 modes with the following settings. Full scan: resolution 60,000, scan range 100–600 m/z, RF Lens (%) 70. Targeted MS2 scan: protonated steroid exact masses were selected for MS/MS using 30% normalized collision energy, and the MS/MS scan was set automatically with a resolution of 15,000. Data acquisition and analysis were performed using the TraceFinder 5.1. clinical software (Thermo Fisher Scientific, Bremen, Germany). Figure S1B shows a chromatogram of a urine sample, and Table S1 indicates the retention times and quantitative ions.

2.5. Method Validation

2.5.1. Linearity of the Calibration Curves

Linearity was evaluated over a range between 12.5 and 1000 µg/L using six standards. Complete calibration curves were analyzed on 5 separate days for both methods. A 1/X weighted linear regression was used to plot the peak area ratio (steroids relative to IS) versus the corresponding concentration. An isotopic IS was used for each steroid. The slope, y-intercept, and correlation coefficient were calculated for each standard curve. A minimum value of $r^2 = 0.99$ was required to pass this validation step. Precision and accuracy versus the nominal concentration of the standards were also calculated. The back-calculated concentrations of the calibrators were acceptable when within ±15% of the nominal values. The lower limit of quantification and the upper limit of quantification were set at the lowest (12.5 µg/L) and highest (1000 µg/L) calibration standard values, respectively [32]. For the LLoQ, accuracy had to be within 100 ± 20% and the RSD below 20% [32].

The analytical responses of the four steroids were assessed to ensure that the calibration curve built in the methanol standards could be used to quantify the urine samples. The slope coefficients (α) of the 6-point steroid-spiked curves in human urine from four different

sources were compared with their respective curves in methanol. The response factors (RF) were calculated as $\alpha_{\text{spiked-urine}}/\alpha_{\text{methanol}}$. The back-calculated concentrations of the urine samples with and without RF correction were used to calculate the sum of the absolute values of the relative residuals $(C_{\text{spiked-urine}} - C_{\text{nominal}})/C_{\text{nominal}})$.

2.5.2. Accuracy and Imprecision

To evaluate the accuracy and precision of both methods, back-calculated results of multiple analyses of the two QCs and two urine samples were used. Inter-assay accuracy and precision were calculated on five different days. Accuracy was determined as the difference between the calculated concentrations of the metabolites and the theoretical concentrations of the QCs expressed as percentages following the formula $1 + ((C_{\text{obtained}} - C_{\text{theoretical}})/(C_{\text{theoretical}}))$. To pass the accuracy test, the mean values had to be within $100 \pm 15\%$ of the theoretical value. The imprecision at each concentration level was expressed as the relative standard deviation (%RSD) for each QC and urine sample, which should not exceed 15% [32]. The accuracy and imprecision of the GC-MS method for cortisol measurements were also evaluated according to analysis (n = 5) of the human serum cortisol certified reference material ERM-DA192, as this method was shown to be free of the matrix effect in the human serum samples.

The accuracy of both the GC-MS and LC-HRMS methods was also assessed by adding cortisol, cortisone, 6β-hydroxycortisol, and 18-hydroxycortisol to urine samples and comparing the expected and obtained concentrations with the formula: Accuracy (%) $= (C_{\text{observed}} - C_{\text{expected}})/C_{\text{spiked}}$.

2.5.3. The Selectivity, Carry-Over, and Stability of the Extracts and Comparison between Methods

The selectivity was investigated by analyzing 10 different human urine sources and was indicated by the absence of any endogenous interference at the retention times of the metabolites. The carry-over was evaluated by injecting 2 µL of cyclohexane (GC-MS method) or 3 µL of the mobile phase (LC-HRMS method) immediately after the injection of the higher standard on three separate occasions. The stability of the extracts in the autosampler was evaluated by reanalyzing the QC and urine samples stored inside the autosampler at ambient temperature (GC-MS) or 8 °C (LC-HRMS) for up to 72 h. Finally, ten urine samples were analyzed using both the GC-MS and LC-HRMS methods.

2.6. Process Efficiency

Due to the presence of endogenous concentrations in the blank urine, the process efficiency of the LC-HRMS method was assessed by comparing the areas of the ISs in the extracted urine samples (3 individual sources) with the areas of the non-extracted ISs according to the formula: $100 \times (A_{\text{urine}}/A_{\text{standard}})$. Three different concentrations of the ISs were evaluated (12.5, 100 and 250 µg/L).

2.7. Cross-Reactivity with Two Common Cortisol Immunoassays

The cross-reactivity of cortisone, 6β-hydroxycortisol, and 18-hydroxycortisol were determined for the Atellica IM1600 (Siemens Healthineers, Erlangen, Germany) and Liaison XL (Diasorin, Saluggia, Italy) cortisol immunoassays. Interference studies were performed in both aqueous solutions without extraction (n = 4) and the urine samples extracted with dichloromethane (n = 4). Cortisol, cortisone, 6β-hydroxycortisol, or 18-hydroxycortisol were spiked into water or normal human urine (before dichloromethane extraction) at final concentrations of 100, 300, and 500 µg/L. The cross-reactivity of each steroid in the cortisol assays in non-extracted aqueous solutions was calculated using the formula $C_{\text{spiked steroid}}/C_{\text{spiked cortisol (100 µg/L)}}$. The cross-reactivity of each steroid in the cortisol assays in the urine samples was calculated using the formula $C_{\text{spiked urine sample}} - C_{\text{unspiked urine sample}})/C_{\text{unspiked urine sample}}$.

2.8. Method Application

The cortisol, cortisone, 6β-hydroxycortisol, and 18-hydroxycortisol concentrations were measured using LC-HRMS in 24 h urine samples (n = 60) from 46 patients (23 males, 23 females, 21 to 85 years old) with clinical suspicion of hypercortisolism or with CS in follow-up. Cortisol in urine was also measured using immunoassay (Liaison), and the results were compared with those obtained using LC-HRMS using Deming regression, Bland–Altman, and *t*-student analyses. In addition, linear correlations between cortisol excretion and the excretion of cortisone, 6β-hydroxycortisol, and 18-hydroxycortisol were determined using Pearson's correlation coefficient (r). A sample with an extremely high urine cortisol excretion (8745 μg/day by LC-HRMS) was excluded from the statistical analyses. Finally, the effect of antisteroidogenic drugs on 11β-hydroxysteroid dehydrogenase and CYP3A4 activities was assessed by calculating the ratios cortisol/cortisone and 6β-hydroxycortisol/cortisol, respectively. The antisteroidogenic drugs included ketoconazole, metyrapone, and osilodrostat, which are used in patients as a medical treatment for hypercortisolism. The concentration results are expressed as means ± SEM, and p values were calculated using one-way ANOVA with Tukey's multiple comparisons test. Statistical analyses were performed using GraphPad Prism 6 (GraphPad Prism Software Inc., San Diego, CA, USA). The study was performed in agreement with the criteria of the Investigation and Ethics Committee of the Hospital Clinic (Barcelona, Spain).

3. Results

3.1. Linearity of the Calibration Curves

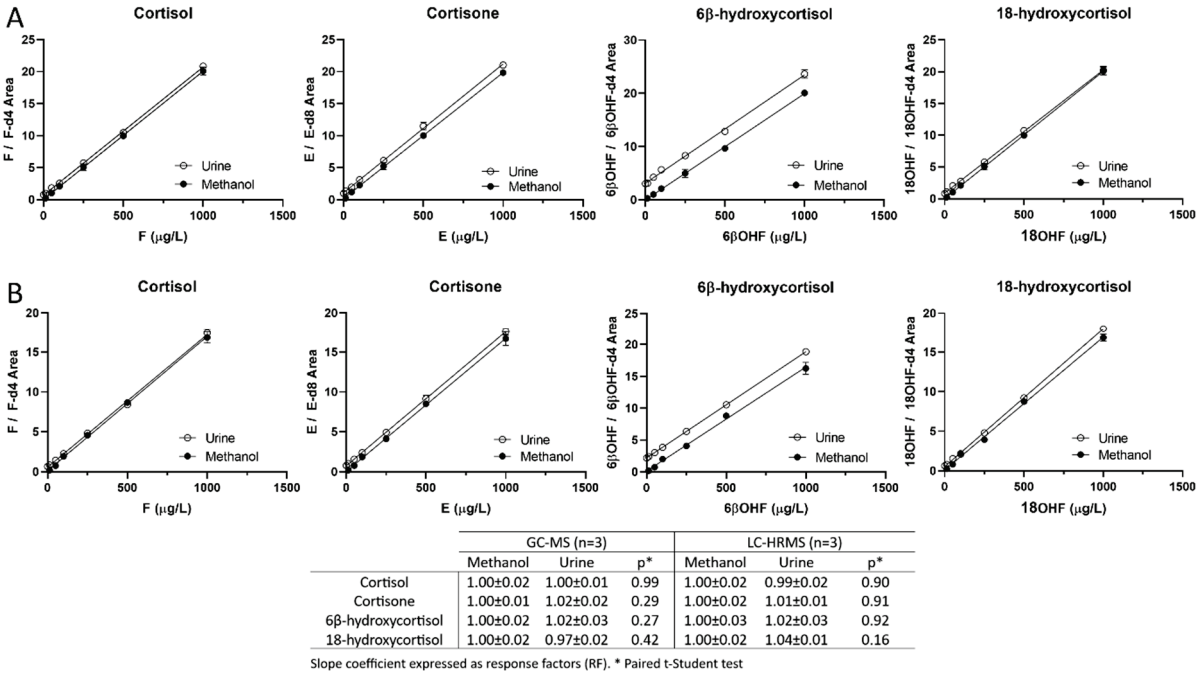
For the GC-MS quantification measurements, the SIM areas of each specific ion of the analytes and of the IS were used. Similarly, for the LC-MS quantifications, only the areas of the HRMS target ions (Table S1) were used. The MS/MS scans were not used for the LC-MS quantification. Calibration curves were prepared according to dilution of the working solution in methanol to avoid the potential bias resulting from endogenous steroids being present at different levels in the urine. Both the GC-MS and LC-HRMS methods were linear for the four steroids, obtaining r^2 values > 0.99. The calibration samples showed an accuracy ranging from 93 to 105% and from 96 to 107%, respectively, for the GC-MS and LC-HRMS methods, and the RSD was <7% (Table 1). Although isotopic ISs were used for each steroid to compensate for any variations during the sample processing, additional validation procedures were necessary to evaluate the appropriateness of the preparation of the calibrations in methanol. Experiments were performed to evaluate the differences in recoveries between the urine samples and methanolic standard solutions. As shown in Figure 1, no significant differences were observed between the slope coefficients (α) of the methanolic solutions and the steroid-spiked curves in urine. The response factors (RF) were calculated as αspiked urine/αmethanol. The implementation of RFs for the samples spiked in urine did not result in better accuracy or precision. Thus, an RF was not necessary despite using a different matrix for the calibration curves and the clinical urine samples. These results support the parsimonious approach of not compensating for different matrices.

Table 1. Inter-day accuracy and imprecision values of the calibration curve standards (n = 5 independent calibration runs). A: accuracy; RSD: relative standard deviation.

	GC-MS method							
	Cortisone		**Cortisol**		**6β-Hydroxycortisol**		**18-Hydroxycortisol**	
μg/L	A (%)	RSD (%)	A (%)	RSD (%)	A (%)	RSD (%)	A (%)	RSD (%)
12.5	98.1	4.8	92.8	6.1	93.0	6.4	95.5	5.4
50	100.3	2.2	95.4	2.2	98.5	5.0	97.7	2.2
100	102.4	1.8	103.3	2.5	103.8	4.3	105.4	1.8
250	99.2	2.1	102.1	2.3	101.2	2.6	100.8	1.7
500	100.8	1.6	97.5	1.4	97.3	2.7	101.4	0.6
1000	100.3	1.5	98.8	1.8	101.7	2.3	101.1	0.8

Table 1. *Cont.*

	LC-MS method							
	Cortisone		**Cortisol**		**6β-Hydroxycortisol**		**18-Hydroxycortisol**	
µg/L	A (%)	RSD (%)	A (%)	RSD (%)	A (%)	RSD (%)	A (%)	RSD (%)
12.5	97.2	5.9	104.2	6.1	106.8	6.8	105.3	4.2
50	102.5	4.3	98.3	5.4	95.6	4.1	96.2	3.3
100	104.3	2.7	103.0	4.1	99.1	2.2	101.8	1.9
250	98.5	2.2	98.6	1.2	99.7	2.7	101.3	3.2
500	100.5	1.8	101.2	2.5	101.0	2.1	99.5	1.6
1000	100.2	0.8	99.1	1.0	100.5	2.1	100.7	1.8



	GC-MS (n=3)			LC-HRMS (n=3)		
	Methanol	Urine	p*	Methanol	Urine	p*
Cortisol	1.00±0.02	1.00±0.01	0.99	1.00±0.02	0.99±0.02	0.90
Cortisone	1.00±0.01	1.02±0.02	0.29	1.00±0.02	1.01±0.01	0.91
6β-hydroxycortisol	1.00±0.02	1.02±0.03	0.27	1.00±0.03	1.02±0.03	0.92
18-hydroxycortisol	1.00±0.02	0.97±0.02	0.42	1.00±0.02	1.04±0.01	0.16

Slope coefficient expressed as response factors (RF). * Paired t-Student test

Figure 1. Steroid-spiked curves in human urine compared with the respective curves in methanol measured using the GC-MS (**A**) and LC-HRMS (**B**) methods. F: cortisol, E: cortisone, 6βOHF: 6β-hydroxycortisol, 18OHF: 18-hydroxycortisol. Four replicates were obtained from distinct methanol samples and an additional four from separate serum sources.

3.2. Accuracy and Imprecision

The values of the inter-assay accuracy and imprecision of the two QC levels and the values of the inter-assay imprecision of the two urine samples also met the validation requirements and are summarized in Table 2. The lowest calibrator (12.5 µg/L) was chosen for the low limit of quantification. The inter-day accuracy and RSD of the low limits of quantification also met the validation requirement: the accuracy was 93–98% and 97–107%, respectively, for the GC-MS and LC-HRMS methods, and the RSD was <7% (Table 1). In addition, the accuracy and RSD of the cortisol measurements using the GC-MS method evaluated using the human serum certified reference material ERM-DA192 were 96.8% and 5.2%, respectively (Figure S2). Finally, the accuracy was also analyzed by spiking the analytes in human urine samples. The GC-MS method presented mean accuracies ranging from 99 to 107%, obtained by processing three replicates of a urine sample spiked with 125 µg/L of each steroid (Table S2). The LC-HRMS method's mean recoveries ranged from 91 to 107%, obtained by processing three different urine samples spiked with 12.5 µg/L and 25 µg/L of each steroid (Table S3).

Table 2. Inter-day accuracy and imprecision values of quality controls and inter-day imprecision values of urine samples (n = 5). A: accuracy. RSD: relative standard deviation. QC: quality control.

	GC-MS		
	µg/L	**A (%)**	**RSD (%)**
Cortisol			
QC	25	103.2	3.2
QC	125	112.7	5.1
Urine	58	-	4.2
Urine	184	-	3.7
Cortisone			
QC1	25	100.0	5.1
QC2	125	106.5	5.1
Urine	67	-	6.3
Urine	193	-	4.6
6β-hydroxycortisol			
QC1	25	100.8	3.9
QC2	125	108.2	4.5
Urine	219	-	6.2
Urine	353	-	8.3
18-hydroxycortisol			
QC1	25	99.6	4.8
QC2	125	109.5	5.2
Urine	52	-	7.6
Urine	175	-	5.1
	LC-HRMS		
	µg/L	**A (%)**	**RSD (%)**
Cortisol			
QC	80	98.9	4.0
QC	160	95.8	4.7
Urine	18	-	9.7
Urine	106	-	3.0
Cortisone			
QC	80	99.1	4.3
QC	160	97.3	4.2
Urine	40	-	5.6
Urine	126	-	4.4
6β-hydroxycortisol			
QC	80	98.0	4.2
QC	160	96.2	3.8
Urine	86	-	5.1
Urine	168	-	2.8
18-hydroxycortisol			
QC	80	95.8	7.0
QC	160	93.8	4.7
Urine 1	40	-	10.5
Urine 2	112	-	5.5

3.3. Selectivity, Carry-Over, and Stability of the Extracts and Method Comparison

The analysis of 20 different human urine samples revealed the endogenous presence of the four analytes in all the samples. However, no additional interfering signals were observed. Similar ion ratios were observed between the quantification ions and two other main ions. In addition, there were no carry-over effects after injecting blank samples following an injection of a standard with the highest concentration. The extracts in the autosampler at ambient temperature (GC-MS) or 8 °C (LC-HRMS) were stable for at least 72 h, except for 18-hydroxycortisol measured using LC-HRMS, which was stable for up to 24 h (Table S4). Finally, a comparison of ten urine samples showed good agreement

between GC-MS and LC-HRMS for the four steroids without significant bias (Deming's regression slopes ranged from 0.97 to 1.02).

3.4. Process Efficiency

The values for process efficiency were determined by comparing the peak areas of the isotopically labeled ISs between the extracted urine samples and the non-extracted standards. As shown in Table S5, the average values for process efficiency at three different levels were dependent on the amount of steroid present in the urine and ranged from 47% to 75% (cortisol), 47% to 86% (cortisone), 10 to 28% (6β-hydroxycortisol), and 25 to 42% (18-hydroxycortisol).

3.5. Cross-Reactivity of Two Common Cortisol Immunoassays

Figure 2 shows the cross-reactivity of the non-extracted standards (in aqueous solution) of cortisone, 6β-hydroxycortisol, and 18-hydroxycortisol with both the Liaison (Figure 2A) and Atellica (Figure 2B) cortisol immunoassays. The Liaison immunoassay presented high cross-reactivity with 6β-hydroxycortisol, lower cross-reactivity with cortisone (<10% up to 500 μg/L), and no cross-reactivity with 18-hydroxycortisol up to 500 μg/L. The Atellica cortisol immunoassay presented significant cross-reactivity with both cortisone and 6β-hydroxycortisol (≈10% at 100 μg/L and ≈20% at 500 μg/L), whereas no-cross reactivity was observed with 18-hydroxycortisol up to 500 μg/L.

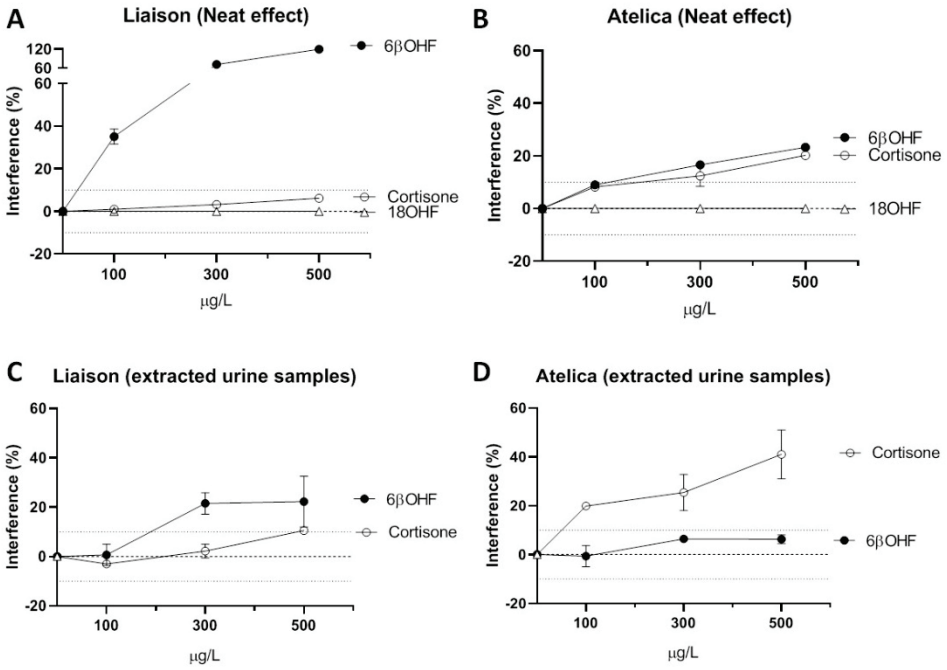


Figure 2. (**A**,**B**) Assessment of interference in urine cortisol immunoassays of varying concentrations of cortisone, 6β-hydroxycortisol (6βOHF), and 18-hydroxycortisol (18OH) standards. (**C**,**D**) Assessment of interference in urine cortisol immunoassays of varying concentrations of cortisone and 6β-hydroxycortisol (6βOHF) following addition of varying concentrations of metabolites to urine samples.

The degree of interference was also obtained in a set of urine samples prepared by spiking the same amounts of cortisone and 6β-hydroxycortisol before the extraction of the urine with dichloromethane. The liaison cortisol immunoassay showed significant interference with 6β-hydroxycortisol (cortisol results > 20% in urine samples spiked with 300 and 500 μg/L of 6β-hydroxycortisol), and also with cortisone (cortisol levels 10% higher at 500 μg/L of cortisone) (Figure 2C). In contrast, the Atellica cortisol immunoassay interfered more with cortisone (cortisol levels 20%, 25%, and 41% higher in urine samples,

respectively, spiked with 100, 300, and 500 μg/L of cortisone) than 6β-hydroxycortisol (cortisol results 6% higher in urine samples spiked with 500 μg/L of 6β-hydroxycortisol) (Figure 2D).

3.6. Method Application

Significantly higher urine cortisol results were obtained using immunoassay (Liaison) in comparison with LC-HRMS, with a mean positive bias of 82 ± 32% (Figure 3). Despite a good correlation coefficient (r^2 = 0.95), the slope of Deming's regression line was significantly different from 1 (Liaison = 1.60 × LC-HRMS + 55.3). A paired *t*-test indicated significant differences between the urine cortisol results obtained using immunoassay and LC-HRMS (238 ± 38 vs. 114 ± 24 μg/day; $p < 0.001$).

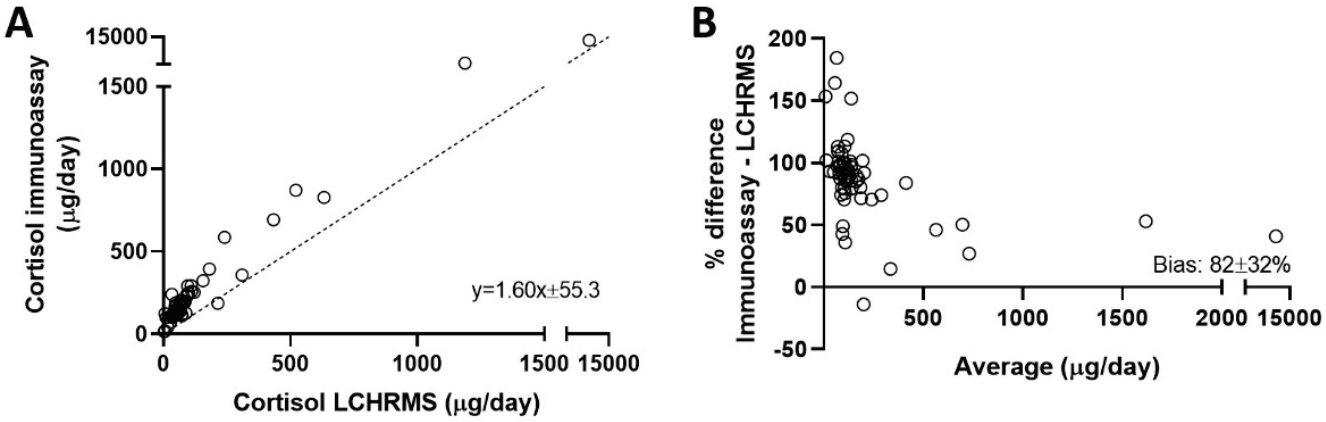
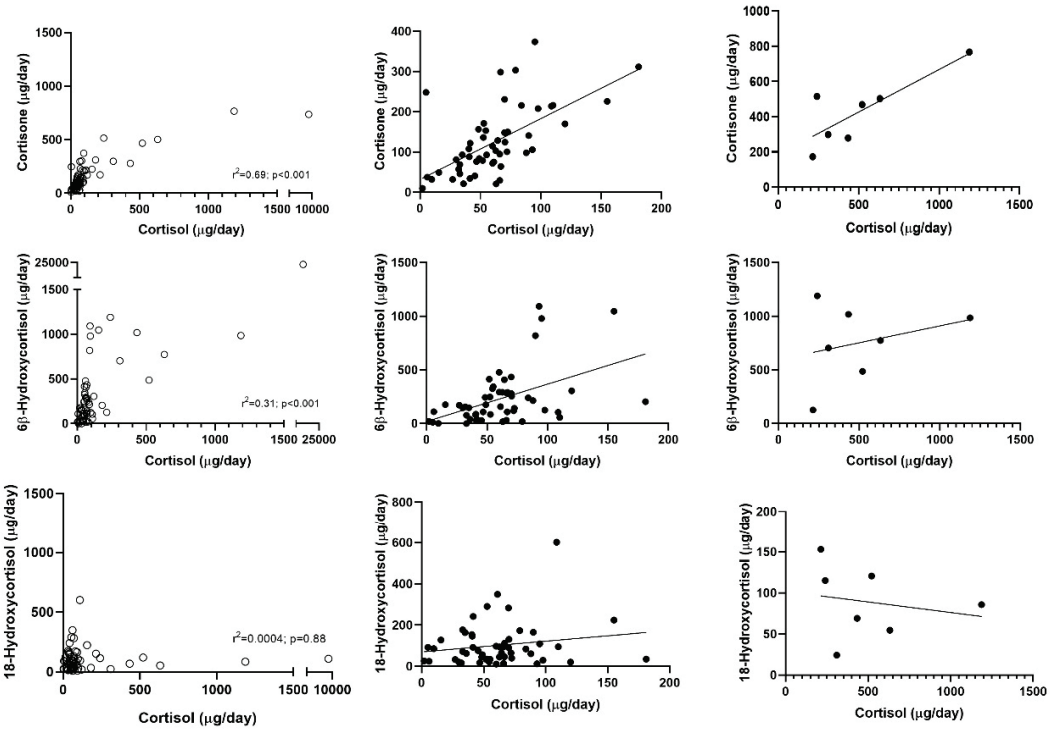


Figure 3. Deming's regression (**A**) and Bland–Altman bias (**B**) plots of cortisol in urine measured using Liaison immunoassay compared with the LC-HRMS method.

The LC-HRMS cortisol concentrations were significantly correlated with cortisone (r^2 = 0.69; $p < 0.001$) and 6β-hydroxycortisol (r^2 = 0.31; $p < 0.001$) in the whole range. However, notable differences were observed in the slope of linear regression when considering high cortisol concentrations (>200 μg/day) or lower concentrations (<200 μg/day). Thus, the slope of the linear regression of cortisol with cortisone lowered from 1.5 to 0.5, and the slope of the linear regression of cortisol with 6β-hydroxycortisol lowered from 3.5 to 0.3 (cortisol < 200 μg/day vs. cortisol > 200 μg/day) (Figure 4). In contrast to cortisone and 6β-hydroxycortisol, no significant correlation was observed between the 18-hydroxycortisol and cortisol concentrations in the urine (Figure 4).

The patients treated with antisteroidogenic drugs presented reduced CYP3A4 activity as assessed via the 6β-hydroxycortisol/cortisol urine concentration ratio. The urine of the patients without antisteroidogenic drugs (n = 41), with metyrapone (n = 12), with ketoconazole (n = 4), and with osilodrostat (n = 3) presented, respectively, 6β-hydroxycortisol/cortisol ratios of 4.1 ± 0.5, 2.2 ± 0.5, 1.5 ± 0.6, and 0.1 ± 0.1 (Figure 5A). In contrast, no differences were observed between the patients without antisteroidogenic drugs and those treated with metyrapone, ketoconazole, or osilodrostat in terms of the 11β-HSD2 activity, calculated as the ratio cortisol/cortisone, which was 0.6 ± 0.1, 0.8 ± 0.1, 0.6 ± 0.2, and 0.4 ± 0.1, respectively (Figure 5B).



x	y	n	p	Slope	p	Regression
Cortisol	Cortisone	59	<0.0001	0.64±0.06	<0.0001	y=0.64x+87.6
Cortisol <200 µg/day	Cortisone	52	<0.0001	1.51±0.27	<0.0001	y=1.51x+32.1
Cortisol >200 µg/day	Cortisone	7	0.02	0.48±0.05	0.02	y=0.48x+185
Cortisol	6β-hydroxycortisol	59	<0.0001	0.95±0.19	<0.0001	y=0.95x+187
Cortisol <200 µg/day	6β-hydroxycortisol	52	0.0004	3.48±0.91	0.0004	y=3.48x+19.6
Cortisol >200 µg/day	6β-hydroxycortisol	7	0.52	0.31±0.46	0.52	y=0.31x+596
Cortisol	18-hydroxycortisol	59	0.88	-0.01±0.07	0.88	y=-0.01x+102
Cortisol <200 µg/day	18-hydroxycortisol	52	0.22	0.52±0.42	0.22	y=0.52x+70.0
Cortisol >200 µg/day	18-hydroxycortisol	7	0.67	-0.03±0.06	0.67	y=-0.03x+102

Figure 4. Linear correlation and regression between LC-HRMS measurements of cortisol and cortisone (**top**), 6β-hydroxycortisol (**middle**), and 18-hydroxycortisol (**bottom**) across the whole range, cortisol < 200 µg/day and cortisol > 200 µg/day.

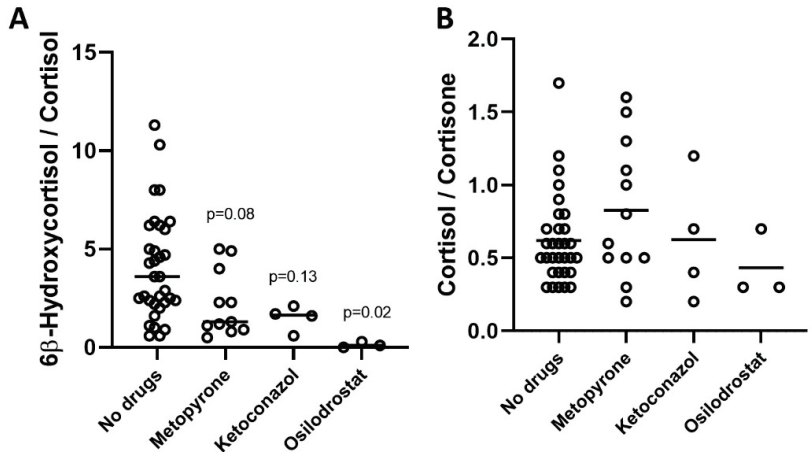


Figure 5. Ratios of 6β-hydroxycortisol/cortisol (**A**) and cortisol/cortisone (**B**) in the urine of patients without antisteroidogenc drugs and on treatment with metyrapone, ketoconazole, and osilodrostat. One-way ANOVA with Tukey's multiple comparisons test.

4. Discussion

The current study presents an accurate and reproducible LC-HRMS method for the quantification of free cortisol, cortisone, 6β-hydroxycortisol, and 18-hydroxycortisol in urine that is suitable for clinical diagnosis. On account of the high selectivity of LC-HRMS, our method uses only the exact mass (protonated) of each steroid for quantification. In addition, full scan acquisition allows us to obtain the full spectra of the analytes, together with untargeted compounds, at a high resolution, which may be helpful for detecting, for instance, synthetic steroids, the most common cause of CS [33].

The accuracy of measurements of endogenous analytes is challenging. For this reason, different approaches have been proposed to calculating the concentration of the analytes in samples, including the surrogate matrix approach [32]. Our method used liquid–liquid extraction with dichloromethane to yield clean extracts, stable isotope-labeled ISs for each compound, and HRMS m/z detection. As a result, the comparison between the calibration curves in urine and methanol showed parallel changes across the range of the method, which were linear in terms of the steroid concentrations, covering most of the expected results in CS and non-CS. Therefore, no other surrogate matrices like artificial urine were evaluated. The accuracy, precision, and recoveries of the added steroids also met the current guidelines for analysis [32]. This method includes the use of commercial mobile phases to facilitate routine implementation and the use of micro-LC results with very low volumes of the mobile phase per analytical run (<0.4 mL/sample). However, the mobile phases are part of an LC-MS kit, and their exact chemical composition has not been disclosed.

The current study also presents a GC-MS method for the quantification of the same steroids with high accuracy and precision, which correlates well with LC-HRMS. This GC-MS method is based on the previous GC-MS method developed by Shackleton et al. for the simultaneous quantification of the same four steroids [31]. Although still less straightforward than the LC-HRMS method, there are, however, some differences between our GC-MS method and the one developed by Shackleton et al. that favor its application in routine. Thus, our method takes advantage of the current commercial availability of ISs for each steroid and uses liquid– liquid extraction instead of solid-phase extraction. Both methods use a two-step derivatization procedure to form methyloxime-trimethylsilyl ethers (MO-TMS) to improve the volatility and thermal stability of the four steroids, which contain a combination of hydroxyl and ketonic groups. However, in our method, silylation is achieved using microwave irradiation, which reduces the incubation time from overnight incubation to 2 min. The feasibility and optimization of this microwave-assisted derivatization procedure, and comparison of the derivatization yields for cortisol, cortisone, and 6β-hydroxycortisol under different experimental conditions, have been previously described [34]. Our results on the evaluation of the extract stability in the autosampler (up to 72 h) also support the efficacy of this derivatization approach. Supplementary Table S6 compares the characteristics of the LC-HRMS and both GC-MS methods.

Both urine and serum were free of matrix effects in the GC-MS method, which allowed further evaluation of the accuracy of the cortisol measurements using a certified reference serum material. The Liaison immunoassay grossly overestimated the UFC concentrations compared with GC-MS, as clearly indicated by the Bland–Altman plot (Figure 3B). The inaccuracy of cortisol immunoassays for urine measurements is a well-known analytical limitation [1,2,35–37], attributed to cross-reactivity with structurally related metabolites such as tetrahydrocortisol and dihydrocortisol [36]. Therefore, we evaluated whether cortisone, 6β-hydroxycortisol, or 18-hydroxycortisol would also cross-react with two common cortisol immunoassays. The results showed the very high cross-reactivity of the Liaison immunoassay with 6β-hydroxycortisol, which greatly decreased in the extracted urine samples (Figure 2). This may be explained by the higher water solubility of 6β-hydroxycortisol, which results in a lower extraction efficiency in dichloromethane (Table S5). Despite this, the Liaison immunoassay presented cortisol results 20% higher when 6β-hydroxycortisol was added at 300 μg/L. This is a level already found in many normal urine samples since 6β-hydroxycortisol's normal excretion in urine is 3–15-fold higher than that of corti-

sol [12,13,31]. Altogether, these results show a significant bias in the Liaison immunoassay due to 6β-hydroxycortisol.

The Atellica immunoassay showed a bias produced by both the unextracted 6β-hydroxycortisol and cortisone standards. The bias produced by 6β-hydroxycortisol highly decreased (<10%) in the extracted urine samples, whereas the bias produced by cortisone remained significant after urine extraction, most likely due to the higher extraction efficiency of the latter (Table S5). Altogether, these results show significant bias in the Atellica immunoassay after dichloromethane extraction due to cortisone and evidence high differences in the cross-reactivities between immunoassays. It should be noted, however, that although mass spectrometry is the gold-standard method for measuring true cortisol, a recent meta-analysis did not observe a higher clinical sensitivity in screening for CS compared to immunoassays [3,4]. It is possible, therefore, that interfering precursors or metabolites of cortisol causing analytical inaccuracy in the immunoassays (cross-reactivity) may contribute to evaluation of the overall adrenal cortisol production.

LC-HRMS measurements of 60 urine samples of patients screened or on follow-up for CS showed good correlations of cortisol with cortisone and 6β-hydroxycortisol but not with 18-hydroxycortisol. In agreement, one sample with an extremely high level of cortisol (8745 μg/day) also presented a very high level of cortisone (737 μg/day) and 6β-hydroxycortisol (22176 μg/day) but not of 18-hydroxycortisol (110 μg/day), which may be related to the more complex metabolism of the latter [16]. The mean cortisol/cortisone ratio was 0.66 at cortisol levels < 200 μg/L and 2.1 at cortisol levels > 200 μg/L, suggesting saturation of the 11βHSD2 enzyme conversion of cortisol into cortisone at high levels of cortisol, as previously observed by Shackleton et al. [38]. A similar pattern was observed with the 6β-hydroxycortisol/cortisol ratio, which suggests a similar enzymatic effect of cortisol excess on 6β-hydroxylation. Finally, although the urine of the patients treated with steroidogenic inhibitors did not show changes in 11βHSD2 activity, a reduction in CYP3A4 activity was observed. Although the causal effect of each drug on CYP3A4 activity cannot be concluded from this study due to the small number of patients and concomitant medications, the results show that patients treated with steroidogenesis inhibitors may present with significant changes in their excretion of free steroid metabolites, as previously observed in a total steroid urine profile [39]. Although the clinical relevance of monitoring these changes in cortisol metabolism should be further assessed, the results point to a considerable impact on the follow-up of these patients if urine cortisol measurements are performed using immunoassay and support the use of mass spectrometry measurements for a proper and comprehensive evaluation of the effects.

5. Conclusions

A routine LC-HRMS method was validated for the quantitative measurement of free cortisol, cortisone, 6β-hydroxycortisol, and 18-hydroxycortisol in human urine, which is helpful for evaluating hypercortisolism and other disorders of glucocorticoid and mineralocorticoid metabolism. Simultaneous full scan acquisition allows for additional untargeted high-resolution compound detection of clinically relevant metabolites or drugs. A GC-MS method was also validated for measurement of the same steroids, and significant interference from 6β-hydroxycortisol and cortisone was demonstrated in cortisol immunoassays, which may impact their reliability for monitoring in hypercortisolism medical therapies.

Supplementary Materials: The following supporting information can be downloaded at https://www.mdpi.com/article/10.3390/biom14050558/s1, Table S1: Retention times and monitored ions of the analytes and internal standards (LC-HRMS); Table S2: Recovery of added steroids in human urine (n = 3), GC-MS method; Table S3: Accuracy of added steroids in human urine (n = 3), LC-HRMS method; Table S4: Stability in the autosampler at 8 °C (GC-MS method) and room temperature (LC-HRMS method); Table S5: Efficiency of the extraction procedure; Table S6: Summary comparison of the characteristics of the LC-HRMS and GC-MS methods validated in this study and the GC-MS method published by Shackleton et al. [31]; Figure S1: Chromatogram of urine samples measured using the GC-MS and LC-HRMS methods; Figure S2: (A) Concentration results from the cortisol

measurements of the human serum cortisol certified reference material ERM-DA192 using the GC-MS method. (B) Cortisol-spiked curves in human serum (n = 3) compared with the respective curves in methanol measured using the GC-MS method.

Author Contributions: Conceptualization, G.C. and F.A.H.; methodology, M.A.B., A.Z., I.M. and M.M.; writing—original draft preparation, G.C. and F.A.H.; writing—review and editing, M.A.B., A.Z., I.M., G.F.-V., M.M. and M.M.-R. All authors have read and agreed to the published version of the manuscript.

Funding: This research was supported by the Instituto de Salud Carlos III (PI19/00774 to G. C. and G. F.-V.) and Agencia Estatal de Investigación (PID2022-138243OB-I00 and MCIN/AEI/10.13039/501100011033/FEDER UE to MM-R), co-financed by FEDER, the European Union, "A way of making Europe"; Consolidated Research Group, Departament de Recerca i Universitats, Generalitat de Catalunya (2021 SGR 00881).

Institutional Review Board Statement: The study was conducted in accordance with the Declaration of Helsinki and approved by the Ethics Committee of Hospital Clínic de Barcelona (HCB/2019/0179).

Informed Consent Statement: Informed consent was obtained from all the subjects involved in the study.

Data Availability Statement: Data is contained within the article or Supplementary Materials.

Conflicts of Interest: The funders had no role in the design of the study, in the collection of data, or in the analyses.

References

1. Murphy, B.E.P. How much "UFC" is really cortisol? *Clin Chem.* **2000**, *46*, 793–794. [CrossRef] [PubMed]
2. Turpeinen, U.; Hämäläinen, E. Determination of cortisol in serum, saliva and urine. *Best. Pract. Res. Clin. Endocrinol. Metab.* **2013**, *27*, 795–801. [CrossRef]
3. Galm, B.P.; Qiao, N.; Klibanski, A.; Biller, B.M.; Tritos, N.A. Accuracy of Laboratory Tests for the Diagnosis of Cushing Syndrome. *J. Clin. Endocrinol. Metab.* **2020**, *105*, 2081–2094. [CrossRef]
4. Petersenn, S. Biochemical diagnosis of Cushing's disease: Screening and confirmatory testing. *Best. Pr. Res. Clin. Endocrinol. Metab.* **2021**, *35*, 101519. [CrossRef]
5. Grund, B.; Marvin, L.; Rochat, B. Quantitative performance of a quadrupole-orbitrap-MS in targeted LC–MS determinations of small molecules. *J. Pharm. Biomed. Anal.* **2016**, *124*, 48–56. [CrossRef] [PubMed]
6. Maurer, H.H. Hyphenated high-resolution mass spectrometry-the "all-in-one" device in analytical toxicology? *Anal. Bioanal. Chem.* **2021**, *413*, 2303–2309. [CrossRef]
7. Rochat, B. From targeted quantification to untargeted metabolomics: Why LC-high-resolution-MS will become a key instrument in clinical labs. *TrAC Trends Anal. Chem.* **2016**, *84*, 151–164. [CrossRef]
8. Cerqueira, L.B.; Fachi, M.M.; Kawagushi, W.H.; Pontes, F.L.D.; de Campos, M.L.; Pontarolo, R. New Validated Method. for Quantification of Glycated Hemoglobin by LC-QToF-MS: Is. HRMS Able to Quantify Clinical Samples? *J. Am. Soc. Mass. Spectrom.* **2020**, *31*, 1172–1179. [CrossRef] [PubMed]
9. Kritmetapak, K.; Losbanos, L.A.; Hines, J.M.; O'Grady, K.L.; Ulmer, C.Z.; Vesper, H.W.; Enders, F.T.; Singh, R.J.; Kumar, R. Chemical Characterization and Quantification of Circulating Intact PTH and PTH Fragments by High-Resolution Mass Spectrometry in Chronic Renal Failure. *Clin. Chem.* **2021**, *67*, 843–853. [CrossRef]
10. Storbeck, K.-H.; Schiffer, L.; Baranowski, E.S.; Chortis, V.; Prete, A.; Barnard, L.; Gilligan, L.C.; Taylor, A.E.; Idkowiak, J.; Arlt, W.; et al. Steroid Metabolome Analysis in Disorders of Adrenal Steroid Biosynthesis and Metabolism. *Endocr. Rev.* **2019**, *40*, 1605–1625. [CrossRef]
11. Ceccato, F.; Trementino, L.; Barbot, M.; Antonelli, G.; Plebani, M.; Denaro, L.; Regazzo, D.; Rea, F.; Frigo, A.C.; Concettoni, C.; et al. Diagnostic accuracy of increased urinary cortisol/cortisone ratio to differentiate ACTH-dependent Cushing's syndrome. *Clin. Endocrinol.* **2017**, *87*, 500–507. [CrossRef] [PubMed]
12. Ohno, M.; Yamaguchi, I.; Saiki, K.; Yamamoto, I.; Azuma, J. Specific determination of urinary 6beta-hydroxycortisol and cortisol by liquid chromatography-atmospheric pressure chemical ionization mass spectrometry. *J. Chromatogr. B Biomed. Sci. Appl.* **2000**, *746*, 95–101. [CrossRef] [PubMed]
13. Barrett, Y.C.; Akinsanya, B.; Chang, S.-Y.; Vesterqvist, O. Automated on-line SPE LC–MS/MS method to quantitate 6beta-hydroxycortisol and cortisol in human urine: Use of the 6beta-hydroxycortisol to cortisol ratio as an indicator of CYP3A4 activity. *J. Chromatogr. B* **2005**, *821*, 159–165. [CrossRef] [PubMed]
14. Lutz, U.; Bittner, N.; Ufer, M.; Lutz, W.K. Quantification of cortisol and 6 beta-hydroxycortisol in human urine by LC-MS/MS, and gender-specific evaluation of the metabolic ratio as biomarker of CYP3A activity. *J. Chromatogr. B* **2010**, *878*, 97–101. [CrossRef] [PubMed]

15. Benzi, J.R.L.; Moreira, F.L.; Marques, M.P.; Duarte, G.; Suarez-Kurtz, G.; Lanchote, V.L. A background subtraction approach for determination of endogenous cortisol and 6β-hydroxycortisol in urine by UPLC-MS/MS with application in a within-day variability study in HIV-infected pregnant women. *J. Chromatogr. B Analyt Technol. Biomed. Life Sci.* **2020**, *1144*, 122074. [CrossRef]
16. Lenders, J.W.M.; Williams, T.A.; Reincke, M.; Gomez-Sanchez, C.E. Diagnosis of endocrine disease: 18-Oxocortisol and 18-hydroxycortisol: Is there clinical utility of these steroids? *Eur. J. Endocrinol.* **2018**, *178*, R1–R9. [CrossRef]
17. Taylor, R.L.; Machacek, D.; Singh, R.J. Validation of a High-Throughput Liquid Chromatography–Tandem Mass Spectrometry Method for Urinary Cortisol and Cortisone. *Clin. Chem.* **2002**, *48*, 1511–1519. [CrossRef]
18. Fong, B.M.-W.; Tam, S.; Leung, K.S.-Y. Improved liquid chromatography–tandem mass spectrometry method in clinical utility for the diagnosis of Cushing's syndrome. *Anal. Bioanal. Chem.* **2009**, *396*, 783–790. [CrossRef]
19. Marcos, J.; Renau, N.; Casals, G.; Segura, J.; Ventura, R.; Pozo, O.J. Investigation of endogenous corticosteroids profiles in human urine based on liquid chromatography tandem mass spectrometry. *Anal. Chim. Acta* **2014**, *812*, 92–104. [CrossRef]
20. Cuzzola, A.; Mazzini, F.; Petri, A. A comprehensive study for the validation of a LC–MS/MS method for the determination of free and total forms of urinary cortisol and its metabolites. *J. Pharm. Biomed. Anal.* **2014**, *94*, 203–209. [CrossRef]
21. Antonelli, G.; Artusi, C.; Marinova, M.; Brugnolo, L.; Zaninotto, M.; Scaroni, C.; Gatti, R.; Mantero, F.; Plebani, M. Cortisol and cortisone ratio in urine: LC-MS/MS method validation and preliminary clinical application. *Clin. Chem. Lab. Med.* **2013**, *52*, 213–220. [CrossRef] [PubMed]
22. Zhai, X.; Chen, F.; Zhu, C.; Lu, Y. A simple LC–MS/MS method for the determination of cortisol, cortisone and tetrahydro-metabolites in human urine: Assay development, validation and application in depression patients. *J. Pharm. Biomed. Anal.* **2015**, *107*, 450–455. [CrossRef] [PubMed]
23. Kosicka, K.; Siemiątkowska, A.; Pałka, D.; Szpera-Goździewicz, A.; Bręborowicz, G.H.; Główka, F.K. Detailed analysis of cortisol, cortisone and their tetrahydro- and allo-tetrahydrometabolites in human urine by LC-MS/MS. *J. Pharm. Biomed. Anal.* **2017**, *140*, 174–181. [CrossRef] [PubMed]
24. Dasenaki, M.; Papatzani, M.; Gounari, E.; Magnisali, P.; Papadopoulou-Marketou, N.; Kanaka-Gantenbein, C.; Moutsatsou, P. Thomaidis NS. Simultaneous determination of free cortisol, cortisone and their tetrahydrometabolites in urine by single solvent extraction and liquid chromatography–tandem mass spectrometry. *Anal. Lett.* **2019**, *52*, 2764–2781. [CrossRef]
25. Li, Z.M.; Kannan, K. Determination of 19 Steroid Hormones in Human Serum and Urine Using Liquid Chromatography-Tandem Mass Spectrometry. *Toxics* **2022**, *10*, 687. [CrossRef]
26. Ray, J.A.; Kish-Trier, E.; Johnson, L.M. Measurement of Urinary Free Cortisol and Cortisone by LC-MS/MS. *Methods Mol. Biol.* **2022**, *2546*, 119–128. [PubMed]
27. Jin, S.; Wada, N.; Takahashi, Y.; Hui, S.P.; Sakurai, T.; Fuda, H.; Takeda, S.; Fujikawa, M.; Yanagisawa, K.; Ikegawa, S.; et al. Quantification of urinary 18-hydroxycortisol using LC-MS/MS. *Ann. Clin. Biochem.* **2013**, *50*, 450–456. [CrossRef] [PubMed]
28. Zhao, B.; Bian, J.; Rao, M.; She, X.; Lou, Y.; Cai, J.; Ma, W. A dilute-and-shoot liquid chromatography-tandem mass spectrometry method for urinary 18-hydroxycortisol quantification and its application in establishing reference intervals. *J. Clin. Lab. Anal.* **2022**, *36*, e24580. [CrossRef] [PubMed]
29. Wang, Y.; Fujioka, N.; Xing, C. Quantitative profiling of cortisol metabolites in human urine by high-resolution accurate-mass MS. *Bioanalysis* **2018**, *10*, 2015–2026. [CrossRef] [PubMed]
30. Arioli, F.; Gamberini, M.C.; Pavlovic, R.; Di Cesare, F.; Draghi, S.; Bussei, G.; Mungiguerra, F.; Casati, A.; Fidani, M. Quantification of cortisol and its metabolites in human urine by LC-MSn: Applications in clinical diagnosis and anti-doping control. *Anal. Bioanal. Chem.* **2022**, *414*, 6841–6853. [CrossRef]
31. Palermo, M.; Gomez-Sanchez, C.; Roitman, E.; Shackleton, C.H. Quantitation of cortisol and related 3-oxo-4-ene steroids in urine using gas chromatography/mass spectrometry with stable isotope-labeled internal standards. *Steroids* **1996**, *61*, 583–589. [CrossRef] [PubMed]
32. European Medicines Agency. *European Medicines Agency, Guideline on Bioanalytical Method Validation*; European Medicines Agency: Amsterdam, The Netherlands, 2011.
33. Sharma, S.T.; Nieman, L.K.; Feelders, R.A. Cushing's syndrome: Epidemiology and developments in disease management. *Clin. Epidemiol.* **2015**, *7*, 281–293. [PubMed]
34. Casals, G.; Marcos, J.; Pozo, O.J.; Alcaraz, J.; Martínez de Osaba, M.J.; Jiménez, W. Microwave-assisted derivatization: Application to steroid profiling by gas chromatography/mass spectrometry. *J. Chromatogr. B Analyt Technol. Biomed. Life Sci.* **2014**, *960*, 8–13. [CrossRef] [PubMed]
35. McCann, S.J.; Gillingwater, S.; Keevil, B.G. Measurement of urinary free cortisol using liquid chromatography-tandem mass spectrometry: Comparison with the urine adapted ACS:180 serum cortisol chemiluminescent immunoassay and development of a new reference range. *Ann. Clin. Biochem.* **2005**, *42*, 112–118. [CrossRef] [PubMed]
36. Wood, L.; Ducroq, D.H.; Fraser, H.L.; Gillingwater, S.; Evans, C.; Pickett, A.J.; Rees, D.W.; John, R.; Turkes, A. Measurement of urinary free cortisol by tandem mass spectrometry and comparison with results obtained by gas chromatography-mass spectrometry and two commercial immunoassays. *Ann. Clin. Biochem.* **2008**, *45*, 380–388. [CrossRef] [PubMed]
37. Aranda, G.; Careaga, M.; Hanzu, F.A.; Patrascioiu, I.; Ríos, P.; Mora, M.; Morales-Romero, B.; Jiménez, W.; Halperin, I.; Casals, G. Accuracy of immunoassay and mass spectrometry urinary free cortisol in the diagnosis of Cushing's syndrome. *Pituitary* **2016**, *19*, 496–502. [CrossRef] [PubMed]

38. Palermo, M.; Shackleton, C.H.; Mantero, F.; Stewart, P.M. Urinary free cortisone and the assessment of 11 beta-hydroxysteroid dehydrogenase activity in man. *Clin. Endocrinol.* **1996**, *45*, 605–611. [CrossRef]
39. Vega-Beyhart, A.; Laguna-Moreno, J.; Díaz-Catalán, D.; Boswell, L.; Mora, M.; Halperin, I.; Casals, G.; Hanzu, F.A. Ketoconazole- and Metyrapone-Induced Reductions on Urinary Steroid Metabolites Alter the Urinary Free Cortisol Immunoassay Reliability in Cushing Syndrome. *Front. Endocrinol.* **2022**, *13*, 833644. [CrossRef]

Disclaimer/Publisher's Note: The statements, opinions and data contained in all publications are solely those of the individual author(s) and contributor(s) and not of MDPI and/or the editor(s). MDPI and/or the editor(s) disclaim responsibility for any injury to people or property resulting from any ideas, methods, instructions or products referred to in the content.

biomolecules

MDPI

Article

Cisplatin Dependent Secretion of Immunomodulatory High Mobility Group Box 1 (HMGB1) Protein from Lung Cancer Cells

Kevin P. Gillespie, Ross Pirnie, Clementina Mesaros and Ian A. Blair *

Center of Excellence in Environmental Toxicology, Department of Systems Pharmacology and Translational Therapeutics, University of Pennsylvania, Philadelphia, PA 19104, USA
* Correspondence: ianblair@upenn.edu; Tel.: +1-610-529-0610

Abstract: High mobility group box 1 (HMGB1) is secreted from activated immune cells, necrotic cells, and certain cancers. Previous studies have reported that different patterns of post-translational modification, particularly acetylation and oxidation, mediate HMGB1 release and confer distinct extracellular HMGB1 signaling activity. Here we report that cisplatin but not carboplatin induces secretion of HMGB1 from human A549 non-small cell lung cancer (NSCLC) cells. Cisplatin-mediated HMGB1 secretion was dose-dependent and was regulated by nuclear exportin 1 (XPO1) also known as chromosomal maintenance 1 (CRM1) rather than adenosine diphosphate (ADP)-ribosylation, acetylation, or oxidation. HMGB1, as well as lysine acetylation and cysteine disulfide oxidation of secreted HMGB1, were monitored by sensitive and specific assays using immunoprecipitation, stable isotope dilution, differential alkylation, and nano liquid chromatography parallel reaction monitoring/high-resolution mass spectrometry (nano-LC-PRM/HRMS). A major fraction of the HMGB1 secreted by low-dose cisplatin treatment of A549 NSCLC cells was found to be in the fully reduced form. In contrast, mainly oxidized forms of HMGB1 were secreted by dimethyl sulfoxide (DMSO)-mediated apoptosis. These findings suggest that inhibition of XPO1 could potentiate the anti-tumor activity of cisplatin by increasing the nuclear accumulation of HMGB1 protein, an inhibitor of cisplatin DNA-adduct repair. Furthermore, low-dose cisplatin therapy could modulate the immune response in NSCLC through the established chemokine activity of extracellular reduced HMGB1. This could potentially enhance the efficacy of subsequent immunotherapy treatment.

Keywords: platinum drugs; acetylation; oxidation; immune response; mass spectrometry; chromatography

1. Introduction

HMGB1 was first isolated among other "high-mobility group" proteins in 1973, so designated because of their high mobilities in polyacrylamide gel electrophoresis relative to other extracted non-histone chromosomal proteins [1]. It is a 30 kDa protein with two nuclear localization signals (NLSs) and an acidic tail of 30 amino acids (Figure 1). HMGB1 interacts with DNA and other nuclear proteins to regulate replication [2], translation [3], and DNA repair [4]. Beyond its nuclear function, HMGB1 has a dual second role as a danger-associated molecular pattern (DAMP) by mediating an immune response when secreted from activated immune cells [5] or passively secreted from necrotic cells [6]. Secreted HMGB1 can activate the receptor for advanced glycation end products (RAGE) [7] as well as toll-like receptor (TLR)-2 and TLR-4 [8]. Among other consequences, activation of these receptors initiates cell-signaling cascades that activate nuclear factor kappa B (NF-κB), a key transcription factor in both innate and adaptive immune responses [8]. The mechanisms that regulate the shift between HMGB1′s dual nuclear and DAMP activities and their impact in human disease have been the subject of much of the research into HMGB1 as a potential therapeutic target [9,10].

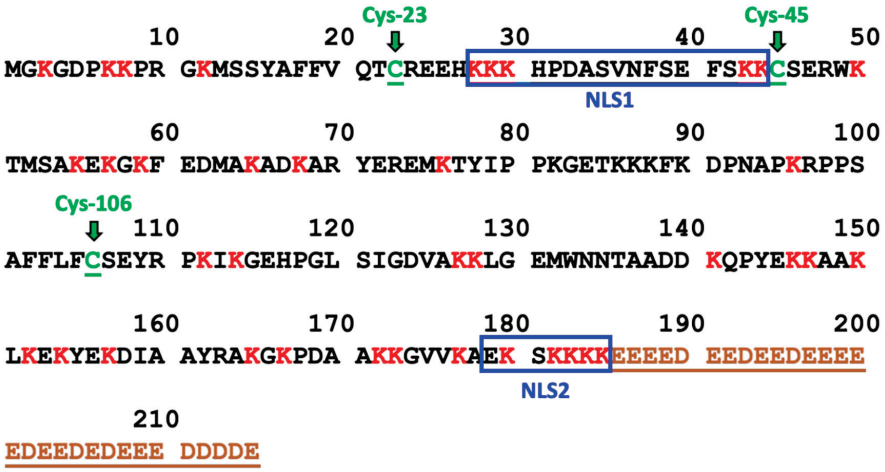


Figure 1. Amino Acid Sequence of HMGB1. The 43 lysine residues are labeled in red and the 3 cysteine residues (Cys-23, Cys-45, and Cys-106) are labeled in green. NLS1 consists of residues 28–44 and NLS2 consists of residues 179–185. The acidic tail (residues 186–215) is labeled in brown.

The role of HMGB1 in the etiology of cancer is complex because of its involvement in both DNA repair and extracellular signaling [11,12]. Growth and metastasis of tumors is thought to be sustained by signaling from HMGB1 and other DAMPs released by necrotic cells following chemotherapy or radiation [13,14]. Extracellular HMGB1 promotes invasion and metastasis by stimulating cell migration and by mediating interactions among components of the extracellular matrix and the tumor microenvironment. Due to these functions, circulating HMGB1 is considered to be an indicator of tumor progression in many cancers [reviewed in [15]]. However, intracellular HMGB1 also has effects on tumor progression by mediating DNA repair mechanisms [4] and NF-κB signaling [8]. Although HMGB1 overexpression has been reported to be common in many types of cancer, including non-small cell lung cancer (NSCLC) [16,17], breast cancer [18], colorectal cancer [19], pancreatic cancer [20], and malignant mesothelioma [21], the ability of different types of tumors to produce their own pool of circulating HMGB1 remains uncertain. In addition, increased tumor HMGB1 mRNA and protein expression correlates with the progression of NSCLC patients [22]. The mechanisms that regulate HMGB1 localization to the nucleus, cytosol, and extracellular space are unclear and may vary among different contexts and cell types.

Platinum-based chemotherapies such as cisplatin and carboplatin are important therapeutic options for the treatment of NSCLC [23,24]. The cytotoxicity of platinum drugs in lung cancer cells is thought to result from DNA damage, especially 1,2-d(GpG) intrastrand crosslinks, which interferes with DNA replication and eventually activates apoptosis [25]. HMGB1 secretion during the treatment of NSCLC has been reported, although the studies were flawed by the analysis of HMGB1 in serum instead of plasma [26,27]. Regrettably, a significant number of studies of HMGB1 secretion have been conducted using serum instead of plasma [28] Our study utilizing matched plasma and serum samples from twenty healthy control subjects revealed that HMGB1 is released when blood is allowed to clot and form serum [15]. The process of clotting led to a substantial 30-fold increase in HMGB1 concentrations, escalating from 0.2 ng/mL in plasma to 6 ng/mL in serum [15]. Consequently, the reliable detection of an elevation in HMGB1 release from tissues into the plasma becomes very difficult to interpret when the protein is quantified in serum. Measurements conducted solely in serum only indicate the ability of blood cells to generate HMGB1 and fail to reflect the actual circulating levels of HMGB1. Despite this fundamental issue, serum is still frequently employed in biomarker studies to quantify HMGB1 secreted from tissues in various pathological conditions.

Various post-translational modifications (PTMs) of HMGB1 have been implicated as mediators of HMGB1 mobility and secretion. These modifications include acetyla-

tion [29–32] methylation [33], poly-ADP ribosylation [34], serine phosphorylation [30,31], and cysteine (Cys) oxidation [31]. A paradigm has emerged relating various circulating HMGB1 proteoforms with corresponding mechanisms of release, where hyperacetylated HMGB1 undergoes regulated secretion from immune cells during inflammation [3], and hypoacetylated HMGB1 is passively released from necrotic cells after tissue injury [35]. Similarly, secretion of the HMGB1 proteoform with an intramolecular disulfide between Cys-23 and Cys-45 (Figure 1) has been associated with inflammation and oxidative stress, whereas reduced HMGB1 with no intramolecular disulfide bond has been associated with passive release from necrotic cells [36,37]. However, many of the studies supporting this conceptual framework have been discredited or retracted [reviewed in [28]]. Therefore, we considered that it was important to definitively characterize distinct patterns of HMGB1 PTMs arising from chemotherapy-induced HMGB1 secretion.

PTMs could play a role in mediating the mobility of HMGB1 in cisplatin-treated cells. For example, HMGB1 is a substrate of poly [ADP-ribose] polymerase 1 (PARP1) [38,39], and DNA damage is a potent inducer of PARP1 activity [38]. Therefore, secreted HMGB1 could conceivably be ADP-ribosylated prior to secretion. Similarly, in vitro experiments have demonstrated that acetylation and phosphorylation of HMGB1 can modulate its DNA-binding properties [40,41]. Furthermore, the binding affinity between cisplatin-modified DNA and reduced HMGB1 is 10-fold greater than with oxidized HMGB1 in vitro [42], which suggests that differences in cellular redox state could contribute to variability in cellular response to platinum drugs. Therefore, characterizing the PTMs and oxidation state of HMGB1 is necessary to fully understand the mechanism by which it is secreted from NSCLC cells resulting from platinum drug treatment.

In the current study, we determined whether platinum drugs could induce regulated HMGB1 translocation and secretion in the human A549 NSCLC cell line. We report a sensitive and specific assay to quantify HMGB1 proteoforms in cells and cell culture media using immunoprecipitation (IP) with magnetic beads covalently crosslinked with dimethyl pimelimidate (DMP) to an HMGB1 polyclonal antibody (pAb) coupled with nano liquid chromatography parallel reaction monitoring/high-resolution mass spectrometry (LC-PRM/HRMS). A differential alkylation approach with iodoacetamide (IAA) and N-ethylmaleimide (NEM) modification of Cys residues was used in combination with a [$^{13}C^{15}N$]-HMGB1 internal standard to characterize and accurately quantify the redox state of HMGB1 Cys residues. Post-IP acetylation with *D*6-acetic anhydride was used to convert all acetylated and nonacetylated HMGB1 into a single molecular form, to characterize and accurately quantify endogenous acetylation of HMGB1 lysine residues. These sensitive and specific methods revealed, surprisingly, that cisplatin, but not carboplatin or transplatin, could induce HMGB1 release from A549 cells prior to cell death or loss of plasma membrane integrity. Furthermore, the secretion was mediated by nuclear transport rather than by acetylation, ADP-ribosylation, phosphorylation, or oxidation.

2. Materials and Methods

2.1. Chemicals and Reagents

Reagents and solvents were LC/MS-grade quality unless otherwise noted. Burdick and Jackson (Muskegon, MI, USA) supplied LC/MS grade water and acetonitrile. Cambridge Isotope Laboratories (Andover, MA, USA): [$^{13}C_6{}^{15}N_2$] lysine, [$^{13}C_9{}^{15}N_1$] tyrosine and [$^{2}H_6$] acetic anhydride. EMSCO/FISHER (Philadelphia, PA, USA) supplied Pierce Protein A/G magnetic agarose beads, formic acid, Dulbecco's phosphate buffered saline (PBS). Fisher Scientific (Pittsburgh, PA, USA) supplied ammonium hydroxide (Optima). MilliporeSigma (Billerica, MA, USA) supplied the anti-HMGB1 rabbit pAb raised against the C-terminal acidic tail of HMGB1 (H9539), ethylenediaminetetraacetic acid (EDTA)-free protease inhibitor cocktail, L-cysteine, chloramine-T hydrate, triethanolamine, and ethanolamine. Abcam (Waltham, MA, USA) supplied the rabbit anti-HMGB2 monoclonal antibody (mAb) raised against an N-terminal HMGB2 peptide of unspecified sequence (ab124670). Anti-histone H3 rabbit pAb (cat. # PA5-16183) and anti-fatty acid synthase (FASN) rabbit pAb

(cat. # MA5-14887) were purchased from Invitrogen (Carlsbad, CA, USA). Novus Biologicals (Centennial, CO, USA) supplied early apoptosis-specific stain polarity Sensitive Indicator of Viability and Apoptosis (pSIVA) and propidium iodide (PI) fluorescent stains. Promega (Madison, WI, USA) supplied mass spectrometry grade trypsin endo-proteinase. Thermo Fisher Scientific (Waltham, MA, USA) supplied tris(2-carboxyethyl)phosphine (TCEP), endoproteinase Glu-C from *Staphylococcus aureus* V8, Tris HCl pH 8 solution, and dimethyl pimelimidate (DMP). Horseradish peroxidase (HRP) was supplied by Santa Cruz Biotechnology, (Dallas, TX, USA). Perkin Elmer (Waltham, MA, USA) supplied the Western Lightning Plus electrochemical luminescence (ECL) reagent. REN and EMMESO malignant mesothelioma cells were a kind gift from Dr. Steven M. Albelda, University of Pennsylvania. Platinum drugs were dissolved in PBS because dimethyl sulfoxide (DMSO) can cause oxidative stress and apoptosis [43–45].

2.2. Platinum Treatments and Lung Cancer Cell Models

A549 cells (American Type Culture Collection) were cultured in Dulbecco's Modified Eagle's Medium/Ham's F-12 Nutrient Mixture media with 15 mM HEPES and 2 mM glutamine (Thermo Fisher Gibco, 11330-032), supplemented with 1% Penicillin-Streptomycin (Thermo Fisher Gibco 15140-122) and 5% FBS (Sigma Aldrich F2442). Cells were seeded at a density of 3×10^6 cells per 35 × 10 mm plate and cultured at 37 °C with 5% CO_2. Cisplatin, transplatin, and carboplatin were prepared as 5 mM stocks in PBS with 30 s pulse sonication and diluted into 10 mL cell culture media for treatment. After 24 h, media was collected and subjected to centrifuge to remove any cell debris (1000 g, 10 min, 4 °C) and the supernatant was transferred to fresh 15-mL tubes. REN and EMMSO cell lines were cultured in RPMI Media with 2 mM glutamine, supplemented with 1% Penicillin-Streptomycin and 5% FBS.

2.3. Cell Culture Media Western Blots and Fluorescent Cell Staining

After collection, aliquots (100 µL) of A549 media were dried under N_2 gas and prepared in LDS sample buffer for electrophoresis separation and membrane transfer. HMGB1 was detected via an HMGB1 rabbit pAb (ab79823) and antirabbit HRP secondary antibody and visualized with an ImageQuant LAS 4000 camera. HMGB2 was similarly detected via an HMGB2 rabbit pAb (ab124670) and antirabbit HRP. Western blots were developed with ECL reagents. Fluorescent staining for nuclear DNA, necrosis, and apoptosis was done with Hoechst 33342, pSIVA, and PI dyes (Novus, NBP2-29382), respectively, following washing of live cells with PBS. Fluorescent microscopy was performed with BioTek Gen5 3.04 Imager. Images were generated from overlaying the blue, green, and magenta filters, respectively.

2.4. Expression and Purification of Stable Isotope Labeling by Amino Acids in Cell Culture (SILAC) Labeled HMGB1

HEK293T cells were cultured in DMEM/F12 SILAC medium containing 0.5 mM [$^{13}C_6{}^{15}N_2$]-lysine and 0.2 mM [$^{13}C_9{}^{15}N_1$]-tyrosine for at least three passages. HMGB1-FLAG tag plasmid (Origene RC205918) was transfected into HEK293T cells by use of lipofectamine 3000 transfection reagent (Invitrogen) following the manufacturer's instructions. Transfected cells were harvested in NP-40 lysis buffer [150 mM NaCl, 50 mM Tris-HCl, pH 7.5, 1 mM EDTA, 0.5% Triton X-100, 0.5% NP-40, and 1 mM DTT, dithiothreitol (DTT)] containing protease inhibitor cocktail after 48 h transfection. Harvested cells were subjected to pulse sonication on ice (30 s) and centrifuged (17,720 g, 15 min, 4 °C) before cell lysate supernatant was carefully transferred to fresh tubes. Anti-FLAG M2 magnetic beads (Sigma Aldrich) were washed twice with NP-40 lysis buffer and added to each tube and incubated overnight at 4 °C with gentle rotation. After removal of the supernatant, the beads were washed with the following solutions sequentially: NP-40 lysis buffer × 3, 0.5 M KCl in NP-40 lysis buffer × 1, 1 M KCl in NP-40 lysis buffer × 1, and PBS × 2. SILAC HMGB1 was eluted from beads with glycine elution buffer (0.1 M glycine-HCl, pH 2.5) for 20 min

and subsequently with 10 mM NH_4HCO_3 for 10 min. Aliquots of 250 mM NH_4HCO_3 were added to pooled eluent until pH was neutral.

2.5. Crosslinked Magnetic Bead Immunoprecipitation and Trypsin Digestion

Protein A/G magnetic beads were gently vortexed and 40 µL dispersed beads were transferred to two 2-mL protein LoBind microcentrifuge tubes (Eppendorf, 022431102). Beads were washed twice with PBS and twice with Buffer A (0.1 M sodium phosphate, pH 7.4). Each tube was incubated with 100 µL buffer A and 100 µL of either H9539 (Sigma Aldrich) or ab79823 (Abcam) anti-HMGB1 rabbit pAb for 2 h at 4 °C with gentle rotation, followed by the addition of 400 µL buffer A and further overnight incubation at 4 °C. The pAb solutions were removed and beads were gently washed twice with buffer A and then twice with 1 mL of cross-linking buffer (0.2 M triethanolamine, pH 8). After washes, the beads were suspended in 1 mL of 25 mM DMP prepared in cross-linking buffer and incubated at room temperature for 1 h with gentle rotation. The DMP solution was removed, and the beads were washed with 1 mL of blocking buffer (0.1 M ethanolamine, pH 8.2) and then incubated at room temperature for 30 min in 1 mL of blocking buffer. The blocking buffer was then removed, and the beads were washed twice with PBS. The PBS was removed, and the beads were incubated in glycine elution buffer for 15 min at room temperature with gentle rotation to remove any residual non-crosslinked antibody from the beads. After removing the glycine elution buffer and two final washes with PBS, beads with both HMGB1 pAbs were equally aliquoted into fresh protein LoBind tubes containing 1 mL A549 media, SILAC FLAG-HMGB1 internal standard (800 ng) and 100 µL IP lysis buffer. Media immunoprecipitation samples were incubated overnight at 4 °C with gentle rotation and gently washed twice with PBS. HMGB1 was eluted with 15 min vigorous shaking of beads in 100 µL elution buffer and then with 5 min vigorous shaking 50 µL 10 mM NH_4HCO_3. The two eluents of each sample were combined and subsequently neutralized with 50 µL 250 mM NH_4HCO_3. The combined elute was dried under N_2 for subsequent resuspension in 25 mM NH_4HCO_3 pH 8 and digested with 400 ng trypsin protease per sample overnight at 37 °C with 600 RPM shaking. We have also previously shown that the IP procedure can efficiently isolate acetylated forms of HMGB1 [15].

2.6. Cell Fractionation

Nuclear and cytosolic subcellular fractions were prepared with ProteoExtract Subcellular Proteome Extraction Kit (Millipore Sigma, 539790) following a protocol adapted from the manufacturer's instructions. After removing cell culture media, cell plates were gently washed twice with PBS and aspiration. Cells were gently lifted in 1 mL PBS and pelleted by centrifugation (600× *g*, 6 min, 4 °C). The PBS supernatant was discarded, and cells were resuspended in 300 µL wash buffer and gently rocked (5 min, 4 °C) before centrifugation (600× *g*, 6 min, 4 °C). This entire wash step was repeated, and then the cells were resuspended in 200 µL extraction buffer I with 2 µL protease inhibitor and gently rocked (5 min, 4 °C) to extract the cytosolic fraction. The cell sample was subjected to centrifugation (1000× *g*, 10 min, 4 °C) and the supernatant was transferred to a clean tube to provide the cytosolic fraction. The remaining pellet was resuspended in 200 µL provided Extraction Buffer II with 2 µL provided protease inhibitor and gently rocked (30 min, 4 °C) before centrifugation (6000× *g*, 10 min, 4 °C). The supernatant was discarded, and the remaining pellet was resuspended in 100 µL extraction buffer III with 2 µL d protease inhibitor and 1 µL benzonase nuclease. The cell sample was gently rocked (10 min, 4 °C) to extract the nuclear fraction. Finally, the sample was subjected to centrifugation (7000× *g*, 10 min, 4 °C) and the supernatant was transferred to a clean tube to provide the nuclear fraction. Cytosolic and nuclear fraction were tested with immunoblotting for FASN and Histone-3/Histone-4 antibodies, respectively.

2.7. In-Solution D6-Acetic Anhydride D_3-Acetylation and GluC and Chymotrypsin Digestion

Following glycine-HCl and NH_4HCO_3 elution of HMGB1, 100 µL 250 mM NH_4HCO_3 was added to each sample to elevate pH to 8.5. A working stock of *D*6-acetic anhydride (Cambridge Isotopes DLM-1162-PK) was diluted 14*X* in acetonitrile. Successive additions of 30 µL ammonium hydroxide (Fisher A470) and 140 µL working stock *D*6-acetic anhydride were added to each sample and incubated for 1 h at 37 °C with 600 RPM shaking. Following the acetylation reaction, samples were dried under N_2 gas and resuspended in 200 µL 50 mM NH_4HCO_3 pH 8 for Glu-C protease digestion or 200 µL pH 8 for Chymotrypsin digestion.

2.8. IAA/NEM Cys Derivatization

SILAC FLAG-HMGB1 stock was reduced in 50 mM TCEP (Thermo Scientific 77720) for 1 h at pH 7 and 30 °C with 600 RPM shaking. Then stock was diluted to 20 ng/µL with Optima water. Iodoacetamide was prepared away from light as a 500 mM stock in 250 mM NH_4HCO_3. Reduced SILAC FLAG-HMGB1 internal standard (400 ng) was added to each 1-mL A549 media sample, followed by addition of iodoacetamide solution for a 60 min reaction with 50 mM iodoacetamide at pH 8.5 and 25 °C in the dark with 600 RPM shaking. Residual iodoacetamide was then quenched with 100 mM L-Cys at pH 8.5 and 30 °C in the dark with 600 RPM shaking and the sample pH was brought to neutral with 0.5 M HCl (Fisher SA48-500). Then more reduced SILAC internal standard (400 ng) was added to each sample, followed by 100 µL IP lysis buffer for 1 mM BME final concentration. Both HMGB1 pAbs were equally aliquoted into samples for overnight immunoprecipitation and subsequent elution as previously described [15]. Following elution, samples were reduced with a large excess (25 mM) TCEP for 1 h at pH 6 and 30 °C with 600 RPM shaking. The high concentration of TCEP prevented its consumption by any NAD^+ that might have been present in the eluate [46]. N-ethylmaleimide was prepared in the dark as a 300 mM stock in water, and aliquots were added to each sample for a 60 min reaction with 30 mM N-ethylmaleimide at pH 7 and 25 °C in the dark with 600 RPM shaking. Samples were then dried under N_2 gas and tryptic digests were prepared as previously described [15]. Glu-C digests were prepared following *D*6-acetic anhydride acetylation steps as previously described [15].

2.9. NanoLC-PRM/HRMS

UHPLC-MS was conducted on a Q Exactive HF hybrid quadrupole-Orbitrap mass spectrometer coupled to a Dionex Ultimate 3000 RSLCnano with capillary flowmeter chromatographic system (Thermo Fisher Scientific, San Jose, CA, USA). The nanoLC system was composed of two columns, including a trapping column (Acclaim PepMap C18 cartridge (0.3 mm × 5 mm, 100 Å, Thermo Scientific) for preconcentration purposes and an analytical column (C18 AQ nano-LC column with a 10 µm pulled tip (75 µm × 25 cm, 3 µm particle size; Columntip, New Haven, CT, USA) to separate digested peptides; two pumps, including one nanopump delivering solvents to analytical column and a micropump connecting to the trapping column; and a 10-port valve. The nanoLC system was controlled by Xcalibur software from the Q-Exactive mass spectrometer. Samples (8 µL) were injected via microliter-pickup injection mode. Loading solvent was water/acetonitrile (99.7:0.3 v/v) containing 0.2% formic acid. A 10-port valve was set at the loading position (1–2) with the loading solvent at 10 µL/min for 3 min. The valve was then changed to the analysis position (1–10), at which time the trapping column was connected with the analytical column, and samples loaded on the loading column were back-flushed into the analytical column. The valve was maintained in the analysis position for 10 min before the end of the run, when it was switched to the loading position ready for the next analysis. Samples were eluted with a linear gradient at a flow rate of 0.35 µL/min: 2% B at 2 min, 5% B at 15 min, 35% B at 40 min, 95% B at 45–55 min, 2% B at 58–70 min. Solvent A was water/acetonitrile (99.5:0.5 v/v) containing 0.1% formic acid, and solvent B was acetonitrile/water (98:2 v/v) containing 0.1% formic acid. Nanospray Flex ion source (Thermo Scientific) was used.

MS operating conditions were as follows: spray voltage 2500 V, ion transfer capillary temperature 250 °C, ion polarity positive, S-lens RF level 55, in-source collision-induced dissociation (CID) 1.0 eV. Both full-scan and parallel reaction monitoring (PRM) were used. The full-scan parameters were resolution 60,000, automatic gain control (AGC) target 1×10^6, maximum IT 200 ms, scan range m/z 290–1600. The PRM parameters were resolution 60,000, AGC target 2×10^5, maximum IT 80 ms, loop count 5, isolation window 1.0 Da, NCE 25.

2.10. Quantification of HMGB1

Standard curve samples for tryptic and Glu-C digests of HMGB1 were prepared in media in triplicate. Recombinant HMGB1 was serially diluted in water and added to each media sample, followed by 800 ng SILAC internal standard. Two peptides per digest with three of the best nano-LC-PRM/HRMS transitions (H^{31}PDASVNFSEFSK^{43} and G^{115}EHPGLSIGDVAK^{127}) were used to generate the standard curves with mean values of light-to-heavy ratios of peak areas of the non-Cys tryptic peptides (Figure S1) from cisplatin-treated A549 media. A549 media HMGB1 was quantified by light-to-heavy ratios of peak areas using the generated standard curves (Figure S2).

2.11. Quantification of HMGB1 Lysine Acetylation and Cys Oxidation

Lysine acetylation was quantified as previously described [15]. Briefly, PRM transitions for all possible CH_3-acetylated and CD_3-acetylated lysine residues were selected in the relevant samples from Glu-C and Chymotrypsin digests. The ratio of each light peptide peak area to the corresponding SILAC peptide peak area was calculated by Xcalibur QuanBrowser and qualified by Skyline. Cys oxidation was quantified by comparing the light-to-heavy ratio of peak areas in CAM- and NEM-modified Cys-containing peptides in the relevant trypsin and Glu-C digests. CAM- and NEM-modified Cys-containing peptides were confirmed by MS2 mass spectra (Figures S9 and S10). The CAM ratio compared to NEM ratio for a given Cys-containing peptide represents the ratio of reduced to disulfide oxidized Cys. The percentage of disulfide oxidation of a given Cys residue was calculated by NEM L/H divided by the sum of CAM L/H and NEM L/H and averaged for three PRM transitions per peptide.

2.12. Inhibitor Co-Treatments and ImageJ Blot Quantification

A549 cells were seeded in 6-well cell culture plates at 0.5×10^6 cells per well. Olaparib, GO-6983, Rottlerin, and KPT-330 were prepared as stocks in DMSO and LMB was provided in a 70/30 Methanol/Water (v/v) solution. Cell culture media was replaced fresh in each well right before inhibitor solutions and vehicle controls were added to each well. Following 3 h in the cell culture incubator, cisplatin or PBS vehicle control was added to each well for 24 h incubation. After 24 h, media was collected and subjected to centrifuge to remove any cell debris (1000 g, 10 min, 4 °C) and the supernatant was transferred to fresh 2-mL tubes. Western blots for HMGB1 were performed as previously described [15]. Following imaging, Western blots were quantified with ImageJ software by subtracting the membrane background signal from each blot using the same area and normalizing the signal to the calculated signal from the blot of HMGB1 (50 ng) on the membrane.

2.13. Trypan Blue Exclusion Assay for A549 Proliferation and Viability

Trypan blue exclusion assays were performed on A549 cells evenly split into 35×10 mm plates for a target density of 3×10^6 cells per plate. After all cells had re-adhered, they were treated with either cisplatin or PBS vehicle control (N = 5). For the trypan blue exclusion assays, cell culture media was aspirated, and cells were lifted by gentle washing with 2.5 mL trypsin-EDTA 0.5% and 2.5 mL PBS. Aliquots of 200 µL cell suspension were mixed with 200 µL trypan blue solution, and 2×11 µL of the mixture was then added to cell counter slides for analysis for cell count and viability by an automated cell counter (LUNA Automated Cell Counter L10001, Logos). The values obtained from the A and B

sides of each slide were averaged and used to calculate the total viable and dead cells on a given plate.

2.14. Asp-N Protease Digests of A549 Subcellular Fractions

A549 subcellular fractions were collected as previously described [47]. Partial aliquots were taken from each fraction for sodium dodecyl sulfate polyacrylamide gel electrophoresis (SDS-PAGE) sample preparation. SILAC HMGB1 was distributed equally to each partial aliquot. SDS-PAGE was run as previously described [15], followed by overnight Colloidal Blue staining (Thermo Fisher, LC6025). Following staining, gels were briefly rinsed with deionized water, and gel pieces between 25 kDa and 37 kDa were excised from each lane to cut into approximately 1 mm^3 pieces and added to fresh microcentrifuge tubes. Gel pieces were rinsed by gentle shaking in 25 mM ammonium bicarbonate in 50% acetonitrile by volume and the solution aspirated before the pieces were dried with 200 µL aliquots of acetonitrile and gentle shaking. After drying the acetonitrile was aspirated and 5 µL *D6*-acetic anhydride was added to each tube of gel pieces to absorb, followed by 50 µL of 100 mM ammonium bicarbonate. After absorption, 150 µL of 100 mM ammonium bicarbonate and 15 µL were added to each tube to bring the pH to approximately 8.5. Samples were incubated for 1 h at 37 °C with 600 RPM shaking, followed by removal of the supernatant, rinsing again with 25 mM ammonium bicarbonate in 50% acetonitrile, and drying again with acetonitrile. A working stock of Asp-N protease was prepared in water 25 ng/µL. After removing acetonitrile, 30 µL (750 ng) Asp-N protease was added to each tube for absorption by the gel pieces. Following absorption, 200 µL 25 mM ammonium bicarbonate was added to each tube and samples were incubated overnight at 37 °C with 600 RPM shaking. Following incubation, the digest supernatant was removed and added to fresh tubes. Residual peptides were extracted from the gel pieces by 45 min bath sonication with 150 µL extraction buffer (3% formic acid in 50% aqueous acetonitrile). The supernatants from this extraction were recombined with the corresponding digest supernatants, and the samples were dried under N_2 gas and prepared for LC-MS analysis as previously described [15].

3. Results

3.1. Cisplatin Induces Regulated HMGB1 Secretion from Lung Cancer Cells

By examining anti-HMGB1 immunoblots of cell culture media, we found that HMGB1 was secreted by the A549 NSCLC cell line with cisplatin treatment in a dose-dependent relationship (Figure 2A). Among the tested platinum chemotherapeutics, cisplatin was the most effective, with the stereoisomer transplatin and the analogue carboplatin showing little effect on HMGB1 release. Conversely, DMSO, an inducer of oxidative stress [43] and apoptosis [44,45], also induced extracellular release of HMGB1. Mesothelioma cell lines REN and EMMESO both constitutively secreted HMGB1 in the absence of platinum drugs, but A549 cells showed no such constitutive secretion (Figure 2A). To accurately quantify cisplatin-secreted HMGB1 from the A549 NSCLC cells, we used a nanoLC-PRM/HRMS platform to analyze tryptic HMGB1 peptides [15].

SILAC methodology was applied to generate lysine- and tyrosine-labeled SILAC (K*Y*-SILAC) HMGB1, which was then used as the internal standard for quantification of HMGB1 isolated from cell culture media by IP, then subjected to trypsin digestion and nanoLC-PRM/HRMS analysis. Calibration curves were made with recombinant HMGB1 and SILAC HMGB1 for tryptic peptide nanoLC-PRM/HRMS transitions H^{31}PDASVNFSEFSK^{43} dehydration, H^{31}PDASVNFSEFSK^{43} y12, G^{115}EHPGLSIGDVAK^{127} b7, and G^{115}EHPGLSIGDVAK^{127} y10 (Figures S1 and S2). NanoLC-PRM/MS analysis confirmed the immunoblot data by showing that there was dose-dependent secretion of HMGB1 with cisplatin at 20 µM [551.4 ± 76.3 ng; mean ± standard deviation (SD)] and 100 µM (1139 ± 102 ng) (Figure 2B). This was significantly different from PBS (204.9 ± 3.3 ng) at 20 µM ($p = 0.0014$) and 100 µM ($p < 00001$), respectively (Figure 2B). There was also increased HMGB1 secretion with DMSO (345.8 ± 30.5, $p < 0.0014$) when

compared with PBS, and there was a minimal effect with other cisplatin analogs that were tested (Figure 2B).

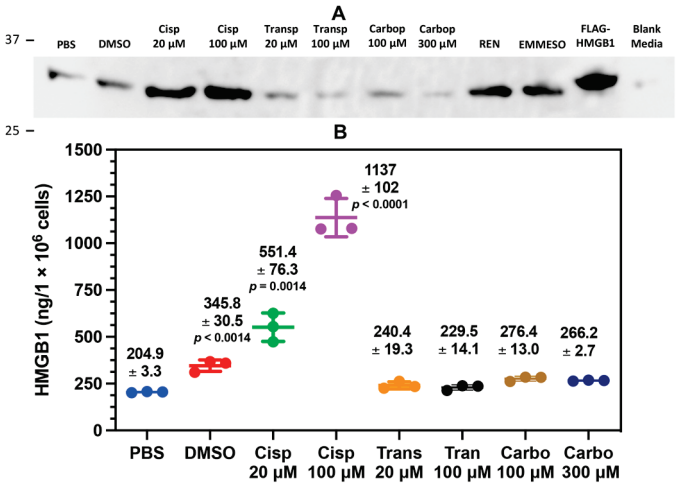


Figure 2. Cisplatin induces HMGB1 secretion from lung cancer cells. Assays were performed following 24 h incubation A549 cells with cisplatin (Cisp, 20 μM), Cisp (100 μM, transplatin (Transp, 20 μM), Transp (100 μM), carboplatin (Carbo, 100 μM) and Carbo (300 μM). (**A**) Representative HMGB1 immunoblots of biological replicates (n = 3) comparing A549 cell culture media to media from untreated malignant mesothelioma cell lines REN and EMMESO. An anti-HMGB1 rabbit pAb against the C-terminal acidic tail of HMGB1 was used. (**B**) absolute quantification of secreted HMGB1 by nano liquid chromatography parallel reaction monitoring/high-resolution mass spectrometry. Significant differences compared to PBS were determined using unpaired Student's *t*-tests. Error bars show ± SD.

3.2. Specific Cisplatin-Mediated Secretion of HMGB1 from Lung Cancer Cells

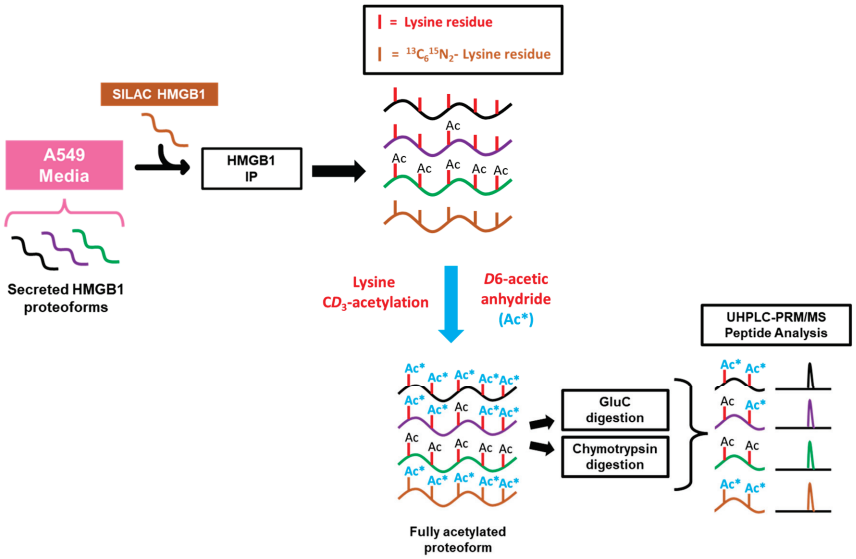
To evaluate if cisplatin treatment specifically induced the extracellular release of HMGB1, and not all nuclear proteins, we examined the nuclear, cytosolic, and media fractions of A549 cells for HMGB1 and HMGB2. Anti-HMGB1 and anti-HMGB2 immunoblotting showed specificity for HMGB1 (Figure S3A) and HMGB2 (Figure S3B), respectively, as demonstrated with recombinant proteins (Figure S3A,B). Although HMGB1 and HMGB2 were both abundant nuclear proteins, there was much more HMGB1 in A549 cytosol (Figure S3A) than HMGB2 (Figure S3B). Cisplatin treatment induced significant secretion of HMGB1 into the A549 cell culture media (Figure S3A), but no secretion of HMGB2 (Figure S3B). We also assessed the subcellular fractions by anti-histone H4 and anti-FASN immunoblotting (Figure S3A, which confirmed robust enrichment of the nuclear and cytosolic fractions and provided evidence that there was no evidence of leakage of histone H4 or FASN into the cell culture media with cisplatin treatment (Figure S3A).

To provide orthogonal analysis of HMGB1 and HMGB2 subcellular distribution with cisplatin treatment, we performed qualitative nano-LC-HRMS/MS analysis of HMGB1- and HMGB2-specific Asp-N peptides (Figures S4–S6). Nuclear, cytosolic, and extracellular media fractions from cisplatin-treated A549 cells were spiked with SILAC HMGB1, separated, and prepared for Asp-N protease digestion. Asp-N was carefully chosen to generate multiple peptides that could be used to distinguish HMGB1 from HMGB2 in the subcellular fraction samples, and CD_3-acetylation (Ac*) was used to improve the chromatography of these peptides. We compared HMGB2 Asp-N peptides D^{124}TAKKLGEMWSEQSAK^{139}, D^{140}KQPYEQKAAKLK^{152}, and D^{158I}AAYRAKGKS^{168} with HMGB1 Asp-N peptides D^{124}VAKKLGEMWNNTAA^{138}, D^{139}DKQPYEKKAAKLK^{152}, and D^{158}IAAYRAKGKP^{168}, respectively, in the nuclear (Figure S4) and cytosolic fractions (Figure S5) as well as the media (Figure S6). Although differences between HMGB1 and HMGB2 sequences precluded a quantitative comparison in this context, the results confirmed that abundant HMGB1 and

HMGB2 peptides were present in the nuclear fraction after protease digestion (Figure S4). However, only HMGB1 peptides were present after protease digestion of the A549 cytosol (Figure S5) or the media after cisplatin treatment of A49 cells (Figure S6). No signals for HMGB2 peptides were detected in the A549 cytosol or A549 cell media after cisplatin treatment (Figures S5 and S6, blue arrows).

3.3. HMGB1 Secreted from Cisplatin-Treated Lung Cancer Cells Is Not Acetylated

To investigate the mechanisms regulating cisplatin-mediated HMGB1 secretion, we first decided to probe acetylation of lysine residues on secreted HMGB1. In order to quantify site-specific acetylation, we adapted a previously reported strategy using HMGB1 IP and nanoLC-PRM/HRMS analysis where we showed that acetylated HMGB1 is isolated by the IP procedure [15]. SILAC HMGB1 internal standard was added to cell culture media samples collected from A549 cells, and light and heavy HMGB1 was immunopurified from these samples (Scheme 1). These samples were treated with *D*6-acetic anhydride to CD_3-acetylate all unmodified HMGB1 lysine residues. This process converts all HMGB1 proteoforms to one universally acetylated molecular form, only differing in mass of the acetyl-lysine modifications. We primarily targeted the most often reported regions of HMGB1 acetylation in other models, including NLS1 (K28-30), NLS2 (K180-185) and the N-terminal region (K3-K12), and we designed our PRM/MS method to analyze all possible combinations of acetylation within them.



Scheme 1. Procedure for preparation and analysis of acetylation in secreted HMGB1. A549 cell culture media was collected and spiked with K*Y*-stable isotope labeling by amino acids in cell culture (SILAC) high mobility group box 1 (HMGB1) internal standard. HMGB1 proteoforms were isolated by overnight IP and eluted with glycine-HCl before CD_3-acetylation (Ac*) with *D*6-acetic anhydride in ammonium bicarbonate/acetonitrile buffer. Samples were subjected to either Glu-C, chymotrypsin, or Asp-N protease digests, and acetylated peptides were analyzed by nano liquid chromatography parallel reaction monitoring/high-resolution mass spectrometry with acetylation status determined by differences in m/z.

NanoLC-PRM/HRMS analysis of the acetylation state of NLS1, NLS2, and N-terminal region of secreted HMGB1 is shown in the chromatograms in Figure 3A–C. Chromatograms for the b11 transitions from the NLS1 Glu-C peptide $HK^{28}K^{29}K^{30}$HPDASVNFSE revealed no signal for triple, double, or single CH_3-acetylation of this peptide (Figure 3A). In contrast, signals were observed from the fully CD_3-acetylated peptide (Figure 3A), which confirmed that K-28, K-29, and K-30 all had no endogenous acetylation. Similarly, chromatograms of the b4 transitions from the NLS2 Glu-C peptide $K^{180}SK^{182}K^{183}K^{184}K^{185}E$

revealed no CH_3-acetylation for any of the peptide's five lysine residues, with multiple transitions analyzed for the same parent ion to check for possible CH_3-acetylation on either MS fragment produced by the b4 transition of this peptide (Figure 3B). As with the NLS1 peptide, $K^{180}SK^{182}K^{183}K^{184}K^{185}E$ was fully CD_3-acetylated, confirming that HMGB1 K180, K182, K183, K184, and K185 all had no endogenous CH_3-acetylation. Additional MRM transitions were used to confirm universal CD_3-acetylation of NLS1 (b10, b11, b12; Figure S7A) and NLS2 (b3, b4, b5; Figure S7B), as shown in the relevant chromatograms. Chromatograms of the y8 transitions for the N-terminal chymotrypsin peptide $GK^3GDPK^7K^8PRGK^{12}MSSY$ (Figure 3C) also showed no endogenous CH_3-acetylation for any of its four lysine residues or the N-terminal amino moiety. We again used multiple transitions analyzed for the same parent m/z to check for possible CH_3-acetylation on either MS fragment produced by the y8 transition of this peptide (Figure 3C). As with the NLS peptides, $GK^3GDPK^7K^8PRGK^{12}MSSY$ was fully CD_3-acetylated, indicating that HMGB1 K3, K7, K8, K12, and the N-terminal amino moiety of HMGB1 all had no endogenous acetylation with cisplatin-mediated secretion (Figure 3C).

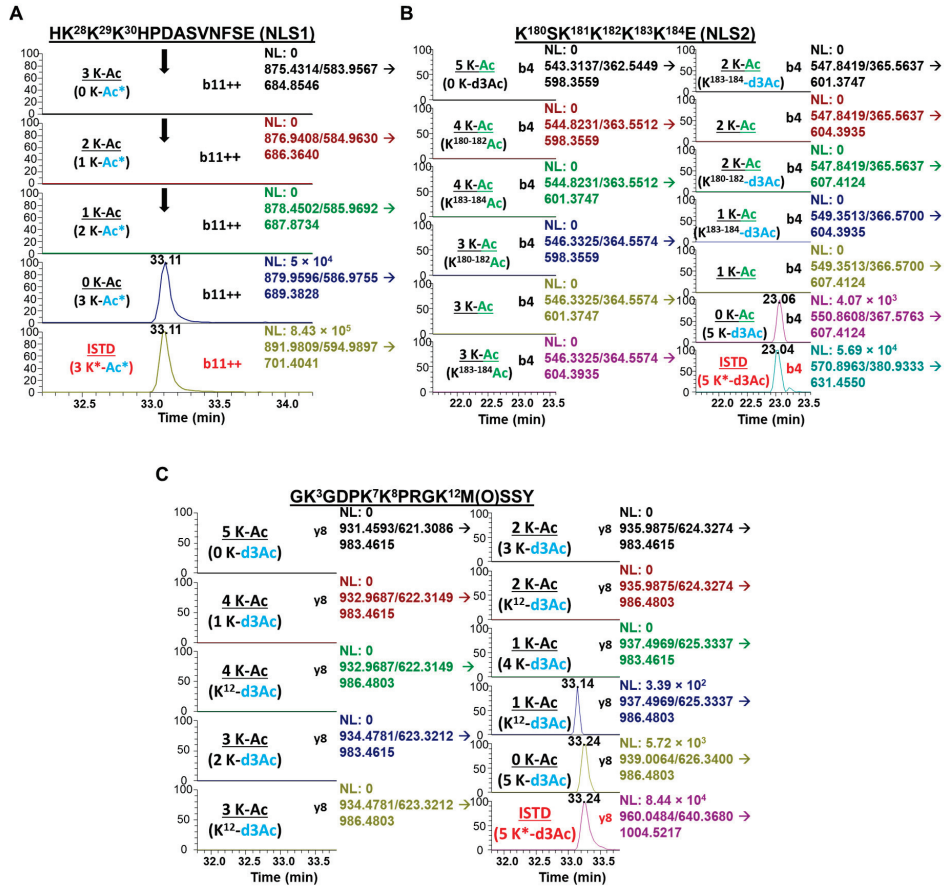


Figure 3. Cisplatin-induced secretion of unacetylated HMGB1. Lysine-containing peptides from cisplatin-treated A549 media were analyzed for acetylation by nano liquid chromatography parallel reaction monitoring/high-resolution mass spectrometry (nanoLC-PRM/HRMS). Chromatograms show light (black) and heavy (red) transitions with CD_3 (*) or endogenous CH_3-acetylation. (**A**) NanoLC-PRM/HRMS chromatograms for NLS1 peptide $HK^{28}K^{29}K^{30}$HPDASVNFSE comparing b11 transitions for triply (first panel), doubly (second panel), and singly (third panel) acetylated NLS1 compared to unacetylated NLS1 peptide (fourth panel) and heavy NLS1 peptide (fifth panel). (**B**) NanoLC-PRM/HRMS chromatograms for NLS2 peptide $K^{180}SK^{181}K^{182}K^{183}K^{184}$ comparing y8 transitions of different possible acetylation states. (**C**) NanoLC-PRM/HRMS chromatograms for N-terminal peptide $GK^3GDPK^7K^8PRGK^{12}$M(O)SSY comparing b4 transitions of different possible acetylation states.

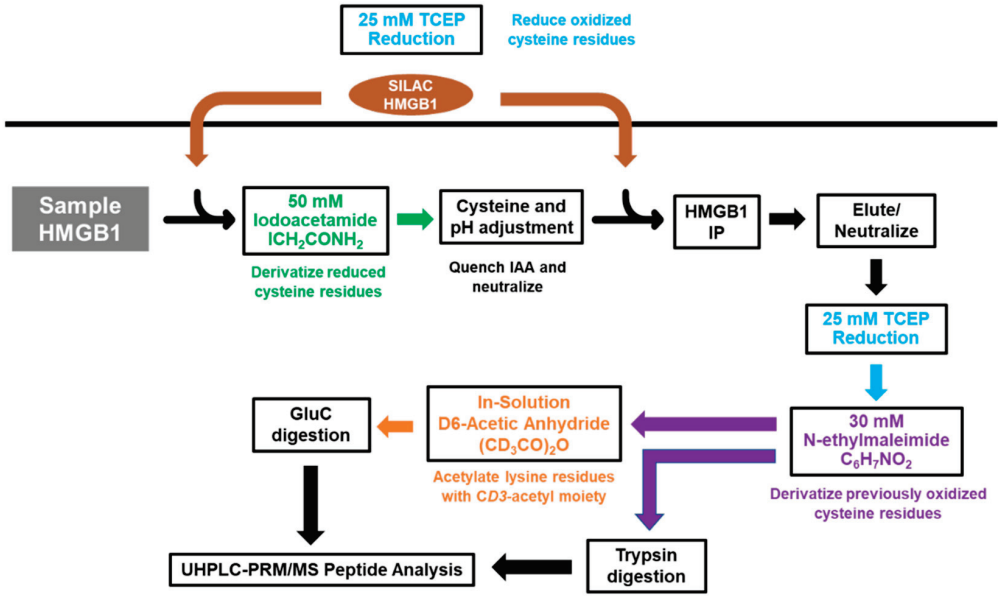
3.4. Non-Targeted Analysis of Acetylation Sites on HMGB1 Secreted from Cisplatin-Treated Lung Cancer Cells

In addition to the targeted nanoLC-PRM/HRMS analysis of acetylation in the specific regions described above, we wanted to apply full-scan nanoLC-high resolution tandem mass spectrometry (HRMS/MS) analysis to other lysine residues within secreted HMGB1. We carefully chose Glu-C, chymotrypsin, and Asp-N proteases to generate as many possible lysine-containing peptides to with maximal coverage of HMGB1′s 43 lysine residues (Figure 1). In total, we were able to probe acetylation on 34 of HMGB1′s 43 lysine residues by nanoLC-HRMS/MS, the results of which are summarized in Table S1. We confirmed each peptide with the corresponding heavy peptide generated from SILAC HMGB1, and we checked for possible CH_3-acetylation by analyzing all possible product ions. Therefore, we found no evidence of endogenous acetylation at any lysine residue in HMGB1 secreted with cisplatin treatment. Furthermore, HMGB1 secreted with DMSO treatment also showed no sign of endogenous acetylation (Figure S8). The data were essentially the same as those discussed above for cisplatin-mediated secretion of HMGB1 (Figure 3A–C).

3.5. Cisplatin Mediates Secretion of Reduced HMGB1

We next interrogated the redox status of the Cys residues on HMGB1 in A549 cell culture media. To distinguish between free (reduced) and disulfide (oxidized) Cys residues on HMGB1, we used a differential alkylation approach with iodoacetamide (IAA) and N-ethylmaleimide (NEM), in which Cys disulfides that were precluded from forming carbamidomethyl (CAM) derivatives with IAA were reduced to free thiols with TCEP prior to the NEM reaction (Scheme 2). A549 media samples were subjected to HMGB1 IP and elution for downstream protease digestion and nanoLC-PRM/HRMS analysis. To control for variation in reaction completeness, IP recovery, efficiency of protease digest, and ionization efficiency of modified peptides among all samples, we used two aliquots of SILAC HMGB1 internal standard, added separately for each of the IAA and NEM reaction steps. Following IAA reaction, residual IAA was quenched to prevent the second aliquot of SILAC HMGB1 internal standard from reacting with IAA on Cys residues. A second aliquot of SILAC HMGB1 was added prior to HMGB1 immunopurification to ensure that ratios of CAM-modified and NEM-modified HMGB1 peptides were not affected by variation in IP and elution efficiency among samples or batches. Reactions with TCEP and NEM were performed post-elution following IP to remove IAA and Cys from the samples. Although trypsin digestion generated sufficient peptides for analysis of Cys-23 with MSSYAFFQTC^{23}R and Cys-106 RPPSAFFLFC^{106}SEYRPK, no tryptic peptide was obtained for analysis of Cys-45 oxidation.

We therefore prepared a second set of A549 media samples in parallel, in which we performed in-solution CD_3-acetylation with *D*6-acetic anhydride and carefully chose Glu-C protease digestion to generate enough peptide for analysis of the Cys-45 in FSKKC^{45}SE. CD_3-acetylation of the lysine residues was used to significantly improve chromatography as well as to facilitate the concurrent analysis of lysine acetylation on this peptide. We found that, in comparison to other treatment conditions, cisplatin induced the secretion of significantly more fully reduced HMGB1, as defined by the redox status of Cys-23, Cys-45, and Cys-106 (Figure 1). There was 228 $\pm$ 39.6 ng and 353 $\pm$ 44.4 ng of reduced HMGB1 secreted at 20 μM and 100 μM cisplatin, respectively (Figure 4A). This result was significantly different from PBS (59.8 $\pm$ 3.1 ng) at both 20 μM (cisplatin $p = 0.0039$) and 100 μM cisplatin ($p = 0.0007$). Although DMSO treatment also increased HMGB1 secretion compared with PBS (Figure 2B), the amount of reduced HMGB1 (37.9 $\pm$ 3.1) was slightly lower than that secreted by PBS (Figure 4A). In contrast, there was significantly more oxidation at Cys-23 ($p < 0.0008$, $p < 0.0026$; Figure 4(Ba)), Cys-45 ($p < 0.001$, $p < 0.001$; Figure 4(Bb)), and Cys-106 ($p < 0.0014$, $p < 0.0006$; Figure 4(Bc)) after DMSO treatment than the HMGB1 secreted by 20 μM and 100 μM cisplatin, respectively.



Scheme 2. Procedure for preparation and redox analysis of secreted HMGB1. A549 cell culture media samples are incubated with iodoacetamide (IAA) to carbamidomethylate free (reduced) Cys residues. tris(2-carboxyethyl)-phosphine (TCEP)-reduced (SILAC) HMGB1 is added both before and after the reaction to act as an internal standard for both free (reduced) and disulfide (oxidized) HMGB1. HMGB1 is immunoprecipitated, eluted, and reduced with TCEP prior to N-ethylmaleimide derivatization. Tryptic peptides for PRM analysis are prepared by overnight trypsin digestion, whereas Glu-C peptides are prepared by overnight Glu-C digestion following in-solution CD_3-acetylation of the lysine residues with *D*6-acetic anhydride.

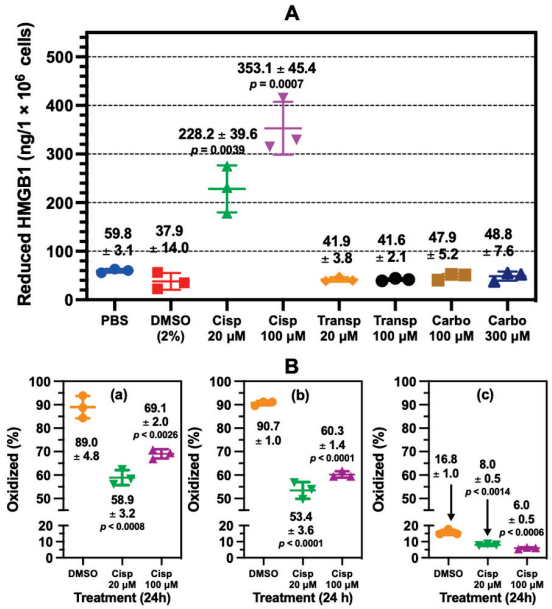


Figure 4. Cisplatin mediated the release of reduced and oxidized HMGB1 from lung cancer cells. (**A**) absolute quantification of reduced HMGB1 released by A549 cells (n = 3) determined by nano liquid chromatography parallel reaction monitoring/high-resolution mass spectrometry (nanoLC-PRM/HRMS) analysis. An unpaired Student's *t*-test was used to compare cisplatin with PBS. (**B**) Site-specific cysteine (Cys) oxidation percentages calculated from nanoLC-PRM/HRMS analysis of carbamidomethyl (CAM)- and N-ethyl maleimide (NEM)-modified peptides in HMGB1 secreted from A549 cells (n = 3). (**a**) Cys-23. (**b**) Cys-45 (**c**) Cys-106. An unpaired Student's t-test was used to compare cisplatin with DMSO. Error bars show ± SD.

Across all treatments, Cys-23 and Cys-45 were oxidized to a similar extent (Figure 4(Ba,Bb)) but there was also more oxidization at these residues than at Cys-106 (Figure 4(Bc)). NanoLC-PRM/HRMS analysis of the redox status of Cys-containing peptides of secreted HMGB1 is shown in the chromatograms in Figure 5. For HMGB1 secreted with cisplatin treatment, assigned MS/MS spectra for Cys-23, Cys-45, and Cys-106 peptides are shown in Figures S9 and S10, for CAM and NEM modifications, respectively. Chromatograms in Figure 5A show the y6, y7, y8, and b2 transitions of tryptic peptide MSSYAFFQTC^{23}R with CAM (left panel) and NEM (right panel) modifications. The relevant ratios of the area under the curves (AUCs) reflect the amount of reduced Cys-23 (CAM) peptide compared with the oxidized Cys-23 (NEM) peptide (Figure 5A).

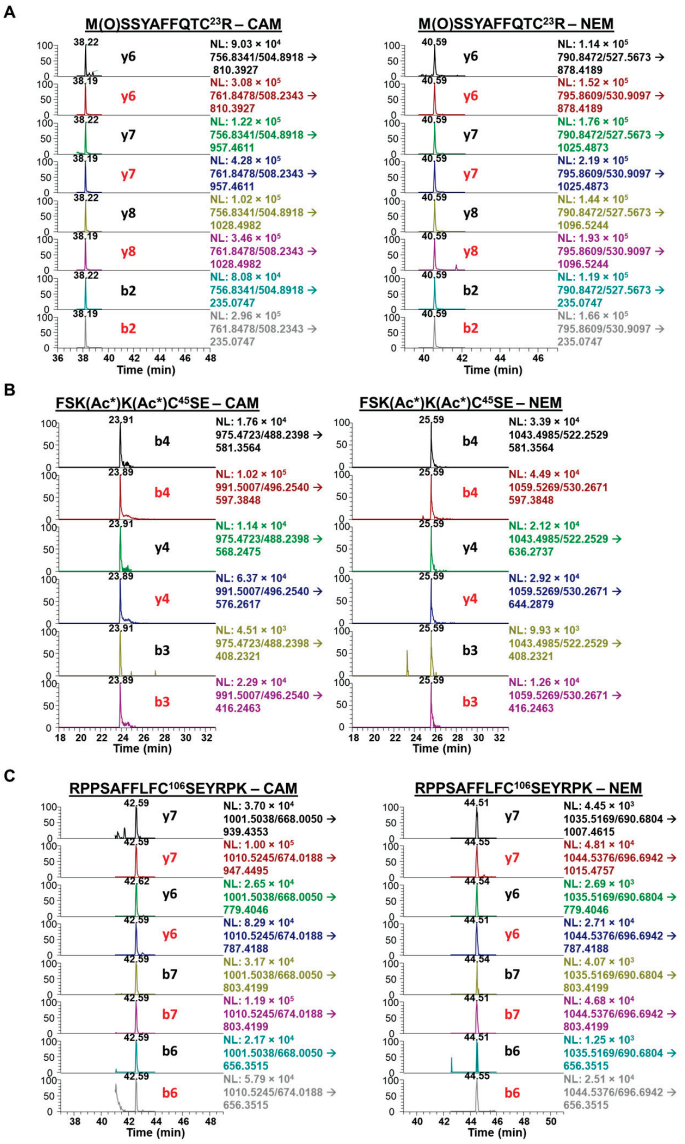


Figure 5. Nano liquid chromatography parallel reaction monitoring/high-resolution mass spectrometry analysis of Cys-containing peptides from cisplatin-treated A549 media. Chromatograms show corresponding light (black) and heavy (red) transitions. Carbamidomethyl (CAM)-modified transitions indicate free (reduced) Cys proteoforms and N-ethyl maleimide (NEM)-modified transitions indicate disulfide (oxidized) Cys proteoforms. (**A**) tryptic peptide M(O)SSYAFFQTC^{23}R with CAM-modified transitions (**left**) and NEM-modified transitions (**right**). (**B**) Glu-C peptide FSK(Ac*)K(Ac*)C^{45}SE with CAM-modified transitions (**left**) and NEM-modified transitions (**right**). (**C**) tryptic peptide RPPSAFFLFC^{106}SEYRPK with CAM-modified transitions (**left**) and NEM-modified transitions (**right**).

Chromatograms of the heavy MSSYAFFQTC^{23}R transitions produced from SILAC HMGB1 were used to calculate light-to-heavy ratios of the AUCs for each corresponding CAM- and NEM-modified peptide transition (Figure 5A). The mean of four MRM transitions (b2, y6, y7, y8) in Figure 5A was used to calculate the oxidized Cys-23 (disulfide) percentage shown in Figure 4B. Similarly, chromatograms show the b4, y4, and b3 MRM transitions of Glu-C peptide FSKKC^{45}SE with CAM (left panel) and NEM (right panel) modifications. The relevant AUC ratios reflect the amount of reduced Cys-45 (CAM) peptide compared with the oxidized Cys-45 (NEM) peptide (Figure 5B). The mean of all three MRM transitions was used to calculate the Cys-45 disulfide oxidation percentage in Figure 4B. Chromatograms also show the y7, y6, b7, and b6 transitions of tryptic peptide RPPSAFFLFC^{106}SEYRPK with CAM (left panel) and NEM (right panel) modifications. The relevant AUC ratios reflect the amount of reduced Cys-106 (CAM) peptide compared with the oxidized Cys-106 (NEM) peptide (Figure 5C). A mean of the three MRM transitions (b3, b5, y4) shown in Figure 5C was used to calculate the oxidized Cys-106 (disulfide) peptide percentage shown in Figure 4B.

3.6. Nuclear Exportin 1 (XPO1) Regulates Cisplatin-Mediated HMGB1 Secretion

We investigated whether cisplatin-mediated HMGB1 secretion is regulated by other post-translational modifications by examining the effects of different pharmacological inhibitors on this process. A549 cells were pre-treated with a different inhibitor or vehicle control, followed by treatment for 24 h with either 50 μM cisplatin or PBS vehicle control, and the cell culture media was assayed by anti-HMGB1 immunoblot (Figure 6). We found that PARP1 inhibitor Olaparib (Figure 6A) had no effect on cisplatin-mediated HMGB1 secretion. Similarly, pan-PKC inhibitors GO-6983 (Figure 6B) and Rottlerin (Figure 6C) had no effect on HMGB1 secretion. Conversely, XPO1 (chromosomal maintenance 1; CRM1) inhibitors leptomycin B (LMB, Figure 6D) and KPT-330 (Figure 6E) significantly attenuated cisplatin-induced HMGB1 secretion from A549 cells. Relative quantification of these immunoblots showed that LMB and KPT-330 inhibited cisplatin-mediated HMGB1 secretion by 95% (Figure 6F) and 52%, (Figure 6G), respectively ($p = 0.0012$ and $p = 0.0030$, respectively; Figure 6F,G).

3.7. Inhibition of Nuclear Exportin 1 (XPO1) Increased Cisplatin-Mediated Nuclear HMGB1 Accumulation and Decreased HMGB1 Secretion

Western blot analysis had revealed that HMGB1 was present in the nucleus and cytosol (Figure S3). However, Western blots were not useful for assessing the precise amount of HMGB1 that was present in the subcellular compartments. Therefore, nanoLC-PRM-HRMS was used to quantify the nuclear and cytosolic HMGB1 and compared with the HMGB1 that was secreted after treating the A549 cells with 50 μM cisplatin or 50 μM cisplatin with 4.5 nM LMB for 24 h (Figure 7). This revealed that there was a highly significant increase in nuclear HMGB1 from 2599 ± 182 ng/10^6 cells in untreated cells to 3764 ± 237 ng/10^6 cells ($p < 0.0025$, Figure 7A) after cisplatin treatment. Nuclear HMGB1 was further increased by 488 ng/10^6 cells to 4272 ± 248 ng/10^6 cells with a combination of cisplatin and LMB (Figure 7A). The high nuclear HMGB1 content after cisplatin treatment relative to the amount secreted (888 ± 33 ng/10^6 cells, Figure 7C) meant that the increase did not quite meet the criteria for statistical significance with a p value of <0.0628). However, cytosolic HMGB1 was significantly lower ($p < 0.0433$) with a combination of cisplatin and LMB (2398 ± 268 ng/10^6 cells) than untreated cells (3164 ± 367 ng/10^6 cells), whereas cytosolic HMGB1 after treatment with cisplatin alone (2851 ± 846 ng/10^6 cells) was not significantly different from untreated cells (Figure 7B). Conversely, there was a significant increase in the amount of HMGB1 secreted from the A549 cells from 206 ± 5 ng/10^6 cells in untreated cells to 898 ± 13 ng/10^6 cells after cisplatin treatment ($p < 0.0001$, Figure 7C). Secreted HMGB1 was reduced significantly to 437 ± 19 ng/10^6 cells by a combination of cisplatin and LMB ($p < 0.001$, Figure 7C).

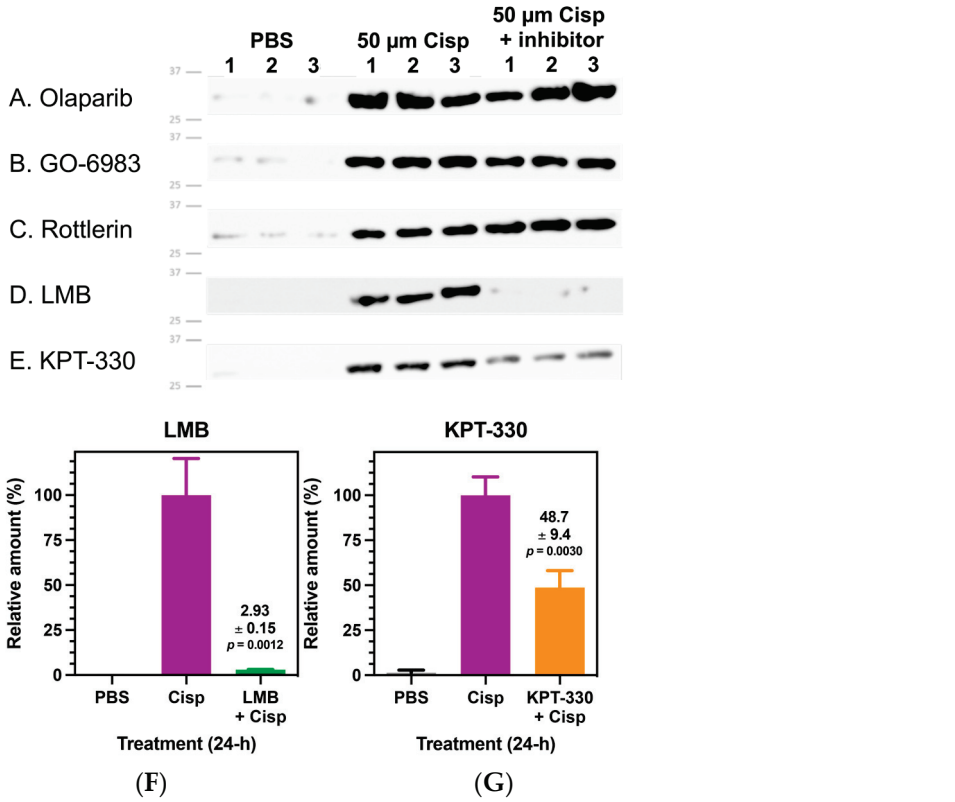


Figure 6. Cisplatin-mediated high mobility group box 1 (HMGB1) secretion is regulated by nuclear exportin 1 (XPO1). Representative anti-HMGB1 immunoblots from biological replicates (n = 3) of A549 cell culture media using anti-HMGB1 rabbit pAb against the C-terminal acidic tail of HMGB1. (**A**) Olaparib (50 µM) (**B**) GO-6983 (120 nM), and (**C**) Rottlerin (100 µM) treatments showed no effect on cisplatin (50 µM)-mediated HMGB1 secretion from A549 cells. Conversely, XPO1 (chromosomal maintenance 1; CRM1) inhibitors (**D**) leptomycin B (LMB) (4.5 nM) and (**E**) KPT-330 (75 nM) significantly attenuated cisplatin-mediated HMGB1 secretion. Normalized immunoblot quantification of HMGB1 in A549 cell culture media comparing effects of XPO1 inhibitors on cisplatin-mediated HMGB1 secretion. (**F**) LMB (4.5 nM). (**G**) KPT-330 (75 nM). Significant differences were determined using an unpaired Student's *t*-test). Error bars show ± SD.

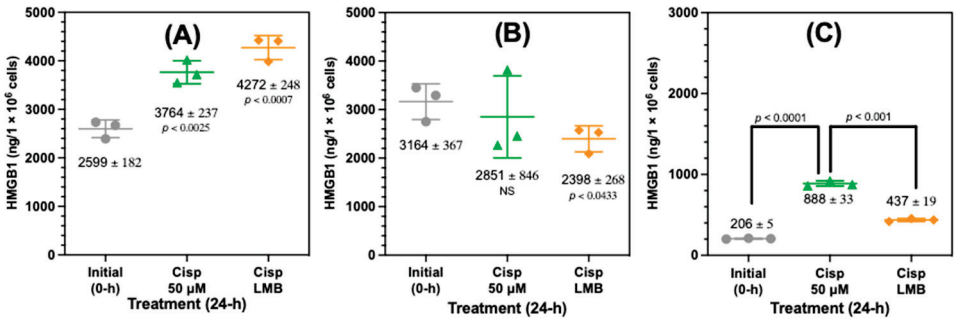


Figure 7. Increased cisplatin-mediated nuclear HMGB1 accumulation and decreased secretion after inhibition of nuclear transporter 1 (XPO1). HMGB1 levels were quantified in A549 cells by nano liquid chromatography-parallel reaction monitoring/high resolution/mass spectrometry in A549 subcellular fractions and A549 cell media after treatment with 50 µM cisplatin and a combination of 50 µM cisplatin with 4.5 nM leptomycin B (LMB). (**A**). Nuclear fraction. (**B**) Cytosolic fraction. (**C**) Cell media. Values are mean ± standard deviation. Statistical analysis was conducted using an unpaired Student's *t*-test.

3.8. Effects of Platinum Drugs and DMSO on Lung Cancer Cell Viability

Since DMSO and cisplatin both induced extracellular release of HMGB1 (Figure 2B), we investigated whether in both cases its release resulted from passive diffusion through compromised nuclear and plasma membranes during A549 cell death. Following these treatments, we stained A549 cells with DNA stain Hoechst, pSIVA and necrosis-specific stain PI for imaging by fluorescence microscopy. We found that DMSO and cisplatin differed significantly in their effects on A549 viability and membrane integrity (Figure S11). When compared with the control (Figure S11A), DMSO-treated cells demonstrated robust apoptosis and secondary necrosis, with significantly compromised integrity of nuclear and plasma membranes (Figure S11B). Conversely, A549 cells treated with 20 μM cisplatin showed no signs of apoptosis or necrosis after 24 h (Figure S11C), with necrotic cells beginning to appear with 100 μM cisplatin (Figure S11D).

3.9. Carboplatin and Transplatin Are Less Effective than Cisplatin at Decreasing Cell Count and Viability

The decrease in the A549 cell count induced by 20 μM transplatin ($6.6 \times 10^6 \pm 1.5 \times 10^5$, $p < 0.0001$), 100 μM transplatin ($6.4 \times 10^6 \pm 1.1 \times 10^5$, $p < 0.0001$), 100 μM carboplatin ($5.5 \times 10^6 \pm 2.7 \times 10^5$, $p < 0.0001$), and 300 μM carboplatin ($4.7 \times 10^6 \pm 1.8 \times 10^5$, $p < 0.0001$), was significantly less than 20 μM cisplatin ($3.8 \pm 3.2 \times 10^5$) (Figure S12). Similarly, the A549 cell viability induced by 20 μM transplatin ($95.3 \pm 1.0\%$, $p < 0.0001$), 100 μM transplatin ($94.2 \pm 0.9\%$, $p < 0.0001$), and 100 μM carboplatin ($94.3 \pm 0.6\%$, $p < 0.0001$) was also significantly lower than 20 μM cisplatin ($91.4 \pm 0.4\%$). However, there was no significant difference in cell viability between 20 μM cisplatin and 300 μM carboplatin ($94.2 \pm 2.1\%$).

3.10. Cisplatin and Leptomycin B (LMB) and Synergistically Attenuate A549 Cell Growth and Increase A549 Cell Death

The minimal amount of PI staining of cisplatin-treated cells indicated that the secretion of HMGB1 from A549 cells was not dependent on loss of nuclear and plasma membrane integrity (Figure S11). To further evaluate this result with an alternative approach, we analyzed cisplatin-treated A549 cells with trypan blue exclusion assays (Figure 8). These assays showed that 24 h treatment with 50 μM cisplatin primarily induced a decrease in cell proliferation ($p < 0.001$, Figure 8A upper) and viability ($p < 0.001$, Figure 8B upper) after 24 h when compared with PBS. There was a very modest increase in cell death ($5.9 \pm 1.4 \times 10^5$ cells; $p < 0.044$) when compared with PBS ($4.3 \pm 0.5 \times 10^5$ cells) at 24 (Figure 8C upper). A combination of 50 μM cisplatin with 16 nM leptomycin B (LMB) significantly increased cell death at 24 h to $7.4 \pm 1.4 \times 10^5$ cells when compared with 50 μM cisplatin alone ($p < 0.0246$) (Figure 8C, upper).

There remained a significant decrease in cell proliferation ($p < 0.0001$, Figure 8A lower) and viability ($p < 0.0001$, Figure 8B lower) after 50 μM cisplatin treatment when compared with PBS at 48 h with no additional increase in cell death ($4.3 \pm 0.9 \times 10^5$; $p < 0.042$, Figure 8C lower). However, a combination of cisplatin and LMB resulted in a highly significant increase in cell death at 48 h of $10.2 \pm 1.6 \times 10^5$ cells when compared with LMB alone ($p < 0.0001$) or cisplatin alone ($p < 0.0001$) (Figure 8C, lower).

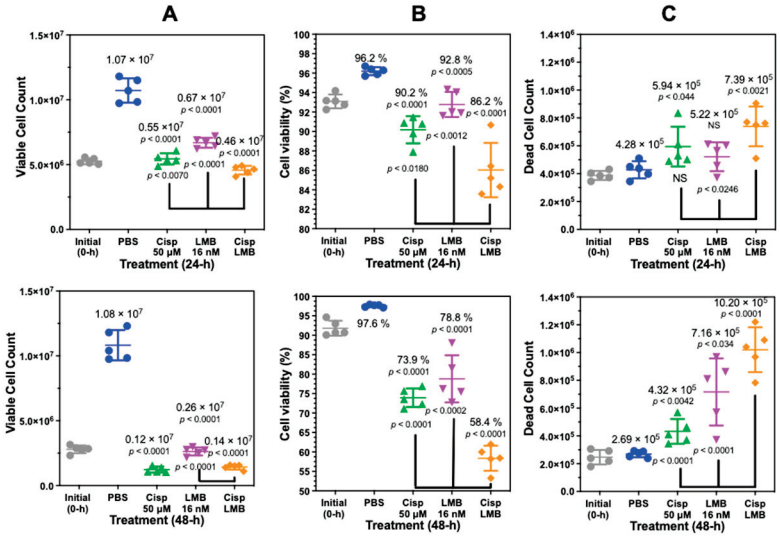


Figure 8. Cisplatin and leptomycin B (LMB) attenuate A549 cell growth and increase A549 cell death. Trypan Blue exclusion assay on biological replicates (n = 5) after cisplatin (50 µM), LMB (16 nM) and a combination of cisplatin (50 µM) and LMB (16 nM) treatment after 24-h. (**A**) Cell count after 24 h (upper) and 48 h (lower). (**B**) Cell viability (%) after 24 h and 48 h. (**C**) Dead cell count after 24 h and 48 h.

4. Discussion

Numerous quantitative studies of protein expression using MS-based methodology have relied on the utilization of stable isotopically labeled standards known as AQUA peptides [48]. These AQUA peptides offer exceptional precision by compensating for variations in ionization efficiency within the mass spectrometer. However, their accuracy is compromised, particularly when IP is employed for protein isolation, as they fail to account for losses that occur during the isolation procedure. Moreover, they do not consider inter-sample differences in protein digestion efficiency, as demonstrated in our research on apolipoprotein (Apo)A1 protein in human serum [49]. The inclusion of an AQUA peptide before protease digestion results in differential loss of the peptide during digestion when compared to the protein-derived peptide [49], rendering this approach unsuitable. Fortunately, these challenges can be effectively overcome by utilizing Stable Isotope Labeling by Amino Acids in Cell Culture (SILAC) protein internal standards, as we have successfully demonstrated for HMGB1 in serum and plasma [15], as well as in various other scenarios. For instance, SILAC internal standards have proven effective for quantifying oxidized HMGB1 in cell media [6], amyloid-β proteins in cerebrospinal fluid (CSF) [50], apolipoprotein-A1 in serum [51], human frataxin-M and human frataxin-E proteins in whole blood [52], and mouse frataxin-M proteins in mouse heart, brain, and liver tissues [47]. The SILAC protein internal standard method establishes a ratio between the SILAC-labeled protein and the corresponding endogenous protein at the beginning of the isolation procedure. This ratio remains constant throughout the entire process and is employed to calculate the quantity of endogenous protein using a standard curve constructed simultaneously with an authentic protein standard. Additionally, the SILAC protein serves as a carrier to enhance the recovery of low-level tissue proteins that may be lost due to non-selective binding to glassware and plastic surfaces. This effect was convincingly demonstrated in our assay for amyloid-β proteins in CSF [50], where most of the amyloid proteinsare lost in the absence of a stable isotope carrier through binding to surfaces during isolation and analysis.

Immunoblotting of cell culture media with an anti-HMGB1 pAb demonstrated that REN and EMMESO mesothelioma cell lines constitutively secrete significant amounts of HMGB1. However, A549 NSLC cells do not secrete HMGB1 unless treated with cisplatin. In contrast, HMGB2, despite being found in similar amounts to HMGB1 in the nucleus of A549

cells, is not secreted. Absolute quantification with LC-MS on immunocaptured HMGB1 from A549 cell culture media revealed that cisplatin was very effective at inducing HMGB1 release (Figure 2B). This suggested that cisplatin has a unique biological activity, which causes HMGB1 secretion. In keeping with such a possibility, neither cisplatin's stereoisomer transplatin nor the platinum drug analog carboplatin caused significant HMGB1 release, even at much higher doses. Both cisplatin [53] and carboplatin [54] form the same 1,2-(GpG) intrastrand crosslinks, suggesting that the slower kinetics of carboplatin's reactivity with DNA might be sufficient to result in disparate effects on HMGB1 release, or the that activity might even be distinct from their effects on DNA damage. Trypan blue exclusion assays demonstrated that 100 μM carboplatin was less effective than 20 μM and 100 μM cisplatin in attenuating A549 cell proliferation and viability after 24 h, suggesting less impact on DNA replication, presumably through less reactivity with nuclear DNA (Figure S12). However, there was no difference in cell viability between 20 μM cisplatin and 300 μM carboplatin, which means that it is not simply a difference in the ability of platinum drugs to induce A549 cell death that is responsible for the increase in cisplatin-mediated HMGB1 release.

DMSO ($p < 0.0014$) and cisplatin at 20 μM ($p < 0.0014$) and 100 μM ($p < 0.0001$) induced significantly increased amounts of HMGB1 secretion from A549 cells when compared with PBS controls (Figure 2B). DMSO is known to cause cellular oxidative stress and DNA oxidation [43] as well as apoptosis [44]. Therefore, we reasoned that both DMSO and cisplatin might function similarly by causing the passive release of HMGB1 due to loss of nuclear and plasma membrane integrity following apoptosis and secondary necrosis. However, analysis with fluorescence microscopy revealed that DMSO caused robust apoptosis and necrosis (Figure S11B), whereas low-dose cisplatin had very little effect after 24 h at doses up to 100 μM (Figure S11C,D). Trypan blue exclusion assays confirmed this finding, showing that 24 h cisplatin treatment with 50 μM cisplatin primarily induced a significant decrease in cell proliferation (Figure 8A upper) and viability (Figure 8B upper) after 24 h compared to PBS. There was a very modest increase in cell death ($5.9 \pm 1.4 \times 10^5$ cells; $p < 0.044$) when compared to PBS ($4.3 \pm 0.5 \times 10^5$ cells) at 24 h (Figure 8C upper). Given that A549 cells showed significant secretion of HMGB1 with cisplatin despite intact nuclear and plasma membranes after 24-h, we reasoned that secretion was through a regulated mechanism rather than a passive release of nuclear proteins. It is noteworthy that there remained a significant decrease in cell proliferation ($p < 0.0001$, Figure 8A lower) and viability ($p < 0.0001$, Figure 8B lower) when compared with PBS at 48 h with no additional increase in cell death (Figure 8C lower).

To confirm that cisplatin treatment specifically induced the secretion of HMGB1, and not all nuclear proteins, we examined the nuclear, cytosolic, and media fractions of A549 cells for HMGB1 and HMGB2. Anti-HMGB1 and anti-HMGB1 immunoblotting showed specificity for HMGB1 and HMGB2, respectively, as demonstrated with recombinant proteins (Figure S3A,B). HMGB1 was detected in nuclear and cytosolic fractions (Figure S3A), whereas HMGB2 was only detected in the nucleus. (Figure S3B). Anti-histone 4 and anti-FASN immunoblotting confirmed robust enrichment of the nuclear and cytosolic fractions and showed that there was no leakage of A549 cellular proteins into the cell culture media (Figure S3A). HMGB1 and HMGB2 are nuclear proteins that are 93% homologous and 80% identical [55]. Surprisingly, we found that only HMGB1 was secreted in significant amounts into the A549 cell culture media after cisplatin treatment. This finding was confirmed by qualitative LC-MS analysis of HMGB1- and HMGB2-specific peptides in subcellular fractions (Figures S4–S6). It has been previously reported that HMGB2 can be secreted from myeloid cells [56] and has been detected in serum of patients with coronary artery in-stent restenosis [57], which provides further evidence that cisplatin is unique in its ability to selectively induce HMGB1 release in the presence of high levels of HMGB2.

There are several reports that acetylation of HMGB1 at K-3, K-7, or K-12 can modulate its ability to inhibit the repair of cisplatin DNA adducts [4,58–60]. Unfortunately, in vitro, and in vivo studies with cisplatin have been unable to confirm that these PTMs are present on secreted HMGB1. To address this issue by quantifying acetylation at K-3, K-7, and K-12,

a SILAC HMGB1 internal standard was added to cell culture media samples collected from A549 cells (Scheme 1). HMGB1 was isolated by IP of these samples and treated with *D*6-acetic anhydride to trideuteroacetylate (CD_3-acetylate) all unacetylated HMGB1 lysine residues. This process converted each of the HMGB1-derived peptides into one molecular form that only differed in the mass of the acetyl-lysine modification. In a previous study, we showed the IP procedure can isolate HMGB1 containing acetylated lysine residues [15]. Using this approach, we were unable to detect acetylation on K-3, K-7, or K-12 residues using a highly specific nanoLC-PRM/HRMS method (Scheme 1). There is also substantial evidence suggesting that HMGB1 NLS1 and NLS2 acetylation is required to facilitate its secretion [31,32,41,61], although many of the key studies have been retracted or statements of concern issued [28]. Consequently, it is perhaps not surprising that we were unable to detect any acetylated forms of HMGB1 secreted after treatment of A549 lung cells with cisplatin. Therefore, we investigated whether cisplatin-mediated HMGB1 secretion was regulated by other PTMs.

The oxidation state of HMGB1′s three Cys residues has been considered especially important in regulating both HMGB1′s secretion and its extracellular signaling activity. However, there are contradictory reports that relate the redox status of extracellular HMGB1 to its mechanism of secretion. This is because most approaches in interrogating the redox state of HMGB1 lack the necessary quantitative parameters for site-specific analysis to accurately measure labile modifications like disulfide bonds. Therefore, we developed a novel differential alkylation approach using SILAC HMGB1 internal standard to control for any differences in HMGB1 recovery, digestion, or peptide ionization efficiency among differentially alkylated HMGB1 proteoforms. This made it possible to conduct site-specific quantification of HMGB1 Cys-disulfides (Scheme 2). Although other tested treatments induced the release of some reduced HMGB1 with free Cys-23 and C-45, cisplatin induced the secretion of significantly more reduced HMGB1. The association of this reduced proteoform of HMGB1 with chemokine activity [62–64] indicates that cisplatin mediated HMGB1 secretion could activate immune cells during cancer chemotherapy.

We also explored whether other PTMs might be involved in the regulation of cisplatin-mediated HMGB1 secretion by testing the effects of different pharmacological inhibitors of PTM formation and examining immunoblots of the cell culture media. Although ADP-ribosylation by PARP1 has been implicated in the regulation of HMGB1 mobility, including a model of DNA damage-associated subcellular translocation [65], the PARP1 inhibitor Olaparib [66] had no effect on cisplatin-mediated HMGB1 secretion (Figure 6A). Similarly, although HMGB1 phosphorylation by PKCs has been suggested to increase HMGB1 secretion, we found that pan-PKC inhibitors GO-6983 [67] and Rottlerin [68] had no effect on cisplatin-mediated HMGB1 secretion from A549 cells (Figure 6B,C). Furthermore, we were unable to detect any other modifications with lysine, tyrosine, serine, or threonine using LC-HRMS/MS analysis of Asp-N, Glu-C, or chymotryptic peptides.

Misinterpretation of much of the original MS data on HMGB1 secretion led to the erroneous concept that acetylation was required for HMGB1 secretion to occur [69]. Nevertheless, this early study did convincingly show that inhibition of nuclear export with LMB prevented the transport of HMGB1 from the nucleus to the cytosol [69]. However, this study did not report that LMB also inhibits secretion of the substantial amounts of HMGB1 that are present in the cytosol (Figure 7B). LMB is known to inhibit the nuclear export of proteins through binding and inhibition of XPO1 (CRM1) (Figure 9) [70,71]. Inhibition of XPO1 might also prevent the nuclear export of pro-secretory proteins and so prevent the secretion of cytosolic proteins [72]. We reasoned that LMB could inhibit the secretion of HMGB1 by concentrating it in the nucleus and inhibiting secretion of the residual HMGB1 from the cytosol (Figure 9). LMB caused an increase in cell death (Figure 8C) and is known to be cytotoxic [73].

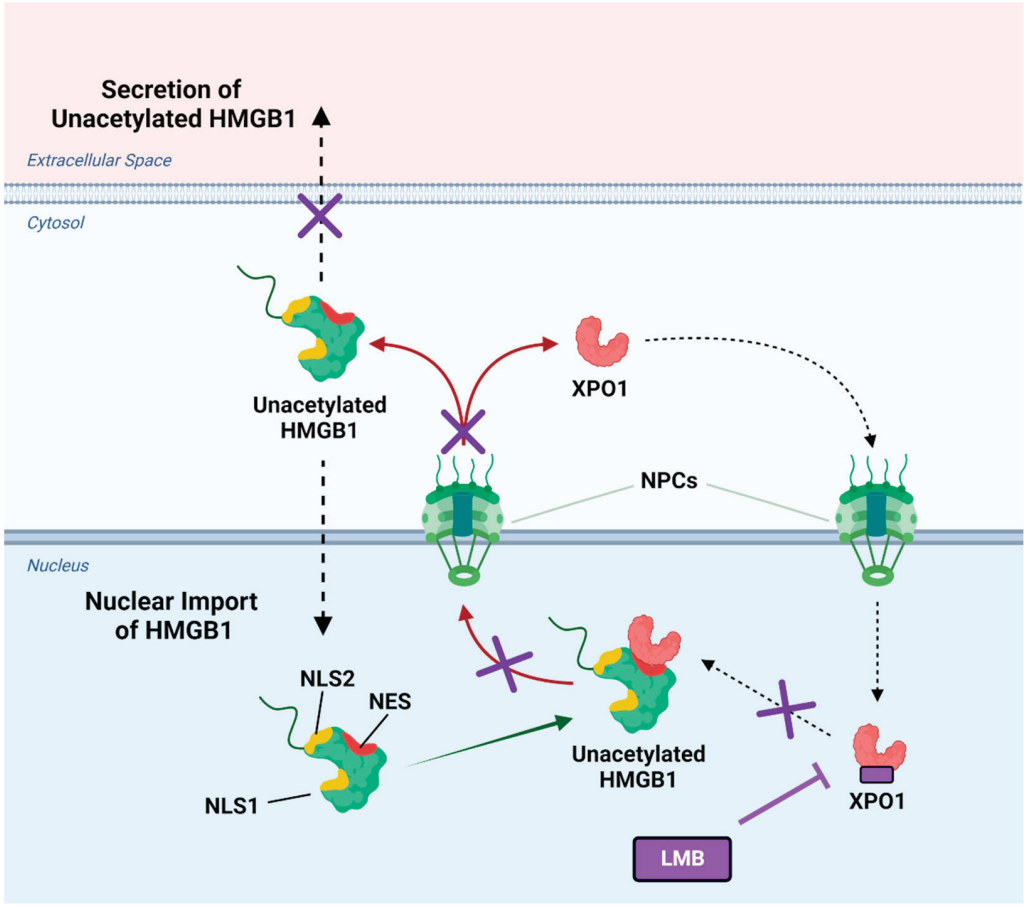


Figure 9. Cisplatin-mediated high mobility group box (HMGB1) secretion is regulated by nuclear exportin 1 (XPO1). HMGB1 contains two reported nuclear localization sequences (NLS1 and NLS2) and a potential nuclear export sequence (NES). Upon treatment of lung cancer cells with cisplatin, XPO1 (also known as chromosomal maintenance 1; CRM1) facilitates the nuclear export of unacetylated HMGB1 through the nuclear pore complexes (NPCs) into the cytosol (indicated by arrows). This translocation allows HMGB1 to be subsequently secreted into the extracellular space. Inhibitors of XPO1 such as leptomycin B (LMB) inhibit the binding of XPO1 to HMGB1, thereby preventing XPO1-regulated secretion of HMGB1 in the presence of cisplatin (indicated by cross signs on arrows). Figure created in Biorender.

Consequently, there is a narrow concentration range where a decrease in HMGB1 secretion can be observed before it induces necrotic cell death and releases HMGB1. We found that the addition of LMB caused a significant inhibition of cisplatin-mediated HMGB1 secretion (Figures 6D,F and 7C). We also showed that the XPO1 inhibitor KPT-330 [74,75] also caused a significant decrease in HMGB1 secretion (Figure 6E,G). A combination of cisplatin and LMB resulted in an additive increase in A549 cell death at 24 h and 48 h when compared with LMB alone or cisplatin alone (Figure 8C). There was a concomitant increase in nuclear HMGB1 with a decrease in cytosolic HMGB1 (Figure 7B) and inhibition of HMGB1 secretion (Figure 7C) as would be predicted if nuclear export were inhibited (Figure 9). HMGB1 binds more tightly to cisplatinated DNA than unmodified DNA, and this binding inhibits the repair of cisplatin-derived 1,2-(GpG) DNA intrastrand crosslinks, which in turn interferes with DNA replication and eventually activates apoptosis [25]. Cisplatin treatment causes increased HMGB1 concentration in the nucleus (Figure 7A), and cancer cells seem to partially survive treatment with cisplatin by transporting HMGB1 from the nucleus into the cytosol where it is then secreted into the extracellular milieu. Therefore, our data are consistent with the concept that LMB-mediated accumulation of HMGB1 in the nucleus facilitates the known ability of HMGB1 to inhibit 1,2-(GpG) DNA intrastrand

repair [4,58–60] and so potentiates the ability of cisplatin to induce A549 NSCLC viability and cell death (Figure 7).

5. Conclusions

We developed a stable isotope dilution nano-LC-PRM/HRMS assay for the precise and accurate quantification of nuclear, cytosolic, and secreted HMGB1 proteoforms. This revealed that inhibition of nuclear transport (Figure 9) inhibits cisplatin-mediated HMGB1 secretion (Figure 6) and causes HMGB1 accumulation in the nucleus (Figure 7A), which is known to inhibit of the repair of 1,2-(GpG) intrastrand crosslinks [4,58–60]. Inhibition of DNA repair by the increased nuclear HMGB1 was most likely responsible for the decreased cell viability (Figure 8B) and increased cell death that was observed (Figure 8C) [25]. This offers the potential for a novel approach to increasing the antitumor activity of low-dose cisplatin by co-administration with low doses of XPO1 inhibitors such as KPT-330 (Selinexor). The difference between A549 NSCLC cells and malignant mesothelioma REN and EMMESO cells regarding HMGB1 secretion (Figure 2A) suggests that different cancer cells will differ in their capacity to secrete HMGB1 in response to cisplatin therapy. The findings of this research have established a different mechanism of HMGB1 secretion in a NSCLC model than has previously been reported. Therefore, future research will benefit from examining this new mechanism in additional cancer cell lines.

It is intriguing that the nano-LC-PRM/HRMS assay also revealed that cisplatin but not carboplatin stimulated HMGB1 secretion from A549 NSCLC cells (Figure 2) as these chemotherapeutic agents are typically thought to have identical modes of action. HMGB1 is an immunomodulator through activation of RAGE, TLR2, and TLR4 [7,8]. The immunomodulatory activity of HMGB1 arises primarily through activity of the fully reduced form, a major proteoform secreted from A549 cells by treatment with doses of cisplatin that slow cell growth but cause minimal cell death after 24 h (<100 μM). Finally, there is increasing interest in combining low-dose (metronomic) chemotherapy in combination with immunotherapy for treating NSCLC [76,77]. Consequently, low-dose cisplatin-mediated HMGB1 release could be used to stimulate the immune system prior to treatment of NSCLC patients with immunotherapy. Furthermore, optimization of dose regimens could be informed by monitoring HMGB1 proteoform levels in the plasma using the methodology that we have reported previously [15].

Supplementary Materials: The following supporting information can be downloaded at: https://www.mdpi.com/article/10.3390/biom13091335/s1. Table S1. Lysine-containing peptides in HMGB1 analyzed by PRM/HRMS. Figure S1. NanoLC-PRM/HRMS chromatograms of non-cysteine tryptic peptides from cisplatin-treated A549 media. Figure S2. Calibration curves with HMGB1 tryptic peptide transitions constructed in cell culture media. Figure S3. HMGB1 and HMGB2 in nuclear, cytosolic, and media fractions of A549 cells. Figure S4. HMGB1 and HMGB2 in nuclear fractions of cisplatin-treated A549 cells. Figure S5. HMGB1 and HMGB2 in cytosolic fractions of cisplatin-treated A549 cells. Figure S6. HMGB1 and HMGB2 in media from cisplatin-treated A549 cells. Figure S7. NLS1 and NLS2 transitions of unacetylated HMGB1 secreted with cisplatin treatment. Figure S8. DMSO induces secretion of unacetylated HMGB1. Figure S9. Assigned mass spectra in cysteine-containing peptides in HMGB1 secreted with cisplatin treatment I. Figure S10. Assigned mass spectra in cysteine-containing peptides in HMGB1 secreted with cisplatin treatment II. Figure S11. Cisplatin-mediated secretion of HMGB1 fromA549 cells is not dependent on necrosis. Figure S12. Cisplatin attenuates A549 cell growth and decreases viability more than other platinum drug analogs. Figure S13. Original full-size Western blots.

Author Contributions: I.A.B., C.M. and K.P.G. conceived and coordinated the study. K.P.G. and R.P. performed the experiments. C.M. and K.P.G. analyzed the data. I.A.B., C.M. and K.P.G. wrote the paper. All authors have read and agreed to the published version of the manuscript.

Funding: This work was supported by the National Institutes of Health grants P30ES01350 and T32ES019851.

Data Availability Statement: The data presented in this study are available on request from Ian A. Blair.

Conflicts of Interest: The authors declare that they have no conflict of interest with the contents of this article.

References

1. Tsuda, K.; Kikuchi, M.; Mori, K.; Waga, S.; Yoshida, M. Primary structure of non-histone protein HMG1 revealed by the nucleotide sequence. *Biochemistry* **1988**, *27*, 6159–6163. [CrossRef] [PubMed]
2. Stros, M. HMGB proteins: Interactions with DNA and chromatin. *Biochim. Biophys. Acta* **2010**, *1799*, 101–113. [CrossRef] [PubMed]
3. Yang, H.; Antoine, D.J.; Andersson, U.; Tracey, K.J. The many faces of HMGB1: Molecular structure-functional activity in inflammation, apoptosis, and chemotaxis. *J. Leukoc. Biol.* **2013**, *93*, 865–873. [CrossRef]
4. Ugrinova, I.; Zlateva, S.; Pashev, I.G.; Pasheva, E.A. Native HMGB1 protein inhibits repair of cisplatin-damaged nucleosomes in vitro. *Int. J. Biochem. Cell Biol.* **2009**, *41*, 1556–1562. [CrossRef]
5. Lu, B.; Wang, C.; Wang, M.; Li, W.; Chen, F.; Tracey, K.J.; Wang, H. Molecular mechanism and therapeutic modulation of high mobility group box 1 release and action: An updated review. *Expert. Rev. Clin. Immunol.* **2014**, *10*, 713–727. [CrossRef] [PubMed]
6. Pirnie, R.; Gillespie, K.P.; Weng, L.; Mesaros, C.; Blair, I.A. Characterization and Quantification of Oxidized High Mobility Group Box 1 Proteoforms Secreted from Hepatocytes by Toxic Levels of Acetaminophen. *Chem. Res. Toxicol.* **2022**, *35*, 1893–1902. [CrossRef] [PubMed]
7. Park, J.S.; Gamboni-Robertson, F.; He, Q.; Svetkauskaite, D.; Kim, J.Y.; Strassheim, D.; Sohn, J.W.; Yamada, S.; Maruyama, I.; Banerjee, A.; et al. High mobility group box 1 protein interacts with multiple Toll-like receptors. *Am. J. Physiol. Cell Physiol.* **2006**, *290*, C917–C924. [CrossRef]
8. Park, J.S.; Svetkauskaite, D.; He, Q.; Kim, J.Y.; Strassheim, D.; Ishizaka, A.; Abraham, E. Involvement of toll-like receptors 2 and 4 in cellular activation by high mobility group box 1 protein. *J. Biol. Chem.* **2004**, *279*, 7370–7377. [CrossRef]
9. Venereau, E.; De Leo, F.; Mezzapelle, R.; Careccia, G.; Musco, G.; Bianchi, M.E. HMGB1 as biomarker and drug target. *Pharmacol. Res.* **2016**, *111*, 534–544. [CrossRef]
10. Vijayakumar, E.C.; Bhatt, L.K.; Prabhavalkar, K.S. High Mobility Group Box-1 (HMGB1): A Potential Target in Therapeutics. *Curr. Drug Targets* **2019**, *20*, 1474–1485. [CrossRef]
11. Lange, S.S.; Vasquez, K.M. HMGB1: The jack-of-all-trades protein is a master DNA repair mechanic. *Mol. Carcinog.* **2009**, *48*, 571–580. [CrossRef] [PubMed]
12. Tang, D.; Kang, R.; Cheh, C.W.; Livesey, K.M.; Liang, X.; Schapiro, N.E.; Benschop, R.; Sparvero, L.J.; Amoscato, A.A.; Tracey, K.J.; et al. HMGB1 release and redox regulates autophagy and apoptosis in cancer cells. *Oncogene* **2010**, *29*, 5299–5310. [CrossRef] [PubMed]
13. Krynetskaia, N.F.; Phadke, M.S.; Jadhav, S.H.; Krynetskiy, E.Y. Chromatin-associated proteins HMGB1/2 and PDIA3 trigger cellular response to chemotherapy-induced DNA damage. *Mol. Cancer Ther.* **2009**, *8*, 864–872. [CrossRef] [PubMed]
14. Wang, L.; He, L.; Bao, G.; He, X.; Fan, S.; Wang, H. Ionizing Radiation Induces HMGB1 Cytoplasmic Translocation and Extracellular Release. *Guo Ji Fang. She Yi Xue He Yi Xue Za Zhi* **2016**, *40*, 91–99.
15. Weng, L.; Guo, L.; Vachani, A.; Mesaros, C.; Blair, I.A. Quantification of Serum High Mobility Group Box 1 by Liquid Chromatography/High-Resolution Mass Spectrometry: Implications for Its Role in Immunity, Inflammation, and Cancer. *Anal. Chem.* **2018**, *90*, 7552–7560. [CrossRef]
16. Wang, J.L.; Wu, D.W.; Cheng, Z.Z.; Han, W.Z.; Xu, S.W.; Sun, N.N. Expression of high mobility group box-B1 (HMGB-1) and matrix metalloproteinase-9 (MMP-9) in non-small cell lung cancer (NSCLC). *Asian Pac. J. Cancer Prev.* **2014**, *15*, 4865–4869. [CrossRef] [PubMed]
17. Ma, Y.; Kang, S.; Wu, X.; Han, B.; Jin, Z.; Guo, Z. Up-regulated HMGB1 in the pleural effusion of non-small cell lung cancer (NSCLC) patients reduces the chemosensitivity of NSCLC cells. *Tumori* **2018**, *104*, 338–343. [CrossRef]
18. Sun, S.; Zhang, W.; Cui, Z.; Chen, Q.; Xie, P.; Zhou, C.; Liu, B.; Peng, X.; Zhang, Y. High mobility group box-1 and its clinical value in breast cancer. *Onco Targets Ther.* **2015**, *8*, 413–419. [CrossRef]
19. Cheng, K.J.; Alshawsh, M.A.; Mejia Mohamed, E.H.; Thavagnanam, S.; Sinniah, A.; Ibrahim, Z.A. HMGB1: An overview of its versatile roles in the pathogenesis of colorectal cancer. *Cell Oncol (Dordr)* **2020**, *43*, 177–193. [CrossRef]
20. Kang, R.; Tang, D. The Dual Role of HMGB1 in Pancreatic Cancer. *J. Pancreatol.* **2018**, *1*, 19–24. [CrossRef]
21. Tabata, C.; Shibata, E.; Tabata, R.; Kanemura, S.; Mikami, K.; Nogi, Y.; Masachika, E.; Nishizaki, T.; Nakano, T. Serum HMGB1 as a prognostic marker for malignant pleural mesothelioma. *BMC Cancer* **2013**, *13*, 205. [CrossRef]
22. Shen, X.; Hong, L.; Sun, H.; Shi, M.; Song, Y. The expression of high-mobility group protein box 1 correlates with the progression of non-small cell lung cancer. *Oncol. Rep.* **2009**, *22*, 535–539. [CrossRef]
23. Fennell, D.A.; Summers, Y.; Cadranel, J.; Benepal, T.; Christoph, D.C.; Lal, R.; Das, M.; Maxwell, F.; Visseren-Grul, C.; Ferry, D. Cisplatin in the modern era: The backbone of first-line chemotherapy for non-small cell lung cancer. *Cancer Treat. Rev.* **2016**, *44*, 42–50. [CrossRef]
24. de Castria, T.B.; da Silva, E.M.; Gois, A.F.; Riera, R. Cisplatin versus carboplatin in combination with third-generation drugs for advanced non-small cell lung cancer. *Cochrane Database Syst. Rev.* **2013**, *8*, CD009256. [CrossRef]

25. Wang, D.; Lippard, S.J. Cellular processing of platinum anticancer drugs. *Nat. Rev. Drug Discov.* **2005**, *4*, 307–320. [CrossRef] [PubMed]
26. Naumnik, W.; Nilklinska, W.; Ossolinska, M.; Chyczewska, E. Serum levels of HMGB1, survivin, and VEGF in patients with advanced non-small cell lung cancer during chemotherapy. *Folia Histochem. Cytobiol.* **2009**, *47*, 703–709. [CrossRef] [PubMed]
27. Niki, M.; Yokoi, T.; Kurata, T.; Nomura, S. New prognostic biomarkers and therapeutic effect of bevacizumab for patients with non-small-cell lung cancer. *Lung Cancer (Auckl)* **2017**, *8*, 91–99. [CrossRef]
28. Pirnie, R.; P Gillespie, K.; Mesaros, C.; Blair, I.A. Reappraisal of oxidized HMGB1 as a mediator and biomarker. *Future Sci. OA* **2022**, *8*, FSO828. [CrossRef] [PubMed]
29. Ge, X.; Antoine, D.J.; Lu, Y.; Arriazu, E.; Leung, T.M.; Klepper, A.L.; Branch, A.D.; Fiel, M.I.; Nieto, N. High mobility group box-1 (HMGB1) participates in the pathogenesis of alcoholic liver disease (ALD). *J. Biol. Chem.* **2014**, *289*, 22672–22691. [CrossRef] [PubMed]
30. He, Y.; Ding, Y.; Wang, D.; Zhang, W.; Chen, W.; Liu, X.; Qin, W.; Qian, X.; Chen, H.; Guo, Z. HMGB1 bound to cisplatin-DNA adducts undergoes extensive acetylation and phosphorylation in vivo. *Chem. Sci.* **2015**, *6*, 2074–2078. [CrossRef] [PubMed]
31. Wang, M.; Gauthier, A.; Daley, L.; Dial, K.; Wu, J.; Woo, J.; Lin, M.; Ashby, C.; Mantell, L.L. The Role of HMGB1, a Nuclear Damage-Associated Molecular Pattern Molecule, in the Pathogenesis of Lung Diseases. *Antioxid. Redox Signal* **2019**, *31*, 954–993. [CrossRef] [PubMed]
32. Chen, R.; Kang, R.; Tang, D. The mechanism of HMGB1 secretion and release. *Exp. Mol. Med.* **2022**, *54*, 91–102. [CrossRef] [PubMed]
33. Ito, I.; Fukazawa, J.; Yoshida, M. Post-translational methylation of high mobility group box 1 (HMGB1) causes its cytoplasmic localization in neutrophils. *J. Biol. Chem.* **2007**, *282*, 16336–16344. [CrossRef] [PubMed]
34. Li, Y.; Xie, J.; Li, X.; Fang, J. Poly (ADP-ribosylation) of HMGB1 facilitates its acetylation and promotes HMGB1 translocation-associated chemotherapy-induced autophagy in leukaemia cells. *Oncol. Lett.* **2020**, *19*, 368–378. [CrossRef]
35. Lundback, P.; Stridh, P.; Klevenvall, L.; Jenkins, R.E.; Fischer, M.; Sundberg, E.; Andersson, U.; Antoine, D.J.; Harris, H.E. Characterization of the Inflammatory Properties of Actively Released HMGB1 in Juvenile Idiopathic Arthritis. *Antioxid. Redox Signal* **2016**, *24*, 605–619. [CrossRef]
36. Hoppe, G.; Talcott, K.E.; Bhattacharya, S.K.; Crabb, J.W.; Sears, J.E. Molecular basis for the redox control of nuclear transport of the structural chromatin protein Hmgb1. *Exp. Cell Res.* **2006**, *312*, 3526–3538. [CrossRef]
37. Antoine, D.J.; Harris, H.E.; Andersson, U.; Tracey, K.J.; Bianchi, M.E. A systematic nomenclature for the redox states of high mobility group box (HMGB) proteins. *Mol. Med.* **2014**, *20*, 135–137. [CrossRef]
38. Ditsworth, D.; Zong, W.X.; Thompson, C.B. Activation of poly(ADP)-ribose polymerase (PARP-1) induces release of the pro-inflammatory mediator HMGB1 from the nucleus. *J. Biol. Chem.* **2007**, *282*, 17845–17854. [CrossRef]
39. Yang, Z.; Li, L.; Chen, L.; Yuan, W.; Dong, L.; Zhang, Y.; Wu, H.; Wang, C. PARP-1 mediates LPS-induced HMGB1 release by macrophages through regulation of HMGB1 acetylation. *J. Immunol.* **2014**, *193*, 6114–6123. [CrossRef]
40. Pelovsky, P.; Pashev, I.G.; Pasheva, E. Interplay between in vitro acetylation and phosphorylation of tailless HMGB1 protein. *Biochem. Biophys. Res. Commun.* **2009**, *380*, 138–142. [CrossRef]
41. Lv, W.L.; Arnesano, F.; Carloni, P.; Natile, G.; Rossetti, G. Effect of in vivo post-translational modifications of the HMGB1 protein upon binding to platinated DNA: A molecular simulation study. *Nucleic Acids Res.* **2018**, *46*, 11687–11697. [CrossRef] [PubMed]
42. Park, S.; Lippard, S.J. Redox state-dependent interaction of HMGB1 and cisplatin-modified DNA. *Biochemistry* **2011**, *50*, 2567–2574. [CrossRef] [PubMed]
43. Mangal, D.; Vudathala, D.; Park, J.H.; Lee, S.H.; Penning, T.M.; Blair, I.A. Analysis of 7,8-dihydro-8-oxo-2′-deoxyguanosine in cellular DNA during oxidative stress. *Chem. Res. Toxicol.* **2009**, *22*, 788–797. [CrossRef]
44. Hanslick, J.L.; Lau, K.; Noguchi, K.K.; Olney, J.W.; Zorumski, C.F.; Mennerick, S.; Farber, N.B. Dimethyl sulfoxide (DMSO) produces widespread apoptosis in the developing central nervous system. *Neurobiol. Dis.* **2009**, *34*, 1–10. [CrossRef] [PubMed]
45. Banic, B.; Nipic, D.; Suput, D.; Milisav, I. DMSO modulates the pathway of apoptosis triggering. *Cell Mol. Biol. Lett.* **2011**, *16*, 328–341. [CrossRef] [PubMed]
46. Patel, S.M.; Smith, T.G.; Morton, M.; Stiers, K.M.; Seravalli, J.; Mayclin, S.J.; Edwards, T.E.; Tanner, J.J.; Becker, D.F. Cautionary Tale of Using Tris(alkyl)phosphine Reducing Agents with NAD(+)-Dependent Enzymes. *Biochemistry* **2020**, *59*, 3285–3289. [CrossRef]
47. Weng, L.; Laboureur, L.; Wang, Q.; Guo, L.; Xu, P.; Gottlieb, L.; Lynch, D.R.; Mesaros, C.; Blair, I.A. Extra-mitochondrial mouse frataxin and its implications for mouse models of Friedreich's ataxia. *Sci. Rep.* **2020**, *10*, 15788. [CrossRef] [PubMed]
48. Chahrour, O.; Cobice, D.; Malone, J. Stable isotope labelling methods in mass spectrometry-based quantitative proteomics. *J. Pharm. Biomed. Anal.* **2015**, *113*, 2–20. [CrossRef]
49. Wang, Q.; Zhang, S.; Guo, L.; Busch, C.M.; Jian, W.; Weng, N.; Snyder, N.W.; Rangiah, K.; Mesaros, C.; Blair, I.A. Serum apolipoprotein A-1 quantification by LC-MS with a SILAC internal standard reveals reduced levels in smokers. *Bioanalysis* **2015**, *7*, 2895–2911. [CrossRef]
50. Oe, T.; Ackermann, B.L.; Inoue, K.; Berna, M.J.; Garner, C.O.; Gelfanova, V.; Dean, R.A.; Siemers, E.R.; Holtzman, D.M.; Farlow, M.R.; et al. Quantitative analysis of amyloid beta peptides in cerebrospinal fluid of Alzheimer's disease patients by immunoaffinity purification and stable isotope dilution liquid chromatography/negative electrospray ionization tandem mass spectrometry. *Rapid Commun. Mass. Spectrom.* **2006**, *20*, 3723–3735. [CrossRef]

51. Wang, Q.; Guo, L.; Strawser, C.J.; Hauser, L.A.; Hwang, W.T.; Snyder, N.W.; Lynch, D.R.; Mesaros, C.; Blair, I.A. Low apolipoprotein A-I levels in Friedreich's ataxia and in frataxin-deficient cells: Implications for therapy. *PLoS ONE* **2018**, *13*, e0192779. [CrossRef]
52. Rojsajjakul, T.; Wu, L.; Grady, C.B.; Hwang, W.T.; Mesaros, C.; Lynch, D.R.; Blair, I.A. Liquid Chromatography-Mass Spectrometry Analysis of Frataxin Proteoforms in Whole Blood as Biomarkers of the Genetic Disease Friedreich's Ataxia. *Anal. Chem.* **2023**, *95*, 4251–4260. [CrossRef] [PubMed]
53. Ober, M.; Lippard, S.J. A 1,2-d(GpG) cisplatin intrastrand cross-link influences the rotational and translational setting of DNA in nucleosomes. *J. Am. Chem. Soc.* **2008**, *130*, 2851–2861. [CrossRef] [PubMed]
54. Blommaert, F.A.; van Dijk-Knijnenburg, H.C.; Dijt, F.J.; den Engelse, L.; Baan, R.A.; Berends, F.; Fichtinger-Schepman, A.M. Formation of DNA adducts by the anticancer drug carboplatin: Different nucleotide sequence preferences in vitro and in cells. *Biochemistry* **1995**, *34*, 8474–8480. [CrossRef]
55. Starkova, T.; Polyanichko, A.; Tomilin, A.N.; Chikhirzhina, E. Structure and Functions of HMGB2 Protein. *Int. J. Mol. Sci.* **2023**, *24*, 8334. [CrossRef]
56. Pusterla, T.; de Marchis, F.; Palumbo, R.; Bianchi, M.E. High mobility group B2 is secreted by myeloid cells and has mitogenic and chemoattractant activities similar to high mobility group B1. *Autoimmunity* **2009**, *42*, 308–310. [CrossRef]
57. He, Y.H.; Wang, X.Q.; Zhang, J.; Liu, Z.H.; Pan, W.Q.; Shen, Y.; Zhu, Z.B.; Wang, L.J.; Yan, X.X.; Yang, K.; et al. Association of Serum HMGB2 Levels With In-Stent Restenosis: HMGB2 Promotes Neointimal Hyperplasia in Mice With Femoral Artery Injury and Proliferation and Migration of VSMCs. *Arterioscler. Thromb. Vasc. Biol.* **2017**, *37*, 717–729. [CrossRef] [PubMed]
58. Sterner, R.; Vidali, G.; Allfrey, V.G. Studies of acetylation and deacetylation in high mobility group proteins. Identification of the sites of acetylation in HMG-1. *J. Biol. Chem.* **1979**, *254*, 11577–11583. [CrossRef]
59. Sterner, R.; Vidali, G.; Allfrey, V.G. Studies of acetylation and deacetylation in high mobility group proteins. Identification of the sites of acetylation in high mobility group proteins 14 and 17. *J. Biol. Chem.* **1981**, *256*, 8892–8895. [CrossRef]
60. Ugrinova, I.; Mitkova, E.; Moskalenko, C.; Pashev, I.; Pasheva, E. DNA bending versus DNA end joining activity of HMGB1 protein is modulated in vitro by acetylation. *Biochemistry* **2007**, *46*, 2111–2117. [CrossRef]
61. Tripathi, A.; Shrinet, K.; Kumar, A. HMGB1 protein as a novel target for cancer. *Toxicol. Rep.* **2019**, *6*, 253–261. [CrossRef]
62. Venereau, E.; Casalgrandi, M.; Schiraldi, M.; Antoine, D.J.; Cattaneo, A.; De Marchis, F.; Liu, J.; Antonelli, A.; Preti, A.; Raeli, L.; et al. Mutually exclusive redox forms of HMGB1 promote cell recruitment or proinflammatory cytokine release. *J. Exp. Med.* **2012**, *209*, 1519–1528. [CrossRef] [PubMed]
63. Schiraldi, M.; Raucci, A.; Munoz, L.M.; Livoti, E.; Celona, B.; Venereau, E.; Apuzzo, T.; De Marchis, F.; Pedotti, M.; Bachi, A.; et al. HMGB1 promotes recruitment of inflammatory cells to damaged tissues by forming a complex with CXCL12 and signaling via CXCR4. *J. Exp. Med.* **2012**, *209*, 551–563. [CrossRef] [PubMed]
64. Venereau, E.; Schiraldi, M.; Uguccioni, M.; Bianchi, M.E. HMGB1 and leukocyte migration during trauma and sterile inflammation. *Mol. Immunol.* **2013**, *55*, 76–82. [CrossRef] [PubMed]
65. Ryabokon, N.I.; Cieslar-Pobuda, A.; Rzeszowska-Wolny, J. Inhibition of poly(ADP-ribose) polymerase activity affects its subcellular localization and DNA strand break rejoining. *Acta Biochim. Pol.* **2009**, *56*, 243–248. [CrossRef]
66. Paik, J. Olaparib: A Review as First-Line Maintenance Therapy in Advanced Ovarian Cancer. *Target. Oncol.* **2021**, *16*, 847–856. [CrossRef]
67. Young, L.H.; Balin, B.J.; Weis, M.T. Go 6983: A fast acting protein kinase C inhibitor that attenuates myocardial ischemia/reperfusion injury. *Cardiovasc Drug Rev* **2005**, *23*, 255–272. [CrossRef]
68. Maioli, E.; Torricelli, C.; Valacchi, G. Rottlerin and cancer: Novel evidence and mechanisms. *ScientificWorldJournal* **2012**, *2012*, 350826. [CrossRef]
69. Bonaldi, T.; Talamo, F.; Scaffidi, P.; Ferrera, D.; Porto, A.; Bachi, A.; Rubartelli, A.; Agresti, A.; Bianchi, M.E. Monocytic cells hyperacetylate chromatin protein HMGB1 to redirect it towards secretion. *EMBO J.* **2003**, *22*, 5551–5560. [CrossRef]
70. Turner, J.G.; Dawson, J.; Sullivan, D.M. Nuclear export of proteins and drug resistance in cancer. *Biochem. Pharmacol.* **2012**, *83*, 1021–1032. [CrossRef]
71. Gao, W.; Lu, C.; Chen, L.; Keohavong, P. Overexpression of CRM1: A Characteristic Feature in a Transformed Phenotype of Lung Carcinogenesis and a Molecular Target for Lung Cancer Adjuvant Therapy. *J. Thorac. Oncol.* **2015**, *10*, 815–825. [CrossRef] [PubMed]
72. Leskov, K.S.; Araki, S.; Lavik, J.P.; Gomez, J.A.; Gama, V.; Gonos, E.S.; Trougakos, I.P.; Matsuyama, S.; Boothman, D.A. CRM1 protein-mediated regulation of nuclear clusterin (nCLU), an ionizing radiation-stimulated, Bax-dependent pro-death factor. *J. Biol. Chem.* **2011**, *286*, 40083–40090. [CrossRef] [PubMed]
73. Marshall, J.A.; Mikowski, A.M.; Bourbeau, M.P.; Schaaf, G.M.; Valeriote, F. Leptostatin: A synthetic hybrid of the cytotoxic polyketides callystatin A and leptomycin B. *Bioorg Med. Chem. Lett.* **2006**, *16*, 320–323. [CrossRef]
74. Wu, M.; Gui, H.; Feng, Z.; Xu, H.; Li, G.; Li, M.; Chen, T.; Wu, Y.; Huang, J.; Bai, Z.; et al. KPT-330, a potent and selective CRM1 inhibitor, exhibits anti-inflammation effects and protection against sepsis. *Biochem. Biophys. Res. Commun.* **2018**, *503*, 1773–1779. [CrossRef] [PubMed]
75. Nie, D.; Huang, K.; Yin, S.; Li, Y.; Xie, S.; Ma, L.; Wang, X.; Wu, Y.; Xiao, J.; Wang, J.; et al. KPT-330 inhibition of chromosome region maintenance 1 is cytotoxic and sensitizes chronic myeloid leukemia to Imatinib. *Cell Death Discov.* **2018**, *4*, 48. [CrossRef]

76. Skavatsou, E.; Semitekolou, M.; Morianos, I.; Karampelas, T.; Lougiakis, N.; Xanthou, G.; Tamvakopoulos, C. Immunotherapy Combined with Metronomic Dosing: An Effective Approach for the Treatment of NSCLC. *Cancers* **2021**, *13*, 1901. [CrossRef]
77. Forde, P.M.; Spicer, J.; Lu, S.; Provencio, M.; Mitsudomi, T.; Awad, M.M.; Felip, E.; Broderick, S.R.; Brahmer, J.R.; Swanson, S.J.; et al. Neoadjuvant Nivolumab plus Chemotherapy in Resectable Lung Cancer. *N. Engl. J. Med.* **2022**, *386*, 1973–1985. [CrossRef]

Disclaimer/Publisher's Note: The statements, opinions and data contained in all publications are solely those of the individual author(s) and contributor(s) and not of MDPI and/or the editor(s). MDPI and/or the editor(s) disclaim responsibility for any injury to people or property resulting from any ideas, methods, instructions or products referred to in the content.

International Journal of
Molecular Sciences

MDPI

Communication

The Mechanism of Hepatic Encephalopathy Induced by Thioacetamide Based on Metabolomics and Proteomics: A Preliminary Study

Honghui Guo [1,2,3,†], Guang Wang [4,†], Wei Huang [1,2,3], Lingrui Li [1,2,3], Yang Bai [1,2,3], Haifeng Wang [1,2,3] and Lina Gao [1,2,3,*]

[1] Liaoning Province Key Laboratory of Forensic Bio-Evidence Sciences, Shenyang 110122, China; 18856834146@163.com (H.G.); vivihuang98@163.com (W.H.)
[2] China Medical University Center of Forensic Investigation, Shenyang 110122, China
[3] Department of Forensic Analytical Toxicology, China Medical University, Shenyang 110122, China
[4] Department of Laboratory Animal Science, China Medical University, Shenyang 110122, China; gwang@cmu.edu.cn
* Correspondence: lngao@cmu.edu.cn; Tel.: +86-189-0091-0140
† These authors contributed equally to this work.

Abstract: Hepatic encephalopathy (HE) is a central nervous system dysfunction syndrome caused by acute and chronic liver failure or various portal systemic shunt disorders. HE arises from metabolic disorder and excludes other known types of encephalopathy. HE is a major cause of death in people with liver disease. Early diagnosis and timely treatment are key to improving HE prognosis. Herein, we established a model of HE and performed metabolomics to identify 50 significantly differential metabolites between the HE group and control group. The main metabolic pathways associated with these differential metabolites were the purine metabolism, pyrimidine metabolism, aminoacyl tRNA biosynthesis, and glucose metabolism. Through proteomics analysis, we identified 226 significantly differential proteins (52 up-regulated and 174 down-regulated). The main (Kyoto Encyclopedia of Genes and Genomes) enrichment pathways were the *Staphylococcus aureus* infection, vitamin digestion and absorption, and complement and coagulation cascades. Through the conjoint analysis of proteomics and metabolomics, the differentially present proteins and metabolites were found to be involved in vitamin digestion and absorption, and ferroptosis pathways. In HE, malondialdehyde was significantly elevated, but glutathione was significantly diminished, and the redox balance was destroyed, thus leading to changes in proteins' levels associated with the ferroptosis pathway. In conclusion, this study preliminarily explored the molecular and metabolic mechanisms underlying HE.

Keywords: thioacetamide; proteomics; metabolomics; ferroptosis; hepatic encephalopathy

1. Introduction

Hepatic encephalopathy (HE) is a syndrome of central nervous system dysfunction caused by acute and chronic liver failure or various portal systemic shunt disorders; it is based on metabolic disorder and excludes other known types of encephalopathy [1]. HE is the third most serious complication of decompensated liver cirrhosis and affects at least 30% of people with cirrhosis [2]. HE is characterized by a series of neuropsychiatric syndromes as diverse as subclinical changes and coma, including abnormal changes in cognitive function, emotion, behavior, and motor function. Clinically, HE is divided primarily into type A, type B, and type C. Type A is caused by acute liver failure, which is characterized by an acute onset, a long course of disease, and a mortality rate as high as 80%. The pathological basis of HE is complex, and its pathogenesis is not yet clear. Beyond the ammonia poisoning theory [3], inflammatory cytokines [4–7], neurosteroids [8–10],

endogenous benzodiazepines [11], bile acids [12,13], and manganese [8] may participate in the occurrence of HE. In recent years, many researchers have found that the influence of ammonia on neurotransmitters plays an important role in the pathogenesis of HE [14,15]. In 2000, Butterworth [16] reported that the primary cause of HE is neurotransmitter abnormalities rather than energy failure. Jones [17] has clearly shown that the occurrence of HE is due to an imbalance between inhibitory neurotransmitters (γ-aminobutyric acid (GABA)) and excitatory neurotransmitters (glutamate), thus leading to a net increase in inhibitory neurotransmitters. The molecular and metabolic mechanisms of HE have not been fully elucidated, and current clinical interventions primarily decrease the formation and absorption of ammonia. On the basis of the pathogenesis of HE, the clinical application of non-absorbable disaccharides, rifaximin, and L-ornithine-L-aspartate (LOLA) is used to decrease circulating ammonia. Probiotics and fecal microbiota transplantation have been used to modulate the gut microbiota composition and ameliorate gastrointestinal disorders; other treatments such as human albumin therapy and branched chain amino acid therapy are also commonly applied [18–25]. To develop more effective treatments and therapies, basic research on the pathogenesis of HE is essential and urgently needed.

An experimental model of HE using thioacetamide (TAA) in mice has been validated [26,27] and involves a dose of 200 mg/kg, injected intraperitoneally for 3 consecutive days, thus achieving a final dose of 600 mg/kg [28,29]. The model mimics human acute progressive hepatic disorders with the concomitant involvement of the brain [30]. TAA is extensively metabolized to very reactive metabolites that bind liver macromolecules, thus resulting in hepatic necrosis, hyper-ammonemia [31], and extensive oxidative stress [32].

Proteomic methods such as high-resolution mass spectrometry are used to study protein composition and changes in cells, tissues, or organisms. The study of the proteome can provide a theoretical basis and solutions for elucidating many disease mechanisms. Through the comparative analysis of the proteome between normal individuals and those with pathologies, disease-specific protein molecules can be identified. Tandem mass tag technology, developed by Thermo Scientific (Waltham, MA, USA) [33], enables relative and absolute quantification, and is often used in quantitative proteomics. Metabolomics, a component of systems biology, is a research method applying genomics and proteomics to quantitatively analyze all metabolites in any organism, and determine the relationships of metabolites with both physiological and pathological changes.

Herein, we sought to explore the mechanism of HE induced by TAA by using metabolomics and proteomics. To our knowledge, we report the first joint analysis of proteomics and metabolomics initially revealing the molecular and metabolic mechanisms of HE.

2. Results

2.1. H&E Staining

The pathological results of the liver in mice in each group are shown in Figure 1. The liver lobular structure of mice in the normal group was normal, and there was no degeneration or necrosis of the liver cells. The mild and moderate watery degeneration of hepatocytes was observed in the experimental group. There was obvious hepatocyte lysis and necrosis, inflammatory cell infiltration, and lobular structure disorder in the necrotic area.

The brain pathological results of mice in each group are shown in Figure 2. The cell structure of the brain tissue of mice in the normal group was normal and complete with a full nucleus, while the cell structure of the brain tissue of mice in the experimental group was disordered with glial cell hyperplasia.

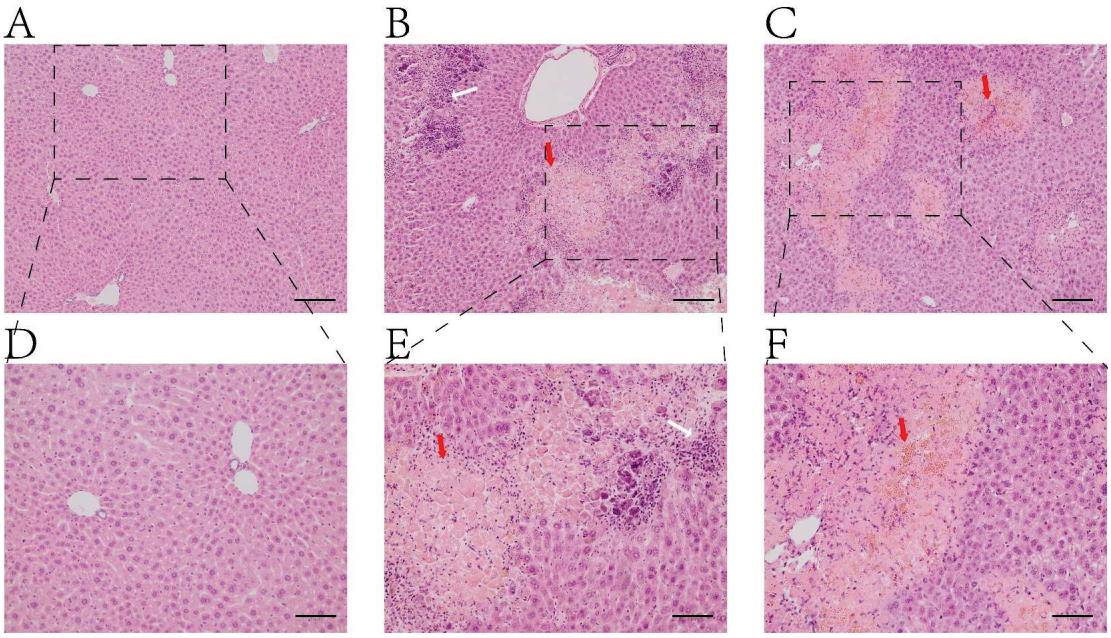


Figure 1. Histopathological examinations of H&E stain of liver. (**A**,**D**): Normal group; (**B**,**C**,**E**,**F**): TAA-induced model group. (**A**–**C**): 100× magnifications, bar = 100 μm; (**D**–**F**): 200× magnifications, bar = 50 μm. White arrow: infiltrations of inflamed cells; Red arrow: Ballooning degeneration and hepatic sinus congestion.

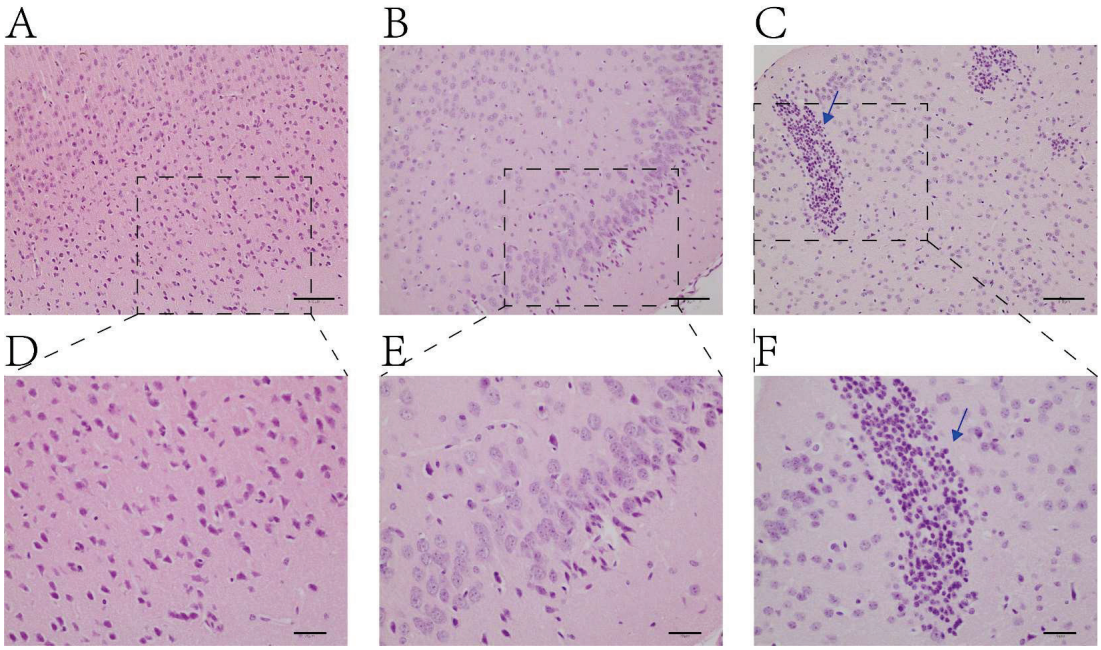


Figure 2. Histopathological examinations of H&E stain of brain. (**A**,**D**): Control group; (**B**,**C**,**E**,**F**): TAA-induced model group. (**A**–**C**): 200× magnifications, bar = 50 μm; (**D**–**F**): 400× magnifications, bar = 20 μm. Blue arrow: Glial cells proliferate and accumulate.

2.2. Results of ALT, AST, GSH, and MDA

As shown in Figure 3, compared with the control group, the levels of ALT (alanine transaminase) and AST (aspartate aminotransferase) in the serum of mice in the HE group were significantly increased ($p \leq 0.01$), indicating the liver injury of mice after modeling. Compared with the control group, the content of GSH in the serum of the model group decreased significantly ($p \leq 0.01$), and the activity of MDA increased significantly.

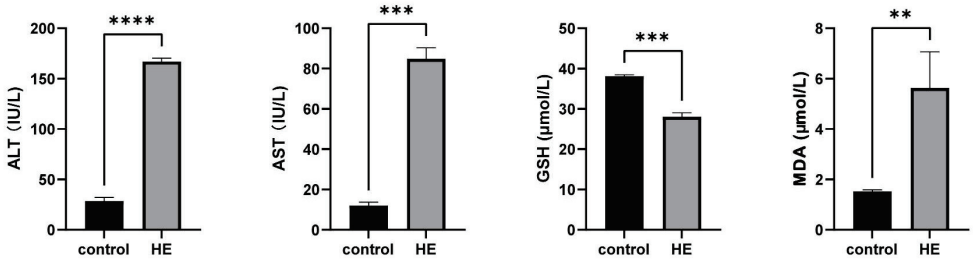


Figure 3. The effects of thioacetamide on mouse serum biochemistry. The levels of ALT, AST, GSH, and MDA in serum of mice are shown. AST and ALT are important indicators of liver function, and their simultaneous elevation indicates liver cell damage and abnormal liver function. The decrease of GSH indicates the occurrence of oxidative damage. Lipid peroxidation as determined by MDA content. Values shown are means ± SEM; The symbols show the following significances: $p < 0.01$ = **; $p < 0.001$ = ***; $p < 0.0001$ = ****.

2.3. Results of Metabolomics

2.3.1. Sample Quality Control

The Pearson correlation coefficient between QC samples is calculated based on the relative quantitative value of metabolites. The higher the correlation of QC samples (the closer R2 is to 1), the better the stability of the whole detection process and the higher the data quality. The correlation of QC samples is shown in Supplementary Figure S1.

2.3.2. PCA and PLS-DA Results

We found that the HE group was significantly different from the control group through principal component analysis (PCA) (as shown in Figure 4A,B) and partial least squares discrimination analysis (PLS-DA) (as shown in Figure 4C,D). We tested whether the model was "overfitted". Whether the model is "overfitted" reflects the accuracy of the model construction. Failure to be "overfitted" indicates that the model can better describe the sample. These results are shown in Figure 4E,F.

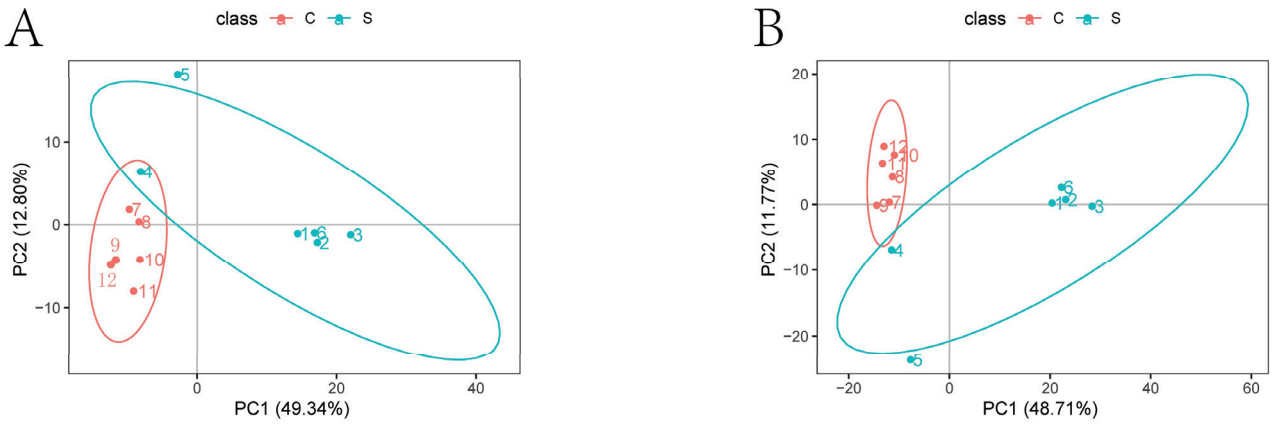


Figure 4. *Cont.*

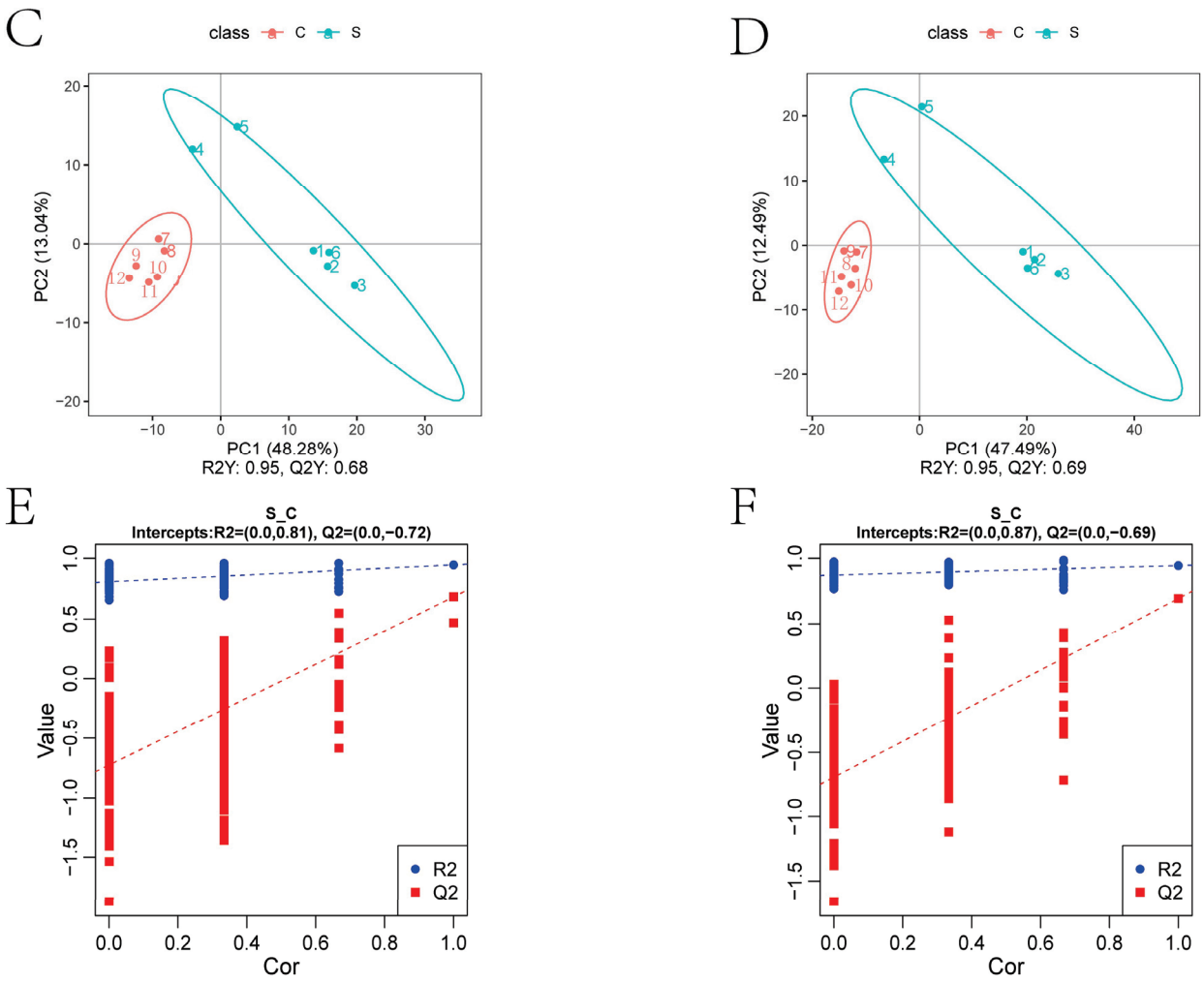


Figure 4. Metabolic profile of mouse brain tissue (**A**,**B**): PCA (principal component analysis); (**C**,**D**): Score plot of the partial least squares discriminant analysis (PLS-DA): abscissa is the score of the sample in the first principal component, the ordinate is the score of the sample in the second principal component, R2Y represents the interpretation rate of the model, Q2Y was used to evaluate the predictive power of the PLS-DA model, and when R2Y is greater than Q2Y, the model is well established; (**E**,**F**): Sort validation graph of Partial least squares discriminant analysis, R2 displays the variance explained in the model and indicates the goodness of fit. Q2 displays the variance in the data predictable by the model and indicates the predictability. In each part, the left one was obtained in the negative polarity mode, and the right one was obtained in the positive polarity mode.

2.3.3. Volcano Plots and Hierarchical Clustering Analysis of Differential Metabolites

The volcano plot can directly show the overall distribution of differential metabolites, the abscissa represents the difference fold change of metabolites in different groups ($\log_2$FoldChange), the ordinate indicates the difference significance level ($-$log10 *p*-value), each point in the volcano plot represents a metabolite, significantly up-regulated metabolites are represented by red dots, significantly down-regulated metabolites are represented by green dots, and the size of the dot represents the VIP value, as shown in Figure 5. Hierarchical clustering analysis of the obtained differential metabolites was performed to obtain the differences in the metabolic expression patterns between and within two groups for the same comparison, as shown in Figure 6. For a more intuitive view of differential metabolites, we listed significantly divergent representative metabolites, as shown in Table 1.

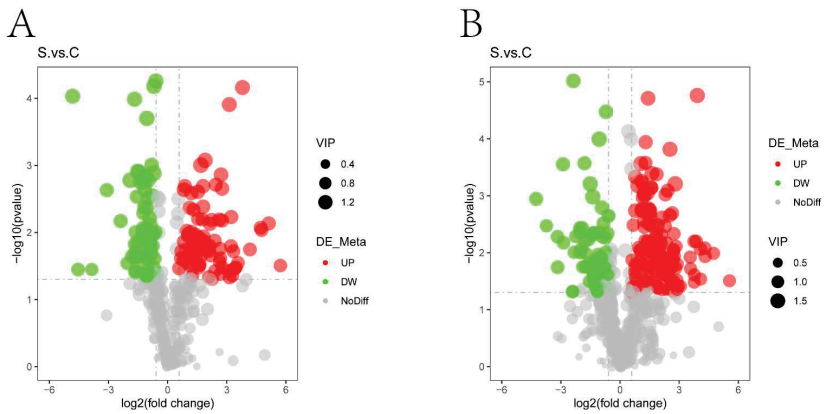


Figure 5. Volcano plots and metabolite heatmaps of differential metabolites. (**A**,**B**): Volcano plots of differential metabolites in (**A**) negative and (**B**) positive polarity mode. Significant difference for the *p* value on vertical ordinate (Base 10 logarithmic transformation). Red represents up-regulation, green represents down-regulation in the HE group, gray represents that there is no distinguished difference between the HE group and the control group, and VIP represents the importance projection value of this substance obtained in the PLS-DA model between different groups.

Table 1. Significant differential metabolites between the HE group and the control group.

No.	Name	log_2FC	*p* Value	ROC	VIP	Up/Down
1	L-Glutamic acid	−0.7148	0.0000	1.0000	1.7550	down
2	Adenine	−1.8026	0.0003	1.0000	1.4061	down
3	Adenosine	−4.2551	0.0011	1.0000	1.3706	down
4	Cytidine	−1.3588	0.0256	0.8611	1.0604	down
5	L-Glutathione (reduced)	−2.0501	0.0288	0.9167	1.0914	down
6	UDP-N-acetylglucosamine	−1.5685	0.0290	0.8611	1.1164	down
7	S-Adenosylmethionine	−1.8971	0.0177	1.0000	1.1697	down
8	N-Acetyl-DL-glutamic acid	−0.9836	0.0323	0.7778	1.1143	down
9	5′-S-Methyl-5′-thioadenosine	−1.2561	0.0350	0.7222	1.1118	down
10	ϒ-Glutamylcysteine	−1.1471	0.0426	0.7222	1.0854	down
11	5-Hydroxyindole-3-acetic acid	−0.8199	0.0470	0.7778	1.0177	down
12	Cytidine 5′-monophosphate (hydrate)	−0.8442	0.0475	0.8056	1.0850	down
13	Inosine	−0.7601	0.0481	0.7778	1.0709	down
14	α-Aspartylphenylalanine	−2.4091	0.0482	0.8056	1.1948	down
15	L-Glutathione oxidized	−1.1454	0.0490	0.8333	1.0628	down
16	α-D-Glucose-1,6-bisphosphate	−1.6690	0.0388	0.8333	1.0271	down
17	N-Acetylneuraminic acid	−0.5952	0.0001	1.0000	1.4531	down
18	5-Aminolevulinic acid	−0.9738	0.0017	1.0000	1.2759	down
19	Adenosine 5′-monophosphate	−3.0832	0.0023	0.9444	1.2062	down
20	Ascorbic acid	−0.9980	0.0129	0.8889	1.1806	down
21	O-Phosphorylethanolamine	−1.0382	0.0368	0.9444	1.0457	down
22	Uridine monophosphate (UMP)	−1.6295	0.0232	0.8611	1.1090	down
23	Guanosine monophosphate (GMP)	−1.6259	0.0234	0.9167	1.0563	down
24	N6-Acetyl-L-lysine	0.5880	0.0499	0.8333	1.0435	up
25	N-Acetyl-L-tyrosine	2.1337	0.0158	0.9167	1.1105	up
26	L-Histidine	2.2341	0.0065	1.0000	1.2401	up
27	Hippuric acid	2.6338	0.0273	0.8611	1.0633	up
28	N2-Methylguanosine	2.7800	0.0330	0.7222	1.0859	up
29	Xanthosine	4.1746	0.0179	0.8611	1.1467	up
30	N-Acetyl-L-phenylalanine	2.1029	0.0189	0.9167	1.1265	up
31	L-Tyrosine	1.2616	0.0443	0.7222	1.0675	up
32	N-Acetyl-DL-tryptophan	1.7116	0.0223	0.8333	1.0564	up
33	Argininosuccinic acid	1.0689	0.0018	0.9444	1.2466	up
34	N3,N4-Dimethyl-L-arginine	2.6446	0.0020	0.9722	1.3649	up
35	L-Phenylalanine	1.4515	0.0031	1.0000	1.3137	up

Table 1. *Cont.*

No.	Name	log_2FC	*p* Value	ROC	VIP	Up/Down
36	Uracil	1.8273	0.0047	1.0000	1.2165	up
37	DL-Tryptophan	1.4018	0.0062	1.0000	1.2632	up
38	L(+)-Ornithine	3.8581	0.0063	0.8611	1.2678	up
39	Proline	3.7575	0.0063	0.8611	1.2684	up
40	γ-aminobutyric acid	2.3444	0.0067	1.0000	1.2419	up
41	Thiamine	0.9335	0.0081	0.9444	1.1754	up
42	Indole-3-acetic acid	1.0212	0.0089	0.9167	1.1264	up
43	Nicotinamide	3.0732	0.0388	0.7222	1.0653	up
44	DL-Lysine	2.0674	0.0141	0.9167	1.1979	up
45	L-Isoleucine	1.7751	0.0158	0.9444	1.1804	up
46	L-(+)-Citrulline	3.7701	0.0245	0.8611	1.1390	up
47	Threonine	0.8236	0.0246	0.8333	1.0965	up
48	N-Acetyl-L-leucine	2.3822	0.0442	0.7222	1.0795	up
49	Riboflavin	1.9154	0.0260	0.8611	1.0731	up
50	Leukotriene B4	1.0947	0.0405	0.8333	1.0335	up

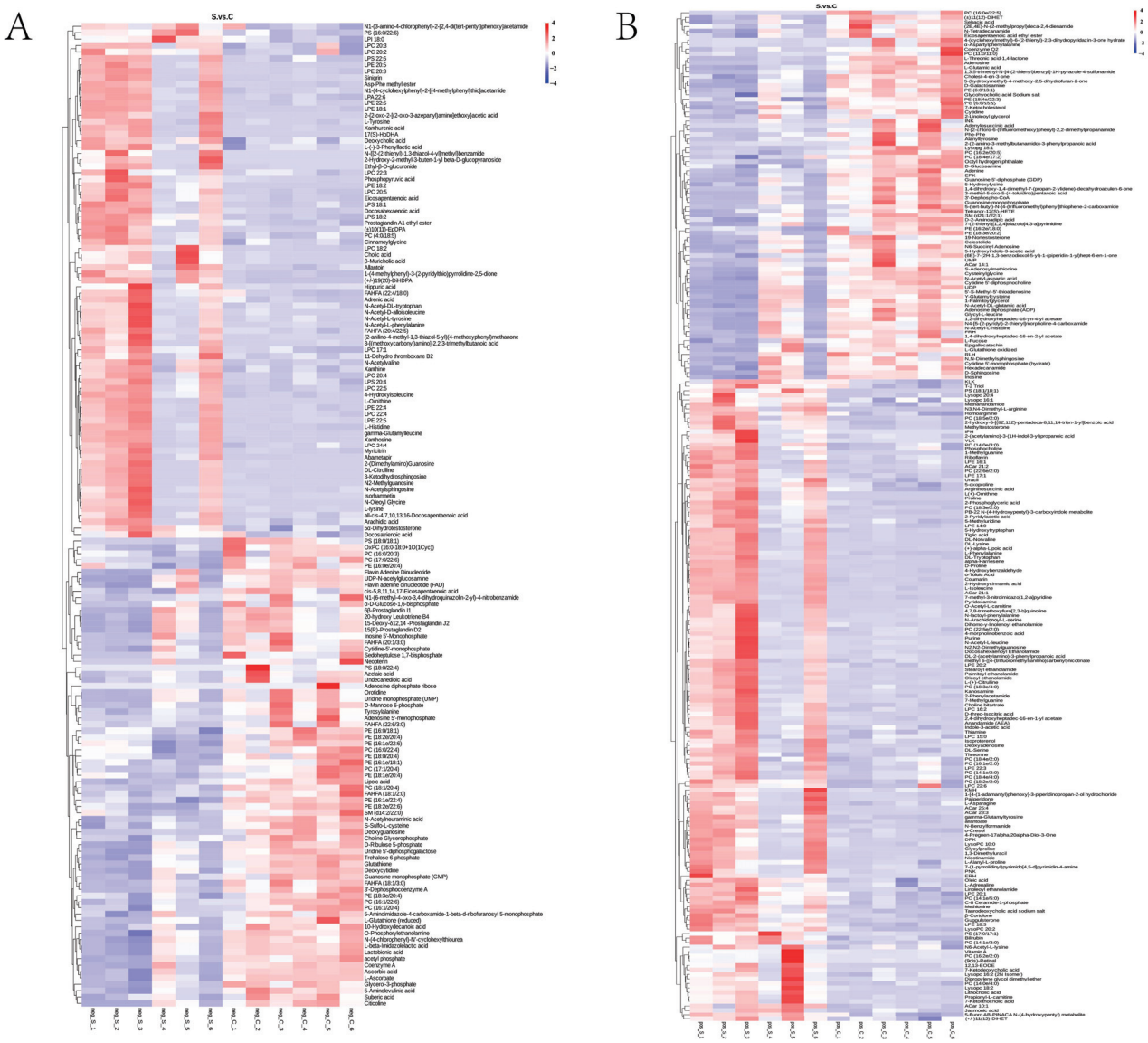


Figure 6. Metabolite heatmaps of differential metabolites. (**A**,**B**): The heatmaps of the metabolites between different groups in (**A**) negative and (**B**) positive polarity mode.

2.3.4. KEGG Pathway Enrichment Analysis

The differential metabolites were also enriched for the KEGG metabolic pathways; the enrichment KEGG pathways are the purine metabolism, pyrimidine metabolism, aminoacyl-tRNA biosynthesis, and glutathione metabolism, as shown in Figure 7.

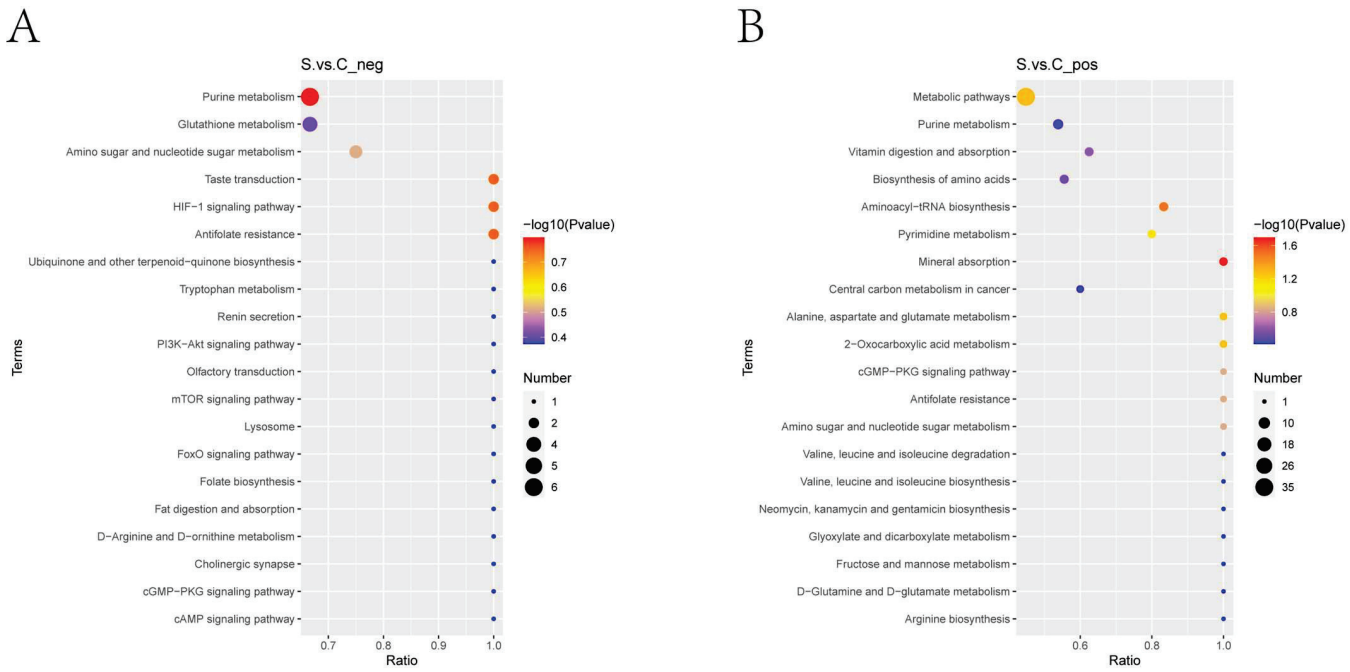


Figure 7. The KEGG pathway that the distinguished metabolites take part in between the HE group and the control group. Terms in the same category were ranked based on the *p*-values. (**A**): the negative polarity mode; (**B**): the positive polarity mode. The abscissa in the figure is the ratio of the number of different metabolites in the corresponding pathway to the number of identified total metabolites. The higher the ratio, the higher the concentration of differential metabolites in the pathway. The color of the dot represents the *p*-value of the hypergeometric test. The smaller the *p*-value, the greater the reliability and the more statistically significant the test. The size of the dot represents the quantity of differential metabolites in the corresponding pathway. A larger point size indicates more different metabolites in the pathway. S represents the HE group; C represents the control group.

2.4. Results of Proteomics

2.4.1. Differential Protein Results for Presentation, Volcano Plots, and Heatmap Plots

Protein difference analysis first selects the sample pairs that need to be compared, and takes the ratio of the mean of all biological repeated quantitative values of each protein in the comparison sample pair as the fold change (FC). In order to judge the significance of the difference, the relative quantitative value of each protein in the two comparison samples was tested by a t-test, and the corresponding *p*-value was calculated as the significance index, with the default *p*-value ≤ 0.05. The number of up- and down-regulated proteins screened according to this condition is shown in Supplementary Table S1. As a result, we found 52 up-regulated proteins and 174 down-regulated proteins.

Differentially expressed proteins (DEPs) are shown by a volcano plot and heatmap, as shown in Figures 8 and 9. DEPs are displayed in a volcano graph, where the black dots represent indifferent proteins, and the up-regulated and down-regulated proteins are represented by red and green dots, respectively.

Cluster analysis was carried out for the relative content of DEPs in each sample and the up-regulation and down-regulation of DEPs among the comparison groups were observed in the cluster analysis of DEPs. When the fold change (FC) $\geq$ 1.2 and the *p*-value < 0.05, up-regulated expressed proteins were screened. When the FC $\leq$ 0.83 and the *p*-value < 0.05, down-regulated expressed proteins were screened.

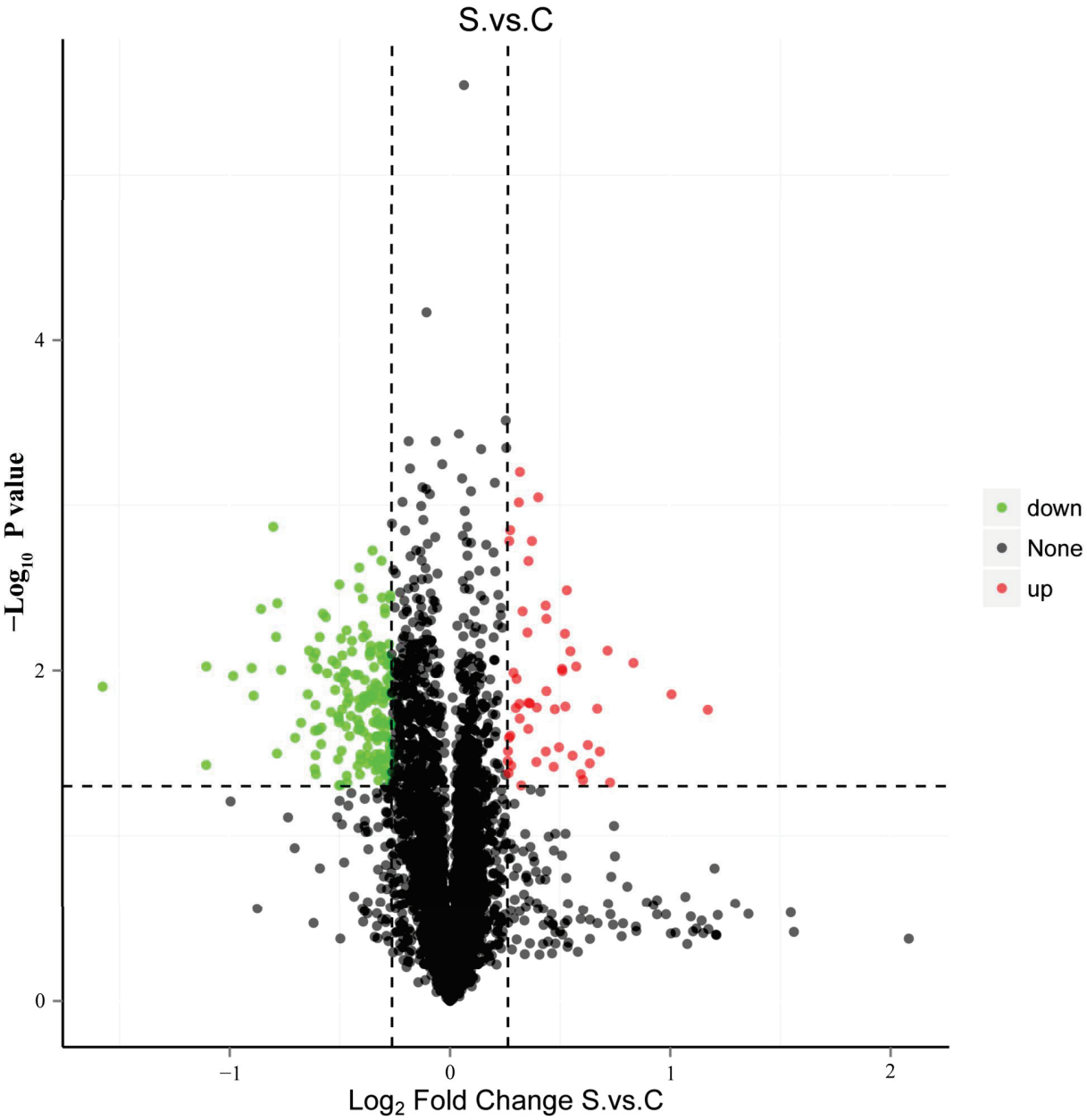


Figure 8. Volcano plots of proteins with differential expression (FC > 1.2 or FC < 0.83, *p* value < 0.05). Significant difference for the *p* value on vertical ordinate (Base 10 logarithmic transformation). Red dots represent up-regulated, green dots represent down-regulated, and black dots represent no significant difference. S represents the HE group; C represents the control group.



Figure 9. The heatmaps of DEPs between the HE group and the control group. Red represents up-regulation; blue represents down-regulation. S represents the HE group; C represents the control group.

2.4.2. DEPs of Gene Ontology (GO) Function Enrichment Analysis

Bioinformatics GO enrichment analysis can indicate what biological functions are significantly related to DEPs. As shown in Figure 10, compared with the control group, the related biological processes of the screened DEPs in the HE group were ion transport, cellular component organization, cytoskeleton organization, organelle organization, etc. These DEPs are mainly located in the extracellular region and cytoskeleton and their main molecular functions were transition metal ion binding, cytoskeletal protein binding, ion transmembrane transporter activity, and zinc ion binding, etc.

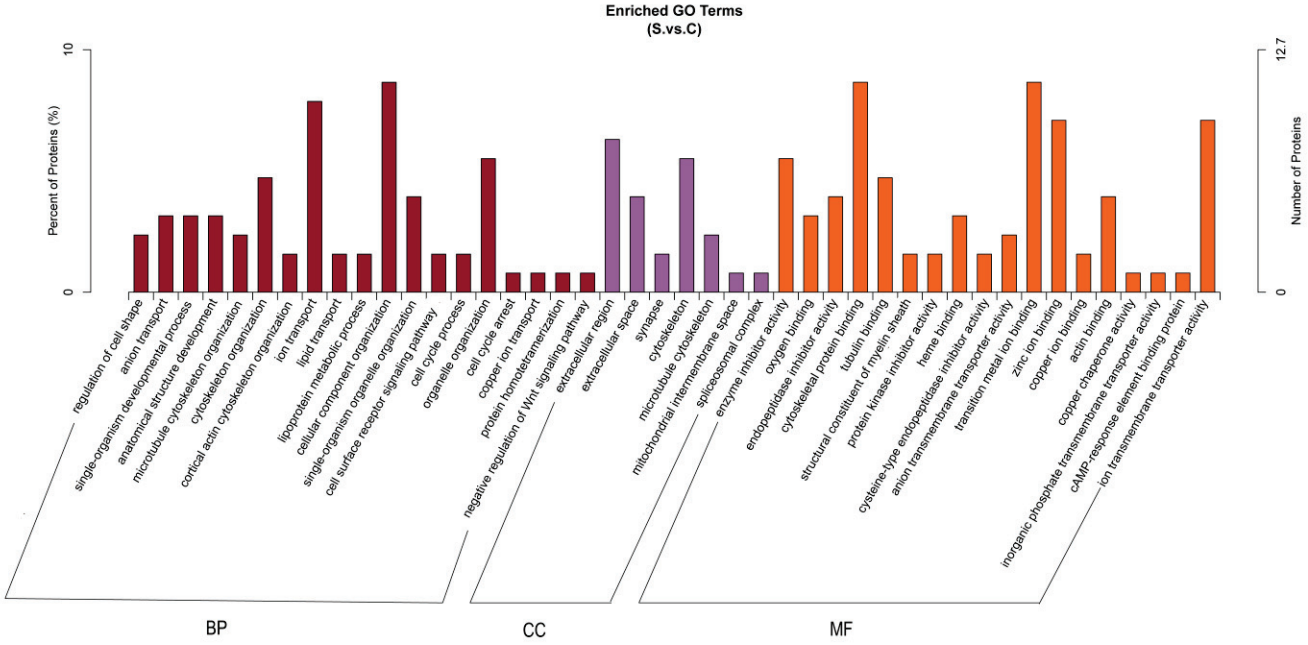


Figure 10. Gene ontology (GO) term (including biological process, cellular component, and molecular function) enrichment for differentially expressed proteins between the HE group and the control group. BP: biological Process, CC: Cellular Component, MF: Molecular Function. The left ordinate represents the number of detected differential proteins associated with the GO as a percentage of the number of differential proteins annotated by GO, and the right ordinate represents the number of detected differential proteins associated with the GO. S represents the HE group; C represents the control group.

2.4.3. Enrichment of Kyoto Encyclopedia of Genes and Genomes (KEGG) Pathway Analysis

The significant enrichment of a pathway can determine the main biochemical metabolic and signal transduction pathways involved in DEPs, as shown in Figure 11. According to the enrichment results, the enriched KEGG pathways were plotted (only the results of the Top 20 are shown). Compared with the control group, the main enriched pathways in the HE group were complement and coagulation cascades, vitamin digestion, and absorption.

2.5. Joint Analysis of Metabolomics and Proteomics

Through the joint analysis of metabolomics and proteomics, as shown in Figure 12, the main enrichment pathways are vitamin digestion and absorption and the ferroptosis pathway. The metabolites and proteins related to vitamin digestion and absorption are pyridoxamine, thiamine, nicotinamide, vitamin A, riboflavin, and aldehyde dehydrogenase. The metabolites and proteins related to the ferroptosis pathway are adrenic acid, coenzyme A, glutathione, STEAP family member 3, and ceruloplasmin serotransferrin.

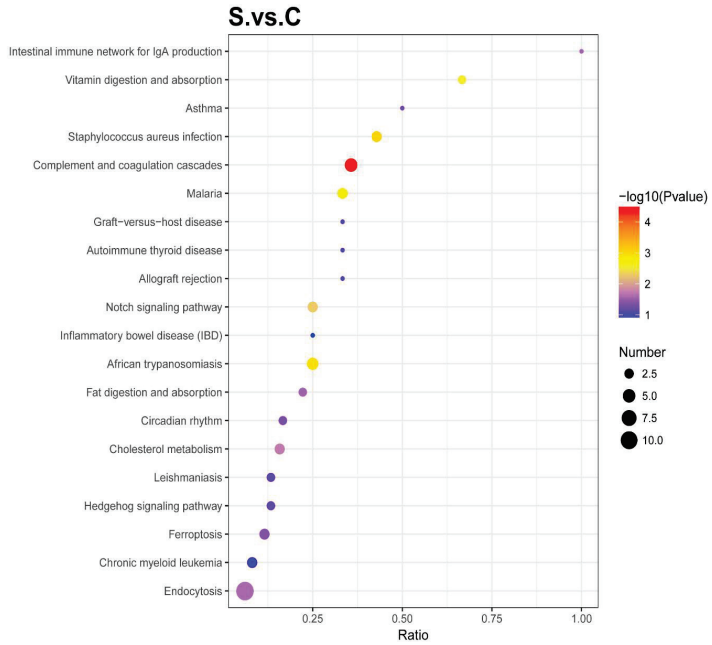


Figure 11. Enrichment KEGG pathway. The abscissa represents the ratio of the number of differential proteins associated with the pathway to the number of background (all) proteins associated with the pathway. The redder the bubble represents the smaller the *p* value, the bluer the bubble represents the larger the *p* value, and the larger the bubble represents the more differential proteins detected. (Top 20 between the HE group and the control group; S represents the HE group; C represents the control group.)

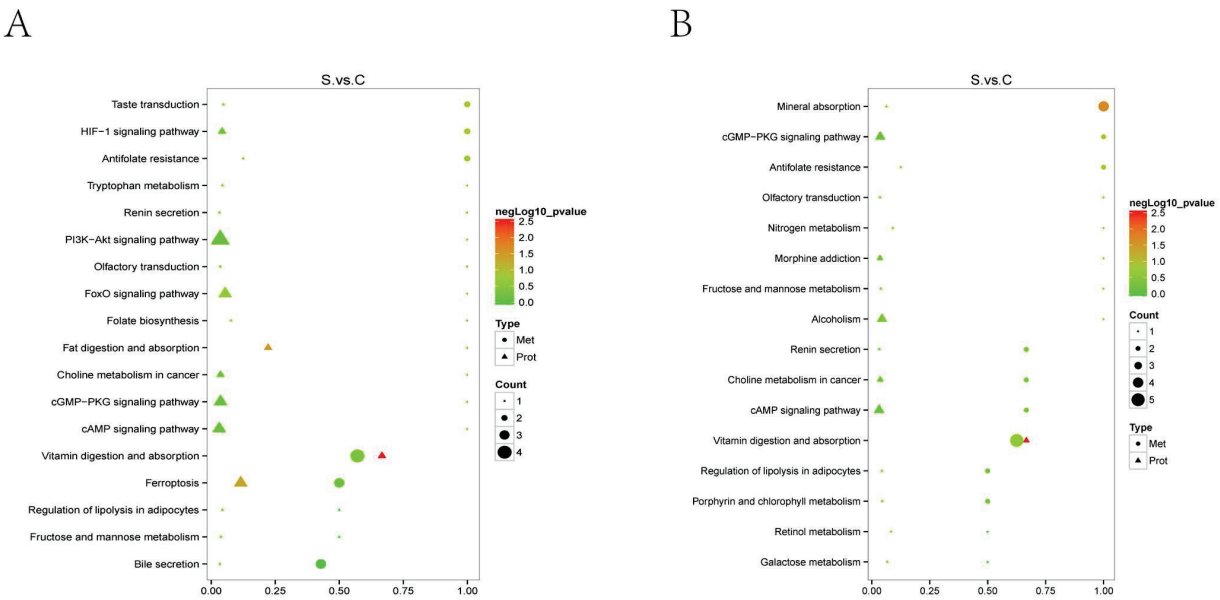


Figure 12. Joint analysis of metabolomics and proteomics. The abscissa in the figure is the ratio of the number of differential metabolites or DEPs in the corresponding pathway to the number of identified total metabolites or proteins. The color of the dot represents the *p*-value of the hypergeometric test. The smaller the *p*-value, the greater the reliability and the more statistically significant the test. The size of the dot represents the quantity of differential metabolites or DEPs in the corresponding pathway. Triangle represents DEPs, Circles represent differential metabolites. S represents the HE group; C represents the control group. (**A**): the negative polarity mode; (**B**): the positive polarity mode.

2.6. Detect Ferroptosis-Related Gene Expression in Mouse Brain Tissue

A range of ferroptosis-related gene expressions, including GPX4 (Glutathione peroxidase 4), was examined. GPX4, SLC7A11, and FTH1 mRNA levels (Figure 13) were dramatically decreased in mice of thioacetamide treatment.

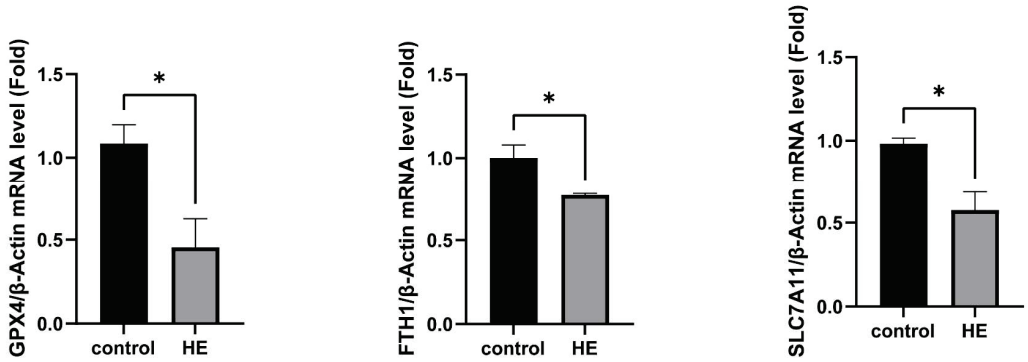


Figure 13. Quantification of relative mRNA expression normalized to β-actin. Ferroptosis-related mRNA expression is decreased in HE group. The relative mRNA levels of GPX4, FTH1, and SLC7A11 in mouse brain tissue injected with or without thioacetamide. Values shown are means ± SEM; The symbols show the following significances: $p \leq 0.05$ = *.

3. Discussion

In this study, the TAA induction method was used to establish a model of acute HE. TAA is metabolized by cytochrome P450 oxidase in liver cells, thus producing toxic TAA sulfur oxide, and subsequently causing lipid peroxidation, liver metabolic disorder, and other damage. Subsequently, inflammatory cells infiltrate the liver tissue, and hepatocyte necrosis and other changes occur; finally, acute liver failure induces type A HE. In this study, liver biochemical indicators and brain tissue staining in the HE group significantly differed from those in the control group, thus indicating the successful establishment of a mouse model of acute HE.

Applying metabolomics, we selected 50 differential metabolites between the HE group and the control group. These metabolites were concentrated primarily in the up-regulation of amino acids (including threonine, citrulline, isoleucine, lysine, proline, ornithine, tryptophan, and phenoylalanine). Some differential metabolites were involved in energy metabolism pathways (down-regulated metabolites included adenine, adenosine, cytidine, uridine diphosphate N-acetylglucosamine, cytidine 5′-monophosphate, inosine, adenosine 5′-monophosphate, uridine monophosphate, guanosine monophosphate, and glucose-1,6-bisphosphate; up-regulated metabolites included N2-methylguanosine, xanthosine, uracil, and argininosuccinic acid) and the reduction of antioxidant properties such as ascorbic acid and glutathione. Glutathione maintains the redox balance in the body. In the HE group, metabolites related to glutathione, such as γ-glutamylcysteine, S-adenosylmethionine, and L-glutathione, were all significantly down-regulated in the HE group. By measuring the content of GSH and MDA, we determined that TAA causes oxidative stress damage to brain and liver tissues. This finding was consistent with the TAA-induced lipid peroxidation and oxidative damage reported by Essam et al. [34]. In addition, metabolites associated with inflammation, such as L-histidine and leukotriene B4, were also significantly up-regulated in the HE group, thus indicating that the inflammatory response played an important role in the pathological process of HE [35,36]. Large amounts of inflammatory mediators and high levels of blood ammonia synergistically affected the brain, thereby triggering inflammatory reactions in the central nervous system.

In the HE group, compared with the control group, GABA was higher and glutamic acid was lower, in agreement with previous findings indicating that HE is associated with neurotransmitter disorder [9]. The roles of abnormal neurotransmitters in the pathogenesis of HE have attracted substantial research attention. Jones has reported that HE occurs because of an imbalance between inhibitory neurotransmitters such as GABA and excitatory neurotransmitters such as glutamate [11].

Proteomic analysis indicated that the functions of DEPs were concentrated in complement and coagulation cascades, and vitamin digestion and absorption. Some studies have also shown that complement and coagulation cascade pathways are involved in degenerative disease [37]. The vitamin digestion and absorption pathways arose from changes in metabolites (such as thiamine, nicotinamide, and riboflavin) and proteins (aldehyde dehydrogenase) in the HE group compared with the control group.

According to a joint proteomic and metabolomic analysis, the main KEGG pathways in the TAA-induced HE model were the HIF-1 signaling pathway, PI3K-Akt signaling pathway, and ferroptosis pathway. Previous studies have indicated that the HIF-1 signaling pathway is involved in molecular mechanisms in liver fibrosis models [38]. Some studies have reported that the PI3K-Akt signaling pathway contributes to the brain molecular mechanism of HE [39,40]. In this study, the joint analysis demonstrated that the changes in the ferroptosis pathway involved the small molecule glutathione, and the proteins six-transmembrane epithelial antigen of prostate 3 (STEAP3), ceruloplasmin, and serotransferrin in the HE group. STEAP3, a key regulator of iron uptake, is involved in immunity and apoptotic processes in various cell types [41,42]. Studies have shown that this protein participates in the regulation of liver ischemia-reperfusion injury, hepatocellular carcinoma, myocardial hypertrophy, and other diseases. Moreover, Ding et al. [41] have found that the expression of STEAP3 is up-regulated in nonalcoholic fatty liver disease. Furthermore, Guo et al. have reported that STEAP3 knockout protects the liver against ischemia-reperfusion injury [42]. In the present study, STEAP3 was found to be up-regulated in the HE group, thus suggesting its involvement in this syndrome. In the HE model, up-regulated serotransferrin suggested that iron metabolism was affected. These findings suggested that the ferroptosis pathway may play a role in the TAA-induced HE model.

According to quantitative RT-PCR analysis, GPX4, SLC7A11 and FTH1 mRNA levels were dramatically diminished in the HE group. Glutathione peroxidase 4 (GPX4) is a recognized ferroptosis gatekeeper with a central role in limiting lipid peroxidation [43]. GPX4 uses glutathione to protect cells against ferroptosis by eliminating phospholipid peroxides [44]. The brain has the second highest concentration of lipids among the diverse organs of the human body; moreover, the high oxygen consumption rate of the brain makes this organ particularly vulnerable and sensitive to lipid peroxidation [45]. GPX4 is the most widely expressed GPX isoform in the brain, and it acts as a powerful antioxidant [46]. GPX4 expression has been found to be down-regulated in many brain diseases [47,48].

SLC7A11 and FTH1 also play important roles in many brain diseases associated with ferroptosis. SLC7A11, the cystine/glutamate antiporter involved in GSH synthesis, neutralizes oxidative substances in the cell membrane [49]. FTH1 has ferroxidase activity, catalyzing the conversion of ferrous (Fe^{2+}) to ferric (Fe^{3+}) iron for storage in ferritin nanocages, thereby attenuating the iron-mediated catalysis of reactive oxygen species. In our study, GPX4, SLC7A11, and FTH mRNA expression was significantly down-regulated in the HE group, thus suggesting the involvement of ferroptosis in our model of TAA-induced HE. As shown in Figure 14, TAA-induced hepatocyte injury leading to HE may be associated with ferroptosis in brain tissue.

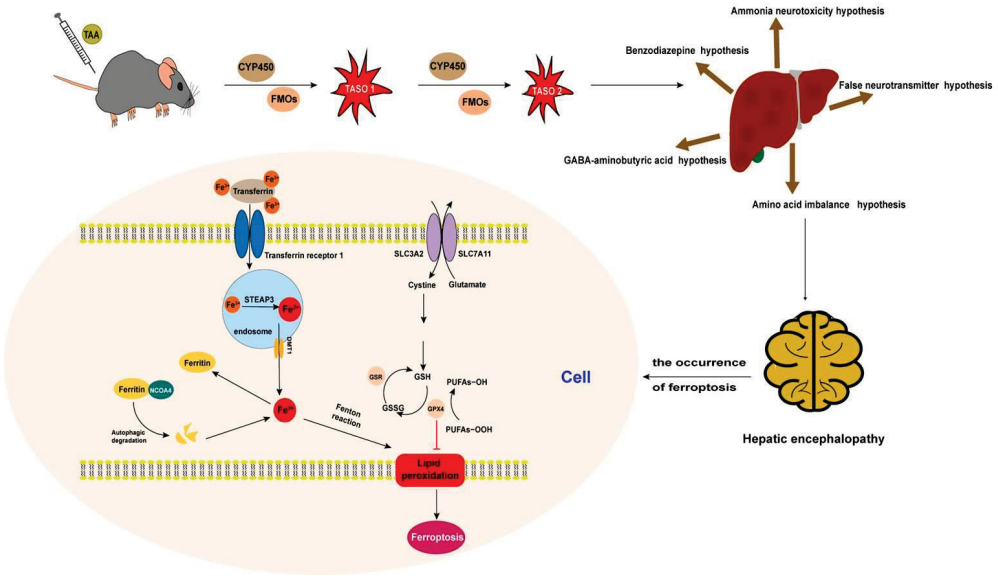


Figure 14. Hepatic encephalopathy after intraperitoneal injection of thioacetamide may be associated with ferroptosis.

4. Materials and Methods

4.1. Reagents

Liquid chromatography–Mass spectrometry (LC-MS)-grade ultrapure water, LC-MS-grade acetonitrile, and LC-MS-grade formic acid were purchased from Thermo Fisher Chemical (Waltham, MA, USA). Acetone was purchased from Beijing Chemical Works Co., Ltd. (Beijing, China). ProteoMiner Low Abundance Protein Enrichment Kit was purchased from Bio-Rad (Hercules, CA, USA). LC-MS/MS analysis was performed by Novogene Co., Ltd. (Beijing, China). Aspartate aminotransferase (AST) enzyme-linked immunosorbent assay (ELISA) and alanine aminotransferase (ALT) ELISA kits were purchased from Shanghai Enzyme-linked Biotechnology Co., Ltd. (Shanghai, China). GSH and SOD Biochemical Assay Kit were purchased from Elabscience Biotechnology Co., Ltd. (Wuhan, China). Liquid chromatography–mass spectrometry (LC–MS)-grade water, acetonitrile (ACN), Methanol (MeOH), and formic acid (FA) were purchased from Thermo Fisher Scientific (Waltham, MA, USA). LC–MS/MS analysis was performed by Novogene Co., Ltd. (Beijing, China). AG RNAex Pro Reagent, Evo M-MLV RT Mix Kit with gDNA Clean for Qpcr, and SYBR® Green Premix Pro Taq HS qPCR Kit were purchased from Accurate Biotechnology(Human)Co., Ltd. (Changsha, China).

4.2. Animal Model and Sample Collection

All animal experiments were approved by the Animal Ethics Committee of China Medical University and performed according to the National Institutes of Health guide for the care and use of Laboratory animals (NIH Publications No. 8023, revised 1978) and to the Guidelines for the Care and Use of Laboratory Animals of China Medical University (ethical approval code is KT2022353). Six-week-old, specific pathogen-free (SPF)-grade male Kunming mice (KM mice, originated from Swiss mice, the largest outbred group in China and widely used in pharmacology, toxicology, and other fields of research) weighing 30 ± 5 g were obtained from Beijing Huafukang Biotechnology Co., Ltd. (Beijing, China). A total of 12 KM mice were randomly divided into the HE groups and the control group (n = 6 in each group). The HE group were given thioacetamide by intraperitoneal injection at the dose of 200 mg/kg at three alternative days. The control group was injected with normal saline every other day, and all were sacrificed on the sixth day of the experiment. At the end of the experiment, the mice were euthanized via compressed gas in their home cage by trained personnel. Death was confirmed after checking for lack of respiration and

faded eye color in each mouse. The brain was excised and the cerebrum quickly separated. Serum samples were stored at −80 °C for detection of GSH activity and MDA content. Parts of the cerebral cortex were homogenized in cold phosphate-buffered saline (PBS), centrifuged, and the clear homogenate was collected for biochemical assays.

4.3. Proteomics

4.3.1. Total Protein Extraction

The cerebrum was ground individually in liquid nitrogen and lysed with PASP lysis buffer (100 mM NH_4HCO_3, 8 M Urea, pH 8), followed by 5 min of ultrasonication on ice. The lysate was centrifuged at 12,000× *g* for 15 min at 4 °C and the supernatant was reduced with 10 mM DTT for 1 h at 56 °C, and subsequently alkylated with sufficient IAM for 1 h at room temperature in the dark.

Then samples were completely mixed with 4 times volume of precooled acetone by vortexing, and incubated at −20 °C for at least 2 h. Samples were then centrifuged at 12,000× *g* for 15 min at 4 °C and the precipitation was collected. After washing with 1 mL cold acetone, the pellet was dissolved by dissolution buffer (8 M Urea, 100 mM TEAB, pH 8.5).

4.3.2. TMT Labeling of Peptides

Each protein sample was taken and the volume was made up to 100 µL with DB dissolution buffer (8 M Urea, 100 mM TEAB, pH 8.5). Trypsin and 100 mM TEAB buffer were added, and sample was mixed and digested at 37 °C for 4 h. Then, trypsin and $CaCl_2$ were added, and sample was digested overnight. Formic acid was mixed with digested sample, adjusted pH under 3, and centrifuged at 12,000× *g* for 5 min at room temperature. The supernatant was slowly loaded to the C18 desalting column, washed with washing buffer (0.1% formic acid, 3% acetonitrile) 3 times, then eluted by some elution buffer (0.1% formic acid, 70% acetonitrile). The eluents of each sample were collected and lyophilized. Next, 100 µL of 0.1 M TEAB buffer was added to reconstitute, and 41 µL of acetonitrile-dissolved TMT labeling reagent was added; sample was mixed with shaking for 2 h at room temperature. Then, the reaction was stopped by adding 8% ammonia. All labeling samples were mixed with equal volume, desalted, and lyophilized.

4.3.3. Separation of Fractions

Mobile phase A (2% acetonitrile, adjusted pH to 10.0 using ammonium hydroxide) and B (98% acetonitrile) were used to develop a gradient elution as shown in Table 2. The lyophilized powder was dissolved in solution A and centrifuged at 12,000× *g* for 10 min at room temperature. The sample was fractionated using a C18 column (Waters BEH C18, 4.6 × 250 mm, 5 µm) on a Rigol L3000 HPLC system and the column oven was set as 45 °C. The eluates were monitored at UV 214 nm, collected for a tube per minute and combined into 10 fractions finally. All fractions were dried under vacuum and then reconstituted in 0.1% (*v*/*v*) formic acid in water.

Table 2. Peptide fraction separation liquid chromatography elution gradient table.

Time (min)	Flow Rate (mL/min)	Mobile Phase A (%)	Mobile Phase B (%)
0	1	97	3
10	1	95	5
30	1	80	20
48	1	60	40
50	1	50	50
53	1	30	70
54	1	0	100

4.3.4. LC-MS/MS Analysis

For transition library construction, shotgun proteomics analyses were performed using an EASY-nLCTM 1200 UHPLC system (Thermo Fisher) coupled with a Q ExactiveTM HF-X mass spectrometer (Thermo Fisher) operating in the data-dependent acquisition (DDA) mode. For this, 1 μg sample was injected into a home-made C18 Nano-Trap column (4.5 cm × 75 μm, 3 μm). Peptides were separated in a home-made analytical column (15 cm × 150 μm, 1.9 μm) using a linear gradient elution, as listed in Table 3. The separated peptides were analyzed by Q Exactive TM HF-X mass spectrometer (Thermo Fisher), with ion source of Nanospray Flex™ (ESI), spray voltage of 2.1 kV, and ion transport capillary temperature of 320 °C. Full scan range was from m/z 350 to 1500 with resolution of 60,000 (at m/z 200), an automatic gain control (AGC) target value was 3×10^6, and a maximum ion injection time was 20 ms. The top 40 precursors of the highest abundant in the full scan were selected and fragmented by higher energy collisional dissociation (HCD) and analyzed in MS/MS, where resolution was 30,000 (at m/z 200) for 6 plex, the automatic gain control (AGC) target value was 5 × 104, the maximum ion injection time was 54 ms, a normalized collision energy was set as 32%, an intensity threshold was 1.2×10^5, and the dynamic exclusion parameter was 20 s. The raw data of MS detection were named ".raw".

Table 3. Liquid chromatography elution gradient table.

Time (min)	Flow Rate (mL/min)	Mobile Phase A (%)	Mobile Phase B (%)
0	0.6	94	6
2	0.6	85	15
48	0.6	60	40
50	0.6	50	50
51	0.6	45	55
60	0.6	0	100

4.3.5. Data Analysis

The Identification and Quantitation of Protein

The resulting spectra from each run were searched separately against Mus_musculus_uniprot_2021_7_15.fasta (86,544 sequences) by the search engines: Proteome Discoverer 2.4 (PD 2.4, Thermo). The searched parameters were set as follows: Mass tolerance for precursor ion was 10 ppm and mass tolerance for product ion was 0.02 Da. Carbamidomethyl was specified as fixed modifications, Oxidation of methionine (M) and TMT plex were specified as dynamic modification. Acetylation, TMT plex, Met-loss. and Met-loss+Acetyl were specified as N-Terminal modifications in PD 2.4. A maximum of 2 missed cleavage sites were allowed.

In order to improve the quality of analysis results, the software PD 2.4 further filtered the retrieval results: Peptide Spectrum Matches (PSMs) with a credibility of more than 99% were identified PSMs. The identified protein contained at least 1 unique peptide. The identified PSMs and protein were retained and performed with FDR of no more than 1.0%. The protein quantitation results were statistically analyzed by T-test. The proteins whose quantitation significantly differed between experimental and control groups ($p < 0.05$ and $|\log_2 FC| > 0.08$ (FC > 1.2 or FC < 0.83 [fold change, FC]) were defined as differentially expressed proteins (DEPs).

The Functional Analysis of Protein and DEP

Gene Ontology (GO) and InterPro (IPR) functional analysis were conducted using the interproscan program against the non-redundant protein database (including Pfam, PRINTS, ProDom, SMART, ProSite, and PANTHER), and the databases of COG (Clusters of Orthologous Groups) and KEGG (Kyoto Encyclopedia of Genes and Genomes) were used to analyze the protein family and pathway. DEPs were used for Volcanic map analysis, cluster heat map analysis, and enrichment analysis of GO and KEGG. The mass spectrometry proteomics data have been deposited to the ProteomeXchange Consortium

(http://proteomecentral.proteomexchange.org (accessed on 14 October 2021)) via the iProX partner repository with the dataset identifier PXD043126.

4.4. Metabolomics

4.4.1. Metabolites Extraction

Tissues (100 mg) were individually grounded with liquid nitrogen and the homogenate was resuspended with prechilled 80% methanol by well vortex. The samples were incubated on ice for 5 min and then were centrifuged at 15,000× g, 4 °C, for 20 min. Some of supernatant was diluted to final concentration containing 53% methanol by LC-MS-grade water. The samples were subsequently transferred to a fresh Eppendorf tube and then were centrifuged at 15,000× g, 4 °C, for 20 min. Finally, the supernatant was injected into the LC-MS/MS system analysis.

4.4.2. UHPLC-MS/MS Analyses

UHPLC-MS/MS analyses were performed using a Vanquish UHPLC system (Thermo Fisher, Wilmington, DE, USA) coupled with an Orbitrap Q ExactiveTM HF mass spectrometer (Thermo Fisher, Wilmington, DE, USA) in Novogene Co., Ltd. (Beijing, China). Samples were injected onto a Hypesil Goldcolumn (100 × 2.1 mm, 1.9 µm) using a 17 min linear gradient at a flow rate of 0.2 mL/min. The eluents for the positive polarity mode were eluent A (0.1% FA in Water) and eluent B (Methanol). The eluents for the negative polarity mode were eluent A (5 mM ammonium acetate, pH 9.0) and eluent B (Methanol).The solvent gradient was set as follows: 2% B, 1.5 min; 2–85% B, 3 min; 100% B, 10 min; 100–2% B, 10.1 min; and 2% B, 12 min. Q ExactiveTM HF mass spectrometer was operated in positive/negative polarity mode with spray voltage of 3.5 kV, capillary temperature of 320 °C, sheath gas flow rate of 35 arb and aux gas flow rate of 10 arb, S-lens RF level of 60, and Aux gas heater temperature of 350 °C.

4.4.3. Data Processing and Metabolite Identification

The raw data files generated by UHPLC-MS/MS were processed using the Compound Discoverer 3.1 (CD3.1, Thermo Fisher) to perform peak alignment, peak picking, and quantitation for each metabolite. After that, peak intensities were normalized to the total spectral intensity. The normalized data were used to predict the molecular formula based on additive ions, molecular ion peaks, and fragment ions. And then peaks were matched with the mzCloud (https://www.mzcloud.org/ (accessed on 12 October 2021)), mzVault, and MassList database to obtain the accurate qualitative and relative quantitative results. Statistical analyses were performed using the statistical software R (R version R-3.4.3), Python (Python 2.7.6 version), and CentOS (CentOS release 6.6).

4.4.4. Data Analysis

These metabolites were annotated using the KEGG database (https://www.genome.jp/kegg/pathway.html (accessed on 14 October 2021)), HMDB database (https://hmdb.ca/metabolites (accessed on 14 October 2021)), and LIPIDMaps database (http://www.lipidmaps.org/ (accessed on 14 October 2021)). Principal components analysis (PCA) and Partial least squares discriminant analysis (PLS-DA) were performed at metaX [50] (a flexible and comprehensive software for processing metabolomics data).We applied univariate analysis (t-test) to calculate the statistical significance (p-value).The metabolites with VIP > 1, p-value < 0.05, and fold change $\geq$ 2 or FC $\leq$ 0.5 were considered to be differential metabolites. Volcano plots were used to filter metabolites of interest based on $\log_2$(FoldChange) and $-\log_{10}$(p-value) of metabolites by ggplot2 in R language.

For clustering heat maps, the data were normalized using z-scores of the intensity areas of differential metabolites and were plotted by Pheatmap package in R language. The correlations between differential metabolites were analyzed by cor () in R language (method = Pearson). Statistical significance of correlations between differential metabolites was calculated by cor.mtest() in R language. p-value < 0.05 was considered as statistically signif-

icant and correlation plots were plotted by corrplot package in R language. The functions of these metabolites and metabolic pathways were studied using the KEGG database. The metabolic pathways enrichment of differential metabolites was performed. When ratios were satisfied by x/n > y/N, metabolic pathways were considered as having enrichment; when *p*-value of metabolic pathway <0.05, metabolic pathways were considered as having statistically significant enrichment.

4.5. Hematoxylin and Eosin (H&E) Staining

Liver and brain specimens from the different treatment groups were fixed in 4% paraformaldehyde for 24 h, embedded in paraffin after being washed in PBS, dehydrated in gradient alcohol, dealcoholized in xylene, and then sliced into 5 μm sections. Sections were stained using standard H&E staining methods and examined by two blinded pathologists. Finally, the sections were mounted with neutral gum and captured by an Olympus microscope (Olympus Corp., Tokyo, Japan).

4.6. Determination of ALT, AST, MDA, and GSH

Levels of ALT, AST, MDA, and GSH in serum samples were evaluated using detection kits, according to the manufacturer's instructions.

4.7. RNA Extraction and Quantitative Real-Time PCR (qPCR)

RNAex Pro Reagent (AG; 21102) was used to extract total RNA, as indicated by the supplier, and the Reverse Transcription Premix kit (AG; 11728) was used to produce cDNA following the manufacturer's recommendations. Quantitative real-time PCR was performed using SYBR Green Pro Taq HS qPCR kit (AG; 11701) and LightCycler480 (Roche, Mannheim, Germany). Actin was used as the internal standard control to normalize gene expression using the $2^{-\Delta\Delta Ct}$ method. The sequences of the qPCR primers are listed in Supplementary Table S2.

4.8. Statistical Analysis

ALT, AST, MDA, and GSH levels were presented as means ± standard deviation (SD) and analyzed using IBM SPSS Statistics for Macintosh, Version 26.0 (SPSS Inc., Chicago, IL, USA). Student's test was used if a significant difference was determined. $p < 0.05$ was considered statistically significant.

5. Conclusions

In conclusion, the mechanism of hepatic encephalopathy may be correlated to the energy metabolism, amino acid metabolism, complement and coagulation cascades, vitamin digestion and absorption, and neurotransmitter imbalance in this experiment, based on the metabolomics and proteomics. More importantly, we found that the mechanism of hepatic encephalopathy may be related to the ferroptosis pathway. However, the specific pathway and mechanism of differential expression proteins still need to be further studied. Meanwhile, the sample size of this study need to be increased.

Supplementary Materials: The following supporting information can be downloaded at: https://www.mdpi.com/article/10.3390/ijms25010284/s1.

Author Contributions: L.G. provided experimental concepts and design, offered scientific direction, and reviewed the manuscript. H.G. and G.W. performed the experiments, researched data, and drafted the manuscript. L.L. and Y.B. analyzed all the data. W.H. and H.W. contributed to reagents and materials. All authors have read and agreed to the published version of the manuscript.

Funding: This research received no external funding.

Informed Consent Statement: Not applicable.

Data Availability Statement: All study data are included in the article and Supplementary Materials.

Conflicts of Interest: The authors declare no conflict of interest.

Abbreviations

ACN	acetonitrile
AGC	automatic gain control
ALT	alanine transaminase
AST	aspartate aminotransferase
BCAAs	branched chain amion acids
BP	biological Process
CC	Cellular Component
COG	clusters of orthologous groups
CYP450	cytochrome P450
DEPs	differentially expressed proteins
ELISA	enzyme-linked immunosorbent assay
FA	formic acid
FC	fold change
FMO	flavin-containing monooxygenase
FMT	fecal microbiota transplantation
FTH1	ferritin heavy chain 1
GABA	γ-aminobutyric acid
Glu	glutamate
GMP	guanosine monophosphate
GO	gene ontology
GPX4	glutathione peroxidase 4
GSH	glutathione
HCD	higher-energy collisional dissociation
HE	hepatic encephalopathy
HRMS	high-resolution mass spectrometry
KEGG	Kyoto Encyclopedia of Genes and Genomes
LC-MS	Liquid chromatography–Mass spectrometry
LOLA	L-ornithine-L-aspartate
MDA	malondialdehyde
MeOH	Methanol
MF	Molecular Function
NAFLD	nonalcoholic fatty liver disease
NCOA4	nuclear receptor coactivator 4
PBS	phosphate-buffered saline
PCA	principal component analysis
PLS-DA	partial least squares discrimination analysis
PSMs	peptide spectrum matches
PUFA	polyunsaturated fatty acid
QC	quality control
ROS	reactive oxygen species
SEM	standard error of mean
SPF	specific pathogen-free
STEAP3	six-transmembrane epithelial antigen of prostate 3
TAA	thioacetamide
TMT	tandem mass tags
UMP	uridine monophosphate
VIP	variable importance in projection

References

1. Bajaj, J.S.; Wade, J.B.; Sanyal, A.J. Spectrum of neurocognitive impairment in cirrhosis: Implications for the assessment of hepatic encephalopathy. *Hepatology* **2009**, *50*, 2014–2021. [CrossRef] [PubMed]
2. Balzano, T. Active Clinical Trials in Hepatic Encephalopathy: Something Old, Something New and Something Borrowed. *Neurochem. Res.* **2023**, *48*, 2309–2319. [CrossRef] [PubMed]
3. Patel, D.; McPhail, M.J.; Cobbold, J.F.; Taylor-Robinson, S.D. Hepatic encephalopathy. *Br. J. Hosp. Med.* **2012**, *73*, 79–85. [CrossRef] [PubMed]

4. Tranah, T.H.; Vijay, G.K.; Ryan, J.M.; Shawcross, D.L. Systemic inflammation and ammonia in hepatic encephalopathy. *Metab. Brain Dis.* **2013**, *28*, 1–5. [CrossRef] [PubMed]
5. Vidal-Cevallos, P.; Chavez-Tapia, N.C.; Uribe, M. Current approaches to hepatic encephalopathy. *Ann. Hepatol.* **2022**, *27*, 100757. [CrossRef] [PubMed]
6. Ramakrishna, K.; Sinku, S.; Majumdar, S.; Singh, N.; Gajendra, T.A.; Rani, A.; Krishnamurthy, S. Indole-3-carbinol ameliorated the thioacetamide-induced hepatic encephalopathy in rats. *Toxicology* **2023**, *492*, 153542. [CrossRef]
7. Mincheva, G.; Gimenez-Garzo, C.; Izquierdo-Altarejos, P.; Martinez-Garcia, M.; Doverskog, M.; Blackburn, T.P.; Hallgren, A.; Backstrom, T.; Llansola, M.; Felipo, V. Golexanolone, a GABA(A) receptor modulating steroid antagonist, restores motor coordination and cognitive function in hyperammonemic rats by dual effects on peripheral inflammation and neuroinflammation. *CNS Neurosci. Ther.* **2022**, *28*, 1861–1874. [CrossRef]
8. Liu, X.F.; Lu, J.J.; Li, Y.; Yang, X.Y.; Qiang, J.W. Ferrous sulfate reverses cerebral metabolic abnormality induced by minimal hepatic encephalopathy. *Metab. Brain Dis.* **2023**, *38*, 1613–1620. [CrossRef]
9. Butterworth, R.F. Pathogenesis of hepatic encephalopathy and brain edema in acute liver failure. *J. Clin. Exp. Hepatol.* **2015**, *5*, S96–S103. [CrossRef]
10. Xu, X.Y.; Ding, H.G.; Li, W.G.; Jia, J.D.; Wei, L.; Duan, Z.P.; Liu, Y.L.; Ling-Hu, E.Q.; Zhuang, H.; Hepatology, C.S.O.; et al. Chinese guidelines on management of hepatic encephalopathy in cirrhosis. *World J. Gastroenterol.* **2019**, *25*, 5403–5422. [CrossRef]
11. Jones, E.A.; Basile, A.S.; Yurdaydin, C.; Skolnich, P. Do benzodiazepine ligands contribute to hepatic encephalopathy? *Adv. Exp. Med. Biol.* **1993**, *341*, 57–69. [CrossRef] [PubMed]
12. Williams, E.; Chu, C.; DeMorrow, S. A critical review of bile acids and their receptors in hepatic encephalopathy. *Anal. Biochem.* **2022**, *643*, 114436. [CrossRef] [PubMed]
13. Kong, W.; Sun, X.; Yu, S.; Liu, P.; Zheng, X.; Zhang, J.; Zhu, L.; Jiang, T.; Jin, M.; Gao, J.; et al. Bile duct ligation increased dopamine levels in the cerebral cortex of rats partly due to induction of tyrosine hydroxylase. *Br. J. Pharmacol.* **2023**, *180*, 1690–1709. [CrossRef] [PubMed]
14. Johansson, M.; Agusti, A.; Llansola, M.; Montoliu, C.; Stromberg, J.; Malinina, E.; Ragagnin, G.; Doverskog, M.; Backstrom, T.; Felipo, V. GR3027 antagonizes GABAA receptor-potentiating neurosteroids and restores spatial learning and motor coordination in rats with chronic hyperammonemia and hepatic encephalopathy. *Am. J. Physiol. Gastrointest. Liver Physiol.* **2015**, *309*, G400–G409. [CrossRef] [PubMed]
15. Llansola, M.; Montoliu, C.; Agusti, A.; Hernandez-Rabaza, V.; Cabrera-Pastor, A.; Gomez-Gimenez, B.; Malaguarnera, M.; Dadsetan, S.; Belghiti, M.; Garcia-Garcia, R.; et al. Interplay between glutamatergic and GABAergic neurotransmission alterations in cognitive and motor impairment in minimal hepatic encephalopathy. *Neurochem. Int.* **2015**, *88*, 15–19. [CrossRef] [PubMed]
16. Butterworth, R.F. Neurosteroids in hepatic encephalopathy: Novel insights and new therapeutic opportunities. *J. Steroid Biochem. Mol. Biol.* **2016**, *160*, 94–97. [CrossRef]
17. Jones, E.A. Ammonia, the GABA neurotransmitter system, and hepatic encephalopathy. *Metab. Brain Dis.* **2002**, *17*, 275–281. [CrossRef]
18. Kircheis, G.; Luth, S. Pharmacokinetic and Pharmacodynamic Properties of L-Ornithine L-Aspartate (LOLA) in Hepatic Encephalopathy. *Drugs* **2019**, *79*, 23–29. [CrossRef]
19. Hassouneh, R.; Bajaj, J.S. Gut Microbiota Modulation and Fecal Transplantation: An Overview on Innovative Strategies for Hepatic Encephalopathy Treatment. *J. Clin. Med.* **2021**, *10*, 330. [CrossRef]
20. Philips, C.A.; Augustine, P. Gut Barrier and Microbiota in Cirrhosis. *J. Clin. Exp. Hepatol.* **2022**, *12*, 625–638. [CrossRef]
21. Alimirah, M.; Sadiq, O.; Gordon, S.C. Novel Therapies in Hepatic Encephalopathy. *Clin. Liver Dis.* **2020**, *24*, 303–315. [CrossRef] [PubMed]
22. Gluud, L.L.; Dam, G.; Les, I.; Marchesini, G.; Borre, M.; Aagaard, N.K.; Vilstrup, H. Branched-chain amino acids for people with hepatic encephalopathy. *Cochrane Database Syst. Rev.* **2017**, *5*, CD001939. [CrossRef] [PubMed]
23. Sharma, B.C.; Singh, J.; Srivastava, S.; Sangam, A.; Mantri, A.K.; Trehanpati, N.; Sarin, S.K. Randomized controlled trial comparing lactulose plus albumin versus lactulose alone for treatment of hepatic encephalopathy. *J. Gastroenterol. Hepatol.* **2017**, *32*, 1234–1239. [CrossRef] [PubMed]
24. Bass, N.M.; Mullen, K.D.; Sanyal, A.; Poordad, F.; Neff, G.; Leevy, C.B.; Sigal, S.; Sheikh, M.Y.; Beavers, K.; Frederick, T.; et al. Rifaximin treatment in hepatic encephalopathy. *N. Engl. J. Med.* **2010**, *362*, 1071–1081. [CrossRef] [PubMed]
25. Sharma, B.C.; Sharma, P.; Agrawal, A.; Sarin, S.K. Secondary prophylaxis of hepatic encephalopathy: An open-label randomized controlled trial of lactulose versus placebo. *Gastroenterology* **2009**, *137*, 885–891.e1. [CrossRef] [PubMed]
26. Schnur, J.; Oláh, J.; Szepesi, A.; Nagy, P.; Thorgeirsson, S.S. Thioacetamide-induced hepatic fibrosis in transforming growth factor beta-1 transgenic mice. *Eur. J. Gastroenterol. Hepat.* **2004**, *16*, 127–133. [CrossRef]
27. Amirshahrokhi, K.; Niapour, A. Carvedilol attenuates brain damage in mice with hepatic encephalopathy. *Int. Immunopharmacol.* **2022**, *111*, 109119. [CrossRef]
28. Miranda, A.S.; Rodrigues, D.H.; Vieira, L.B.; Lima, C.X.; Rachid, M.A.; Vidigal, P.V.; Gomez, M.V.; Reis, H.J.; Guatimosim, C.; Teixeira, A.L. A thioacetamide-induced hepatic encephalopathy model in C57BL/6 mice: A behavioral and neurochemical study. *Arq. Neuropsiquiatr.* **2010**, *68*, 597–602. [CrossRef]

29. Avraham, Y.; Grigoriadis, N.C.; Magen, I.; Poutahidis, T.; Vorobiav, L.; Zolotarev, O.; Ilan, Y.; Mechoulam, R.; Berry, E.M. Capsaicin affects brain function in a model of hepatic encephalopathy associated with fulminant hepatic failure in mice. *Br. J. Pharmacol.* **2009**, *158*, 896–906. [CrossRef]
30. Butterworth, R.F. Pathophysiology of Hepatic Encephalopathy: Studies in Animal Models. In *Metabolic Encephalopathy*; McCandless, D.W., Ed.; Springer: New York, NY, USA, 2009; pp. 149–180.
31. Swapna, I.; Kumar, K.V.; Reddy, P.V.; Murthy Ch, R.; Reddanna, P.; Senthilkumaran, B. Phospholipid and cholesterol alterations accompany structural disarray in myelin membrane of rats with hepatic encephalopathy induced by thioacetamide. *Neurochem. Int.* **2006**, *49*, 238–244. [CrossRef]
32. Sathyasaikumar, K.V.; Swapna, I.; Reddy, P.V.; Murthy Ch, R.; Roy, K.R.; Dutta Gupta, A.; Senthilkumaran, B.; Reddanna, P. Co-administration of C-Phycocyanin ameliorates thioacetamide-induced hepatic encephalopathy in Wistar rats. *J. Neurol. Sci.* **2007**, *252*, 67–75. [CrossRef] [PubMed]
33. Ross, P.L.; Huang, Y.N.; Marchese, J.N.; Williamson, B.; Parker, K.; Hattan, S.; Khainovski, N.; Pillai, S.; Dey, S.; Daniels, S.; et al. Multiplexed protein quantitation in Saccharomyces cerevisiae using amine-reactive isobaric tagging reagents. *Mol. Cell Proteom.* **2004**, *3*, 1154–1169. [CrossRef] [PubMed]
34. Essam, R.M.; Saadawy, M.A.; Gamal, M.; Abdelsalam, R.M.; El-Sahar, A.E. Lactoferrin averts neurological and behavioral impairments of thioacetamide-induced hepatic encephalopathy in rats via modulating HGMB1/TLR-4/MyD88/Nrf2 pathway. *Neuropharmacology* **2023**, *236*, 109575. [CrossRef] [PubMed]
35. Asano, F.; Moriwaki, H.; Shiratori, Y.; Shimazaki, M.; Sakai, T.; Koshino, Y.; Murakami, N.; Sugihara, J.; Ohnishi, H.; Saito, K.; et al. Enhanced production of leukotriene B4 by peripheral blood mononuclear cells in patients with fulminant hepatitis. *J. Gastroenterol. Hepatol.* **1993**, *8*, 228–231. [CrossRef] [PubMed]
36. Bissonnette, J.; Rose, C.F. Hepatic Encephalopathy: Pathophysiology—Brain. In *Diagnosis and Management of Hepatic Encephalopathy: A Case-based Guide*; Bajaj, J.S., Ed.; Springer International Publishing: Cham, Switzerland, 2018; pp. 15–29.
37. Ma, S.X.; Seo, B.A.; Kim, D.; Xiong, Y.; Kwon, S.H.; Brahmachari, S.; Kim, S.; Kam, T.I.; Nirujogi, R.S.; Kwon, S.H.; et al. Complement and Coagulation Cascades are Potentially Involved in Dopaminergic Neurodegeneration in alpha-Synuclein-Based Mouse Models of Parkinson's Disease. *J. Proteome Res.* **2021**, *20*, 3428–3443. [CrossRef] [PubMed]
38. Yang, X.; Wang, Z.; Kai, J.; Wang, F.; Jia, Y.; Wang, S.; Tan, S.; Shen, X.; Chen, A.; Shao, J.; et al. Curcumol attenuates liver sinusoidal endothelial cell angiogenesis via regulating Glis-PROX1-HIF-1alpha in liver fibrosis. *Cell Prolif.* **2020**, *53*, e12762. [CrossRef] [PubMed]
39. Arenas, Y.M.; Felipo, V. Sustained Hyperammonemia Activates NF-kappaB in Purkinje Neurons Through Activation of the TrkB-PI3K-AKT Pathway by Microglia-Derived BDNF in a Rat Model of Minimal Hepatic Encephalopathy. *Mol. Neurobiol.* **2023**, *60*, 3071–3085. [CrossRef]
40. Abdelaziz, R.R.; Abdelrahman, R.S.; Abdelmageed, M.E. SB332235, a CXCR2 antagonist, ameliorates thioacetamide-induced hepatic encephalopathy through modulation of the PI3K/AKT pathways in rats. *Neurotoxicology* **2022**, *92*, 110–121. [CrossRef]
41. Ding, T.; Chen, S.; Xiao, W.; Liu, Z.; Tu, J.; Yu, Y.; Dong, B.; Chen, W.; Zeng, Y. Six-Transmembrane Epithelial Antigen of Prostate 3 Promotes Hepatic Insulin Resistance and Steatosis. *J. Lipid Res.* **2023**, *64*, 100318. [CrossRef]
42. Guo, W.Z.; Fang, H.B.; Cao, S.L.; Chen, S.Y.; Li, J.; Shi, J.H.; Tang, H.W.; Zhang, Y.; Wen, P.H.; Zhang, J.K.; et al. Six-Transmembrane Epithelial Antigen of the Prostate 3 Deficiency in Hepatocytes Protects the Liver Against Ischemia-Reperfusion Injury by Suppressing Transforming Growth Factor-beta-Activated Kinase 1. *Hepatology* **2020**, *71*, 1037–1054. [CrossRef]
43. Chen, X.; Li, J.; Kang, R.; Klionsky, D.J.; Tang, D. Ferroptosis: Machinery and regulation. *Autophagy* **2021**, *17*, 2054–2081. [CrossRef] [PubMed]
44. Stockwell, B.R.; Jiang, X.; Gu, W. Emerging Mechanisms and Disease Relevance of Ferroptosis. *Trends Cell Biol.* **2020**, *30*, 478–490. [CrossRef] [PubMed]
45. Costa, I.; Barbosa, D.J.; Benfeito, S.; Silva, V.; Chavarria, D.; Borges, F.; Remiao, F.; Silva, R. Molecular mechanisms of ferroptosis and their involvement in brain diseases. *Pharmacol. Ther.* **2023**, *244*, 108373. [CrossRef] [PubMed]
46. Cardoso, B.R.; Hare, D.J.; Bush, A.I.; Roberts, B.R. Glutathione peroxidase 4: A new player in neurodegeneration? *Mol. Psychiatry* **2017**, *22*, 328–335. [CrossRef] [PubMed]
47. Wang, C.; Chen, S.; Guo, H.; Jiang, H.; Liu, H.; Fu, H.; Wang, D. Forsythoside A Mitigates Alzheimer's-like Pathology by Inhibiting Ferroptosis-mediated Neuroinflammation via Nrf2/GPX4 Axis Activation. *Int. J. Biol. Sci.* **2022**, *18*, 2075–2090. [CrossRef]
48. Zhan, S.; Lu, L.; Pan, S.S.; Wei, X.Q.; Miao, R.R.; Liu, X.H.; Xue, M.; Lin, X.K.; Xu, H.L. Targeting NQO1/GPX4-mediated ferroptosis by plumbagin suppresses in vitro and in vivo glioma growth. *Br. J. Cancer* **2022**, *127*, 364–376. [CrossRef]
49. Mao, C.; Liu, X.G.; Zhang, Y.L.; Lei, G.; Yan, Y.L.; Lee, H.M.; Koppula, P.; Wu, S.Q.; Zhuang, L.; Fang, B.L.; et al. DHODH-mediated ferroptosis defence is a targetable vulnerability in cancer. *Nature* **2021**, *593*, 586–590, Erratum in *Nature* **2021**, *596*, E13. [CrossRef]
50. Wen, B.; Mei, Z.; Zeng, C.; Liu, S. metaX: A flexible and comprehensive software for processing metabolomics data. *BMC Bioinform.* **2017**, *18*, 183. [CrossRef]

Disclaimer/Publisher's Note: The statements, opinions and data contained in all publications are solely those of the individual author(s) and contributor(s) and not of MDPI and/or the editor(s). MDPI and/or the editor(s) disclaim responsibility for any injury to people or property resulting from any ideas, methods, instructions or products referred to in the content.

separations

MDPI

Article

Development and Application of a UPLC–MRM–MS Method for Quantifying Trimethylamine, Trimethylamine-N-Oxide, and Related Metabolites in Individuals with and Without Metabolic Syndrome

Mohammed E. Hefni [1,2,*] and Cornelia M. Witthöft [1]

[1] Department of Chemistry and Biomedical Sciences, Faculty of Health and Life Sciences, Linnaeus University, 392 31 Kalmar, Sweden; cornelia.witthoft@lnu.se
[2] Food Industries Department, Faculty of Agriculture, Mansoura University, P.O. Box 46, Mansoura 35516, Egypt
* Correspondence: mohammed.hefni@lnu.se; Tel.: +46-480-44-61-30

Abstract: Trimethylamine-N-oxide (TMAO) is associated with various chronic diseases. TMAO is a downstream oxidative metabolite of trimethylamine (TMA) that is generated by the gut microbiota from dietary choline, carnitine, and betaine. Current analytical methods predominantly target TMAO only, due to the challenge of efficiently extracting and quantifying TMA. The present study demonstrates a simple and rapid UPLC–MRM–MS method for concurrent quantification of TMAO, TMA, and related precursors (choline, betaine, and various carnitines) following a methanol extraction from plasma and derivatization using iodoacetonitrile (IACN). Pure methanol resulted in a higher extractability of TMA (up to two-fold) compared to both pure acetonitrile and various methanol/acetonitrile mixtures. The quantification method showed high linearity within the tested range of 0.0625–100 µmol/L (determination coefficient > 0.999) and an intra- (n = 3) and inter-day (n = 9) precision of 2–8% along with an average recovery of above 94% for all metabolites (TMAO, TMA, choline, betaine, L-carnitine, acetyl-L-carnitine, and propionyl-L-carnitine). The method's applicability was confirmed through a comparison of TMAO and its precursor concentrations in plasma samples of overnight-fasted subjects with (n = 12) and without (n = 21) metabolic syndrome.

Keywords: methylamines; TMAO; TMA; plasma samples; extraction; UPLC–MRM–MS

1. Introduction

TMAO has been recognized as a significant risk factor that is associated with increased adverse outcomes of several chronic diseases, such as cardiovascular disease, colorectal cancer, diabetes, and chronic kidney disease [1–4]. TMAO is a small metabolite that can be directly obtained from one's diet, e.g., seafood [5], or derived from the oxidation of TMA by hepatic flavin monooxygenases into TMAO [6]. TMA is produced by the gut microbial enzymes from nutrients in animal-based foods, e.g., carnitine(s) and choline [7], through two primary pathways (choline and betaine pathways). The key enzymes involved are choline TMA-lyase (CutC/D) and carnitine-oxygenase (CntA/B) [8,9]. Betaine can also be converted to TMA by an enzyme complex (YeaW/X) [8,9]. Thus, the quantification of TMA levels can provide insight into the composition and the activity of the gut microbiota, as well as the activity of flavin monooxygenases. Deficiency of the latter leads to trimethylaminuria (fish odor syndrome) [10]. Establishing a rapid and accurate quantitative method for the

quantification of TMAO and its related metabolites is needed for research advancement and clinical diagnosis.

Liquid chromatography, coupled with mass spectrometry, is the most common method for analyzing TMAO, TMA, and related metabolites [11–16]. Unlike TMAO and the other metabolites, which can be measured directly using MS/MS, TMA typically requires derivatization [12,14,15,17,18] due to its low mass (59 Da), which results in poor fragmentation using UPLC–MRM–MS [18]. Additionally, ionization of TMA, without fragmentation, produces a weak signal of protonated ions at $m/z = 60$ [18]. Consequently, this additional derivatization step limited the development of a UPLC–MRM–MS method for TMA quantification, highlighting a gap in TMA-specific methodological optimization. This has led to TMAO becoming the primary focus of several UPLC–MRM–MS methods developed to study the role of TMAO in health and disease. To address this, this study focused on systematically optimizing the extraction procedure and chromatographic conditions to develop ultra-performance liquid chromatography–multiple reaction monitoring–tandem mass spectrometry (UPLC–MRM–MS) for the analysis of TMA, TMAO, and related metabolites in plasma.

The method was internally validated and applied on a subsample of plasma samples from overnight fasted subjects (both with and without metabolic syndrome) to determine and compare TMAO, TMA, and related metabolites between the two groups. Metabolic syndrome is a cluster of conditions—including obesity, high blood pressure, dyslipidemia, and insulin resistance—that occur together, thus increasing the risk of cardiovascular disease and type 2 diabetes [19]. TMAO has been implicated in cardiovascular diseases and metabolic disorders, rendering it a relevant biomarker [6].

2. Materials and Methods

2.1. Reagents and Solutions

TMAO, TMA, betaine, choline, L-carnitine, propionyl-L-carnitine, acetyl-L-carnitine, and L-carnitine chloride-d9 (Table 1) were purchased from Sigma-Aldrich (St. Louis, MO, USA). Other deuterated compounds (TMA-d9, TMAO-d9, betaine-d11, L-carnitine-d3, acetyl-L-carnitine-d3) (Table 1) were purchased from Cambridge Isotope Laboratories, Inc. (Andover, MA, USA). All the other chemicals and solvents were purchased from Sigma-Aldrich (St. Louis, MO, USA). All chemicals in this study were of LCMS grade, except iodoacetonitrile (IACN), which was of p.a. grade. Water (MQ) was purified using a Milli-Q Water Purification System (Merck, Darmstadt, Germany).

Table 1. Mass transition collision energy of analyzed metabolites.

Metabolite	Precursor Ion	Quantifier Ion/ Qualifier Ion	Collision Energy (eV)
Trimethylamine-acetonitrile	99.01	58.1 59.1	29 17
Trimethylamine-N-oxide	76.01	58.1 59.1	21 13
Choline	104.01	60.1 45.1	17 25
Betaine	118.01	58.2 59.2	33 21
Acetyl-L-carnitine	204.01	85.1 29.2	21 50

Table 1. *Cont.*

Metabolite	Precursor Ion	Quantifier Ion/ Qualifier Ion	Collision Energy (eV)
L-Carnitine	162.01	43.2 60.2	33 17
Propionyl-L-carnitine *	218.2	85.1 29.2	21 49
Internal standards (ISs)			
Trimethylamine-acetonitrile-d9	108.01	66.2 68.2	33 17
Trimethylamine-N-oxide-d9	85.01	66.2 68.1	25 13
Choline-d9	113.01	69.2 45.2	21 25
Betaine-d11	129.01	66.2 68.2	37 21
Acetyl-L-carnitine-d3	204.01	85.1 29.3	21 50
L-Carnitine-d3	165.01	43.2 103.1	41 17

* D_3-L-carnitine was used as an IS for the quantification of propionyl-L-carnitine. Dwell time was 50 milliseconds (ms), cell accelerator voltage 4 V, and fragmentor voltage 166 V.

Individual stock solutions of TMAO, TMA, betaine, choline, L-carnitine, propionyl-L-carnitine, and acetyl-L-carnitine were prepared in MQ water at a concentration of 10 mmol/L and stored at −30 °C. Aqueous calibration solutions were prepared using serial dilution to contain 0.0625, 0.125, 0.25, 0.5, 1, 2, 5, 10, 20, 50, and 100 µmol/L of the individual compounds and stored at −30 °C. Individual stock solutions of internal standards (ISs) were prepared in MQ water at a concentration of 10 mmol/L and stored at −30 °C. A mixture of IS (10 µmol/L of each compound) was prepared in water and stored at −30 °C.

2.2. Optimization of Chromatographic Conditions

A standard solution containing a mix of external standards (50 µmol/L) and ISs (10 µmol/L) was used to optimize the UPLC method and the ion source and to establish mass transition settings. All analysis was carried out using a UPLC 1260 II Infinity system (Agilent Technologies, Santa Clara, CA, USA) coupled with a triple quadrupole mass spectrometer (Agilent Technologies, Santa Clara, CA, USA) that was equipped with an AJS-ES source (Agilent Jet Stream ionization source).

Methylamines were separated on a neutral UPLC–HILIC column (ACE 1.7 HILIC-N, 75 × 2.1 mm) (Chromtech ACE, Scantec Nordic, Aberdeen, Scotland), along with a guard column(ACE 1.7 HILIC-N, 3.0 × 2.1 mm)(Chromtech ACE, Scantec Nordic, Aberdeen, Scotland). Isocratic elution was performed using a mobile phase consisting of 70% ammonium formate (10 mmol/L) in MQ water (solvent A) and 30% acetonitrile (ACN) (solvent B) as described earlier [14]. The flow rate was set at 0.2 mL/min and the injection volume was 1 µL. The total run time was 6 min, and the first 0.5 min was diverted to waste. The column was thermostatically controlled at 25 °C, while the autosampler temperature was kept at 5 °C. The injector was washed using 20% methanol in water.

Optimization of ion source parameters was carried out using Source Optimizer Software (version B.08.00, Mass Hunter workstation, Agilent Technologies, Santa Clara, CA, USA). A wide range of the following parameters was optimized: capillary voltage (0–2000 V, step size 500), nozzle voltage (0–2000 V, step size 500), drying gas temperature (100–280 °C, step size 30), drying gas flow (10–20 L/min, step size 1), sheath gas temperature (225–400 °C, step size 25), sheath gas flow (5–12 L/min, step size 1), nebulizer (15–60 psi, step size 5), high-pressure flow (70–210 V, step size 20), and low pressure flow (40–160 V, step size 20). The optimized parameters were applied during the analysis of plasma samples and were set as follows: drying gas temperature 160 °C, drying gas flow 11.0 L/min, nebulizer pressure 35 psi, sheath gas temperature 400 °C, sheath gas flow 12 L/min, capillary voltage +2000 V (positive ionization), nozzle voltage 0 V, iFunnel high pressure 110 V, and low pressure 60 V (positive mode).

AJS-ES was used and operated in Multiple Reaction Monitoring (MRM) mode. Mass transitions were also optimized using method optimizer software (version 10.1, Mass Hunter workstation, Agilent Technologies, Santa Clara, CA, USA). Four product ions were acquired, and a wide range (5–50 eV) of collision energy was tested (Table 1). The most intense transition was used for the quantification (quantifier transition) (Table 1), and the second was used for confirmation (qualifier transition).

2.3. Optimization of Extraction Conditions and Derivatization of TMA

Optimization of extraction conditions was carried out using a non-fasted human plasma from a single donor stored in aliquots of 250–500 µL at −80 °C. Before the analysis of TMAO and its related metabolites, the plasma was thawed at room temperature. Various extraction solvent mixtures of MeOH/ACN (100:0, 90:10, 50:50, 10:90, 0:100) were evaluated using a fixed volume (25 µL) of the plasma sample. Two different solvent-to-sample ratios were examined (100:25 and 200:25), and a fixed amount of IS (10 µL, containing 10 µmol/L of each deuterated compound) was added. Different extraction times (5, 10, and 20 min) were also checked.

The optimized extraction conditions were applied to all plasma samples. In brief, 25 µL of plasma samples were transferred to a 1.5 mL Eppendorf tube and mixed with 100 µL of pure methanol, and 10 µL of an IS (containing 10 µmol/L of each deuterated compound) was added. To generate the calibration curve, 25 µL of each external standard level was transferred to a 1.5 mL Eppendorf tube and mixed with 100 µL of pure methanol and 10 µL of the IS. Both plasma samples and standards were then vortexed, shaken for 10 min at room temperature, and centrifuged (13,000× *g*, 8 min). After extraction, samples were derivatized as previously described [14,20] with minor modifications. Briefly, 100 µL of the supernatant was then transferred to a 1.5-mL microcentrifuge tube, and 890 µL of ACN, 5 µL of concentrated NH_4OH, and 5 µL of IACN were added. Samples were vortexed and shaken (10 min at room temperature). The reaction was stopped by adding 2 µL formic acid. Samples were centrifuged (13,000× *g*, 5 min). The supernatant was transferred into HPLC vials.

2.4. Quality Control of Analytical Method

To control for within- and between-day variations, plasma samples were analyzed (four analysis occasions, duplicate samples). Recovery was carried out by spiking the plasma samples with TMA, TMAO, betaine, choline, L-carnitine, acetyl-L-carnitine, and propionyl-L-carnitine each at the levels of 5, 10, 20, 50, and 100 µmol/L (5 levels as duplicate samples, $n = 10$). The linearity of the added standards was investigated using linear regression. The limit of detection (LOD) and limit of quantification (LOQ) were estimated from calibration curve data using LOD = (3.3 × SD)/b; LOQ = (10 × SD)/b,

where SD is the residual standard deviation of the linear regression and b is the slope of the regression line.

2.5. Method Application on Clinical Plasma Samples

To demonstrate the utility of the method, plasma samples from the 33 subjects with (n = 12) and without (n = 21) metabolic syndrome, aged 57 ± 6.7, after overnight fasting (≈12 h), were analyzed to determine and compare TMAO, TMA, and related metabolites in both groups. The analyzed plasma samples represent a subsample of plasma samples from subjects participating in an intervention trial to determine the effects of animal food ingestion (meat and eggs) on postprandial plasma concentrations of methylamines. Blood samples were collected from January to May 2020 and from December 2022 to May 2023 (the interruption was due to the COVID-19 pandemic). Blood samples (3 mL) were withdrawn using an intravenous catheter into EDTA K2 vacutainers, which were centrifuged (2000× g, 10 min) for plasma separation. Subsamples from the collected plasma (250 µL) were stored at −80 °C until analysis. The human trial was approved by the Swedish Ethical Review Authority (Dnr: 2019-04354).

2.6. Calculations and Statistics

The coefficient of variation (CV) for between-day variation was calculated for clinical samples (n = 8, four analysis occasions as duplicate samples). The recovery (R) was calculated according to the following Equation (1):

$$R\ (\%) = \left(\frac{\left(C_{found} - C_{sample}\right)}{C_{added}} \right) \times 100 \quad (1)$$

where C_{found} is the measured concentration in the spiked sample, C_{sample} is the measured concentration in the sample before spiking, and C_{added} is the added concentration.

The linearity of each calibration curve was determined using regression analyses. Extraction efficacy of different solvents was compared using a one-way analysis of variance (ANOVA). Data of methylamines in clinical plasma samples were expressed as mean ± standard deviation (SD). A t-test was performed at a 0.05 level of significance to examine the difference in methylamine concentrations between subjects with and without metabolic syndrome. Statistical analyses were carried out using GraphPad Prism (Prism 10, GraphPad, La Jolla, CA, USA) at a significance level of $p < 0.05$.

3. Results

3.1. Extraction and Derivatization

Pure methanol or methanol/ACN (9:1) demonstrated similar higher efficacy in extracting TMA, both yielding up to 2-fold higher, compared to pure ACN and other various mixtures of methanol/ACN (Figure 1). The extractability of the other metabolites did not differ significantly when using methanol, ACN, or various mixtures of methanol/ACN (Figure 1). A volume of 100 µL of methanol was found to be adequate for the extraction of 25 µL plasma, as no significant difference was observed when compared to using 200 µL of solvent. IACN proved to be a suitable derivatizing reagent in the presence of 5 µL NH_4OH, and a duration of 10 min was sufficient for complete derivatization of TMA. Formic acid is necessary to terminate the reaction and to stabilize the derivatized TMA.

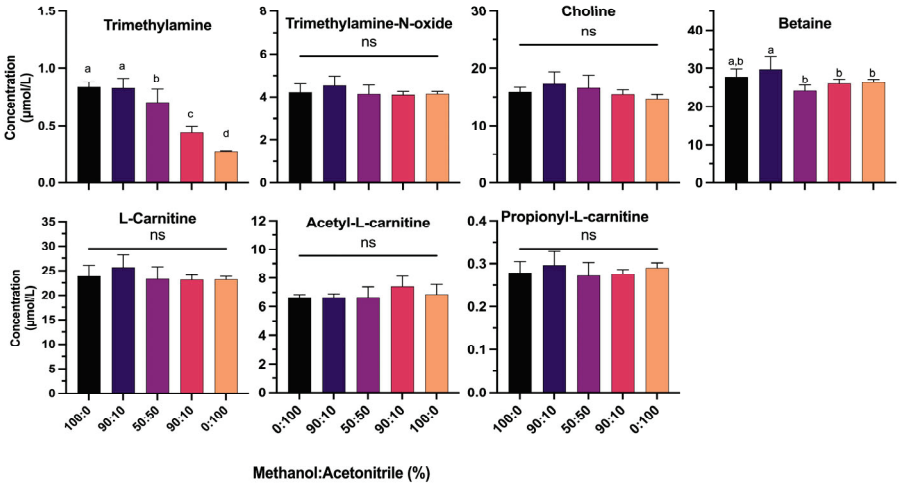


Figure 1. The effect of different methanol/acetonitrile mixtures (100:0, 90:10, 50:50, 10:90, 0:100) as extraction solvents on the extractability of TMAO and related metabolites (µmol/L) from plasma (n = 5 replicates). Different letters a–d indicate significant differences, ns, not significant.

3.2. Optimized Chromatographic Conditions

Isocratic elution with a mobile phase consisting of 70% mobile phase A (10 mmol/L ammonium formate in MQ water) and 30% mobile phase B (pure ACN) showed a satisfying resolution of TMAO, TMA, choline, betaine, and propionyl-, acetyl-, and L-carnitine using a UPLC–HILIC-N (neutral) column (Figure 2) at 0.2 mL/min flow rate.

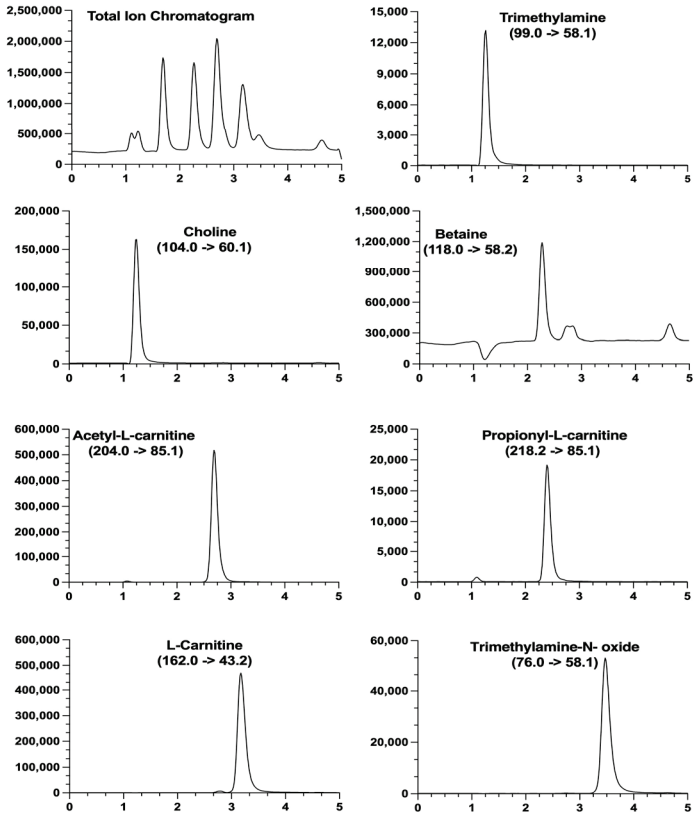


Figure 2. Typical total ion chromatogram and MRM spectrum (positive ionization mode) of methylamines in a plasma sample. The concentrations (µmol/L) were as follows: 0.5 for trimethylamine, 2.1 for trimethylamine-N-oxide, 9.7 for choline, 46.7 for betaine, 4.6 for acetyl-L-carnitine, 0.4 for propionyl-L-carnitine, and 37.4 for L-carnitine.

Mass transitions (Table 1) and ion source parameters were optimized using two product ions as quantifiers (the most abundant ion) and qualifiers (the second most abundant) for confirmation purposes. The optimized conditions resulted in a total run time of 6 min, with good sensitivity (Table 2) and reproducibility. The calibration curves of all metabolites were linear up to the tested level of 100 µmol/L ($R^2 > 0.9991$) (Table 2). The LOQs ranged from 0.06 µmol/L for L-carnitine to 0.24 µmol/L for propionyl-L-carnitine, which proved suitable for clinical samples. The average recovery of individual metabolites after standard addition (duplicate samples at each addition level, five levels, $n = 10$) ranged from 94% for choline to 114% for TMA (Table 3) and resulted in coefficients of determination R^2 above 0.9953 (Figure 3). The between-day variation (CV%, $n = 8$, duplicate samples at four consecutive days) for all metabolites in plasma samples was below 10%.

Table 2. Method quality control parameters of aqueous calibration curve, limit of detection, and limit of quantification ($n = 3$, three different occasions).

Metabolites	Calibration			Limits (µmol/L)	
	Slope	Intercept	R^2	LOD	LOQ
TMA	0.0591	−0.018	0.9996	0.06 ± 0.01	0.18 ± 0.02
TMAO	0.0855	0.0003	0.9997	0.03 ± 0.02	0.09 ± 0.08
Choline	0.0575	−0.0095	0.9999	0.03 ± 0.00	0.09 ± 0.01
Betaine	0.0769	−0.0192	0.9998	0.05 ± 0.03	0.1 ± 0.06
Acetyl-L-carnitine	0.0630	−0.0372	0.9991	0.08 ± 0.01	0.26 ± 0.02
L-carnitine	0.0604	0.0011	0.9999	0.02 ± 0.01	0.06 ± 0.02
Propionyl-L-carnitine	0.2505	−0.0969	0.9996	0.08 ± 0.03	0.24 ± 0.01

TMA: trimethylamine, TMAO: trimethylamine-N-oxide, R^2: coefficient of determination; LOD = limit of detection, LOQ = limit of quantification. LOD and LOQ were based on the residual standard deviation (R), and the slope (b) of the regression line using the following equation: LOD = (3.3 × SD)/b; LOQ = (10 × SD)/b.

Table 3. Concentrations of methylamines (µmol/L) in spiked and non-spiked plasma samples ($n = 2$).

Level of Addition (µmol/L)	Average Concentration (µmol/L)							Average Recovery (% ± SD)
		0	5	10	20	50	100	
TMA	C_{found}	0.4	6.4	11.7	19.5	64.1	113.0	
	Recovery (%)		118	113	95	128	112	114 ± 1
TMAO	C_{found}	1.9	7.3	11.9	18.9	52.9	103.6	
	Recovery (%)		105	99	85	101	101	95 ± 5
Choline	C_{found}	10.6	15.3	19.7	29.7	58.2	104.6	
	Recovery (%)		93	91	96	96	94	94 ± 2
Betaine	C_{found}	41.9	46.4	51.1	61.2	93.5	132.3	
	Recovery (%)		104	99	100	105	91	98 ± 5
Acetyl-L-carnitine	C_{found}	4.8	9.8	14.9	21.3	63.4	113.2	
	Recovery (%)		101	100	82	117	108	102 ± 3
L-carnitine	C_{found}	30.6	35.8	40.9	51.3	82.9	128.5	
	Recovery (%)		104	103	104	105	98	103 ± 3
Propionyl-L-carnitine	C_{found}	0.3	5.3	9.8	19.3	51.2	103	
	Recovery (%)		98.9	95.4	95.2	102	103	98 ± 8

Recovery trials were carried out using a non-fasted human plasma from a single donor stored in aliquots of 250–500 µL at −80 °C, with duplicate samples ($n = 2$) at each addition level (five levels). Variation between measured concentrations in duplicates was £ 10%. Recovery was calculated according to Equation (1).

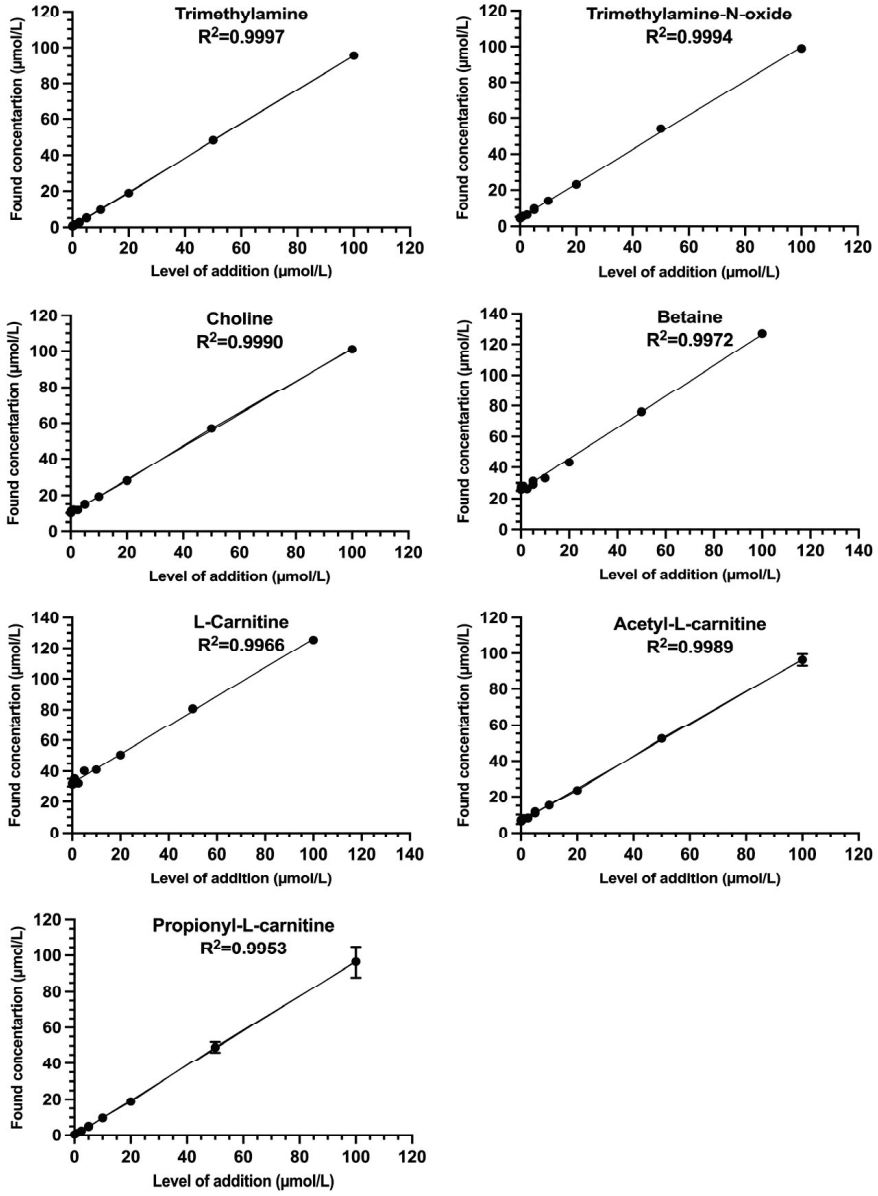


Figure 3. Coefficients of determination of added trimethylamine (TMA), trimethylamine-N-oxide (TMAO), choline, betaine, L-carnitine, acetyl-L-carnitine, and propionyl-L-carnitine to a plasma sample (n = 3). The intercept of linearity lines is not at zero due to baseline concentrations of methylamines in the unspiked sample (TMA 0.4, TMAO 1.9, choline 10.6, betaine 41.9, acetyl-L-carnitine 4.8, L-carnitine 30.6, and propionyl-L-carnitine 0.3 µmol/L).

3.3. Method Application

The method was successfully applied to determine methylamines in fasted plasma samples of subjects with (n = 12) and without (n = 21) metabolic syndrome. In all plasma samples, the metabolites trimethylamine N-oxide, trimethylamine, choline, betaine, and acetyl-, propionyl-, and L-carnitine were simultaneously quantified. TMA concentrations were the same in both groups; however, TMAO, propionyl-L-carnitine, and L-carnitine concentrations were higher in individuals with metabolic syndrome. Other metabolites did not differ between both groups (Table 4).

Table 4. Concentrations of methylamines (μmol/L) in plasma of 21 healthy subjects, collected on two occasions (n = 42), and 12 subjects with metabolic syndrome, collected on two occasions (n = 24).

Variable	Healthy (n = 21)	Metabolic Syndrome (n = 12)	Unpaired t-Test
Trimethylamine	1.6 ± 0.3	1.6 ± 0.3	ns
Trimethylamine N-oxide *	4.6 ± 6.3	9.5 ± 14.4	0.03
Choline	9.1 ± 1.9	9.4 ± 2.1	ns
Betaine	29.1 ± 6.5	30.2 ± 8.8	ns
Acetyl-L-carnitine	6.6 ± 2.2	6.8 ± 1.9	ns
L-Carnitine	30.4 ± 5.7	36.0 ± 6.7	0.0005
Propionyl-L-carnitine	0.27 ± 0.1	0.33 ± 0.1	0.02

ANOVA repeated measurement (mixed model) was used to analyze the individual variation across the two time-points and between the two groups. As no significant differences were observed within the groups over time, time was not considered in the model. Instead, an unpaired t-test was used to compare the groups. All variables were normally distributed except for TMAO; therefore, the data were log transferred. * TMAO values presented in the table show the untransformed and not the log-transformed data. ns, not significant.

4. Discussion

4.1. Analytical Findings

The method was partially validated in alignment with ICH guidelines [21], following approaches established in our previous work and other published studies [11–14,18]. This study emphasizes TMA extraction and detection, as the current literature mainly targeted its oxidized metabolite, TMAO (a hepatic flavin monooxygenase-derived metabolite), highlighting a gap in TMA-specific methodological optimization. Quantifying TMA, however, offers unique insights into gut microbial activity and host metabolic function and might enable the diagnosis of trimethylaminuria and therapeutic strategies to disrupt the TMA-TMAO axis. Challenges in TMA quantification are mainly due to difficulties in detection and here we demonstrate that the selection of extraction solvent significantly impacts TMA extractability. The low molecular weight of TMA led to poor fragmentation, with fragments appearing in a mass region filled with the interferences, which resulted in a noisy baseline and low sensitivity. We also observed that analysis of TMA without fragmentation (CE = 0) produced a weak signal at m/z = 60 ($C_3H_9N^+$ H); similar observations were reported by others [18]. Additionally, ACN can form adducts with ammonium ions producing a signal at m/z = 59, which may interfere with the TMA detection [20]. ACN can also be hydrolyzed to produce acetamide (mass 59.1) [20], which contributed to the high background signal observed when monitoring the molecular ion expected for TMA at m/z = 60.1. Therefore, derivatizing TMA is necessary to achieve reliable and accurate results. In this study, TMA was derivatized using IACN, which proved to be a suitable and fast reaction, as previously described [14]. However, we observed that the addition of formic acid was crucial to terminate the derivatization reaction, thus ensuring the samples' stability in the autosampler. The absence of formic acid resulted in the formation of a peak that shares the same retention time as derivatized TMA but possesses different qualifier ratios. Previously, we showed that the alkaline conditions employed during the derivatization maintained TMAO in an uncharged state, preventing any cross-reactions with TMAO or other methylamines [14].

Moreover, ensuring a high extractability of TMA was a challenging aspect of this study, as the sample extraction method affects the metabolite profile and data quality [22]. Indeed, during this study, we found that the use of the previously chosen extraction medium methanol/ACN (10:90) [14] resulted in lower TMA extractability. In contrast, using pure methanol significantly improved the extractability (up to two-fold increase) of TMA (Figure 1) and the reproducibility. This finding aligns with previous studies [22,23] and indicates a lower protein interference, a more comprehensive metabolite profile, and greater reproducibility when methanol was used as the extraction solvent compared to

ACN. Another contributing factor could be the higher polarity of methanol, a protic solvent that can form hydrogen bonds by donating protons (H+), which facilitates the dissolution and extractability of highly polar compounds (e.g., TMA). In contrast, ACN, an aprotic solvent, lacks the ability to form hydrogen bonds, relying mainly on dipole–dipole interactions, which may be less effective for extracting highly polar compounds compared to the hydrogen bonding mechanism facilitated by methanol.

The limit of quantification for all methylamines in the present study (ranging from 0.06 μmol/L for L-carnitine to 0.24 μmol/L for propionyl-L-carnitine) is comparable to those obtained by others using UPLC–MRM–MS [12,15]. This allows an accurate quantification of physiological concentrations of TMA, which exists in very low concentrations in plasma, as observed in this study. The quantification using MRM is highly selective and shows less interference from co-eluting compounds, which eliminates the need for complete chromatographic separation, whereas the use of a UPLC–HILIC column results in nearly complete separation of all metabolites in a short run time of 6 min. The use of labeled ISs ensured the precision of the quantification by correcting for variation from sample preparation, as well as instrumental detection [24].

The optimized extraction procedure (pure methanol, 10 min), derivatization (IACN, 10 min), and chromatographic conditions resulted in significant improvements in the quantification, particularly of TMA.

4.2. Method Application

In line with previous studies [25,26], we observed higher TMAO and L-carnitine concentrations in subjects with metabolic syndrome. Previous studies have also found a positive correlation between plasma TMAO and BMI in adults [4] and children [27]. Andraos et al. [28] reported a positive correlation between TMAO precursors and metabolic syndrome in children and adults, but notably not with TMAO itself. The increased levels of L-carnitine and particularly TMAO in subjects with metabolic syndrome were assumed to reflect underlying metabolic disturbances and an altered gut microbiota profile [29]. Further, the high L-carnitine concentrations observed in individuals with metabolic syndrome are well in line with data reported in other studies [26,28]. L-carnitine plays an important role in fatty acid metabolism by facilitating the transport of long-chain fatty acids into the mitochondria for β-oxidation; hence, L-carnitine supplement has been used in weight treatment [30].

There is also research to suggest that a diet high in L-carnitine is linked to increased body fat and negative health effects [26], which may, however, not be observed for L-carnitine supplements [26]. The relationship between the origin of dietary L-carnitine (from food versus supplement), plasma levels, and the condition of metabolic syndrome warrants further investigation.

To summarize, an MRM triple quadrupole mass spectrometry (UPLC–MRM–MS) method suitable for quantifying TMA, TMAO, betaine, choline, and acetyl-, propionyl- and L-carnitine was developed. The method involves a robust and fast extraction and derivatization step and was successfully applied to quantify TMAO and related methylamines in the plasma of both healthy subjects and subjects with metabolic syndrome.

Author Contributions: Conceptualization, M.E.H.; methodology, M.E.H.; validation, M.E.H.; formal analysis, M.E.H.; investigation, M.E.H. and C.M.W.; resources, M.E.H. and C.M.W.; data curation, M.E.H. and C.M.W.; writing—original draft preparation M.E.H.; writing—review and editing, M.E.H. and C.M.W.; visualization, M.E.H. and C.M.W.; project administration, M.E.H. and C.M.W.; funding acquisition, M.E.H. and C.M.W. All authors have read and agreed to the published version of the manuscript.

Funding: This research was funded by Crafoord Foundation: grant number 20180874 for execution of the human study and grant number 20231220 for purchase of UPLC–MSMS equipment.

Institutional Review Board Statement: The study was conducted in accordance with the Declaration of Helsinki, and approved by the Institutional Review Board (or Ethics Committee) of the Swedish Ethical Review Authority (protocol code 2019-04354, approved 30 September 2019).

Informed Consent Statement: Informed consent was obtained from all subjects involved in the study.

Data Availability Statement: The data supporting the study findings are available from the corresponding author upon request.

Acknowledgments: We are most grateful to all subjects for their participation in the study. We would like to thank Annelie Franzén-Eriksson, Amanda Hellström, and Patrik Hellström for their help with blood collection, and Eva Lundin Adolfsson for providing access to the Training Health Clinic in Kalmar.

Conflicts of Interest: The authors declare no conflicts of interest.

Abbreviations

The following abbreviations are used in this manuscript:

ACN	Acetonitrile
IACN	Iodoacetonitrile
IS	Internal Standards
LOD	Limit of Detection
LOQ	Limit of Quantification
R	Recovery
R^2	Coefficient of determination
SD	Standard Deviation
TMA	Trimethylamine
TMAO	Trimethylamine-N-oxide
UPLC–MRM–MS	Ultra Performance Liquid Chromatography–Multiple Reaction Monitoring–Mass Spectrometry

References

1. Wang, Z.; Klipfell, E.; Bennett, B.J.; Koeth, R.; Levison, B.S.; DuGar, B.; Feldstein, A.E.; Britt, E.B.; Fu, X.; Chung, Y.-M.; et al. Gut flora metabolism of phosphatidylcholine promotes cardiovascular disease. *Nature* **2011**, *472*, 57–63. [CrossRef] [PubMed]
2. Qi, J.; You, T.; Li, J.; Pan, T.; Xiang, L.; Han, Y.; Zhu, L. Circulating trimethylamine N-oxide and the risk of cardiovascular diseases: A systematic review and meta-analysis of 11 prospective cohort studies. *J. Cell. Mol. Med.* **2018**, *22*, 185–194. [CrossRef] [PubMed]
3. Heianza, Y.; Ma, W.; Manson, J.E.; Rexrode, K.M.; Qi, L. Gut Microbiota Metabolites and Risk of Major Adverse Cardiovascular Disease Events and Death: A Systematic Review and Meta-Analysis of Prospective Studies. *J. Am. Heart Assoc.* **2017**, *6*, e004947. [CrossRef] [PubMed]
4. Barrea, L.; Annunziata, G.; Muscogiuri, G.; Di Somma, C.; Laudisio, D.; Maisto, M.; De Alteriis, G.; Tenore, G.C.; Colao, A.; Savastano, S. Trimethylamine-N-oxide (TMAO) as Novel Potential Biomarker of Early Predictors of Metabolic Syndrome. *Nutrients* **2018**, *10*, 1971. [CrossRef]
5. Wang, Z.; Tang, W.H.W.; O'Connell, T.; Garcia, E.; Jeyarajah, E.J.; Li, X.S.; Jia, X.; Weeks, T.L.; Hazen, S.L. Circulating trimethylamine N-oxide levels following fish or seafood consumption. *Eur. J. Nutr.* **2022**, *61*, 2357–2364. [CrossRef]
6. Janeiro, M.H.; Ramírez, M.J.; Milagro, F.I.; Martínez, J.A.; Solas, M. Implication of Trimethylamine N-Oxide (TMAO) in Disease: Potential Biomarker or New Therapeutic Target. *Nutrients* **2018**, *10*, 1398. [CrossRef]
7. Evans, M.; Dai, L.; Avesani, C.M.; Kublickiene, K.; Stenvinkel, P. The dietary source of trimethylamine N-oxide and clinical outcomes: An unexpected liaison. *Clin. Kidney J.* **2023**, *16*, 1804–1812. [CrossRef]
8. Craciun, S.; Balskus, E.P. Microbial conversion of choline to trimethylamine requires a glycyl radical enzyme. *Proc. Natl. Acad. Sci. USA* **2012**, *109*, 21307–21312. [CrossRef]

9. Koeth, R.A.; Levison, B.S.; Culley, M.K.; Buffa, J.A.; Wang, Z.; Gregory, J.C.; Org, E.; Wu, Y.; Li, L.; Smith, J.D.; et al. γ-Butyrobetaine Is a Proatherogenic Intermediate in Gut Microbial Metabolism of L-Carnitine to TMAO. *Cell Metab.* **2014**, *20*, 799–812. [CrossRef]
10. Messenger, J.; Clark, S.; Massick, S.; Bechtel, M. A review of trimethylaminuria: (fish odor syndrome). *J. Clin. Aesthet. Dermatol.* **2013**, *6*, 45–48.
11. Yu, W.B.; Xu, C.C.; Li, G.M.; Hong, W.P.; Zhou, Z.Y.; Xiao, C.X.; Zhao, Y.Q.; Cai, Y.F.; Huang, M.; Jin, J. Simultaneous determination of trimethylamine N-oxide, choline, betaine by UPLC-MS/MS in human plasma: An application in acute stroke patients. *J. Pharm. Biomed. Anal.* **2018**, *152*, 179–187. [CrossRef] [PubMed]
12. Zhao, X.Q.; Zeisel, S.H.; Zhang, S.C. Rapid LC-MRM-MS assay for simultaneous quantification of choline, betaine, trimethylamine, trimethylamine N-oxide, and creatinine in human plasma and urine. *Electrophoresis* **2015**, *36*, 2207–2214. [CrossRef] [PubMed]
13. Wang, Z.N.; Levison, B.S.; Hazen, J.E.; Donahue, L.; Li, X.M.; Hazen, S.L. Measurement of trimethylamine-N-oxide by stable isotope dilution liquid chromatography tandem mass spectrometry. *Anal. Biochem.* **2014**, *455*, 35–40. [CrossRef]
14. Hefni, M.E.; Bergstrom, M.; Lennqvist, T.; Fagerstrom, C.; Witthoft, C.M. Simultaneous quantification of trimethylamine N-oxide, trimethylamine, choline, betaine, creatinine, and propionyl-, acetyl-, and L-carnitine in clinical and food samples using HILIC-LC-MS. *Anal. Bioanal. Chem.* **2021**, *413*, 5349–5360. [CrossRef] [PubMed]
15. Xu, C.; Zhang, M.; Zhang, S.; Wang, P.; Lai, C.; Meng, D.; Chen, Z.; Yi, X.; Gao, X. Simultaneous determination of choline, L-carnitine, betaine, trimethylamine, trimethylamine N-oxide, and creatinine in plasma, liver, and feces of hyperlipidemic rats by UHPLC-MS/MS. *J. Chromatogr. B* **2024**, *1243*, 124210. [CrossRef] [PubMed]
16. Korytowska-Przybylska, N.; Michorowska, S.; Wyczałkowska-Tomasik, A.; Pączek, L.; Giebułtowicz, J. Development of a novel method for the simultaneous detection of trimethylamine N-oxide and creatinine in the saliva of patients with chronic kidney disease—Its utility in saliva as an alternative to blood. *J. Pharm. Biomed. Anal.* **2023**, *234*, 115519. [CrossRef]
17. Cho, C.E.; Taesuwan, S.; Malysheva, O.V.; Bender, E.; Tulchinsky, N.F.; Yan, J.; Sutter, J.L.; Caudill, M.A. Trimethylamine-N-oxide (TMAO) response to animal source foods varies among healthy young men and is influenced by their gut microbiota composition: A randomized controlled trial. *Mol. Nutr. Food Res.* **2017**, *61*, 1600324. [CrossRef]
18. Valdivia-Garcia, M.A.; Bi, Y.; Abaakil, K.; V Li, J. Derivatization to reduce background interferences for simultaneous quantitation of trimethylamine (TMA) and trimethylamine-N-oxide (TMAO) using liquid chromatography with tandem mass spectrometry. *J. Pharm. Biomed. Anal.* **2025**, *252*, 116480. [CrossRef]
19. Rochlani, Y.; Pothineni, N.V.; Kovelamudi, S.; Mehta, J.L. Metabolic syndrome: Pathophysiology, management, and modulation by natural compounds. *Ther. Adv. Cardiovasc. Dis.* **2017**, *11*, 215–225. [CrossRef]
20. McEntyre, C.J. Liquid Chromatography—Mass Spectrometry Methods for Investigating Osmolytes and Related One-Carbon Metabolites in Health and Disease. Ph.D. Thesis, University of Canterbury, Christchurch, New Zealand, 2016.
21. European Medicines Agency. *ICH Guideline M10 on Bioanalytical Method Validation and Study Sample Analysis*; European Medicines Agency: Amsterdam, The Netherlands, 2022.
22. Yang, Y.; Cruickshank, C.; Armstrong, M.; Mahaffey, S.; Reisdorph, R.; Reisdorph, N. New sample preparation approach for mass spectrometry-based profiling of plasma results in improved coverage of metabolome. *J. Chromatogr. A* **2013**, *1300*, 217–226. [CrossRef]
23. Lepoittevin, M.; Blancart-Remaury, Q.; Kerforne, T.; Pellerin, L.; Hauet, T.; Thuillier, R. Comparison between 5 extractions methods in either plasma or serum to determine the optimal extraction and matrix combination for human metabolomics. *Cell. Mol. Biol. Lett.* **2023**, *28*, 43. [CrossRef]
24. Wu, J.; Wiegand, R.; LoRusso, P.; Li, J. A stable isotope-labeled internal standard is essential for correcting for the interindividual variability in the recovery of lapatinib from cancer patient plasma in quantitative LC–MS/MS analysis. *J. Chromatogr. B* **2013**, *941*, 100–108. [CrossRef]
25. León-Mimila, P.; Villamil-Ramírez, H.; Li, X.S.; Shih, D.M.; Hui, S.T.; Ocampo-Medina, E.; López-Contreras, B.; Morán-Ramos, S.; Olivares-Arevalo, M.; Grandini-Rosales, P.; et al. Trimethylamine N-oxide levels are associated with NASH in obese subjects with type 2 diabetes. *Diabetes Metab.* **2021**, *47*, 101183. [CrossRef]
26. Gao, X.; Tian, Y.; Randell, E.; Zhou, H.; Sun, G. Unfavorable Associations Between Serum Trimethylamine N-Oxide and L-Carnitine Levels With Components of Metabolic Syndrome in the Newfoundland Population. *Front. Endocrinol.* **2019**, *10*, 168. [CrossRef]
27. Mihuta, M.S.; Paul, C.; Borlea, A.; Roi, C.M.; Pescari, D.; Velea-Barta, O.-A.; Mozos, I.; Stoian, D. Connections between serum Trimethylamine N-Oxide (TMAO), a gut-derived metabolite, and vascular biomarkers evaluating arterial stiffness and subclinical atherosclerosis in children with obesity. *Front. Endocrinol.* **2023**, *14*, 1253584. [CrossRef]
28. Andraos, S.; Jones, B.; Lange, K.; Clifford, S.A.; Thorstensen, E.B.; Kerr, J.A.; Wake, M.; Saffery, R.; Burgner, D.P.; O'Sullivan, J.M. Trimethylamine N-oxide (TMAO) is not Associated with Cardiometabolic Phenotypes and Inflammatory Markers in Children and Adults. *Curr. Dev. Nutr.* **2021**, *5*, nzaa179. [CrossRef]

29. Liu, Y.; Dai, M. Trimethylamine N-Oxide Generated by the Gut Microbiota Is Associated with Vascular Inflammation: New Insights into Atherosclerosis. *Mediat. Inflamm.* **2020**, *2020*, 4634172. [CrossRef]
30. Talenezhad, N.; Mohammadi, M.; Ramezani-Jolfaie, N.; Mozaffari-Khosravi, H.; Salehi-Abargouei, A. Effects of L-carnitine supplementation on weight loss and body composition: A systematic review and meta-analysis of 37 randomized controlled clinical trials with dose-response analysis. *Clin. Nutr. ESPEN* **2020**, *37*, 9–23. [CrossRef]

Disclaimer/Publisher's Note: The statements, opinions and data contained in all publications are solely those of the individual author(s) and contributor(s) and not of MDPI and/or the editor(s). MDPI and/or the editor(s) disclaim responsibility for any injury to people or property resulting from any ideas, methods, instructions or products referred to in the content.

separations

MDPI

Article

HPLC-MS/MS Analysis for Sphingosine 1-Phosphate after the Dephosphorylation by Hydrogen Fluoride

Hee-Jung Kim †, Seo-Hyeon Jung †, Shokhid Gulyamov , Hyun-Gy Lee, Oybek Boyjigitov and Yong-Moon Lee *

College of Pharmacy, Chungbuk National University, Cheongju 28160, Republic of Korea;
rlagmlwnd94@naver.com (H.-J.K.); sherry987@naver.com (S.-H.J.); shohid9395@gmail.com (S.G.);
hglee38@gmail.com (H.-G.L.); oybek.boyjigitov.97@mail.ru (O.B.)
* Correspondence: ymleefn@cbnu.ac.kr; Tel.: +82-1071817139; Fax: +82-43-268-2732
† These authors contributed equally to this work.

Abstract: Sphingosine 1-phosphate (S1P) is a signaling lipid molecule involved in various cellular processes. It is important to develop a quantitative method for S1P to determine endogenous levels and to investigate its functions. As S1P is a tiny lipid component of most biological samples, highly sensitive analysis by LC-MS/MS is required. The main challenge in S1P analysis by chromatography is peak-broadening due to the presence of a polar phosphate and the fact that S1P is indeed a zwitterion itself. In this study, we used hydrogen fluoride (HF) to efficiently remove a phosphate and then analyzed the surrogate, sphingosine, as a sharp peak by LC-ESI-MS/MS. We optimized the dephosphorylation reaction in terms of temperature and reaction time. Multiple reaction monitoring (MRM) for a dephosphorylated form of S1P and C17-S1P as an internal standard at *m/z* transition 300.4 > 282.4 (quantification ion), 300.4 > 262.4 (qualification ion), 286.3 > 268.2 (internal standard) was conducted. This method was validated by essential parameters such as specificity, linearity, range, LOQ, LOD, accuracy, precision, and repeatability. To confirm this new method, we quantified S1P levels in various serum products (100.0~284.4 nM). In the sample pretreatment conditions for extracting S1P, the concern about potential sphingosine contamination in serum was negligible. The dephosphorylation efficiency by this method was about two-fold higher than that of alkaline phosphatase (APase). To apply the method in vivo, we analyzed S1P in plasma and kidney tissues obtained from a chronic kidney disease (CKD) mouse model. S1P levels were increased only in CKD kidney tissue but not in plasma. In conclusion, by applying the dephosphorylation step with HF, we established a new, sensitive LC-MS/MS quantitative method for S1P that can be applied to biological samples.

Keywords: mass spectrometry; sphingosine 1-phosphate; dephosphorylation; hydrogen fluoride; multiple reaction monitoring; serum; chronic kidney disease

1. Introduction

One of the sphingolipid metabolites, sphingosine-1-phosphate (S1P), is endogenously synthesized by two sphingosine kinases (SphK1 and SphK2). Sphk1 is predominantly localized in the cytosol and cell membrane, whereas Sphk2 is mainly present in the nucleus, mitochondria, and endoplasmic reticulum [1].

S1P act intracellularly as a second messenger, regulating calcium release, cell death, and cell proliferation. It can also be translocated extracellularly by transporter and then act as a ligand of S1P receptors (S1PRs). S1PRs, with five subtypes (S1P1-5), are high-affinity G protein-coupled receptors, coupling to G proteins to activate a downstream cascade [2].

S1P is a minor lipid component in most biological samples. To determine the endogenous S1P level and investigate its functions, it is essential to develop a reliable, highly sensitive method for S1P. Recently, liquid chromatography-tandem mass chromatography (LC-MS/MS) with electrospray ionization (ESI) has been widely used for S1P analysis because of its high specificity and sensitivity [3–5].

The main challenges to the development of an S1P quantitative method are peak-broadening due to the presence of a polar phosphate head group, and zwitterion formation in S1P [6]. The negatively charged phosphate in S1P can also interact with the column metal ion, resulting in severe peak-tailing and decreased detectability. To improve this peak-broadening problem, modified methods using a highly acidic mobile phase [7,8] or specific metal-free column have been applied [9]. However, these conventional methods cannot completely solve the problem and require a specially designed column. An alternative breakthrough was the elimination of the phosphate group in S1P, which releases stable sphingosine free from the peak-broadening problem. The use of specific enzyme alkaline phosphatase (APase) of bovine intestine origin for S1P dephosphorylation was successful [10]. However, this APase in animal origin is limited for use by critical problems on the activity changes, expensive and has an infection issue of bovine spongiform encephalopathy (BSE).

The hydrogen fluoride (HF), both in organic and aqueous solution, can selectively cleave phosphorus-oxygen chemical bond. The first report of dephosphorylation reaction on nucleotides and alkyl phosphates by HF was published [11,12]. Similarly, LC-MS/MS analysis after dephosphorylation of phosphoryl peptides showed the efficiency of HF in eliminating a phosphate group [13]. In this regard, we investigated the utility of HF on the dephosphorylation of the sphingolipid S1P.

In this study, we established a new method by using HF to easily remove a phosphate from S1P and overcame the peak-broadening problem by analyzing the surrogate sphingosine by LC-MS/MS. In addition, this method was successfully used to analyze S1P levels in serum and kidney tissues in an animal model of chronic kidney disease (CKD) induced by adenosine.

2. Materials and Methods

2.1. Materials and Reagents

D-erythro-sphingosine-1-phosphate (S1P) and C17-sphingosine-1-phosphate (C17-S1P) were purchased from Avanti Polar Lipids, Inc. (Alabaster, AL, USA). Both were dissolved in methanol for stock solution. Hydrogen fluoride in pyridine (~70% HF) was purchased from Sigma Aldrich (Catalog No. 184225; St. Louis, MO, USA). Serum was purchased from Cytiva (Marlborough, MA, USA). All organic solvents were purchased from Honeywell Burdick & Jackson (Charlotte, NC, USA). Male Wistar rats were provided by Samtako Bio Korea (Osan, Republic of Korea). Animals were maintained under a controlled temperature at 21–22 °C, and optimized humidity conditions with 12/12-h cycles. They were provided with standard chow and access to water. All animal experiments in this study were performed in accordance with the institutional animal care and use committees of Chungbuk National University.

2.2. CKD Animal Model

Rats were divided into 2 groups after 1 week of acclimatization. For CKD group (n = 6), 600 mg/kg body weight adenine in 0.5% CMC was applied by oral gavage for 10 days. On the other hand, 0.5% CMC (2 mL/200 g body weight) was applied to the control group (n = 6). On the 11th day, the rats were sacrificed. Blood samples were collected immediately and transferred to Eppendorf tubes containing anticoagulant. The tubes were centrifuged at 3000 rpm for 3 min and the supernatant was transferred to new tubes. Kidney tissues were obtained by surgery and rinsed with PBS. All kidney tissues were stored at −80 °C until further analysis.

Plasma samples collected from control and CKD group rats were analyzed for creatinine, tryptophan, and kynurenine, which are widely accepted biomarkers for CKD diagnosis. The change in plasma creatinine levels was determined by the Jaffé method using LabAssay^{TM}. Creatinine Kit (Fujifilm Wako Pure Chemical Corporation, Osaka, Japan). An aliquot of 50 μL of plasma proteins were deproteinized with 300 μL of deproteinization reagent. 100 μL of the supernatant was transferred to a 96-well plate and

mixed with 50 µL of picric acid reagent and 50 µL of 0.75 M sodium hydroxide solution. The mixture was kept at an ambient temperature for 20 min before measurement using a microplate reader at a wavelength of 520 nm. For plasma tryptophan and kynurenine, 33 µL of 2M perchloric acid was added to 100 µL of rat plasma. Samples were vortexed vigorously for 1 min and centrifuged at 14,000 rpm for 30 min at 4 °C. The supernatant was transferred to an HPLC vial and 20 µL of the supernatant was injected into the HPLC system. The Agilent Technologies 1100 series LC system with DAD detector was used to detect tryptophan and kynurenine. Compounds were eluted with 92% acetonitrile (ACN) containing 5mM sodium acetate (pH = 7.15) at a flow rate of 1.0 mL/min in a Waters C18 column (250 × 4.6 mm I.D., 5 µm particle size) at 25 °C. Tryptophan and kynurenine were detected at 365 and 267 nm, respectively.

2.3. S1P Extraction

Kidney samples were homogenized by ultra-sonication in RIPA lysis buffer (10 mM Tris-HCl, pH 8.0, 1 mM EDTA, 0.5 mM EGTA, 1% Triton X-100, 0.1% sodium deoxycholate, 0.1% SDS, 140 mM NaCl) containing protease inhibitors. After complete homogenization, the tubes were centrifuged at 14,000 rpm, 4 °C for 10 min. The supernatant was collected for protein assay and S1P extraction. Protein assay was performed according to the instructions of the Thermo protein assay kit (Pierce, IL, USA). Plasma samples were thawed at 37 °C. An aliquot of 100 µL of each sample was placed in an Eppendorf tube, and then 250 µL of methanol containing 0.6 µL of concentrated HCl and 30 pmol of C17-S1P as an internal standard was added. The tube was ultrasonicated in an ice-cold water bath for 5 min. After sonication, 250 µL $CHCl_3$, 250 µL 1 M NaCl and 25 µL 3 N NaOH were added. The tube was vortexed vigorously for 10 min and centrifuged at 14,000 rpm for 5 min. The alkaline aqueous phase containing S1P was transferred to a new tube. The remaining lower layer was re-extracted with 125 µL methanol, 125 µL 1 M NaCl, and 13 µL 3 N NaOH. The combined aqueous fraction of the s1p extract was then mixed with 600 µL $CHCl_3$ and 50 µL 6 N HCl. The tube was vortexed and centrifuged again. The $CHCl_3$ phase was transferred to a new tube and dried with a vacuum concentrator. The entire extraction scheme is described in Figure 1.

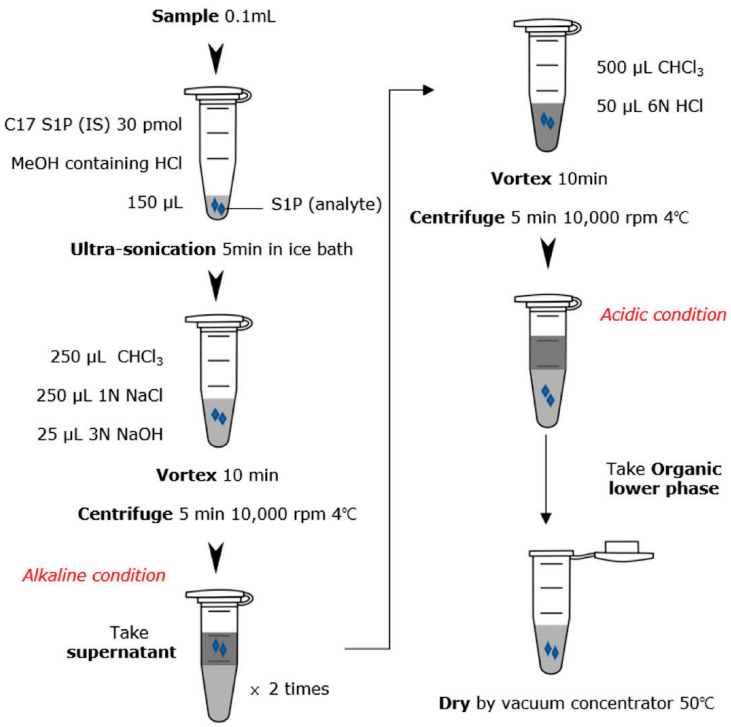


Figure 1. Extraction scheme.

2.4. S1P Dephosphorylation

The dried residue was reconstituted with 80 µL methanol. The tube was vortexed and then sonicated in a water bath for 10 min. Hydrogen fluoride (~70% HF in pyridine) 100 µL was added to each sample and sealed with parafilm in an ice bath. The tube was vortexed and incubated at 25 °C. After 1 h, HF was evaporated under a nitrogen stream. The reaction was quenched by adding 300 µL of 10 N NaOH. This was followed by 300 µL of dichloromethane (DCM) for the organic fraction and the tube was vortexed vigorously. The tube became cloudy due to precipitation of sodium fluoride. The tube was centrifuged at 14,000 rpm for 5 min, and the dephosphorylated S1P in the DCM layer was extracted twice. The combined DCM fraction was washed with alkaline water and evaporated through vacuum concentrators. Methanol was added to the dried residue prior to mass spectrometry injection.

2.5. LC-MS/MS Analysis

To determine S1P levels, liquid chromatography-tandem mass spectrometry (LC-MS/MS) was performed on an AB Sciex QTRAP 3200 mass spectrometer coupled to a Shiseido Nanospace SI-2 HPLC system. Electrospray ionization (ESI) with a positive ion mode was used as the ionization source. According to the manual tuning of direct infusion, the transition from precursor to product ions was found at optimized collision energies. The optimized ESI parameters are listed in Table 1. The analytes were separated on an Inertsil ODS-3 column (100 × 3.0 mm, 3 µm) maintained at 40 °C. The mobile phase consisted of (A) 0.1% formic acid in water containing 10 mM ammonium acetate, (B) 0.1% formic acid in acetonitrile:2-propanol (4:3, *v*/*v*). A gradient elution condition at a flow rate of 0.3 mL/min was as follows: 0–1 min, 30% B; 1–3 min, 95% B; 3–7 min, 100% B; 7–9 min, hold 100% B; 9–10 min. 30% B, 10–14 min, hold 30% B for re-equilibration. The injection volume was 20 µL.

Table 1. (A). HPLC separation condition. (B). MS/MS detection condition.

(A) Liquid Chromatography Conditions				
Column	Inertsil ODS-3 100 × 3.0 mm, 3 µm			
Column Temp	40 °C			
Mobile phase A	0.1% Formic acid and 10 mM CH_3COONH_4 in water			
Mobile phase B	0.1% Formic acid + 10 mM CH_3COONH_4 in Acetonitrile: 2-PrPanol (4:3, *v*/*v*)			
Injection volume	20 µL			
flow rate	0.3 mL/min			
Gradient condition	time (min)	A (vol %)	B (vol %)	
	0.0~1.0	70	30	
	1.0~3.0	70→5	30→95	
	3.0~7.0	5→0	95→100	
	7.0~9.0	0	100	
	9.0~10.0	0→70	100→30	
	10.0~14.0	70	30	
	14.01	Controller stop		
(B) Mass Spectrometer Condition				
Ionization mode	ESI (+) MRM			
Ion Source Gas 1	40			
Temperature	300			
Ion Source Gas 2	50			
Ion Spray Voltage	5500			
Curtain Gas (CUR)	20			
Collision Gas (CAD)	5			
Component	MRM condition			
	m/*z*	DP (V)	CE (eV)	CXP (eV)
S1P	300.4 > 282.4 (quantifier)	40	15	5
	300.4 > 264.4 (qualifier)	40	28	4
C17 S1P	286.3 > 268.2	80	20	5

2.6. Method Validation

The method was validated for specificity, linearity, precision, accuracy, reproducibility, limit of quantitation (LOQ), limit of detection (LOD) in line with the ICH Q2(R1) guidelines. A standard solution diluted with stock solution by methanol was used to determine specificity, linearity, LOQ, LOD. Specificity was evaluated by the presence of interference at the same retention time of the analyte. The correlation coefficient (R^2) value of the calibration curve with a standard solution for 3 different days was used to determine linearity. The signal-to-noise ratio (S/N ratio) was calculated to confirm LOQ and LOD. For LOQ, an S/N ratio of 10 was accepted and for LOD, an S/N ratio of 3. 2% BSA solution spiked with S1P and C17-S1P was used as the precision, accuracy, and reproducibility samples. Precision and accuracy were evaluated by relative standard deviation (RSD, %) and recovery (%) at 3 different concentrations with 3 individuals. A low concentration spiked sample was injected 6 times and the RSD % was calculated for reproducibility.

3. Results

3.1. S1P Extraction

A two-step extraction procedure was used to determine S1P levels in biological samples. The extraction procedure was modified according to the previous report [14]. In a mixture of aqueous alkaline solution, methanol, and chloroform, S1P with polarity exists in the upper aqueous layer after centrifugation, while sphingosine and other major lipid components move to the organic solvent layer. After transfer of the aqueous phase, an acidic aqueous solution was added to decrease the polarity of the phosphate group of S1P. Under acidic conditions, S1P was followed in the lower chloroform phase and then injected into LC-MS/MS. Because the mass transitions of HF-derived dephosphorylated S1P are the same as those of sphingosine, it is important to separate S1P and sphingosine in the first extraction step. Without separation, S1P levels could be overestimated due to the sphingosine background. To confirm sphingosine contamination, fetal bovine serum (FBS), kidney tissue extracts with, and without, HF treatment were prepared. The S1P peak area of each group was compared in the same injection batch (n = 3). The results are summarized in Table 2. It was confirmed that the background was very low compared to the S1P peak area contained in the biological sample.

Table 2. Contaminated sphingosine levels during the S1P analysis in biological samples.

Sample (n = 3)	Peak Area		Relative Amount (%)
	Without HF	With HF	
FBS	657	27,774	2.4
Kidney tissue	341	7257	4.5

3.2. Optimization for S1P Dephosphorylation

The reaction condition of hydrogen fluoride (HF) dephosphorylation was optimized by considering the reaction temperature and time. The HF was treated with S1P standard solution dissolved in methanol, and then tubes were kept overnight at 4 °C, 25 °C, 40 °C to determine the optimal temperature. After being kept overnight, the HF was evaporated, and the remaining solution was prepared for mass spectrometry as described above. As shown in Figure 2A, reaction at 25 °C was optimal to eliminate the phosphate group at S1P. The optimal reaction time for dephosphorylation was examined by varying the reaction time of the S1P standard solution with HF at 25 °C. The dephosphorylation yield increased and then became stable after 60 min, as shown in Figure 2B. Thus, a 60 min incubation time was sufficient for the reaction with S1P and hydrogen fluoride.

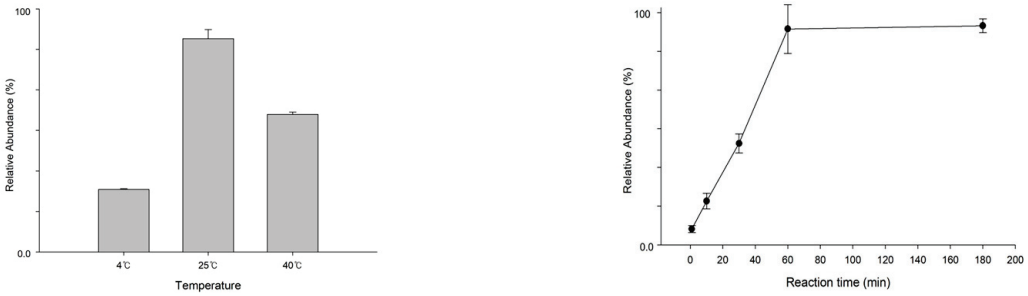


Figure 2. Optimization for S1P dephosphorylation: (**A**) reaction temperature; and (**B**) reaction time at 25 °C.

3.3. S1P Analysis by LC-MS/MS

To confirm the MRM transition, S1P and C17-S1P (IS) standard solutions were injected directly into the mass spectrometer after dephosphorylation. Both compounds predominantly generated $[M + H]^+$ form at m/z 300.4 (S1P) and m/z 286.3 (C17-S1P) as precursor ions in the positive ion mode. The precursor ions then produced fragment ions in the collision energy product ion scan mode. The product ion mass spectra obtained by selecting these precursor ions are shown in Figure 3. For S1P, m/z 282.4 was the abundant product ion corresponding to $[M + H\text{-}H_2O]^+$, the minor fragment ion m/z 264.4 corresponding to $[M + H\text{-}2H_2O]^+$. C17-S1P, which was used as an internal standard in our study, had the same pattern, thus m/z 268.2 was obtained for the major product ion. This result showed that HF selectively eliminated the phosphate group from S1P, since the fragmentation pattern was consistent with that of sphingosine. Therefore, MRM transitions of m/z 300.4 → 282.4 were selected for S1P quantification, m/z 300.4 → 264.4 for S1P qualification, and m/z 286.3 → 268.2 for C17-S1P (IS).

For high ionization yield, 10 mM ammonium acetate and 0.1% formic acid were added. The addition of formic acid also has the advantage of peak separation. For high resolution, isopropanol was used in combination with acetonitrile. With optimized gradient conditions, the retention time of S1P in our chromatography system was 5.99 min (Figure 4A) and C17-S1P was 5.74 min (Figure 4B).

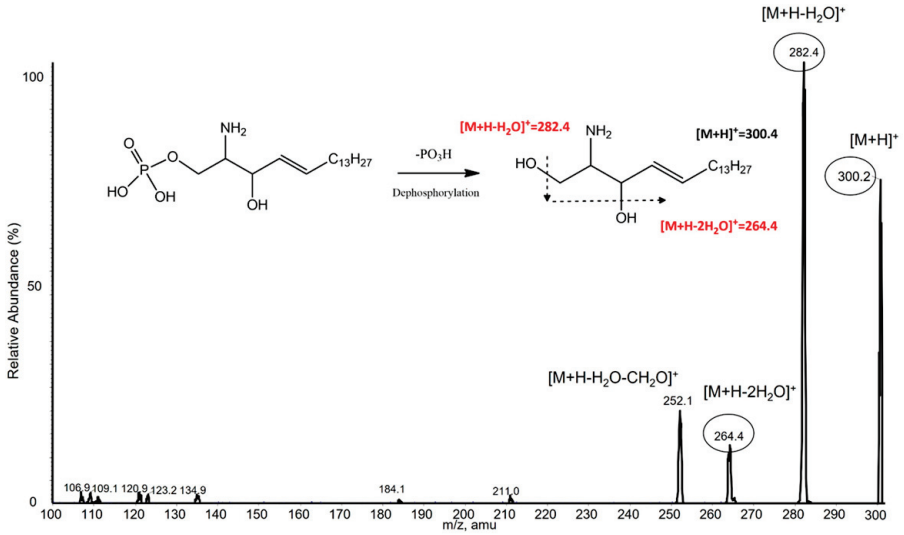


Figure 3. MS fragmentation pattern of S1P.

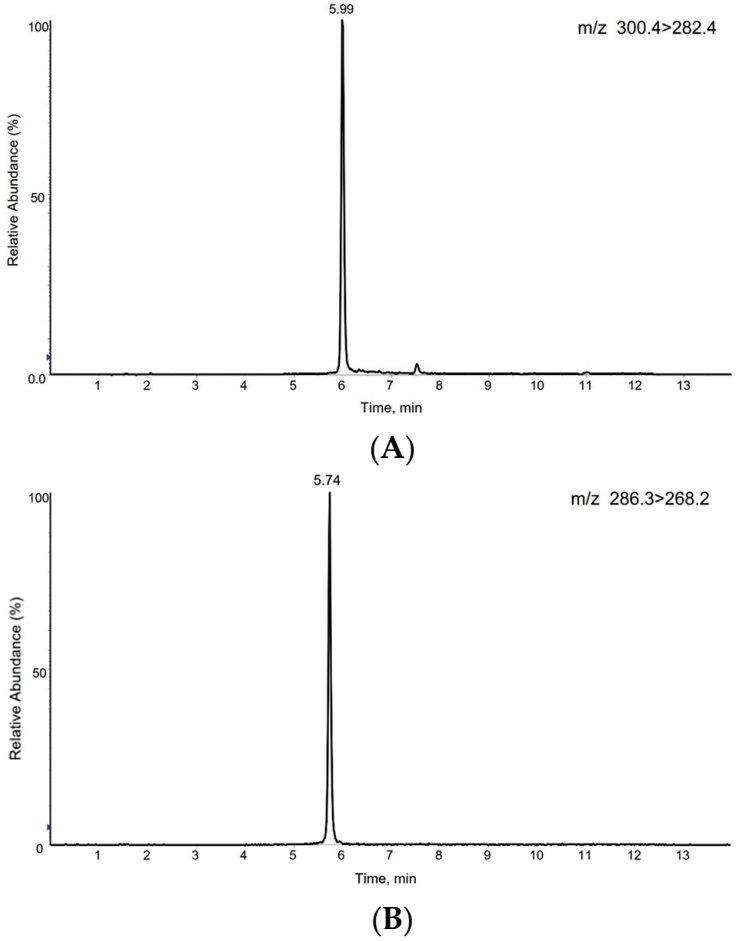


Figure 4. Typical LC-MS/MS elution profile of S1P (**A**); and C17-S1P (**B**).

3.4. Method Validation

The peak of the analyte and internal standard were well separated and had no interference, as shown in Figure 4. A calibration curve was drawn by peak ratio using C17-S1P as an internal standard and had good linearity with standard samples, as described in the material and methods. The calibration equation was y = 0.0074x + 0.0516 (n = 3) and the correlation coefficient (R^2) value was 0.9996 (n = 3) in a range of 10~1000 nM (pmol/mL). Linearity data are shown in Table 3. The limit of quantification was 10 nM (signal-to-noise ratio > 10), and the limit of detection (signal-to-noise ratio > 3) was 5 nM. The relative standard deviation (RSD) in three different concentrations for precision ranged from 0.0~2.7%. For accuracy, the recovery rate was 98.5~106.0% at 30, 250, 800 nM (pmol/mL) spiking samples with three individuals. The RSD at 30 nM spiking sample with six replicates for reproducibility was 4.7%. Detailed results are summarized in Table 4.

Table 3. Standard curve for S1P analysis.

No.	Slope	Intercept	R^2
1	0.0075	0.0760	0.9996
2	0.0074	0.0161	0.9997
3	0.0073	0.0626	0.9987
Average	0.0074	0.0516	0.9996
S.D.	0.0001	0.0314	0.0006

Table 4. Precision, Accuracy and Reproducibility.

	Nominal Concentration (pmol/mL)	Mean (pmol/mL)	S.D. (pmol/mL)	Precision (RSD, %)	Accuracy (Recovery, %)
Precision & Accuracy (n = 3)	30	29.8	0.5	0.0	99.5
	250	246.2	2.7	2.7	98.5
	800	848.1	46.7	0.1	106.0
Reproducibility (n = 6)	30	31.4	1.5	4.7	104.5

3.5. S1P Levels in CKD Animal Model

To apply our method to biological samples, we first determined S1P in commercial serum, fetal bovine serum (FBS), fetal calf serum (FCS), and horse serum. The S1P level in FBS was determined to be 100.0 ± 5.3 pmol/mL, FCS 106.5 ± 4.5 pmol/mL, and horse serum 284.4 ± 11.3 pmol/mL (mean ± SD) (Figure 5).

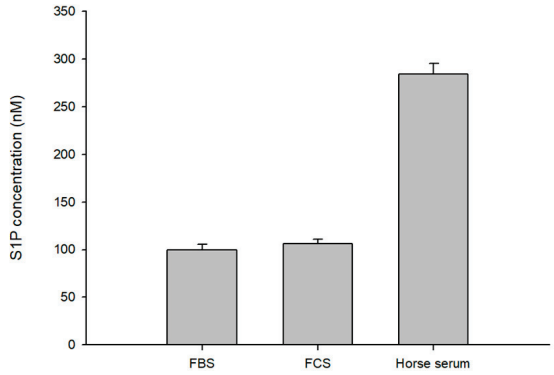


Figure 5. Measured S1P levels in serum products.

Second, we analyzed endogenous S1P in the CKD rat model (Figure 6). To confirm that the CKD rat model treated with adenine for 10 days successfully induced CKD, we examined several biomarkers representing renal functions (Table 5). Plasma creatinine was increased from 0.3 dm/mL to 1.4 dm/mL in the CKD group, expressing the deterioration of glomerular filtration. The kynurenine level was doubled in the plasma of CKD rats, while tryptophan was reduced by 1.7-fold. The body mass of CKD rats remained unchanged, while control group rats gained about 50 g during the experiment. Conversely, the kidneys of CKD rats were enlarged and weighed almost 2.8 times more than those of the controls.

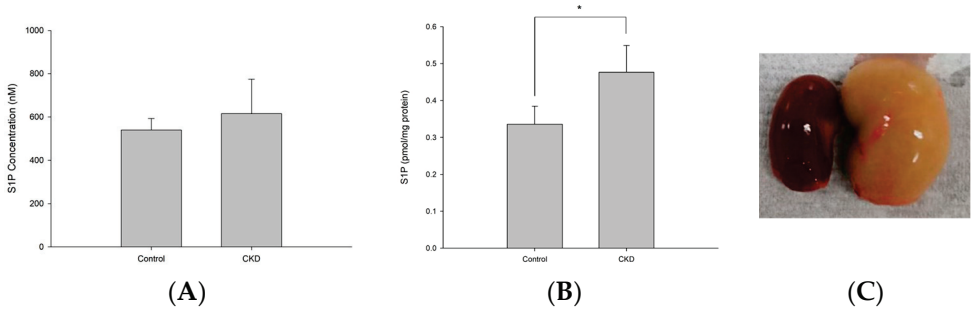


Figure 6. Measured S1P levels in plasma (**A**); and kidney tissue (**B**) (* $p < 0.05$) in CKD animals. (**C**) Morphological changes in the kidney: Control (left); CKD (right).

Table 5. Changes in typical CKD biomarkers.

CKD Biomarkers	Control Group (n = 6)	CKD Group (n = 6)
Creatinine (mg/dL)	0.31 ± 0.03	1.38 ± 0.55
Kynurenine (μg/mL)	0.60 ± 0.18	1.01 ± 0.55
Tryptophan (μg/mL)	12.25 ± 1.42	7.39 ± 1.01

As shown in Figure 6, the plasma S1P level of the control group was 540.3 ± 53.1 pmol/mL, and that of the CKD group was 615.0 ± 159.2 pmol/mL. Figure 6A showed slightly increased but not significant (p value > 0.05) levels. As shown in Figure 6B, a significant increase in the S1P level in kidney tissue was observed in the CKD group (p value < 0.05). The S1P concentrations in the control and CKD group showed 0.336 ± 0.05 and 0.477 ± 0.07 pmol/mg protein (mean ± SD), respectively. The reported plasma concentration is about 100~700 pmol/mL and the tissue concentration are about 1~10 pmol/mL [15], which correlate with the results of our study.

4. Discussion

In this study, we developed a new method for the quantification of S1P by LC-MS/MS. The method described here has high sensitivity with the use of an HF dephosphorylation process. The dephosphorylation mechanism in S1P involves the removal of the phosphate group through a hydration reaction by the addition of HF and regeneration of the hydroxyl group in the sphingoid backbone. The specific affinity of the fluoride anion to the oxygen–phosphorus bond is a very important factor in effecting this cleavage [13]. In addition, the analysis can be performed on the general C18 column, which is the most popular and widely used reverse-phase column, without any peak-tailing problem. Using C17-S1P as the internal standard, we can obtain reproducible S1P quantification results. When internal standard substances with very different structures are used in biological sample analysis, errors in quantification may be severe, due to differences in ionization rates. To minimize these concerns, C17-S1P, which is structurally similar to S1P, was used, and the quantitative value of S1P among biological samples analyzed by this method was found to be not significantly different to conventional method results. Therefore, C17-S1P is often used as an internal standard in papers quantifying S1P with LC-MS/MS. There was no problem with the quantification of S1P in plasma, cultured cells, and kidney tissue analyzed within a limited biological sample. Method validation was performed on several parameters and showed good specificity, linearity, precision, and accuracy. The LOD of this method was 5 pmol/mL, with which it was possible to detect low levels of endogenous S1P in tissues similar to other recently reported methods.

In this study, we compared the dephosphorylation reaction efficiency of HF and APase with an S1P standard solution and a C17 sphingosine standard solution as the internal standard (Figure 7). The dephosphorylation ability of HF exhibited clearly better efficiency than APase. HF is easier to obtain in the laboratory and the cost is much lower than APase.

HF was an effective reagent for the analysis of S1P by dephosphorylation, but careful handling was required. In addition, HF produces corrosive fumes that can easily penetrate the skin and cause severe burns [16]. Researchers should use appropriate safety equipment and always work in a fume hood. HF can dissolve glass containers; thus for transfer, the use of tightly sealed plastic bottles or tubes is required [17].

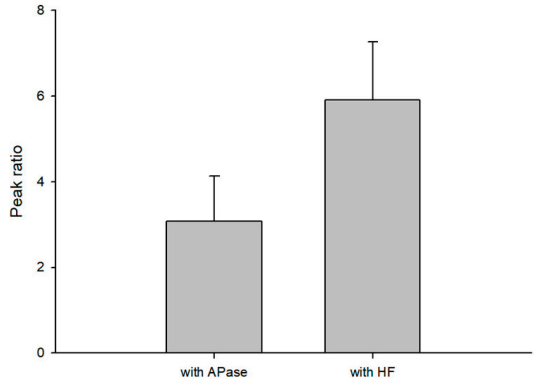


Figure 7. Dephosphorylation reaction efficiency of HF.

We analyzed serum S1P levels in three different sera. As shown in Figure 5, fetal bovine serum and fetal calf serum have similar concentrations. However, horse serum has a higher level of S1P. We thought this was due to the difference in erythrocyte levels between different species. The reference interval of bovine erythrocytes is 4.9–7.5 $\times$ 10^6/μL [18] and that of horse erythrocytes is 6.10–11.0 $\times$ 10^6/μL [19]. Since S1P is highly abundant in mature erythrocytes with high activity of Sphk1, higher levels of erythrocyte species seem to produce higher levels of S1P in serum [20,21].

The role of S1P in CKD has not been fully established, although the protective role of S1P has been suggested in renal fibrosis, which is a clinical manifestation of CKD [22]. Several studies have reported upregulation of renal Sphk1 in various kidney disease models [23,24]. In addition, S1P2 is highly expressed in renal ischemia and reperfusion injury, which may lead to renal fibrosis [25,26]. According to our experimental results, kidney tissues of CKD group showed increased S1P levels, while there was no significant increase in plasma. During the progression of CKD, inflammatory cytokines, including transforming growth factor-β (TGF-β), are secreted, which cause renal fibrosis. Since TGF-β is known to stimulate Sphk1, we can correlate elevated S1P levels with CKD kidney tissue [27]. Further research will be necessary to elucidate plasma S1P levels in CKD models, as well as to determine the S1P function and therapeutic target in CKD.

5. Conclusions

In conclusion, we established a new S1P analysis method with HF dephosphorylation by LC-MS/MS, which was highly sensitive and effective in quantifying an S1P level with comparable sensitivity levels [15]. Since S1P is zwitterion, this method solved the problem of S1P peak-broadening when analyzing directly by conventional methods. The pretreatment method using HF was very simple, and a one-hour reaction at room temperature was sufficient for quantitative dephosphorylation of S1P. With this new method, we compared S1P level in the plasma and kidney tissue of a chronic kidney disease model. The method can also be used in various biological samples and determine the therapeutic role of S1P in various diseases, including CKD.

Author Contributions: Conceptualization, Y.-M.L.; methodology, S.G., H.-J.K. and S.-H.J.; validation, H.-J.K.; formal analysis, H.-J.K., S.G. and H.-G.L.; investigation, H.-G.L.; data curation, H.-J.K., S.-H.J. and O.B.; writing—original draft preparation, H.-J.K., S.-H.J. and Y.-M.L.; writing—review and editing, O.B. and Y.-M.L. All authors have read and agreed to the published version of the manuscript.

Funding: This work was supported by a funding for the academic research program of Chungbuk National University in 2022.

Institutional Review Board Statement: The animal study was approved by the Institutional Animal Care and Use Committees of Chungbuk National University (protocol code CBNU-2165-23-02 and date of approval is on 31 July 2023).

Data Availability Statement: The data presented in this study are available within the article.

Conflicts of Interest: The authors declare no conflict of interest.

References

1. Nguyen, T.Q.; Vu, T.M.; Tukijan, F.; Muralidharan, S.; Foo, J.C.; Li Chin, J.F.; Hasan, Z.; Torta, F.; Nguyen, L.N. Erythrocytes efficiently utilize exogenous sphingosines for S1P synthesis and export via Mfsd2b. *J. Biol. Chem.* **2021**, *296*, 100201. [CrossRef] [PubMed]
2. Constantinescu, V.; Haase, R.; Akgun, K.; Ziemssen, T. S1P receptor modulators and the cardiovascular autonomic nervous system in multiple sclerosis: A narrative review. *Ther. Adv. Neurol. Disord.* **2022**, *15*, 17562864221133163. [CrossRef]
3. Luth, A.; Neuber, C.; Kleuser, B. Novel methods for the quantification of (2E)-hexadecenal by liquid chromatography with detection by either ESI QTOF tandem mass spectrometry or fluorescence measurement. *Anal. Chim. Acta* **2012**, *722*, 70–79. [CrossRef] [PubMed]
4. Bielawski, J.; Pierce, J.S.; Snider, J.; Rembiesa, B.; Szulc, Z.M.; Bielawska, A. Sphingolipid analysis by high performance liquid chromatography-tandem mass spectrometry (HPLC-MS/MS). *Adv. Exp. Med. Biol.* **2010**, *688*, 46–59. [CrossRef] [PubMed]
5. Oizumi, H.; Sugimura, Y.; Totsune, T.; Kawasaki, I.; Ohshiro, S.; Baba, T.; Kimpara, T.; Sakuma, H.; Hasegawa, T.; Kawahata, I.; et al. Plasma sphingolipid abnormalities in neurodegenerative diseases. *PLoS ONE* **2022**, *17*, e0279315. [CrossRef]
6. Demont, E.H.; Arpino, S.; Bit, R.A.; Campbell, C.A.; Deeks, N.; Desai, S.; Dowell, S.J.; Gaskin, P.; Gray, J.R.; Harrison, L.A.; et al. Discovery of a brain-penetrant S1P(3)-sparing direct agonist of the S1P(1) and S1P(5) receptors efficacious at low oral dose. *J. Med. Chem.* **2011**, *54*, 6724–6733. [CrossRef]
7. Saigusa, D.; Shiba, K.; Inoue, A.; Hama, K.; Okutani, M.; Iida, N.; Saito, M.; Suzuki, K.; Kaneko, T.; Suzuki, N.; et al. Simultaneous quantitation of sphingoid bases and their phosphates in biological samples by liquid chromatography/electrospray ionization tandem mass spectrometry. *Anal. Bioanal. Chem.* **2012**, *403*, 1897–1905. [CrossRef]
8. Frej, C.; Andersson, A.; Larsson, B.; Guo, L.J.; Norstrom, E.; Happonen, K.E.; Dahlback, B. Quantification of sphingosine 1-phosphate by validated LC-MS/MS method revealing strong correlation with apolipoprotein M in plasma but not in serum due to platelet activation during blood coagulation. *Anal. Bioanal. Chem.* **2015**, *407*, 8533–8542. [CrossRef]
9. Gowda, S.G.B.; Nakahashi, A.; Yamane, K.; Nakahashi, S.; Murai, Y.; Siddegowda, A.K.C.; Hammam, M.A.S.; Monde, K. Facile Chemoselective Strategy toward Capturing Sphingoid Bases by a Unique Glutaraldehyde-Functionalized Resin. *ACS Omega* **2018**, *3*, 753–759. [CrossRef]
10. Min, J.K.; Yoo, H.S.; Lee, E.Y.; Lee, W.J.; Lee, Y.M. Simultaneous quantitative analysis of sphingoid base 1-phosphates in biological samples by o-phthalaldehyde precolumn derivatization after dephosphorylation with alkaline phosphatase. *Anal. Biochem.* **2002**, *303*, 167–175. [CrossRef]
11. Lenard, J. Reactions of proteins, carbohydrates, and related substances in liquid hydrogen fluoride. *Chem. Rev.* **1969**, *69*, 625–638. [CrossRef] [PubMed]
12. Adler, M.; Bobrow, E. Hydrolysis of purine and pyrimidine ribosides and 2-deoxyribosides with liquid hydrogen fluoride. *Mt. Sinai J. Med.* **1970**, *37*, 206–212. [PubMed]
13. Kuyama, H.; Toda, C.; Watanabe, M.; Tanaka, K.; Nishimura, O. An efficient chemical method for dephosphorylation of phosphopeptides. *Rapid Commun. Mass. Spectrom.* **2003**, *17*, 1493–1496. [CrossRef]
14. Ruwisch, L.; Schafer-Korting, M.; Kleuser, B. An improved high-performance liquid chromatographic method for the determination of sphingosine-1-phosphate in complex biological materials. *Naunyn-Schmiedeberg's Arch. Pharmacol.* **2001**, *363*, 358–363. [CrossRef] [PubMed]
15. Berdyshev, E.V.; Gorshkova, I.A.; Garcia, J.G.; Natarajan, V.; Hubbard, W.C. Quantitative analysis of sphingoid base-1-phosphates as bisacetylated derivatives by liquid chromatography-tandem mass spectrometry. *Anal. Biochem.* **2005**, *339*, 129–136. [CrossRef]
16. Schwerin, D.L.; Hatcher, J.D. Hydrofluoric Acid Burns. In *StatPearls*; StatPearls Publishing LLC.: Treasure Island, FL, USA, 2023.
17. Ghoreishi, S.M.; Beiggy, M.; Mazloum Ardekani, M. Optimization of gas chromatography using short glass capillary column with mass spectrometry for identification and evaluation of commercial heavy alkylbenzene structures. *Anal. Bioanal. Chem.* **2003**, *375*, 1212–1220. [CrossRef]
18. Roland, L.; Drillich, M.; Iwersen, M. Hematology as a diagnostic tool in bovine medicine. *J. Vet. Diagn. Investig.* **2014**, *26*, 592–598. [CrossRef]
19. Mauricio, C.R.; Schneider, F.K.; Dos Santos, L.C. Image-based red cell counting for wild animals blood. *Annu. Int. Conf. IEEE Eng. Med. Biol. Soc.* **2010**, *2010*, 438–441. [CrossRef]
20. Hanel, P.; Andreani, P.; Graler, M.H. Erythrocytes store and release sphingosine 1-phosphate in blood. *FASEB J.* **2007**, *21*, 1202–1209. [CrossRef]
21. Selim, S.; Sunkara, M.; Salous, A.K.; Leung, S.W.; Berdyshev, E.V.; Bailey, A.; Campbell, C.L.; Charnigo, R.; Morris, A.J.; Smyth, S.S. Plasma levels of sphingosine 1-phosphate are strongly correlated with haematocrit, but variably restored by red blood cell transfusions. *Clin. Sci.* **2011**, *121*, 565–572. [CrossRef]
22. Du, C.; Ren, Y.; Yao, F.; Duan, J.; Zhao, H.; Du, Y.; Xiao, X.; Duan, H.; Shi, Y. Sphingosine kinase 1 protects renal tubular epithelial cells from renal fibrosis via induction of autophagy. *Int. J. Biochem. Cell Biol.* **2017**, *90*, 17–28. [CrossRef]
23. Lee, S.Y.; Kim, D.H.; Sung, S.A.; Kim, M.G.; Cho, W.Y.; Kim, H.K.; Jo, S.K. Sphingosine-1-phosphate reduces hepatic ischaemia/reperfusion-induced acute kidney injury through attenuation of endothelial injury in mice. *Nephrology* **2011**, *16*, 163–173. [CrossRef] [PubMed]

24. Koch, A.; Pfeilschifter, J.; Huwiler, A. Sphingosine 1-phosphate in renal diseases. *Cell Physiol. Biochem.* **2013**, *31*, 745–760. [CrossRef] [PubMed]
25. Romero, D.J.; Pescio, L.G.; Santacreu, B.J.; Mosca, J.M.; Sterin-Speziale, N.B.; Favale, N.O. Sphingosine-1-phosphate receptor 2 plays a dual role depending on the stage of cell differentiation in renal epithelial cells. *Life Sci.* **2023**, *316*, 121404. [CrossRef] [PubMed]
26. Matsuyama, M.; Funao, K.; Kuratsukuri, K.; Tanaka, T.; Kawahito, Y.; Sano, H.; Chargui, J.; Touraine, J.L.; Yoshimura, N.; Yoshimura, R. Expression of sphingosine-1 phosphate receptor in rat renal ischemia-reperfusion injury. *Mol. Med. Rep.* **2010**, *3*, 233–236.
27. Wang, T.N.; Chen, X.; Li, R.; Gao, B.; Mohammed-Ali, Z.; Lu, C.; Yum, V.; Dickhout, J.G.; Krepinsky, J.C. SREBP-1 Mediates Angiotensin II-Induced TGF-beta1 Upregulation and Glomerular Fibrosis. *J. Am. Soc. Nephrol.* **2015**, *26*, 1839–1854. [CrossRef]

Disclaimer/Publisher's Note: The statements, opinions and data contained in all publications are solely those of the individual author(s) and contributor(s) and not of MDPI and/or the editor(s). MDPI and/or the editor(s) disclaim responsibility for any injury to people or property resulting from any ideas, methods, instructions or products referred to in the content.

Journal of
Clinical Medicine

MDPI

Article

Comparative Analysis of Serum Amino Acid Profiles in Patients with Myasthenia Gravis and Multiple Sclerosis

Piotr Kośliński [1,*], Łukasz Rzepiński [2,3], Marcin Koba [1], Zdzisław Maciejek [2,3], Mariusz Kowalewski [4] and Emilia Daghir-Wojtkowiak [5]

[1] Department of Toxicology and Bromatology, Collegium Medicum in Bydgoszcz, Nicolaus Copernicus University in Toruń, Dr. A. Jurasza 2, 85-089 Bydgoszcz, Poland; kobamar@cm.umk.pl
[2] Department of Neurology, 10th Military Research Hospital and Polyclinic, Powstańców Warszawy 5, 85-681 Bydgoszcz, Poland; luk.rzepinski@gmail.com (Ł.R.); z.maciejek@wp.pl (Z.M.)
[3] Sanitas—Neurology Outpatient Clinic, 85-010 Bydgoszcz, Poland
[4] Multiple Sclerosis Foundation, 78-449 Borne Sulinowo, Poland
[5] International Centre for Cancer Vaccine Science, University of Gdansk, 80-309 Gdansk, Poland; emilia.daghir-wojtkowiak@ug.edu.pl
* Correspondence: piotr.koslinski@cm.umk.pl

Abstract: Background: Multiple sclerosis (MS) and myasthenia gravis (MG) are autoimmune diseases that attack the central nervous system (CNS) and the neuromuscular junction, respectively. As the common pathogenesis of both diseases is associated with an autoimmune background and the involvement of T and B lymphocytes, the overlapping of selected clinical symptoms may cause difficulties in the differential diagnosis of both diseases. **Methods**: The aim of the study was to use Liquid Chromatography–Electrospray Ionization–Mass Spectrometry (LC–ESI–MS/MS) in conjunction with multivariate statistical analyses to examine the changes in amino acid metabolic profiles between patients with MG, MS, and a control group. **Results**: Comparative analysis of amino acids (AA) between patients with MG, MS, and within the control group allowed for the identification of statistically significant differences in the amino acid profile. Comparing the patients (patients with MS and MG) with the control group, and after taking the results of multiple tests into account, it was observed that amino acids such as ARG, PRO, TRP, CIT were significantly different between the groups. When considering the comparison between the AA concentrations in MS and MG patients, we found three AAs that were significantly different in the MS and MG groups, after correcting for multiple testing (CIT, GABA, and AAA). Higher concentrations of amino acids that showed significant differences were observed in patients with myasthenia gravis. **Conclusions**: Our results have indicated AAs that may prove valuable for improving the diagnostics of MS and MG patients. To better assess the potential utility of these markers, their performance requires further validation in a larger study group and limitation of possible confounding factors, e.g., medications and diet.

Keywords: myasthenia gravis; multiple sclerosis; amino acids; biomarkers

1. Introduction

Neurological diseases that are based on immunological mechanisms have been studied for years, and many aspects still remain unclear [1]. Autoimmune mechanisms are associated with both myasthenia gravis (MG) and multiple sclerosis (MS). These diseases are characterized by inflammation and immune deregulation. In the case of MG, antibodies are formed against proteins at the postsynaptic neuromuscular junctions (NMJ), which leads to a unique set of clinical symptoms such as variable muscle fatigue and respiratory complications [2]. In MS, the dysfunction of regulatory T cells (Tregs) ultimately leads to an unregulated T cell response against the myelin structures of the central nervous system (CNS) [3]. MG and MS have been found to affect women more than men in terms of prevalence and incidence. The female to male ratio in patients with MG and MS has

been described as approximately 2:1 and 3:1, respectively, but varies depending on age and/or type of disease [4,5]. Although the mechanisms underlying impaired self-tolerance in these and other autoimmune diseases have not been fully elucidated, one possibility is numerical, functional, and/or migratory deficits in T regulatory (Treg) cells. Dysregulation of suppressive and migratory markers on Tregs has been linked to the pathogenesis of both MS and MG. It seems that the discovery of a common pathway in the pathogenesis of related autoimmune diseases may guide future methods of their diagnosis and therapy [6].

The application of metabolomics towards understanding the manifestation and progression of complex neurological diseases represents a powerful means to identify the earliest markers associated with disease progression and treatment response [7]. Results of the previous studies focusing on non-targeted and targeted metabolic analysis in MG and MS patients have allowed us to confirm the differences in metabolic profiles between the study and control group. The results obtained by Lu et al. using untargeted serum metabolic analysis allowed for the separation of healthy people from MG patients based on their metabolic profiles [8]. The use of a double control group (a group of healthy people and patients with rheumatoid arthritis) made it possible to distinguish seropositive patients with MG from the reference autoimmune disease, i.e., rheumatoid arthritis, based on metabolic profiles [9]. Rispoli et al., in their review, offered evidence in support of the potential of metabolomics as a biomarker and drug discovery tool in MS [10].

The interest in amino acids (AA) in MS and MG has resulted from their role in the autoimmune process. AAs are important in the functioning of T lymphocytes, and their disturbed metabolism may be associated with the process of autoimmunity [11–13]. AA metabolic profiling has many applications including screening, diagnosis, and treatment monitoring. Scientific research is still being developed to assess the possible use of AAs in the diagnosis and monitoring of therapy in neurodegenerative diseases [14], Alzheimer's disease [15], Parkinson's disease [16], autoimmune diseases [17], and cancer [18]. The available literature data indicate that the observed abnormalities in AA metabolic pathways may be related to various clinical aspects (i.e., etiology, pathogenesis, diagnosis, prognosis and treatment) of both multiple sclerosis [19–21] and myasthenia gravis [9,22].

Our previous research analyzed the profile of AAs in the serum of MS patients and of MG patients, as well as compared them with the control group, taking into account the differences depending on the disease outcomes. The study revealed different patterns of serum AA profiles between the patients and control group, as well as between the patient groups with various disease types [20,22,23].

It is believed that it is very important to include, in the metabolomic analysis, both a comparative analysis of a group of patients with a control group of healthy people, as well as a comparison of the metabolic profiles of patients from the same group of diseases, e.g., autoimmune diseases. This allows for the detection of more specific changes that may accompany specific diseases such as MG or MS. According to the available knowledge, there are no studies allowing for a direct comparison of the AA profile in patients with MG and MS. Therefore, the aim of the presented work is to use HPLC with mass spectrometry detection, combined with multivariate statistical analyses, to compare AA metabolic profiles in patients with MS and MG in order to identify specific changes.

2. Materials and Methods

2.1. Subjects and Serum Samples

Patients were recruited from the Neurology Outpatient Clinic at Sanitas (Bydgoszcz, Poland) and the MS Rehabilitation Centre (Borne Sulinowo, Poland). The study population was divided into three groups as follows: 28 patients with generalized or ocular subtype of MG, 121 patients with MS, and 53 healthy volunteers with no history of autoimmune diseases (mean age $\pm$ SD: 58.38 $\pm$ 12.78; 30 men, 23 women). The concentration data of 29 AAs were centered and standardized prior to analysis. The clinical and demographic characteristics of the patients are presented in Table 1.

Table 1. Demographic and clinical data of patients.

	MS	MG
Number of subjects (n)	121	28
Sex (male/female)	42/80 (34%/66%)	3/25 (10.7%/89.3%)
Age, years	52.5 ± 11.61 Min–Max: 23–77	48.92 ± 12.61 Min–Max: 29–75
Disease duration (years) [range]	16 ± 8.4	7.85 ± 6.53
Median EDSS score (IQR)	6 (4.0–6.5)	n.a.
MS type n (%)	RRMS: 41 (34%)	n.a.
	SPMS: 55 (45%)	
	PPMS: 25 (21%)	
MG type n (%)		GMG: 25 (89.3%)
		OMG: 3 (10.7%)
AChRAb		Yes: 21 (75%)
		No: 7 (25%)

MS—multiple sclerosis; MG—myasthenia gravis, RRMS—relapsing–remitting multiple sclerosis; SPMS—secondary progressive multiple sclerosis; PPMS—primary progressive multiple sclerosis; EDSS—Expanded Disability Status Scale; IQR—interquartile range; GMG—generalized myasthenia gravis; OMG—ocular myasthenia gravis, AChRAb—acetylcholine receptor antibody, n.a.—not applicable.

Blood samples were collected from patients in the morning, following an overnight fast. The collected samples were centrifuged, and the serum was frozen at −80 °C until analysis. AA profiling of the collected samples was performed using the EZ:faast kit. The EZ:faast AA analysis procedure consisted of three sequential steps, i.e., solid-phase extraction, derivatization, and liquid–liquid extraction. The prepared samples were then analyzed using liquid chromatography–mass spectrometry.

2.2. Chemicals and Reagents

In the present study, the following reagents were used: HPLC-grade methanol (Merck Darmstadt, Germany), ammonium acetate and formic acid (Sigma-Aldrich Co., St. Louis, MO, USA), and the EZ:faast^{TM} amino acid kit (Phenomenex, Inc., Torrance, CA, USA). Water was prepared using the Milli-Q system (Millipore, Bedford, MA, USA).

Quantitative analysis was performed using the internal standard method. A mixture of three standards was used as internal standards, namely homoarginine (HARG), methionine-D3 (Met-D3), and homophenylalanine (HPHE).

2.3. Instrumentation and Conditions

The quantitative and qualitative analyses of samples were performed using the High-Performance Liquid Chromatograph Nexera XR LC-20 AD pump (Shimadzu, Kyoto, Japan) and a Nexera XR SIL-20AC autosampler (Shimadzu, Kyoto, Japan), coupled with a mass spectrometer equipped with an electrospray ion source (ESI), the LCMS-8045 Mass Spectrometer (Shimadzu, Kyoto, Japan). The instrument was controlled, and the recorded data were processed using LabSolutions LCMS Ver.5.6 software.

Chromatographic separation was carried on the EZ:faast AA analysis–mass spectrometry column (250 × 3.0 mm, 4 µm) at a column temperature of 35 °C with the corresponding binary mobile phase. Solvent A was 10 mM ammonium formate in water and solvent B was 10 mM ammonium formate in methanol. The mobile phase flow was 0.25 mL/min and took place in a gradient system of 68% B–83% B in 13 min. The injection volume was 1 µL. The mass spectrometry (MS) data were acquired in positive ion mode. Multiple reacting monitoring was used for quantification by monitoring the ion transition of the AAs.

2.4. Statistical Analysis

The Kruskal–Wallis test was used to assess differences between the continuous variables' distribution (age, AA concentration). Post hoc analysis was further used to explore differences between means while controlling the family error rate. Considering non-normally distributed data, differences between the two groups were evaluated using Mann–Whitney U test statistics. Bonferroni correction was used to adjust for multiple testing. Pearson's correlation was used to study the linear correlation between AAs. All analyses and figures were formulated with Python [24].

3. Results

3.1. Comparison of AA Concentration between a Group of Patients (MS + MG Patients) and a Control Group of Healthy People

The concentration data of 29 AA were centered and standardized prior to analysis. In a combined analysis of patients with MS and MG, at a significance level of $\alpha = 0.05$, we found significant differences in AA concentrations between the study group and the healthy control group for the following amino acids: Glutamine (GLN) ($p = 0.015$), Arginine (ARG) ($p = 0.0001$), Citrulline (CIT) ($p = 0.0008$), 1-Methyl-L-histidine (1MHIS) ($p = 0.00002$), 4-Hydroxyproline (HYP) ($p = 0.02$), Sarcosine (SAR) ($p = 0.041$), α-Aminobutyric acid (ABA) ($p = 0.0008$), Proline (PRO) ($p = 0.0001$), Valine (VAL) ($p = 0.001$), Tryptophan (TRP) ($p = 0.0006$), and Cystine (CC) ($p = 0.005$) (Figure 1). After applying the Bonferroni correction (corrected p-value = 0.0017), the concentrations of ARG, CIT, 1MHIS, ABA, PRO, and TRP remained significantly different.

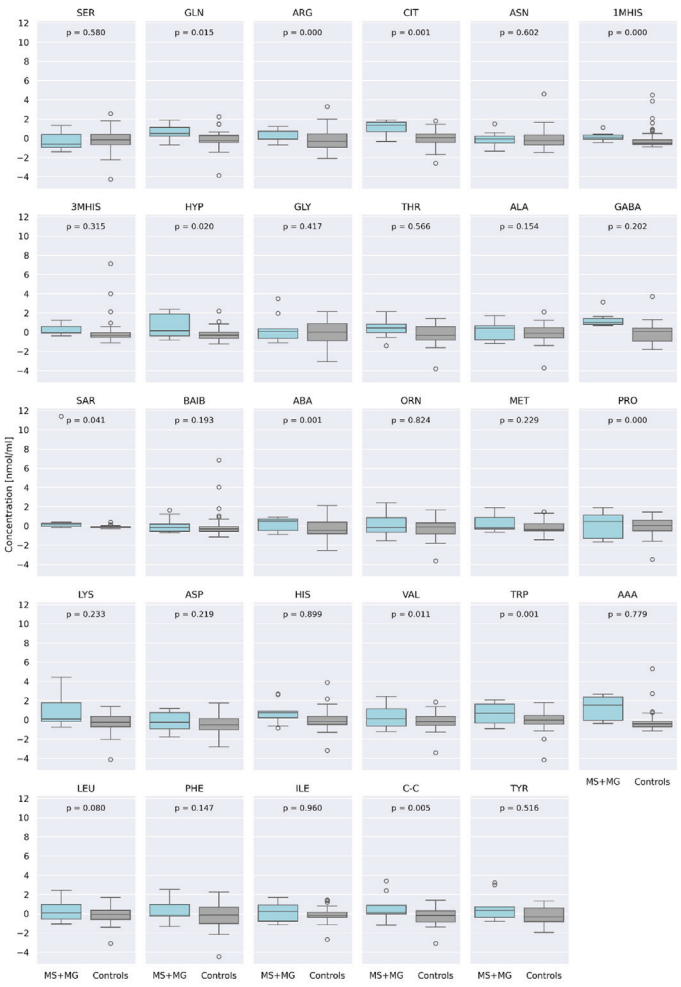


Figure 1. Centered and standardized AA concentrations between two groups—study group (MS and MG (blue) and controls (grey) represented as boxplots. The dots denote outlying observations. Serine (SER), Glutamine (GLN), Arginine (ARG), Citrulline (CIT), Asparagine (ASN), 1-Methyl-L-histidine

(1MHIS), 3-Methyl-L-histidine (3MHIS), 4-Hydroxyproline (HYP), Glycine (GLY), Threonine (THR), Alanine (ALA), Gamma-aminobutyric acid (GABA), Sarcosine (SAR), Beta-aminoisobutyric Acid (BAIB), α-Aminobutyric acid (ABA), Ornithine (ORN), Methionine (MET), Proline (PRO), Lysine (LYS), Aspartic acid (ASP), Histidine (HIS), Valine (VAL), Glutamic acid (GLU), Tryptophan (TRP), α-Aminoadipic acid (AAA), Leucine (LEU), Phenylalanine (PHE), Isoleucine (ILE), Cystine (C-C), Tyrsine (TYR).

The next step in the analysis involved evaluating AA concentrations as a function of age between the case and control groups. The goal was to determine if there was a trend in AA concentrations related to the age of the study population. Among the patients, no linear trend (positive or negative) was observed with increasing age. However, in the control group, there was a slight negative trend (decrease) in the concentrations of SER, ASN, GLY, GABA, ORN, and ASP, and a slight positive trend (increase) in the concentrations of ARG and CC.

3.2. Comparison of AA Concentration between MS and MG Patients

In the next stage of the work, the focus was on comparing the median distribution of AA concentration between the patients with MS and MG. At $\alpha = 0.05$, we observed a group of AA concentrations, GLN ($p = 0.015$), CIT ($p = 0.0007$), GABA ($p = 0.00009$), SAR ($p = 0.01$), His ($p = 0.048$), and AAA ($p = 0.0008$), to be significantly different between the MS and MG patients.

After Bonferroni correction (corrected p-value = 0.0017) concentration of CIT, GABA, and AAA remained significant. The comparison between MS and MG patients in terms of those three AA concentrations is presented as a boxplot (Figure 2).

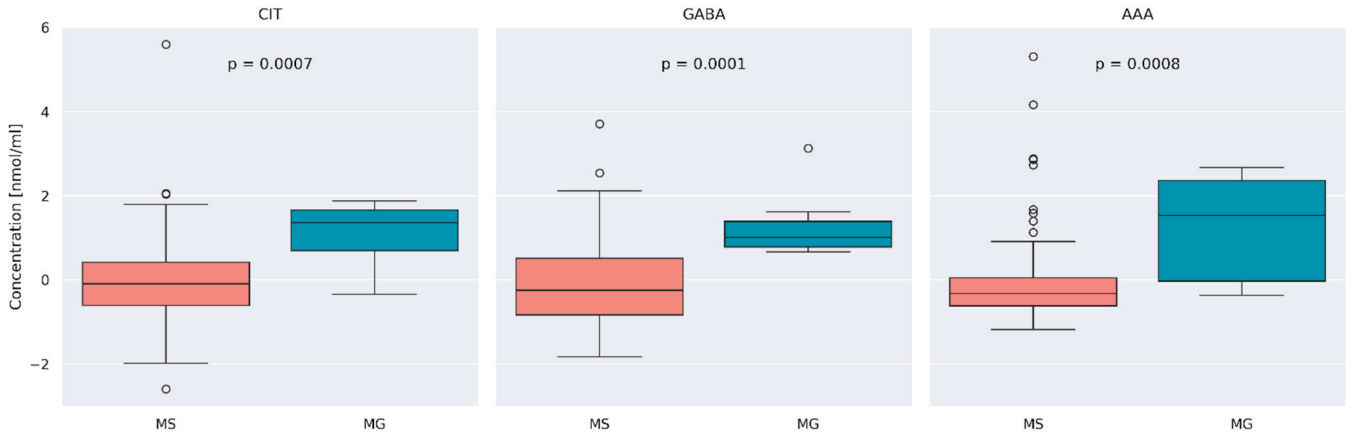


Figure 2. Centered and standardized concentration of Citrulline (CIT)), Gamma-aminobutyric acid (GABA) and α-Aminoadipic acid (AAA) between MS and MG patients. Black dots represent outlying observations.

To further explore those differences in the concentrations of CIT, GABA, and AAA between the MS and MG patients, we visualized these concentrations according to sexes (Figure 3). Due to the small number of men in the MG group, only women were included in the comparison.

As can be seen in Figure 3, as well as in the case of unification of the study groups in terms of gender, we observe statistically significantly higher concentrations of CIT, GABA, and AAA in the group of patients with MG.

To further explore the nature of the AA correlations, we examined their relationships with each other. Given that each AA's distribution approximates a normal distribution, and that the AAs follow similar pathways, a linear relationship between them is anticipated. Therefore, we utilized Pearson's correlation analysis to assess the degree of linear correlation between the variables.

Figure 4 presents a correlation matrix showing the degree of linear relationship between the AAs in MS and MG patients, and Figure 5 shows that of the control group. As can be seen from this figure, the vast majority of correlations are weakly positive (a positive trend is expected given that the origin of AA may be driven by a similar mechanism).

Several AAs are highly positively correlated with other AAs (R2 > 0.8, dark blue), meaning that they essentially carry the same information.

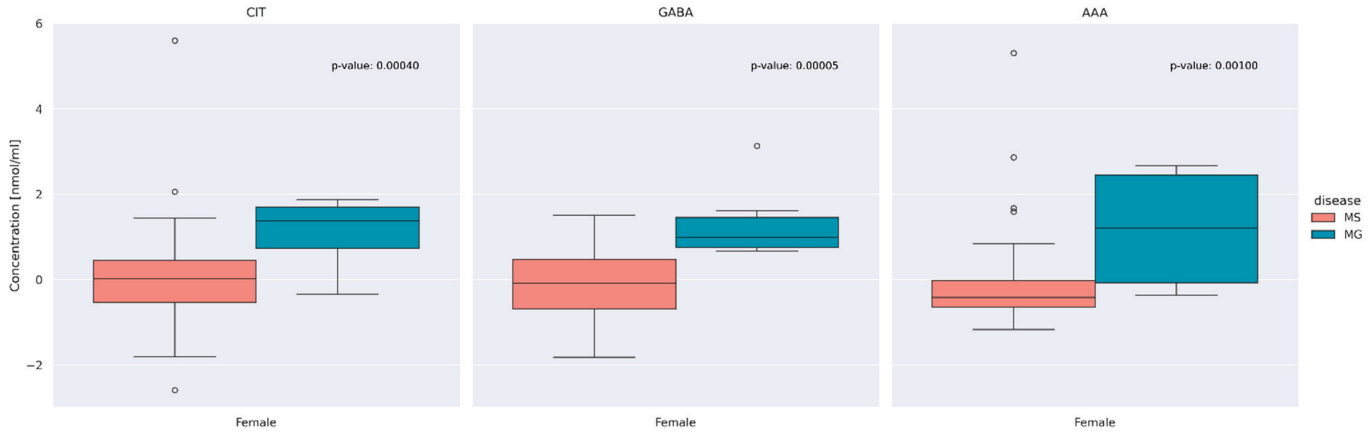


Figure 3. Centered and standardized concentration of Citrulline (CIT), Gamma-aminobutyric acid (GABA) and α-Aminoadipic acid (AAA) between MS and MG patients according to sex. The dots represent outlying observations.

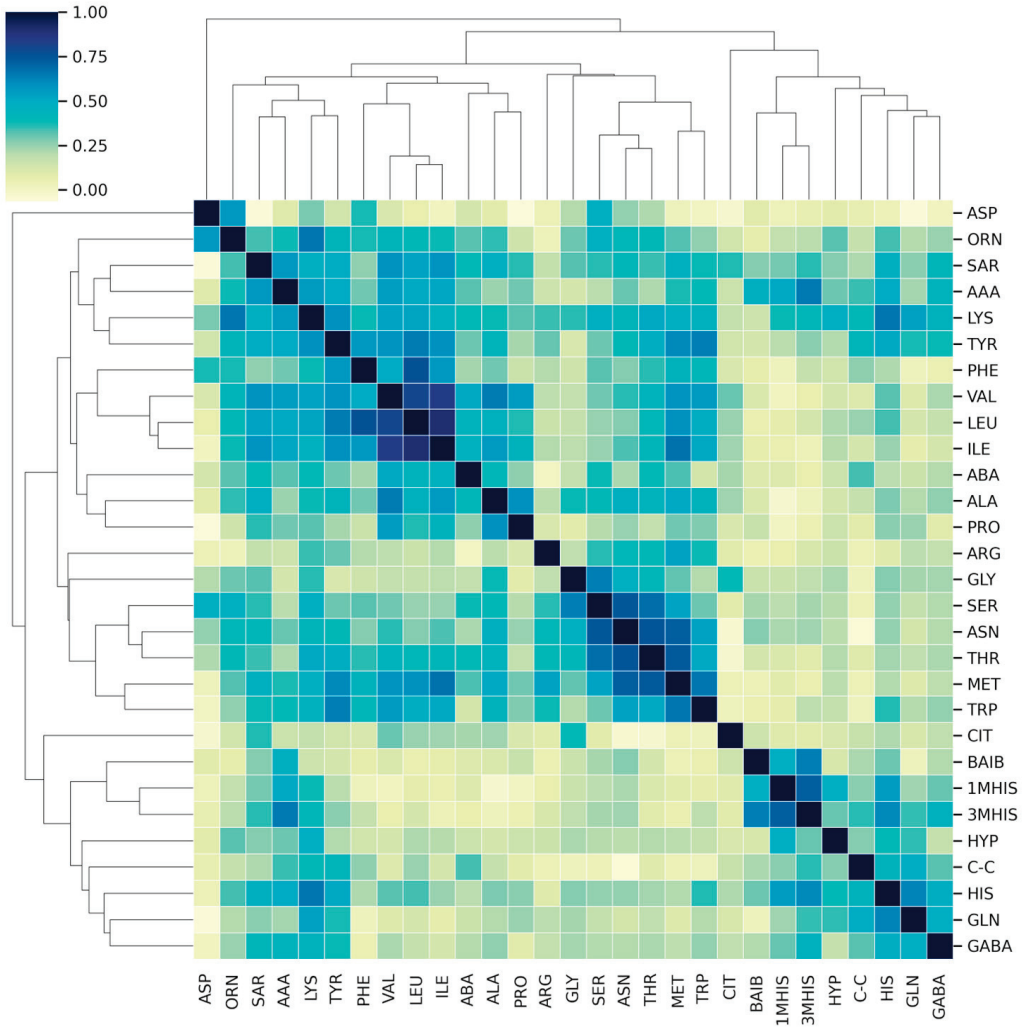


Figure 4. Correlation matrix demonstrating the degree of linear correlation between AAs in the MS and MG patient groups.

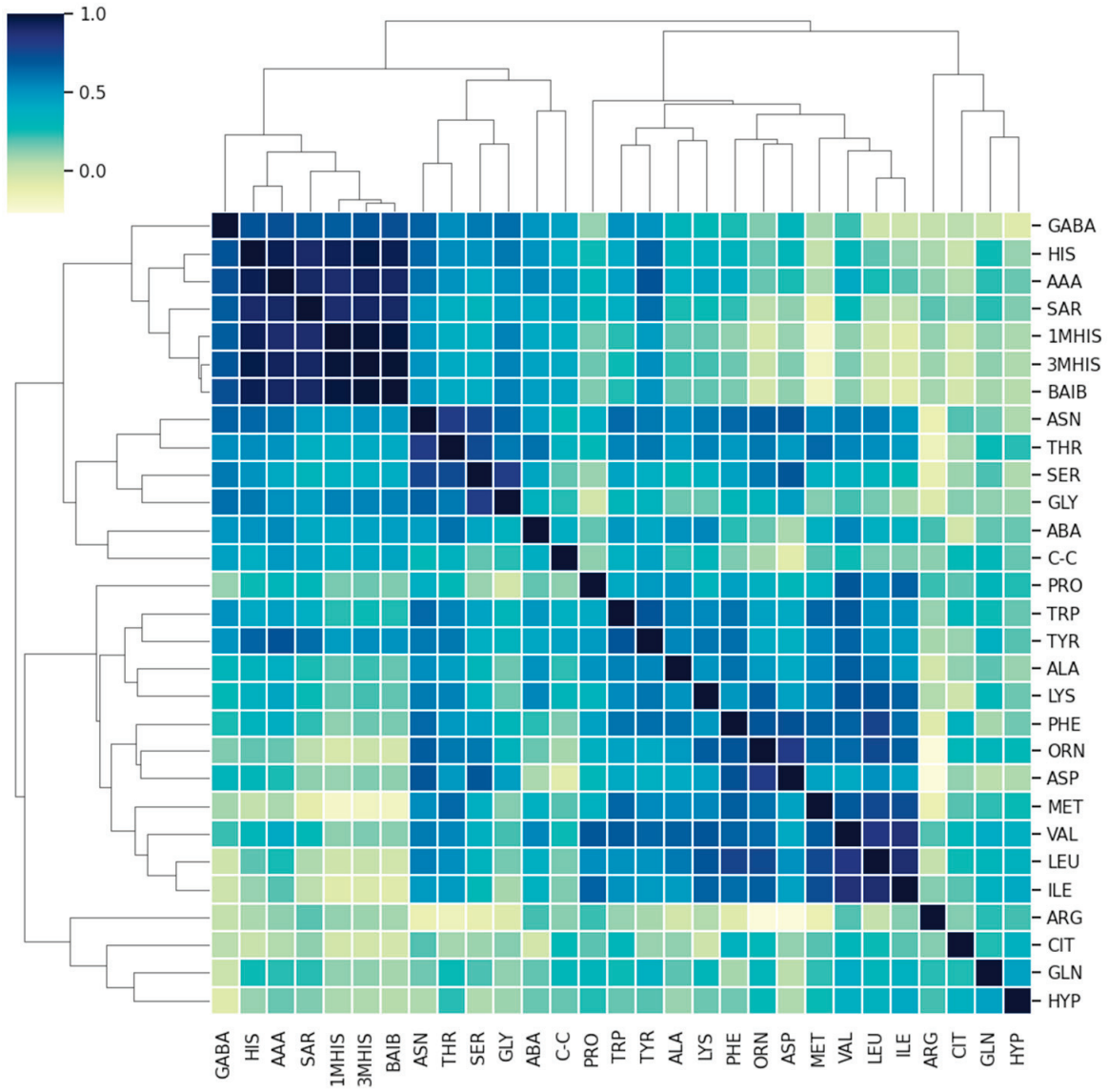


Figure 5. Correlation matrix demonstrating the degree of correlation between AAs in the control group.

3.3. Evaluation of Differences between Overall AA Concentrations according to the Type of Disease

In the next stage, it was assessed whether there were differences between the general concentrations of AA depending on the type of disease. Patients with MS were divided into three main types of MS, each defined by how far the disease has progressed (RRMS—relapsing–remitting multiple sclerosis; SPMS—secondary progressive multiple sclerosis; PPMS—primary progressive multiple sclerosis). The study included patients with generalized myasthenia gravis (GMG). The Kruskal–Wallis test showed the existence of differences between the disease types in terms of AA concentrations ($p = 1.04 \times 10^{-12}$). The post hoc analysis revealed the significant differences of AA concentrations between the following:

(i) PPMS (n = 26) and RRMS (n = 41) ($p = 0.008$)
(ii) PPMS (n = 26) and GMG (n = 25) ($p = 0.03$)
(iii) RRMS (n = 41) and GMG (n = 25) ($p = 0.00001$)
(iv) SPMS (n = 55) and GMG (n = 25) ($p = 0.0008$)

However, at this point, it should be highlighted that the differences mentioned may be a consequence of the existence of outlying points (Figure 6).

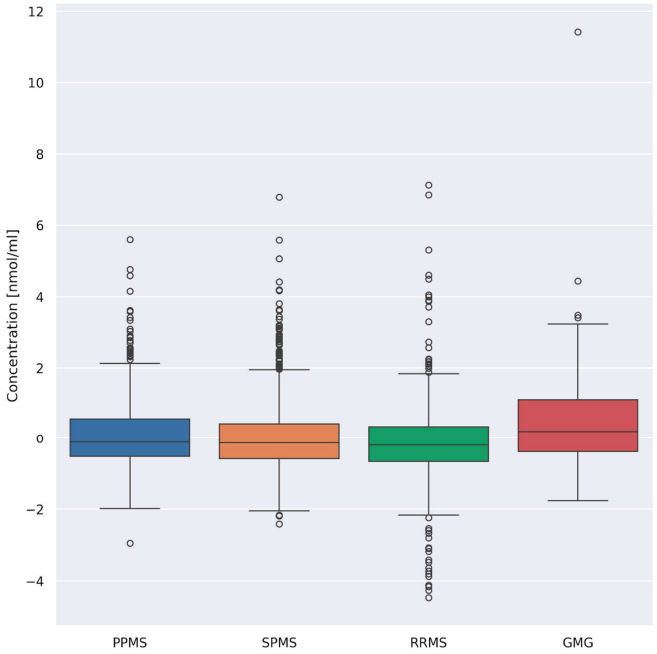


Figure 6. Centered and standardized AA concentrations for each disease type, MS and MG (PPMS—primary progressive multiple sclerosis, SPMS—secondary progressive multiple sclerosis, RRMS—relapsing–remitting multiple sclerosis; GMG—generalized myasthenia gravis).

The trend of AA concentrations was then checked with the duration of MS/MG (patients only) (Figure 7). From visual inspection, there is no trend of AA concentrations with the course of disease duration.

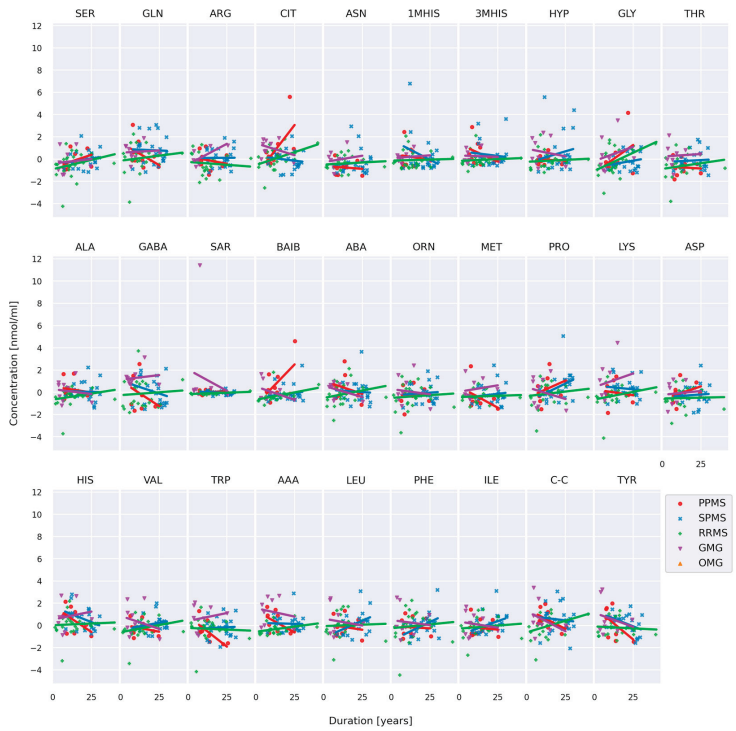


Figure 7. Centered and standardized AA concentration in a function of duration stratified by MS/MG subtypes. (PPMS—primary progressive multiple sclerosis, SPMS—secondary progressive multiple sclerosis, RRMS—relapsing–remitting multiple sclerosis; GMG—generalized myasthenia gravis, OMG—ocular myasthenia gravis).

3.4. Comparison of AA Concentration between Two Groups of Patients: RRMS (n = 41) and MG (n = 28)

Typically, multiple sclerosis (MS) begins with an initial relapsing–remitting course (RRMS). RRMS and myasthenia gravis (MG) share many similarities, including a relapsing course with a wide range of clinical signs, genetic predisposition, and a favorable response to anti-CD20 monoclonal antibodies or other forms of immunosuppressive therapies [25]. Notably, the potential clinical course, characterized by spontaneous or steroid-induced regression of neurological deficits, can complicate the initial differential diagnosis of both diseases. Thus, identifying a serum biomarker that can differentiate between these conditions would be highly beneficial. Consequently, in this study, a group of patients with RRMS was isolated for a comparative analysis with patients with MG. When comparing AA concentrations between the two groups—RRMS (n = 41) and MG (n = 28)—statistically significant differences in total AA concentration were observed (Figure 8).

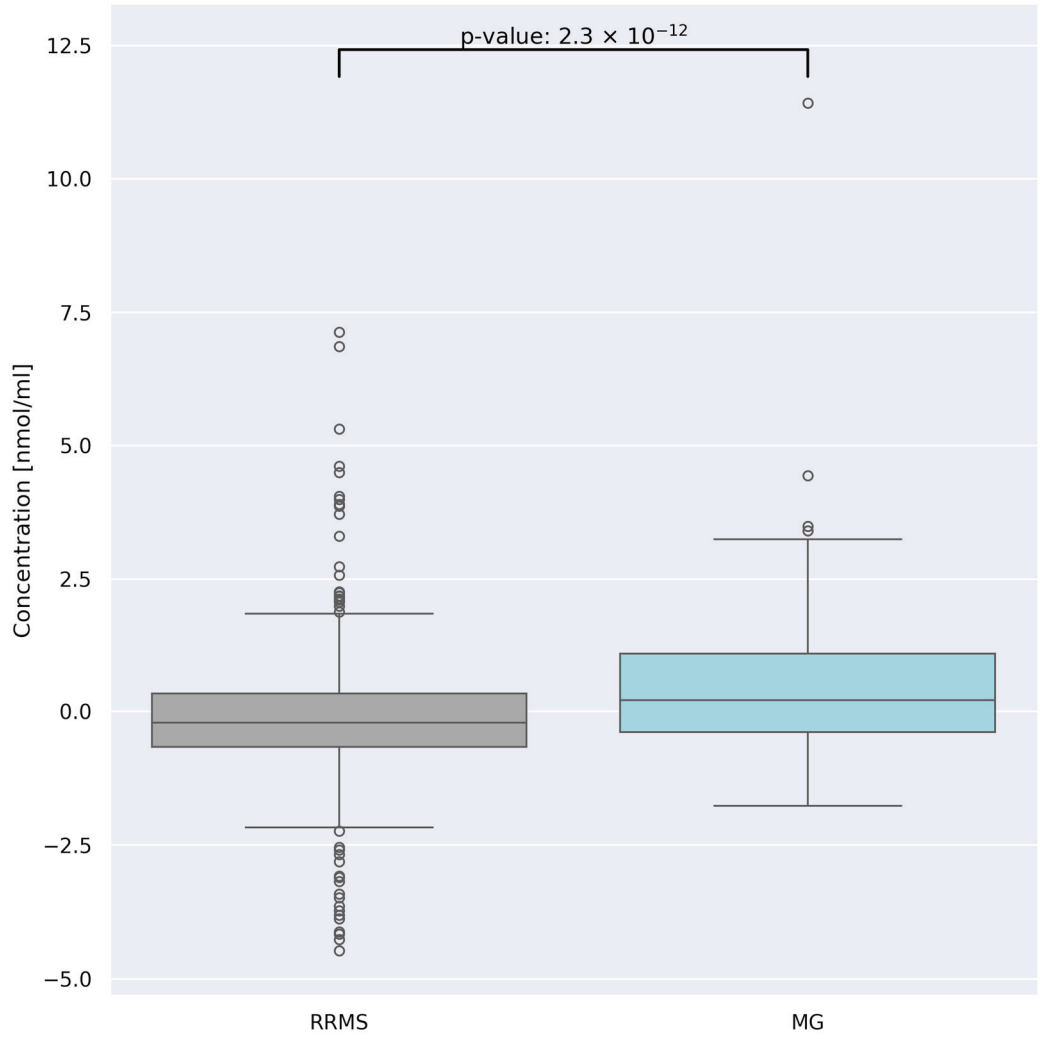


Figure 8. Centered and standardized AA concentrations for two groups: relapsing–remitting multiple sclerosis (RRMS) and myasthenia gravis (MG) patients. The dots represent outlying observations.

At $\alpha = 0.05$, we observed a group of AA concentrations to be significantly different between RRMS and MG patients (Figure 9), i.e., 1MHIS ($p = 0.0003$), 3MHIS ($p = 0.00015$), HYP ($p = 0.027$), AAA ($p = 0.006$), and PHE ($p = 0.034$). After Bonferroni correction (corrected p-value = 0.0017), 3MHIS remained significant. Median concentration of 3MHIS is higher in MG compared to that of RRMS patients ($p = 0.00015$).

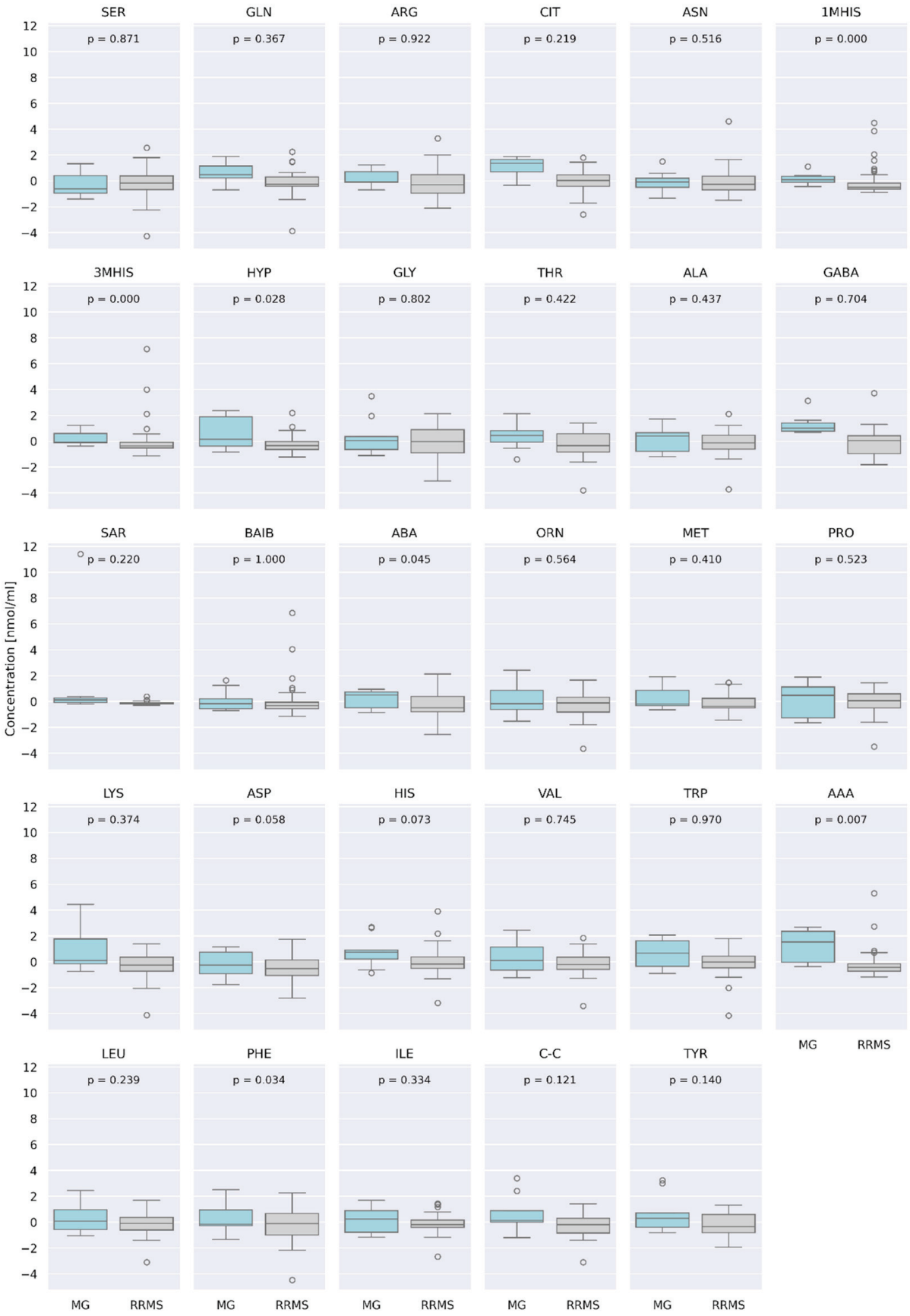


Figure 9. Centered and standardized AA concentrations between two groups, relapsing–remitting multiple sclerosis (RRMS—gray) and myasthenia gravis (MG—blue, represented as boxplots. The dots denote outlying observations.

To further investigate the nature of the amino acids (AAs), we examined the correlations between them. Given that the distribution of each AA approximates a normal distribution and that they originate from similar pathways, a linear relationship between them is expected. Therefore, we used Pearson's correlation to measure the linear dependence between variables. Below, we present a correlation matrix showing the degree of linear relationship between AAs in patients with MG and RRMS (Figure 10). Generally, the correlations are positive, with several AAs showing strong positive correlations with others ($R^2 > 0.8$, dark blue), indicating that they essentially carry the same information. A visual inspection reveals that the correlation plots differ significantly between the two groups, with weaker linear correlations observed in the RRMS patient group.

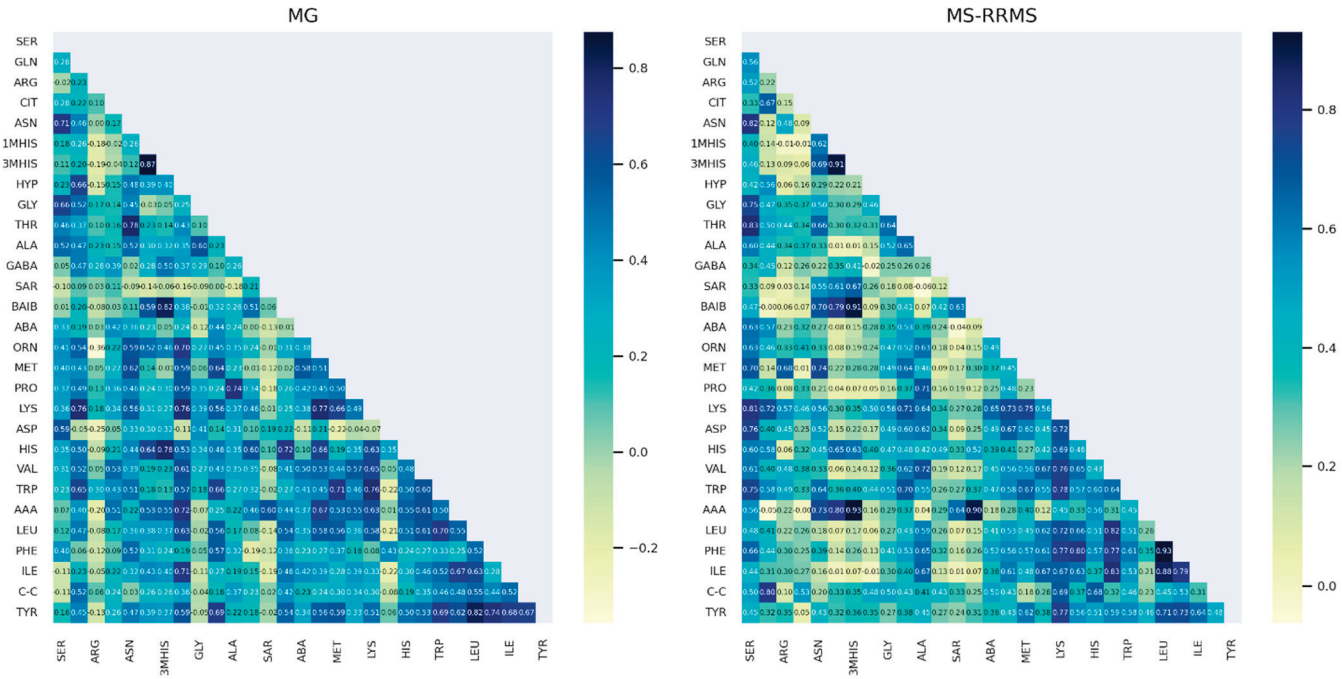


Figure 10. Correlation matrix demonstrating the degree of linearity in AA between the RRMS and MG patient groups. The number on the heatmaps denote R^2.The lighter the color, the lower the correlation coefficient value between two AAs.

4. Discussion

Although MS and MG are separate autoimmune diseases, some studies suggest that they coexist. The co-occurrence of MG and MS occurs more frequently than expected based on a chance association, and this association may be underdiagnosed due to the possible overlap of symptoms, especially bulbar and ocular manifestations, in which MG or MS may mimic each other, leading to an underestimation of the incidence combined occurrence of MG and MS [26]. In particular, two early symptoms of the disease—fatigue and diplopia—require caution in the proper diagnosis of the underlying disease. This aspect is important in the case of early MS symptoms in the complete absence or presence of only a single demyelinating lesion in the brain and/or spinal cord and existing contraindications to lumbar puncture. Moreover, with the increasing incidence of late-onset MG, patients may have foci of vascular damage in the central nervous system, some of which may be difficult to distinguish from demyelinating changes [6]. In such cases, patients are particularly vulnerable to misdiagnosis and having a peripheral marker that can distinguish MG from MS may be of significant support to clinicians.

Despite the differences in the pathologies of MS and MG, there are immunological similarities. Both MS and MG are considered largely T cell mediated [6]. Although the primary cause of MG development is autoantibodies against Ach receptors at the neuromuscular junction, the mechanism underlying the autoimmune response appears

to be initiated by T cell activation. Alternatively, although multiple sclerosis is primarily mediated by T cells, there is some evidence that B cells and self-reactive antibodies also play a role in the pathogenesis of multiple sclerosis [26].

In T cells, AA are involved in many functions that include, but are not limited to, providing the building blocks of proteins, nucleotides, and lipids, regulating the epigenome, and maintaining redox balance, which are crucial for maintaining T cell function and differentiation capacity [27].

Comparing the patients (patients with MS and MG, n = 149) with the control group (n = 53), we found statistically significant differences in the concentrations of AAs, such as: ARG, CIT, M1HIS, ABA, PRO, TRP. Four of them, ARG, PRO, TRP, CIT, remained significant after taking multiple testing into account. Previous studies have indicated a differentiation between the control group of healthy people and patients with MG and MS due to the concentration of ARG [20–22].

AAs such as arginine and tryptophan seem particularly interesting due to their involvement in the regulation of the immune response [28]. Arginine, by participating in the synthesis of non-protein compounds such as nitric oxide or polyamines, plays an important role in vasodilation, calcium release, neurotransmission, and immune response. The research results indicate an important role of NO-dependent processes in both autoimmune diseases and chronic inflammation. Increasing the amount of NO in the body is associated with exacerbation of inflammation [29]. ARG catabolism occurs through multiple pathways, including degradation by iNOS to nitric oxide (NO) and CIT, as well as arginase-mediated degradation to produce PROs, urea, ornithine, and polyamines. Therefore, the higher serum ARG and PRO concentrations with lower CIT concentration found in our study may indicate a shift in ARG metabolism towards reduced degradation by iNOS [30].

When considering the comparison between AA concentrations in MS and MG patients we found three AAs that were significantly different in the MS and MG groups after correcting for multiple testing (CIT, GABA, and AAA). Higher concentrations of AAs that showed significant differences were observed in patients with myasthenia gravis. Based on the comparative analysis by gender, no significant differences were observed between women and men in the MS group. Previous studies did not show any differences in concentration between MG and MS patients and a control group of healthy people [20,22].

Knowledge about AAA function or the potential mechanisms linking AAA to the disease processes is limited. AAA is produced by the breakdown of the essential AA lysine and is metabolized mainly in the mitochondria. AAA is structurally similar to glutamate. In studies conducted on animal models, it was observed that AAA significantly reduces glutamate uptake. Furthermore, AAA induced the production of reactive oxygen and nitrogen species, lipid peroxidation, and protein oxidation, in addition to reducing antioxidant defense. It has been indicated that the disruption of glutamatergic neurotransmission and redox homeostasis by AAA may play a role in the neurological symptoms, among others, accompanying α-ketoadipic acidosis [31,32].

The obtained research results indicate reduced CIT concentration in MS patients compared to MG. The study by Rzepliński et al. indicated a reduced level of CIT in patients with MS compared to the control group, which was probably related to the disorder of Arg metabolism [20]. Reduced Arg levels in MS patients compared to MG may confirm this hypothesis. However, it is worth noting that another study hypothesized that demyelination in multiple sclerosis leads to increased release of citrulline from the brain into the circulation [33].

Most circulating citrulline is produced by the transformation of dietary glutamine and arginine by enterocytes of the intestinal epithelium. The released CIT is largely taken up by the kidneys, where almost 100% of it is metabolized by arginosuccinate synthetase and lyase to produce arginine [34]. In addition to the gut–renal axis and post-translational deamination, citrulline can be produced by the action of two other substances. First, citrulline acts as an intermediate in the urea cycle, where it is synthesized from ornithine

and carbamoyl phosphate by ornithine carbamoyl transferase. Second, citrulline is a byproduct of NO production by nitric oxide synthase (NOS) from arginine [35].

Another AA that allowed for the statistically significant differentiation of the MS patient group from the MG patient group was gamma-aminobutyric acid (GABA). GABA is the main inhibitory neurotransmitter in the mammalian central nervous system and is directly responsible for the regulation of muscle tone in humans. GABA is also a modulator of the immune system [36]. The results obtained in our study indicate higher GABA concentrations in patients with MG compared to MS. Reduced GABA concentration in the CSF compared to the control group of healthy people has also been confirmed in other studies [21,37,38].

The model course of MS is an initial relapsing–remitting phase (RRMS), which, after a certain period, progresses to disability and transitions to a secondary progressive phase (SPMS). Due to diagnostic difficulties in differentiating myasthenia gravis and multiple sclerosis in their initial phase, we decided to isolate a group of patients with RRMS and myasthenia gravis to assess possible differences in the AA profiles of these groups. Both groups are similar in terms of age and sex distribution.

We reported that there were differences in the overall AA concentrations between the two disease subtypes (MG vs. RRMS); however, a lot of outlying observations were present in the patients' data and the results should be treated with caution.

When considering the comparison between RRMS and myasthenia patients, we found differences in several AA concentrations (1MHIS, HYP, AAA, PHE), with 3MHIS being significantly higher in MG patients when correcting for multiple testing.

The increased 3MHIS concentration in MG patients compared to the healthy controls has been confirmed in previous studies [22]. It has been found that 3-methylhistidine (3MH) is formed as a result of the post-translational modification of histidine residues, which is an essential AA with a wide range of functions in the body. It is believed that the presence of free 3MH in the body is the result of the breakdown of myofibrillar proteins, therefore its possible use as a marker of myofibrillar protein catabolism is indicated [39,40]. An increase in the loss of muscle proteins is observed, among others, in neuromuscular diseases such as MG or Duchenne syndrome [41].

The visual inspection of AA concentration in a function of age between RRMS and MG patients showed a positive linear trend with age. No clear direction of linear trend was observed for AA concentrations in a function of duration (the same reported when duration was divided into two categories). A correlation plot visualizing the linear relationship between the AAs showed a vast majority of positive correlations in both groups of patients. Visually, both correlation plots are quite different, with RRMS patients characterized by weaker linear relationships between AA.

5. Conclusions

Multiple sclerosis and myasthenia gravis are autoimmune neurological diseases. Research indicates the possible involvement of AA in the modification of the immune response, which is a key mechanism in the initiation of autoimmune diseases.

In the presented work, the metabolic profiles of 29 AAs were determined using LC–MS/MS in order to capture specific changes in AA profiles between a group of patients with MG and MS.

Comparison of the AA concentrations between the groups showed statistically significant differences ($\alpha = 0.05$) between GLN, CIT, GABA, SAR, His, AAA. After Bonferroni correction (corrected p-value = 0.0017), the concentrations of CIT, GABA, and AAA remained significant.

Statistical tests showed the existence of differences between disease types (RRMS, PPMS, SPMS, GMG) in terms of AA concentrations. RRMS and MG share many similarities, therefore a comparative analysis of AA profiles between these groups of patients was also performed. Bonferroni correction confirmed a significantly higher concentration of 3MHIS in MG compared to RRMS patients.

This study showed that AAs may be involved in the mechanisms underlying the pathogenesis of MG and MS diseases. The demonstrated differences may result from the participation of AA in immune responses, neurodegeneration processes, and construction of muscle proteins. The common pathogenesis of both diseases associated with an autoimmune background, involvement of T and B lymphocytes, and overlapping selected clinical symptoms may cause difficulties in the differential diagnosis of both diseases. At the same time, the identification of changes in AA metabolism in MS and MG can more precisely determine which of them are more likely to be attributed to autoimmune diseases of the neuromuscular junction and to the central nervous system. The obtained results may indicate AAs as potential biomarkers of autoimmune neurological diseases. The presented study has some limitations, including balancing the size of the study groups and the gender distribution in the group of patients with MG.

Further work is necessary, including a larger study group, limiting possible confounding factors, e.g., medications and diet, in order to correlate the results of previous studies with other possible autoimmune neurological diseases.

Author Contributions: Conceptualization, P.K.; Formal Analysis, P.K. and E.D.-W.; Investigation, P.K.; Methodology, P.K.; Project Administration, P.K.; Resources, Ł.R., M.K. (Marcin Koba), Z.M. and M.K. (Mariusz Kowalewski); Supervision, P.K.; Writing—Original Draft, P.K.; Writing—Review and Editing, P.K. and Ł.R. All authors have read and agreed to the published version of the manuscript.

Funding: This research received no external funding.

Institutional Review Board Statement: The study was conducted in accordance with the Declaration of Helsinki and approved by the Ethics Committee of the Nicolaus Copernicus University in Toruń and Collegium Medicum in Bydgoszcz (consent number: KB 499/2021, of 12.10.2021).

Informed Consent Statement: Informed consent was obtained from all subjects involved in the study.

Data Availability Statement: Data are unavailable due to privacy or ethical restrictions.

Acknowledgments: We gratefully acknowledge Poland's high-performance Infrastructure PLGrid ACK Cyfronet AGH, for providing computer facilities and support within computational grant no PLG/2023/016653.

Conflicts of Interest: The authors declare no conflicts of interest.

References

1. DeMaio, A.; Mehrotra, S.; Sambamurti, K.; Husain, S. The Role of the Adaptive Immune System and T Cell Dysfunction in Neurodegenerative Diseases. *J. Neuroinflamm.* **2022**, *19*, 251. [CrossRef] [PubMed]
2. Ha, J.C.; Richman, D.P. Myasthenia Gravis and Related Disorders: Pathology and Molecular Pathogenesis. *Biochim. Biophys. Acta (BBA)-Mol. Basis Dis.* **2015**, *1852*, 651–657. [CrossRef]
3. Ghasemi, N.; Razavi, S.; Nikzad, E. Multiple Sclerosis: Pathogenesis, Symptoms, Diagnoses and Cell-Based Therapy. *Cell J.* **2017**, *19*, 1–10.
4. Dong, D.; Chong, M.K.C.; Wu, Y.; Kaminski, H.; Cutter, G.; Xu, X.; Li, H.; Zhao, C.; Yin, J.; Yu, S.; et al. Gender Differences in Quality of Life among Patients with Myasthenia Gravis in China. *Health Qual. Life Outcomes* **2020**, *18*, 296. [CrossRef]
5. Harbo, H.F.; Gold, R.; Tintora, M. Sex and Gender Issues in Multiple Sclerosis. *Ther. Adv. Neurol. Disord.* **2013**, *6*, 237–248. [CrossRef] [PubMed]
6. Danikowski, K.M.; Jayaraman, S.; Prabhakar, B.S. Regulatory T Cells in Multiple Sclerosis and Myasthenia Gravis. *J. Neuroinflamm.* **2017**, *14*, 117. [CrossRef]
7. Kohler, I.; Verhoeven, A.; Derks, R.J.; Giera, M. Analytical Pitfalls and Challenges in Clinical Metabolomics. *Bioanalysis* **2016**, *8*, 1509–1532. [CrossRef]
8. Lu, Y.; Wang, C.; Chen, Z.; Zhao, H.; Chen, J.; Liu, X.; Kwan, Y.; Lin, H.; Ngai, S. Serum Metabolomics for the Diagnosis and Classification of Myasthenia Gravis. *Metabolomics* **2012**, *8*, 704–713. [CrossRef]
9. Blackmore, D.; Siddiqi, Z.; Li, L.; Wang, N.; Maksymowych, W. Beyond the Antibodies: Serum Metabolomic Profiling of Myasthenia Gravis. *Metabolomics* **2019**, *15*, 109. [CrossRef]
10. Rispoli, M.G.; Valentinuzzi, S.; De Luca, G.; Del Boccio, P.; Federici, L.; Di Ioia, M.; Digiovanni, A.; Grasso, E.A.; Pozzilli, V.; Villani, A.; et al. Contribution of Metabolomics to Multiple Sclerosis Diagnosis, Prognosis and Treatment. *Int. J. Mol. Sci.* **2021**, *22*, 11112. [CrossRef] [PubMed]

11. Ling, Z.N.; Jiang, Y.F.; Ru, J.N.; Lu, J.H.; Ding, B.; Wu, J. Amino Acid Metabolism in Health and Disease. *Signal Transduct. Target. Ther.* **2023**, *8*, 345. [CrossRef]
12. Kurniawan, H.; Soriano-Baguet, L.; Brenner, D. Regulatory T Cell Metabolism at the Intersection between Autoimmune Diseases and Cancer. *Eur. J. Immunol.* **2020**, *50*, 1626–1642. [CrossRef]
13. Antony, I.R.; Wong, B.H.S.; Kelleher, D.; Verma, N.K. Maladaptive T-Cell Metabolic Fitness in Autoimmune Diseases. *Cells* **2023**, *12*, 2541. [CrossRef] [PubMed]
14. Socha, E.; Koba, M.; Kośliński, P. Amino Acid Profiling as a Method of Discovering Biomarkers for Diagnosis of Neurodegenerative Diseases. *Amino Acids* **2019**, *51*, 367–371. [CrossRef] [PubMed]
15. Corso, G.; Cristofano, A.; Sapere, N.; La Marca, G.; Angiolillo, A.; Vitale, M.; Fratangelo, R.; Lombardi, T.; Porcile, C.; Intrieri, M.; et al. Serum Amino Acid Profiles in Normal Subjects and in Patients with or at Risk of Alzheimer Dementia. *Dement. Geriatr. Cogn. Disord. Extra* **2017**, *7*, 143–159. [CrossRef]
16. Figura, M.; Kuśmierska, K.; Bucior, E.; Szlufik, S.; Koziorowski, D.; Jamrozik, Z.; Janik, P. Serum Amino Acid Profile in Patients with Parkinson's Disease. *PLoS ONE* **2018**, *13*, e0191670. [CrossRef] [PubMed]
17. Kono, M.; Yoshida, N.; Tsokos, G.C. Amino Acid Metabolism in Lupus. *Front. Immunol.* **2021**, *12*, 623844. [CrossRef]
18. Lieu, E.L.; Nguyen, T.; Rhyne, S.; Kim, J. Amino Acids in Cancer. *Exp. Mol. Med.* **2020**, *52*, 15–30. [CrossRef] [PubMed]
19. Negrotto, L.; Correale, J. Amino Acid Catabolism in Multiple Sclerosis Affects Immune Homeostasis. *J. Immunol.* **2017**, *198*, 1900–1909. [CrossRef]
20. Rzepiński, Ł.; Kośliński, P.; Kowalewski, M.; Koba, M.; Maciejek, Z. Serum Amino Acid Profiling in Differentiating Clinical Outcomes of Multiple Sclerosis. *Neurol. I Neurochir. Pol.* **2023**, *57*, 414–422. [CrossRef]
21. Pashaei, S.; Yarani, R.; Mohammadi, P.; Emami Aleagha, M.S. The Potential Roles of Amino Acids and Their Major Derivatives in the Management of Multiple Sclerosis. *Amino Acids* **2022**, *54*, 841–858. [CrossRef] [PubMed]
22. Kośliński, P.; Rzepiński, Ł.; Daghir-Wojtkowiak, E.; Koba, M.; Maciejek, Z. Serum Amino Acid Profiles in Patients with Myasthenia Gravis. *Amino Acids* **2023**, *55*, 1157–1172. [CrossRef] [PubMed]
23. Rzepiński, Ł.; Kośliński, P.; Gackowski, M.; Koba, M.; Maciejek, Z. Amino Acid Levels as Potential Biomarkers of Multiple Sclerosis in Elderly Patients: Preliminary Report. *J. Clin. Neurol.* **2022**, *18*, 529–534. [CrossRef] [PubMed]
24. Van Rossum, G.; Drake, F.L. *Python 3 Reference Manual*; CreateSpace: Scotts Valley, CA, USA, 2009.
25. Rzepiński, Ł.; Zawadka-Kunikowska, M.; Newton, J.L.; Zalewski, P. Cardiac Autonomic Dysfunction in Myasthenia Gravis and Relapsing-Remitting Multiple Sclerosis—A Pilot Study. *J. Clin. Med.* **2021**, *10*, 2173. [CrossRef] [PubMed]
26. Dehbashi, S.; Hamouda, D.; Shanina, E. Co-Occurrence of Multiple Sclerosis and Myasthenia Gravis: A Case Report and Review of Immunological Theories. *Mult. Scler. Relat. Disord.* **2019**, *34*, 135–136. [CrossRef]
27. Hope, H.C.; Salmond, R.J. The Role of Non-Essential Amino Acids in T Cell Function and Anti-Tumour Immunity. *Arch. Immunol. Ther. Exp.* **2021**, *69*, 29. [CrossRef] [PubMed]
28. Bröer, S.; Bröer, A. Amino Acid Homeostasis and Signalling in Mammalian Cells and Organisms. *Biochem. J.* **2017**, *474*, 1935–1963. [CrossRef]
29. Sellebjerg, F.; Giovannoni, G.; Hand, A.; Madsen, H.O.; Jensen, C.V.; Garred, P. Cerebrospinal Fluid Levels of Nitric Oxide Metabolites Predict Response to Methylprednisolone Treatment in Multiple Sclerosis and Optic Neuritis. *J. Neuroimmunol.* **2002**, *125*, 198–203. [CrossRef]
30. Virarkar, M.; Alappat, L.; Bradford, P.G.; Awad, A.B. L-Arginine and Nitric Oxide in CNS Function and Neurodegenerative Diseases. *Crit. Rev. Food Sci. Nutr.* **2013**, *53*, 1157–1167. [CrossRef]
31. Desine, S.; Gabriel, C.L.; Smith, H.M.; Antonetti, O.R.; Wang, C.; Calcutt, M.W.; Doran, A.C.; Silver, H.J.; Nair, S.; Terry, J.G.; et al. Association of Alpha-Aminoadipic Acid with Cardiometabolic Risk Factors in Healthy and High-Risk Individuals. *Front. Endocrinol.* **2023**, *14*, 1122391. [CrossRef]
32. da Silva, J.C.; Amaral, A.U.; Cecatto, C.; Wajner, A.; dos Santos Godoy, K.; Ribeiro, R.T.; de Mello Gonçalves, A.; Zanatta, Â.; da Rosa, M.S.; Loureiro, S.O.; et al. α-Ketoadipic Acid and α-Aminoadipic Acid Cause Disturbance of Glutamatergic Neurotransmission and Induction of Oxidative Stress In Vitro in Brain of Adolescent Rats. *Neurotox. Res.* **2017**, *32*, 276–290. [CrossRef] [PubMed]
33. Vyver, M.V.; Beelen, R.; De Keyser, J.; Nagels, G.; Van Binst, A.M.; Verborgh, C.; D'haeseleer, M. Plasma Citrulline Levels Are Increased in Patients with Multiple Sclerosis. *J. Neurol. Sci.* **2018**, *387*, 174–178. [CrossRef] [PubMed]
34. Crenn, P.; Coudray-Lucas, C.; Thuillier, F.; Cynober, L.; Messing, B. Postabsorptive Plasma Citrulline Concentration Is a Marker of Absorptive Enterocyte Mass and Intestinal Failure in Humans. *Gastroenterology* **2000**, *119*, 1496–1505. [CrossRef]
35. Breuillard, C.; Cynober, L.; Moinard, C. Citrulline and Nitrogen Homeostasis: An Overview. *Amino Acids* **2015**, *47*, 685–691. [CrossRef]
36. Watanabe, M.; Maernura, K.; Kanbara, K.; Tamayama, T.; Hayasaki, H. GABA and GABA Receptors in the Central Nervous System and Other Organs. *Int. Rev. Cytol.* **2002**, *213*, 1–47. [PubMed]
37. Gao, F.; Yin, X.; Edden, R.A.E.; Evans, A.C.; Xu, J.; Cao, G.; Li, H.; Li, M.; Zhao, B.; Wang, J.; et al. Altered Hippocampal GABA and Glutamate Levels and Uncoupling from Functional Connectivity in Multiple Sclerosis. *Hippocampus* **2018**, *28*, 813–823. [CrossRef] [PubMed]
38. Nantes, J.C.; Proulx, S.; Zhong, J.; Holmes, S.A.; Narayanan, S.; Brown, R.A.; Hoge, R.D.; Koski, L. GABA and Glutamate Levels Correlate with MTR and Clinical Disability: Insights from Multiple Sclerosis. *NeuroImage* **2017**, *157*, 705–715. [CrossRef] [PubMed]

39. Nagasawa, T.; Yoshizawa, F.; Nishizawa, N. Plasma N-Methylhistidine Concentration Is a Sensitive Index of Myofibrillar Protein Degradation during Starvation in Rats. *Biosci. Biotechnol. Biochem.* **1996**, *60*, 501–502. [CrossRef]
40. Sjijlin, J.; Hjort, G.; Friman, G.; Hambraeus, L. Urinary Excretion of L-Methylhistidine: A Qualitative Indicator of Exogenous 3-Methylhistidine and Intake of Meats From Various Sources. *Metabolism* **1987**, *36*, 1175–1184. [CrossRef]
41. Mary, P.; Servais, L.; Vialle, R. Neuromuscular Diseases: Diagnosis and Management. *Orthop. Traumatol. Surg. Res.* **2018**, *104*, S89–S95. [CrossRef]

Disclaimer/Publisher's Note: The statements, opinions and data contained in all publications are solely those of the individual author(s) and contributor(s) and not of MDPI and/or the editor(s). MDPI and/or the editor(s) disclaim responsibility for any injury to people or property resulting from any ideas, methods, instructions or products referred to in the content.

Journal of
Clinical Medicine

MDPI

Article

An Integrated Approach Based on Clinical Data Combined with Metabolites and Biomarkers for the Assessment of Post-Operative Complications after Cardiac Surgery

Peter Meinarovich †, Alisa Pautova *,†, Evgenii Zuev, Ekaterina Sorokina, Ekaterina Chernevskaya and Natalia Beloborodova

Federal Research and Clinical Center of Intensive Care Medicine and Rehabilitology, 25-2 Petrovka Str., 107031 Moscow, Russia; pmejnarovic@gmail.com (P.M.); zuev17ev@gmail.com (E.Z.); esorokina@fnkcrr.ru (E.S.); echernevskaya@fnkcrr.ru (E.C.); nvbeloborodova@yandex.ru (N.B.)

* Correspondence: alicepau@mail.ru; Tel.: +7-905-773-89-81

† These authors contributed equally to this work.

Abstract: Background: Early diagnosis of post-operative complications is an urgent task, allowing timely prescribing of appropriate therapy and reducing the cost of patient treatment. The purpose of this study was to determine whether an integrated approach based on clinical data, along with metabolites and biomarkers, had greater predictive value than the models built on fewer data in the early diagnosis of post-operative complications after cardiac surgery. **Methods**: The study included patients (n = 62) admitted for planned cardiac surgery (coronary artery bypass grafting with cardiopulmonary bypass) with (n = 26) or without (n = 36) post-operative complications. Clinical and laboratory data on the first day after surgery were analyzed. Additionally, patients' blood samples were collected before and on the first day after surgery to determine biomarkers and metabolites. **Results**: Multivariate PLS-DA models, predicting the presence or absence of post-operative complications, were built using clinical data, concentrations of metabolites and biomarkers, and the entire data set (ROC-AUC = 0.80, 0.71, and 0.85, respectively). For comparison, we built univariate models using the EuroScore2 and SOFA scales, concentrations of lactate, the dynamic changes of 4-hydroxyphenyllactic acid, and the sum of three sepsis-associated metabolites (ROC-AUC = 0.54, 0.79, 0.62, 0.58, and 0.70, respectively). **Conclusions:** The proposed complex model using the entire dataset had the best characteristics, which confirms the expediency of searching for new predictive models based on a variety of factors.

Keywords: aromatic microbial metabolites; sepsis-associated metabolites; 4-hydroxyphenyllactic acid; prognostic models; SOFA

1. Introduction

The incidence of complications after cardiac surgery has decreased due to the development of new technologies and treatment methods, as well as improved qualifications of surgeons. However, the development of various complications still remains a serious problem that can lead to increasing expense for treatment, mortality, or deterioration in the patient's quality of life after surgery [1]. The Society of Thoracic Surgeons has identified five major post-operative complications: stroke, renal failure, prolonged intubation, unplanned reoperation, and deep sternal wound infection. The frequency of complications may vary depending on the type of operation, the patient's condition before surgery, and the professionalism of the operating team of cardiac surgeons [2]. To reduce the risks of post-operative complications, various measures are used, such as careful planning of the operation, preparing the patient before the operation, and strict monitoring in the post-operative period.

The use of biomarkers is a powerful tool that can improve the quality of the diagnostics and treatment of patients, help to understand the patient's condition, and promptly identify possible complications. These biomarkers are lactate [3], procalcitonin (PCT), interleukin-6 (IL6), N-terminal pro B-type natriuretic peptide (NT-proBNP), protein S100 [4], and high-sensitivity troponin T (HST-T) [5]. They have different sensitivity and specificity for the prognosis of the post-cardiosurgical complications, however, none of them is an excellent biomarker with 100% sensitivity and specificity.

Various metabolites have increasingly been used in clinical practice and actively studied for early diagnosis [6–10]. The value of metabolites lies in their ability to mark not only changes in the human body. The gut microbiota is known to influence host physiology, including through the production of multiple metabolites [11]. There is a concept pertaining to the relationship between the gut microbiota and the heart, the so-called gut–heart axis, which has led to novel treatment and prevention strategies by studying and targeting the composition of the gut microbiome and its metabolites [4,12,13]. Most metabolomic studies in cardiac surgery are usually related to the development of certain complications, such as acute kidney injury [7,14,15] and post-operative delirium [8,16]. However, our hypothesis is that an altered microbiome both before and in the early post-operative period and, as a consequence, its altered metabolic function, may be the cause of the development of any type of post-operative complication.

In one of our recent single-center studies on aortic prosthetics, aromatic microbial metabolites were increased in the early post-operative period (6 h after the end of the surgery) in the group of patients with all types of post-operative complications (n = 43) and, in particular, in patients with infectious complications (n = 26) [17]. In our other single-center pilot study on patients undergoing cardiac surgery (n = 24), those who developed infectious complications (n = 12) in the early post-operative period had a distinct gut microbiota taxonomy, with a predominance of potentially pathogenic species, even before the surgery [18]. In the current study, we decided to further analyze certain metabolites in all cardiac surgery patients from this study, as well as examine known biomarkers to try to predict complications that may occur. Therefore, the aim of this study was to identify the value of metabolite and biomarker monitoring for predicting post-operative complications in cardiac surgery in comparison with clinical data.

2. Materials and Methods

2.1. Study Design

This study was performed in the N. Pirogov National Medical Surgical Center, Moscow, Russian Federation. The local Ethics Committee approved the study (no. 04 from 22 May 2018), which was conducted in accordance with the ethical standards of the Declaration of Helsinki. Informed consent for participation in this study was also obtained from each patient or his/her legal representative.

The criteria for inclusion in the study were the following: the patient was over 18 years old, had planned cardiovascular surgery that corresponded to one of the following categories of cardiac surgery— coronary artery bypass grafting (CABG) or combination of CABG with other types of cardiac surgery. Also, serum samples should be collected before the surgery (point 0) or within a day following the surgery (point 1). Additionally, the patient gave informed consent to participate in the study.

Patients with the following criteria were not considered in this study: the presence of active infectious endocarditis, emergency surgery, previous bacterial infectious diseases in the past three months, antibiotic use within the past three months, or refusal to participate in the study.

Exclusion criteria included off-pump CABG and the absence of one of the collected samples (point 0 or point 1). All patients were divided into two groups retrospectively: with post-surgical complications (n = 26) and without post-surgical complications (n = 36). Complications included post-operative bleeding (n = 9, 15%), respiratory disorders (n = 7, 11%), atrial fibrillation (n = 5, 8%), myocardial ischemia (n = 5, 8%), and delirium (n = 2, 3%).

Some patients had multiple organ failure (n = 3, 5%). Demographic and peri-operative information, comorbidity, scales, and laboratory parameters were retrospectively analyzed from medical documentation.

Initially, 72 patients were included in the study, however, only 62 of them met the necessary criteria for inclusion, i.e., had a cardiopulmonary bypass during the cardiac surgery and had serum samples in both points 0 and 1. Patients (n = 62, including 44 males and 18 females) had different types of planned cardiovascular surgery. All patients had coronary artery bypass grafting—CABG (n = 62, 100%); some patients had combined operations—CABG and plastics of aortic or mitral valve (PAMV) (n = 12, 19%), CABG, and post-infarction left ventricular aneurysm resection (n = 2, 3%). All surgeries were performed with a cardiopulmonary bypass. Some patients had the following concomitant diseases: chronic heart failure (n = 54, 87%), chronic gastritis (n = 45, 73%), hypertension (n = 44, 71%), diabetes (n = 10, 16%), atrial fibrillation (n = 7, 11%), obesity (n = 5, 8%), gastric ulcers (n = 4, 7%), and chronic pancreatitis (n = 4, 7%). The median (interquartile range 25, 75%) age was 62 (57, 68) years, ejection fraction (EF) was 60 (49, 64) %. All patients used peri-operative antibiotic prophylaxis, using 2 g of cefazolin three times within 24 h. Summary information concerning the included and excluded patients is presented in Figure 1.

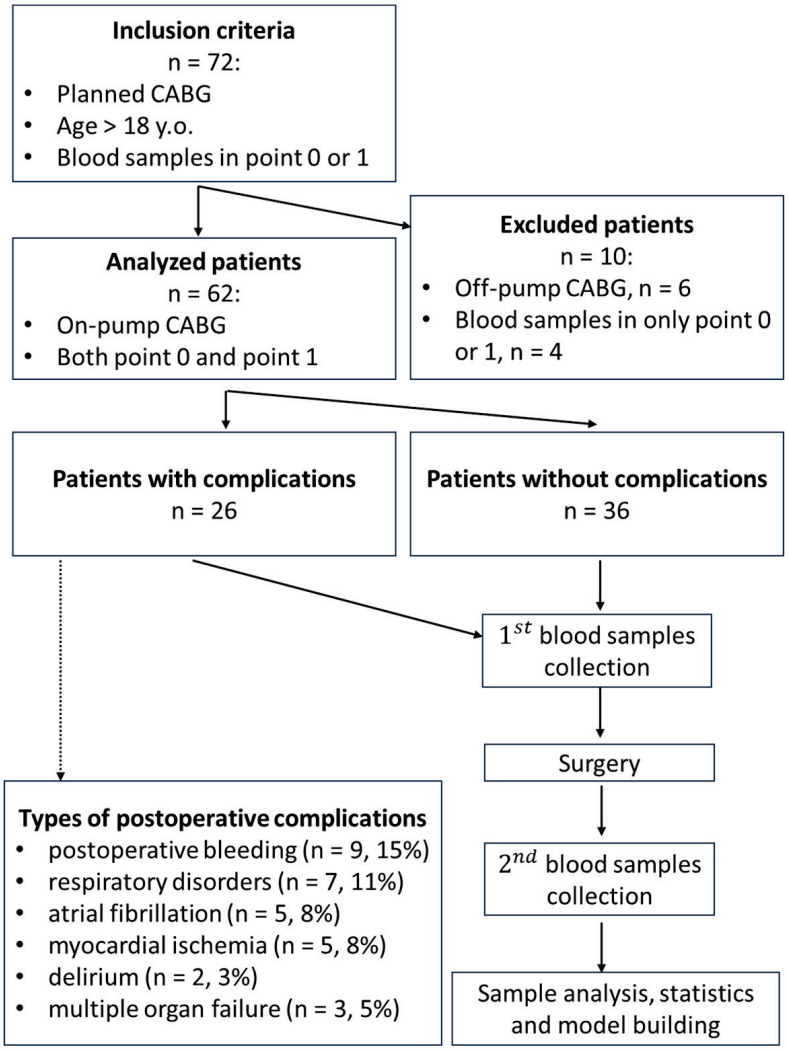


Figure 1. Study design summary (CABG—coronary artery bypass grafting).

2.2. Blood Sample Collection

The collection of patients' blood samples was performed before the surgery (point 0) and within a day after the surgery (point 1). There were also 48 blood samples from healthy donors (n = 48), which were used to reveal reference values for aromatic and dicarboxylic acid concentrations [17]. Serum samples were obtained by blood centrifuging at 1500× g for 10 min on the same day. The total number of serum samples (n = 172) included 124 from patients and 48 from healthy volunteers.

Data on the following parameters were taken from the medical documentation: EF% before surgery, hemoglobin (Hb), leucocytes, the highest value of lactate for the first day (lactate), pH max, pH min, infusion volume, on-pump time, number of erythrocytes transfusions, and total blood loss. Additionally, some specific analyses were conducted in the Federal Research and Clinical Center of Intensive Care Medicine and Rehabilitology in Moscow, Russia. Gas chromatography-mass spectrometry (GC-MS) analyses using a Trace GC 1310 gas chromatograph and ISQ LT mass spectrometer from the Thermo Electron Corporation (Santa Clara, CA, USA) were conducted to measure the concentration of various aromatic and dicarboxylic acids (benzoic acid—BA, phenylacetic acid—PhAA, phenylpropionic acid—PhPA, phenyllactic acid—PhLA, 4-hydroxybenzoic acid—p-HBA, 4-hydroxyphenylacetic acid—p-HPhAA, 4-hydroxyphenylpropionic acid—p-HPhPA, homovanillic acid—HVA, 4-hydroxyphenyllactic acid—p-HPhLA, succinic acid—SA, and fumaric acid—FA). The limit of quantitation for all acids was 0.5 μmol/L with a relative standard deviation of 10–30%, and the calibration curve was linear for all metabolites within the clinically significant concentration range (0.5–15 μmol/L). The sample preparation for the analytes and the details on the GC-MS analysis were previously described [19]. Several biomarkers were measured (IL6, PCT, NT-proBNP, protein S100, and HST-T) by electrochemiluminescence (Cobas e411, Roche, Basel, Switzerland).

2.3. Statistical Analysis

The Shapiro–Wilk test was used to assess the normality of the data distribution and, as a result, there were no data distributed normally. Continuous variables were described in tables using median and interquartile ranges; categorial variables were described using a number of cases and percentages. The Mann–Whitney U-test (two-sided) and Chi-square test were used for primary descriptive statistics in Section 3.1, and p-value < 0.05 was chosen as significant. All statistical tests were performed with Scipy 1.14.1, Python. The proportion of missing data was less than 5%, primarily in biomarkers. A k-nearest neighbors (KNN) imputer was used to fill in missing values. To achieve dimensional reduction for visualization and machine learning, partial least squares (PLS) regression was used (Section 3.2). Variable importance in projection (VIP) scores were computed to evaluate the importance of variables. Three multivariate and five univariate models were built. For multivariate models, initial lists of variables were used for fitting PLS data with important features (VIP score > 1) then transformed by PLS and used for the fitting of logistic regression and binary classification (PLS-DA). The schematic pipeline is shown in Figure 2. For univariate models, receiver operating characteristic (ROC) analysis was performed. All models were performed with Sklearn 1.3.1 (Python) and metrics (area under the ROC curve (ROC-AUC), sensitivity, specificity) with 95% confidence intervals (95% CI) computed and evaluated with k-fold cross-validation (k = 7).

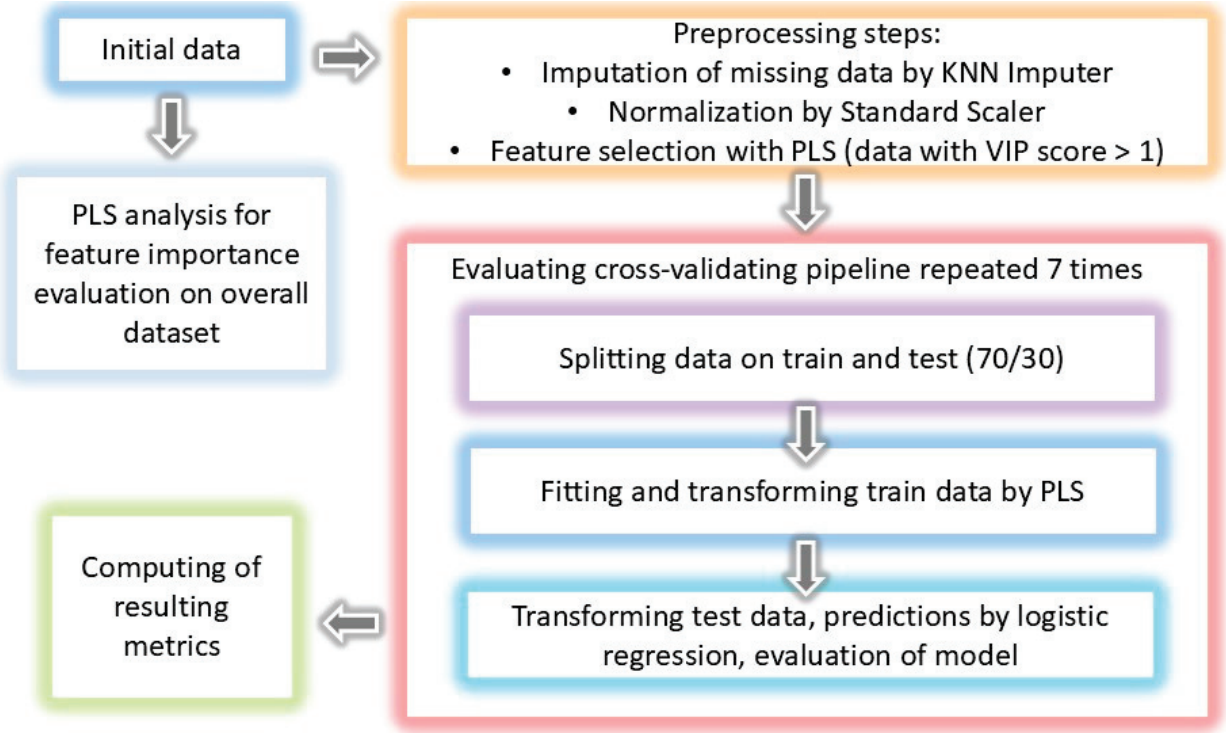


Figure 2. Resulting pipeline for building multivariate predictive models.

3. Results

3.1. Comparison of Uncomplicated and Complicated Patient Groups

Table 1 describes the medical and demographic characteristics, intraoperative parameters, and the serum concentrations of metabolites and biomarkers in all patients (n = 62), which were compared to the corresponding reference values or donors' concentrations for metabolites, and the differences between patients without (n = 36) and with (n = 26) complications before (point 0) and within a day after the surgery (point 1).

In point 0 there were patients with the following parameters that were beyond the reference values: hemoglobin (n = 23, 37%), leucocytes (n = 58, 94%), lactate (n = 62, 100%), pH (n = 39, 63%), IL6 (n = 33, 53%), NT-proBNP (n = 50, 81%,), S100 (n = 8, 13%), and HST-T (n = 48, 77%). According to the criterion that 95% CI of the parameter should not contain the minimum or maximum level of the corresponding reference range, the following parameters should be considered as significantly beyond the reference range: leukocytes in all patients—95% CI (11.3 – 20.8) $\times$ 10^9 (beyond reference range (4–9) $\times$ 10^9) and lactate in all patients—95% CI 2.82 – 7.51 mmol/L (higher than the maximum reference level of 2 mmol/L).

Usage of vasopressors (p = 0.02), time of mechanic ventilation (p < 0.001), infusion volume (p < 0.001), on-pump time (p < 0.001), number of erythrocyte transfusions (p = 0.03), blood loss on the 1st day (p = 0.04), Sepsis-related Organ Failure Assessment (SOFA) scores (p < 0.001), and HST-T after the surgery (p = 0.03) were significantly higher in patients with complications compared to uncomplicated ones.

In serum samples of donors and all patients before the surgery (in point 0), differences in concentrations of BA (p < 0.001), PhAA (p < 0.001), p-HBA (p = 0.03), p-HPhAA (p < 0.001), sum of sepsis-associated PhLA, p-HPhAA and p-HPhLA—Σ3AMM (p = 0.04), SA (p < 0.001), and FA (p < 0.001) were statistically significant. Within a day after the surgery, all metabolites differed statistically in all donors and patients.

The dynamics of the metabolites and biomarkers were evaluated as the difference (Δ) between their levels in points 1 and 0 (1–0). The differences in the level of Σ3AMM (p = 0.03), PCT (p = 0.01), NT-proBNP (p = 0.01), and HST-T (p = 0.01) were statistically significant.

Table 1. Medical and demographic characteristics, intraoperative parameters, and serum concentrations of metabolites and biomarkers before (point 0) and within a day after the surgery (point 1) in all patients (n = 62), uncomplicated (n = 36), and complicated (n = 26) groups of patients. The statistically significant differences between uncomplicated and complicated groups of patients are highlighted in bold ($p < 0.05$).

Parameter	Reference Values/ Concentrations of Metabolites in Donors	All Patients (n = 62)	Uncomplicated Group (n = 36)	Complicated Group (n = 26)	Uncomp. vs. Comp., p-Value	All Patients vs. Donors, p-Value
Age, years	-	62 (57, 67)	61 (57, 67)	63 (56, 67)	0.62	-
Sex (males), n, %	-	44, 71.0%	13, 36.1%	5, 19.2%	0.15 *	-
Diabetes Mellitus, n, %	-	10, 16.1%	6, 16.7%	4, 15.4%	0.72 *	-
EF (%)	-	60 (49, 63)	58 (48, 63)	60 (51, 66)	0.33	-
EuroScore 2	-	0.91 (0.75, 1.16)	0.94 (0.78, 1.08)	0.90 (0.71, 1.35)	0.84	-
Hemoglobin, g/L	110–160	114.5 (107.0, 125.5)	113.0 (107.0, 124.5)	118.0 (103.3, 125.5)	0.89	ns
Leucocytes, 10^9	4–9	16.10 (13.50, 19.87)	16.20 (13.65, 18.54)	15.98 (12.56, 20.62)	0.85	**
Vasopressors > 6 h	-	45, 72.6%	22, 61.1%	23, 88.5%	**0.02** *	-
Mechanic ventilation > 12 h	-	9, 14.5%	0, 0%	9, 34, 6%	**0.001** *	-
Lactate, mmol/L	<2	5.17 (3.54, 7.08)	4.84 (3.46, 6.08)	5.85 (3.94, 7.94)	0.07	**
Infusion volume, mL	-	5928 (5175, 6897)	5560 (4822, 6425)	6825 (5888, 7600)	**0.001**	-
On-pump time, h	-	85.50 (76.25, 108.75)	78.50 (67.50, 98.50)	102.00 (85.00, 129.75)	**0.001**	-
pH max	7.35–7.45	7.47 (7.45, 7.50)	7.47 (7.44, 7.49)	7.49 (7.45, 7.50)	0.21	ns
pH min	7.35–7.45	7.33 (7.29, 7.36)	7.33 (7.29, 7.36)	7.33 (7.29, 7.35)	0.40	ns
SOFA on the 1st day	-	4 (3, 6)	4 (2, 4)	6 (4, 6)	**0.001**	-
Number of erythrocytes transfusions	-	1 (0, 2)	1 (0, 2)	2 (1, 3)	**0.03**	-
Blood loss on the 1st day, mL	-	1275 (1050, 1400)	1200 (1050, 1300)	1350 (1075, 1487)	**0.04**	-
			Before surgery, point 0			
BA_0, µmol/L	<0.5 (<0.5, <0.5)	1.8 (1.3, 2.4)	1.7 (1.3, 2.3)	2.1 (1.5, 2.6)	0.13	**0.001**
PhAA_0, µmol/L	<0.5 (<0.5, 0.6)	0.9 (0.6, 1.2)	1.0 (0.6, 1.5)	0.9 (0.6, 1.0)	0.24	**0.001**
PhPA_0, µmol/L	<0.5 (<0.5, 0.5)	<0.5 (<0.5, <0.5)	<0.5 (<0.5, 0.5)	<0.5 (<0.5, <0.5)	0.33	0.75
PhLA_0, µmol/L	<0.5 (<0.5, <0.5)	<0.5 (<0.5, <0.5)	<0.5 (<0.5, <0.5)	<0.5 (<0.5, <0.5)	0.85	0.79
p-HBA_0, µmol/L	<0.5 (<0.5, <0.5)	<0.5 (<0.5, <0.5)	<0.5 (<0.5, <0.5)	<0.5 (<0.5, <0.5)	0.19	**0.03**
p-HPhAA_0, µmol/L	<0.5 (<0.5, <0.5)	0.7 (0.5, 1.0)	0.7 (0.5, 1.1)	0.6 (0.5, 0.9)	0.45	**0.001**
p-HPhPA_0, µmol/L	<0.5 (<0.5, <0.5)	<0.5 (<0.5, <0.5)	<0.5 (<0.5, <0.5)	<0.5 (<0.5, <0.5)	1.00	1
HVA_0, µmol/L	<0.5 (<0.5, <0.5)	<0.5 (<0.5, <0.5)	<0.5 (<0.5, <0.5)	<0.5 (<0.5, <0.5)	0.74	0.13
p-HPhLA_0, µmol/L	1.2 (1.0, 1.6)	1.2 (1.0, 1.4)	1.2 (1.0, 1.4)	1.2 (1.1, 1.4)	0.72	0.37
Σ3AMM_0, µmol/L	1.9 (1.5, 2.2)	2.1 (1.8, 2.7)	2.1 (1.8, 2.8)	2.0 (1.7, 2.5)	0.55	**0.04**
SA_0, µmol/L	4.8 (4.4, 6.0)	20.2 (17.0, 25.2)	19.9 (16.9, 25.8)	20.7 (17.6, 24.0)	0.86	**0.001**
FA_0, µmol/L	1.3 (1.1, 1.5)	1.7 (1.5, 2.1)	1.7 (1.4, 2.1)	1.7 (1.5, 2.4)	0.93	**0.001**
IL6_0, pg/mL	<7	9.0 (6.8, 13.6)	9.5 (7.0, 13.6)	8.7 (6.2, 14.2)	0.75	ns
PCT_0, ng/mL	<0.5	<0.5 (<0.5, <0.5)	<0.5 (<0.5, <0.5)	<0.5 (<0.5, <0.5)	0.59	ns
NT-proBNP_0, pg/mL	<300	564.8 (216.0, 883.0)	478.3 (213.7, 790.3)	625.2 (239.8, 883.0)	0.72	ns
S100_0, pg/mL	<0.5	<0.5 (<0.5, <0.5)	<0.5 (<0.5, <0.5)	<0.5 (<0.5, <0.5)	0.27	ns
HST-T_0, pg/mL	<0.5	24.2 (16.2, 40.3)	29.2 (16.5, 45.3)	22.5 (15.6, 30.4)	0.16	ns

Table 1. *Cont.*

Parameter	Reference Values/ Concentrations of Metabolites in Donors	All Patients (n = 62)	Uncomplicated Group (n = 36)	Complicated Group (n = 26)	Uncomp. vs. Comp., p-Value	All Patients vs. Donors, p-Value
A day after surgery, point 1						
BA_1, µmol/L	<0.5 (<0.5, <0.5)	1.4 (0.9, 2.8)	1.2 (0.9, 2.1)	1.6 (1.1, 3.1)	0.15	**0.001**
PhAA_1, µmol/L	<0.5 (<0.5, 0.60)	<0.5 (<0.5, 0.5)	<0.5 (<0.5, 0.5)	<0.5 (<0.5, <0.5)	0.99	**0.001**
PhPA_1, µmol/L	<0.5 (<0.5, 0.52 < 0)	5 (<0.5, <0.5)	<0.5 (<0.5, <0.5)	<0.5 (<0.5, <0.5)	1.00	**0.001**
PhLA_1, µmol/L	<0.5 (<0.5, <0.5)	<0.5 (<0.5, <0.5)	<0.5 (<0.5, <0.5)	<0.5 (<0.5, <0.5)	0.96	**0.001**
p-HBA_1, µmol/L	<0.5 (<0.5, <0.5)	<0.5 (<0.5, <0.5)	<0.5 (<0.5, <0.5)	<0.5 (<0.5, <0.5)	0.77	**0.03**
p-HPhAA_1, µmol/L	<0.5 (<0.5, <0.5)	<0.5 (<0.5, <0.5)	<0.5 (<0.5, <0.5)	<0.5 (<0.5, <0.5)	0.49	**0.001**
p-HPhPA_1, µmol/L	<0.5 (<0.5, <0.5)	<0.5 (<0.5, <0.5)	<0.5 (<0.5, <0.5)	<0.5 (<0.5, <0.5)	1.00	**0.001**
HVA_1, µmol/L	<0.5 (<0.5, <0.5)	1.6 (0.7, 3.0)	1.1 (<0.5, 3.0)	2.3 (1.1, 3.3)	0.06	**0.001**
p-HPhLA_1, µmol/L	1.3 (1.0, 1.6)	1.6 (1.3, 2.4)	1.6 (1.3, 2.3)	1.6 (1.3, 2.4)	0.56	**0.001**
Σ3AMM_1, µmol/L	1.9 (1.5, 2.2)	2.2 (1.8, 3.3)	2.4 (1.7, 3.3)	2.2 (1.8, 3.2)	0.98	**0.001**
SA_1, µmol/L	4.8 (4.4, 5.9)	16.2 (12.7, 21.7)	15.8 (12.2, 20.0)	16.9 (14.3, 23.3)	0.34	**0.001**
FA_1, µmol/L	1.3 (1.1, 1.5)	2.2 (1.5, 3.8)	2.2 (1.5, 4.5)	2.1 (1.8, 3.4)	0.91	**0.001**
IL6_1, pg/mL	<7	67.6 (38.0, 101.1)	58.7 (34.8, 102.8)	76.4 (43.7, 100.0)	0.64	**
PCT_1, ng/mL	<0.5	3.3 (0.7, 8.8)	1.5 (<0.5, 7.3)	4.2 (1.1, 16.8)	0.06	**
NT-proBNP_1, pg/mL	<300	981.9 (608.9, 1409.3)	964.1 (468.8, 1329.8)	1181.5 (817.8, 1878.8)	0.13	**
S100_1, pg/mL	<0.5	<0.5 (<0.5, <0.5)	<0.5 (<0.5, <0.5)	<0.5 (<0.5, <0.5)	0.81	ns
HST-T_1, pg/mL	<0.5	356.7 (202.4, 614.0)	261.9 (194.2, 455.0)	575.5 (216.9, 745.5)	**0.03**	**
Differences between point 1 and point 0 (Δ)						
ΔBA, µmol/L	-	−0.3 (−2.5, 1.9)	−0.4 (−2.0, 1.3)	−0.2 (−3.0, 2.5)	0.89	-
ΔPhAA, µmol/L	-	−0.8 (−1.4, −0.2)	−0.8 (−1.5, −0.1)	−0.7 (−1.2, −0.3)	0.32	-
ΔPhPA, µmol/L	-	0.0 (−0.2, 0.2)	0.0 (−0.3, 0.3)	0.0 (−0.1, 0.1)	0.37	-
ΔPhLA, µmol/L	-	0.0 (−0.2, 0.2)	0.0 (−0.3, 0.3)	0.0 (−0.2, 0.2)	0.65	-
Δp-HBA, µmol/L	-	0.0 (−0.8, 0.8)	0.0 (−0.9, 0.9)	0.0 (−0.5, 0.5)	0.28	-
Δp-HPhAA, µmol/L	-	−0.6 (−1.8, 0.7)	−0.7 (−2.1, 0.7)	−0.5 (−1.4, 0.3)	0.22	-
Δp-HPhPA, µmol/L	-	0.0 (0.0, 0.0)	0.0 (0.0, 0.0)	0.0 (0.0, 0.0)	0.99	-
ΔHVA, µmol/L	-	1.7 (−2.4, 5.8)	1.1 (−2.4, 4.7)	2.3 (−2.2, 6.7)	0.08	-
Δp-HPhLA, µmol/L	-	0.5 (−0.3, 1.3)	0.4 (−0.2, 1.1)	0.6 (−0.3, 1.5)	0.20	-
ΔΣ3AMM, µmol/L	-	0.3 (−1.2, 1.9)	0.0 (−1.5, 1.5)	0.7 (−0.8, 2.2)	**0.03**	-
ΔSA, µmol/L	-	−4.4 (−16.3, 7.6)	−4.9 (−15.8, 5.9)	−2.3 (−14.9, 10.4)	0.29	-
ΔFA, µmol/L	-	0.5 (−8.7, 9.7)	0.4 (−11.0, 11.7)	0.5 (−4.2, 5.3)	0.96	-
ΔIL6, pg/mL	-	60.8 (−28.6, 150.1)	51.6 (−31.2, 134.4)	69.3 (−28.4, 167.0)	0.97	-
ΔPCT, ng/mL	-	3.6 (−11.6, 18.8)	1.5 (−4.2, 7.1)	4.9 (−16.2, 25.9)	**0.01**	-
ΔNT-proBNP, pg/mL	-	493.6 (−1878.4, 2865.7)	264.4 (−871.4, 1400.1)	720.6 (−2547.1, 3988.3)	**0.01**	-
ΔS100, pg/mL	-	0.0 (−0.3, 0.3)	0.0 (−0.2, 0.2)	0.0 (−0.4, 0.5)	0.67	-
ΔHST-T, pg/mL	-	390.7 (47.8, 733.6)	247.0 (−106.4, 600.4)	569.5 (270.4, 868.6)	**0.01**	-

*—Chi-square test; **—reference values out of 95% CI, the differences are significant; ns—not significant differences.

3.2. Models for the Prognosis of the Post-Operative Complications

Data that were collected before and within a day after the surgery were used to fit models to predict if a patient would have complications or not. PLS analysis was performed for the importance evaluation of all parameters included in the model (Figure 3). The threshold value for VIP scores was chosen as 1. SOFA and time of mechanic ventilation > 12 h took leading positions in the VIP scores rating, and the clinical parameters higher than the threshold were on-pump time, infusion volume, total blood loss, number of erythrocytes transfusions, and lactate. Differences in certain metabolites and biomarkers (NT-proBNP, HVA, PCT, p-HPhLA, Σ3AMM, PhLA, and BA) were more than the chosen threshold.

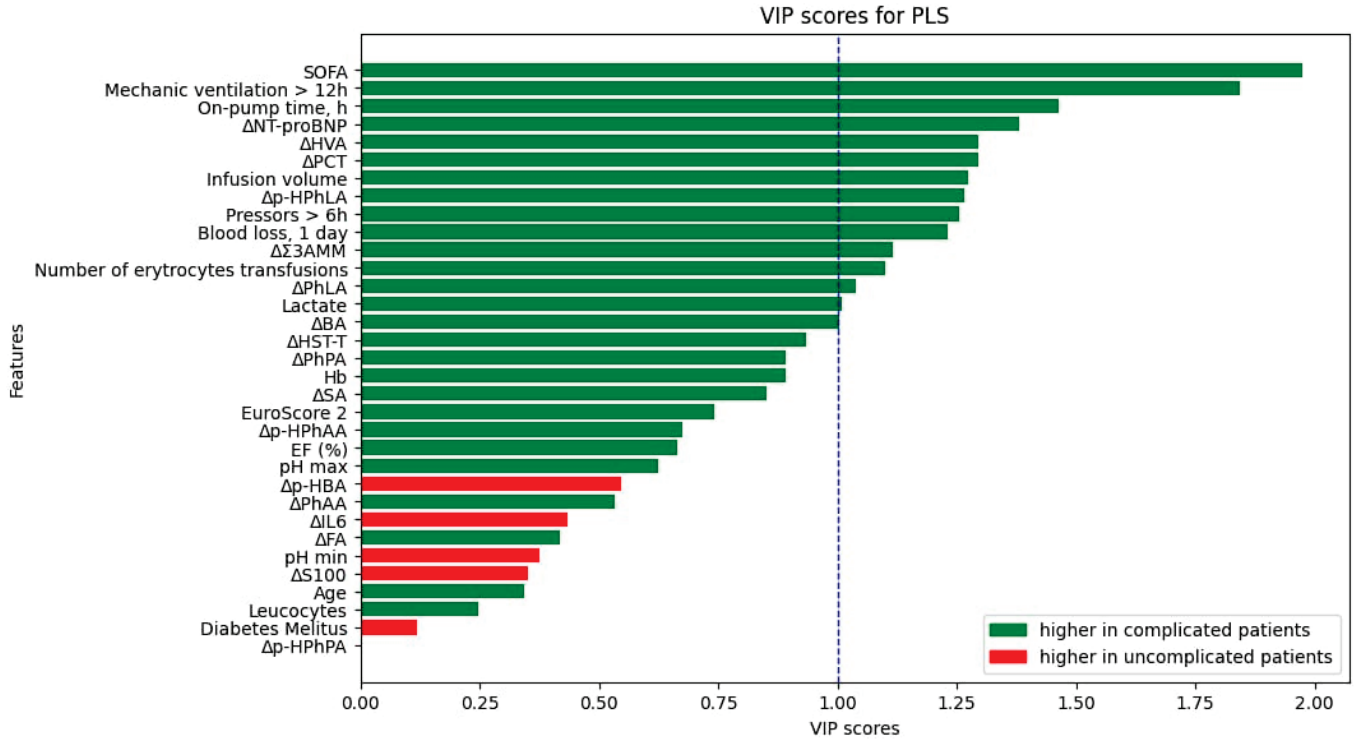
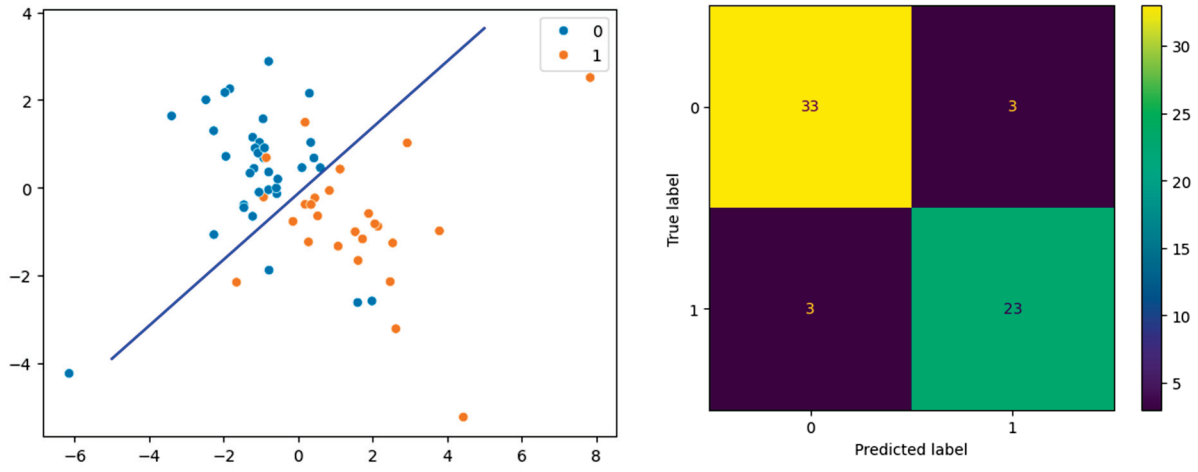


Figure 3. VIP scores for PLS analysis. The blue line marks the threshold of importance (VIP score > 1.0).

The resulting pipeline included transforming data with PLS and then predicting the development of complications by the logistic regression. Computed coordinates that are explained as a scatter plot (Figure 4a) show linear discrimination between groups. A confusion matrix shows the quality of classification of the final model on all data (Figure 4b). Three samples were misclassified in the uncomplicated group of patients (false negative samples) and three samples were misclassified in the complicated group of patients (false positive samples).

Multivariate PLS-DA models were constructed. We built model-fits on all data (ROC-AUC = 0.85), on only clinical data (ROC-AUC = 0.80), and on only metabolites and biomarkers (ROC-AUC = 0.71). We compared our models with univariate models built on SOFA (ROC-AUC = 0.79) and EuroScore 2 (ROC-AUC = 0.54) scores, lactate (ROC-AUC = 0.62), Δp-HPhLA (ROC-AUC = 0.58), and ΔΣ3AMM (ROC-AUC = 0.70). All data obtained were accumulated in Table 2 and Figure 5.

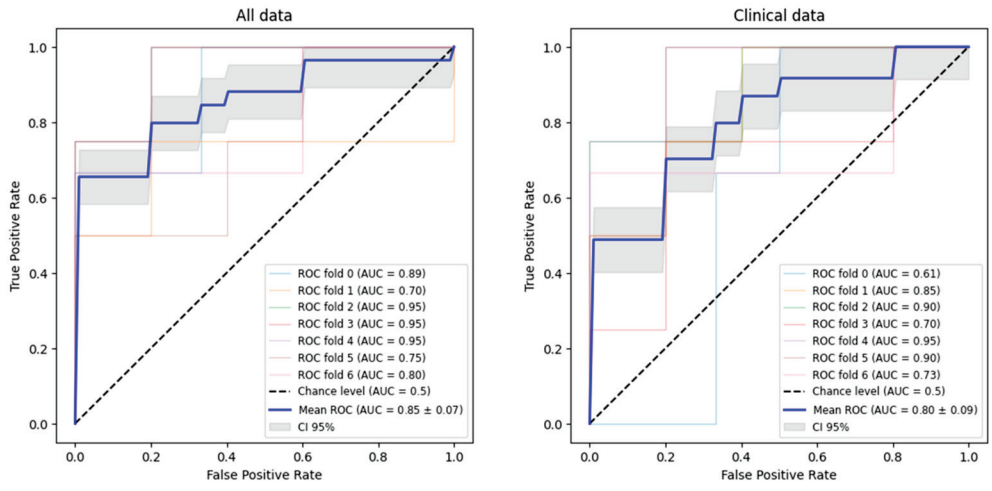


(a) (b)

Figure 4. Classification results of the final model fit on all data: scatter plot (**a**) and confusion matrix (**b**). Blue points (0) correspond to patients without complications (n = 36), orange points (1) correspond to patients with complications (n = 26) in (**a**).

Table 2. Characteristics of multi- and univariate predictive models for the post-operative cardiac complications.

Models	ROC-AUC, 95% CI	Sensitivity, 95% CI	Specificity, 95% CI
Multivariate models			
All data	0.85 (0.78, 0.92)	0.81 (0.77, 0.85)	0.79 (0.75, 0.83)
Clinical data	0.80 (0.71, 0.89)	0.66 (0.63, 0.69)	0.78 (0.72, 0.84)
Metabolites and biomarkers	0.71 (0.56, 0.86)	0.72 (0.69, 0.75)	0.47 (0.43, 0.51)
Univariate models			
SOFA	0.79 (0.73, 0.85)	0.67 (0.62, 0.72)	0.84 (0.75, 0.93)
ΔΣ3AMM	0.70 (0.62, 0.78)	0.59 (0.55, 0.73)	0.79 (0.75, 0.83)
Lactate	0.62 (0.42, 0.82)	0.74 (0.66, 0.82)	0.61 (0.56, 0.66)
Δp-HPhLA	0.58 (0.47, 0.69)	0.85 (0.80, 0.90)	0.48 (0.41, 0.55)
EuroScore2	0.54 (0.38, 0.70)	0.49 (0.3, 0.55)	0.63 (0.59, 0.67)



(a) (b)

Figure 5. *Cont.*

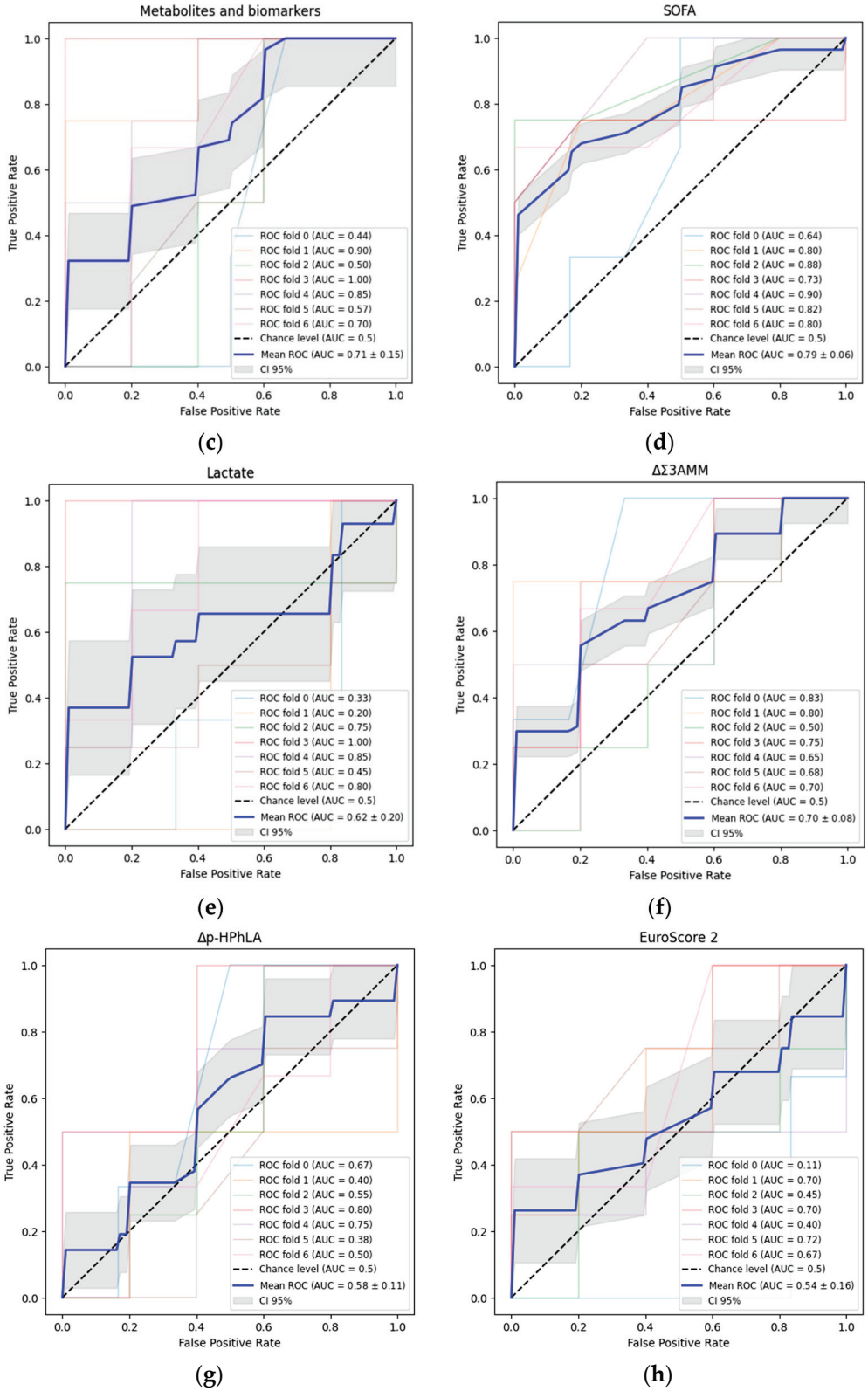


Figure 5. ROC curves for three multivariate models based on all data (**a**), clinical data (**b**), metabolites and biomarkers (**c**); and five univariate models based on SOFA (**d**), lactate (**e**), ΔΣ3AMM (**f**), Δp-HPhLA (**g**), and EuroScore2 (**h**). Blue lines explain means of true positive rate/false positive rate co-ordinates. Other lines show different cross-validation splits. Grey zone demonstrates 95% CI.

4. Discussion

Cardiac surgery remains one of the types of operation after which complications can arise, despite the development of medicine and the improvement in the quality of medical care provided. Early prediction of post-operative complications is crucial. In the early post-operative period, either medical prophylaxis or simply stricter monitoring can be performed to effectively avoid undesirable consequences of invasive treatment [16]. This was the main reason why we focused on data that were available in the pre-operative and early peri-operative periods in the current study.

Researchers have identified various risk factors for the development of post-operative complications. They can be divided into three groups: patient characteristics (female sex, obesity, smoking), clinician characteristics (volume of infusion, duration of surgery, doses of assigned medications), and post-operative factors (clinical decisions and nursing) [2,20]. The use of cardiopulmonary bypass in cardiac surgery is considered to be one of the main risk factors that disrupts metabolic pathways, mainly due to the activation of oxidative stress [21]. This fact served as the basis for including in our study only those patients who had cardiac surgery with a cardiopulmonary bypass, to search for parameters that could distinguish patients with and without complications. In our study, clinical parameters that significantly differ in patients with and without complications were infusion volume, on-pump time, SOFA, number of erythrocytes transfusion, and blood loss in the 1st day (Table 1). Data on on-pump time correlated with another study where this parameter was also higher in the complicated group of patients [22].

Biomarkers are widely used in cardiac surgery. All of them generally explain one or a few types of complication. NT-proBNP marks atrial wall distraction [23], cardiac troponins—biomarkers of ischemic processes in cardiac tissue [5,24], PCT and IL6—markers of inflammation and infectious processes [25], lactate—a marker of tissue hypoxia [26] in prediction of post-operative complications after cardiac surgery. Inflammatory biomarkers IL6 and PCT are not always specific for assessing the severity of the infectious process in cardiac surgery patients. Cardiac surgery causes an increase in the PCT level, even in the absence of complications, but its level usually does not exceed 5 ng/mL. Patients with a complicated post-operative course, with infection or sepsis, showed higher PCT and IL6 levels than patients with an uncomplicated course [27–29]. Endogenous intoxication due to infection can worsen the function of the heart, which can manifest itself both clinically and in a laboratory. NT-proBNP is used in the diagnosis of heart failure. Its values always increase during the first few days after open heart surgery, with a further gradual decrease if there are no complications. Typically, NT-proBNP values are higher in more severe patients receiving inotropic therapy. Another promising biomarker to evaluate post-operative complications is HST-T, the release of which should be expected after all CABG procedures. It depends on the procedure, the nature of the cardioplegia, and many other factors. The peak HST-T concentration usually occurs within 24 to 48 h after the operation [30]. In this study, the level of HST-T in the complicated group was significantly higher than in the group of patients without complications. This can be explained by the fact that infectious complications developed more in those patients who had primary cardiac complications in the intraoperative or early post-operative periods: myocardial infarction, myocardial injury, and severe heart failure. Patients with primary cardiac complications have a greater risk of bacterial infection [31]. However, our findings correlate with data from a study that included 1318 patients after CABG surgery, with a peak HST-T level greater than 400 ng/L, measured within 24 h, and associated with a major adverse cardiac or cerebrovascular event, 30-day mortality, myocardial infection, and ICU stay>48 h [32].

Various studies were conducted to reveal metabolic changes after cardiac surgery [7,8,10]. In our previous study, higher serum concentrations of metabolites of phenylalanine and tyrosine in the complicated group of cardiac surgery patients were detected [17]. In the current study, among metabolites and biomarkers, only HST-T after the surgery differed significantly in two groups of patients, but differences between metabolites and biomarkers (point 1–point 0) were statistically significant among a few characteristics (ΔΣ3AMM, ΔPCT,

ΔNT-pro-BNP, ΔHST-T). These facts show that dynamic changes are important for the prediction of post-operative complications. In our previous study, additional statistically significant differences in Δp-HPhAA and Δp-HPhLA were obtained [17], which we did not observe in the current study, but we obtained statistically significant differences in the dynamics of the sum of p-HPhAA and Δp-HPhLA, together with PhLA—ΔΣ3AMM. These two studies repeatedly demonstrated the altered metabolism of phenylalanine and tyrosine in high-risk patients, with a predominance of the sepsis-associated metabolites of microbial origin [33].

Machine learning is a powerful tool that can be used for the prediction of post-operative complications. In cardiac surgery, it has been successfully used for the prognostication of post-operative atrial fibrillation [12] and acute kidney injury [34]. Although some studies have described the results as applying predictive models built only on clinical data, they have demonstrated different predictive ability. Zhang et al. reported predictive models with ROC-AUC = 0.94 for XGBoost and ROC-AUC = 0.75 for support vector machines built on records of monitoring during off-pump CABG [35]. Li et al. demonstrated ROC-AUC for different models lower than 0.70 [22]. Despite the relatively good predictive ability of clinical data, prognostic models based on metabolomic data have shown growing popularity in diagnostics because of their potential. In particular, in patients with aortic dissection, there have been results showing the marking of impaired metabolic pathways, and suggesting potential biomarkers for different conditions and diseases [10]. There have also been attempts to use metabolites and biomarkers with clinical data in machine learning for the prediction of post-operative delirium and acute kidney injury [16,36]. Our PLS-DA models fitted on metabolites and biomarkers demonstrated moderate predictive value with ROC-AUC = 0.71 and sensitivity/specificity 0.72/0.47. The model fitted only on clinical data demonstrated better predictive value with ROC-AUC = 0.80 and sensitivity/specificity 0.66/0.78. Finally, the best results were obtained for the model with the entire set of data—ROC-AUC = 0.85 and sensitivity/specificity of 0.81/0.79. This fact gives us the opportunity to suppose that the use of metabolites and biomarkers in predictive models in cardiac surgery may improve their sensitivity and specificity for recognizing post-surgical complications.

As additional data and for comparison, we built a series of univariate models. In the current study, EuroScore2 scale performed poorly on patient group discrimination (ROC-AUC = 0.54 and sensitivity/specificity of 0.49/0.63). As noted, baseline microbiome parameters (microbial metabolites) and biomarkers did not show significant differences between the groups of patients with and without complications in our study. Accordingly, the prognostic value of these parameters was not confirmed in this cohort. Although the EuroScore2 scale is a widely accepted tool for pre-operative risk assessment based on clinical and demographic data risks [37], a direct comparison with other models was not necessary or appropriate in this study. This is because the studied approaches assess different aspects of risk. However, our results indicate the need for further studies with a larger sample of patients to more accurately assess the prognostic value of the microbial metabolites and biomarkers.

The SOFA scale showed the best results in univariate models with the best specificity (ROC-AUC = 0.79 and sensitivity/specificity of 0.67/0.84), despite the fact that it is usually used for mortality prediction and it may have different predictive ability for various pathologic conditions [38]. We also examined the model on lactate—ROC-AUC = 0.62 and sensitivity/specificity of 0.74/0.61, and it may be compared with data on the predictive ability of this biomarker with those in other conditions, despite the fact that lactate is not used as a specific biomarker for cardiac surgery [39,40].

In our previous study, we received ROC-AUC = 0.71 and sensitivity/specificity of 0.81/0.56 for Σ3AMM and ROC-AUC = 0.69, and sensitivity/specificity of 0.79/0.47 for p-HPhLA for the prediction of all types of post-operative complications after aortic prosthetics [17]. In the current study, two univariate models using ΔΣ3AMM and Δp-HPhLA for the prediction of complications were built, and demonstrated predictive ability with

ROC-AUC = 0.70 and sensitivity/specificity of 0.59/0.79 for ΔΣ3AMM, and ROC-AUC = 0.58, with the best sensitivity among all models—0.85 and poor specificity—0.50 for Δp-HPhLA.

Our pilot single-center study has a number of limitations. Firstly, the number of patients was relatively low, which meant we could not evaluate the contribution of sex, age, comorbidity, and off-pump surgeries on the statistics and quality of predictive models. Secondly, we considered all types of complication, despite the fact that different types of complication have different developmental pathophysiology. However, we supposed that the microbiota disruption, indirectly assessed by the level of microbial metabolites, could affect the development of all types of complication. Also, there were data on some serum samples in the latest days (the third and sixth) after surgery that were not analyzed. The short follow-up period of the study restricted the ability to assess long-term outcomes and complications. A longer follow-up would provide a more comprehensive understanding of the predictive value of the proposed integrated approach. However, making therapeutic decisions at the earliest stages, namely before surgery or in the early post-operative period, is most important in cardiac surgery for the successful management of patients in the post-operative period.

In cardiac surgery patients who developed infectious complications in the post-operative period, statistically significant changes in the taxonomic composition of the microbiota were detected, even before surgery, compared to patients without complications, while there were no differences in routine clinical and specific biochemical markers [18]. This is a potential target for reducing the risks of infectious complications. In this work, we assessed only a part of the clinical parameters, microbiota metabolites, and biomarkers, and perhaps expanding their range in the future will allow us to identify complications specific to the development, even before surgery, which will make diagnosis faster and more accessible.

5. Conclusions

Using levels of certain metabolites and biomarkers circulating in the blood, in combination with clinical data, can help improve the predictive ability of diagnostic algorithms. It is essential to explore methods to regulate microbiota metabolism to improve surgical outcomes in the future by finding alternatives to compensate for its functions. For these purposes, it is important to organize and conduct multi-center studies in which it would be possible to study various approaches to pre-operative influences on the microbiota of patients in order to reduce the incidence of any type of post-operative complication in cardiac surgery.

Author Contributions: Conceptualization, E.Z. and N.B.; methodology, E.Z., A.P. and E.C.; formal analysis, P.M.; investigation, E.Z., A.P., E.S. and E.C.; resources, E.Z. and N.B.; data curation, E.Z. and N.B.; writing—original draft preparation, A.P., P.M. and E.S.; writing—review and editing, E.Z., N.B. and E.C.; visualization, P.M.; supervision, A.P., N.B. and E.C.; project administration, A.P. and E.Z.; funding acquisition, N.B. All authors have read and agreed to the published version of the manuscript.

Funding: This research received no external funding.

Institutional Review Board Statement: The study was conducted in accordance with the Declaration of Helsinki, and approved by the local Ethics Committee of N. Pirogov National Medical Surgical Center, Moscow, Russian Federation (protocol no. 04 from 22 May 2018).

Informed Consent Statement: Informed consent was obtained from all subjects involved in the study.

Data Availability Statement: The original contributions presented in the study are included in the article, further inquiries can be directed to the corresponding author.

Conflicts of Interest: The authors declare no conflicts of interest.

References

1. Crawford, T.C.; Magruder, J.T.; Grimm, J.C.; Suarez-Pierre, A.; Sciortino, C.M.; Mandal, K.; Zehr, K.J.; Conte, J.V.; Higgins, R.S.; Cameron, D.E.; et al. Complications After Cardiac Operations: All Are Not Created Equal. *Ann. Thorac. Surg.* **2017**, *103*, 32–40. [CrossRef]
2. Montrief, T.; Koyfman, A.; Long, B. Coronary artery bypass graft surgery complications: A review for emergency clinicians. *Am. J. Emerg. Med.* **2018**, *36*, 2289–2297. [CrossRef] [PubMed]
3. Lazzeri, C.; Valente, S.; Chiostri, M.; Gensini, G.F. Clinical significance of Lactate in acute cardiac patients. *World J. Cardiol.* **2015**, *7*, 483. [CrossRef]
4. Chen, X.; Li, H.-Y.; Hu, X.-M.; Zhang, Y.; Zhang, S.-Y. Current understanding of gut microbiota alterations and related therapeutic intervention strategies in heart failure. *Chin. Med. J.* **2019**, *132*, 1843–1855. [CrossRef] [PubMed]
5. Kavsak, P.A.; Belley-Cote, E.P.; Whitlock, R.P.; Lamy, A. Cardiac troponin testing in cardiac surgery. *Expert Rev. Cardiovasc. Ther.* **2023**, *21*, 729–731. [CrossRef]
6. Gowda, G.N.; Zhang, S.; Gu, H.; Asiago, V.; Shanaiah, N.; Raftery, D. Metabolomics-based methods for early disease diagnostics. *Expert Rev. Mol. Diagn.* **2008**, *8*, 617–633. [CrossRef]
7. Cui, H.; Shu, S.; Li, Y.; Yan, X.; Chen, X.; Chen, Z.; Hu, Y.; Chang, Y.; Hu, Z.; Wang, X.; et al. Plasma Metabolites-Based Prediction in Cardiac Surgery-Associated Acute Kidney Injury. *J. Am. Heart Assoc.* **2021**, *10*, e021825. [CrossRef] [PubMed]
8. Tripp, B.A.; Dillon, S.T.; Yuan, M.; Asara, J.M.; Vasunilashorn, S.M.; Fong, T.G.; Metzger, E.D.; Inouye, S.K.; Xie, Z.; Ngo, L.H.; et al. Targeted metabolomics analysis of postoperative delirium. *Sci. Rep.* **2021**, *11*, 1521. [CrossRef] [PubMed]
9. Gregory, A.J.; Noss, C.D.; Chun, R.; Gysel, M.; Prusinkiewicz, C.; Webb, N.; Raymond, M.; Cogan, J.; Rousseau-Saine, N.; Lam, W.; et al. Perioperative Optimization of the Cardiac Surgical Patient. *Can. J. Cardiol.* **2023**, *39*, 497–514. [CrossRef]
10. Gong, Y.; Li, T.; Liu, Q.; Wang, X.; Deng, Z.; Cheng, L.; Yu, B.; Liu, H. Analysis of differential metabolites in serum metabolomics of patients with aortic dissection. *BMC Cardiovasc. Disord.* **2024**, *24*, 1–10. [CrossRef]
11. Dodd, D.; Spitzer, M.H.; Van Treuren, W.; Merrill, B.D.; Hryckowian, A.J.; Higginbottom, S.K.; Le, A.; Cowan, T.M.; Nolan, G.P.; Fischbach, M.A.; et al. A gut bacterial pathway metabolizes aromatic amino acids into nine circulating metabolites. *Nature* **2017**, *551*, 648–652. [CrossRef] [PubMed]
12. Lu, X.; Liu, J.; Zhou, B.; Wang, S.; Liu, Z.; Mei, F.; Luo, J.; Cui, Y. Microbial metabolites and heart failure: Friends or enemies? *Front. Microbiol.* **2022**, *13*, 956516. [CrossRef]
13. Chernevskaya, E.A.; Getsina, M.L.; Cherpakov, R.A.; Sorokina, E.A.; Shabanov, A.K.; Moroz, V.V.; Beloborodova, N.V. Sepsis-Associated Metabolites and Their Biotransformation by Intestinal Microbiota. *Gen. Reanimatol.* **2023**, *19*, 4–12. [CrossRef]
14. Bai, Y.; Huang, W.; Jiang, X.; Xu, W.; Li, Y.; Wang, Y.; Huang, S.; Wu, K.; Hu, L.; Chen, C. Metabolomic interplay between gut microbiome and plasma metabolome in cardiac surgery-associated acute kidney injury. *Rapid Commun. Mass Spectrom.* **2023**, *37*, e9504. [CrossRef] [PubMed]
15. Davidson, J.A.; Robison, J.; Khailova, L.; Frank, B.S.; Jaggers, J.; Ing, R.J.; Lawson, S.; Iguidbashian, J.; Ali, E.; Treece, A.; et al. Metabolomic profiling demonstrates evidence for kidney and urine metabolic dysregulation in a piglet model of cardiac surgery-induced acute kidney injury. *Am. J. Physiol. Physiol.* **2022**, *323*, F20–F32. [CrossRef]
16. Wiredu, K.; O'Connor, S.; Naseem, H.; Brauer, B.L.; Kettenbach, A.N.; Frost, H.R.; Shaefi, S.; Gerber, S.A. Intraoperative plasma proteomic changes in cardiac surgery: In search of biomarkers of post-operative delirium. *PROTEOMICS—Clin. Appl.* **2023**, *17*, e2200066. [CrossRef]
17. Beloborodova, N.; Pautova, A.; Grekova, M.; Yadgarov, M.; Grin, O.; Eremenko, A.; Babaev, M. Microbiota Metabolism Failure as a Risk Factor for Postoperative Complications after Aortic Prosthetics. *Biomedicines* **2023**, *11*, 1335. [CrossRef]
18. Chernevskaya, E.; Zuev, E.; Odintsova, V.; Meglei, A.; Beloborodova, N. Gut Microbiota as Early Predictor of Infectious Complications before Cardiac Surgery: A Prospective Pilot Study. *J. Pers. Med.* **2021**, *11*, 1113. [CrossRef] [PubMed]
19. Pautova, A.K.; Burnakova, N.A.; Beloborodova, N.V.; Revelsky, A.I. Simultaneous Determination of Aromatic, Short-Chain Fatty and Dicarboxylic Acids in Blood Serum and Cerebrospinal Fluid by Gas Chromatography–Mass Spectrometry. *J. Anal. Chem.* **2023**, *78*, 1942–1954. [CrossRef]
20. Ruslyakova, I.A.; Belyakov, K.S.; Abdulrazakov, A.A.; Marinin, V.A. Predictors of Complications Related to Cardiac Ablation for Atrial Arrhythmias. *Gen. Reanimatol.* **2024**, *20*, 4–14. [CrossRef]
21. Gonenc, A.; Hacışevki, A.; Griffiths, H.R.; Torun, M.; Bakkaloglu, B.; Simsek, B. Free radical reaction products and antioxidant capacity in beating heart coronary artery surgery compared to conventional bypass. *Biochemistry* **2011**, *76*, 677–685. [CrossRef] [PubMed]
22. Li, Q.; Lv, H.; Chen, Y.; Shen, J.; Shi, J.; Zhou, C. Development and validation of a machine learning predictive model for perioperative myocardial injury in cardiac surgery with cardiopulmonary bypass. *J. Cardiothorac. Surg.* **2024**, *19*, 384. [CrossRef]
23. Turagam, M.K.; Mirza, M.; Werner, P.H.; Sra, J.; Kress, D.C.; Tajik, A.J.; Jahangir, A. Circulating Biomarkers Predictive of Postoperative Atrial Fibrillation. *Cardiol. Rev.* **2016**, *24*, 76–87. [CrossRef] [PubMed]
24. Forner, J.; Schupp, T.; Weidner, K.; Rusnak, J.; Jawhar, S.; Dulatahu, F.; Brück, L.M.; Behnes, M.; Hoffmann, U.; Bertsch, T.; et al. Cardiac Troponin I Reveals Diagnostic and Prognostic Superiority to Aminoterminal Pro-B-Type Natriuretic Peptide in Sepsis and Septic Shock. *J. Clin. Med.* **2022**, *11*, 6592. [CrossRef]
25. Bavare, A.; Rissmiller, B.; Devaraj, S.; Guffey, D.; Rajapakshe, D.; Weiner, H.; Caldarone, C.; Shekerdemian, L. Perioperative Procalcitonin in Predicting Infection in Children Undergoing Surgical Procedures. *J. Surg. Res.* **2021**, *258*, 332–338. [CrossRef]

26. Stephens, E.H.; Epting, C.L.; Backer, C.L.; Wald, E.L. Hyperlactatemia: An Update on Postoperative Lactate. *World J. Pediatr. Congenit. Heart Surg.* **2020**, *11*, 316–324. [CrossRef]
27. Sponholz, C.; Sakr, Y.; Reinhart, K.; Brunkhorst, F. Diagnostic value and prognostic implications of serum procalcitonin after cardiac surgery: A systematic review of the literature. *Crit. Care* **2006**, *10*, 1–11. [CrossRef] [PubMed]
28. Sander, M.; von Heymann, C.; von Dossow, V.; Spaethe, C.; Konertz, W.F.; Jain, U.; Spies, C.D. Increased Interleukin-6 After Cardiac Surgery Predicts Infection. *Anesth. Analg.* **2006**, *102*, 1623–1629. [CrossRef]
29. Xie, M.; Chen, Y.T.; Zhang, H.; Zhang, H.T.; Pan, K.; Chen, X.F.; Xie, X.L. Diagnostic Value of Procalcitonin and Interleukin-6 on Early Postoperative Pneumonia after Adult Cardiac Surgery: A Prospective Observational Study. *Heart Surg. Forum* **2022**, *25*, E020–E029. [CrossRef]
30. Gu, Y.; Shan, L.; Liu, B.; Lv, M.; Chen, X.; Yan, T.; Shi, Y.; Chen, J.; Li, Z.; Zhang, Y. Release Profile of Cardiac Troponin T and Risk Factors of Postoperative Myocardial Injury in Patients Undergoing CABG. *Int. J. Gen. Med.* **2021**, *14*, 2541–2551. [CrossRef]
31. Singh, N.; Anchan, R.K.; Besser, S.A.; Belkin, M.N.; Cruz, M.D.; Lee, L.; Yu, D.; Mehta, N.; Nguyen, A.B.; Alenghat, F.J. High sensitivity Troponin-T for prediction of adverse events in patients with COVID-19. *Biomarkers* **2020**, *25*, 626–633. [CrossRef] [PubMed]
32. Nellipudi, J.A.; Baker, R.A.; Dykes, L.; Krieg, B.M.; Bennetts, J.S. Prognostic Value of High-Sensitivity Troponin T After On-Pump Coronary Artery Bypass Graft Surgery. *Heart Lung Circ.* **2021**, *30*, 1562–1569. [CrossRef]
33. Zhizhin, K.Y.; Turyshev, E.S.; Pautova, A.K.; Beloborodova, N.V.; Kuznetsov, N.T. Methodology for the determining aromatic monocarboxylic acids as products of phenylalanine and tyrosine metabolism: Current advances and trends. *Russ. Chem. Rev.* **2024**, *93*, RCR5119. [CrossRef]
34. Jia, T.; Xu, K.; Bai, Y.; Lv, M.; Shan, L.; Li, W.; Zhang, X.; Li, Z.; Wang, Z.; Zhao, X.; et al. Machine-learning predictions for acute kidney injuries after coronary artery bypass grafting: A real-life muticenter retrospective cohort study. *BMC Med. Inform. Decis. Mak.* **2023**, *23*, 270. [CrossRef]
35. Zhang, Y.; Li, L.; Li, Y.; Zeng, Z. Machine learning model-based risk prediction of severe complications after off-pump coronary artery bypass grafting. *Adv. Clin. Exp. Med.* **2022**, *32*, 185–194. [CrossRef]
36. Chen, Z.; Chen, L.; Yao, G.; Yang, W.; Yang, K.; Xiong, C. Novel Blood Cytokine-Based Model for Predicting Severe Acute Kidney Injury and Poor Outcomes After Cardiac Surgery. *J. Am. Heart Assoc.* **2020**, *9*, 18004. [CrossRef]
37. van Dijk, W.B.; Leeuwenberg, A.M.; Grobbee, D.E.; Siregar, S.; Houterman, S.; Daeter, E.J.; de Vries, M.C.; Groenwold, R.H.H.; Schuit, E.; Bramer, S.; et al. Dynamics in cardiac surgery: Trends in population characteristics and the performance of the EuroSCORE II over time. *Eur. J. Cardio-Thoracic Surg.* **2023**, *64*, 301. [CrossRef]
38. Schoe, A.; Bakhshi-Raiez, F.; de Keizer, N.; van Dissel, J.T.; de Jonge, E. Mortality prediction by SOFA score in ICU-patients after cardiac surgery; comparison with traditional prognostic–models. *BMC Anesthesiol.* **2020**, *20*, 65. [CrossRef]
39. Meyer, Z.C.; Schreinemakers, J.M.J.; de Waal, R.A.L.; van der Laan, L. Searching for predictors of surgical complications in critically ill surgery patients in the intensive care unit: A review. *Surg. Today* **2015**, *45*, 1091–1101. [CrossRef]
40. Cho, H.; Jung, J.-Y.; Yoon, H.-K.; Yang, S.-M.; Lee, H.-J.; Kim, W.H.; Jung, C.-W.; Suh, K.-S. Serum neutrophil gelatinase-associated lipocalin and lactate level during surgery predict acute kidney injury and early allograft dysfunction after liver transplantation. *Sci. Rep.* **2023**, *13*, 8643. [CrossRef] [PubMed]

Disclaimer/Publisher's Note: The statements, opinions and data contained in all publications are solely those of the individual author(s) and contributor(s) and not of MDPI and/or the editor(s). MDPI and/or the editor(s) disclaim responsibility for any injury to people or property resulting from any ideas, methods, instructions or products referred to in the content.

molecules

MDPI

Article

Quantitative Analysis of Cenobamate and Concomitant Anti-Seizure Medications in Human Plasma via Ultra-High Performance Liquid Chromatography–Tandem Mass Spectrometry

Linda Molteni [1,*], Bruno Charlier [2,3], Albino Coglianese [2,4], Viviana Izzo [2,3], Giovanni Assenza [5], Pierantonio Menna [5,6], Ugo de Grazia [1,†] and Annachiara D'Urso [1,*]

[1] SSD Laboratory Medicine, Fondazione IRCCS "Istituto Neurologico Carlo Besta", 20133 Milan, Italy; ugo.degrazia@virgilio.it
[2] Department of Medicine, Surgery and Dentistry "Scuola Medica Salernitana", University of Salerno, Baronissi, 84081 Salerno, Italy; bcharlier@unisa.it (B.C.); albino.cog@gmail.com (A.C.); vizzo@unisa.it (V.I.)
[3] University Hospital "San Giovanni di Dio e Ruggi d'Aragona", 84131 Salerno, Italy
[4] Graduate School in Clinical Pathology and Clinical Biochemistry, University of Salerno, Baronissi, 84081 Salerno, Italy
[5] Fondazione Policlinico Universitario Campus Bio-Medico, 00128 Rome, Italy; g.assenza@policlinicocampus.it (G.A.); p.menna@policlinicocampus.it (P.M.)
[6] Department of Science and Technology for Sustainable Development and One Health, University Campus Biomedico di Roma, 00128 Rome, Italy
* Correspondence: linda.molteni@istituto-besta.it (L.M.); annachiara.durso@istituto-besta.it (A.D.)
† Current address: Pharmacotoxicology Unit, Centro Diagnostico Italiano C.D.I., 20147 Milan, Italy.

Abstract: Cenobamate (CNB) is a new anti-seizure medication (ASM) recently introduced in clinical practice after approval by the FDA and EMA for the add-on treatment of focal onset seizures in adult patients. Although its mechanism of action has not been fully understood, CNB showed promising clinical efficacy in patients treated with concomitant ASMs. The accessibility of CNB could pave a way for the treatment of refractory or drug-resistant epilepsies, which still affect at least one-third of the patients under pharmacological treatment. In this context, therapeutic drug monitoring (TDM) offers a massive opportunity for better management of epileptic patients, especially those undergoing combined therapy. Here, we describe the first fully validated ultra-high performance liquid chromatography-tandem mass spectrometry (UHPLC–MS/MS) method for the quantification of CNB and concomitant ASMs in human plasma, with samples extracted either manually or by means of a liquid handler. Our method was validated according to the most recent ICH International Guideline M10 for Bioanalytical Method Validation and Study Sample Analysis. The method proved to be selective for CNB and displayed a linear range from 0.8 to 80 mg/L; no matrix effect was found (98.2 ± 4.1%), while intra-day and inter-day accuracy and precision were within the acceptance range. Also, CNB short- and long-term stability in plasma under different conditions was assessed. Leftover human plasma samples were employed as study samples for method validation. Our method proved to be highly sensitive and selective to quantify CNB and concomitant ASMs in human plasma; therefore, this method can be employed for a routinely TDM-based approach to support physicians in the management of an epileptic patient.

Keywords: cenobamate; anti-seizure medications; therapeutic drug monitoring; pharmacokinetics; UHPLC–MS/MS

1. Introduction

Epilepsy is one of the most common and heterogeneous neurological disorders, affecting about 70 million people worldwide. It is estimated that in industrialized countries

almost 3–4% of people will develop epilepsy during their lifetime; the risk is higher in developing countries, exacerbating the deleterious effects on physical, psychological, and social well-being [1,2].

The treatment of epilepsies is merely symptomatic, with no currently available therapies able to correct the underlying disorder, instead only aimed at suppressing seizure manifestation [3]. For this reason, people with epilepsies will need a lifelong treatment, characterized by frequent changes in medicaments and polytherapy [1,3,4].

The administration of anti-seizure medications (ASMs) is considered the mainstay treatment against epilepsies [1,4]; even though novel ASMs have been introduced in recent years, along with first-, second-, and third-generation drugs already available for pharmacological treatment, there is no evidence of any improvement in treatment outcomes in patients with newly diagnosed epilepsies within the past two decades [3,5].

In a previous study, it was found that barely two-thirds of the patients with newly diagnosed epilepsies have reached seizure freedom, intended as 100% seizure reduction after ASMs treatment, while one-third of patients continued to have partial seizure control. In particular, those who did not respond to the first or second ASM regimen were more prone to develop refractory or drug-resistant epilepsies [6,7]. It has also been shown that the probability of becoming seizure-free decreases with subsequent ineffective ASM treatments [3,5]. In this scenario, it is clear that refractory epilepsies still represent a great challenge, with an unmet need for new treatment strategies aimed at ensuring long-term seizure control [8].

Cenobamate (CNB) ([(*R*)-1-(2-chlorophenyl)-2-(2*H*-tetrazol-2-yl)ethyl]) is a tetrazole alkyl carbamate derivative (Figure 1), recently introduced in clinical practice as an ASM. In November 2019, the Food and Drug Administration (FDA) approved XCOPRI®, marketed by SK Life Science Inc. (Paramus, NJ, USA) for the adjunctive treatment of focal onset seizures with or without secondary generalization in adult patients. Afterwards, in March 2021, the European Medicines Agency (EMA) approved Ontozry®, marketed by Arvelle Therapeutics Netherlands B.V. (Amsterdam, The Netherlands) [9,10].

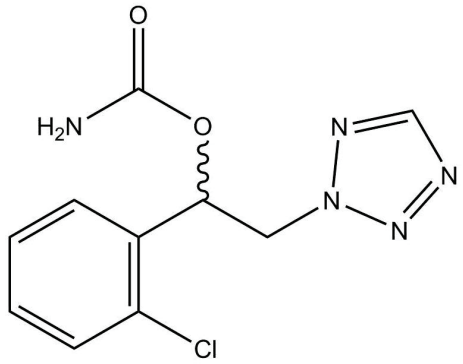


Figure 1. Chemical structure of CNB.

CNB's short-term efficacy was demonstrated in two randomized, double-blind, multicenter, placebo-controlled clinical trials (YKP3089C013; NCT01397968 and YKP3089C017; NCT01866111) in which CNB was administrated once daily as an adjunctive treatment in adults with drug-resistant focal seizures. It was found that CNB reduced seizure frequency by at least 50% in 50.1% of the patients randomized to receive CNB adjunctively to their existing ASMs, compared to placebo and in a dose-dependent manner. In addition, seizure freedom rates were higher and dose-dependent in the CNB group compared to placebo, with 27.5% of patients achieving seizure freedom in the first trial [11–14]. Subsequent open-label extended clinical trials demonstrated that seizure freedom was maintained for up to 30 months [15]. CNB was well tolerated, with few central adverse events mainly due to the rate of the titration process (including dizziness, insomnia, diplopia, disturbances in gait and coordination) [16,17].

CNB showed a more favorable relationship between efficacy and tolerability when compared with other ASMs, suggesting that it may have a different and unique mechanism of action responsible for its clinical efficacy [9,18]. The precise mechanism of action of CNB has not been established yet, but in vitro data suggest that CNB might regulate both excitatory and inhibitory transmission. Nakamura et al. have shown that CNB targets voltage-gated sodium channels and inhibits the persistent component of the sodium ion current (I_{NaP}) in hippocampal CA3 neurons, thus, hindering repetitive firing [19]. Moreover, Sharma et al. have demonstrated that CNB acts as a positive allosteric modulator of human γ-aminobutyric acid (GABA) receptors by binding to non-benzodiazepine sites, hence, regulating both phasic and tonic currents [20].

In this context, CNB's suggested mechanism of action represents a novelty in the sphere of ASMs; only phenytoin (PHT) shares a similar action on I_{NaP}. However, despite this analogy, PHT shows a narrower anti-seizure profile when compared to CNB. Moreover, the more conventional sodium-blocker ASMs act on the transient component of the sodium ion currents (I_{NaT}), which is primarily responsible for the rapid depolarization of the action potential, rather than on I_{NaP}, which is suggested to be involved in the amplification of subthreshold synaptic potentials and the facilitation of repetitive firing in neurons [21]. This implies that the inhibition of I_{NaP} could play a crucial but not sufficient role in order to explain CNB's clinical efficacy. The combination of both excitatory and inhibitory regulation is thought to contribute to the broad anti-seizure spectrum of CNB and could explain its promising efficacy [9,18].

In the abovementioned clinical trials, CNB was administered as an adjunctive treatment with one to three other concomitant ASMs. Thus, it is of crucial importance to evaluate both pharmacokinetics (PK) and pharmacodynamics (PD) interactions between CNB and co-administered ASMs [16]. After a single oral administration, CNB is rapidly adsorbed (t_{max} = 1–4 h), showing high bioavailability (88%), and is moderately bound to plasma proteins (60%). Its plasma exposure increases with drug concentration, with a more than proportional increase at high doses. CNB showed a long half-life ($t_{1/2}$ = 50–60 h) within the therapeutic dose range (100–400 mg/die). The prolonged $t_{1/2}$ and the more than proportional plasma exposure of CNB at high doses suggest a non-linear process of distribution and elimination. CNB is primarily metabolized in the liver by both phase II and phase I reactions, the latter carried out by several cytochrome P450 (CYP) isoforms, including CYP2E1, CYP2A6, CYP2B6, CYP2C19, and CYP3A4/5. As a CYP substrate, CNB affects CYP activity by inhibiting or inducing different CYP isoenzymes, including CYP2C19 or CYP2C8. Interestingly, it can also inhibit or induce CYP2B6 and CYP3A4 isoforms. No effect on transporter proteins has been shown [10,22].

Several studies were carried out to assess drug–drug interactions (DDIs) between CNB and other concomitant ASMs. It was shown, for example, that PHT and phenobarbital (PB) reduced the area under the curve (AUC) of CNB; interestingly, by inhibiting CYP2C19, CNB was also able to increase plasma concentrations of PB, PHT, brivaracetam (BRV), and cannabidiol. Moreover, by inducing CYP3A4, CNB was able to reduce the plasma concentrations of lamotrigine (LTG) and carbamazepine (CBZ). A decrease in plasma concentrations of clonazepam, ethosuximide (ETS), felbamate, midazolam, perampanel (PMP), and zonisamide (ZNS) is also expected. CNB interactions were assessed on other types of drugs, including omeprazole, oral contraceptives, and bupropion, following the same mechanisms [10,16]. Despite this preliminary evidence, more extensive clinical studies will be needed to better clarify both DDIs induced by CNB and, most importantly, its mechanism of action, which has not been fully characterized yet.

As previously mentioned, CNB represents an add-on therapy to concomitant ASMs; therefore, its introduction in routine therapeutic drug monitoring (TDM), as already performed for the other ASMs, could be of crucial advantage. The measurement of CNB plasma concentrations might allow for a better definition of therapeutic ranges and give pivotal information on its PK under different conditions and when co-administered with

other ASMs. TDM of CNB could also help with concerns related to patient management in terms of efficacy and safety by identifying a personalized therapeutic plan.

Here, we describe an update of our previously validated method [23] for the simultaneous quantification of CNB and concomitant ASM plasma concentrations, including pregabalin (PGB), gabapentin (GBP), levetiracetam (LEV), ethosuximide (ETS), lamotrigine (LTG), primidone (PRM), lacosamide (LCS), zonisamide (ZNS), rufinamide (RUF), 10-OH-monohydroxycarbazepine (10-OH-MHD), brivaracetam (BRV), carbamazepine-epoxide (CBZ-E), topiramate (TPM), tiagabine (TGB), perampanel (PMP), and stiripentol (STP). CBZ, PB, PHT, and valproic acid (VPA) were excluded from this study, as in our laboratories these drugs are routinely monitored by immunochemistry assays.

Our UHPLC–MS/MS analytical method was validated according to the most recent ICH Guideline M10 on Bioanalytical Method Validation and Study Sample Analysis [24]. To the best of our knowledge, this represents the first fully validated UHPLC–MS/MS method for the simultaneous quantification of CNB and other ASMs in human plasma samples.

2. Results and Discussion

2.1. Comparison of Existing Methods

Thus far, only a few analytical methods have been developed for the quantification of CNB in plasma samples (Table 1). Oh et al. first developed a method for the quantification of CNB in rat plasma, paving the way for the determination of CNB using LC-MS/MS [25]. This method employed a simple protein precipitation extraction with carisbamate as internal standard and showed a short run time; however, the calibration range was quite limited (0.01–5 mg/L).

During phase 1 and phase 2 clinical studies, human plasma samples were analyzed to validate an LC-MS/MS method for the quantification of CNB; however, methodological and analytical procedures were not reported in detail [22]. The calibration range was limited (0.02–10 mg/L) and a simple protein precipitation extraction was employed; phenacetin was used as internal standard.

Other LC-MS/MS methods in human plasma were developed and applied for pharmacokinetic studies of CNB with both a single-ascending dose (SAD) and multiple-ascending dose (MAD) [26]. The first method, which was employed for both SAD and MAD studies, showed a calibration range from 0.02 to 25 mg/L; CNB was extracted with a simple protein precipitation extraction with acetonitrile, and phenacetin was used as internal standard. The second method was employed for MAD studies only and showed a more limited calibration range (0.02–10 mg/L); the samples were precipitated with acetonitrile and the obtained supernatant was evaporated and reconstituted with acetonitrile and water. Phenacetin was once again used as internal standard. The third and last method described by Vernillet et al. [26], employed for MAD studies, showed a more extended calibration range (0.05–40 mg/L) and a more complicated extraction procedure was used; lipid extraction with methyl tertiary-butyl ether was performed and the supernatant was then evaporated and reconstituted with methanol and water. This time, d4-cenobamate was introduced as internal standard, thus allowing a more robust quantification.

Most recently, our group has developed and validated a UHPLC–MS/MS method for the monitoring of CNB plasma concentrations in two patients who underwent CNB dose titration and concomitant ASM regimens [23]. This method represented a fast, simple, and robust tool for the quantification of CNB in a calibration range from 0.05 to 20 mg/L. A simple protein precipitation extraction with acetonitrile and lamotrigine-C13-d3 as internal standard was performed. The chromatographic separation was fast, with a 3.5 min run time.

Table 1. Comparison of existing analytical methods for the quantification of CNB in LC-MS/MS. EDTA = ethylenediamine tetraacetic acid; AcN = acetonitrile; MeOH = methanol; APCI = atmospheric pressure chemical ionization; ESI = electrospray ionization.

Methods	Calibration Range for CNB	Co-Detected Compounds	Matrix (Anticoagulant)	Extraction	Internal Standard	Chromatographic Separation			Mass Spectrometry Analysis	
						Column	Mobile Phase	Run Time	Instrument	Source
Drug Approval Package: XCOPRI [22]	0.02–10.00 mg/L	/	Human plasma (heparin)	Protein precipitation	Phenacetin	/	/	/	AB/MDS Sciex API 4000 (triple quadrupole)	/
Oh et al., 2019 [25]	0.01–5.00 mg/L	/	Rat plasma	Protein precipitation (AcN)	Carisbamate (30 mg/L)	C18 column	60:40 (*v*/*v*) ammonium formate (10 mM):AcN	3 min	AB/MDS Sciex API 4000 (triple quadrupole)	ESI
Vernillet et al., 2020 [26]	0.02–25.00 mg/L	/	Human plasma (sodium heparin)	Protein precipitation (AcN)	Phenacetin (0.01 mg/L)	C18 column	62:38 (*v*/*v*) ammonium acetate (2 mM):MeOH	/	Triple quadrupole mass spectrometer	Heated nebulizer source
	0.02–10.00 mg/L	/		Protein precipitation (AcN), evaporation and reconstitution with 40:60 (*v*/*v*) AcN:H_2O	Phenacetin (0.01 mg/L)	C18 column	62:38 (*v*/*v*) ammonium acetate (2 mM):MeOH	/	Triple quadrupole mass spectrometer	APCI
	0.05–40.00 mg/L	/		Lipid extraction (methyl tertiary-butyl ether), evaporation and reconstitution with 3:2 (*v*/*v*) MeOH:H_2O	d4-cenobamate (100 mg/L)	/	A: 1000; 1.00; 0.40 (*v*/*v*) H_2O:HCOOH:ammonium hydroxide B: 1000; 1.00; 0.40 (*v*/*v*) MeOH:HCOOH:ammonium hydroxide	/	Triple quadrupole mass spectrometer	TurboIon Spray®
Charlier et al., 2022 [23]	0.05–20.00 mg/L	/	Human plasma (EDTA)	Protein precipitation (AcN)	Lamotrigine-C13-d3 (2 mg/L)	Pentafluoro-phenyl column	A: H_2O:0.1% HCOOH B: AcN:0.1% HCOOH	3.5 min	Endura TSQ (triple quadrupole)	ESI
Our Method	0.80–80.00 mg/L	Other 16 ASMs	Human plasma (lithium heparin)	Protein precipitation (AcN) and dilution with mobile phase	Lamotrigine-C13-d3	C18 column	M1: H_2O:0.1% HCOOH M2: AcN:0.1% HCOOH	7 min	Xevo TQ-XS (triple quadrupole)	ESI

As a result of the introduction of CNB into a clinical practice in which several other ASMs are co-administered, the need to develop a single method for the simultaneous quantification of all other available ASMs has undoubtedly emerged. In this framework, our method provides a simple, robust, and rather fast quantification of CNB and 16 other ASMs within a single run. The plasma samples are extracted with a simple protein precipitation and, as in our previous method, lamotrigine-C13-d3 is used as internal standard. Employed by Vernillet et al. [26], d4-cenobamate represents the gold standard for the normalization of CNB signal, however, it is difficult to obtain; conversely, lamotrigine-C13-d3 is already used for the internal normalization of lamotrigine and was also found to provide good normalization capabilities for CNB. The chromatographic separation is simple and has a relatively short run time of 7 min. Moreover, the calibration range was extended from 0.80 to 80 mg/L, reflecting the plasma concentrations reported in the previous articles and those described by de Grazia et al. [27]. Finally, the simultaneous quantification of CNB and other ASMs within a single method allows us to save both reagent costs and time, also providing a tool for a more efficient clinical management of the patient.

2.2. Method Validation

The analytical method was fully validated for CNB, given that the quantification methods for the other compounds have been previously validated by the kit manufacturer and the CE/IVD kit for the quantification of other ASMs is already in use in our laboratory for routine TDM. Data on partial kit validation, as recommended by ICH Guideline M10 [24], for the quantification of concomitant ASMs are reported in Supplementary Material and are also discussed in a previous study [28].

The method proved to be selective and sensitive, since no chromatographic peaks from interfering components, including other ASMs, were observed, with a response higher than 20% of the lower limit of quantification (LLOQ) signal. Figure 2 shows representative chromatograms of blank plasma and samples spiked with CNB.

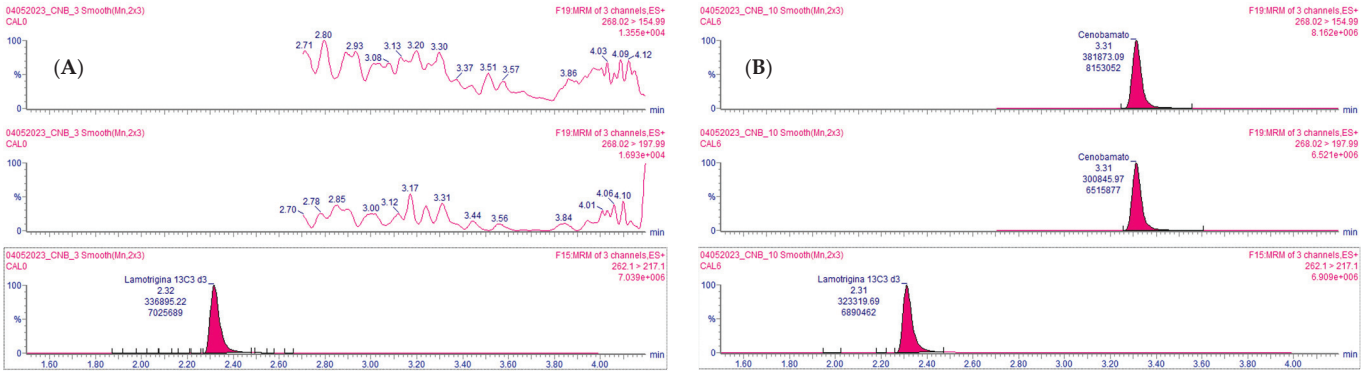


Figure 2. Representative CNB chromatograms in blank plasma samples extracted with internal standard (IS) (**A**), and in plasma samples spiked with CNB and extracted with IS (**B**).

A seven-point calibration curve was built, as well as three concentration levels of quality control (QC) samples. The calibration range was determined based on a recent publication by de Grazia et al. [27], in which expected CNB plasma concentrations were reported within 5–60 mg/L. In our previous study, the calibration curve was limited to 20 mg/L; since the reported CNB plasma concentrations were higher, we decided to extend the calibration range above these values.

A 1/x weighted linear regression model was applied and the method showed good linearity over the calibration range, as shown in Figure 3. LLOQ was set at 0.8 mg/L for CNB and was included in the calibration curves, as well as for those of the other measured compounds (shown in Supplementary Material—Table S1).

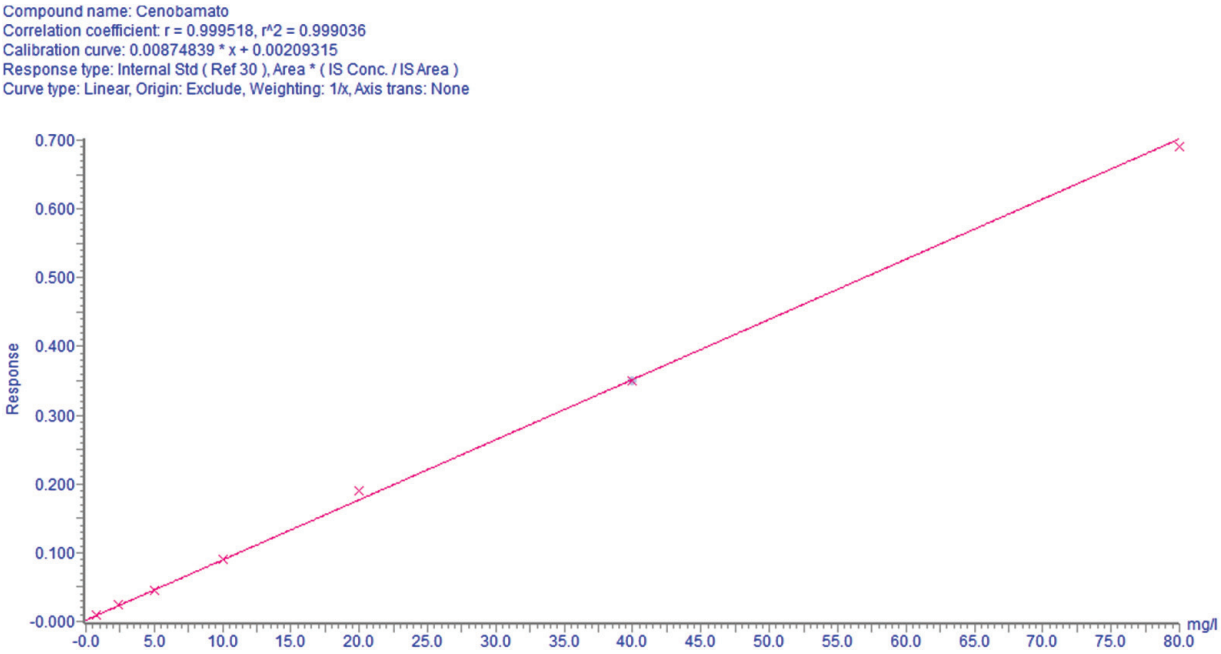


Figure 3. CNB calibration curve in plasma. The curve equation is y = 0.00874839x + 0.00209315. R^2 is 0.999.

No carry-over was observed: six blank injections of samples at high concentrations showed a mean signal of 8.3 ± 1.8% of LLOQ response for CNB.

Dilution integrity was assessed by measuring precision and accuracy of diluted samples (n = 5): mean bias% and CV% were, respectively, 9.5% and 4.0% for the 1:2 dilution factor and 10.5% and 3.7% for the 1:16 dilution factor.

No matrix effect (ME) could be found for CNB when measured at low QC (LQC) and high QC (HQC), while recovery (RE) was acceptable, as shown in Table 2.

Table 2. Summary of matrix effect (ME) and recovery (RE) data and internal standard normalized (ISn) values (n = 7) for CNB. LQC = low QC (3 mg/L); HQC = high QC (60 mg/L); CV = coefficient of variation.

		Matrix 1	Matrix 2	Matrix 3	Matrix 4	Matrix 5	Matrix 6	Matrix 7
ME%	LQC	107	106	105	112	111	113	107
	HQC	102	103	109	111	114	111	112
RE%	LQC	105	101	106	105	105	99	106
	HQC	107	98	101	102	98	106	108
ISn-ME%	LQC	99	92	99	101	105	102	92
	HQC	90	97	98	99	99	101	100
ISn-RE%	LQC	112	112	101	106	99	97	111
	HQC	111	98	104	111	107	113	114

Precision and accuracy were assessed at LLOQ, LQC, medium QC (MQC), and HQC, following a 5 × 5 scheme. Bias% and CV% values for inter-day and intra-day measurements are shown in Table 3. All values met the acceptance criteria.

Table 3. Inter-day and intra-day precision and accuracy of the quantification method in human plasma. QCs = quality control samples; LLOQ = lower limit of quantification (0.8 mg/L); LQC = low QC (3 mg/L); MQC = medium QC (30 mg/L); HQC = high QC (60 mg/L); CV = coefficient of variation.

		INTER-DAY					INTRA-DAY
QCs		**Day 1**	**Day 2**	**Day 3**	**Day 4**	**Day 5**	
LLOQ	Bias%	7.2	18.4	−11.9	−16.3	−6.7	−1.9
	CV%	4.4	2.6	10.2	9.2	3.4	14.6
LQC	Bias%	5.4	−1.7	−0.9	4.5	12.4	3.9
	CV%	3.4	3.2	5.2	7.4	6.1	5.5
MQC	Bias%	−0.6	−5.3	10.3	1.4	4.8	2.1
	CV%	6.1	5.3	5.8	9.3	7.8	5.8
HQC	Bias%	−0.2	−13.7	−0.5	−1.2	−1.5	−3.4
	CV%	3.6	5.5	6.5	3.2	7.1	6.0

Accuracy and precision were also assessed for the other measured compounds in order to evaluate the robustness of the bioanalytical method. Data are shown in Supplementary Material (Tables S2 and S3).

Reinjection reproducibility was evaluated by measuring accuracy and precision of a reinjected run. All values were within the acceptance criteria.

Stability was assessed under different storing conditions (Table 4). CNB in plasma proved to be stable up to 1 week at 4 °C, up to 1 month at −40 °C, and up to 24 h when stored in the autosampler compartment (10 °C). Freeze-thaw samples at −20 °C showed an overall good stability, as well as samples stored at −20 °C for 1 month. CNB concentration in plasma samples stored at room temperature (RT) for 72 h was shown to be highly unstable.

Table 4. Short-term and medium-term stability in plasma samples and extracts for different storage times and conditions (n = 3). Stability is expressed as percentage difference from T0 (% of degradation). LQC = low QC (3 mg/L); HQC = high QC (60 mg/L).

Storage Conditions	**QCs**	**% Difference from T0**		
		48 h	**72 h**	**1 week**
4 °C	LQC	10.6	−14.6	−11.6
	HQC	−0.8	−11.3	−13.6
		72 h		
RT	LQC	−27.8		
	HQC	−19.6		
		24 h		
Autosampler (10 °C)	LQC	−7.9		
	HQC	−0.6		
		1 month	**Freeze-thaw**	
−20 °C	LQC	−19.5	−16.5	
	HQC	5.1	−9.6	
		1 month		
−40 °C	LQC	−11.9		
	HQC	−3.4		

Incurred sample reanalysis (ISR) of study samples was performed on 15 out of the 29 samples included in the method validation; 80% of the repeated values showed a percentage difference below ±20% when compared to the initial values.

Automated Sample Extraction Validation

Partial method validation, according to the most recent ICH Guideline M10 for Bioanalytical Method Validation [24], was also carried out for CNB when an automated sample extraction procedure was employed.

No carry-over was observed: six blank samples dispensed after the handling of samples at high concentrations showed a mean signal of 3.5 ± 1.8% of CNB LLOQ response (3.4 ± 2.2% for the first handling tip and 3.5 ± 1.5% for the second handling tip).

No ME was found for CNB, while RE was acceptable. Internal standard normalized ME (ISn-ME) was 97.6 ± 5.9% for LQC and 101.5 ± 5.2% for HQC, while internal standard normalized RE (ISn-RE) was 94.0 ± 6.7% for LQC and 105.6 ± 3.8% for HQC.

2.3. Analysis of Patient Samples

The analysis of anonymized real samples is a necessary step in the validation process of a bioanalytical method, as reported in the ICH Guideline M10 [24]. Leftover plasma samples collected for routine TDM of ASMs from patients in co-therapy with CNB treated at Fondazione IRCCS Istituto Neurologico Carlo Besta were analyzed as study samples in order to assess method robustness. In total, 29 samples from 14 patients in co-therapy with CNB were collected and processed. Patients' features are described in Supplementary Material (Table S4).

Our patients are 60% male while 40% are female and their age ranges from 20 to 75 years old. The daily administered CNB dose ranges from 12.5 to 400 mg, as a reflection of the titration process; the measured CNB concentrations span from 0.9 to 54.2 mg/L, in agreement with the concentration ranges previously described [27]. No concentration values were found above the upper quantification limit of 80 mg/L, while a few samples were found below the LLOQ, even though patients were reported to consume CNB.

Our data suggest a linear PK of CNB, with a positive correlation between CNB daily dose and CNB plasma concentrations. A linear correlation was also reported when CNB daily dose pro kg was employed (Figure 4). Moreover, a high inter-subject variability is observed, presumably due to intrinsically different patient features and to the potential interactions with other concomitant therapies. Amongst our patients, the co-administered ASMs were VPA, CBZ, PB, TMP, BRIVA, LCS, PMP, clobazam, LEV, PGB, LMT, ZNS, and PHT; unfortunately, due to the small population, no considerations about DDIs reported among our patients can be drafted. In this context, as a result of the great inter-individual variability and of the strong influence of DDIs on CNB PK [10], the quantification of CNB plasma concentrations represents a necessary step for the identification of a personalized drug regimen.

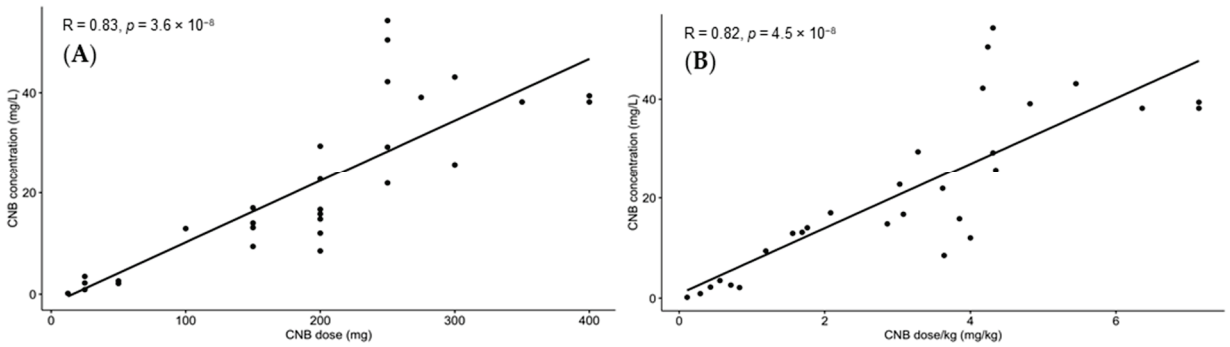


Figure 4. Significant ($p < 0.0001$) linear correlation (Pearson test) between daily dose and the plasma concentration of CNB (**A**), and between daily dose pro kg and the plasma concentration of CNB (**B**). Statistical analysis was performed with R software (version 4.3.2).

2.4. Method Comparison

The performance of the method was evaluated by analyzing 99 patient samples, and the results are shown in the Passing–Bablok regression plot [slope with 95% confidence interval (CI) and intercept with 95% CI] (Figure 5). Regression analysis (regression equation y = 0.328472 + 0.785880x) showed an intercept of 0.3285 (95% CI, 0.01928–0.4516) and a slope of 0.7859 (95% CI, 0.7419–0.8434). No significant deviation from linearity was observed (p = 0.51). The correlation coefficient was 0.961 with a 95% CI (0.942–0.973) with $p < 0.0001$.

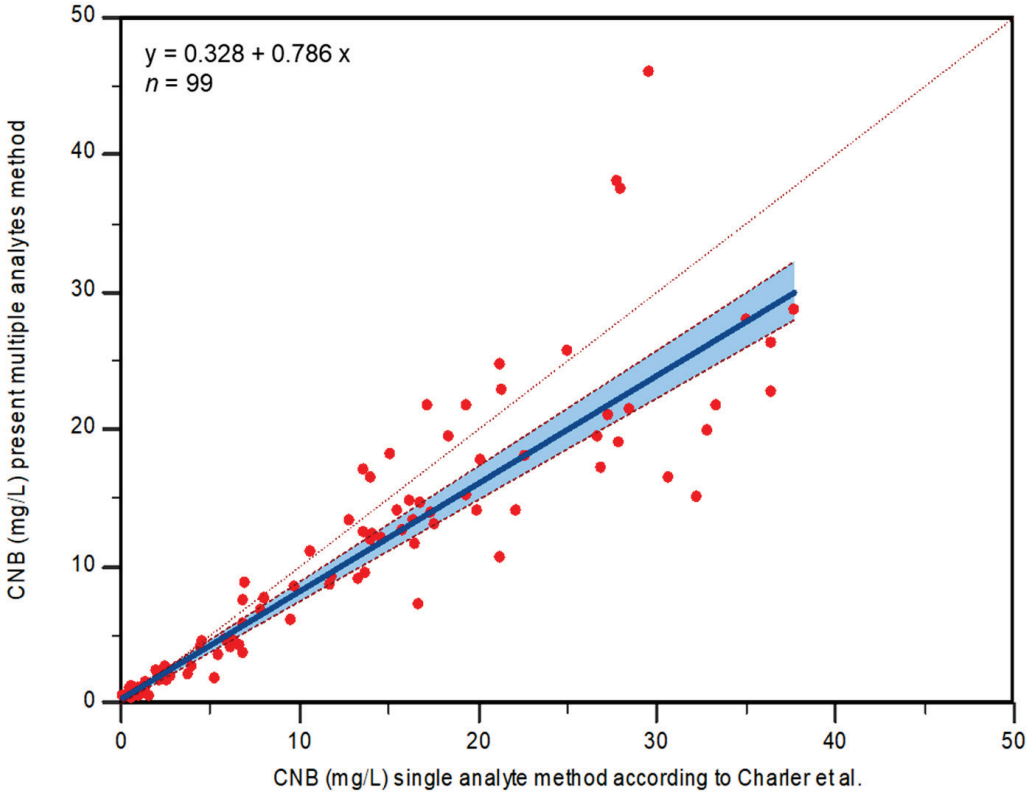


Figure 5. Passing–Bablok correlation plot of CNB plasma concentrations (mg/L) obtained with reference method [23] (*X*-axis) compared with those obtained with the method here presented (*Y*-axis). Thick line, regression line; thin line, identity line; dashed line, confidence interval for the regression line.

The Bland–Altman plot (bias with 95% CI, 95% limits of agreement) (Figure 6) showed a mean bias of 10.1% (95% CI, 1.9405–18.2033).

CNB concentrations in patients' samples, when determined with the reference method, ranged from 0.1 to 37.7 mg/L (mean 12.3 mg/L, median 10.6 mg/L), while the present method varied from 0.4 to 46.0 mg/L (mean 10.42 mg/L, median 8.7 mg/L).

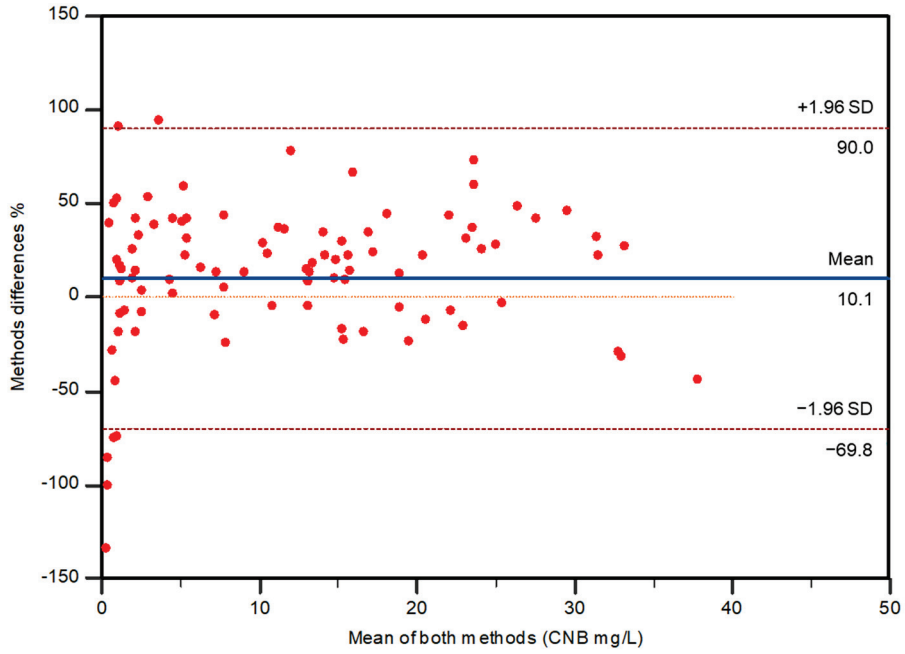


Figure 6. Bland–Altman plot includes the reference line for no difference (at 0 mg/L) (dotted line), the solid line indicating mean % difference and the 95% limits of agreement of the methods (dashed lines).

3. Materials and Methods

3.1. Chemicals and Reagents

Cenobamate (racemic mixture) was purchased from Alsachim (Illkirch, France). A stock solution was prepared in water at the nominal concentration of 0.8 mg/mL and stored at −20 °C.

Ultrapure water was obtained from a Milli-Q water purification system (Millipore, Milan, Italy). LC-MS/MS grade acetonitrile and methanol were purchased from Merck (Milan, Italy).

As reference method, a commercial CE/IVD kit for the quantification of antiepileptic drugs in human serum/plasma ("Plasmatic AEDs in the LC-MS—Deuterated Internal Standards") was purchased from Eureka Lab Division, a division of Sentinel Diagnostic (Milan, Italy).

3.2. Calibration Curves and Quality Control Samples

Calibration curves and QC samples were obtained by reconstituting the lyophilized material provided by the commercial kit with 1 mL of Milli-Q water, following the manufacturer instructions. CNB was added to the highest calibration standard, which was then serially diluted with blank plasma from healthy donors to obtain a seven-point calibration curve (0.0, 2.4, 5.0, 10.0, 20.0, 40.0, and 80.0 mg/L). To obtain QC samples, CNB was added to the fifth level of the blank calibration curve, which was then serially diluted with blank plasma from healthy donors to obtain 3 levels of QCs, defined as LQC, MQC, and HQC (3.0, 30.0, and 60.0 mg/L). Nominal concentration values of the calibration curve and QC samples for the other detected compounds are shown in Supplementary Material (Table S1).

3.3. Sample Preparation

3.3.1. Manual Sample Preparation

Fresh whole blood was collected by venipuncture in lithium-heparin-containing tubes; after collection, tubes were centrifuged at 3500× *g* for 15 min and plasma was collected. Plasma samples were either processed or stored at −20 °C until further analysis.

Samples were extracted by following the analytical procedure indicated by the kit manufacturer. A total of 50 µL of sample was dispensed into a 1.5 mL tube and 25 µL

of mobile phase A (Water, 0.1% HCOOH) was added; the sample underwent a protein precipitation step by adding 500 µL of acetonitrile (ACN) spiked with IS to the tube (IS are listed in Table S5). Samples were then vortex mixed and incubated at −20 °C for 15 min. The tubes were then centrifuged at 16,000× *g* for 15 min; 50 µL of supernatant was added to 450 µL of mobile phase A in an autosampler vial. A total of 1 µL of the obtained solution was injected into the instrument.

3.3.2. Automated Sample Preparation

In order to automatize and standardize the sample preparation procedure, the samples were also extracted by employing a Tecan Freedom EVO 100 liquid-handling unit equipped with Freedom EVOware Version 2.8 SP2 software (Tecan Italia S.r.l., Cernusco sul Naviglio, Italy).

A sample of 50 µL was dispensed into a 96-well plate and 25 µL of mobile phase A (Water, 0.1% HCOOH) was added; the sample underwent a protein precipitation step by adding 500 µL of ACN spiked with IS (IS are listed in Table S5). The plate was then mixed by vortexing, incubated at −20 °C for 15 min, and then centrifuged at 3500× *g* for 20 min; subsequently, 50 µL of supernatant was added to 450 µL of mobile phase A in a clean plate. A total of 1 µL of the obtained solution was injected into the instrument.

3.4. Instrument Setup and Parameters

LC-MS/MS analysis was carried out on a Waters Xevo TQ-XS triple quadrupole mass spectrometer coupled to a Waters Acquity UPLC I-Class System (Waters Corporation, Sesto San Giovanni, Italy). Chromatographic separation was performed on an Agilent InfinityLab Poroshell EC-C18 column (2.1 × 50 mm, 1.9 µm particle size) (Agilent, Santa Clara, CA, USA) with two mobile phases, A (Water, 0.1% HCOOH) and B (ACN, 0.1% HCOOH). Elution was performed in gradient elution mode: at a flow rate of 0.5 mL/min, the gradient was stepped from 2% B to 13% B in 0.5 min and held for 1.3 min; then, it was stepped to 21% B in 0.1 min and held for 1 min, stepped to 50% B in 0.5 min and held for 0.5 min, and stepped to 80% B in 0.1 min and held for 0.3 min. Column was washed at 95% B for 0.6 min and restored to the initial condition of 2% B for column equilibration. Total run time was 7 min; column oven was set at 35 °C.

MS analysis was performed using a triple quadrupole mass spectrometer equipped with an electrospray ionization (ESI) source operated both in positive and negative ion mode. Method parameters were the following: source temperature 150 °C, capillary voltage +1.5 kV, desolvation temperature 500 °C, cone gas flow rate 150 L/h, collision gas flow rate 0.15 mL/min, and desolvation gas flow rate 1000 L/h. Dwell time was automatically calculated. Waters MassLynx (V 4.2) and TargetLynx (V 4.2) software was used to acquire and process data (Waters Corporation, Sesto San Giovanni, Italy).

All compounds were detected in multiple reaction monitoring (MRM) mode as described in Supplementary Material (Table S5). The detecting conditions for CNB were obtained by directly infusing the standard solution at 100 ng/mL and were the following: precursor ion 268.02 *m*/*z*, cone voltage 20 V, quantifier ion 154.99 *m*/*z* (collision energy 14 V), qualifier ion 197.99 *m*/*z* (collision energy 10 V), ion mode ES+, retention time 3.32 min.

Similarly to our previous study, available deuterated standards such as felbamate-d4, topiramate-d12, and lamotrigine-13C-d3 were tested to be employed as IS. Lamotrigine-13C-d3 was found to provide better results, both in terms of chromatographic resolution and recovery, and showed good normalization capabilities [23].

3.5. Method Validation

Method validation for CNB was performed according to the most recent ICH Guideline M10 for Bioanalytical Method Validation and Study Sample Analysis [24], which requires the following assays: selectivity and specificity, calibration curve linearity, carry-over, dilution integrity, matrix effect, accuracy and precision, reinjection reproducibility, stability,

and incurred sample reanalysis. A partial validation was performed on the modified kit in order to assess its robustness and reliability in the monitoring of concomitant ASMs.

3.5.1. Selectivity and Specificity

Method selectivity and specificity were assessed by analyzing six different lots of blank matrices, including (i) reconstituted highest calibration standard (without CNB), (ii) two matrices of blank plasma from healthy donors, and (iii) three matrices of Li-Heparin plasma containing other ASMs. The absence of significant response accountable to interfering components at analyte retention time was assessed; response should not be greater than 20% of analyte response at LLOQ.

3.5.2. Linearity

Calibration curves were built by plotting analyte/IS peak area ratio against corresponding analyte nominal concentrations and fitted by using a 1/x weighted linear regression model.

To assess the LLOQ, CNB-spiked plasma samples at concentrations of 2, 0.8, 0.5, and 0.4 mg/L were prepared and analyzed in triplicate. LLOQ was defined as the lowest concentration level at which accuracy and precision were within ±20%.

3.5.3. Carry-Over

Carry-over was assessed by analyzing six blank plasma samples from healthy donors after the injection of the highest calibration standard. Response should not be greater than 20% of analyte response at LLOQ.

3.5.4. Dilution Integrity

Dilution integrity was performed to assess the feasibility of the dilution procedure. A high-concentrated plasma sample (120 mg/L CNB) was serially diluted with blank plasma to obtain 1:2 and 1:16 dilutions falling within the calibration range. Diluted samples were analyzed in triplicate. The mean accuracy and precision of diluted samples should be within ±15%.

3.5.5. Recovery and Matrix Effect

RE and ME for CNB were assessed at two concentration levels (LQC and HQC) by analyzing seven different lots of matrices in triplicate, including (i) lipemic Li-Heparin plasma containing other ASMs, (ii) normal Li-Heparin plasma containing other ASMs, (iii) hemolyzed Li-Heparin plasma containing other ASMs, (iv) three matrices of blank plasma from healthy donors, and (v) reconstituted blank calibration standard. RE and ME were calculated according to Matuszewski [29]; IS normalization was applied as described in De Nicolò et al. [30], thus, ISn-ME and Isn-RE values are shown.

3.5.6. Accuracy and Precision

Intra-day and inter-day accuracy and precision were assessed at four concentration levels (LLOQ, LQC, MQC, and HQC) with a 5 × 5 scheme, consisting of five replicates for each concentration level in five analytical runs over five non-consecutive days.

Accuracy is expressed as relative error, or bias%, which is calculated as the percentage difference between measured and nominal concentrations, while precision is expressed as CV%. Mean accuracy and precision values within ±15% for LQC, MQC, and HQC, and within ±20% for LLOQ, were considered acceptable.

3.5.7. Reinjection Reproducibility

Reinjection reproducibility was assessed to establish the viability of processed samples. One run from accuracy and precision experiments was reinjected after storage in the autosampler compartment (10 °C) for 24 h and accuracy and precision of reinjected QCs were assessed.

3.5.8. Stability

Sample stability was measured at two concentration levels (LQC and HQC) in triplicate. Short-term stability was assessed at RT for 72 h and at 4 °C for 48 h, 72 h, and 1 week; autosampler stability was assessed by storing extracts in the autosampler compartment at 10 °C for 24 h. Medium-term stability at −40 °C for 1 month and freeze-and-thaw (FT) stability at −20 °C were assessed.

The mean concentration values obtained from each measurement were compared to the concentrations measured at T0 before storage. Stability data are expressed as percentage difference from T0.

3.5.9. Incurred Sample Reanalysis

ISR is aimed at assessing the accuracy of the reported analyte concentration in study samples, since they may differ from calibration standards due to matrix issues.

From 29 study samples, 15 samples were reanalyzed. The percentage difference between the initial concentration and the concentration measured during ISR was calculated as the percentage ratio between the difference of repeated and initial value and the mean value.

For at least 2/3 of the repeats the percentage difference should be within ±20%.

3.5.10. Automated Sample Extraction Validation

The method was also partially validated for CNB when an automated sample extraction procedure was employed, as described in Section 3.3.2., according to the most recent ICH Guideline for Bioanalytical Method Validation [24]. Carry-over, RE, and ME were assessed.

Carry-over was assessed by analyzing six blank plasma samples from healthy donors after the dispensation of the highest calibration standard. Response should not be greater than 20% of analyte response at LLOQ.

RE and ME were assessed at LQC and HQC by analyzing seven different lots of matrices in triplicate, including (i) lipemic Li-Heparin plasma containing other ASMs, (ii) normal Li-Heparin plasma containing other ASMs, (iii) hemolyzed Li-Heparin plasma containing other ASMs, (iv) three matrices of blank plasma from healthy donors, and (v) reconstituted blank calibration standard. RE and ME were calculated according to Matuszewski [29]; IS normalization was applied as described in De Nicolò et al. [30], thus, IS normalized ME (ISn-ME) and IS normalized RE (ISn-RE) values are shown.

3.6. Method Comparison

Finally, to assess the robustness and validity of the new method, the concentration of 99 samples obtained from the three hospitals participating in this study (Fondazione IRCCS Istituto Neurologico Carlo Besta, Milano; Azienda Ospedaliero-Universitaria "San Giovanni di Dio e Ruggi d'Aragona-Scuola Medica Salernitana", Salerno; Fondazione Policlinico Universitario Campus Biomedico, Roma) were compared with those obtained with the previously published method. Patients are described in the following table (Table 5).

Table 5. Summary of patients' data used for method comparison (n = 47, samples n = 99).

Gender		
	Woman	16 (34%)
	Man	31 (66%)
Age (year), median (range)		26.21 (18–60)
Body weight (kg), median (range) (n = 37)		66.62 (54–107)
Cenobamate dose (mg) (n = 86)		
	Mean (SD)	115 (81)
	Median (range)	100 (12.5–250)
Cenobamate plasma concentration (mg/L)		
	Mean (SD)	10 (10)
	Median (range)	7 (0.4–46)
Patients with no data		7
Patients with unknown concomitant ASMs		19
Patients with 1 concomitant ASM		4
Patient with 2 or more concomitant ASMs		17

Statistical Analysis

Method cross-validation was performed considering the previously published LC-MS/MS assay as the reference method and the one here described as the test method. Methods were compared by Passing–Bablok regression and Bland–Altman plot, obtained with MedCalc Statistical Software version 22.014 (MedCalc Software, Mariakerke, Belgium) and MetComp Software version 1 (GdS SIBioC, Novara, Italy) [31].

4. Conclusions

As a result of CNB's recent approval as an ASM, limited information is available regarding its plasmatic therapeutic ranges and its real-life interactions with other concomitant drugs. Also, since the titration process represents a crucial step for drug safety [16], the determination of plasma concentrations could provide the clinician with useful information for the identification of tailor-made therapeutic regimens during both the titration and maintenance periods.

For this reason, we provide the development and validation of a UHPLC–MS/MS quantification method for the detection of CNB and other ASMs, starting from a commercially CE/IVD validated kit for the quantification of antiepileptic drugs in human plasma and serum. Our method was validated for CNB but also allowed the detection and quantification of other drugs, which are often administered in co-therapy with CNB. The simultaneous detection of 17 compounds may represent a saving in terms of both reagent costs and time, and provides a more efficient clinical management of the patient.

Overall, our method showed a good performance, with a simple extraction procedure and a relatively short run time for the detection of a total of 17 compounds. The absence of interferences between CNB and the other compounds within the analytical determination is of crucial importance for the introduction of CNB into routine TDM of ASMs.

Future studies will be needed in order to improve our understanding of CNB's pharmacological features and interactions, and for the determination of a therapeutic reference range aimed at identifying personalized drug regimens and ensuring drug clinical efficacy and safety.

Supplementary Materials: The following supporting information can be downloaded at: https://www.mdpi.com/article/10.3390/molecules29040884/s1, Table S1: Nominal concentrations of calibration curves and quality control (QC) samples; Table S2: Intra-day precision and accuracy of the quantification method in human plasma for the detection of the other detected ASMs; Table S3: Inter-day precision and accuracy of the quantification method in human plasma for the detection of the other detected ASMs; Table S4: Demographic and therapeutic features of patients receiving CNB as co-ASMs in polytherapy at Fondazione IRCCS Istituto Neurologico Carlo Besta; Table S5: MS method transitions, parameters, and retention times.

Author Contributions: Conceptualization, L.M., A.D. and U.d.G.; methodology, L.M. and A.D.; validation, L.M., B.C., A.C. and A.D.; data curation, L.M. and A.D.; writing—original draft preparation, L.M., A.D. and U.d.G.; writing—review and editing, V.I., P.M., G.A., B.C., A.C. and U.d.G. All authors have read and agreed to the published version of the manuscript.

Funding: This work was supported by the Italian Ministry of Health (RRC2023), L.M., U.d.G., and A.D.

Institutional Review Board Statement: The analysis of anonymized real samples is a necessary step in the validation process of a bioanalytical method as reported in the ICH Guideline M10 for Bioanalytical Method Validation and Study Sample Analysis [24]. We referred to the European Regulation on in vitro diagnostic medical devices (EU 2017/746), a regulation of the European Union that is currently in force (recital 73; article 58). Leftover plasma samples collected for routine TDM of ASMs from patients in co-therapy with CNB treated at Fondazione IRCCS Istituto Neurologico Carlo Besta (Milano); Azienda Ospedaliero-Universitaria "San Giovanni di Dio e Ruggi d'Aragona-Scuola Medica Salernitana", (Salerno); and Fondazione Policlinico Universitario Campus Biomedico, Roma) were analyzed as study samples in order to assess method robustness. Ethical standards of the Institutional and National Research Committee and the 1975 Declaration of Helsinki, revised in 2013, were observed.

Informed Consent Statement: Written informed consent for the collection of anonymized residual samples after routine clinical analysis was obtained from all patients in accordance with the privacy regulations of the institutes involved in the study.

Data Availability Statement: Data are contained within the article and supplementary materials.

Acknowledgments: Authors wish to thank all colleagues and lab technicians that helped in developing this study.

Conflicts of Interest: The authors declare no conflicts of interest.

References

1. Perucca, P.; Scheffer, I.E.; Kiley, M. The management of epilepsy in children and adults. *Med. J. Aust.* **2018**, *208*, 226–233. [CrossRef]
2. Beghi, E. The Epidemiology of Epilepsy. *Neuroepidemiology* **2019**, *54*, 185–191. [CrossRef]
3. Chen, Z.; Brodie, M.J.; Liew, D.; Kwan, P. Treatment Outcomes in Patients with Newly Diagnosed Epilepsy Treated with Established and New Antiepileptic Drugs: A 30-Year Longitudinal Cohort Study. *JAMA Neurol.* **2018**, *75*, 279. [CrossRef]
4. Perucca, E.; Tomson, T. The pharmacological treatment of epilepsy in adults. *Lancet Neurol.* **2011**, *10*, 446–456. [CrossRef]
5. Hauser, W.A. Questioning the Effectiveness of Newer Antiseizure Medications. *JAMA Neurol.* **2018**, *75*, 273. [CrossRef]
6. Kwan, P.; Brodie, M.J. Early Identification of Refractory Epilepsy. *N. Engl. J. Med.* **2000**, *342*, 314–319. [CrossRef]
7. Kwan, P. Drug-Resistant Epilepsy. *N. Engl. J. Med.* **2011**, *365*, 919–926. [CrossRef]
8. Golyala, A.; Kwan, P. Drug development for refractory epilepsy: The past 25 years and beyond. *Seizure* **2017**, *44*, 147–156. [CrossRef] [PubMed]
9. Guignet, M.; Campbell, A.; White, H.S. Cenobamate (XCOPRI): Can preclinical and clinical evidence provide insight into its mechanism of action? *Epilepsia* **2020**, *61*, 2329–2339. [CrossRef] [PubMed]
10. Roberti, R.; De Caro, C.; Iannone, L.F.; Zaccara, G.; Lattanzi, S.; Russo, E. Pharmacology of Cenobamate: Mechanism of Action, Pharmacokinetics, Drug–Drug Interactions and Tolerability. *CNS Drugs* **2021**, *35*, 609–618. [CrossRef] [PubMed]
11. Krauss, G.L.; Klein, P.; Brandt, C.; Lee, S.K.; Milanov, I.; Milovanovic, M.; Steinhoff, B.J.; Kamin, M. Safety and efficacy of adjunctive cenobamate (YKP3089) in patients with uncontrolled focal seizures: A multicentre, double-blind, randomised, placebo-controlled, dose-response trial. *Lancet Neurol.* **2020**, *19*, 38–48. [CrossRef]
12. Sperling, M.R.; Klein, P.; Aboumatar, S.; Gelfand, M.; Halford, J.J.; Krauss, G.L.; Rosenfeld, W.E.; Vossler, D.G.; Wechsler, R.; Borchert, L.; et al. Cenobamate (YKP3089) as adjunctive treatment for uncontrolled focal seizures in a large, phase 3, multicenter, open-label safety study. *Epilepsia* **2020**, *61*, 1099–1108. [CrossRef] [PubMed]

13. Chung, S.S.; French, J.A.; Kowalski, J.; Krauss, G.L.; Lee, S.K.; Maciejowski, M.; Rosenfeld, W.E.; Sperling, M.R.; Mizne, S.; Kamin, M. Randomized phase 2 study of adjunctive cenobamate in patients with uncontrolled focal seizures. *Neurology* **2020**, *94*, e2311–e2322. [CrossRef]
14. Vossler, D.G. Remarkably High Efficacy of Cenobamate in Adults with Focal-Onset Seizures: A Double-Blind, Randomized, Placebo-Controlled Trial. *Epilepsy Curr.* **2020**, *20*, 85–87. [CrossRef] [PubMed]
15. Klein, P.; Aboumatar, S.; Brandt, C.; Dong, F.; Krauss, G.L.; Mizne, S.; Sánchez-Álvarez, J.C.; Steinhoff, B.J.; Villanueva, V. Long-term Efficacy and Safety From an Open-Label Extension of Adjunctive Cenobamate in Patients With Uncontrolled Focal Seizures. *Neurology* **2022**, *99*, e989–e998. [CrossRef]
16. Buckley, C.T.; Waters, O.R.; DeMaagd, G. Cenobamate: A New Adjunctive Agent for Drug-Resistant Focal Onset Epilepsy. *Ann. Pharmacother.* **2021**, *55*, 318–329. [CrossRef]
17. French, J.A. Cenobamate for focal seizures—A game changer? *Nat. Rev. Neurol.* **2020**, *16*, 133–134. [CrossRef]
18. Löscher, W.; Sills, G.J.; White, H.S. The ups and downs of alkyl-carbamates in epilepsy therapy: How does cenobamate differ? *Epilepsia* **2021**, *62*, 596–614. [CrossRef]
19. Nakamura, M.; Cho, J.-H.; Shin, H.; Jang, I.-S. Effects of cenobamate (YKP3089), a newly developed anti-epileptic drug, on voltage-gated sodium channels in rat hippocampal CA3 neurons. *Eur. J. Pharmacol.* **2019**, *855*, 175–182. [CrossRef] [PubMed]
20. Sharma, R.; Nakamura, M.; Neupane, C.; Jeon, B.H.; Shin, H.; Melnick, S.M.; Glenn, K.J.; Jang, I.-S.; Park, J.B. Positive allosteric modulation of GABAA receptors by a novel antiepileptic drug cenobamate. *Eur. J. Pharmacol.* **2020**, *879*, 173117. [CrossRef]
21. Sills, G.J.; Rogawski, M.A. Mechanisms of action of currently used antiseizure drugs. *Neuropharmacology* **2020**, *168*, 107966. [CrossRef] [PubMed]
22. Drug Approval Package: XCOPRI. Available online: https://www.accessdata.fda.gov/drugsatfda_docs/nda/2019/212839Orig1s000TOC.cfm (accessed on 11 July 2023).
23. Charlier, B.; Coglianese, A.; Operto, F.F.; Coppola, G.; de Grazia, U.; Menna, P.; Filippelli, A.; Piaz, F.D.; Izzo, V. Development and Validation of a UHPLC–MS/MS-Based Method to Quantify Cenobamate in Human Plasma Samples. *Molecules* **2022**, *27*, 7325. [CrossRef] [PubMed]
24. ICH Guideline M10 on Bioanalytical Method Validation and Study Sample Analysis. Available online: https://www.ema.europa.eu/en/documents/scientific-guideline/ich-guideline-m10-bioanalytical-method-validation-step-5_en.pdf (accessed on 10 February 2023).
25. Oh, J.-H.; Jeong, J.-W.; Ji, Y.-G.; Shin, Y.-M.; Lee, K.-R.; Cho, K.H.; Koo, T.-S. Development of a liquid chromatography-tandem mass spectrometry method for assaying cenobamate in rat plasma. *J. Liq. Chromatogr. Relat. Technol.* **2018**, *41*, 992–997. [CrossRef]
26. Vernillet, L.; Greene, S.A.; Kamin, M. Pharmacokinetics of Cenobamate: Results From Single and Multiple Oral Ascending-Dose Studies in Healthy Subjects. *Clin. Pharmacol. Drug Dev.* **2020**, *9*, 428–443. [CrossRef]
27. de Grazia, U.; Menna, P.; Cantù, M.; Baldelli, S.; Goffredo, B.M.; Deleo, F.; D'Urso, A. Indicazioni per l'armonizzazione degli intervalli di riferimento nel monitoraggio terapeutico di farmaci antiepilettici. *Biochim. Clin.* **2023**, *47*, 82. [CrossRef]
28. de Grazia, U.; D'Urso, A.; Ranzato, F.; De Riva, V.; Contarato, G.; Billo, G.; Perini, F.; Galloni, E. A Liquid Chromatography-Mass Spectrometry Assay for Determination of Perampanel and Concomitant Antiepileptic Drugs in the Plasma of Patients With Epilepsy Compared with a Fluorescent HPLC Assay. *Ther. Drug Monit.* **2018**, *40*, 477–485. [CrossRef]
29. Matuszewski, B.K.; Constanzer, M.L.; Chavez-Eng, C.M. Strategies for the Assessment of Matrix Effect in Quantitative Bioanalytical Methods Based on HPLC−MS/MS. *Anal. Chem.* **2003**, *75*, 3019–3030. [CrossRef]
30. De Nicolò, A.; Cantù, M.; D'Avolio, A. Matrix effect management in liquid chromatography mass spectrometry: The internal standard normalized matrix effect. *Bioanalysis* **2017**, *9*, 1093–1105. [CrossRef]
31. Vidali, M.; Tronchin, M.; Dittadi, R. Protocollo per la comparazione di due metodi analitici di laboratorio. *Biochim. Clin.* **2016**, *40*, 129–142. [CrossRef]

Disclaimer/Publisher's Note: The statements, opinions and data contained in all publications are solely those of the individual author(s) and contributor(s) and not of MDPI and/or the editor(s). MDPI and/or the editor(s) disclaim responsibility for any injury to people or property resulting from any ideas, methods, instructions or products referred to in the content.

molecules

MDPI

Article

Development and Validation of a New LC-MS/MS Bioanalytical Method for the Simultaneous Determination of Levodopa, Levodopa Methyl Ester, and Carbidopa in Human Plasma Samples

Linda Molteni [1,*,†], Bruno Charlier [2,3,†], Viviana Izzo [2,3], Albino Coglianese [2,4], Valeria Conti [2,3], Roberto Eleopra [5], Roberto Cilia [5,*], Chiara Capelli [1], Annachiara D'Urso [1] and Ugo de Grazia [1]

[1] Laboratory of Neurological Biochemistry and Neuropharmacology, Fondazione IRCCS Istituto Neurologico Carlo Besta, 20133 Milano, Italy; chiara.capelli02@universitadipavia.it (C.C.); annachiara.durso@istituto-besta.it (A.D.); ugo.degrazia@istituto-besta.it (U.d.G.)
[2] Department of Medicine, Surgery and Dentistry "Scuola Medica Salernitana", University of Salerno, Baronissi, 84081 Salerno, Italy; bcharlier@unisa.it (B.C.); vizzo@unisa.it (V.I.); albino.cog@gmail.com (A.C.); vconti@unisa.it (V.C.)
[3] University Hospital "San Giovanni di Dio e Ruggi d'Aragona", 84131 Salerno, Italy
[4] Graduate School in Clinical Pathology and Clinical Biochemistry, University of Salerno, Baronissi, 84081 Salerno, Italy
[5] Parkinson and Movement Disorders Unit, Department of Clinical Neurosciences, Fondazione IRCCS Istituto Neurologico Carlo Besta, 20133 Milano, Italy; roberto.eleopra@istituto-besta.it
* Correspondence: linda.molteni@istituto-besta.it (L.M.); roberto.cilia@istituto-besta.it (R.C.)
† These authors contributed equally to this work.

Abstract: Levodopa (L-DOPA) treatment, combined with the administration of dopa-decarboxylase inhibitors (DDCIs), is still the most effective symptomatic treatment of Parkinson's disease (PD). Although its efficacy in the early stage of the disease has been confirmed, its complex pharmacokinetics (PK) increases the variability of the intra-individual motor response, thus amplifying the risk of motor/non-motor fluctuations and dyskinesia. Moreover, it has been demonstrated that L-DOPA PK is strongly influenced by several clinical, therapeutic, and lifestyle variables (e.g., dietary proteins). L-DOPA therapeutic monitoring is therefore crucial to provide personalized therapy, hence improving drug efficacy and safety. To this aim, we have developed and validated an ultra-high performance liquid chromatography–tandem mass spectrometry (UHPLC-MS/MS) method to quantify L-DOPA, levodopa methyl ester (LDME), and the DDCI carbidopa in human plasma. The compounds were extracted by protein precipitation and samples were analyzed with a triple quadrupole mass spectrometer. The method showed good selectivity and specificity for all compounds. No carryover was observed, and dilution integrity was demonstrated. No matrix effect could be retrieved; intra-day and inter-day precision and accuracy values met the acceptance criteria. Reinjection reproducibility was assessed. The described method was successfully applied to a 45-year-old male patient to compare the pharmacokinetic behavior of an L-DOPA-based medical treatment involving commercially available *Mucuna pruriens* extracts and an LDME/carbidopa (100/25 mg) formulation.

Keywords: levodopa; levodopa methyl ester; carbidopa; Parkinson's disease; therapeutic drug monitoring; liquid chromatography–mass spectrometry (LC–MS); analytical method

1. Introduction

Parkinson's disease (PD) is a common neurodegenerative condition characterized by the progressive loss of dopaminergic neurons and subsequent alteration in dopaminergic transmission at nigrostriatal level [1,2].

Dopaminergic substitution is considered the main therapeutic strategy for the symptomatic treatment of PD [3,4]. The administration of the dopamine precursor levodopa (L-DOPA) has remained the main cardinal treatment since its introduction in the 1960s [3,5,6]. Due to its limited bioavailability and the frequent manifestation of adverse events [7], L-DOPA has been promptly combined with the administration of peripheral dopa-decarboxylase inhibitors (DDCIs), which proved to be able to hinder L-amino acid decarboxylase (AADC) activity in the peripheral compartment (mainly at gastrointestinal level) [8,9]. Incapable of crossing the blood-brain barrier (BBB), DDCIs, such as carbidopa and benserazide, increase the concentration of dopamine (DA) in the brain by preventing the bio-activation of L-DOPA at the peripheral level, thus potentiating its therapeutic effect [4,8].

While the introduction of DDCIs has increased the central bioavailability and therapeutic action of L-DOPA by reducing its peripheral metabolism rate, the progression of nigrostriatal terminals loss and individual daily doses of long-term treatment with L-DOPA/DDCIs increase the risk of developing motor/non-motor fluctuations and dyskinesia [10–12]. The occurrence of motor complications is due to several factors, including progressive loss of presynaptic dopaminergic regulation (e.g., dopamine transporter, presynaptic D2 receptors), hindering of the buffering ability against alterations in L-DOPA levels, irregular gastrointestinal emptying, delayed L-DOPA absorption and L-DOPA short plasma half-life [10–13]. Thus, a strict correlation between L-DOPA-related motor complications and its complex pharmacokinetics (PK) can be evinced. In addition, L-DOPA PK can be strongly influenced by several demographic, clinical, and lifestyle factors, such as gender, body mass index (BMI), age, disease duration, and diet (protein redistribution dietary regimen is in fact recommended) [14–21]. Among those, gender seems to be a strong predictor of L-DOPA PK: women show greater L-DOPA bioavailability, higher plasma concentrations, as well as higher AUC and Cmax, and are also more prone to develop L-DOPA-related complications when compared to men [14,15].

In the past decades, the association between motor fluctuations and L-DOPA PK mechanisms became clearer and various strategies were explored to increase L-DOPA bioavailability, particularly by enhancing its absorption. In this context, a more soluble L-DOPA prodrug, levodopa methyl ester (LDME), was introduced [22]. Considering that L-DOPA is still largely unavailable and unaffordable for the majority of patients in many Sub-Saharan African and other low-income countries, growing interest has been also directed towards a leguminous plant, *Mucuna pruriens* variant *utilis*, which seeds are reported to be rich in L-DOPA. Recent studies have shown that *Mucuna pruriens* powder is able to control motor and non-motor symptoms of PD, with a different PK compared to marketed L-DOPA formulations. *Mucuna pruriens* seeds may represent an effective alternative to L-DOPA conventional treatment in low-income areas, where it is unaffordable and inaccessible, although tolerability in the long term is still under investigation [23–26].

In this complex scenario, it is of crucial importance to monitor L-DOPA plasma concentrations to integrate PK data with clinical and demographic information to identify additional predictors of L-DOPA PK within lifestyle and therapeutic variables, which could be really useful to optimize and personalize dopaminergic therapy, thus ensuring drug efficacy and safety [14,15]. Recently, Conti and coworkers [14] described the use of a novel LC-MS/MS method to evaluate L-DOPA plasma concentrations in a clinical study, which aim was to identify L-DOPA PK predictors. In this work, 35 L-DOPA-naïve patients, 19 men and 16 women, were enrolled in a multi-center study involving different Italian hospitals and were treated with a single dose of oral L-DOPA/benserazide (100/25 mg) formulation. Multiple regression analyses were applied to identify PK predictors amongst variables such as gender, age, and BMI; the female sex turned out as a strong predictor of L-DOPA AUC and Cmax, while BMI was identified as a predictor of AUC only. Moreover, only BMI was shown to predict $t_{1/2}$; when stratifying by gender, BMI was confirmed to significantly predict $t_{1/2}$ only in women. According to the results described in this study, women are more prone to develop motor complications when compared to men and this is reflected in higher plasma concentrations, as well as higher Cmax and AUC. Although useful for

its purpose, the main limitation of this methodology was the ability to evaluate the sole L-DOPA plasma concentration. Various LC-MS/MS methods were developed to monitor L-DOPA and carbidopa in human plasma [27–33], but to date, no method was found in the scientific literature for the monitoring of LDME in LC-MS/MS.

In this work, we have developed and validated, according to the most recent guidelines on bioanalytical method validation and study sample analysis [34], a UHPLC-MS/MS method for the simultaneous determination of L-DOPA, LDME, and carbidopa in human plasma. The novel bioanalytical method relies on a simple acidic protein precipitation extraction procedure and provides a rapid simultaneous determination of the pharmacologically active compound L-DOPA, as well as its prodrug LDME and one of the two known DDCIs, carbidopa. The development of this method has allowed performing a study on a 45-year-old male patient aimed at the comparison of the pharmacokinetic behavior of two different L-DOPA-containing formulations, i.e., commercially available *Mucuna pruriens* extracts and LDME/carbidopa (100/25 mg) tablets.

2. Results

2.1. Method Validation

Method validation was performed according to the most recent ICH guidelines for bioanalytical method validation [34], which require the following assays: selectivity and specificity, calibration curve linearity, carry-over, dilution integrity, matrix effect, accuracy and precision, reinjection reproducibility, and stability. Technical details are explained in Section 4.5.

Method selectivity and specificity were assessed by analyzing blank plasma samples from different matrices; no interfering peaks with response higher than 20% and 5%, when compared to lower limit of quantification (LLOQ) and internal standard (IS) signals, were found for any of the compounds tested.

Figure 1 shows spectral data and fragmentation analysis of L-DOPA, LDME, and carbidopa, and Figure 2 shows representative chromatograms of blank plasma and samples spiked with L-DOPA, LDME, and carbidopa.

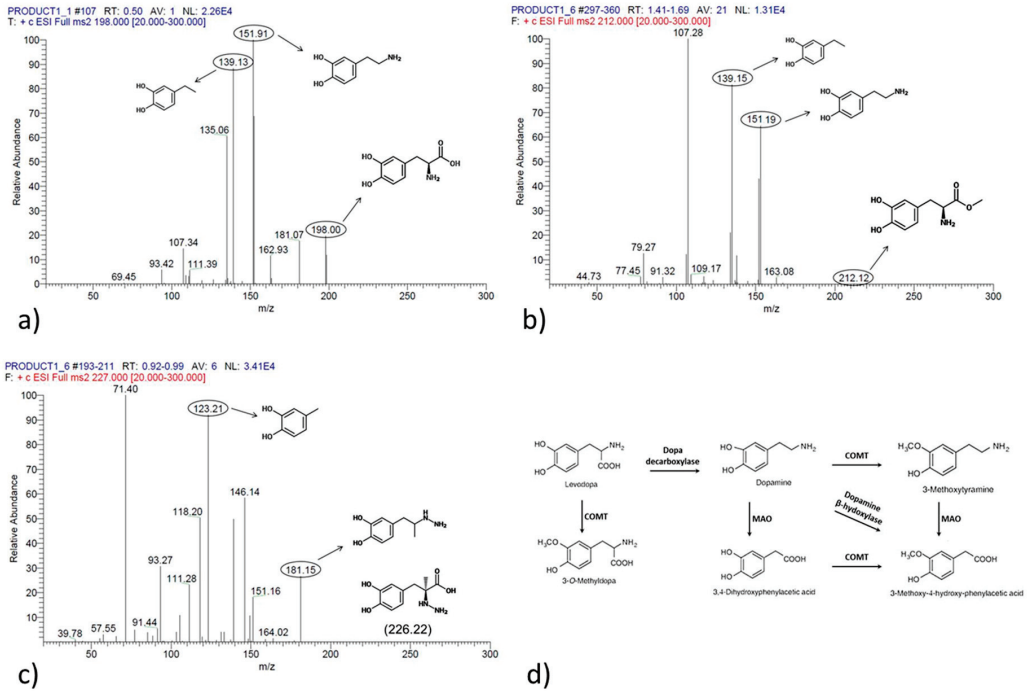


Figure 1. Spectral data and fragment analysis of L-DOPA (panel (**a**)), LDME (panel (**b**)), and carbidopa (panel (**c**)). Panel (**d**) shows L-DOPA metabolism and enzymes involved in sequential transformation (catechol-O-methyltransferase COMT; monoamine oxidases (MAO).

Our method showed to be linear up to 10,000 μg/L L-DOPA and LDME and 6000 μg/L for carbidopa (ULOQ); LLOQ was set at 15 μg/L for all analytes. Although the method is linear up to higher concentration levels, the calibration curve upper quantification limit was set at 2000 μg/L for clinical purposes.

A 1/x weighted linear regression model was applied and the method showed to be linear over the calibration range and beyond. Representative linear equations and regression coefficients are: for L-DOPA, y = 0.00785897x + 0.029, R^2 = 0.998; for LDME, y = 0.0246945x − 0.117, R^2 = 0.995; for carbidopa, y = 0.015161x + 0.004, R^2 = 0.998.

Negligible carryover was observed: six blank injections after samples at ULOQ showed a mean signal of 6.8 ± 1.9% of LLOQ response for L-DOPA, 5.6 ± 6.0% of LLOQ response for LDME, 3.1 ± 2.5% of LLOQ response for carbidopa, and 0.028 ± 0.014% of IS signal for deuterated levodopa (L-DOPA-D3).

Dilution integrity was assessed by measuring the precision and accuracy of diluted samples (n = 5): mean bias% and CV% were, respectively, 1.2% and 1.8% for L-DOPA, 2.7% and 1.9% for LDME, and 3.9% and 2.1% for carbidopa.

No matrix effect (ME) could be found for any of the compounds when measured at low-quality control level (LQC), medium QC level (MQC), and high QC level (HQC) concentrations (as shown in Supplementary Material, Table S1). Mean IS-normalized ME (ISn-ME) values were 106 ± 3.2% for L-DOPA, 98 ± 6.2% for LDME, 107 ± 2.5% for carbidopa, and 97 ± 3.6% for L-DOPA-D3. Mean IS-normalized recovery (ISn-RE) of plasma extraction was 110 ± 3.5% for L-DOPA, 79 ± 3.8% for LDME, 93 ± 3.2% for carbidopa, and 98 ± 5.6% for L-DOPA-D3 (Table S1).

Precision and accuracy were assessed at LLOQ, LQC, MQC, and HQC following a 5 × 5 scheme. Bias% and CV% values for inter-day and intra-day measurements are shown in Table 1a,b, respectively. All values met the acceptance criteria.

Table 1. (**a**) Inter-day precision and accuracy of the quantification method in human plasma. QCs = quality control samples; LLOQ = lower limit of quantification (15 μg/L); LQC = low QC (300 μg/L); MQC = medium QC (900 μg/L); HQC = high QC (1800 μg/L); CV = coefficient of variation. (**b**) Intra-day precision and accuracy of the quantification method in human plasma. QCs = quality control samples; LLOQ = lower limit of quantification (15 μg/L); LQC = low QC (300 μg/L); MQC = medium QC (900 μg/L); HQC = high QC (1800 μg/L); CV = coefficient of variation.

(a)

INTER-DAY

		L-DOPA					**LDME**					**Carbidopa**				
QCs		**D1**	**D2**	**D3**	**D4**	**D5**	**D1**	**D2**	**D3**	**D4**	**D5**	**D1**	**D2**	**D3**	**D4**	**D5**
LLOQ	Bias%	0.6	4.0	−7.9	−5.5	−0.5	6.7	−4.9	11.8	10.7	−17.4	−0.1	5.9	10.2	8.1	−10.1
	CV%	3.4	8.5	2.6	4.0	5.5	8.7	4.1	5.2	5.0	2.9	4.4	6.3	8.2	5.5	9.5
LQC	Bias%	−0.3	11.4	3.1	2.9	−4.1	10.4	−9.4	2.6	7.7	−9.5	2.5	−5.7	1.5	4.3	−9.6
	CV%	3.1	2.9	2.1	2.5	2.7	3.1	4.9	6.3	6.7	2.8	4.1	4.3	5.6	8.1	5.9
MQC	Bias%	−1.0	0.6	−4.3	−1.3	−7.3	8.6	−7.3	−3.1	5.9	−12.7	8.1	−0.1	4.7	9.2	−6.3
	CV%	6.0	4.5	2.3	2.7	1.6	2.3	7.1	5.6	4.0	2.1	2.3	3.6	4.9	4.5	2.1
HQC	Bias%	−2.2	−4.0	−4.7	−5.4	−3.1	−0.1	−7.8	5.3	4.3	−9.4	2.9	−7.3	−0.1	2.5	−3.5
	CV%	2.4	3.4	2.0	2.4	5.0	7.2	4.6	4.5	6.1	3.9	5.0	2.5	4.1	7.3	4.2

(b)

INTRA-DAY

QCs		**L-DOPA**	**LDME**	**Carbidopa**
LLOQ	Bias%	0.7	4.5	1.4
	CV%	7.6	11.0	7.9
LQC	Bias%	−0.3	1.9	−2.5
	CV%	8.6	9.7	6.1
MQC	Bias%	−2.8	1.4	1.8
	CV%	3.0	10.5	5.5
HQC	Bias%	−3.1	1.7	−1.2
	CV%	2.2	10.8	3.9

Reinjection reproducibility was evaluated by measuring the accuracy and precision of a reinjected run. All values were within the acceptance criteria.

Due to the well-known high instability of catecholamines and affiliated compounds, short-term and medium-term stability was assessed (as shown in Supplementary Materials, Figure S1). Short-term stability at room temperature under both light exposure and light protection conditions and at 4 °C was unsatisfactory for all compounds, with the exception of carbidopa when stored at 4 °C. On the other hand, extracts stored in the autosampler compartment were stable for up to 1 week for all compounds. Most importantly, L-DOPA and carbidopa showed good stability in plasma samples when stored at −40 °C up to 2 months and 1 month, respectively; in the same condition, LDME stability was not satisfactory.

2.2. Pharmacokinetic Study

The developed and validated method was applied to real samples obtained from a male patient under treatment at Fondazione IRCCS Istituto Neurologico Carlo Besta. A 45-year-old male patient who was reported to medicate with commercially available *Mucuna pruriens* extracts alone was examined. L-DOPA PK parameters after administration of two tablets of an LDME/carbidopa (100/25 mg) formulation were compared with those obtained after the administration of 500 mg of L-DOPA from *Mucuna pruriens* extracts in off-med conditions from 12 h before (previously treated with L-DOPA/benserazide). In order to maintain the same L-DOPA central bioavailability within the treatments, the *Mucuna pruriens* dose was adjusted by multiplying the conventional L-DOPA dose by five times, hence simulating the theoric absence of DDCIs in *Mucuna pruriens* extract [24]. L-DOPA PK parameters are summarized in Table 2 and plasma concentrations are plotted in Figure 3.

Table 2. PK parameters after administration of two tablets of an LDME/carbidopa (100/25 mg) formulation compared to plasma concentrations after the administration of 500 mg of L-DOPA from commercially available *Mucuna pruriens* extracts.

Formulation	Dose (mg)	Cmax (μg/L)	Tmax (min)	Cmin (μg/L)	$t_{1/2}$ (min)	AUC (μg × h/mL)
LDME/Carbidopa	2 × 100/25	2795	15	323	40	2.687
Mucuna pruriens extract	500	3597	30	1293	141	7.043
		3482	60			

LDME and carbidopa plasma concentrations were also monitored. No LDME could be found when the patient was treated with LDME/carbidopa formulation, thus confirming its complete degradation as a prodrug; carbidopa was detected and its concentration curve, along with L-DOPA, is also shown in Figure 3. No LDME and negligible carbidopa concentrations were detected when the patient was treated with *Mucuna pruriens* extracts.

Noteworthily, the treatment with *Mucuna pruriens* extracts determined higher Cmax and higher AUC compared to the treatment with conventional LDME/carbidopa formulation, in line with the results obtained by Cilia et al. [24]. On the other hand, Tmax was lower when the patient was treated with LDME/carbidopa formulation (Figure 3). The administration of *Mucuna pruriens* extracts was also characterized by higher Cmin and $t_{1/2}$ values when compared with conventional L-DOPA treatment, hence indicating a slower elimination rate.

PK parameters measured after the administration of *Mucuna pruriens* extracts were compared with those presented by Cilia et al. [24]: plasmatic concentration curves in patients administered *Mucuna pruriens* extracts often show double maximum L-DOPA concentration peaks, thus confirming irregular *Mucuna pruriens* PK. It can also be evinced that the activity of the DDCI benserazide was depleted during the 12 h in off-med condition, otherwise, L-DOPA plasma concentration would have been 5 times higher due to inhibition of gastrointestinal AADC activity, which is not hindered when only *Mucuna pruriens* extracts are administered.

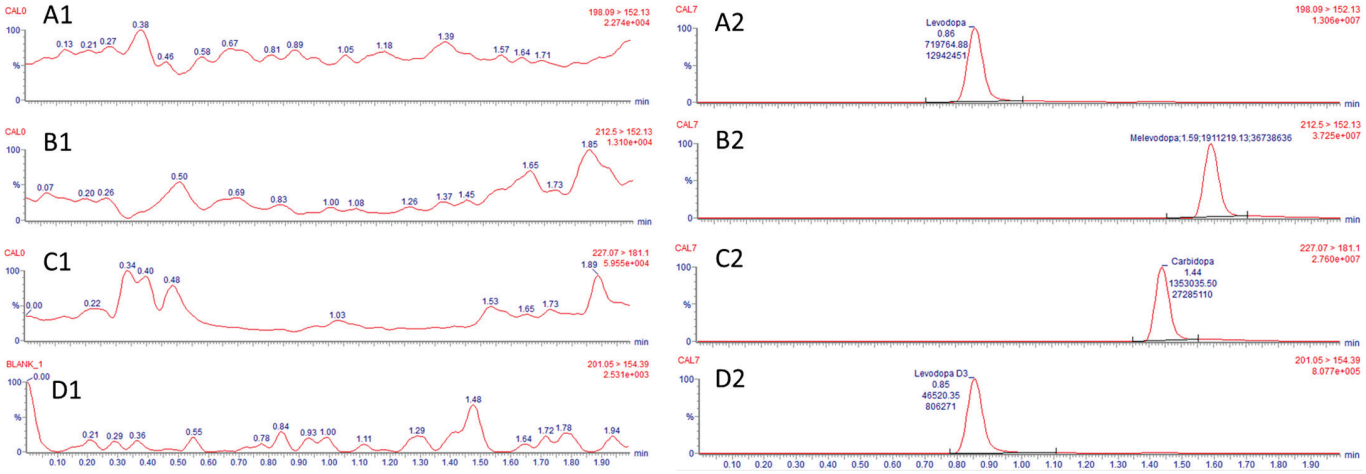
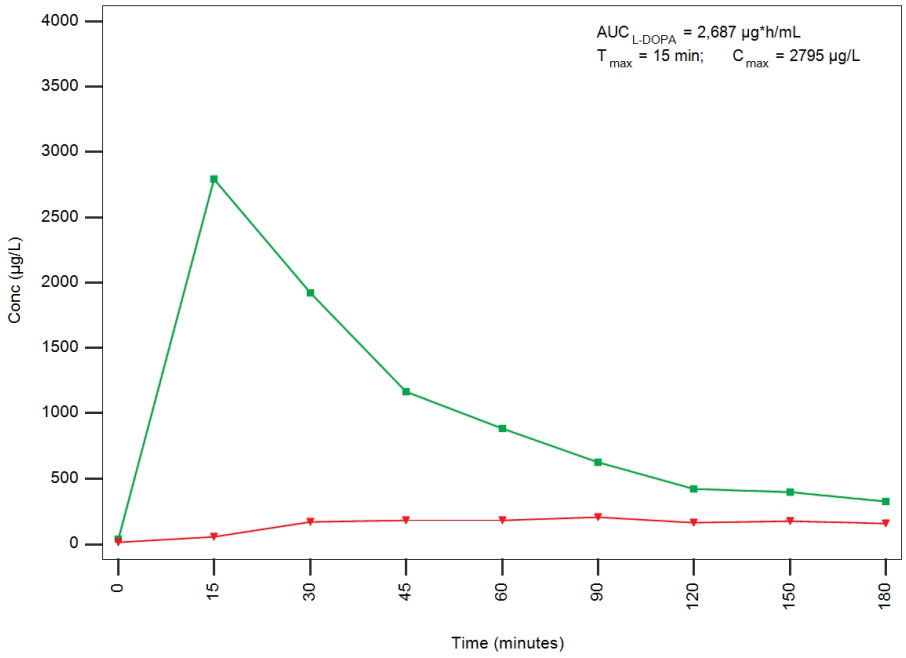


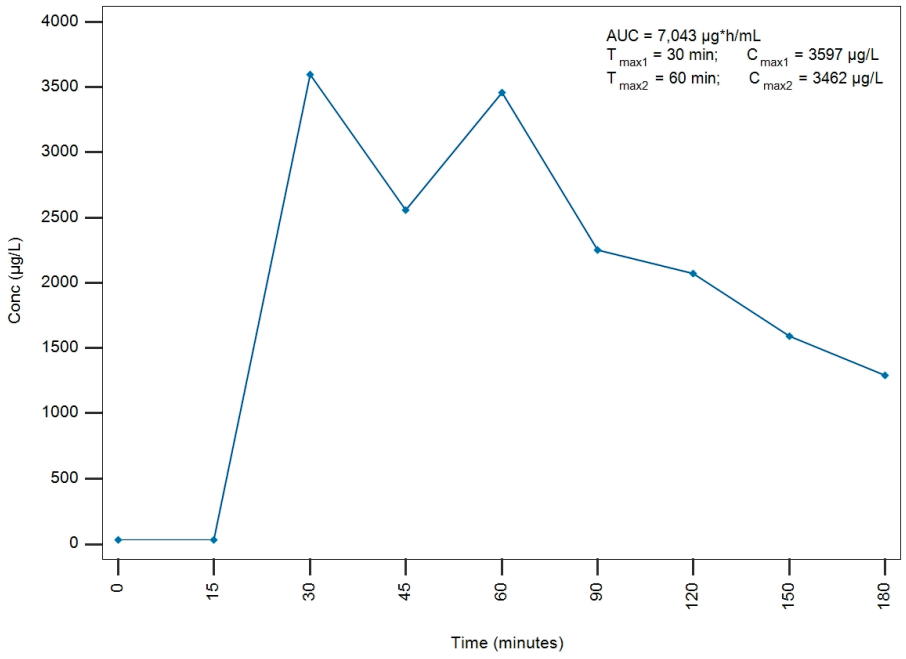
Figure 2. Representative chromatograms of blank plasma (**1**) compared to spiked plasma (**2**). In panel (**A**), L-DOPA (quan 198.09 → 152.13 *m/z*, RT: 0.89 min); in panel (**B**), LDME (quan 212.50 → 152.13 *m/z*, RT: 1.53 min); in panel (**C**), carbidopa (quan 227.07 → 181.11 *m/z*, RT: 1.44 min); in panel (**D**), internal standard L-DOPA-D3 (201.05 → 154.39 *m/z*, RT: 0.85 min). Qualifier ions are described in Table 3.

Table 3. MS method transitions (in bold quantifier ion, in italic qualifier ion), parameters, and retention times.

Compound	Precursor Ion (*m/z*)	Product Ion (*m/z*)	Cone (V)	Collision (V)	Retention Time (min)
L-DOPA	198.09	**152.13** *134.94*	15 20	15 16	0.86
LDME	212.50	**152.13** *134.92*	20 20	14 18	1.59
Carbidopa	227.07	**181.11** *123.08*	20 20	15 27	1.44
L-DOPA-D3	201.05	**154.39**	20	16	0.85



(**A**)



(**B**)

Figure 3. L-DOPA plasma concentrations (µg/L) and PK parameters at 0, 15, 30, 45, 60, 90, 120, 150, and 180 min after administration of two tablets of an LDME/carbidopa (100/25 mg) formulation (L-DOPA concentrations curve in green and carbidopa in red) (**A**) compared to plasma concentrations after the administration of 500 mg of L-DOPA from commercially available *Mucuna pruriens* extracts (*Mucuna pruriens*-derived L-DOPA concentrations curve in blue) (**B**).

3. Discussion

L-DOPA/DDCIs administration is considered the mainstay therapeutic strategy for PD treatment, and its efficacy in the early stage of the disease has been extensively reported [2–5]; with the protracting of the disease, the manifestation of motor complications associated with L-DOPA administration becomes more frequent and causes a rapid de-

crease in PD patients' quality of life [10–13]. As the occurrence of motor complications is strictly associated with the complex L-DOPA PK, the therapeutic monitoring of L-DOPA plasma concentrations plays a crucial role in the management of PD patients [14,15]. In fact, L-DOPA PK is influenced by several clinical, therapeutic, and lifestyle variables, such as gender, BMI, age, disease duration, and severity [14–21]. The identification of other predictors of L-DOPA PK and the integration of these data with plasma concentrations and clinical information could be really helpful to assist clinicians in the optimization of personalized PD therapy, hence ensuring drug efficacy and safety [14,15].

To this aim, we have successfully developed and validated a novel UHPLC-MS/MS bioanalytical method able to quantify in a single run L-DOPA, LDME, and carbidopa in human plasma samples. This method provides the quantification of the pharmacologically active compound, and most importantly allows the monitoring of plasma concentrations of the prodrug LDME and of one of the two known DDCIs, carbidopa, thus ensuring a comprehensive understanding of L-DOPA PK and its alterations. Unfortunately, we could not manage to include the DDCI benserazide due to severe stability issues of the compound; a future perspective will be the overcoming of these issues and the introduction of benserazide within the developed method.

The method proved to be sensitive and selective towards the compounds and was successfully validated according to the most recent guidelines for bioanalytical method validation [34]. Carryover, dilution integrity, matrix effect, accuracy and precision, reinjection reproducibility, and stability were investigated. All parameters were within the acceptance criteria. Nevertheless, the main difficulty we encountered during method validation was the low stability of the compounds in the matrix, in particular when stored at room temperature or at 4 °C. Moreover, LDME was not stable in any of the conditions tested while the other compounds were stable only when frozen and stored at −40 °C up to 1 month for carbidopa and to 2 months for L-DOPA. For this reason, study samples should be processed shortly after drawing to ensure accurate determination of all compounds. Samples should be always handled at low temperatures (e.g., ice bucket, refrigerated centrifuge); samples could also be stored at −40 °C but this process may alter LDME plasma concentrations. Overall, the method performance was good, providing the simultaneous determination of the compound with a short run time and a simple extraction procedure.

As a proof of concept, our method was applied to measure PK parameters in a patient treated with commercially available *Mucuna pruriens* extracts. L-DOPA PK parameters after administration of two tablets of an LDME/carbidopa (100/25 mg) formulation were compared with those obtained after the administration of 500 mg of L-DOPA from *Mucuna pruriens* extracts in off-med conditions from 12 h before. LDME and carbidopa plasma concentrations were also monitored.

The application to real-life PD patients' samples showed that our validated method could be useful to simultaneously monitor L-DOPA plasma concentrations, as well as those of the prodrug LDME and of the DDCI carbidopa, providing a complete overview of L-DOPA PK and its eventual alterations. Indeed, the therapeutic monitoring of L-DOPA and the integration of PK data with clinical and demographic information could be valuable tools for the optimization of what is considered the "gold standard" in the symptomatic treatment of PD.

4. Materials and Methods

4.1. Chemicals and Reagents

L-DOPA, LDME, carbidopa, and L-DOPA-D3 standards were purchased by Merck (Milan, Italy). Stock solutions were prepared in 10 mM HCl at the nominal concentration of 150 μg/mL for L-DOPA, LDME, carbidopa and at the nominal concentration of 50 μg/mL for L-DOPA-D3. Stock solutions were stored at −20 °C.

Trifluoroacetic acid (TFA) was purchased by Merck (Milan, Italy). Ultrapure water was obtained from a Milli-Q water purification system (Millipore, Milan, Italy). LC-MS grade acetonitrile and formic acid were purchased by Merck (Milan, Italy).

4.2. Calibration Curves and Quality Control Samples

Blank plasma from healthy donors was spiked to obtain an eight-point calibration curve (0, 125, 250, 500, 750, 1000, 1500, 2000 μg/L), as well as 3 levels of QC samples at low (LQC, 300 μg/L), medium (MQC, 900 μg/L) and high (HQC, 1800 μg/L) concentrations.

Freshly spiked calibration curves and quality control samples were prepared before each analytical run.

4.3. Sample Preparation

Fresh whole blood was collected by venipuncture in K3-EDTA-containing tubes; after collection, tubes were promptly covered in aluminum foil to ensure light protection and stored at 4 °C until centrifugation. Tubes were centrifuged at 3500× *g* for 15 min at 4 °C and plasma was collected. Plasma samples were either processed or stored at −40 °C until further analysis.

Samples were extracted by acidic protein precipitation. Aliquots of 100 μL of plasma samples were dispensed in 1.5 mL safe-lock tubes; 300 μL of a 10% TFA solution spiked with the IS L-DOPA-D3 at the concentration of 200 μg/L were added to the tubes. Samples were then vortexed for 10 s and centrifuged at 13,000 rpm for 10 min at 4 °C. The supernatant was collected and transferred to a clean 1.5 mL safe-lock tube, which underwent a further step of centrifugation at 13,000 rpm for 5 min at 4 °C. Finally, 250 μL of clean supernatant was collected and transferred to clean glass autosampler vials; 5 μL of sample was injected into the instrument.

4.4. Instrument Setup and Parameters

LC-MS/MS analysis was carried out on a Waters Xevo TQ-XS triple quadrupole mass spectrometer coupled to a Waters Acquity UPLC I-Class System (Waters Corporation, Sesto San Giovanni, Italy). Chromatographic separation was performed on a Kinetex PFP column (50 × 2.1 mm; 2.6 μm particle size) (Phenomenex, Torrance, CA, United States) with two mobile phases: mobile phase A consisted of 0.1% formic acid in water while mobile phase B consisted of 0.1% formic acid in acetonitrile. Elution was performed in gradient elution mode: at a flow rate of 0.4 mL/min, the gradient was stepped from 0% B (100% A) to 30% B (70% A) in 2 min. Then, the column was washed for 1 minute at 70% B (30% A) and restored to the initial condition of 0% B (100% A) for column equilibration. Total run time was 4.5 minutes; column oven was set at 22 °C.

All compounds were detected in multiple reaction monitoring (MRM) mode as described in Table 3. The detecting conditions for each compound were obtained by directly infusing standard solutions in 50% MeOH at 250 μg/L.

MS analysis was performed using a triple quadrupole mass spectrometer equipped with an electrospray ionization (ESI) source. Method parameters were the following: source temperature +150 °C, capillary voltage +1.5 kV, desolvation temperature +500 °C, cone gas flow rate 150 L/h, collision gas flow rate 0.15 mL/min, and desolvation gas flow rate 1000 L/h. Dwell time was set to 0.008 s. Waters MassLynx (V 4.2) and TargetLynx software were used to acquire and process data (Waters Corporation, Sesto San Giovanni, Italy).

4.5. Method Validation

Method validation was performed according to the most recent International Council for Harmonization (ICH) guidelines for bioanalytical method validation "ICH Guideline M10 on Bioanalytical Method Validation and Study Sample Analysis" released by EMA Committee for Medicinal Products for Human Use on 25th July 2022 [34]. Required validation steps are selectivity and specificity, calibration curve linearity, carry-over, dilution integrity, matrix effect, accuracy and precision, reinjection reproducibility, and stability.

4.5.1. Selectivity and Specificity

Method selectivity and specificity were assessed by analyzing six different lots of blank matrices and assessing the absence of significant response accountable to interfering

components at analytes and internal standard retention times. Response should not be greater than 20% of analyte response at LLOQ and 5% of IS response for each matrix.

4.5.2. Linearity

Calibration curves were built by plotting analyte/IS peak areas ratio against corresponding analyte nominal concentrations and fitted by using a 1/x weighted linear regression model.

To assess LLOQ, spiked plasma samples at the concentrations of 100, 75, 50, 25, 15, 10, 5, and 1 μg/L were prepared and analyzed in triplicate. LLOQ was defined as the lowest concentration level at which accuracy and precision were within ±20%.

To assess ULOQ, spiked plasma samples at the concentrations of 3000, 4000, 6000, 8000, and 10,000 μg/L were prepared and analyzed in triplicate. ULOQ was defined as the highest concentration level at which calibration curve maintained its linearity by precision and accuracy being within ±15%.

4.5.3. Carry Over

Carryover was assessed by analyzing six blank plasma samples after the injection of a calibration standard at the ULOQ. Response should not be greater than 20% of analyte response at LLOQ and 5% of IS response for each blank sample.

4.5.4. Dilution Integrity

Dilution integrity was performed to assess the viability of the dilution procedure. A high-concentrated plasma sample (15,000 μg/L for L-DOPA and LDME, 10,000 for carbidopa) was serially diluted with blank plasma to obtain 1:2 and 1:10 dilutions falling within the calibration range. Diluted samples were analyzed in triplicate. The mean accuracy and precision of diluted samples should be within ±15%.

4.5.5. Recovery and Matrix Effect

RE and ME were assessed for each analyte at three concentration levels (LQC, MQC, and HQC) by analyzing six different lots of matrices in triplicate. RE and ME were calculated according to Matuszewski [35]; IS normalization was applied as described in De Nicolò et al. [36]; thus, ISn-ME and ISn-RE values are shown.

4.5.6. Accuracy and Precision

Intra-day and inter-day accuracy and precision were assessed at four concentration levels (LLOQ, LQC, MQC, and HQC) with a 5 × 5 scheme, consisting of five replicates for each concentration level in five analytical runs over five nonconsecutive days.

Accuracy is expressed as relative error, or bias%, which is calculated as the percentual difference between measured and nominal concentrations, while precision is expressed as CV%. Mean accuracy and precision values within ±15% for LQC, MQC, HQC, and within ±20% for LLOQ were considered acceptable.

4.5.7. Reinjection Reproducibility

Reinjection reproducibility was evaluated to establish the viability of processed samples. One run from accuracy and precision experiments was reinjected after storage in the autosampler compartment (10 °C) for 24 h and accuracy and precision of reinjected QCs were assessed.

4.5.8. Stability

Sample stability was measured at two concentration levels (LQC and HQC) in triplicate. Long-term stability was evaluated at −40 °C for 2 weeks, 1 and 2 months; short-term stability was evaluated at room temperature (rt) under light exposure and with light protection and at 4 °C (light protection) for 1, 2, 3, 4, and 7 days. Autosampler stability was

also assessed by storing extracts in the autosampler compartment at 10 °C for 1, 2, 3, 4, and 7 days.

The mean concentration values obtained from each measurement were compared to the concentrations measured at T0 before storage. Stability data are expressed as percentual difference from T0.

4.5.9. Statistical and Graphical Analysis

MedCalc® (version 20.215, MedCalc Software bv, Ostend, Belgium) was used for PK parameters determination.

Supplementary Materials: The following supporting information can be downloaded at: https://www.mdpi.com/article/10.3390/molecules28114264/s1, Figure S1: L-DOPA, LDME, and carbidopa stability; Table S1: Matrix effect (ME) and recovery (RE) data.

Author Contributions: V.I. and U.d.G. conceptualized the study and oversaw the data analysis. L.M., B.C. and U.d.G. drafted the manuscript. L.M., B.C., A.C. and C.C. performed the experiments and data analysis. A.D. and V.C. participated in data analysis and drafting of the manuscript. R.E. and R.C. performed data analysis and participated in the drafting of the manuscript. All authors contributed to the article and approved the submitted version. All authors have read and agreed to the published version of the manuscript.

Funding: This work was partially supported by the Italian Ministry of Health (RC 2022, RC 2023, R.C., U.d.G., L.M., A.D.).

Institutional Review Board Statement: The study was conducted in accordance with the Declaration of Helsinki and approved by the Ethics Committee of Fondazione IRCCS Istituto Neurologico Carlo Besta (protocol code: 054/2023, date of release: 19 May 2023).

Informed Consent Statement: Levodopa pharmacokinetics is routinely performed for diagnostic purposes. Written informed consent has been obtained from the patient to publish this paper.

Data Availability Statement: The data that support the findings of this study are available from the corresponding author upon reasonable request.

Acknowledgments: Authors wish to thank all colleagues and lab technicians that helped in developing this study.

Conflicts of Interest: The authors declare no conflict of interest.

Sample Availability: Not applicable.

References

1. Balestrino, R.; Schapira, A.H.V. Parkinson Disease. *Eur. J. Neurol.* **2020**, *27*, 27–42. [CrossRef] [PubMed]
2. Simon, D.K.; Tanner, C.M.; Brundin, P. Parkinson Disease Epidemiology, Pathology, Genetics, and Pathophysiology. *Clin. Geriatr. Med.* **2020**, *36*, 1–12. [CrossRef] [PubMed]
3. Fahn, S. The History of Dopamine and Levodopa in the Treatment of Parkinson's Disease: Dopamine and Levodopa in the Treatment of PD. *Mov. Disord.* **2008**, *23*, S497–S508. [CrossRef]
4. LeWitt, P.A. Levodopa Therapy for Parkinson's Disease: Pharmacokinetics and Pharmacodynamics: Levodopa Pharmacokinetics and Pharmacodynamics. *Mov. Disord.* **2015**, *30*, 64–72. [CrossRef] [PubMed]
5. Müller, T. Dopaminergic Substitution in Parkinson's Disease. *Expert Opin. Pharmacother.* **2002**, *3*, 1393–1403. [CrossRef]
6. Cotzias, G.C.; Van Woert, M.H.; Schiffer, L.M. Aromatic amino acids and modification of parkinsonism. *N. Engl. J. Med.* **1967**, *276*, 374–379. [CrossRef] [PubMed]
7. Nutt, J.G.; Fellman, J.H. Pharmacokinetics of levodopa. *Clin. Neuropharmacol.* **1984**, *7*, 35–49. [CrossRef]
8. Gershanik, O.S. Improving L-dopa therapy: The development of enzyme inhibitors. *Mov. Disord.* **2015**, *30*, 103–113. [CrossRef]
9. Contin, M.; Martinelli, P. Pharmacokinetics of Levodopa. *J. Neurol.* **2010**, *257*, 253–261. [CrossRef]
10. Cilia, R.; Cereda, E.; Akpalu, A.; Sarfo, F.S.; Cham, M.; Laryea, R.; Obese, V.; Oppon, K.; Del Sorbo, F.; Bonvegna, S.; et al. Natural History of Motor Symptoms in Parkinson's Disease and the Long-Duration Response to Levodopa. *Brain* **2020**, *143*, 2490–2501. [CrossRef]
11. de Bie, R.M.A.; Clarke, C.E.; Espay, A.J.; Fox, S.H.; Lang, A.E. Initiation of Pharmacological Therapy in Parkinson's Disease: When, Why, and How. *Lancet Neurol.* **2020**, *19*, 452–461. [CrossRef] [PubMed]
12. Bloem, B.R.; Okun, M.S.; Klein, C. Parkinson's Disease. *Lancet* **2021**, *397*, 2284–2303. [CrossRef] [PubMed]

13. Nyholm, D.; Lennernäs, H. Irregular Gastrointestinal Drug Absorption in Parkinson's Disease. *Expert Opin. Drug Metab. Toxicol.* **2008**, *4*, 193–203. [CrossRef] [PubMed]
14. Conti, V.; Izzo, V.; Russillo, M.C.; Picillo, M.; Amboni, M.; Scaglione, C.L.M.; Nicoletti, A.; Cani, I.; Cicero, C.E.; De Bellis, E.; et al. Gender Differences in Levodopa Pharmacokinetics in Levodopa-Naïve Patients with Parkinson's Disease. *Front. Med.* **2022**, *9*, 909936. [CrossRef] [PubMed]
15. Contin, M.; Lopane, G.; Belotti, L.M.B.; Galletti, M.; Cortelli, P.; Calandra-Buonaura, G. Sex Is the Main Determinant of Levodopa Clinical Pharmacokinetics: Evidence from a Large Series of Levodopa Therapeutic Monitoring. *J. Park. Dis.* **2022**, *12*, 2519–2530. [CrossRef] [PubMed]
16. Nishikawa, N.; Iwaki, H.; Shiraishi, T.; Mukai, Y.; Takahashi, Y.; Murata, M. Female, Aging, Difference Formulations of DCI, or Lower Body Weight Increases AUC4hr of Levodopa in Patients with Parkinson's Disease. *Park. Relat. Disord.* **2020**, *76*, 16–20. [CrossRef]
17. Kumagai, T.; Nagayama, H.; Ota, T.; Nishiyama, Y.; Mishina, M.; Ueda, M. Sex Differences in the Pharmacokinetics of Levodopa in Elderly Patients with Parkinson Disease. *Clin. Neuropharmacol.* **2014**, *37*, 173–176. [CrossRef]
18. Zappia, M.; Crescibene, L.; Arabia, G.; Nicoletti, G.; Bagalà, A.; Bastone, L.; Caracciolo, M.; Bonavita, S.; Di Costanzo, A.; Scornaienchi, M.; et al. Body Weight Influences Pharmacokinetics of Levodopa in Parkinson's Disease. *Clin. Neuropharmacol.* **2002**, *25*, 79–82. [CrossRef]
19. Müller, T.; Woitalla, D.; Saft, C.; Kuhn, W. Levodopa in Plasma Correlates with Body Weight of Parkinsonian Patients. *Park. Relat Disord.* **2000**, *6*, 171–173. [CrossRef]
20. Contin, M.; Riva, R.; Martinelli, P.; Albani, F.; Baruzzi, A. Effect of Age on the Pharmacokinetics of Oral Levodopa in Patients with Parkinson's Disease. *Eur. J. Clin. Pharm.* **1991**, *41*, 463–466. [CrossRef]
21. Nagayama, H.; Ueda, M.; Kumagai, T.; Tsukamoto, K.; Nishiyama, Y.; Nishimura, S.; Hamamoto, M.; Katayama, Y. Influence of Ageing on the Pharmacokinetics of Levodopa in Elderly Patients with Parkinson's Disease. *Park. Relat Disord.* **2011**, *17*, 150–152. [CrossRef] [PubMed]
22. Stocchi, F.; Marconi, S. Factors Associated with Motor Fluctuations and Dyskinesia in Parkinson Disease: Potential Role of a New Melevodopa Plus Carbidopa Formulation (Sirio). *Clin. Neuropharmacol.* **2010**, *33*, 198–203. [CrossRef] [PubMed]
23. Cassani, E.; Cilia, R.; Laguna, J.; Barichella, M.; Contin, M.; Cereda, E.; Isaias, I.U.; Sparvoli, F.; Akpalu, A.; Budu, K.O.; et al. *Mucuna Pruriens* for Parkinson's Disease: Low-Cost Preparation Method, Laboratory Measures and Pharmacokinetics Profile. *J. Neurol. Sci.* **2016**, *365*, 175–180. [CrossRef] [PubMed]
24. Cilia, R.; Laguna, J.; Cassani, E.; Cereda, E.; Pozzi, N.G.; Isaias, I.U.; Barichella, M.; Pezzolli, G. *Mucuna pruriens* in Parkinson disease: A double-blind, randomized, controlled, crossover study. *Neurology* **2017**, *89*, 432–438. [CrossRef]
25. Cilia, R.; Laguna, J.; Cassani, E.; Cereda, E.; Raspini, B.; Barichella, M.; Pezzoli, G. Daily Intake of *Mucuna pruriens* in Advanced Parkinson's Disease: A 16-Week, Noninferiority, Randomized, Crossover, Pilot Study. *Park. Relat Disord.* **2018**, *49*, 60–66. [CrossRef]
26. Fothergill-Misbah, N.; Maroo, H.; Cham, M.; Pezzoli, G.; Walker, R.; Cilia, R. Could *Mucuna Pruriens* Be the Answer to Parkinson's Disease Management in Sub-Saharan Africa and Other Low-Income Countries Worldwide? *Park. Relat. Disord.* **2020**, *73*, 3–7. [CrossRef]
27. Ferreira, M.S.; Davanço, M.G.; Pepi, G.T.; Previde, N.; Gabbai, J.J.; Martho, A.C.; Brandão, A.H.; Riccio, M.F.; de Campos, D.R.; Meulman, J.; et al. Sensitive LC–MS/MS Method for Quantitation of Levodopa and Carbidopa in Plasma: Application to a Pharmacokinetic Study. *Bioanalysis* **2018**, *10*, 1567–1576. [CrossRef]
28. Martins, H.F.; Pinto, D.P.; Nascimento, V.d.A.; Marques, M.A.S.; Amendoeira, F.C. Determination of Levodopa in Human Plasma by High Performance Liquid Chromatography-Tandem Mass Spectrometry (HPLC-MS/MS): Application to a Bioequivalence Study. *Quím. Nova* **2013**, *36*, 171–176. [CrossRef]
29. Pan, L.; Guo, Y.; Li, Z.; Chen, J.; Jiang, T.; Yu, Y. Simultaneous Determination of Levodopa, Benserazide and 3-O-Methyldopa in Human Serum by LC–MS–MS. *Chroma* **2010**, *72*, 627–633. [CrossRef]
30. Burmaoğlu, R.E.; Sağlık Aslan, S. A Rapid Liquid Chromatography/Tandem Mass Spectrometry Method for Simultaneous Determination of Levodopa, Carbidopa, Entacapone and Their Six Related Compounds in Film-coated Tablets. *Rapid Commun. Mass Spectrom.* **2020**, *34*, e8782. [CrossRef]
31. Ribeiro, R.P.; Gasparetto, J.C.; de Oliveira Vilhena, R.; de Francisco, T.M.G.; Martins, C.A.F.; Cardoso, M.A.; Pontarolo, R.; Athayde Teixeira de Carvalho, K. Simultaneous Determination of Levodopa, Carbidopa, Entacapone, Tolcapone, 3- O -Methyldopa and Dopamine in Human Plasma by an HPLC–MS/MS Method. *Bioanalysis* **2015**, *7*, 207–220. [CrossRef] [PubMed]
32. César, I.C.; Byrro, R.M.; Cardoso, F.F.D.S.E.S.; Mundim, I.M.; Teixeira, L.S.; Gomes, S.A.; Bonfim, R.R.; Pianetti, G.A. Development and validation of a high-performance liquid chromatography-electrospray ionization-MS/MS method for the simultaneous quantitation of levodopa and carbidopa in human plasma. *J. Mass Spectrom.* **2011**, *46*, 943–948. [CrossRef] [PubMed]
33. Jiang, R.; Yang, J.; Mei, S.; Zhao, Z. Determination of Levodopa by Chromatography-Based Methods in Biological Samples: A Review. *Anal. Sci.* **2022**, *38*, 1009–1017. [CrossRef] [PubMed]
34. ICH Guideline M10 on Bioanalytical Method Validation and Study Sample Analysis. Available online: https://www.ema.europa.eu/en/documents/scientific-guideline/ich-guideline-m10-bioanalytical-method-validation-step-5_en.pdf (accessed on 10 February 2023).

35. Matuszewski, B.K.; Constanzer, M.L.; Chavez-Eng, C.M. Strategies for the assessment of matrix effect in quantitative bioanalytical methods based on HPLC-MS/MS. *Anal. Chem.* **2003**, *75*, 3019–3030. [CrossRef]
36. De Nicolò, A.; Cantù, M.; D'Avolio, A. Matrix Effect Management in Liquid Chromatography Mass Spectrometry: The Internal Standard Normalized Matrix Effect. *Bioanalysis* **2017**, *9*, 1093–1105. [CrossRef]

Disclaimer/Publisher's Note: The statements, opinions and data contained in all publications are solely those of the individual author(s) and contributor(s) and not of MDPI and/or the editor(s). MDPI and/or the editor(s) disclaim responsibility for any injury to people or property resulting from any ideas, methods, instructions or products referred to in the content.

biomolecules

MDPI

Article

Variations in *O*-Glycosylation Patterns Influence Viral Pathogenicity, Infectivity, and Transmissibility in SARS-CoV-2 Variants

Sherifdeen Onigbinde †, Cristian D. Gutierrez Reyes †, Mojibola Fowowe, Oluwatosin Daramola, Mojgan Atashi, Andrew I. Bennett and Yehia Mechref *

Department of Chemistry and Biochemistry, Texas Tech University, Lubbock, TX 79409, USA; sonigbin@ttu.edu (S.O.); cristian.d.gutierrez-reyes@ttu.edu (C.D.G.R.); mfowowe@ttu.edu (M.F.); odaramol@ttu.edu (O.D.); mojgan.atashi@ttu.edu (M.A.); andy.bennett@ttu.edu (A.I.B.)

* Correspondence: yehia.mechref@ttu.edu; Tel.: +1-806-742-3059

† These authors contributed equally to this work.

Abstract: The highly glycosylated S protein plays a vital role in host cell invasion, making it the principal target for vaccine development. Differences in mutations observed on the spike (S) protein of SARS-CoV-2 variants may result in distinct glycosylation patterns, thus influencing immunological evasion, infectivity, and transmissibility. The glycans can mask key epitopes on the S1 protein and alter its structural conformation, allowing the virus to escape the immune system. Therefore, we comprehensively characterize *O*-glycosylation in eleven variants of SARS-CoV-2 S1 subunits to understand the differences observed in the biology of the variants. In-depth characterization was performed with a double digestion strategy and an efficient LC-MS/MS approach. We observed that *O*-glycosylation is highly conserved across all variants in the region between the NTD and RBD, whereas other domains and regions exhibit variation in *O*-glycosylation. Notably, omicron has the highest number of *O*-glycosylation sites on the S1 subunit. Also, omicron has the highest level of sialylation in the RBD and RBM functional motifs. Our findings may shed light on how differences in *O*-glycosylation impact viral pathogenicity in variants of SARS-CoV-2 and facilitate the development of a robust vaccine with high protective efficacy against the variants of concern.

Keywords: SARS-CoV-2; mutations; *O*-glycosylation; pathogenicity; transmissibility; LC-MS/MS

1. Introduction

The COVID-19 pandemic, which is caused by the SARS-CoV-2 virus, a member of the β-coronaviruses, caught the world by storm, claiming millions of lives worldwide and altering the pace and fashion of global systems [1]. As of 7 September 2023, 770,563,467 cases of COVID-19 and 6,957,216 deaths were confirmed and reported to the World Health Organization [2]. After the SARS-CoV-2 outbreak in late 2019, there was an 11-month stretch of relative evolutionary stability of the virus. However, since late 2020, SARS-CoV-2 has undergone several mutations at a fast pace to produce variants of concern (VOCs) and variants of interest (VOIs) with observed differences in their transmissibility and infectivity [3,4]. The VOCs include the alpha, beta, delta, gamma, and omicron variants while the others are referred to as VOIs. One of the mutations that emerged and increased in frequency was an amino acid substitution, D614G, within the C-terminal domain (CTD) of the viral spike protein. This mutation was shown by some studies to confer a reasonable benefit for transmissibility [5] and infectivity [6,7]. Another notable missense mutation that emerged within the receptor-binding motif (RBM) of the S1 protein of some variants is N501Y. This mutation has been reported to be more infectious than D614G [8,9] and exists in the current variant of concern, omicron.

The viral transmembrane spike (S) glycoprotein, a trimeric class 1 fusion protein made up of two functional subunits, S1 and S2, is the most essential component of SARS-CoV-2 pathogenesis. It contains the receptor-binding domain (RBD) in the S1 subunit that interacts with the angiotensin-converting enzyme 2 (ACE2) receptor of host cells to facilitate viral entry into the cell [10–14], and the S2 subunit that enables the membrane fusion of viral and host cells [15,16]. The cleavage site at the S1/S2 boundary, which oversees activating β-coronaviruses S proteins, is another important region on the S1 subunit [17,18]. The furin cleavage process plays a crucial role in increasing the receptor binding and fusion activity of the spike protein, contributing significantly to SARS-CoV-2 transmission [19–22]. Of particular interest is the heavy glycosylation of the S1 subunit that serves as a form of "glycan shield" [23,24]. This glycan shield significantly influences the overall pathogenesis of the SARS-CoV-2 virus and protects it from the activity of neutralizing antibodies produced by the host immune response. As a result, the S1 subunit is very important and is the primary target for generating vaccines and neutralizing antibodies in clinical trials [25,26].

Comprehensive research has been conducted to decipher the pattern of *N*-glycosylation on S proteins in SARS-CoV-2 and other members of the β-coronaviruses, such as MERS-CoV and SARS-CoV [16,27–31]. Although SARS-CoV-2 was reported to exhibit a lesser glycan shield with more exposed areas due to fewer *N*-glycosylation sites compared to other β-coronaviruses [27,32], it is still more pathogenic and transmissible [33,34]. *N*-glycosylation plays a crucial role in various aspects of SARS-CoV-2 infection, including viral binding and entrance [35,36], as well as immune recognition and response [37,38]. Thus, an in-depth study of the specific glycosylation patterns of recombinant viral S proteins may provide essential insights into viral biology and direct vaccine design tactics [39,40].

Like viral *N*-glycosylation, *O*-glycosylation also influences viral entrance, spread, and glycan shielding and is linked with infectivity and evolutionary adaptation of the virus [41–44]. Several groups have characterized *O*-glycosylation on the S protein of the wild-type SARS-CoV-2 virus, utilizing different expression systems [29,31,45–49]. A recent study investigated *O*-glycosylation changes in SARS-CoV-2 VOCs, but their findings are limited to the prevalent *O*-glycosylation site T323 [30]. Recent reports have shown that *O*-glycosylation can influence furin-mediated spike cleavage impacting infectivity and transmissibility in SARS-CoV-2 [44,50]. Increased proteolytic processing of spike S protein in some VOCs has been associated with P681 mutation to His or Arg amino acid residues [51–53]. It has been demonstrated that these mutations decrease *O*-glycosylation on Serine (S) or Threonine (T) on a peptide stretch proximal to the furin cleavage site, thereby increasing proteolytic cleavage of S protein into S1 and S2 subunits [44,50]. Consequently, this increase in proteolytic cleavage increases the infectivity of the VOCs. Unlike *N*-glycosylation sites, *O*-glycosylation sites on SARS-CoV-2 S proteins do not have a conserved sequon, a common sugar core, or a high occupancy of glycans; rather, they are occupied with a variety of *O*-linked glycans with low occupancy [27,45,54]. As a result, the comprehensive study of viral *O*-glycosylation is greatly impeded. This necessitates a dire need for greater efforts toward *O*-glycosylation studies of the SARS-CoV-2 S protein.

Since adaptive immunity and infectivity are influenced by viral glycosylation [32,55], mutational alterations in the amino acid sequence of the SARS-CoV-2 S protein variants may produce new sites of glycosylation that could contribute to the specific viral biology of each variant. For example, we identified *O*-glycosylation on mutation points R190S and F490S observed in the Gamma and Lambda variants, respectively. There is limited knowledge about the comprehensive *O*-glycosylation studies of the different SARS-CoV-2 S1 protein variants that exist within the global population. Therefore, we performed a qualitative and quantitative in-depth analysis to determine the *O*-glycosylation patterns of eleven variants of the SARS-CoV-2 S1 protein using high-resolution liquid chromatography–mass spectrometry (LC-MS/MS). To address an accurate and efficient characterization of the S1 protein's *O*-glycosylation, we employed two strategies. Initially, double enzymatic digestion using trypsin and immunomodulating metalloprotease (IMPa) was performed,

followed by a paired MS/MS dissociation strategy using HCD and EThcD. IMPa is an *O*-glycoprotease that cleaves *N*-terminally to S or T linked by a mucin-type *O*-glycan, and sialylation on the *O*-linked glycan does not affect its digestion efficiency [56,57]. This approach allowed a confident assignment of isobaric *O*-glycopeptide forms by differentiating the S or T *O*-glycosylation position. In addition, the analysis revealed an extensive heterogeneity in the *O*-glycosylation pattern in the different SARS-CoV2 S1 protein variants. Thus, by describing the comprehensive *O*-glycosylation patterns of the SARS-CoV-2 S1 protein variants, our findings may reveal how variation in *O*-glycosylation impacts infection and transmission of SARS-CoV-2 variants and serve as a foundation for the development of vaccines with a broad spectrum of functionality.

2. Materials and Methods

2.1. Chemicals and Reagents

Trypsin/Lys-C mix mass spectrometry grade was purchased from Promega (Madison, WI, USA). *O*-glycoprotease (IMPa) was obtained from New England Biolabs (Ipswich, MA). HPL C grade acetonitrile (MeCN) and water were purchased from Fisher Scientific (Fair Lawn, NJ, USA). Formic acid (FA), ammonium bicarbonate (ABC), dithiothreitol (DTT), and iodoacetamide (IAA) were purchased from Sigma Aldrich (St. Louis, MO, USA). SARS CoV-2 (2019-nCoV) Spike S1 protein variants were purchased from Sino Biologicals (US Inc., Wayne, PA, USA) (Table 1).

Table 1. List of the SARS-CoV-2 variants showing the S1 accession ID, name, lineage, and list of mutations.

SARS-CoV-2 S1 Accession ID *	Variant Name	Lineage	Mutations/Deletions/Insertions
40591-V08H12	Alpha	B.1.1.7	HV69-70 deletion, Y144 deletion, N501Y, A570D, D614G, P681H
40591-V08H14	Gamma	P.1	L18F, T20N, P26S, D138Y, R190S, K417T, E484K, N501Y, D614G, H655Y
40591-V08H15	Beta	B.1.351	L18F, D80A, D215G, LAL242-244 deletion, R246I, K417N, E484K, N501Y, D614G
40591-V08H17	Epsilon	B.1.427	W152C, L452R, D614G
40591-V08H23	Delta	B.1.617.2	T19R, G142D, E156G, 157–158 deletion, L452R, T478K, D614G, P681R
40591-V08H28	Iota	B.1.526	L5F, T95I, D253G, S477N, E484K, D614G
40591-V08H29	Eta	B.1.525	Q52R, A67V, 69–70 deletion, 144 deletion, E484K, D614G, Q677H
40591-V08H32	Lambda	C.37	G75V, T76I, RSYLTPG246-252 deletion, D253N, L452Q, F490S, D614G
40591-V08H38	Mu	B.1.621	T95I, Y144S, Y145N, R346K, E484K, N501Y, D614G, P681H
40591-V08H41	Omicron	B.1.1.529	A67V, Δ69-70, T95I, G142D/Δ143-145, Δ211I/L212I, ins214EPE, G339D, S371L, S373P, S375F, K417N, N440K, G446S, S477N, T478K, E484A, Q493R, G496S, Q498R, N501Y, Y505H, T547K, D614G, H655Y, N679K, P681H
40591-V08H1-B	Kappa	B.1.617.1	T95I, G142D, E154K, L452R, E484Q, D614G, P681R

* Vendor part numbers (Sino Biologicals Inc.).

2.2. Tryptic and IMPa Digestion

The tryptic digestion was performed according to the method previously described by Gutierrez Reyes et al. [58]. Briefly, 10 μL of glycoproteins were reconstituted with 40 μL of 50 mM ABC buffer and denatured for 15 min at 90 °C in a water bath. The denatured glycoprotein was reduced by the addition of 1.25 μL of 200 mM DTT and incubated at 60 °C for 45 min. Following that, the glycoprotein was alkylated by adding 5.0 μL of 200 mM IAA and incubated at 37 °C for 45 min. To quench the excess IAA, another 1.25 μL of 200 mM DTT was added and incubated at 37 °C for 30 min. Thereafter, trypsin/Lys-C enzyme was introduced in a 1:25 enzyme-to-protein ratio and incubated at 37 °C for 20 h.

After incubation, the digestion was quenched by heating at 90 °C for 15 min and dried under vacuum in a SpeedVac concentrator (Labconco CentriVap). In a second enzymatic digestion, the tryptic-digested samples were resuspended in 20 mM Tris-HCl solution (pH = 8.0) to a total reaction volume of 50 µL. The IMPa enzyme was added at a 1:10 enzyme-to-protein ratio and incubated at 37 °C for 20 h. The samples were finally dried in a SpeedVac concentrator and resuspended in mobile phase A (MPA) containing 98% water, 2% ACN, and 0.1% formic acid. All samples were prepared in biological triplicates to demonstrate reproducibility.

2.3. LC-MS/MS Analysis

The reconstituted tryptic/IMPa digests were resuspended to a final concentration of 500 ng/µL. Two microliters of the reconstituted sample were injected into an Acclaim PepMap 100 C18 trap (75 mm × 2 cm, 3 mm particle size, Thermo Scientific, Pittsburg, PA, USA) for online purification. Thereafter, the sample was separated on a reversed-phase C18 Acclaim PepMap 100 Å capillary column (150 mm × 75 µm id, Thermo Scientific, Pittsburg, PA, USA) with a temperature of 40 °C and a flow rate of 0.35 µL/min. The chromatographic gradient started at 2% of mobile phase B (MPB) for 5 min and gradually increased to 30% over 35 min, and 70% over 32 min. Then, it was ramped up to 90% of MPB in 1 min and kept constant for 7 min to wash the system. Finally, it was decreased to 2% MPB in 1 min and kept constant for 9 min to equilibrate the column for the next injection. The LC-MS/MS analysis of the *O*-glycopeptide samples was performed with an UltiMate 3000 nano-LC system (Dionex, Sunnyvale, CA, USA) coupled to an Orbitrap Fusion Lumos Tribrid Mass Spectrometer (Thermo Scientific, San Jose, CA, USA). The MPA consisted of 98% water and 2% ACN containing 0.1% FA, and the MPB consisted of 100% ACN containing 0.1% FA. After the LC separation, the *O*-glycopeptide samples were introduced into the mass spectrometer using a nano ESI source in positive ion mode, 2 kV, and a transfer tube temperature of 275 °C. The full MS spectra were acquired in an Orbitrap mass analyzer with a mass range of 500 to 1800 m/z, with a resolving power of 120 K and a mass accuracy of 5 ppm. The RF lens was set at 60% and the maximum injection time was 50 ms. The dynamic exclusion parameters were set as follows: repeat count 1; exclusion duration of 60 s; mass tolerance of 10 ppm; and an intensity threshold of 5.0×10^4. The MS/MS orbitrap scans were generated in data-dependent acquisition (DDA) mode with a duty cycle of 3 s and a selection of the 20 most intense ions from the full MS scan. For the *O*-glycopeptide dissociation, an initial high-energy collision dissociation followed by an electron-transfer/higher-energy collision dissociation (HCD-EThcD) strategy was applied. For the initial HCD, a normalized collision energy (NCE) of 35% and 10 ms of activation time were utilized. The isolation window was 2 m/z with a resolution of 30 k, a fixed scan range of 120 to 4000 m/z, and a maximum injection time of 60 ms. Then, the most intense ions were acquired and sent to a second MS/MS scan using EThcD with an isolation window of 1.6 m/z. A second MS/MS scan was generated using an EThcD dissociation. The Quadrupole was utilized for ion isolation with a window of 1.6 m/z. The ETD reaction time was 50 ms with a reagent target of 2.0×10^5 and a maximum ETD reagent injection time of 200 ms. The supplemental HCD was set at 25%. The generated fragment ions were analyzed in the Orbitrap with a resolution of 30 K, a fixed scan range of 120 to 4000 m/z, and a maximum injection time of 200 ms.

2.4. Data Processing

The raw data files were first processed in Byonic software (version 4.1.10, Protein Metrics, Inc., Cupertino, CA, USA) for *O*-glycopeptide identification, with a mass tolerance of 10 ppm for precursors and 20 ppm for fragment ions. Carbamidomethyl (C) was set as a fixed modification, while oxidation (M), acetyl (protein *N*-terminal), and deamidation (N) were variable modifications. In the digestion parameters, cleavage sites RK and ST were specified with cleavage sides at the C-terminal and *N*-terminal for Trypsin and IMPa, respectively. MetaMorpheus software (version 0.0.320) was also utilized for the

identification of *O*-glycopeptides according to the *O*-pair search method described by Lu et al. [59]. Identification was followed by a manual check of the peak retention time, monoisotopic mass, and mass spectra using XCalibur software® (Version 2.2, Thermo Scientific) to validate the identified *O*-glycopeptides and eliminate false positive ones. The fragment ions were theoretically validated using Glycoworkbench (Version 2.0) [60]. The areas under the peaks were quantified to represent the abundance of each identified *O*-glycopeptide. Relative quantification of the *O*-glycopeptides was accomplished in Microsoft Excel (version 2308) by normalizing the area by the total abundance. The bar plots and heatmaps were generated using GraphPad Prism 9, and Biorender software was used to generate the workflow schematic.

The findings of this study indicate that a significant majority, specifically over 80%, of the *O*-glycopeptides that were unambiguously identified do not possess the consensus sequon required for *N*-glycosylation, which suggests a minimal influence of *N*-linked glycans on the identification of *O*-linked glycans. Nevertheless, in the case of *O*-glycosylation occurring on the serine (S) or threonine (T) amino acid residues neighboring asparagine within the consensus sequon, only glycopeptides classified as level 1 by MetaMorpheus were deemed unequivocal, as the distinctive fragments associated with these glycopeptides accurately pinpoint the glycosylation site on the S/T amino acid residue. This type of glycosylation was manually investigated and validated.

3. Results and Discussion

3.1. Comprehensive Analysis of Site-Specific O-Glycosylation

As shown in Figure 1, we devised an approach to conduct a thorough investigation of the *O*-glycosylation on the S1 proteins from eleven SARS-CoV-2 variants. The investigated variants were kappa, alpha, epsilon, gamma, delta, beta, iota, eta, lambda, mu, and omicron. To rule out any potential bias introduced by the expression of the spike proteins, all the variants utilized for this study were expressed in HEK293 cells. The investigated S1 proteins have different amino acid sequences as a result of mutations including substitution, insertion, or deletion at different regions or domains in the spike proteins of the different SARS-CoV-2 variants, as shown in Table 1. The validation of the mutant S1 glycoproteins was completed through LC-MS proteomics analysis. The protein coverage was calculated utilizing Proteome Discoverer 2.5 software (Thermo Scientific). The results demonstrate the association of the analyzed S1 proteins with the SARS-CoV-2 variants (Supplementary Figure S1).

The *O*-glycoproteomics experiment was initiated with the tryptic digestion of the S1 protein variants. Then, the tryptic digests were subjected to a second digestion using the *O*-glycoprotease IMPa enzyme, which cleaves *N*-terminally to Ser/Thr amino acid residues that are *O*-glycosylated. A high-resolution LC-MS/MS approach was utilized to examine the *O*-glycopeptides. The mutations described by the vendor (Table 1) were used to construct the S1 protein sequences for the different variants. This information was uploaded into Byonic® (version 4.1.10) and MetaMorpheus® software (version 1.0.1) to complete the *O*-glycopeptide identification, followed by manual validation of the detected precursors. The MetaMorpheus® software (version 1.0.1) was utilized according to the *O*-pair search approach described by Lu et al. [59]. The Level 1 searches were reported as spectral evidence that confidently assigns glycans to the glycosites.

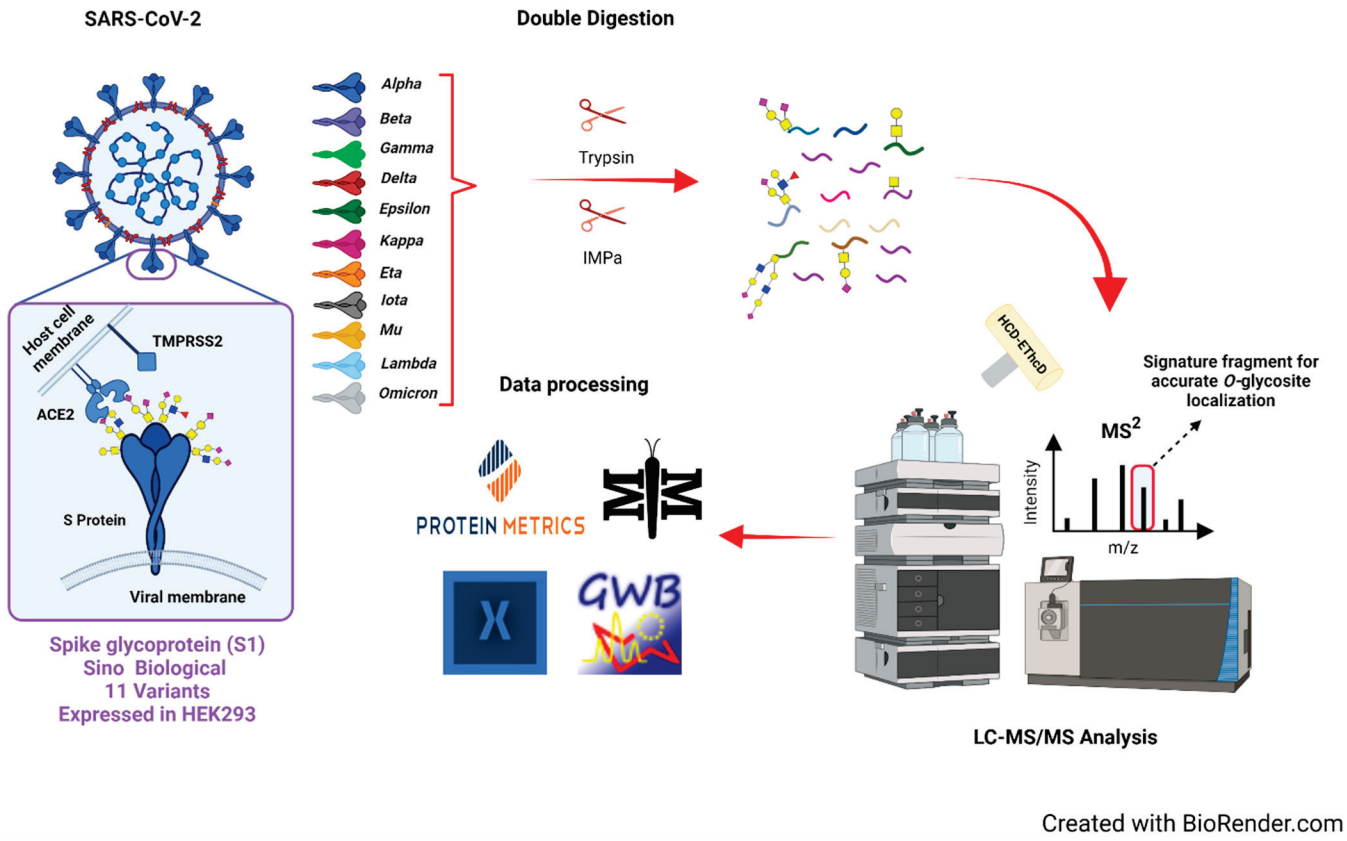


Figure 1. Schematics of the *O*-glycoproteomic workflow employed in this work. Variants of SARS-CoV-2 S1 proteins recombinantly expressed in HEK293 were digested using trypsin followed by IMPa. The glycopeptide digests were analyzed by LC-MS/MS. Glycopeptides were identified using Byonic (version 4.1.10) and MetaMorpheus software (version 1.0.1). The *O*- glycan symbols used in this work: , HexNAc (N); , Hex (H); , Fucose (F); and , NeuAc (A).

The comparisons of the *O*-glycopeptides identified in the S1 subunits of the SARS-CoV-2 variants showed extensive heterogeneity. Figure 2A shows the number of glycosylation sites observed in the analyzed variants, while Figure 2B shows the number of unique *O*-glycans attached to the unambiguously identified *O*-glycosites. The different strains show the distribution of the *O*-glycosylation sites across different regions and domains of the S1 subunit of the SARS-CoV-2 S protein (Figure 2C). These include the *N*-terminal domain (NTD), receptor binding domain (RBD), receptor binding motif (RBM), C-terminal domain (CTD), and the region between the NTD and RBD designated as amino acid residues 305–331. The designation of the different domains and regions of the S1 protein was determined according to the X-ray crystallography structure of SARS-CoV-2 RBD complexed with ACE2 [61]. According to these results, the omicron, eta, and lambda variants were more densely *O*-glycosylated with 23, 18, and 18 sites, respectively. The variants with fewer glycosylation sites were alpha and kappa with 15 and 11 sites, respectively. Importantly, all data were generated in biological triplicates, and identical results were obtained from the replicates, demonstrating the reproducibility of our analytic method. Previously, 11 *O*-glycosylation sites have been identified on the S1 subunit of the wild-type (WT) SARS-CoV-2 spike protein while 6 sites were found on the S2 subunit [46]. Liang and co-workers unambiguously identified 16 *O*-glycosylation sites in the S1 subunit of the WT spike protein and 14 in its D614G mutant expressed in HEK 293 cells [47]. This observation implies that mutations have the potential to influence *O*-glycosylation in spike proteins. Additionally, the authors reported the identification of 6 *O*-glycosylation sites on the S1 subunit of the WT SARS-CoV-2 that was expressed in insects. This significant change in the number of *O*-glycosylation sites may be attributable to the different expression systems

utilized. Wang et al. conducted a comparative analysis of *N*- and *O*-glycosylation patterns in HEK293 and Baculovirus insect cells [48]. Their findings revealed distinct variations in the site-specific glycosylation of spike proteins when expressed in these two different systems. Additionally, it was revealed that there is a notable disparity in the sialylation distribution of *N*-glycans between HEK293 cells and Baculovirus insect cells. The authors suggested that the expression systems may exhibit preferences for *O*-glycosylation enzymes, particularly GalNAcTs, which could account for the observed variances in *O*-glycosylation. Another study has documented notable disparities in the *O*-glycosylation patterns of the receptor-binding domain (RBD) when expressed as a monomer, as opposed to its localization on the dimeric ectodomain of insect cells [45]. However, they reported similarities in *O*-glycosylation patterns between insect and HEK293 ectodomains. In the work of Zhang and colleagues, 3 *O*-glycosites were confidently assigned in the full-length S protein expressed in the insect cell while 11 sites were assigned in only the S1 subunit expressed in the human cell [49]. In addition, the reported sialylation in the S1 subunit expressed in human cells increased compared to insect cells. The utilization of recombinant viral proteins as a foundation for the development of non-mRNA vaccines [62,63] necessitates a comprehensive understanding of the glycosylation characteristics shown by these recombinant viral proteins across various cellular systems. It has been demonstrated that HEK293 cells adhere to the general mammalian glycosylation pathway; thus, it was explored in this study [64]. Figure 2B shows the number of *O*-linked glycans derived from the studied variants. Similar to the work of Dong et al., we have identified some unique *O*-linked glycans in SARS-CoV-2 S1 proteins including H2N3F2, H1N2F2, and H2N3F3 [47]. We have also shown multiple sialylated *O*-glycans such as H1N1A3 and H1N2A3 linked to the S1 protein in some variants. In addition, we identified large *O*-glycans, including H4N6F2 in alpha and lambda; H5N5F3 in lambda; and H4N4F3A1 in lambda, beta, eta, and mu. Overall, our findings showed extensive differences in the *O*-glycosylation of the S1 proteins of SARS-CoV-2 variants.

Important differences in the S1 protein domains and regions were also observed. For example, the RBM was *O*-glycosylated in all the variants except alpha and delta (Figure 2C). In all the SARS-CoV-2 variants characterized in this approach, the region between NTD and RBD with the designated amino acid residues 305–331 was found to be extensively *O*-glycosylated and conserved among all variants. Thr 323 in this region has been reported to be extensively *O*-glycosylated in other studies as well [29–31,65]. While the delta variant exhibits no unambiguous *O*-glycosylation in the RBD and RBM functional motifs, either or both the domain and the motif were mostly *O*-glycosylated in the other variants. In the omicron variant, Roberts et al. identified a unique *O*-glycosite Thr 376 on the RBD that we could not identify in our study [65]. However, their experiment was conducted using the spike protein RBD expressed as a monomer, which may have prompted differentiation in the glycosylation pattern of the RBD [66]. The CTD1 and CTD2 also exhibited varying degrees of *O*-glycosylation. For the CTD1, a few of the variants were *O*-glycosylated in this domain including delta, iota, lambda, and omicron. Conversely, the CDT2 domain was *O*-glycosylated in all the variants except mu. The presence of a mutation on P681 has been found to decrease *O*-glycosylation on Thr678 in CTD2 [44]. Accordingly, our data indicates that *O*-glycosylation was not detected on Thr678 in VOCs except in the gamma variant. This discrepancy may be attributed to the absence of a mutation on residue P681 in gamma.

Another intriguing observation in the glycosylation pattern observed in this analysis was the *O*-glycosylation proximal to *N*-glycosylation sites. Previously, Tian et al. reported *O*-glycosylation in proximity to glycosylated asparagine amino acid residue in wild-type SARS-CoV-2 spike protein, thereby suggesting the "O-Follow-N" rule [67]. We observed *O*-glycosylation on T124, T236, and S151 following potential *N*-glycosylation sites with the sequon NXS/T in some of the analyzed variants (Figure 2C).

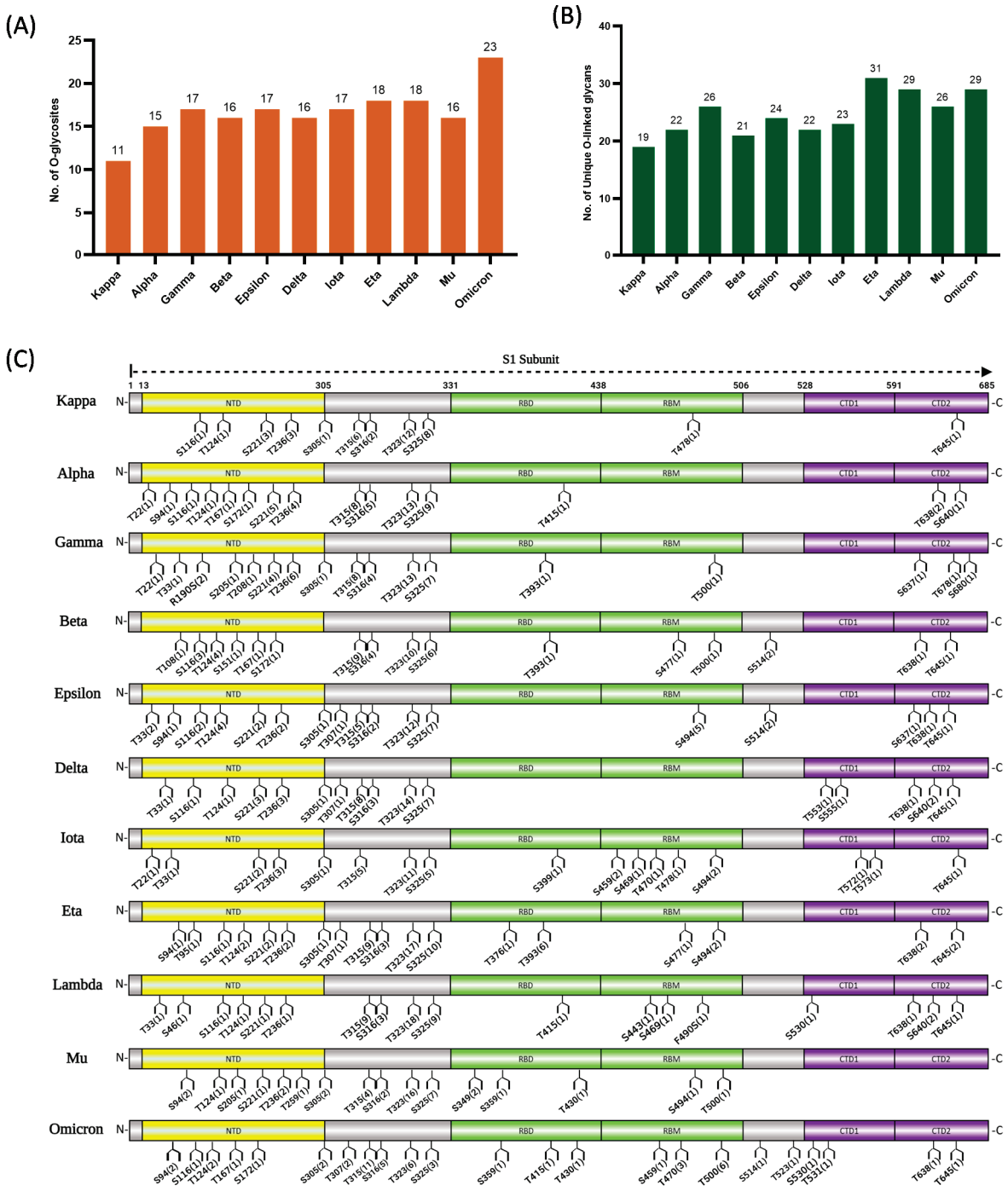


Figure 2. Site-specific localization of *O*-glycoforms in SARS-CoV-2 variants S1 proteins. The bar graphs represent the number of (**A**) unambiguous *O*-glycosylation sites and (**B**) unique *O*-linked glycans observed in each SARS-CoV-2 variant. The error bar represents the standard deviation (n = 3). (**C**) Schematic representation of the 11 SARS-CoV-2 variants S1 glycoprotein showing the position of *O*-linked glycosylation. The domains and regions of the S1 glycoproteins are illustrated as NTD (yellow), the region between NTD and RBD 305–331 (grey), RBD (green), RBM (green), and CTD 1/2 (purple). The identified *O*-glycopeptides are shown in detail in Supplementary Tables S1 and S2 for Byonic and MetaMorpheus, respectively.

3.2. Microheterogeneity of Site-Specific O-Glycosylation

In the previous section, we described the qualitative differences in *O*-glycosylation between the domains and motifs of the S1 protein variants. It is well known that the

site-glycosylation also presents large differences in glycan expression [68,69]. Therefore, we next quantitatively describe the heterogeneity of the identified glycosylation sites across the variants' domains and regions. These include the domains NTD, RBD, RBM, CTD, and the region between the NTD and RBD designated as amino acid residues 305–331. Although the function of the NTD is not clear, it has been shown to be a potential target for therapeutics against SARS-CoV-2 [70]. SARS-CoV-2 binding by ACE2 occurs primarily at the RBD, a critical functional component within the S1 subunit [16,61,71]. The RBM in the RBD is the essential functional motif that facilitates interaction with the human angiotensin-converting enzyme (ACE2) [28]. Additionally, the CTD also functions as the RBD for the ACE2 entry receptor [26]. The data revealed that the relative abundances of *O*-glycosylation were not uniformly distributed across each domain or region, as shown in Figure 3A–E. Across all the variants, the region between the amino acids 305 to 331 contained the highest relative abundance of *O*-glycopeptides with a total average of 88%. It is noteworthy that the omicron variant showed the lowest *O*-glycosylation, with a relative abundance of approximately 61.0% in this region. The comparative analysis of *O*-glycosylation in the NTD revealed that all strains had levels below 11% of relative abundance, where omicron showed the largest abundance with 10.7% in this region. Remarkably, the relative abundance of the RBD domain was less than 3% in all strains except for omicron, with 7.5%. The relative abundance of *O*-glycosylation on the RBM functional motif was similar between iota and omicron with 16.9% and 16.5%, respectively. The *O*-glycosylation relative abundance in the rest of the analyzed strains was less than 6% in this motif. Considering the CTD's involvement in the binding of the ACE2 receptor and the crucial function of the furin S1/S2 cleavage site in mediating the hydrolysis of S protein, we measured the *O*-glycosylation at the CTD 1 and 2 close to the cleavage site. In this domain, the iota strain had the highest relative abundance (10.9%), followed by omicron (4.7%).

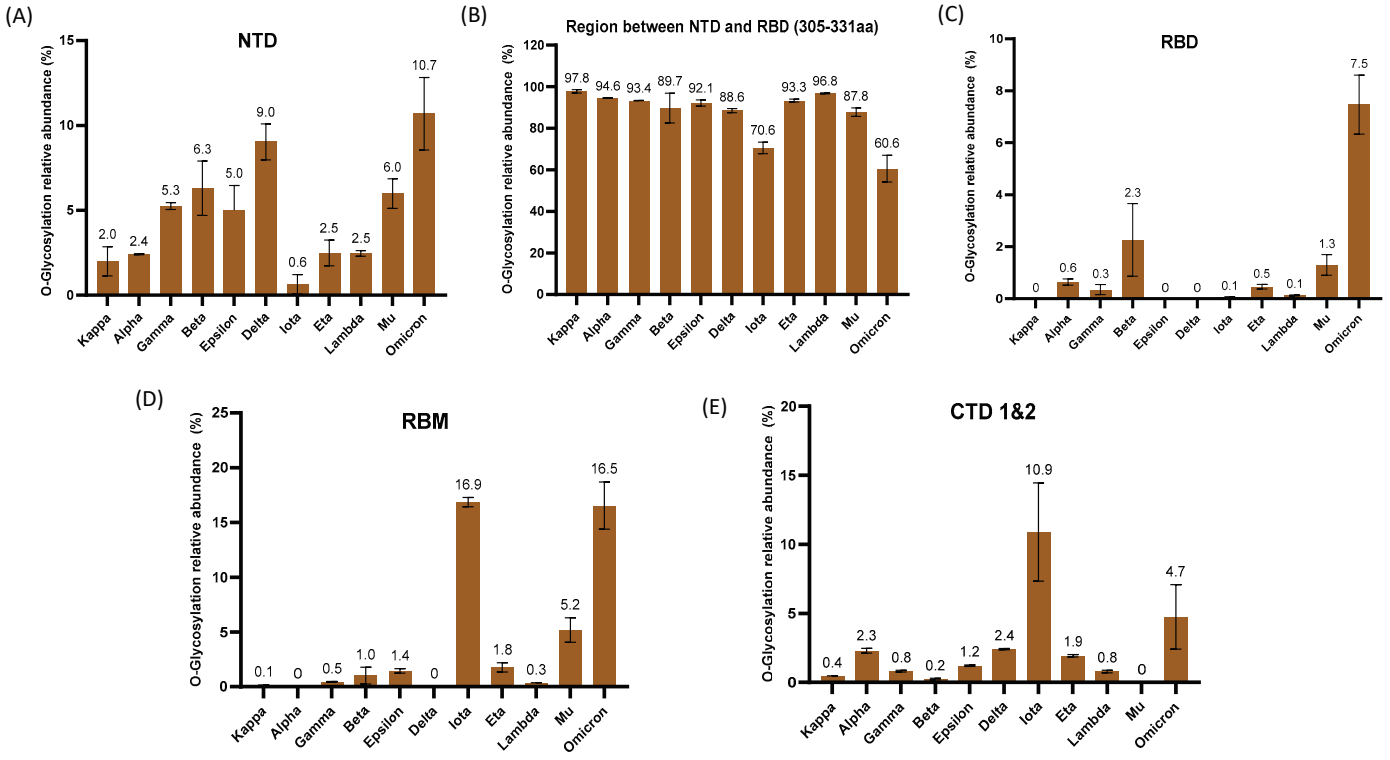


Figure 3. Distribution and quantification of *O*-glycosylation in domains and regions. The bar graphs represent the normalized total *O*-glycosylation abundance on (**A**) the NTD, (**B**) the region between NTD and RBD, (**C**) the RBD, (**D**) the RBM, and (**E**) the CTD 1 and 2 across the different variants. The normalized relative abundances are shown in percentage (%). The error bar represents the standard deviation (n = 3).

Additionally, we analyzed the top five *O*-glycopeptides across all variants and determined that the most abundant *O*-glycan (H1N1A2) was observed on amino acid residue T323/S325 except in omicron (Figure 4). The omicron variant possesses this abundant glycan in position T315/S316. The disialylated core 1 *O*-glycan has been reported to be the most abundant in the wild type of SARS-CoV-2 S protein in many studies [46,72]. The single levels of this glycan varied between 75.0% and 53.4% relative abundance in almost all the evaluated variants (Figure 4). Conversely, the eta and omicron variants presented considerably lower relative abundances of this glycan H1N1A2 with 23.7% and 24.5%, respectively (Figure 4). In this case, both variants showed a uniform *O*-glycan distribution. This observation may be due to the increased number of *O*-glycosylation sites present in both variants. The relative abundances are spread across the multiple *O*-glycosylated sites.

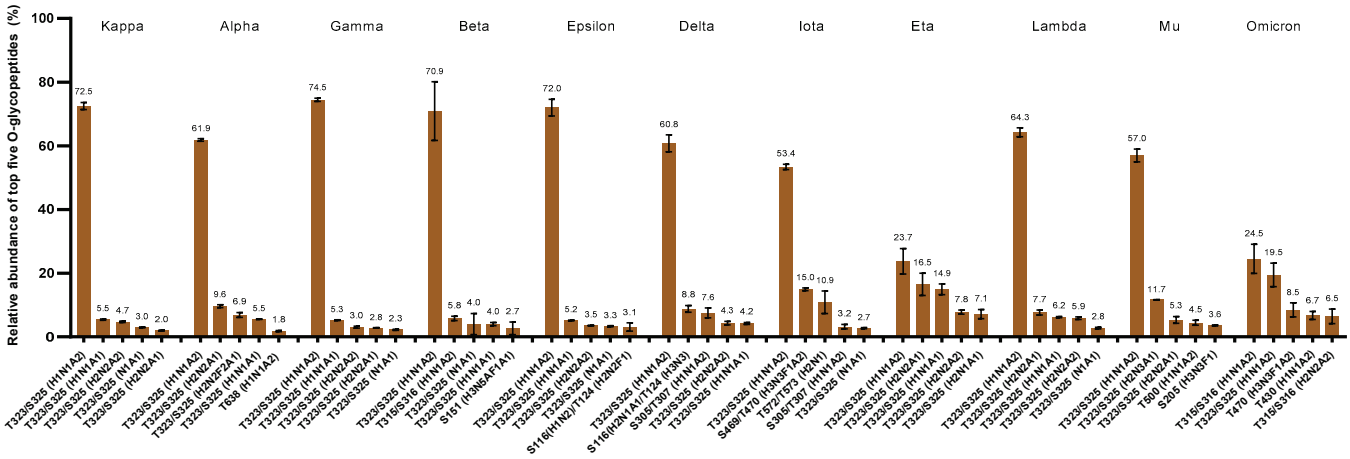


Figure 4. Quantification of the top five *O*-glycopeptides in each variant. The bar graph represents the normalized percentage relative abundance of the top five *O*-glycopeptides across the different variants. The error bar represents the standard deviation (n = 3).

Because the RBD domain is the principal target of neutralizing antibodies, the bulk of SARS-CoV-2 specific antibodies is directed towards it [73]. Several mutations have occurred in the RBD of different SARS-CoV-2 variants that alter their binding by antibodies [74–77]. Reports from previous studies indicate that omicron with many mutations, especially in the spike protein, has the ability to evade the immune system, thereby increasing its infectivity and transmissibility [78,79]. Omicron's RBD contains 15 substitutions, and two of these mutations (including G446S and G496S) have introduced new potential *O*-glycosylation sites. We identified *O*-glycosylation on mutation points G446S; however, this was considered ambiguous due to the lack of sufficient spectral evidence. Accordingly, our results indicated a significant increase in the *O*-glycosylation abundance of this domain in omicron (Figure 3C). These glycans may shield important epitopes aiding the immune evasion seen in omicron variants, thereby increasing its infectivity and transmissibility. Substitutions such as K417N and N501Y have been linked to immune evasion and increased infectivity [8,9,80]. In addition, the E484K mutation lowers antibody neutralization, which would favor escape mutations [81]. Point mutations involving substitution with electropositive amino acid residues such as Q493R and Q498R in the RBD of omicron have been shown to be critical for increased binding of its RBD to its ACE2 receptor [82,83]. The presence of these critical mutations in VOCs may explain their observed increase in infection. In addition to these mutations, the dense *O*-glycosylation observed in omicron may explain its ability to evolve into new variants of concern with enhanced transmissibility and antibody resistance [84]. Among the VOIs, iota has shown a dense distribution of *O*-glycosylation comparable to omicron on its RBM. However, it lacks mutations essential for immune escapism and increased infectivity. Contrary to the other strains of SARS-CoV-2 known to infect the lungs, omicron primarily targets the upper respiratory tract, resulting in milder

symptoms and a greater transmission of the variant [85]. The expression of ACE2 in the upper respiratory tract is significantly low compared to the lungs [86,87]. The extensive *O*-glycosylation seen in the RBD of omicron may explain its ability to mainly infect the upper respiratory tract, which is characterized by poor expression of human ACE2.

N-glycosylation characterization and profiling in SARS-CoV-2 spike proteins have been conducted in many studies [29–31,88,89]. The significance of *N*-glycosylation in the pathogenicity of the virus has been demonstrated since it plays a pivotal role in facilitating viral attachment and entry into the host cell [35,36]. In addition, they can modulate both innate and adaptive immune responses in the virus, which ultimately impacts host recognition and infectivity [37,38]. A recent study investigated the *N*- and *O*-glycosylation profiling of SARS-CoV-2 variants of concern (VOCs) and reported changes in the *N*- and *O*-glycosylation profile [30]. However, the researchers were only able to confirm the presence of *O*-glycosite T323 which may be due to differences in the expression systems or expression methods.

Our results indicated that the omicron variant has a wide distribution of *O*-glycosylation on critical functional domains, which may explain its higher transmissibility and infectivity. Overall, the omicron variant possesses more *O*-glycosylation sites than other strains, with 23 unambiguous *O*-glycosylation sites. Moreover, combined with its extensive *O*-glycosylation, omicron's *N*-glycosylation on the S1 subunit may ensure maximum glycan shielding of the protein potentially contributing to immune evasion.

3.3. Compositional Analysis of O-Glycoform Types

Key components of glycosylation include glycoform types, which play a role in the interaction between the virus and the host [25]. Sialylated glycoforms have been demonstrated to be important in viral pathogenicity and transmission among species by playing crucial functions such as attachment and entry receptors for viruses in host cells [11,90]. Based on this information, it is imperative to carry out a comprehensive analysis of viral sialylation on SARS-CoV-2 variants. Herein, *O*-linked glycoform types generated from the S1 subunit of the SARS-CoV-2 strains were investigated and classified into sialylated, fucosylated, sialofucosylated, and other types, as depicted in Figure 5.

To explore the different glycan types in the S1 proteins of SARS-CoV-2 variants, we computed the total normalized relative abundances of the different *O*-glycoform types (Figure 5A–D). According to our results, the sialylated *O*-glycans were the most abundant of all the variants, demonstrating the importance of sialylation in viral pathogenesis. The total average of sialylation across the investigated variants was 88%, while the iota and omicron strains showed lower relative abundances with 66.4% and 74.1%, respectively (Figure 5A). The top five *O*-glycans were the sialylated type, as can be observed in Figure 4. Of particular interest, the observed deficiency of sialylation of the iota and omicron variants was complemented with a significant increase of 17.6% and 15.3% in sialofucosylation, compared to other SARS-CoV-2 strains (Figure 5B). The most abundant sialofucosylated *O*-glycans were different across the variants. For instance, H2N2F2A1 was the most abundant in alpha, while H3N3F1A2 was the most abundant in omicron and iota (Figure 4). High expression of sialofucosylation has been linked to increased ACE2 binding and decreased sensitivity to neutralizing antibodies [91]. There is still a need for further research to determine the biological significance of *O*-sialofucosylation on the virology of SARS-CoV-2 variants. Additional results showed approximately 7% fucosylated *O*-glycoforms in mu and 6% in omicron, while the other variants exhibited $\leq$4% fucosylation (Figure 5C). The final *O*-glycoform type studied was the glycoforms without sialylation or fucosylation, termed neutral glycan types. In contrast to the other variants, iota had a much larger abundance of this type of *O*-glycosylation with 15.1% relative abundance, while others showed less than 4% (Figure 5D). The role that this glycoform type plays in iota deserves further investigation.

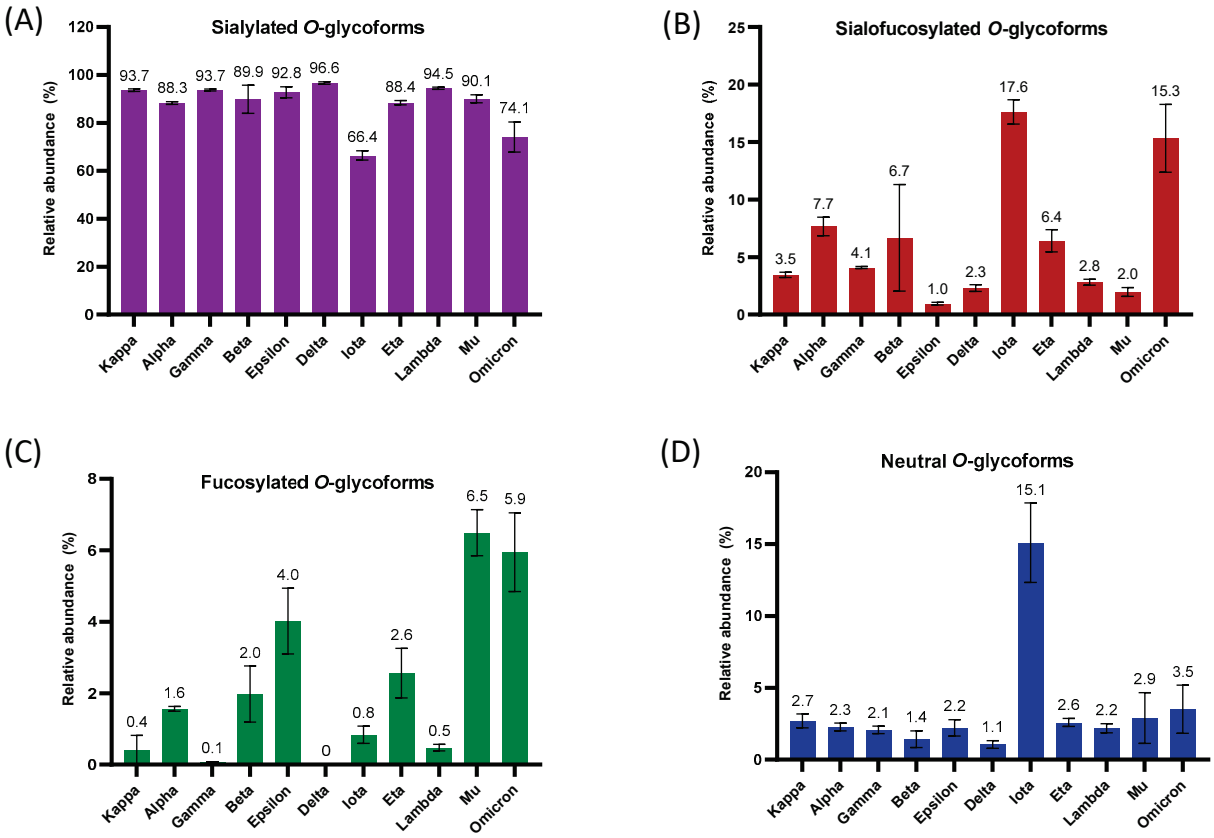


Figure 5. Distribution of *O*-glycoform types in different domains and regions across variants. (**A**) The bar graph represents the normalized percentage relative abundance of sialylated-only *O*-glycoforms across the different variants. (**B**) The bar graph represents the normalized percentage relative abundance of sialofucosylated *O*-glycoforms across the different variants. (**C**) The bar graph represents the normalized percentage relative abundance of fucosylated-only *O*-glycoforms across the different variants. (**D**) The bar graph represents the normalized percentage relative abundance of neutral *O*-glycoforms across the different variants. The error bar represents the standard deviation (n = 3).

Among the top five *O*-glycopeptides across all variants, the most prevalent *O*-glycoform in all variants was disialylated and located between NTD and RBD (Figure 4). Interestingly, among all the analyzed SARS-CoV-2 variants, the top five *O*-glycopeptides identified in only omicron were disialylated, with two of them present on the RBD (T430 and T470) functional domain (Figure 4). The most abundant glycopeptide in all variants was present in the region between the NTD and RBD. There is a need to explore sialylation on functional domains because the abundance of this glycopeptide was greater than 50% in all the examined SARS-CoV-2 S1 variants, except for eta and omicron (<25%).

To further explore the relevance of sialylation in SARS-CoV-2 variant pathogenesis and interspecies transmission, we investigated the total sialylation on the RBD and RBM functional domains in the S1 proteins of the variants. Notably, omicron showed 7.5% sialylation abundance in the RBD; in comparison, all other variants showed less than 1% sialylation in the RBD (Supplementary Figure S2). Prior studies have indicated that the increased sialylation observed in the omicron variant may potentially augment its ability to evade neutralization [91]. Roberts et al. have also reported increased sialylation in the RBD of WT and SARS-CoV-2 variants [65]. In the RBM, there was a comparable sialylation abundance in omicron and iota with 15.5% and 17.8%, respectively, while the others showed less than 6% sialylation in this functional motif (Supplementary Figure S3). This is due to the higher sialylation abundance in the region between NTD and RBD in the other variants that were analyzed.

It is still unknown how the essential amino acid point mutation interacts with proximal *O*-linked glycans in various SARS-CoV-2 variants. According to our results, only the omicron variant exhibited six *O*-glycoforms on position T500 next to the immune escape mutation point N501Y in the RBM, while the other strains had just one *O*-glycoform or none (Figure 2C). More interestingly, the six *O*-glycoforms found on the T500 position in the omicron variant were sialylated, further implicating sialylation in the infectivity and transmissibility of this variant. It is important to reiterate that the RBM on the RBD is the functional motif that interacts directly with the human ACE2 for viral entry [28]. Thus, this type of glycosylation may influence the viral life cycle and host interaction.

After evaluating the abundance of the different *O*-glycoform types, we subsequently employed heat maps to illustrate the normalized abundances of individual glycoforms on the identified glycosites in all analyzed variants of SARS-CoV-2, as depicted in Supplementary Figures S4–S14.

3.4. Differentially Expressed O-Glycosylation among SARS-CoV-2 S1 Protein Variants

In this section, we focus our evaluation on the variants with a denser distribution of *O*-glycosylation on the S1 protein: iota, eta, lambda, mu, and omicron. Interestingly, these variants showed significant differences in the microheterogeneity of glycoforms present on the identified glycosites. To provide useful analytical information, we investigated how these five variants differ in terms of *O*-glycoforms. The results showed 16, 24, 20, 17, and 30 unique *O*-glycopeptides for iota, eta, lambda, mu, and omicron SARS-CoV-2 S1 proteins, respectively. Eleven *O*-glycopeptides were found in common among the evaluated variants (Figure 6A). The list of unique and shared *O*-glycopeptides present in these variants is shown in Supplementary Table S3. It is worth noting that the common *O*-glycopeptides were present in the region between the amino acids 305 to 331. The region observed between the NTD and RBD was the most glycosylated region in all the SARS-CoV-2 S1 proteins analyzed in this approach. Although the eta variant showed the largest number of *O*-linked glycans, omicron had the largest number of unique *O*-glycopeptides prompted by its higher number of identified *O*-glycosites. This information suggests a greater complexity in the *O*-glycosylation of omicron compared to the other variants.

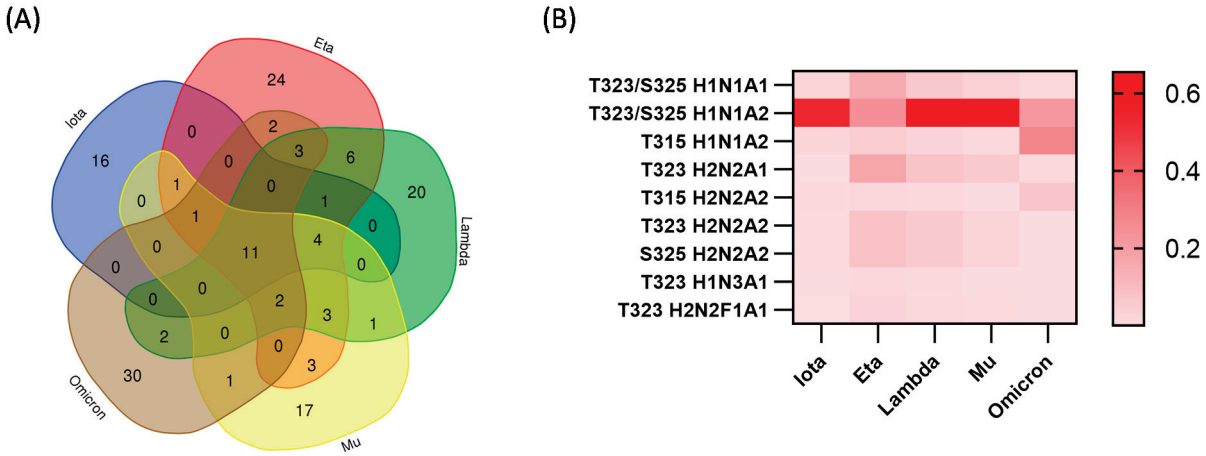


Figure 6. Comparative analysis of microheterogeneity among five variants. (**A**) Venn plot showing the shared and unique *O*-glycopeptides among iota, eta, lambda, mu, and omicron. (**B**) Heatmap of *O*-glycopeptides common to iota, eta, lambda, mu, and omicron illustrating relative abundance.

The relative abundances of the common *O*-glycopeptides shared by the SARS-CoV-2 variants were plotted as a heatmap (Figure 6B). Where the SARS-CoV-2 variants are shown on the x-axis, the glycosylation sites and *O*-linked glycans are shown along the y-axis for comparison of *O*-glycoform expressions. The results showed a significantly higher abundance of H1N1A2 on T323/S325 of the variants iota, lambda, and mu. Conversely, the

eta and omicron variants showed a more uniform *O*-glycan expression, a difference that was also demonstrated in Figure 4. The expression of T315 H1N1A2 may be comparable in the iota, eta, lambda, and mu variants, but it is significantly more abundant in omicron. This comparison demonstrates that common *O*-glycoforms are shared by the SARS-CoV-2 variants, but also highlights the variation in their expressions across the variants.

3.5. HCD-EThcD Dissociation of Tryptic-IMPa Digested O-Glycopeptides

Unlike *N*-glycosylation, the motifs observed for *O*-glycosylation are more complicated. *O*-glycoproteomic analysis is challenging due to differences in glycoforms attached to a glycosylation site and the site occupancy [27,54]. Therefore, the digestion method and instrument methodology employed have a significant impact on the number of identified *O*-glycosylation sites and the quality of MS/MS spectra that will be generated [69,92]. Another difficulty associated with the study of *O*-glycosites using glycoproteomic analysis is the fact that several of these sites are relatively close to one another. Thus, often the final glycopeptides contain more than one glycosylation site occupied with the same or different glycans. A clear example is the heavily glycosylated T323/S325 in the S-protein of SARS-CoV-2, which has posed a significant challenge in deciphering the specific localization of glycosylation in studies conducted by many groups [27,29]. Studies have shown that HCD does not provide a confident assignment of site localization for multiply glycosylated peptides [59,69,93]. To overcome this problem, coupled with double digestion using tryptic and IMPa digestion, we employed an HCD–EThcD pair dissociation method for selective backbone fragmentation to aid the confident assignment of *O*-linked glycans on adjacent S and T present on the same backbone. In this technique, HCD is first used to generate a spectrum that facilitates accurate identification of peptide backbone fragments without localization of the glycan. However, the precursor mass in the HCD spectrum corresponds to a combination of the peptide and the *O*-glycans. Subsequently, the paired EThcD spectrum allows for the site-specific localization of *O*-glycosylation even in multiply glycosylated peptides [59,93,94]. The reporter ions produced by HCD are systematically merged with the signature fragments necessary for *O*-glycosite localization generated by EThCD in a sequential manner [95]. The utilization of this integrated fragmentation technique has the capability to generate a broader range of fragment ions, hence enhancing the analysis of site-specific glycosylation. Moreover, the resulting spectra exhibit a high level of quality [96]. With this novel approach, we have been able to show that both T323 and S325 are *O*-glycosylated. Figure 7A shows the EICs of the positional isomers of the *O*-glycopeptides (VQPT$_{323}$ESIVR) + H1N1A2 and (VQPTES$_{325}$IVR) + H1N1A2. Figure 7B shows the mass spectra of the *O*-glycopeptide (VQPT$_{323}$ESIVR) + H1N1A2. The C4 fragment "VQPT323 + H1N1A2" with an m/z value of 1391.65 shows that T323 is occupied with the *O*-glycan H1N1A2, and a z4 fragment with the rest of the peptide backbone. Figure 7C shows the mass spectra of the *O*-glycopeptide (VQPTES325IVR) + H1N1A2. In this case, the fragment z5 "ES325IVR + H1N1A2" with an m/z value of 1550.65 shows that S325 is occupied with the *O*-glycan H1N1A2. Although our instrumentation generated MS/MS spectra for qualitative identification of these isobaric *O*-glycopeptide ions, we were unable to obtain a good resolution of the peaks with the employed analytical technique. We have also shown the same peptide "VQPTESIVR" that is doubly glycosylated with different glycans confidently assigned to the glycosylation sites T323 and S325, as shown in Supplementary Figure S15. The z5 fragment confirms the linkage of H1N2A1 to S325, while the c6 fragment shows the linkage of H1N1 to T323 and H1N2A1 to S325.

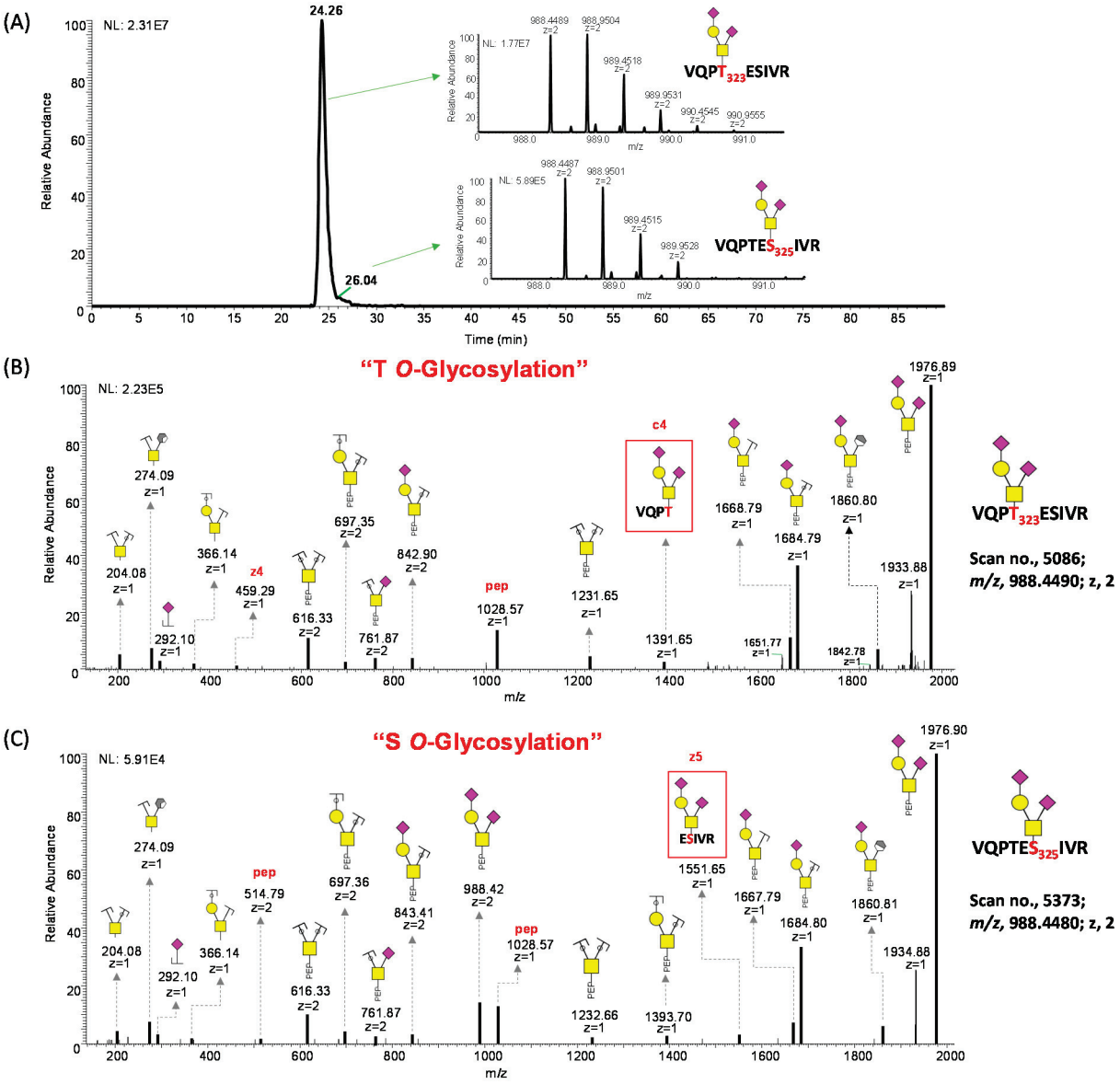


Figure 7. EThcD tandem mass spectra of a tryptic/IMPa digested glycopeptide confirming the occupancy of both T323 and S325 *O*-glycosylation sites in beta variant (H15). (A) An Extracted Ion Chromatogram (EIC) of isobaric *O*-glycopeptide VQPTESIVR-H1N1A1. The insets represent the MS1 spectra for the isobars. The c4 fragment in (**B**) shows that T323 is glycosylated and the z5 fragment in (**C**) shows that S325 is glycosylated.

3.6. O-Glycosylation at Points of Mutation

The mutations in the sequences of the different SARS-CoV-2 variants may alter the conformation of the proteins, which can impact the accessibility of *O*-glycosylation enzymes [97]. This could increase the probability of variant-dependent heterogeneous glycosylation, altering the glycosylation pattern in different variants. To the best of our knowledge, we will be the first to report *O*-glycosylation at points of mutations in SAR-CoV-2 variants. According to our results, the R190S mutation observed in the gamma variant, and F490S in the lambda variant, are shown to be *O*-glycosylated with spectral evidence (Figure 8). In addition, we identified *O*-glycosylation at G446S mutation in omicron, but without confident spectral evidence (Supplementary Table S4). The implications of these changes in the viral life cycle and interaction with the host call for further exploration.

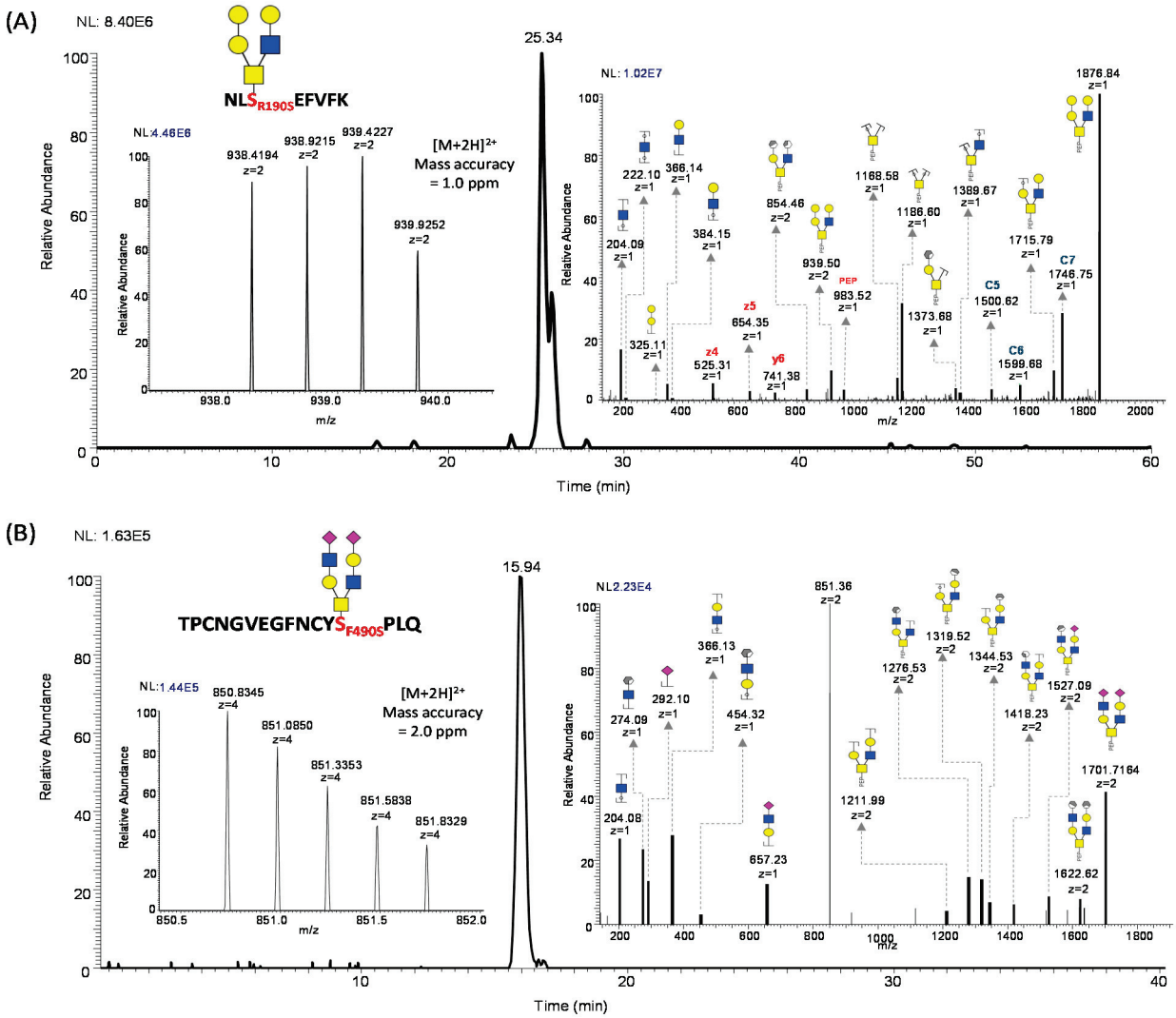


Figure 8. Localization of *O*-glycopeptides on mutation hotspots. The extracted ion chromatogram of *O*-glycopeptide on (**A**) R190S mutation present in gamma variant, (**B**) F490S mutation present in lambda variant.

4. Conclusions

SARS-CoV-2 remains a major health concern despite numerous scientific efforts to contain it. The changes in glycosylation patterns due to mutations in the S protein of SARS-CoV-2 variants necessitate thorough investigation. Here, we have demonstrated site-specific macro- and microheterogeneity in the pattern of *O*-glycosylation across 11 SARS-CoV-2 variants. We examined *O*-glycosylation in various functional domains to assess the effect of mutation on the glycosylation pattern in the S1 protein of SARS-CoV-2 variants. Our findings are important to understand how these glycosylation changes influence viral pathogenicity, tropism, immunological evasion, and virus-host interaction, all of which are critical in the development of a robust activity vaccine for managing the emerging SARS-CoV-2 variants of concern. Furthermore, we discovered *O*-glycosylation at mutation hotspots for the first time. Finally, whether *N*-glycosylation can complement the observed *O*-glycosylation for maximum glycan shielding should be further investigated.

Supplementary Materials: The following supporting information can be downloaded at: https://www.mdpi.com/article/10.3390/biom13101467/s1, Figure S1: Amino acid sequences and purity of the acquired S1 glycoproteins of eleven strains of SARS-CoV-2 that were expressed in human embryonic kidney 293 (HEK293) cells; Figure S2: Sialylation relative abundance on the receptor

binding domain (RBD) of the variants S1 glycoproteins; Figure S3: Sialylation relative abundance on the receptor binding motif (RBM) of the variants S1 glycoproteins; Figure S4: Heatmap showing the relative abundance of individual *O*-glycoforms identified in alpha; Figure S5: Heatmap showing the relative abundance of individual *O*-glycoforms identified in beta; Figure S6: Heatmap showing the relative abundance of individual *O*-glycoforms identified in gamma; Figure S7: Heatmap showing the relative abundance of individual *O*-glycoforms identified in delta; Figure S8: Heatmap showing the relative abundance of individual *O*-glycoforms identified in epsilon; Figure S9: Heatmap showing the relative abundance of individual *O*-glycoforms identified in kappa; Figure S10: Heatmap showing the relative abundance of individual *O*-glycoforms identified in iota; Figure S11: Heatmap showing the relative abundance of individual *O*-glycoforms identified in eta; Figure S12: Heatmap showing the relative abundance of individual *O*-glycoforms identified in lambda; Figure S13: Heatmap showing the relative abundance of individual *O*-glycoforms identified in mu; Figure S14: Heatmap showing the relative abundance of individual *O*-glycoforms identified in omicron; Figure S15: EThcD tandem mass spectra of a tryptic/IMPa digested glycopeptide confirming the occupancy of both T323 and S325 *O*-glycosylation sites; Data extracted from eta variant (H29) with Scan no., 3354; m/z, 751.6761; z, 3; Figure S16: EThcD tandem mass spectra of a tryptic/IMPa digested glycopeptide confirming the occupancy of a mutation point (R190S) in Gamma; Table S1: *O*-glycopeptides identified by Byonic; Table S2: *O*-glycopeptides identified by MetaMorpheus; Table S3: Venn plot results of unique and shared *O*-glycopeptides among five variants. Table S4: Ambiguous *O*-glycopeptides identified on G446*S* in omicron.

Author Contributions: Conceptualization, Y.M. and S.O.; project administration, supervision, and funding acquisition, Y.M.; methodology and formal analysis, S.O. and C.D.G.R.; data curation, S.O., C.D.G.R., M.F., O.D., and M.A.; writing original draft preparation, S.O. and M.F.; writing review and editing, C.D.G.R., A.I.B., S.O., and Y.M. All authors have read and agreed to the published version of the manuscript.

Funding: This work was supported by grants from the National Institutes of Health (1R01GM130091-05, 1U01CA22575305-05), the Robert A. Welch Foundation (No. D-0005), and The CH Foundation.

Institutional Review Board Statement: Not applicable.

Informed Consent Statement: Not applicable.

Data Availability Statement: The mass spectrometry proteomics data have been deposited to the ProteomeXchange Consortium via the PRIDE partner repository with the dataset identifier PXD041282 and 10.6019/PXD041282.

Conflicts of Interest: The authors declare no conflict of interest.

References

1. Zhou, F.; Fan, G.; Liu, Z.; Cao, B. SARS-CoV-2 shedding and infectivity—Authors' reply. *Lancet* **2020**, *395*, 1340. [CrossRef] [PubMed]
2. WHO. Coronavirus (COVID-19) Dashboard. Available online: https://covid19.who.int/ (accessed on 18 September 2023).
3. Harvey, W.T.; Carabelli, A.M.; Jackson, B.; Gupta, R.K.; Thomson, E.C.; Harrison, E.M.; Ludden, C.; Reeve, R.; Rambaut, A.; Peacock, S.J.; et al. SARS-CoV-2 variants, spike mutations and immune escape. *Nat. Rev. Microbiol.* **2021**, *19*, 409–424. [CrossRef] [PubMed]
4. Tao, K.; Tzou, P.L.; Nouhin, J.; Gupta, R.K.; de Oliveira, T.; Kosakovsky Pond, S.L.; Fera, D.; Shafer, R.W. The biological and clinical significance of emerging SARS-CoV-2 variants. *Nat. Rev. Genet.* **2021**, *22*, 757–773. [CrossRef] [PubMed]
5. Volz, E.; Hill, V.; McCrone, J.T.; Price, A.; Jorgensen, D.; O'Toole, Á.; Southgate, J.; Johnson, R.; Jackson, B.; Nascimento, F.F.; et al. Evaluating the Effects of SARS-CoV-2 Spike Mutation D614G on Transmissibility and Pathogenicity. *Cell* **2021**, *184*, 64–75. [CrossRef] [PubMed]
6. Hou, Y.J.; Chiba, S.; Halfmann, P.; Ehre, C.; Kuroda, M.; Dinnon, K.H., III; Leist, S.R.; Schäfer, A.; Nakajima, N.; Takahashi, K.; et al. SARS-CoV-2 D614G variant exhibits efficient replication ex vivo and transmission in vivo. *Science* **2020**, *370*, 1464–1468. [CrossRef] [PubMed]
7. Yurkovetskiy, L.; Wang, X.; Pascal, K.E.; Tomkins-Tinch, C.; Nyalile, T.P.; Wang, Y.; Baum, A.; Diehl, W.E.; Dauphin, A.; Carbone, C.; et al. Structural and Functional Analysis of the D614G SARS-CoV-2 Spike Protein Variant. *Cell* **2020**, *183*, 739–751. [CrossRef]
8. Liu, H.; Zhang, Q.; Wei, P.; Chen, Z.; Aviszus, K.; Yang, J.; Downing, W.; Jiang, C.; Liang, B.; Reynoso, L.; et al. The basis of a more contagious 501Y.V1 variant of SARS-CoV-2. *Cell Res.* **2021**, *31*, 720–722. [CrossRef]

9. Galloway, S.E.; Paul, P.; MacCannell, D.R.; Johansson, M.A.; Brooks, J.T.; MacNeil, A.; Slayton, R.B.; Tong, S.; Silk, B.J.; Armstrong, G.L.; et al. Emergence of SARS-CoV-2 B.1.1.7 Lineage—United States, December 29, 2020-January 12, 2021. *MMWR Morb. Mortal. Wkly. Rep.* **2021**, *70*, 95–99. [CrossRef]
10. Thompson, A.J.; de Vries, R.P.; Paulson, J.C. Virus recognition of glycan receptors. *Curr. Opin. Virol.* **2019**, *34*, 117–129. [CrossRef]
11. Qing, E.; Hantak, M.; Perlman, S.; Gallagher, T. Distinct Roles for Sialoside and Protein Receptors in Coronavirus Infection. *mBio* **2020**, *11*, e02764-19. [CrossRef]
12. Yang, T.-J.; Chang, Y.-C.; Ko, T.-P.; Draczkowski, P.; Chien, Y.-C.; Chang, Y.-C.; Wu, K.-P.; Khoo, K.-H.; Chang, H.-W.; Hsu, S.-T.D. Cryo-EM analysis of a feline coronavirus spike protein reveals a unique structure and camouflaging glycans. *Proc. Natl. Acad. Sci.* **2020**, *117*, 1438–1446. [CrossRef]
13. Kirchdoerfer, R.N.; Cottrell, C.A.; Wang, N.; Pallesen, J.; Yassine, H.M.; Turner, H.L.; Corbett, K.S.; Graham, B.S.; McLellan, J.S.; Ward, A.B. Pre-fusion structure of a human coronavirus spike protein. *Nature* **2016**, *531*, 118–121. [CrossRef] [PubMed]
14. Yuan, M.; Wu, N.C.; Zhu, X.; Lee, C.-C.D.; So, R.T.Y.; Lv, H.; Mok, C.K.P.; Wilson, I.A. A highly conserved cryptic epitope in the receptor binding domains of SARS-CoV-2 and SARS-CoV. *Science* **2020**, *368*, 630–633. [CrossRef]
15. Shajahan, A.; Pepi, L.E.; Rouhani, D.S.; Heiss, C.; Azadi, P. Glycosylation of SARS-CoV-2: Structural and functional insights. *Anal. Bioanal. Chem.* **2021**, *413*, 7179–7193. [CrossRef] [PubMed]
16. Yuan, Y.; Cao, D.; Zhang, Y.; Ma, J.; Qi, J.; Wang, Q.; Lu, G.; Wu, Y.; Yan, J.; Shi, Y.; et al. Cryo-EM structures of MERS-CoV and SARS-CoV spike glycoproteins reveal the dynamic receptor binding domains. *Nat. Commun.* **2017**, *8*, 15092. [CrossRef] [PubMed]
17. Reis, C.A.; Tauber, R.; Blanchard, V. Glycosylation is a key in SARS-CoV-2 infection. *J. Mol. Med.* **2021**, *99*, 1023–1031. [CrossRef]
18. Liu, X.; Wu, Q.; Zhang, Z. Global Diversification and Distribution of Coronaviruses with Furin Cleavage Sites. *Front. Microbiol.* **2021**, *12*, 649314. [CrossRef]
19. Benton, D.J.; Wrobel, A.G.; Xu, P.; Roustan, C.; Martin, S.R.; Rosenthal, P.B.; Skehel, J.J.; Gamblin, S.J. Receptor binding and priming of the spike protein of SARS-CoV-2 for membrane fusion. *Nature* **2020**, *588*, 327–330. [CrossRef]
20. Pak, A.J.; Yu, A.; Ke, Z.; Briggs, J.A.G.; Voth, G.A. Cooperative multivalent receptor binding promotes exposure of the SARS-CoV-2 fusion machinery core. *Nat. Commun.* **2022**, *13*, 1002. [CrossRef]
21. Hoffmann, M.; Kleine-Weber, H.; Pöhlmann, S. A Multibasic Cleavage Site in the Spike Protein of SARS-CoV-2 Is Essential for Infection of Human Lung Cells. *Mol. Cell* **2020**, *78*, 779–784.e5. [CrossRef]
22. Qiao, B.; Olvera de la Cruz, M. Enhanced Binding of SARS-CoV-2 Spike Protein to Receptor by Distal Polybasic Cleavage Sites. *ACS Nano* **2020**, *14*, 10616–10623. [CrossRef] [PubMed]
23. Liu, C.; Zhou, Q.; Li, Y.; Garner, L.V.; Watkins, S.P.; Carter, L.J.; Smoot, J.; Gregg, A.C.; Daniels, A.D.; Jervey, S.; et al. Research and Development on Therapeutic Agents and Vaccines for COVID-19 and Related Human Coronavirus Diseases. *ACS Cent. Sci.* **2020**, *6*, 315–331. [CrossRef]
24. Feng, W.; Newbigging, A.M.; Le, C.; Pang, B.; Peng, H.; Cao, Y.; Wu, J.; Abbas, G.; Song, J.; Wang, D.-B.; et al. Molecular Diagnosis of COVID-19: Challenges and Research Needs. *Anal. Chem.* **2020**, *92*, 10196–10209. [CrossRef] [PubMed]
25. Cho, B.G.; Gautam, S.; Peng, W.; Huang, Y.; Goli, M.; Mechref, Y. Direct Comparison of N-Glycans and Their Isomers Derived from Spike Glycoprotein 1 of MERS-CoV, SARS-CoV-1, and SARS-CoV-2. *J. Proteome Res.* **2021**, *20*, 4357–4365. [CrossRef] [PubMed]
26. Haslwanter, D.; Dieterle, M.E.; Wec, A.Z.; O'Brien, C.M.; Sakharkar, M.; Florez, C.; Tong, K.; Rappazzo, C.G.; Lasso, G.; Vergnolle, O.; et al. A Combination of Receptor-Binding Domain and N-Terminal Domain Neutralizing Antibodies Limits the Generation of SARS-CoV-2 Spike Neutralization-Escape Mutants. *mBio* **2021**, *12*, e0247321. [CrossRef] [PubMed]
27. Watanabe, Y.; Allen, J.D.; Wrapp, D.; McLellan, J.S.; Crispin, M. Site-specific glycan analysis of the SARS-CoV-2 spike. *Science* **2020**, *369*, 330–333. [CrossRef]
28. Walls, A.C.; Tortorici, M.A.; Frenz, B.; Snijder, J.; Li, W.; Rey, F.A.; DiMaio, F.; Bosch, B.J.; Veesler, D. Glycan shield and epitope masking of a coronavirus spike protein observed by cryo-electron microscopy. *Nat. Struct. Mol. Biol.* **2016**, *23*, 899–905. [CrossRef]
29. Shajahan, A.; Supekar, N.T.; Gleinich, A.S.; Azadi, P. Deducing the N- and *O*-glycosylation profile of the spike protein of novel coronavirus SARS-CoV-2. *Glycobiology* **2020**, *30*, 981–988. [CrossRef]
30. Shajahan, A.; Pepi, L.E.; Kumar, B.; Murray, N.B.; Azadi, P. Site specific N- and *O*-glycosylation mapping of the spike proteins of SARS-CoV-2 variants of concern. *Sci. Rep.* **2023**, *13*, 10053. [CrossRef]
31. Sanda, M.; Morrison, L.; Goldman, R. N- and O-Glycosylation of the SARS-CoV-2 Spike Protein. *Anal. Chem.* **2021**, *93*, 2003–2009. [CrossRef]
32. Watanabe, Y.; Berndsen, Z.T.; Raghwani, J.; Seabright, G.E.; Allen, J.D.; Pybus, O.G.; McLellan, J.S.; Wilson, I.A.; Bowden, T.A.; Ward, A.B.; et al. Vulnerabilities in coronavirus glycan shields despite extensive glycosylation. *Nat. Commun.* **2020**, *11*, 2688. [CrossRef] [PubMed]
33. Wrapp, D.; Wang, N.; Corbett, K.S.; Goldsmith, J.A.; Hsieh, C.L.; Abiona, O.; Graham, B.S.; McLellan, J.S. Cryo-EM structure of the 2019-nCoV spike in the prefusion conformation. *Science* **2020**, *367*, 1260–1263. [CrossRef] [PubMed]
34. Shang, J.; Ye, G.; Shi, K.; Wan, Y.; Luo, C.; Aihara, H.; Geng, Q.; Auerbach, A.; Li, F. Structural basis of receptor recognition by SARS-CoV-2. *Nature* **2020**, *581*, 221–224. [CrossRef] [PubMed]
35. Zheng, L.; Ma, Y.; Chen, M.; Wu, G.; Yan, C.; Zhang, X.E. SARS-CoV-2 spike protein receptor-binding domain N-glycans facilitate viral internalization in respiratory epithelial cells. *Biochem. Biophys. Res. Commun.* **2021**, *579*, 69–75. [CrossRef] [PubMed]

36. Casalino, L.; Gaieb, Z.; Goldsmith, J.A.; Hjorth, C.K.; Dommer, A.C.; Harbison, A.M.; Fogarty, C.A.; Barros, E.P.; Taylor, B.C.; McLellan, J.S.; et al. Beyond Shielding: The Roles of Glycans in SARS-CoV-2 Spike Protein. *bioRxiv* **2020**. [CrossRef]
37. Vankadari, N.; Wilce, J.A. Emerging WuHan (COVID-19) coronavirus: Glycan shield and structure prediction of spike glycoprotein and its interaction with human CD26. *Emerg. Microbes Infect.* **2020**, *9*, 601–604. [CrossRef]
38. Grant, O.C.; Montgomery, D.; Ito, K.; Woods, R.J. Analysis of the SARS-CoV-2 spike protein glycan shield reveals implications for immune recognition. *Sci. Rep.* **2020**, *10*, 14991. [CrossRef] [PubMed]
39. Behrens, A.J.; Harvey, D.J.; Milne, E.; Cupo, A.; Kumar, A.; Zitzmann, N.; Struwe, W.B.; Moore, J.P.; Crispin, M. Molecular Architecture of the Cleavage-Dependent Mannose Patch on a Soluble HIV-1 Envelope Glycoprotein Trimer. *J. Virol.* **2017**, *91*, e01894-16. [CrossRef]
40. Cao, L.; Diedrich, J.K.; Kulp, D.W.; Pauthner, M.; He, L.; Park, S.R.; Sok, D.; Su, C.Y.; Delahunty, C.M.; Menis, S.; et al. Global site-specific N-glycosylation analysis of HIV envelope glycoprotein. *Nat. Commun.* **2017**, *8*, 14954. [CrossRef] [PubMed]
41. Bagdonaite, I.; Nordén, R.; Joshi, H.J.; Dabelsteen, S.; Nyström, K.; Vakhrushev, S.Y.; Olofsson, S.; Wandall, H.H. A strategy for O-glycoproteomics of enveloped viruses--the O-glycoproteome of herpes simplex virus type 1. *PLoS Pathog.* **2015**, *11*, e1004784. [CrossRef]
42. Olofsson, S.; Blixt, O.; Bergström, T.; Frank, M.; Wandall, H.H. Viral O-GalNAc peptide epitopes: A novel potential target in viral envelope glycoproteins. *Rev. Med. Virol.* **2016**, *26*, 34–48. [CrossRef]
43. Silver, Z.A.; Antonopoulos, A.; Haslam, S.M.; Dell, A.; Dickinson, G.M.; Seaman, M.S.; Desrosiers, R.C. Discovery of O-Linked Carbohydrate on HIV-1 Envelope and Its Role in Shielding against One Category of Broadly Neutralizing Antibodies. *Cell Rep.* **2020**, *30*, 1862–1869. [CrossRef] [PubMed]
44. Gonzalez-Rodriguez, E.; Zol-Hanlon, M.; Bineva-Todd, G.; Marchesi, A.; Skehel, M.; Mahoney, K.E.; Roustan, C.; Borg, A.; Di Vagno, L.; Kjær, S.; et al. O-Linked Sialoglycans Modulate the Proteolysis of SARS-CoV-2 Spike and Likely Contribute to the Mutational Trajectory in Variants of Concern. *ACS Cent. Sci.* **2023**, *9*, 393–404. [CrossRef] [PubMed]
45. Bagdonaite, I.; Thompson, A.J.; Wang, X.; Søgaard, M.; Fougeroux, C.; Frank, M.; Diedrich, J.K.; Yates, J.R., III; Salanti, A.; Vakhrushev, S.Y.; et al. Site-Specific O-Glycosylation Analysis of SARS-CoV-2 Spike Protein Produced in Insect and Human Cells. *Viruses* **2021**, *13*, 551. [CrossRef]
46. Tian, Y.; Parsons, L.M.; Jankowska, E.; Cipollo, J.F. Site-Specific Glycosylation Patterns of the SARS-CoV-2 Spike Protein Derived From Recombinant Protein and Viral WA1 and D614G Strains. *Front. Chem.* **2021**, *9*, 767448. [CrossRef]
47. Dong, X.; Li, X.; Chen, C.; Zhang, X.; Liang, X. Systematic analysis and comparison of *O*-glycosylation of five recombinant spike proteins in β-coronaviruses. *Anal. Chim. Acta* **2022**, *1230*, 340394. [CrossRef]
48. Wang, Y.; Wu, Z.; Hu, W.; Hao, P.; Yang, S. Impact of Expressing Cells on Glycosylation and Glycan of the SARS-CoV-2 Spike Glycoprotein. *ACS Omega* **2021**, *6*, 15988–15999. [CrossRef]
49. Zhang, Y.; Zhao, W.; Mao, Y.; Chen, Y.; Zheng, S.; Cao, W.; Zhu, J.; Hu, L.; Gong, M.; Cheng, J.; et al. O-Glycosylation Landscapes of SARS-CoV-2 Spike Proteins. *Front. Chem.* **2021**, *9*, 689521. [CrossRef]
50. Zhang, L.; Mann, M.; Syed, Z.A.; Reynolds, H.M.; Tian, E.; Samara, N.L.; Zeldin, D.C.; Tabak, L.A.; Ten Hagen, K.G. Furin cleavage of the SARS-CoV-2 spike is modulated by *O*-glycosylation. *Proc. Natl. Acad. Sci. USA* **2021**, *118*, e2109905118. [CrossRef]
51. Wrobel, A.G.; Benton, D.J.; Roustan, C.; Borg, A.; Hussain, S.; Martin, S.R.; Rosenthal, P.B.; Skehel, J.J.; Gamblin, S.J. Evolution of the SARS-CoV-2 spike protein in the human host. *Nat. Commun.* **2022**, *13*, 1178. [CrossRef]
52. Liu, Y.; Liu, J.; Johnson, B.A.; Xia, H.; Ku, Z.; Schindewolf, C.; Widen, S.G.; An, Z.; Weaver, S.C.; Menachery, V.D.; et al. Delta spike P681R mutation enhances SARS-CoV-2 fitness over Alpha variant. *Cell Rep.* **2022**, *39*, 110829. [CrossRef] [PubMed]
53. Mohammad, A.; Abubaker, J.; Al-Mulla, F. Structural modelling of SARS-CoV-2 alpha variant (B.1.1.7) suggests enhanced furin binding and infectivity. *Virus Res.* **2021**, *303*, 198522. [CrossRef] [PubMed]
54. Zhao, P.; Praissman, J.L.; Grant, O.C.; Cai, Y.; Xiao, T.; Rosenbalm, K.E.; Aoki, K.; Kellman, B.P.; Bridger, R.; Barouch, D.H.; et al. Virus-Receptor Interactions of Glycosylated SARS-CoV-2 Spike and Human ACE2 Receptor. *Cell Host Microbe* **2020**, *28*, 586–601. [CrossRef]
55. Watanabe, Y.; Raghwani, J.; Allen, J.D.; Seabright, G.E.; Li, S.; Moser, F.; Huiskonen, J.T.; Strecker, T.; Bowden, T.A.; Crispin, M. Structure of the Lassa virus glycan shield provides a model for immunological resistance. *Proc. Natl. Acad. Sci. USA* **2018**, *115*, 7320–7325. [CrossRef] [PubMed]
56. Vainauskas, S.; Guntz, H.; McLeod, E.; McClung, C.; Ruse, C.; Shi, X.; Taron, C.H. A Broad-Specificity O-Glycoprotease That Enables Improved Analysis of Glycoproteins and Glycopeptides Containing Intact Complex O-Glycans. *Anal. Chem.* **2022**, *94*, 1060–1069. [CrossRef]
57. Bergstrom, K.S.; Xia, L. Mucin-type O-glycans and their roles in intestinal homeostasis. *Glycobiology* **2013**, *23*, 1026–1037. [CrossRef] [PubMed]
58. Gutierrez Reyes, C.D.; Huang, Y.; Atashi, M.; Zhang, J.; Zhu, J.; Liu, S.; Parikh, N.D.; Singal, A.G.; Dai, J.; Lubman, D.M.; et al. PRM-MS Quantitative Analysis of Isomeric N-Glycopeptides Derived from Human Serum Haptoglobin of Patients with Cirrhosis and Hepatocellular Carcinoma. *Metabolites* **2021**, *11*, 563. [CrossRef]
59. Lu, L.; Riley, N.M.; Shortreed, M.R.; Bertozzi, C.R.; Smith, L.M. O-Pair Search with MetaMorpheus for *O*-glycopeptide characterization. *Nat. Methods* **2020**, *17*, 1133–1138. [CrossRef] [PubMed]
60. Damerell, D.; Ceroni, A.; Maass, K.; Ranzinger, R.; Dell, A.; Haslam, S.M. The GlycanBuilder and GlycoWorkbench glycoinformatics tools: Updates and new developments. *Biol. Chem.* **2012**, *393*, 1357–1362. [CrossRef]

61. Lan, J.; Ge, J.; Yu, J.; Shan, S.; Zhou, H.; Fan, S.; Zhang, Q.; Shi, X.; Wang, Q.; Zhang, L.; et al. Structure of the SARS-CoV-2 spike receptor-binding domain bound to the ACE2 receptor. *Nature* **2020**, *581*, 215–220. [CrossRef]
62. Tian, J.H.; Patel, N.; Haupt, R.; Zhou, H.; Weston, S.; Hammond, H.; Logue, J.; Portnoff, A.D.; Norton, J.; Guebre-Xabier, M.; et al. SARS-CoV-2 spike glycoprotein vaccine candidate NVX-CoV2373 immunogenicity in baboons and protection in mice. *Nat. Commun.* **2021**, *12*, 372. [CrossRef] [PubMed]
63. Le Ru, A.; Jacob, D.; Transfiguracion, J.; Ansorge, S.; Henry, O.; Kamen, A.A. Scalable production of influenza virus in HEK-293 cells for efficient vaccine manufacturing. *Vaccine* **2010**, *28*, 3661–3671. [CrossRef] [PubMed]
64. Wang, Q.; Stuczynski, M.; Gao, Y.; Betenbaugh, M.J. Strategies for Engineering Protein N-Glycosylation Pathways in Mammalian Cells. *Methods Mol. Biol.* **2015**, *1321*, 287–305. [CrossRef] [PubMed]
65. Roberts, D.S.; Mann, M.; Li, B.H.; Kim, D.; Brasier, A.R.; Jin, S.; Ge, Y. Distinct Core Glycan and O-Glycoform Utilization of SARS-CoV-2 Omicron Variant Spike Protein RBD Revealed by Top-Down Mass Spectrometry. *bioRxiv* **2022**. [CrossRef]
66. Chawla, H.; Fadda, E.; Crispin, M. Principles of SARS-CoV-2 glycosylation. *Curr. Opin. Struct. Biol.* **2022**, *75*, 102402. [CrossRef]
67. Tian, W.; Li, D.; Zhang, N.; Bai, G.; Yuan, K.; Xiao, H.; Gao, F.; Chen, Y.; Wong, C.C.L.; Gao, G.F. *O*-glycosylation pattern of the SARS-CoV-2 spike protein reveals an "O-Follow-N" rule. *Cell Res.* **2021**, *31*, 1123–1125. [CrossRef]
68. Franc, V.; Řehulka, P.; Raus, M.; Stulík, J.; Novak, J.; Renfrow, M.B.; Šebela, M. Elucidating heterogeneity of IgA1 hinge-region *O*-glycosylation by use of MALDI-TOF/TOF mass spectrometry: Role of cysteine alkylation during sample processing. *J. Proteom.* **2013**, *92*, 299–312. [CrossRef]
69. Zhang, Y.; Xie, X.; Zhao, X.; Tian, F.; Lv, J.; Ying, W.; Qian, X. Systems analysis of singly and multiply O-glycosylated peptides in the human serum glycoproteome via EThcD and HCD mass spectrometry. *J. Proteom.* **2018**, *170*, 14–27. [CrossRef]
70. Chi, X.; Yan, R.; Zhang, J.; Zhang, G.; Zhang, Y.; Hao, M.; Zhang, Z.; Fan, P.; Dong, Y.; Yang, Y.; et al. A neutralizing human antibody binds to the N-terminal domain of the Spike protein of SARS-CoV-2. *Science* **2020**, *369*, 650–655. [CrossRef]
71. Walls, A.C.; Park, Y.J.; Tortorici, M.A.; Wall, A.; McGuire, A.T.; Veesler, D. Structure, Function, and Antigenicity of the SARS-CoV-2 Spike Glycoprotein. *Cell* **2020**, *181*, 281–292. [CrossRef]
72. Roberts, D.S.; Mann, M.W.; Melby, J.A.; Larson, E.J.; Zhu, Y.; Brasier, A.R.; Jin, S.; Ge, Y. Structural O-Glycoform Heterogeneity of the SARS-CoV-2 Spike Protein Receptor-Binding Domain Revealed by Native Top-Down Mass Spectrometry. *bioRxiv* **2021**. [CrossRef]
73. Du, L.; Yang, Y.; Zhang, X. Neutralizing antibodies for the prevention and treatment of COVID-19. *Cell. Mol. Immunol.* **2021**, *18*, 2293–2306. [CrossRef] [PubMed]
74. Chen, R.E.; Zhang, X.; Case, J.B.; Winkler, E.S.; Liu, Y.; VanBlargan, L.A.; Liu, J.; Errico, J.M.; Xie, X.; Suryadevara, N.; et al. Resistance of SARS-CoV-2 variants to neutralization by monoclonal and serum-derived polyclonal antibodies. *Nat. Med.* **2021**, *27*, 717–726. [CrossRef] [PubMed]
75. Wang, P.; Nair, M.S.; Liu, L.; Iketani, S.; Luo, Y.; Guo, Y.; Wang, M.; Yu, J.; Zhang, B.; Kwong, P.D.; et al. Antibody resistance of SARS-CoV-2 variants B.1.351 and B.1.1.7. *Nature* **2021**, *593*, 130–135. [CrossRef]
76. Starr, T.N.; Greaney, A.J.; Addetia, A.; Hannon, W.W.; Choudhary, M.C.; Dingens, A.S.; Li, J.Z.; Bloom, J.D. Prospective mapping of viral mutations that escape antibodies used to treat COVID-19. *Science* **2021**, *371*, 850–854. [CrossRef]
77. Thomson, E.C.; Rosen, L.E.; Shepherd, J.G.; Spreafico, R.; da Silva Filipe, A.; Wojcechowskyj, J.A.; Davis, C.; Piccoli, L.; Pascall, D.J.; Dillen, J.; et al. Circulating SARS-CoV-2 spike N439K variants maintain fitness while evading antibody-mediated immunity. *Cell* **2021**, *184*, 1171–1187. [CrossRef]
78. Wang, L.; Cheng, G. Sequence analysis of the emerging SARS-CoV-2 variant Omicron in South Africa. *J. Med. Virol.* **2022**, *94*, 1728–1733. [CrossRef]
79. Bayani, F.; Safaei Hashkavaei, N.; Uversky, V.N.; Mozaffari-Jovin, S.; Sefidbakht, Y. Insights into the structural peculiarities of the N-terminal and receptor binding domains of the spike protein from the SARS-CoV-2 Omicron variant. *Comput. Biol. Med.* **2022**, *147*, 105735. [CrossRef]
80. Starr, T.N.; Greaney, A.J.; Hilton, S.K.; Ellis, D.; Crawford, K.H.D.; Dingens, A.S.; Navarro, M.J.; Bowen, J.E.; Tortorici, M.A.; Walls, A.C.; et al. Deep Mutational Scanning of SARS-CoV-2 Receptor Binding Domain Reveals Constraints on Folding and ACE2 Binding. *Cell* **2020**, *182*, 1295–1310. [CrossRef]
81. Moelling, K. Within-Host and Between-Host Evolution in SARS-CoV-2-New Variant's Source. *Viruses* **2021**, *13*, 751. [CrossRef]
82. Barre, A.; Klonjkowski, B.; Benoist, H.; Rougé, P. How Do Point Mutations Enhancing the Basic Character of the RBDs of SARS-CoV-2 Variants Affect Their Transmissibility and Infectivity Capacities? *Viruses* **2022**, *14*, 783. [CrossRef] [PubMed]
83. McCallum, M.; Czudnochowski, N.; Rosen, L.E.; Zepeda, S.K.; Bowen, J.E.; Walls, A.C.; Hauser, K.; Joshi, A.; Stewart, C.; Dillen, J.R.; et al. Structural basis of SARS-CoV-2 Omicron immune evasion and receptor engagement. *Science* **2022**, *375*, 864–868. [CrossRef] [PubMed]
84. Kumar, S.; Karuppanan, K.; Subramaniam, G. Omicron (BA.1) and sub-variants (BA.1.1, BA.2, and BA.3) of SARS-CoV-2 spike infectivity and pathogenicity: A comparative sequence and structural-based computational assessment. *J. Med. Virol.* **2022**, *94*, 4780–4791. [CrossRef] [PubMed]
85. Wolter, N.; Jassat, W.; Walaza, S.; Welch, R.; Moultrie, H.; Groome, M.; Amoako, D.G.; Everatt, J.; Bhiman, J.N.; Scheepers, C.; et al. Early assessment of the clinical severity of the SARS-CoV-2 omicron variant in South Africa: A data linkage study. *Lancet* **2022**, *399*, 437–446. [CrossRef] [PubMed]

86. Salamanna, F.; Maglio, M.; Landini, M.P.; Fini, M. Body Localization of ACE-2: On the Trail of the Keyhole of SARS-CoV-2. *Front. Med.* **2020**, *7*, 594495. [CrossRef]
87. Hikmet, F.; Méar, L.; Edvinsson, Å.; Micke, P.; Uhlén, M.; Lindskog, C. The protein expression profile of ACE2 in human tissues. *Mol. Syst. Biol.* **2020**, *16*, e9610. [CrossRef]
88. Zhang, Y.; Zhao, W.; Mao, Y.; Chen, Y.; Wang, S.; Zhong, Y.; Su, T.; Gong, M.; Du, D.; Lu, X.; et al. Site-specific N-glycosylation Characterization of Recombinant SARS-CoV-2 Spike Proteins. *Mol. Cell. Proteom.* **2021**, *20*, 100058. [CrossRef]
89. Xie, Y.; Butler, M. Quantitative profiling of N-glycosylation of SARS-CoV-2 spike protein variants. *Glycobiology* **2023**, *33*, 188–202. [CrossRef]
90. Stencel-Baerenwald, J.E.; Reiss, K.; Reiter, D.M.; Stehle, T.; Dermody, T.S. The sweet spot: Defining virus-sialic acid interactions. *Nat. Rev. Microbiol.* **2014**, *12*, 739–749. [CrossRef]
91. Zheng, L.; Wang, K.; Chen, M.; Qin, F.; Yan, C.; Zhang, X.E. Characterization and Function of Glycans on the Spike Proteins of SARS-CoV-2 Variants of Concern. *Microbiol. Spectr.* **2022**, *10*, e0312022. [CrossRef]
92. Campos, D.; Girgis, M.; Sanda, M. Site-specific glycosylation of SARS-CoV-2: Big challenges in mass spectrometry analysis. *Proteomics* **2022**, *22*, e2100322. [CrossRef] [PubMed]
93. Zhang, Y.; Zheng, S.; Zhao, W.; Mao, Y.; Cao, W.; Zeng, W.; Liu, Y.; Hu, L.; Gong, M.; Cheng, J.; et al. Sequential Analysis of the N/O-Glycosylation of Heavily Glycosylated HIV-1 gp120 Using EThcD-sceHCD-MS/MS. *Front. Immunol.* **2021**, *12*, 755568. [CrossRef] [PubMed]
94. Bilan, V.; Leutert, M.; Nanni, P.; Panse, C.; Hottiger, M.O. Combining Higher-Energy Collision Dissociation and Electron-Transfer/Higher-Energy Collision Dissociation Fragmentation in a Product-Dependent Manner Confidently Assigns Proteomewide ADP-Ribose Acceptor Sites. *Anal. Chem.* **2017**, *89*, 1523–1530. [CrossRef] [PubMed]
95. Mao, Y.; Wang, S.; Zhao, Y.; Konstantinidi, A.; Sun, L.; Ye, Z.; Vakhrushev, S.Y. Systematic Evaluation of Fragmentation Methods for Unlabeled and Isobaric Mass Tag-Labeled O-Glycopeptides. *Anal. Chem.* **2021**, *93*, 11167–11175. [CrossRef]
96. Zeng, W.; Zheng, S.; Su, T.; Cheng, J.; Mao, Y.; Zhong, Y.; Liu, Y.; Chen, J.; Zhao, W.; Lin, T.; et al. Comparative N-Glycoproteomics Analysis of Clinical Samples Via Different Mass Spectrometry Dissociation Methods. *Front. Chem.* **2022**, *10*, 839470. [CrossRef]
97. Aloor, A.; Aradhya, R.; Venugopal, P.; Gopalakrishnan Nair, B.; Suravajhala, R. Glycosylation in SARS-CoV-2 variants: A path to infection and recovery. *Biochem. Pharmacol.* **2022**, *206*, 115335. [CrossRef]

Disclaimer/Publisher's Note: The statements, opinions and data contained in all publications are solely those of the individual author(s) and contributor(s) and not of MDPI and/or the editor(s). MDPI and/or the editor(s) disclaim responsibility for any injury to people or property resulting from any ideas, methods, instructions or products referred to in the content.

biomolecules

MDPI

Article

Stability Determination of Intact Humanin-G with Characterizations of Oxidation and Dimerization Patterns

Mustafa Ozgul [1,*], Anthony B. Nesburn [1,2], Nader Nasralla [3], Benjamin Katz [4], Enes Taylan [5], Baruch D. Kuppermann [1] and Maria Cristina Kenney [1,6,*]

1 Department of Ophthalmology, Gavin Herbert Eye Institute, University of California Irvine, Irvine, CA 92617, USA
2 Cedars-Sinai Medical Center, Los Angeles, CA 90048, USA
3 IVD Technologies Inc., Santa Ana, CA 92705, USA
4 Department of Chemistry, University of California Irvine, Irvine, CA 92697, USA
5 Department of Obstetrics and Gynecology, University of California Los Angeles, Los Angeles, CA 90095, USA
6 Department of Pathology and Laboratory Medicine, University of California Irvine, Irvine, CA 92617, USA
* Correspondence: ozgulm@hs.uci.edu (M.O.); mkenney@hs.uci.edu (M.C.K.)

Abstract: Humanin is the first identified mitochondrial-derived peptide. Humanin-G (HNG) is a variant of Humanin that has significantly higher cytoprotective properties. Here, we describe the stability features of HNG in different conditions and characterize HNG degradation, oxidation, and dimerization patterns over short-term and long-term periods. HNG solutions were prepared in high-performance liquid chromatography (HPLC) water or MO formulation and stored at either 4 °C or 37 °C. Stored HNG samples were analyzed using HPLC and high-resolution mass spectrometry (HRMS). Using HPLC, full-length HNG peptides in HPLC water decreased significantly with time and higher temperature, while HNG in MO formulation remained stable up to 95% at 4 °C on day 28. HNG peptides in HPLC water, phosphate-buffered saline (PBS) and MO formulation were incubated at 37 °C and analyzed at day 1, day 7 and day 14 using HRMS. Concentrations of full-length HNG peptide in HPLC water and PBS declined over time with a corresponding appearance of new peaks that increased over time. These new peaks were identified to be singly oxidized HNG, doubly oxidized HNG, homodimerized HNG, singly oxidized homodimerized HNG, and doubly oxidized homodimerized HNG. Our results may help researchers improve the experimental design to further understand the critical role of HNG in human diseases.

Keywords: peptides; stability; degradation products; oxidations; high-performance liquid chromatography (hplc); high-resolution mass spectrometry (hrms)

1. Introduction

Mitochondrial DNA (mtDNA) is double-stranded, circular DNA comprised of 16,569 nucleotide pairs that represents 37 genes encoding for 13 peptides, 22 transfer RNAs, and 2 ribosomal RNAs [1,2]. Mitochondria-derived peptides (MDPs), encoded by the human mtDNA, play essential roles in many cellular physiological processes that can affect aging and disease progression [3–9]. Exploring mitochondrial biology, several MDPs, consisting of 16–38 amino acids, have been identified [10]. Humanin (HN), the first identified MDP, contains 24 amino acids (2687.3 Da) [5] and has neuroprotective and anti-apoptotic properties in in vitro and in vivo models [5,11–14]. The serum HN levels decrease significantly with age and are associated with age-related diseases in rodent animal models and human clinical studies [15,16]. HN peptides protect against neurotoxicity in Alzheimer's disease and suppress amyloid-beta-induced neuronal death in vitro [17]. The administration of exogenous HN peptides provides cytoprotective effects in Type-2 diabetes rat models [15] as well as myocardial and cerebral ischemia [18,19] and atherosclerosis [20] mouse models [3].

Humanin-G (HNG) is an HN derivative with a S14G substitution exhibiting 1000-fold more potent cytoprotective properties than HN, and it also demonstrates therapeutic potential for multiple diseases [5,21]. Similar to Humanin, HNG (2657.3 Da) inhibits amyloid-beta (Aβ)-induced death in primary neurons in vitro and demonstrates cytoprotective effects for myocardial ischemia-reperfusion injury in animal models [18,22–24]. HNG also has antitumor effects as shown in neuroblastoma tumor xenograft experiments [25]. The effect was linked to reduced angiogenesis and increased tumor cell apoptosis [25].

Recently, we investigated the effect of HNG in a transmitochondrial cybrid model for age-related macular degeneration (AMD), which is the most common cause of visual impairment in the elderly population. Cybrids are cell lines with identical nuclei but with mitochondria from different individuals with AMD or age-matched normal subjects. The AMD cybrids treated with HNG showed significantly increased levels of humanin receptor proteins and decreased levels of RNA/proteins involved in apoptosis, autophagy, and ER stress pathways [1]. HNG-treated AMD cybrids showed significantly lower levels of cell death and improved functions in vitro [1]. However, conducting in vivo studies has been challenging due to the instability of the HNG peptide because of its tendency to rapidly degrade, oxidize and dimerize. The development of novel formulations to enhance the stability of HNG peptides is a critical first step toward the therapeutic delivery of HNG in retinal degeneration models in vivo and for future clinical investigations to treat several age-related diseases such as AMD, Alzheimer's disease, and diabetic retinopathy. To the best of our knowledge, this is the first study that accurately analyzes the stability features of HNG and identifies its fragments and their therapeutic potential using high-performance liquid chromatography (HPLC) and high-resolution mass spectrometry (HRMS). We also developed a stabilization formula (MO formulation) that significantly improves the HNG peptide stability when stored long term and at 37 °C.

2. Materials and Methods

2.1. Chemicals and Materials

The HNG peptide (Catalog No: AS-60887) was purchased from AnaSpec Inc. (Fremont, CA, US). Acetonitrile, HPLC water, LC-MS water, and formic acid were purchased from Fisher Scientific (Waltham, MA, USA). Analytical grade solvents were used in all experiments.

2.2. Physiochemical Properties

An ExPASy ProtParam bioinformatics software tool was used to determine structural prediction including the instability index value, grand average of hydropathy value (GRAVY), and theoretical isoelectric point (pI). The instability index represents the prediction of peptide instability. When a peptide's instability index is less than 40, the peptide is classified as stable, and if it is higher than 40, the peptide is designated as unstable. The GRAVY method predicts peptide hydrophilicity and hydrophobicity. GRAVY's positive values and negative values represent the hydrophobic and hydrophilic structures, respectively [26–29]. The ExPASy PeptideCutter bioinformatics software tool was utilized to predict potential cleave sites, cleaving enzymes, and chemicals in the HNG peptide [30]. Theoretical charge of HNG peptide over pH change was analyzed using the peptide analysis tool in the Thermo-Fisher Scientific website.

2.3. HNG Solution Preparation and Storage

For HPLC studies, HNG solutions were prepared at 125 μg/mL in HPLC water and at 112.5 μg/mL in the stabilization formula (MO formulation). The MO formulation, a proprietary solution, is a colorless liquid and includes organic acid (pH = 2.4–2.5) that has been found to be non-toxic to cells. We prepared duplicate HNG peptide solutions that were stored at two different temperatures (4 °C and 37 °C). For long-term stability analyses, HNG solutions were stored for 11 months at 4 °C. HNG solutions were filtered using 0.22 μm filters before HPLC analysis. The stability features of the stored HNG

solutions were evaluated by HPLC at seven different time-points (6 h, 21 h, 33 h, day 3, day 7, day 14, and day 28). For HRMS studies, samples with a concentration of 30 µM HNG were prepared from the stored HPLC water and MO-formulation to analyze 11-month-old HNG products.

2.4. High-Performance Liquid Chromatography

The Agilent 1100 system with an Agilent Eclipse XDB-C8 5 µm, 4.6 × 150 mm HPLC column was used to achieve liquid chromatographic separation. HNG was monitored at a wavelength of 200 nm using a Diode Array Detector. Gradient elution was performed with solvent A (water with 0.05% trifluoroacetic acid) and solvent B (acetonitrile with 0.05% trifluoroacetic acid). The gradient started at 30% solvent B with a ramp to 60% solvent B in a period of 10 min. At 12 min, the gradients begin to return to 30% solvent B in 0.1 min. The column was equilibrated from 12.1 min to 20 min at 30% solvent B (Table S1). The flow rate was set to 1 mL/min, and 25 µL of the sample was injected into the column. The column temperature was set at 40 °C.

2.5. High-Resolution Mass Spectrometry

The Waters® Acquity H-class ultra-performance liquid chromatography (UPLC) method was run on a Waters BEH C4 column 300 Å, 1.7 µm, 50 mm × 2.1 using 25 min gradient at 0.3 mL/min from 97% A to 97% B, where A is 0.1% formic acid in water and B is 100% ACN (Table S2). Mass spectrometric analysis was performed using a XEVO G2-XS Quadrupole Time-of-Flight (QTof) mass spectrometer equipped with StepWave ion optics (Waters Corp., MA, USA). The positive electrospray ionization mode was utilized. Measurements were conducted using an ion source desolvation temperature of 350 °C and a cone voltage of 40 V. Argon was utilized as damping gas in the Collision-Induced Dissociation (CID) experiments. A capillary transfer temperature of 300 °C and a spray voltage of 3.0 kV were used to accomplish ionization. A resolution of 30,000 Full Width at Half Maximum (FWHM) was used for a full scan experiment within a range of m/z 100–2000 in addition to 15,000 FWHM with an isolation window adjusted to m/z 2.0 for Parallel Reaction Monitoring (PRM) mode. The instrument was operated in MSE continuum mode, which alternates low-energy (6 V) and high-energy (40 V) scans every 0.5 sec. Leucine Enkephalin was used as a lock mass for nominal mass correction, and a CsNaI ladder was used for detector calibration.

Mass to Charge Calculation Formula for Dimerized Form HNG and their Fragments. The disulfide bridge causes a mass shift of −2 Da. The monoisotopic HNG molecular weight (Mw) is 2657.3.

$$Mass\ to\ Charge\ Ratio = \frac{Peptide\ 1\ Mw + Peptide\ 2\ Mw - Dimerization\ Mass\ Shift + Number\ of\ Protonation}{Charge\ State\ of\ Dimer}$$

Mass to Charge Calculation Formula for oxidized form HNG and their fragments. Oxidation causes a mass shift of +16 Da. The monoisotopic HNG molecular weight (Mw) is 2657.3.

$$Mass\ to\ Charge\ Ratio = \frac{Peptide\ \ Mw + Oxidation\ Mass + Number\ of\ Protonation}{Charge\ State\ of\ Oxidized\ Peptide}$$

2.6. Data Analysis

Collected data were analyzed using MassLynx (version 4.2, 2016) and BiopharmaLynx (version 4.0.27.10, 2015) software programs provided by the Waters Company (Milford, MA, USA).

3. Results

The molecular structure, molecular weights, charges, and amino acid sequences of HNG peptides were characterized using UCSF Chimera software and the ExPASy ProtParam bioinformatics software tool (Figure 1).

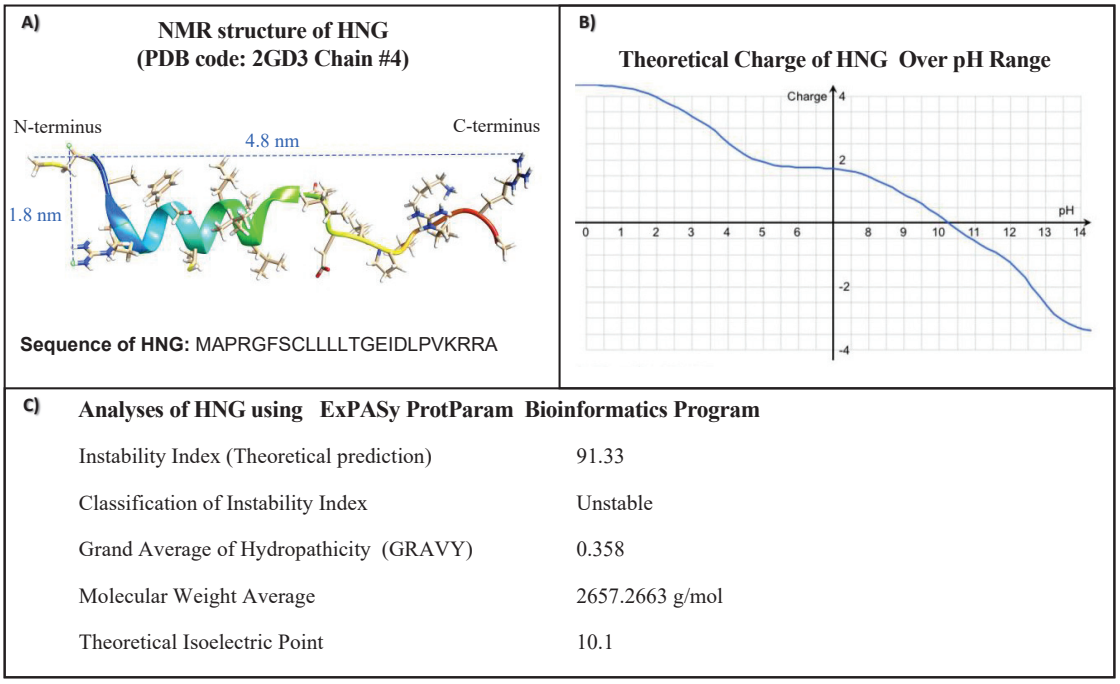


Figure 1. (**A**) The NMR structure of HNG peptide (PDB identifier 2GD3 Chain 8) is visualized using the UCSF Chimera program. The length and width of HNG are ~4 nm and ~1.5 nm, respectively. The sequence of full-length HNG is shown. (**B**) The diagram shows the net charge of HNG as a function of pH. (**C**) Physiochemical properties of HNG.

In Figure 1A, the predicted structure of HNG shows the proposed length and width as approximately 4.8 nm and approximately 1.8 nm, respectively. In Figure 1B, the isoelectric point is 10. 1, indicating it is a basic peptide. The net charge of HNG peptide at pH 7 is 1.9, indicating it is a soluble peptide in neutral water. In Figure 1C, HNG has an Instability Index of 91.33, suggesting it is an unstable peptide. The GRAVY value is 0.358, indicating a hydrophobic property.

We used the ExPASy PeptideCutter bioinformatics software to predict potential cleave sites, cleaving enzymes, and chemicals in the HNG peptide [30]. The functions, hydropathicity, name of cleaving enzymes/chemicals, and properties of each amino acid of HNG peptide are given in Table 1.

Table 1. Functions, hydropathicity, name of cleaving enzymes/chemicals and properties of each amino acids of HNG peptide.

Pos.	Amino Acid	Function	Hydropathicity	Amino Acid Side Chain Properties	Name of Cleaving Enzymes/Chemicals (Theoretical)
1	M	Neuroprotection	1.900	Hydrophobic	Chymotrypsin, Cyanogen Bromide
2	A	Neuroprotection	1.800	Hydrophobic	Proteinase K
3	**P***	**Neuroprotection**	−1.600	Hydrophobic	N/A
4	**R***	**Neuroprotection**	−4.500	Positive Charged (Basic)	Trypsin, Arg-C proteinase, Clostridiopeptidase B

Table 1. *Cont.*

Pos.	Amino Acid	Function	Hydropathicity	Amino Acid Side Chain Properties	Name of Cleaving Enzymes/Chemicals (Theoretical)
5	**G***	**N/D**	−0.400	Hydrophobic	Pepsin, Thermolysin
6	**F***	**IGFBP-3 binding, Beta-Amyloid Binding**	2.800	Hydrophobic	Chymotrypsin, Proteinase K
7	**S***	**Beta-Amyloid Binding, Beta-Amyloid Protection, Dimerization**	−0.800	Polar	2-nitro-5-thiocyanobenzoic acid
8	**C***	**Neuroprotection, BAX, BAD, end tBID binding, Disulfide Bond for dimerization**	2.500	Polar	Pepsin, Thermolysin
9	**L***	**Neuroprotection, Secretion, Dimerization**	3.800	Hydrophobic	Proteinase K, Pepsin, Thermolysin, Chymotrypsin
10	**L***	**Secretion**	3.800	Hydrophobic	Proteinase K, Pepsin, Thermolysin, Chymotrypsin
11	**L***	**Secretion**	3.800	Hydrophobic	Proteinase K, Pepsin, Thermolysin, Chymotrypsin
12	**L***	**Neuroprotection**	3.800	Hydrophobic	Proteinase K, Pepsin, Chymotrypsin
13	**T***	**Neuroprotection**	−0.700	Polar	Proteinase K,
14	**G***	**Neuroprotection**	−0.400	Hydrophobic	Asp-N Endopeptidase
15	**E***	**N/D**	−3.500	Negative Charged (Acidic)	Proteinase K, Glutamyl endopeptidase, Staphylococcal peptidase I
16	**I***	**N/D**	4.500	Hydrophobic	Proteinase K, Asp-N Endopeptidase
17	**D***	**N/D**	−3.500	Negative Charged (Acidic)	Formic acid
18	**L***	**N/D**	3.800	Hydrophobic	Proteinase K, Pepsin
19	**P***	**Beta-Amyloid Protection, Secretion**	−1.600	Hydrophobic	Thermolysin
20	**V***	**Secretion**	4.200	Hydrophobic	Proteinase K, Peptidyl-Lys metalloendopeptidase
21	K	IGFBP-3 binding	−3.900	Positive Charged (Basic)	Lysyl endopeptidase, Trypsin
22	R	N/D	−4.500	Positive Charged (Basic)	Arg-C proteinase, Clostridiopeptidase B, Trypsin
23	R	N/D	−4.500	Positive Charged (Basic)	Thermolysin, Arg-C proteinase, Clostridiopeptidase B, Trypsin
24	A	N/D	1.800	Hydrophobic	N/A

* Neuroprotection core domains are shown in bold font. Pos.; Position, N/D; Not Determined, N/A: Not Available.

3.1. Short-Term Stability of HNG Peptide in Different Conditions

We analyzed the stability of the HNG peptide stored in HPLC water (Figure 2A–I, Left Panel) and MO formulation (Figure 2J–Q, Right Panel) at 4 °C and 37 °C using HPLC at day 0, day 1, day 3, day 7, day 14, and day 28. The concentration of full-length HNG decreases over time, while the concentration of the HNG products (HNG-Pd) simultaneously increased (Figure 2A–R).

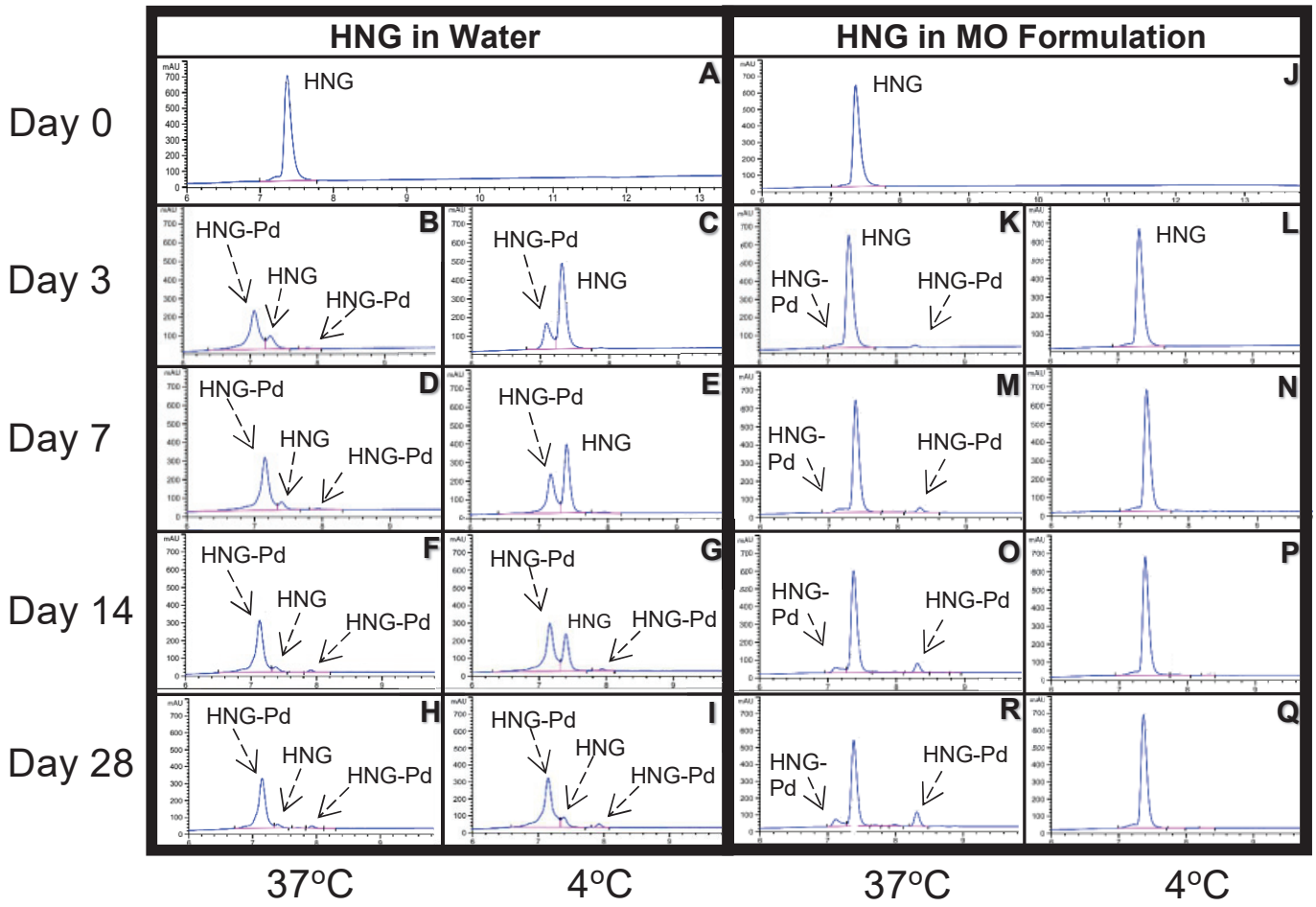


Figure 2. Ion chromatogram results of HNG in HPLC-grade water (Left Panel) and MO formulation (Right Panel). **LEFT PANEL: HNG in Water.** (**A**) Day 0 at RT; (**B**) 3rd day +37 °C; (**C**) 3rd day +4 °C; (**D**) 7th day +37 °C; (**E**) 7th day +4 °C. (**F**) 14th day +37 °C; (**G**) 14th day +4 °C; (**H**) 28th day +37 °C; (**I**) 28th day +4 °C. **RIGHT PANEL: HNG in MO formulation.** (**J**) Day 0 at RT; (**K**) 3rd day +37 °C; (**L**) 3rd day +4 °C; (**M**) 7th day +37 °C; (**N**) 7th day +4 °C; (**O**) 14th day +37 °C; (**P**) 14th day +4 °C; (**R**) 28th day +37 °C; (**Q**) 28th day +4 °C. RT, room temperature: HNG Humanin-G; Pd: Product.

Compared to the MO formulation, we found that the HNG peptide was sensitive to storage temperature and duration. At 21 h after storage, the full-length HNG peptide level in HPLC water stored at 4 °C was 90% compared to 67% at 37 °C (Figure 3). After 33 h of storage, nearly half of the full-length HNG peptides (52%) was found at 37 °C in HPLC water, indicating its half-life at body temperature (Figure 3). By day 28, the full-length HNG stored in HPLC water was further declined to concentrations of 11% at 4 °C and 5% at 37 °C (Figure 3).

When we evaluated the HNG stability stored in the MO formulation, remarkably, we found that the full-length HNG peptide remained stable up to 95% at 4 °C on day 28. Even at 37 °C, the full-length HNG peptide concentration was significantly higher when stored in the MO formulation compared to HPLC water (67% versus 11%, respectively) (Figure 3). These results show that the HNG peptide is highly unstable when stored in HPLC water,

and the stability of the HNG peptide can be successfully improved when stored in our newly developed MO formulation.

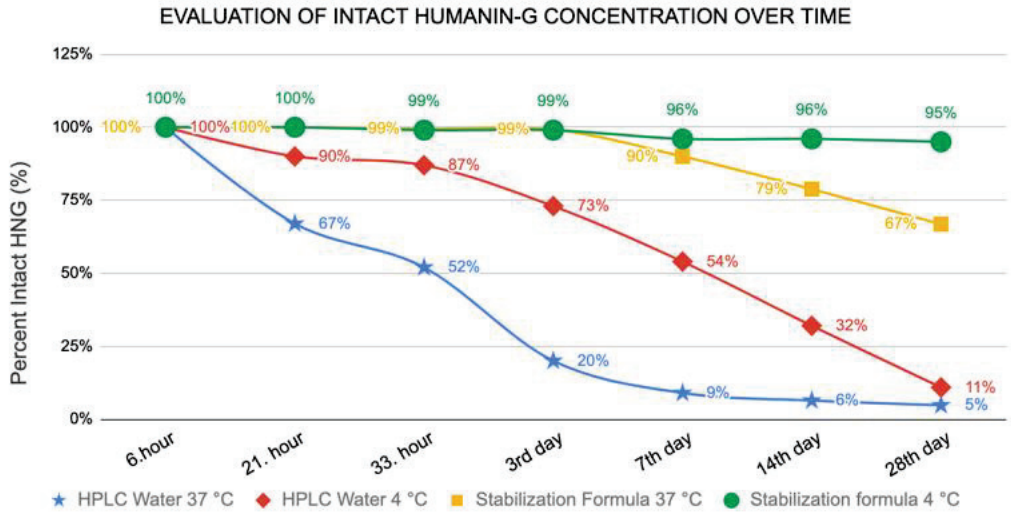


Figure 3. Stable HNG peptide concentration changes over time in HPLC water versus MO formulation at 4 °C and 37 °C.

Overall, the stability of the full-length HNG peptide in HPLC water and MO formulation was measured using HPLC at 4 °C and 37 °C over a 28-day period, and the results showed that the full-length HNG peptide in HPLC-grade water is not stable at 4 °C and 37 °C. Based on the results of these HPLC studies, we saw indications, represented by the other peaks in the graph, of unidentified amino acid sequences of the HNG products. To identify the composition of HNG products that occurred in the three different solutions (HPLC-grade water, PBS, and MO formulation), we performed experiments using UPLC-HRMS. Collected UPLC-HRMS data were analyzed using the BiopharmaLynx program to identify the peptide sequence of each peak (Figures 4–13, Tables S3 and S4).

3.2. Characterization of Full-Length HNG, Its Oxidized and Dimerized Forms

To characterize HNG products using UPLC-HRMS, we prepared a solution of HNG peptide in HPLC-grade water, PBS and MO formulation. Using UPLC-HRMS, the full-length HNG, singly oxidized full-length HNG (SO_x-HNG), doubly oxidized full-length HNG (Dox-HNG), singly oxidized dimerized HNG (SO_x-DM-HNG) and doubly oxidized dimerized HNG (DO_x-DM-HNG) were identified.

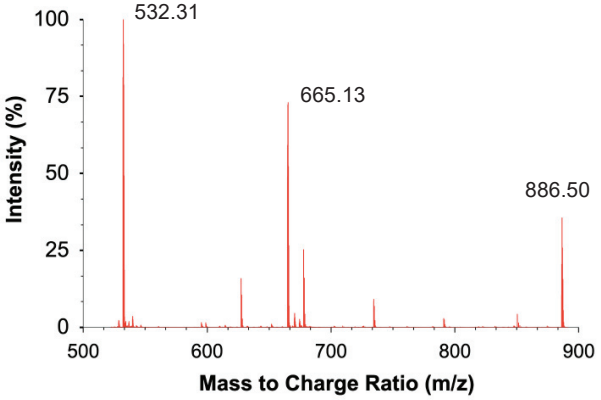
The amino acid sequences and m/z ratio of full-length HNG, singly oxidized HNG, doubly oxidized HNG in PBS on day 14 at 37 °C are represented (Figure 4). In Figure 4A,B, multiple charged full-length HNG peptides (MAPRGFSCLLLLTGEIDLPVKRRA) were observed at *m/z* 532.31 (z = 5), 665.13 (z = 4), and 886.50 (z = 3). In Figure 4C,D, multiple charged singly oxidized (methionine) full-length HNG peptides (SO_x-HNG) were observed at *m/z* 535.50 (z = 5), 669.13 (z = 4), and 891.83 (z = 3). In Figure 4E,F, multiple charged doubly oxidized (methionine and cysteine) full-length HNG peptides (Dox-HNG) were observed at *m/z* 538.70 (z = 5), 673.13 (z = 4), and 897.17 (z = 3).

In Figure 5, the amino acid sequences and m/z ratio of intact homodimerized (cysteine-cysteine disulfide bone) HNG (DM-HNG), singly oxidized homodimerized HNG, and doubly oxidized homodimerized HNG in PBS on day 14 at 37 °C are represented. In Figure 5A,B, multiple charged DM-HNG peptides were observed at 532.21 m/z (DM-HNG 1-24, z = 10), 591.22 m/z (DM-HNG 1-24, z = 9), 665.01 m/z (DM-HNG 1-24, z = 8), 759.86 m/z (DM-HNG 1-24, z = 7), 886.33 m/z (DM-HNG 1-24, z = 6), and 1063.41 m/z (DM-HNG 1-24, z = 5).

A) M A P R G F S C L L L L T G E I D L P V K R R A

Charge States of Intact HNG	m/z Ratio
$[M+5H^+]^{5+}$	532.31
$[M+4H^+]^{4+}$	665.13
$[M+3H^+]^{3+}$	886.50

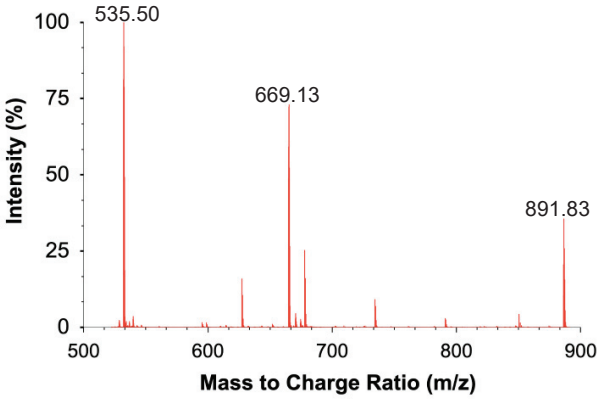
B)



C) M A P R G F S C L L L L T G E I D L P V K R R A

Charge States of Singly-Oxidized Intact HNG (Oxidation of Methionine)	m/z Ratio
$[M+O+5H^+]^{5+}$	535.50
$[M+O+4H^+]^{4+}$	669.13
$[M+O+3H^+]^{3+}$	891.83

D)



E) M A P R G F S C L L L L T G E I D L P V K R R A

Charge States of Doubly-Oxidized Intact HNG (Oxidation of Methionine and Cysteine)	m/z Ratio
$[M+O+O+5H^+]^{5+}$	538.70
$[M+O+O+4H^+]^{4+}$	673.13
$[M+O+O+3H^+]^{3+}$	897.16

F)

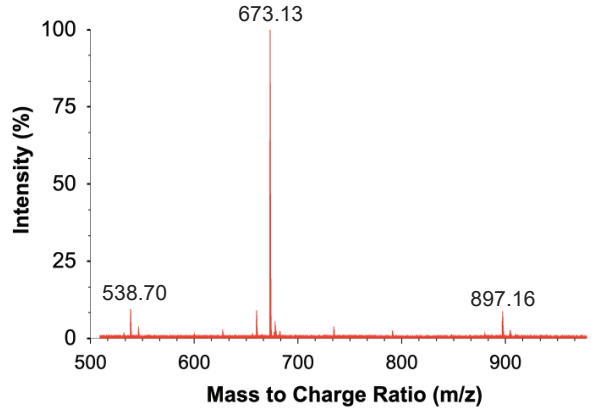
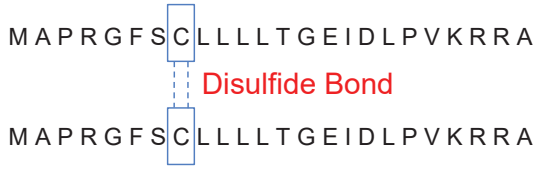


Figure 4. (**A**) Amino acid sequence and m/z ratio of the full-length HNG are represented. (**B**) Representative HRMS precursor ion mass spectra of HNG in PBS. (**C**) Amino acid sequence and m/z ratio of SO_X-HNG are represented. (**D**) Representative HRMS precursor ion mass spectra of SO_X-HNG in PBS. (**E**) Amino acid sequence and m/z ratio of DO_X-HNG HNG are represented. (**F**) Representative HRMS precursor ion mass spectra of DO_X-HNG in PBS.

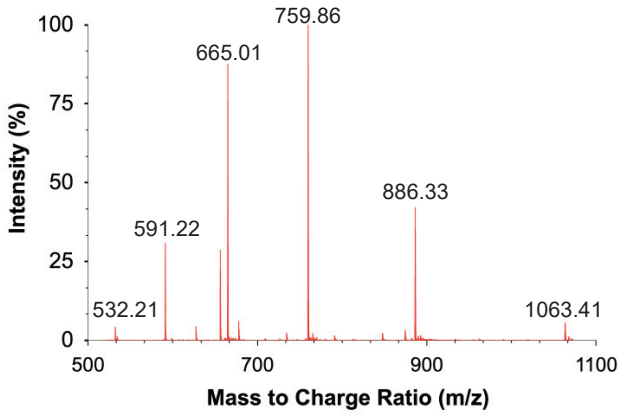
In Figure 5C,D, multiple charged homodimerized HNG with methionine oxidation (singly oxidized homodimerized HNG, SO_x-DM-HNG) were observed at 533.81 m/z (z = 10), 593.01 m/z (z = 9), 667.01 m/z (z = 8), 762.14 m/z (z = 7), 888.99 m/z (z = 6), and 1066.80 m/z (z = 5).

A)

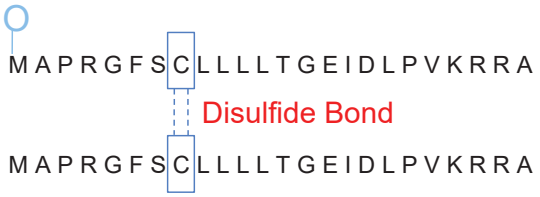


Charge States of Dimerized HNG	m/z Ratio
$[M+M+10H^+]^{10+}$	532.21
$[M+M+9H^+]^{9+}$	591.22
$[M+M+8H^+]^{8+}$	665.01
$[M+M+7H^+]^{7+}$	759.86
$[M+M+6H^+]^{6+}$	886.33
$[M+M+5H^+]^{5+}$	1063.41

B)

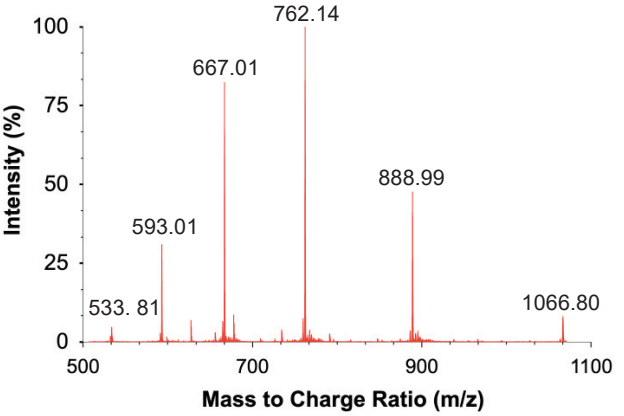


C)

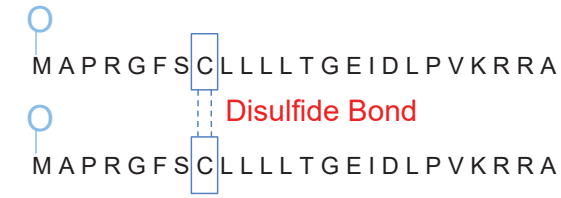


Charge States of Singly-Oxidized Dimerized HNG	m/z Ratio
$[M+M+O+10H^+]^{10+}$	533.81
$[M+M+O+9H^+]^{9+}$	593.01
$[M+M+O+8H^+]^{8+}$	667.01
$[M+M+O+7H^+]^{7+}$	762.14
$[M+M+O+6H^+]^{6+}$	888.99
$[M+M+O+5H^+]^{5+}$	1066.60

D)



E)



Charge States of Doubly-Oxidized Dimerized HNG	m/z Ratio
$[M+M+O+O+10H^+]^{10+}$	532.30
$[M+M+O+O+9H^+]^{9+}$	594.77
$[M+M+O+O+8H^+]^{8+}$	669.01
$[M+M+O+O+7H^+]^{7+}$	764.43
$[M+M+O+O+6H^+]^{6+}$	891.67
$[M+M+O+O+5H^+]^{5+}$	1069.80

F)

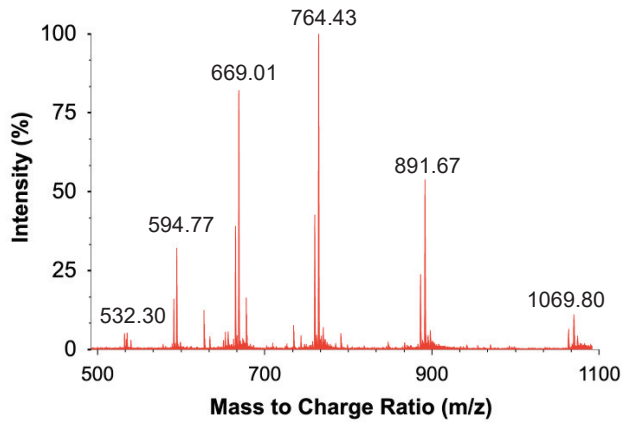


Figure 5. (**A**) Amino acid sequence and m/z ratio of DM-HNG are represented. (**B**) Representative HRMS precursor ion mass spectra of DM-HNG in PBS. (**C**) Amino acid sequence and m/z ratio of SO_X-DM-HNG are represented. (**D**) Representative HRMS precursor ion mass spectra of SO_X-DM-HNG in PBS. (**E**) Amino acid sequence and m/z ratio of DO_X-DM-HNG are represented. (**F**) Representative HRMS precursor ion mass spectra of DO_X-DM-HNG in PBS.

In Figure 5E,F, multiple charged homodimerized HNG with methionine oxidized and cysteine disulfide bonds (doubly oxidized homodimerized HNG, DO_x-DM-HNG) were

observed at 532.30 m/z (z = 10), 594.77 m/z (z = 9), 669.01 m/z (z = 8), 764.43 m/z (z = 7), 891.67 m/z (z = 6), and 1069.80 m/z (z = 5).

HNG solutions were incubated at 37 °C and analyzed at day 1 (Figure 6), day 7 (Figure 7) and day 14 (Figure 8) using ultra-performance liquid chromatography coupled with high-resolution mass spectrometry (Waters® Xevo G2-XS QTof). The presence of full-length HNG and DM-HNG in PBS, HPLC-grade water and MO formulation at the different time periods was analyzed (Figures 6–8). The retention time frames of full-length HNG and DM-HNG ranged from 20.75 to 21.25 min and 22.50 to 23.25 min, respectively (Figures 6–8).

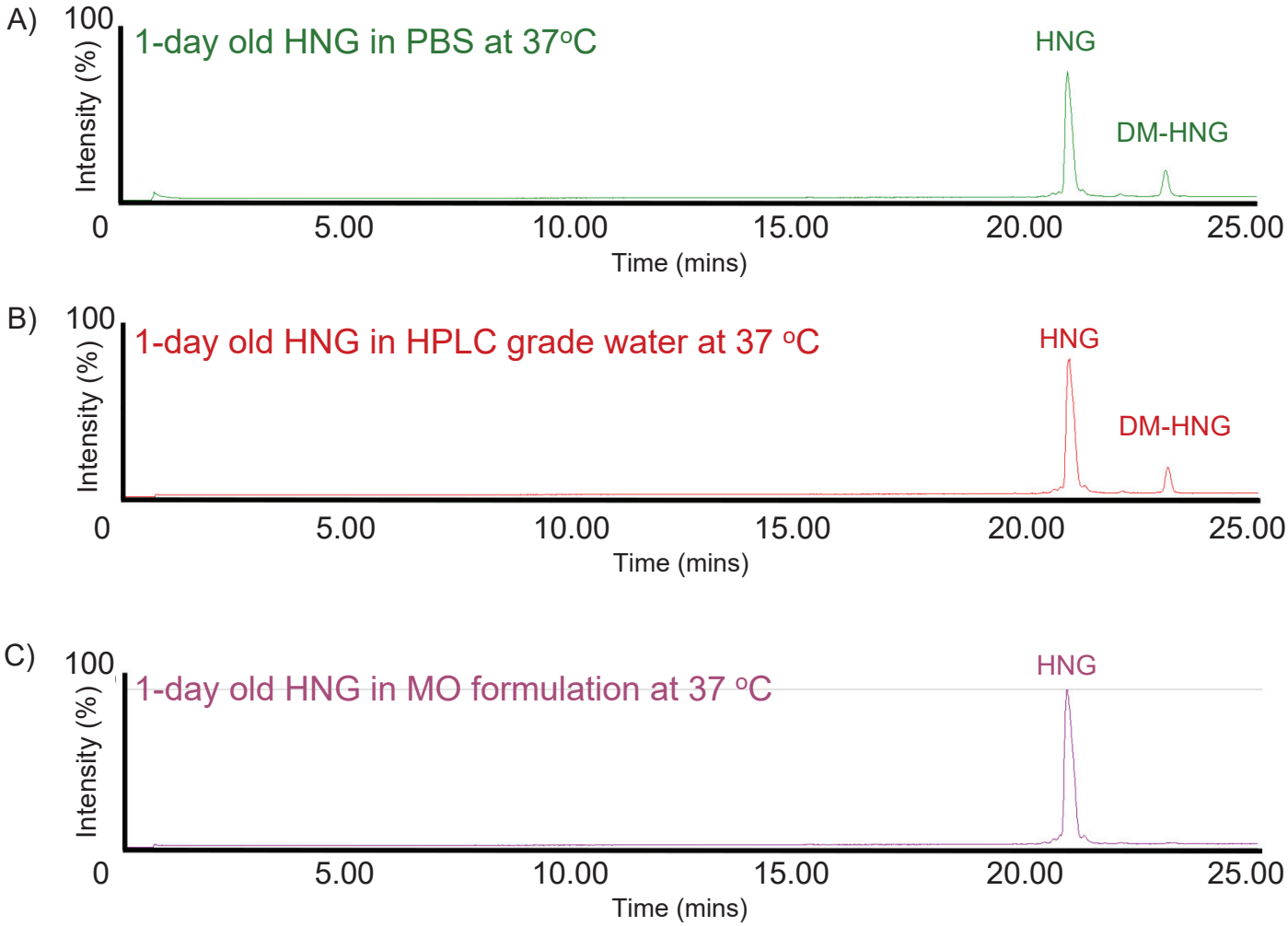


Figure 6. Ion chromatogram results of incubated HNG at 37 °C for 1 day in PBS (**A**), HPLC-grade water (**B**), and MO formulation (**C**).

Concentrations of full-length HNG peptide declined over time with a corresponding appearance of new peaks that increased over time (Figures 6–8). These new peaks were identified as oxidized and/or dimerized HNG products. The DM-HNG was the dominant HNG-Pd at all time points. We found that the full-length HNG peptide had oxidized and dimerized at 37 °C in the PBS, the HPLC-grade water, and MO formulation at day 1 (Figure 6A–C), day 7 (Figure 7A–C) and day 14 (Figure 8A–C). The concentration of the DM-HNG simultaneously increased over time, while the HNG stored in the MO formulation remained mostly intact. (Figures 6–8).

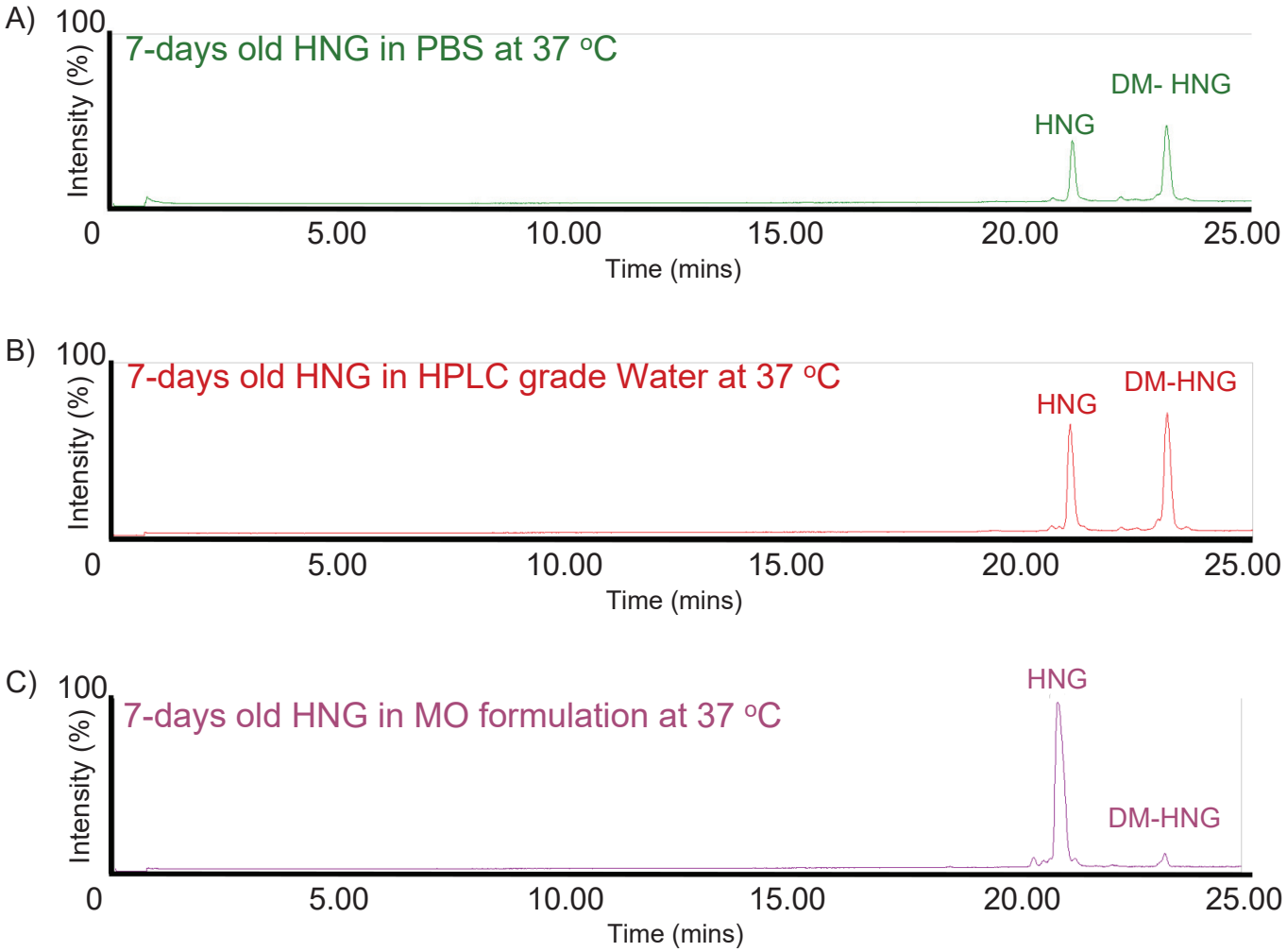


Figure 7. Ion chromatogram results of incubated HNG at 37 °C for 7 days in PBS (**A**), HPLC-grade water (**B**), and MO formulation (**C**).

The full-length HNG, SO_x-HNG and DO_x-HNG were evaluated over time in PBS, HPLC-grade water and MO formulation. In Figure 9A, at day 1, SO_x-HNG and DO_x-HNG were detected in the HPLC-grade water as well as in the PBS and the MO formulation at 37 °C. The highest intensities of full-length HNG, and SO_x-HNG were detected in the MO-formula, and next were those in the HPLC-grade water, with the lowest in the PBS. The highest intensity of DO_x-HNG was detected in the PBS solution, while that in the HPLC-grade water was lower and that in the MO formulation was the lowest.

In Figure 9B, at day 7, higher intensities of SO_x-HNG peptides and full-length HNG were detected in the MO formulation, next were those in the HPLC-grade water and the lowest were in the PBS at 37 °C. The highest intensity of DO_x-HNG was detected in the PBS, that in the HPLC-grade water was lower and that in the MO formulation was lowest.

In Figure 9C, on day 14 at 37 °C, higher intensities of full-length HNG peptides were detected in the MO formulation, next were those in the HPLC-grade water and the lowest were in the PBS at 37 °C. Higher intensities of SO_x-HNG peptides were detected in the MO formulation, next were those in the PBS and the lowest were in the HPLC-grade water. The highest intensity of DO_x-HNG was detected in the HPLC-grade water, that in the PBS was lower and that in the MO formulation was the lowest.

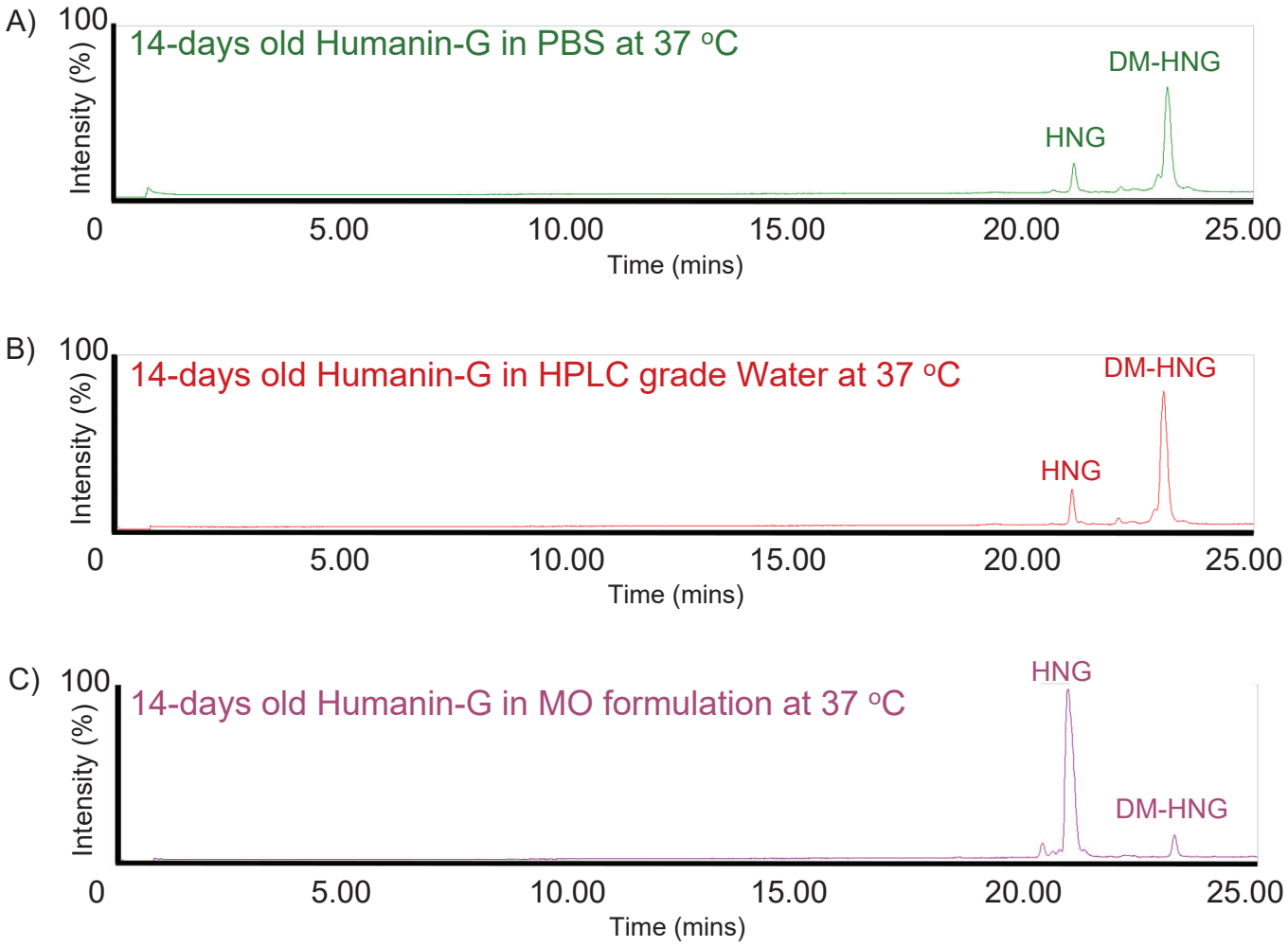


Figure 8. Ion chromatogram results of incubated HNG at 37 °C for 14 days in PBS (**A**), HPLC-grade water (**B**), and MO formulation (**C**).

The homodimerized form of HNG, SO_x-DM-HNG and DO_x-DM-HNG were evaluated over time in PBS, HPLC-grade water and MO formula at 37 °C. In Figure 10A, at day 1, a lower intensity of DM-HNG was detected in MO formula than HPLC-grade water and PBS.

In Figure 10B, on day 7 at 37 °C, higher intensities of SO_x-DM-HNG peptides and DM-HNG were detected in the HPLC-grade water, next were those in the PBS and the lowest were in the MO formulation at 37 °C. The highest intensity of DO_x-DM-HNG was detected in the HPLC-grade water, that in the PBS was lower and that in the MO formulation was lowest.

In Figure 10C, on day 14 at 37 °C, higher intensities of SO_x-DM-HNG peptides and DM-HNG were detected in the HPLC-grade water, next were those in the PBS and the lowest were in the MO-formula at 37 °C. The highest intensity of DO_x-DM-HNG was detected in the PBS, that in the HPLC-grade water was lower and that in the MO-formula was lowest.

In Figure 11A, intensities of SO_x-HNG peptides were evaluated at 37 °C in various solutions at day 1, day 7 and day 14 using UPLC-HRMS. At days 1 and 7, higher intensity of SO_x-HNG were detected in the MO formulation, next were those in the HPLC-grade water, with the lowest in the PBS. At day 14, higher intensities of SO_x-HNG peptides were detected in the MO formulation, next were those in the PBS and the lowest were in the HPLC-grade water.

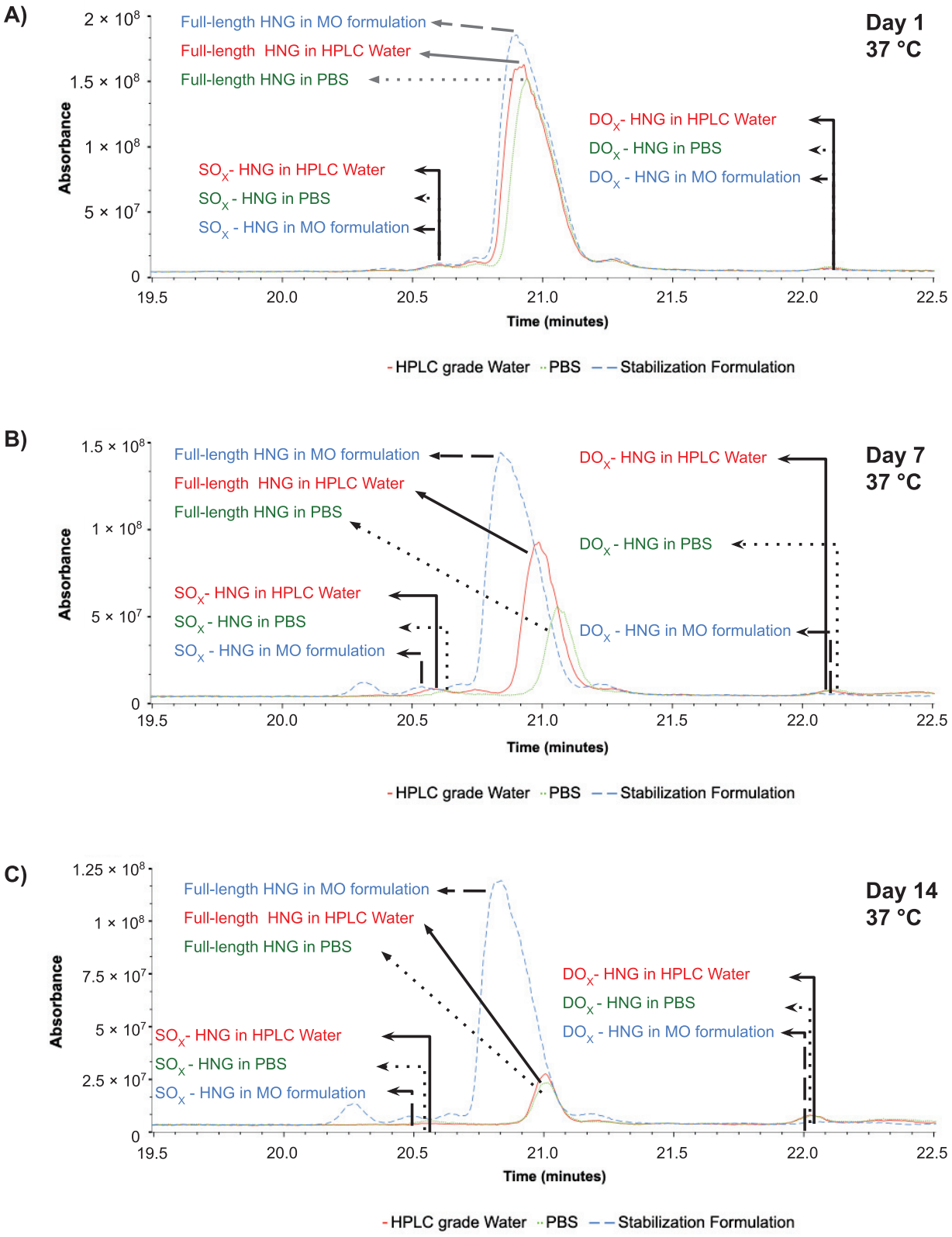


Figure 9. Overlay ion chromatogram (19 min–22.5 min) results of incubated HNG at 37 °C in PBS, HPLC-grade water and MO formulation at day 1 (**A**), at day 7 (**B**), and at day 14 (**C**).

In Figure 11B, intensities of Dox-HNG peptides were evaluated at 37 °C in various solutions at day 1, day 7 and day 14 using UPLC-HRMS. At days 1 and 7, higher intensity of DO_X-HNG was detected in the PBS solution, that in the HPLC-grade water was lower

and that in the MO formulation was the lowest. At day 14, higher intensities of DO_x-HNG peptides were detected in the HPLC-grade water, next were those in the PBS and the lowest were in the MO formulation.

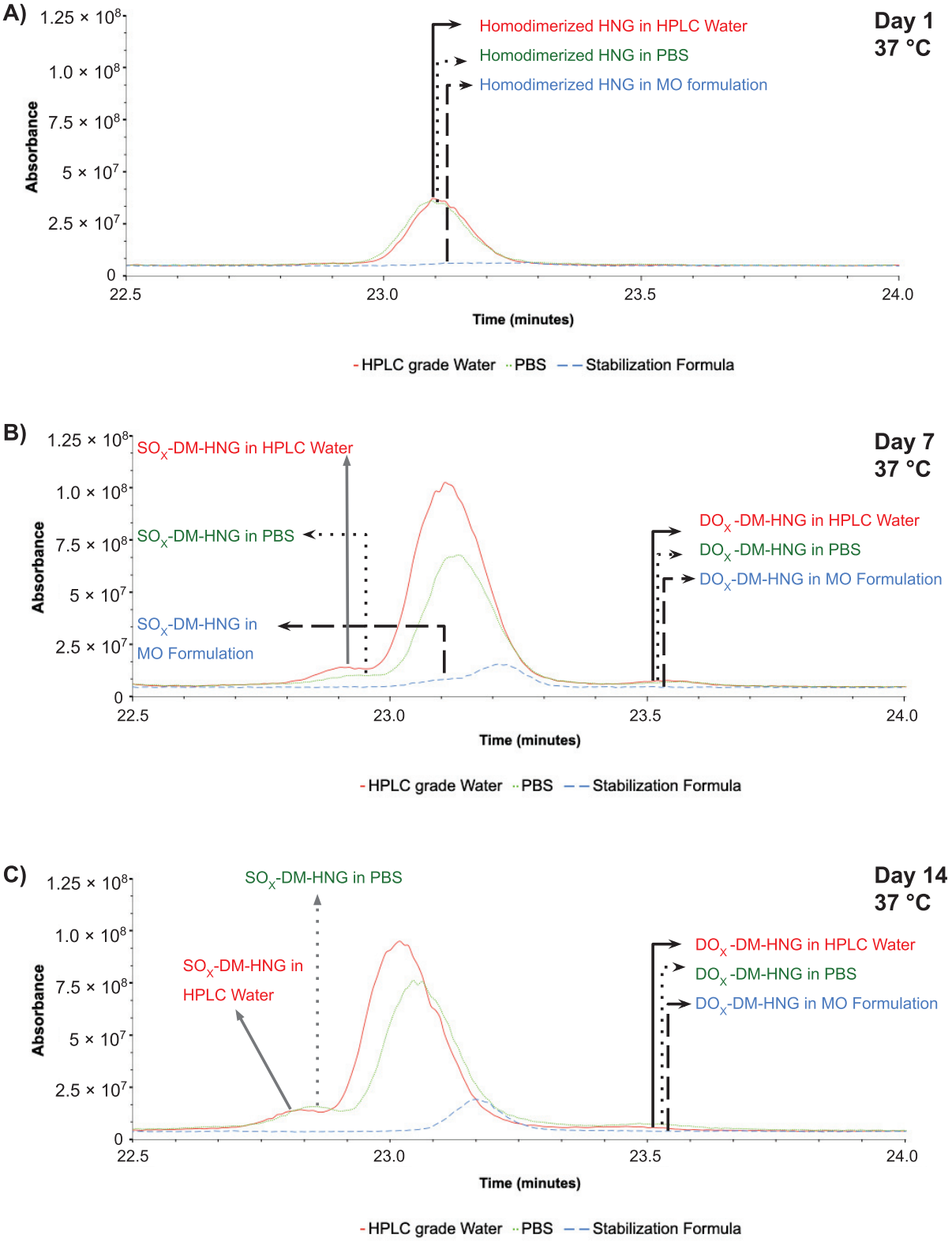


Figure 10. Overlay ion chromatogram (22.5 min–24 min) results of incubated HNG at 37 °C in PBS, HPLC-grade water and MO formulation at day 1 (**A**), at day 7 (**B**), at day 14 (**C**).

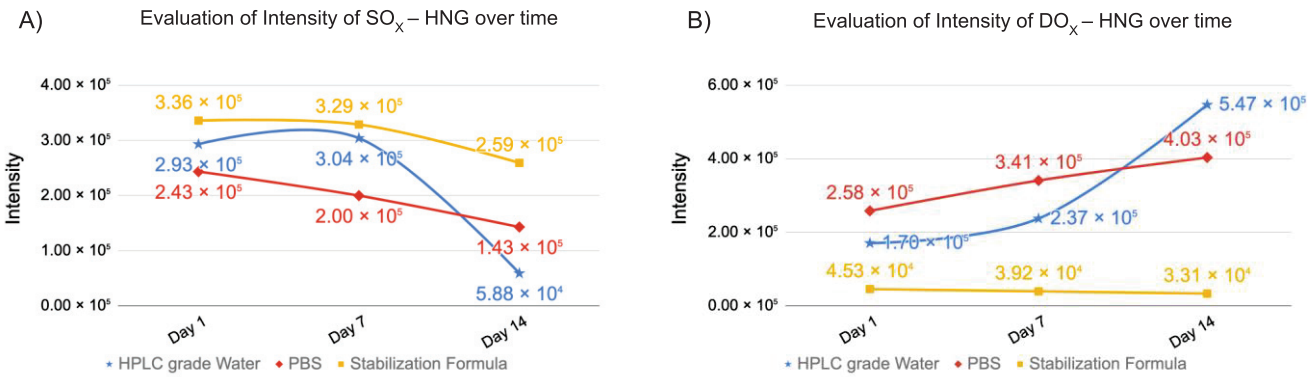


Figure 11. Evaluation of intensity changes of SO_X-HNG (**A**), DOX-HNG (**B**) at day 1, 7 and 14.

In Figure 12A, intensities of DM-HNG peptides were evaluated at 37 °C in various solutions at day 1, day 7 and day 14 using UPLC-HRMS. At day 1, lower intensities of DM-HNG were detected in MO formulation than HPLC-grade water and PBS. At day 7, higher intensities of DM-HNG were detected in the HPLC-grade water, next were those in the PBS and the lowest were in the MO formulation at 37 °C. At day 14, a higher intensity of DM-HNG was detected in the HPLC-grade water, next was that in the PBS and the lowest was in the MO formulation at 37 °C.

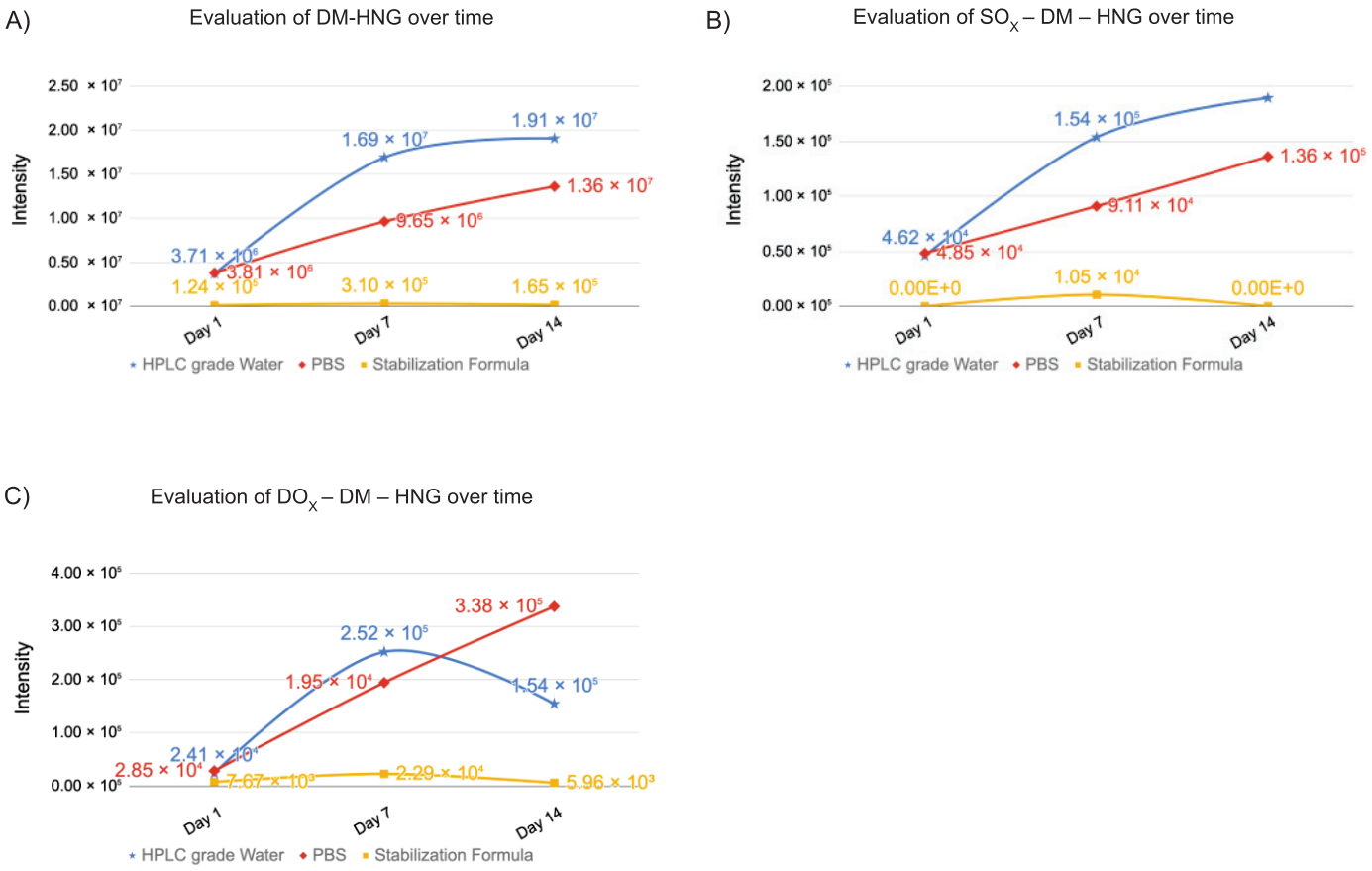


Figure 12. Evaluation of intensity changes of homodimerized form of HNG (**A**), SO_X-DM-HNG (**B**), DO_X-DM-HNG (**C**) at day 1, 7 and 14.

In Figure 12B, intensities of SO_X-DM-HNG were evaluated at 37 °C in various solutions at day 1, day 7 and day 14 using UPLC-HRMS. At day 1, SO_X-DM-HNG was detected in HPLC-grade water and PBS and not detected in MO formulation. At day 7, a higher

intensity of SO_x-DM-HNG was detected in the HPLC-grade water, next was that in the PBS and the lowest was in the MO formulation at 37 °C. At day 14, higher intensities of SO_x-DM-HNG were detected in the HPLC-grade water, next were those in the PBS and the lowest were in the MO formulation at 37 °C.

In Figure 12C, intensities of DO_X-DM-HNG were evaluated at 37 °C in various solutions at day 1, day 7 and day 14 using UPLC-HRMS. At day 1, a lower intensity of DO_X-DM-HNG was detected in MO formulation than HPLC-grade water and PBS. At day 7, higher intensities of DO_x-DM-HNG peptides were detected in the HPLC-grade water, next were those in the PBS and the lowest were in the MO formulation at 37 °C. At day 14, the highest intensity of DO_x-DM-HNG was detected in the PBS, that in the HPLC-grade water was lower and that in the MO formulation was the lowest.

3.3. Long-Term Stability of HNG Peptide in Different Conditions

We evaluated the long-term stability of HNG peptide in the HPLC water and MO formulation stored at 4 °C for 11 months. Collected HRMS data were analyzed using the BiopharmaLynx program to identify peptide sequences (Tables S3 and S4). Identified peptide sequences and HRMS data collected from 11 months old HNG in HPLC water (Table S3) and MO formulation (Table S4) show the full-length HNG peptide, its fragments, and dimerized forms. Mass spectrometry analysis showed that the HNG peptide in HPLC water degraded into multiple fragments (Figure 13B), while in MO formulation, HNG remained mostly intact (Figure 13E). The retention time frames of 11-month-old DM-HNG in HPLC water ranged from 24.2 to 24.6 min (Figure 13A,B, Upper Panel A) and 11-month-old HNG in MO formulation ranged from 22.4 to 22.6 min (Figure 13D,E, Lower Panel B). The 11-month-old HNG peptides in HPLC water showed multiple charged states 532.2 *m/z* (homodimerized-HNG 1-24, z = 10), 591.0 *m/z* (DM-HNG 1-24, z = 9), 664.9 *m/z* (DM-HNG 1-24, z = 8), 759.9 *m/z* (DM-HNG 1-24, z = 7), 886.2 *m/z* (DM-HNG 1-24, z = 6), and 1063.4 *m/z* (DM-HNG 1-24, z = 5) as shown in Figure 13C, Upper Panel A. Many fewer multiple charged intact molecules of 11-month-old HNG peptides in MO formulation were observed at *m/z* 532.3 (HNG 1-24, z = 5), 665.1 (HNG 1-24, z = 4), and 886.5 (HNG 1-24, z = 3) (Figure 13F, Lower Panel B).

As seen in Figure 13, the HNG peptides without a stabilizing formulation were oxidized and dimerized continuously in the HPLC-grade water while the peptide oxidation and dimerization were much slower in the MO formulation. The HNG peptides were stored in the HPLC water (Table S3) and MO formulation (Table S4) over 11 months, and many dimers and oxidized products were identified in both solutions. However, the highest intensities of full-length HNG were found in MO formulation (Table S4), suggesting the potential of the MO formulation for general use in enhancing peptide stability and preventing peptide oxidation.

In summary, our results show that the full-length HNG peptide (24 amino acids) is highly susceptible to chemical modification when placed in HPLC water and PBS at either 4 °C or 37 °C. For example, when placed in HPLC water for 28 days at 4 °C, less than 11% was found in the full-length HNG peptide form (Figure 3), but the HNG peptide was stabilized when placed in the MO formulation (67% and 95% remained full-length HNG at 37 °C or 4 °C, respectively). Using UPLC-HRMS, the full-length HNG was found in both the singly oxidized and doubly oxidized forms (Figure 4); the ionized mass spectra of the SO_X-HNG and DO_X-HNG showed multiple charged states (Figure 4). The ion chromatography of the full-length HNG incubated for 1 to 14 days in PBS, HPLC-grade water or the MO formulations showed increasing loss in the full-length HNG in the PBS and HPLC-grade water, but surprisingly, the full-length HNG in the MO formulation remains mostly stable (Figure 6). Finally, when the full-length HNG was stored for 11 months in HPLC-grade water at 4 °C, we found full-length HNG, along with dimerization and degradation products of HNG, which included three different HNG fragments and four different dimerized forms of HNG fragments (Table S3). When the full-length HNG was stored for 11 months in the MO formulation at 4 °C, there were the full-length HNG, SO_X-

HNG, DO_X-HNG and degradation products of HNG, which includes 28 different HNG fragments and 64 dimerized forms of HNG fragments (Table S4). These data demonstrate that the full-length HNG is fragmented and modified chemically in HPLC-grade water and the MO formulation. Future studies will investigate the biological features of the HNG fragments, the dimerized HNG and oxidized HNG, since these forms may have signaling functions, reflecting increased mitochondrial DNA damage and/or perhaps a positive, rescuing effect for damaged cells.

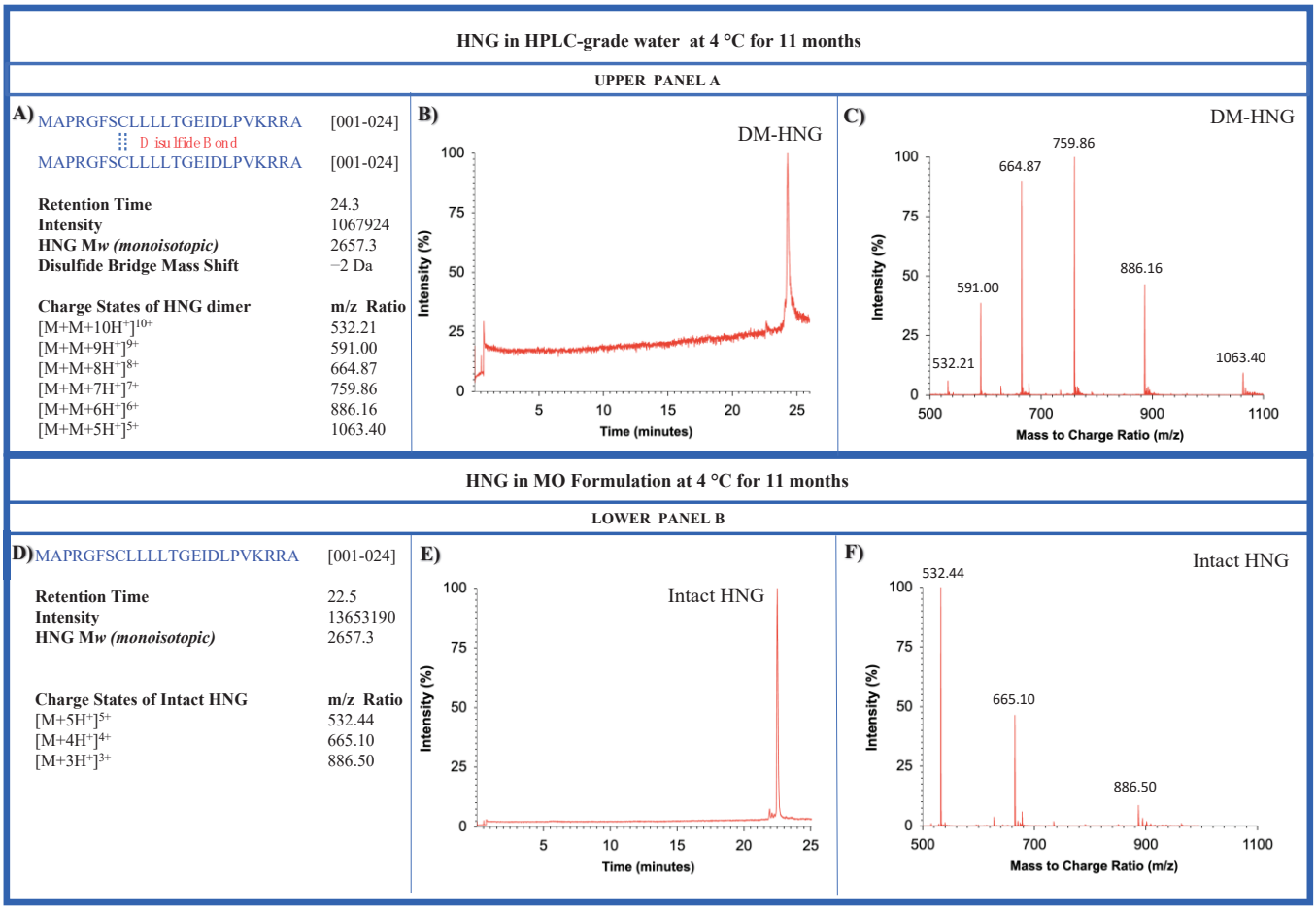


Figure 13. Measurements of HNG in HPLC-grade water (Upper Panel A) and MO formulation (Lower Panel B) at 4 °C for 11 months using HRMS. **UPPER PANEL A,** (**A**) Amino acid sequence and m/z ratio of dimerized form HNG is represented; (**B**,**C**) Representative ion chromatogram and HRMS product ion mass spectra of HNG in HPLC water, respectively. **LOWER PANEL B,** (**D**) Amino acid sequence and m/z ratio of HNG is represented; (**E**,**F**) Representative ion chromatogram and HRMS product ion mass spectra of HNG in MO formulation.

4. Discussion

Despite the promising results that demonstrated the key cellular protective role of HNG, the in vitro and in vivo stability and half-life properties of HNG peptide have not been well studied, and the majority of the reported studies investigating the role of HNG were mostly limited to in vitro cell cultures. Therefore, determining and enhancing the molecular stability properties of HNG is essential to better translate to proper in vivo therapeutic studies. Understanding the stability properties of full-length HNG peptide can help us more accurately determine the dosing and frequency for HNG administration in in vivo animal studies and for possible future clinical studies investigating its role in physiology and disease.

Water and moisture have many effects on peptide degradation [31]. A 28-amino acid Vasoactive Intestinal Peptide, a 29-amino acid peptide Glucagon, vaso-active intestinal peptide and a tricyclic glycopeptide Vancomycin are unstable in aqueous solutions [32–35]. Knoop et al. have reported the instability of the MOTS-c peptide, another mitochondria-derived peptide, in the human plasma [36]. Consistent with those findings, our results showed that HNG in HPLC water is unstable at 37°C, reaching 50% concentration at approximately 33 h. When stored in HPLC water at 4°C, then 54% of the HNG peptide remained stable at day 7, indicating peptide instability even in cold storage conditions in HPLC water. Therefore, researchers investigating the effects of the HNG peptide should consider this newly identified short half-life when determining treatment doses and frequency in cell cultures or in vivo administration to the systemic circulation.

To overcome the low stability issue of the HNG peptide, we developed a special solution (MO formulation) to improve the stability of the molecule. The MO formulation has an acidic property to stabilize the HNG peptide structure. Our proprietary solution demonstrated significant efficiency resulting in 95% full-length HNG peptides after 28 days of storage at 4 °C. Moreover, the MO formulation could provide a 95% stable HNG peptide concentration for up to 7 days at 37 °C. Hence, the MO formulation may significantly improve the efficacy of HNG treatment, and it could reduce administration frequency and costs as well. The increased stability with the MO formulation may provide further processing opportunities such as infusion of HNG and/or potentially other MDPs such as small humanin-like peptides into microspheres for various applications.

Oxidative mechanisms play critical roles in aging and age-related diseases such as ischemia, atherosclerosis, Alzheimer's disease, cataracts, and AMD [37–39]. Peptide oxidation decreases enzymatic activity, accumulates with age, and is related to numerous diseases [38]. Cysteine, methionine, histidine, and tryptophan amino acids are most susceptible to oxidation [38]. Oxidation causes a mass shift of +16 Da. HNG includes methionine and cysteine amino acids, which are susceptible to oxidation. Cysteine oxidation in HNG is responsible for the dimerization of HNG fragments via disulfide bridges. The disulfide bridge causes a mass shift of −2 Da and produces stable, covalently bonded dimers. The high-resolution tandem mass spectrometer provides highly sensitive and accurate results that can identify oxidation sites and disulfide bridges in peptides and dimerized peptides.

Finally, there is a lack of knowledge regarding the degradation products of HNG peptide and their oxidized and dimerized forms. Our study demonstrates that HNG fragments formed homodimers and heterodimers via disulfide bridge interactions (Tables S3 and S4). In the long-term study, our results show that dimerization provides increased stability for the intact HNG and its fragments (Figure 13D,F, Lower Panel B). Consistent with the other studies, several proteins have been shown to increase stability and have functions in dimerized forms, such as human IgG antibody [40], HLA-G dimers on cell surfaces [41], human superoxide dismutase enzymes [42], and glial cell line-derived neurotrophic factor [43]. Disulfide bonds contribute to the structure, functionality stability, and dimerization of peptides and proteins [40–43].

5. Conclusions

For the first time, the short- and long-term stability properties of HNG peptide and its oxidation and degradation products have been analyzed in detail using advanced HPLC and HRMS technologies. Our findings may provide insight for understanding key features in the HNG peptide sequence that define its stability via disulfide bonds. It is currently unknown whether dimerized HNG fragments possess any biological activity. Additionally, we have identified various HNG fragments that may possess different cellular functionalities and/or receptor activities. Future studies will investigate whether there are any such biological functions of these HNG fragments. We also developed a new chemical solution that significantly improves the stability of the HNG peptide in both 4 °C and 37 °C media conditions for up to 28 days. Our results may help researchers design better in vitro

and in vivo experimental parameters to further understand the critical role of Humanin and HNG in physiological conditions and human diseases.

Supplementary Materials: The following supporting information can be downloaded at: https://www.mdpi.com/article/10.3390/biom13030515/s1, Table S1: Represent HPLC gradient run for stability assay. Table S2: Represent UPLC gradient for identification of Humanin-G product. Table S3: Amino acid sequences and mass spectrometric analytical properties of HNG in HPLC water at 11 months. Dimerized HNG and dimerized HNG fragments are ordered by intensity (counts). Table S4: Amino acid sequences and mass spectrometric analytical properties of HNG in MO formulation at 11 months. Dimerized HNG and dimerized HNG fragments are ordered by intensity (counts).

Author Contributions: M.O. and M.C.K. designed the study. M.O. performed HPLC studies with N.N. and carried out HRMS experiments with B.D.K., M.O., B.K. and N.N. analyzed the data. M.O., E.T., N.N. and M.C.K. were involved in preparing the first draft and editing both the original and revised versions of the manuscript. E.T., B.K., N.N. and M.C.K. provided feedback on figures and tables. M.C.K. assisted in strengthening the range and profundity of the manuscript. M.O., A.B.N., N.N., B.K., E.T., B.D.K. and M.C.K. reviewed the data and wrote and/or edited the paper and all have approved it for submission. All authors have read and agreed to the published version of the manuscript.

Funding: This research was supported by Discovery Eye Foundation, the NIH-R01 grant (1R01EY027363-01A1), UCI School of Medicine, Polly and Michael Smith, Roy and Edith Carver, Iris and B. Gerald Cantor Foundation; Research was supported in part by an unrestricted grant from Research to Prevent Blindness.

Institutional Review Board Statement: Not applicable.

Informed Consent Statement: Not applicable.

Data Availability Statement: Not applicable.

Acknowledgments: We owe special thanks to Director Felix Grun in the UCI Mass Spectrometry Facility for discussion and assistance with the mass spectrometry experiments.

Conflicts of Interest: M.C.K.: Her research on mitochondria has been supported by Discovery Eye Foundation (DEF). She serves as a member of the Board for DEF. The University of California, Irvine has reviewed and approved the terms of this arrangement in accordance with conflicts-of-interest policies. M.C.K.: Collaborations with Allegro, Ophthalmics, LLC and Almon Therapeutics, Inc. B.D.K: CLINICAL RESEARCH: Alcon, Alimera, Allegro, Allergan, Apellis, Clearside, Genentech, GSK, Ionis, jCyte, Novartis, Regeneron, ThromboGenics; CONSULTANT: Alimera, Allegro, Allergan, Cell Care, Dose, Eyedaptic, Galimedix, Genentech, Glaukos, Interface Biologics, jCyte, Novartis, Ophthotech, Regeneron, Revana, Theravance Biopharma.

References

1. Nashine, S.; Cohen, P.; Chwa, M.; Lu, S.; Nesburn, A.B.; Kuppermann, B.D.; Kenney, M.C. Humanin G (HNG) Protects Age-Related Macular Degeneration (AMD) Transmitochondrial ARPE-19 Cybrids from Mitochondrial and Cellular Damage. *Cell Death Dis.* **2017**, *8*, e2951. [CrossRef] [PubMed]
2. Riazi-Esfahani, M.; Kuppermann, B.; Kenney, M. The Role of Mitochondria in AMD: Current Knowledge and Future Applications. *J. Ophthalmic Vis. Res.* **2017**, *12*, 424. [CrossRef] [PubMed]
3. Gong, Z.; Tas, E.; Muzumdar, R. Humanin and Age-Related Diseases: A New Link? *Front. Endocrinol.* **2014**, *5*, 210. [CrossRef]
4. Guo, B.; Zhai, D.; Cabezas, E.; Welsh, K.; Nouraini, S.; Satterthwait, A.C.; Reed, J.C. Humanin Peptide Suppresses Apoptosis by Interfering with Bax Activation. *Nature* **2003**, *423*, 456–461. [CrossRef] [PubMed]
5. Hashimoto, Y.; Niikura, T.; Tajima, H.; Yasukawa, T.; Sudo, H.; Ito, Y.; Kita, Y.; Kawasumi, M.; Kouyama, K.; Doyu, M.; et al. A Rescue Factor Abolishing Neuronal Cell Death by a Wide Spectrum of Familial Alzheimer's Disease Genes and Aβ. *Proc. Natl. Acad. Sci. USA* **2001**, *98*, 6336–6341. [CrossRef] [PubMed]
6. Nishimoto, I.; Matsuoka, M.; Niikura, T. Unravelling the Role of Humanin. *Trends Mol. Med.* **2004**, *10*, 102–105. [CrossRef]
7. Hashimoto, Y.; Ito, Y.; Niikura, T.; Shao, Z.; Hata, M.; Oyama, F.; Nishimoto, I. Mechanisms of Neuroprotection by a Novel Rescue Factor Humanin from Swedish Mutant Amyloid Precursor Protein. *Biochem. Biophys. Res. Commun.* **2001**, *283*, 460–468. [CrossRef]

8. Sreekumar, P.G.; Ishikawa, K.; Spee, C.; Mehta, H.H.; Wan, J.; Yen, K.; Cohen, P.; Kannan, R.; Hinton, D.R. The Mitochondrial-Derived Peptide Humanin Protects RPE Cells From Oxidative Stress, Senescence, and Mitochondrial Dysfunction. *Invest. Ophthalmol. Vis. Sci.* **2016**, *57*, 1238. [CrossRef]
9. Lee, C.; Zeng, J.; Drew, B.G.; Sallam, T.; Martin-Montalvo, A.; Wan, J.; Kim, S.-J.; Mehta, H.; Hevener, A.L.; de Cabo, R.; et al. The Mitochondrial-Derived Peptide MOTS-c Promotes Metabolic Homeostasis and Reduces Obesity and Insulin Resistance. *Cell Metab.* **2015**, *21*, 443–454. [CrossRef]
10. Minasyan, L.; Sreekumar, P.G.; Hinton, D.R.; Kannan, R. Protective Mechanisms of the Mitochondrial-Derived Peptide Humanin in Oxidative and Endoplasmic Reticulum Stress in RPE Cells. *Oxidative Med. Cell. Longev.* **2017**, *2017*, 1–11. [CrossRef]
11. Lee, C.; Wan, J.; Miyazaki, B.; Fang, Y.; Guevara-Aguirre, J.; Yen, K.; Longo, V.; Bartke, A.; Cohen, P. IGF-I Regulates the Age-Dependent Signaling Peptide Humanin. *Aging Cell* **2014**, *13*, 958–961. [CrossRef] [PubMed]
12. Tajima, H.; Niikura, T.; Hashimoto, Y.; Ito, Y.; Kita, Y.; Terashita, K.; Yamazaki, K.; Koto, A.; Aiso, S.; Nishimoto, I. Evidence for in Vivo Production of Humanin Peptide, a Neuroprotective Factor against Alzheimer's Disease-Related Insults. *Neurosci. Lett.* **2002**, *324*, 227–231. [CrossRef]
13. Men, J.; Zhang, X.; Yang, Y.; Gao, D. An AD-Related Neuroprotector Rescues Transformed Rat Retinal Ganglion Cells from CoCl2-Induced Apoptosis. *J. Mol. Neurosci.* **2012**, *47*, 144–149. [CrossRef] [PubMed]
14. Niikura, T.; Chiba, T.; Aiso, S.; Matsuoka, M.; Nishimoto, I. Humanin: After the Discovery. *MN* **2004**, *30*, 327–340. [CrossRef]
15. Muzumdar, R.H.; Huffman, D.M.; Atzmon, G.; Buettner, C.; Cobb, L.J.; Fishman, S.; Budagov, T.; Cui, L.; Einstein, F.H.; Poduval, A.; et al. Humanin: A Novel Central Regulator of Peripheral Insulin Action. *PLoS ONE* **2009**, *4*, e6334. [CrossRef] [PubMed]
16. Bachar, A.R.; Scheffer, L.; Schroeder, A.S.; Nakamura, H.K.; Cobb, L.J.; Oh, Y.K.; Lerman, L.O.; Pagano, R.E.; Cohen, P.; Lerman, A. Humanin Is Expressed in Human Vascular Walls and Has a Cytoprotective Effect against Oxidized LDL-Induced Oxidative Stress. *Cardiovasc. Res.* **2010**, *88*, 360–366. [CrossRef] [PubMed]
17. Hashimoto, Y.; Niikura, T.; Ito, Y.; Sudo, H.; Hata, M.; Arakawa, E.; Abe, Y.; Kita, Y.; Nishimoto, I. Detailed Characterization of Neuroprotection by a Rescue Factor Humanin against Various Alzheimer's Disease-Relevant Insults. *J. Neurosci.* **2001**, *21*, 9235–9245. [CrossRef]
18. Muzumdar, R.H.; Huffman, D.M.; Calvert, J.W.; Jha, S.; Weinberg, Y.; Cui, L.; Nemkal, A.; Atzmon, G.; Klein, L.; Gundewar, S.; et al. Acute Humanin Therapy Attenuates Myocardial Ischemia and Reperfusion Injury in Mice. *ATVB* **2010**, *30*, 1940–1948. [CrossRef] [PubMed]
19. Xu, X.; Chua, C.C.; Gao, J.; Hamdy, R.C.; Chua, B.H.L. Humanin Is a Novel Neuroprotective Agent Against Stroke. *Stroke* **2006**, *37*, 2613–2619. [CrossRef]
20. Oh, Y.K.; Bachar, A.R.; Zacharias, D.G.; Kim, S.G.; Wan, J.; Cobb, L.J.; Lerman, L.O.; Cohen, P.; Lerman, A. Humanin Preserves Endothelial Function and Prevents Atherosclerotic Plaque Progression in Hypercholesterolemic ApoE Deficient Mice. *Atherosclerosis* **2011**, *219*, 65–73. [CrossRef]
21. Takeshita, Y.; Hashimoto, Y.; Nawa, M.; Uchino, H.; Matsuoka, M. SH3-Binding Protein 5 Mediates the Neuroprotective Effect of the Secreted Bioactive Peptide Humanin by Inhibiting c-Jun NH2-Terminal Kinase. *J. Biol. Chem.* **2013**, *288*, 24691–24704. [CrossRef] [PubMed]
22. Klein, L.E.; Cui, L.; Gong, Z.; Su, K.; Muzumdar, R. A Humanin Analog Decreases Oxidative Stress and Preserves Mitochondrial Integrity in Cardiac Myoblasts. *Biochem. Biophys. Res. Commun.* **2013**, *440*, 197–203. [CrossRef]
23. Jin, H.; Liu, T.; Wang, W.-X.; Xu, J.-H.; Yang, P.-B.; Lu, H.-X.; Sun, Q.-R.; Hu, H.-T. Protective Effects of [Gly14]-Humanin on β-Amyloid-Induced PC12 Cell Death by Preventing Mitochondrial Dysfunction. *Neurochem. Int.* **2010**, *56*, 417–423. [CrossRef]
24. Yamagishi, Y.; Hashimoto, Y.; Niikura, T.; Nishimoto, I. Identification of Essential Amino Acids in Humanin, a Neuroprotective Factor against Alzheimer's Disease-Relevant Insults. *Peptides* **2003**, *24*, 585–595. [CrossRef] [PubMed]
25. Eriksson, E.; Wickström, M.; Perup, L.S.; Johnsen, J.I.; Eksborg, S.; Kogner, P.; Sävendahl, L. Protective Role of Humanin on Bortezomib-Induced Bone Growth Impairment in Anticancer Treatment. *JNCI J. Natl. Cancer Inst.* **2014**, *106*, djt459. [CrossRef] [PubMed]
26. Kyte, J.; Doolittle, R.F. A Simple Method for Displaying the Hydropathic Character of a Protein. *J. Mol. Biol.* **1982**, *157*, 105–132. [CrossRef]
27. Chang, K.Y.; Yang, J.-R. Analysis and Prediction of Highly Effective Antiviral Peptides Based on Random Forests. *PLoS ONE* **2013**, *8*, e70166. [CrossRef] [PubMed]
28. Enany, S. Structural and Functional Analysis of Hypothetical and Conserved Proteins of Clostridium Tetani. *J. Infect. Public Health* **2014**, *7*, 296–307. [CrossRef] [PubMed]
29. Li, R.-F.; Lu, Z.-F.; Sun, Y.-N.; Chen, S.-H.; Yi, Y.-J.; Zhang, H.-R.; Yang, S.-Y.; Yu, G.-H.; Huang, L.; Li, C.-N. Molecular Design, Structural Analysis and Antifungal Activity of Derivatives of Peptide CGA-N46. *Interdiscip. Sci. Comput. Life Sci.* **2016**, *8*, 319–326. [CrossRef] [PubMed]
30. Bernardo, D.; Sánchez, B.; Al-Hassi, H.O.; Mann, E.R.; Urdaci, M.C.; Knight, S.C.; Margolles, A. Microbiota/Host Crosstalk Biomarkers: Regulatory Response of Human Intestinal Dendritic Cells Exposed to Lactobacillus Extracellular Encrypted Peptide. *PLoS ONE* **2012**, *7*, e36262. [CrossRef]
31. Bell, L.N. Peptide Stability in Solids and Solutions. *Biotechnol. Prog.* **1997**, *13*, 342–346. [CrossRef]
32. Mody, R.; Tramontano, A.; Paul, S. Spontaneous Hydrolysis of Vasoactive Intestinal Peptide in Neutral Aqueous Solution. *Int. J. Pept. Protein Res.* **1994**, *44*, 441–447.

33. Taleb, N.; Coriati, A.; Khazzaka, C.; Bayonne, J.; Messier, V.; Rabasa-Lhoret, R. Stability of Commercially Available Glucagon Formulation for Dual-Hormone Artificial Pancreas Clinical Use. *Diabetes Technol. Ther.* **2017**, *19*, 589–594. [CrossRef] [PubMed]
34. Jackson, M.A.; Caputo, N.; Castle, J.R.; David, L.L.; Roberts, C.T.; Ward, W.K. Stable Liquid Glucagon Formulations for Rescue Treatment and Bi-Hormonal Closed-Loop Pancreas. *Curr. Diabetes Rep.* **2012**, *12*, 705–710. [CrossRef] [PubMed]
35. Cao, M.; Feng, Y.; Zhang, Y.; Kang, W.; Lian, K.; Ai, L. Studies on the Metabolism and Degradation of Vancomycin in Simulated in Vitro and Aquatic Environment by UHPLC-Triple-TOF-MS/MS. *Sci. Rep.* **2018**, *8*, 1–13. [CrossRef]
36. Knoop, A.; Thomas, A.; Thevis, M. Development of a Mass Spectrometry Based Detection Method for the Mitochondrion-Derived Peptide MOTS-c in Plasma Samples for Doping Control Purposes. *Rapid Commun. Mass Spectrom.* **2019**, *33*, 371–380. [CrossRef]
37. Ramkumar, S.; Fan, X.; Wang, B.; Yang, S.; Monnier, V.M. Reactive Cysteine Residues in the Oxidative Dimerization and Cu2+ Induced Aggregation of Human ΓD-Crystallin: Implications for Age-Related Cataract. *Biochim. Biophys. Acta-Mol. Basis Dis.* **2018**, *1864*, 3595–3604. [CrossRef]
38. Schey, K.L.; Finley, E.L. Identification of Peptide Oxidation by Tandem Mass Spectrometry. *Acc. Chem. Res.* **2000**, *33*, 299–306. [CrossRef]
39. Reeg, S.; Grune, T. Protein Oxidation in Aging: Does It Play a Role in Aging Progression? *Antioxid. Redox Signal.* **2015**, *23*, 239–255. [CrossRef]
40. McAuley, A.; Jacob, J.; Kolvenbach, C.G.; Westland, K.; Lee, H.J.; Brych, S.R.; Rehder, D.; Kleemann, G.R.; Brems, D.N.; Matsumura, M. Contributions of a Disulfide Bond to the Structure, Stability, and Dimerization of Human IgG1 Antibody CH3 Domain. *Protein Sci.* **2007**, *17*, 95–106. [CrossRef]
41. Boyson, J.E.; Erskine, R.; Whitman, M.C.; Chiu, M.; Lau, J.M.; Koopman, L.A.; Valter, M.M.; Angelisova, P.; Horejsí, V.; Strominger, J.L. Disulfide Bond-Mediated Dimerization of HLA-G on the Cell Surface. *Proc. Natl. Acad. Sci. USA* **2002**, *99*, 16180–16185. [CrossRef] [PubMed]
42. Banci, L.; Bertini, I.; Durazo, A.; Girotto, S.; Gralla, E.B.; Martinelli, M.; Valentine, J.S.; Vieru, M.; Whitelegge, J.P. Metal-Free Superoxide Dismutase Forms Soluble Oligomers under Physiological Conditions: A Possible General Mechanism for Familial ALS. *Proc. Natl. Acad. Sci. USA* **2007**, *104*, 11263–11267. [CrossRef] [PubMed]
43. Li, T.; Yamane, H.; Arakawa, T.; Narhi, L.O.; Philo, J. Effect of the Intermolecular Disulfide Bond on the Conformation and Stability of Glial Cell Line-Derived Neurotrophic Factor. *Protein Eng. Des. Sel.* **2002**, *15*, 59–64. [CrossRef] [PubMed]

Disclaimer/Publisher's Note: The statements, opinions and data contained in all publications are solely those of the individual author(s) and contributor(s) and not of MDPI and/or the editor(s). MDPI and/or the editor(s) disclaim responsibility for any injury to people or property resulting from any ideas, methods, instructions or products referred to in the content.

Journal of
Clinical Medicine

MDPI

Case Report

Comprehensive GC-MS Measurement of Amino Acids, Metabolites, and Malondialdehyde in Metformin-Associated Lactic Acidosis at Admission and during Renal Replacement Treatment

Rene A. Posma [1], Stephan J. L. Bakker [2], Maarten W. Nijsten [1], Daan J. Touw [3] and Dimitrios Tsikas [4,*]

[1] Department of Critical Care, University of Groningen, University Medical Center Groningen, 9713 GZ Groningen, The Netherlands; r.a.posma@umcg.nl (R.A.P.); m.w.n.nijsten@umcg.nl (M.W.N.)
[2] Division of Nephrology, Department of Internal Medicine, University of Groningen, University Medical Center Groningen, 9713 GZ Groningen, The Netherlands; s.j.l.bakker@umcg.nl
[3] Department of Clinical Pharmacy and Pharmacology, University of Groningen, University Medical Center Groningen, 9713 GZ Groningen, The Netherlands; d.j.touw@umcg.nl
[4] Institute of Toxicology, Core Unit Proteomics, Hannover Medical School, 30623 Hannover, Germany
* Correspondence: tsikas.dimitros@mh-hannover.de

Abstract: Metformin is the most widely used drug in type 2 diabetes. Regular metformin use has been associated with changes in concentrations of amino acids. In the present study, we used valid stable-isotope labeled GC-MS methods to measure amino acids and metabolites, including creatinine as well as malondialdehyde (MDA), as an oxidative stress biomarker in plasma, urine, and dialysate samples in a patient at admission to the intensive care unit and during renal replacement treatment because of metformin-associated lactic acidosis (MALA, 21 mM lactate, 175 μM metformin). GC-MS revealed lower concentrations of amino acids in plasma, normal concentrations of the nitric oxide (NO) metabolites nitrite and nitrate, and normal concentrations of MDA. Renal tubular reabsorption rates were altered on admission. The patient received renal replacement therapy over 50 to 70 h of normalized plasma amino acid concentrations and their tubular reabsorption, as well as the tubular reabsorption of nitrite and nitrate. This study indicates that GC-MS is a versatile analytical tool to measure different classes of physiological inorganic and organic substances in complex biological samples in clinical settings such as MALA.

Keywords: amino acids; GC-MS; intoxication; MALA; oxidative stress; renal replacement therapy

1. Introduction

Metformin (*N*,*N*-dimethylbiguanide) is the most commonly prescribed oral antihyperglycemic drug to treat type 2 diabetes [1]. Metformin is eliminated in urine in its unchanged form via renal secretion [2]. Patients with metformin intoxication can develop metformin-associated lactic acidosis (MALA), a life-threatening condition. MALA is defined as a plasma pH < 7.35, a plasma lactate concentration >5 mM, and a metformin concentration >5 mg/L [3]. The pathophysiology of MALA is characterized by reduced lactate clearance due to impaired gluconeogenesis combined with inhibition of systemic mitochondrial respiration, causing an increase in anaerobic metabolism [4–7]. Patients with MALA are treated in the intensive care unit (ICU), requiring comprehensive supportive care in combination with renal replacement therapy (RRT), such as intermittent hemodialysis (HD) or continuous RRT [8].

Metformin use has been associated with changes in concentrations of amino acids and their metabolites, including homoarginine [9,10]. The effects of metformin-induced post-translational modifications (PTM) at toxic concentrations are scarce [11,12]. In urine of a patient with MALA, we have previously found an accumulation of hydroxy-proline

(OH-Pro) [13]. The aim of the present study was to determine the status of other amino acids, including arginine and some of its metabolites, and of oxidative stress in the MALA patient at ICU admission and during RRT. Free L-arginine (Arg) is the physiological substrate of nitric oxide synthase (NOS) isoforms [14]. Of particular interest were the major metabolites and measures of nitric oxide (NO), namely nitrate and nitrite. Post-translational dimethylation of Arg residues in proteins leads to symmetric dimethylarginine (SDMA) and asymmetric dimethylarginine (ADMA), which are endogenous inhibitors of NOS activity [14]. As dimethyl amine (DMA) is the major urinary metabolite of ADMA [15], it was of interest to investigate potential effects of MALA on this ADMA metabolite. Eventually, malondialdehyde (MDA) was measured as a biomarker of oxidative stress [16] in the MALA patient.

Mass spectrometry coupled to gas chromatography (GC-MS) is a widely used instrumental technique for the reliable quantitative determination of numerous physiological compounds, drugs, and their metabolites in biological samples such as plasma and urine. In the present work, we used previously described validated GC-MS methods for the measurement of the above-mentioned analytes [17–24]. These methods include use of suitable derivatization techniques for the analytes and their stable-isotope labeled analogs (^{2}H, ^{15}N), which serve as internal standards. All GC-MS analyses in this study were performed in the negative-ion chemical ionization (NICI) mode and by using selected-ion monitoring (SIM) of analyte-specific ions.

2. Materials and Methods

2.1. Patient

The case report on metformin intoxication and RRT treatment has been described elsewhere in detail [13] and is briefly summarized below.

The 70-year old female patient (bodyweight, 84 kg) was oliguric, and the plasma creatinine concentration was 606 μM, indicating acute renal failure. The patient was transferred to our hospital to start RRT. At ICU admission, the blood metformin concentration was 175 μM. During hemodialysis, the metformin plasma concentration rapidly decreased, and the acidosis improved, with an increase in pH from 7.26 to 7.40 in approximately 2 h. Likewise, lactate concentration decreased from 21 mM to <2 mM within 12 h. After hemodialysis (HD) was stopped, continuous veno-venous hemodiafiltration (CVVHDF) and, subsequently, continuous veno-venous hemofiltration (CVVH) was applied. Heparin was used as an anticoagulant during CVVHDF, whereas citrate was used during CVVH. After 12 h of ICU admission, the metformin concentration decreased to 39 μM, which is generally considered to be non-toxic [25]. Heparinized plasma, urine, and dialysate samples were centrifuged and stored at −80 °C. Written informed consent was obtained to collect residual material and for publication of this case report. Ethical approval was given by the institutional review board (METc 2014-552).

2.2. GC-MS Analyses in Plasma, Urine, and Dialysate Samples

Metformin, amino acids, nitrate, nitrite, and MDA were analyzed by GC-MS in plasma, urine, and dialysate (effluent) samples after suitable derivatization, as described previously [17–24]. All amino acids were measured simultaneously as methyl ester pentafluoropropionyl derivatives. Nitrate, nitrite, creatinine, and MDA were measured simultaneously as pentafluorobenzyl derivatives. DMA was analyzed after extractive derivatization as a pentafluorobenzamide derivative. In all analyses, commercially available and de novo synthesized stable-isotope labelled analogs were used as internal standards for each analyte.

GC-MS analyses were performed on a single quadrupole mass spectrometer model ISQ, equipped with a Trace 1210 series gas chromatograph, and an AS1310 autosampler (ThermoFisher, Dreieich, Germany). A fused-silica capillary column Optima 17 (15 m length, 0.25 mm I.D., 0.25 μm film thickness) was used (Macherey-Nagel, Düren, Germany). Methane was used as the reagent gas (flow rate of 2.4 mL/min) for NICI. Quantitative analyses were performed in the SIM mode. The GC-MS method for amino acids measures the

sum of citrulline (Cit) and ornithine (Orn), asparagine (Asn) and aspartate (Asp), glutamine (Gln) and glutamate (Glu), leucine (Leu) and isoleucine (Ile). The concentrations of these amino acids are reported as Orn, Asp, Glu, and Leu, respectively. Analyte concentrations in urine were corrected for urinary creatinine excretion and are reported as μmol analyte per mmol creatinine. Creatinine in plasma and urine was also analyzed by GC-MS, as described elsewhere [24]. All analyses were performed at the same time in one laboratory by a single skillful person.

2.3. Calculations and Statistical Analyses

Fractional excretion (FE, %) values were calculated for all analytes by dividing the concentration ratio of creatinine (Crea) in plasma (P) and urine (U), i.e., $[Crea]_P/[Crea]_U$, by the concentration ratio of an analyte (A) in plasma and urine, i.e., $[A]_P/[A]_U$, measured at a certain time point, and by multiplying the result by 100 (see Formula (1)). Tubular reabsorption values (T, %) of analytes were calculated by subtracting the FE values from 100 (see Formula (2)).

$$FE\ (\%) = ([Crea]_P/[Crea]_U)/([A]_P/[A]_U) \times 100\% \quad (1)$$

$$T\ (\%) = 100 - FE\ (\%) \quad (2)$$

Renal clearance was calculated by dividing the elimination rate in urine from the previous time-point, at which urine was collected to the current time-point by the corresponding plasma concentration. The instantaneous plasma clearance by dialysis was calculated by dividing the product of dialysate flow and concentration in the dialysate (i.e., elimination rate) by the plasma concentration. Because the blood samples were not simultaneously obtained together with the effluent samples, the concentration in plasma was linearly interpolated using data from four time-points with the Trend function in Excel (Microsoft, Redmond, WA, USA). Calculating plasma clearance by dialysis using the AV method was not possible because no simultaneous inflow and outflow samples were obtained. To present the average clearance of each compound during CVVHDF and CVVH, respectively, the time-weighted mean clearance was calculated, which is more representative of the true clearance than the arithmetic mean, as it assumes a linear trend between each individual measurement [26].

Data analyses were performed with GraphPad Prism version 7 (GraphPad Software, San Diego, CA, USA) and R version 4.3.2 (R Foundation for Statistical Computing, Vienna, Austria).

3. Results and Discussion

The concentrations of the analytes measured in the samples of the study are presented in Tables 1 and 2 and in Figures 1 and 2. For the sake of clarity and better readability, the results are presented separately for the amino acids and the other analytes. For comparison of analyte concentrations measured in the patient's samples, we used concentrations of the analytes as measured in studies on healthy subjects [17–24,27–37]. These data are summarized in Table 3. The reference interval for plasma creatinine was reported to be 53–115 μM [36].

Table 1. (**a**) Concentrations of metformin, creatinine, and metabolites (all in μM) in plasma samples of the patient during (time in h) RTR. (**b**) Concentrations of metformin (mM), creatinine (mM), and metabolites (all in μM) in urine samples of the patient during (time in h) RTR. (**c**) Concentrations of metformin and metabolites (all in μM) in effluent samples of the patient during (time in h) RTR.

(a)								
Time	**Metformin**	**Creatinine**	**Nitrate**	**Nitrite**	**MDA**	**GAA**	**ADMA**	**SDMA**
5.5	*75*	*388*	*57*	*2.64*	*1.16*	*1.42*	*0.22*	*1.48*
7.2	73	385	59	3.09	0.90	3.46	0.53	1.76

Table 1. *Cont.*

(a)

Time	Metformin	Creatinine	Nitrate	Nitrite	MDA	GAA	ADMA	SDMA
9.0	63	350	56	3.07	1.25	3.63	0.48	1.98
10.7	55	297	55	2.83	0.93	5.30	0.71	2.38
11.3	50	307	58	3.24	0.89	5.31	0.50	1.88
12.6	44	267	51	3.34	0.83	4.09	0.53	1.30
15.9	35	202	53	3.25	0.07	2.83	0.32	0.98
30.8	19	183	57	4.38	1.18	5.85	0.48	1.42
35.0	16	167	53	3.66	0.96	4.72	0.44	1.73
40.3	13	145	51	2.96	1.14	1.93	0.30	1.03
48.8	10	135	58	3.12	0.81	4.74	0.48	1.03
53.3	10	190	53	2.92	1.03	2.82	0.35	2.25
57.0	9	219	57	3.08	1.23	2.62	0.46	1.34
62.0	7	250	53	3.29	0.94	1.96	0.50	1.18
63.0	7	226	56	3.02	0.90	1.91	0.51	1.34
64.7	6	234	56	3.29	0.92	3.35	0.33	2.15
66.6	4	230	60	3.08	0.82	2.28	0.42	1.52

(b)

Time	Metformin	Creatinine	DMA	Nitrate	Nitrite	MDA	GAA	ADMA	SDMA
5.5	*1.46*	*2.5*	*126*	*239*	*10.5*	*1.08*	*13.2*	*1.32*	*12.9*
7.2	1.17	1.88	84	137	10.3	0.98	12.2	1.8	4.3
9.0	1.44	2.23	124	107	9.3	1.79	13.6	2.14	7.2
10.7	1.23	2.11	102	119	7.4	1.09	11.0	1.07	5.0
11.3	1.25	2.19	105	91	5.1	1.08	11.8	1.23	4.8
12.6	2.58	4.84	213	112	9.8	15.07	39.1	2.68	11.8
15.9	3.37	6.14	279	81	5.1	19.52	59.6	4.39	17.8
30.8	3.5	4.88	321	216	24.1	7.31	146.1	7.65	33.7
35.0	2.87	4.49	231	84	10.6	9.66	147.8	4.93	14.8
40.3	4.02	6.29	367	78	7.5	6.64	196.4	6.71	15.1
46.5	5.11	6.39	423	83	5.4	6.88	212.8	8.45	15.6
48.8	3.28	5.43	360	84	1.9	5.28	248.2	5.78	13.3
50.8	2.04	3.33	230	86	1.8	3.53	198.4	4.15	6.1
53.3	1.17	2.56	191	93	2.0	10.81	179.7	3.42	5.4
57.0	0.95	2.61	148	108	2.2	4.22	97.5	3.17	5.7
62.0	0.68	3.17	153	127	2.1	1.81	79.7	3	5.1
63.0	0.64	3.6	157	137	3.3	1.85	81.1	2.79	5.7
64.7	0.6	3.85	162	141	3.1	1.7	59.8	3.15	6.0
66.6	0.5	4.04	233	150	2.3	2.07	59.4	3.85	7.8

(c)

Time	Metformin	DMA	Nitrate	Nitrite	MDA	Creatinine	GAA	ADMA	SDMA
5.0	*28.6*	*3.41*	*31.1*	*9.49*	*0.19*	*155*	*1.67*	*0.16*	*0.54*
8.8	80.9	10.5	32.2	2.70	0.27	344	2.00	0.40	1.52
11.0	69.6	9.09	25.9	4.48	0.25	427	2.49	0.32	1.22
12.0	60.7	7.73	29.0	4.13	0.29	384	2.94	0.31	1.39
13.0	54.9	7.80	24.3	4.12	0.27	423	3.97	0.32	1.31
15.3	45.2	7.92	27.5	3.89	0.23	415	3.04	0.31	1.36
17.6	37.1	6.86	25.3	3.92	0.26	344	2.38	0.28	0.93
19.5	32.5	6.96	21.4	4.10	0.22	256	3.85	0.31	1.09
20.8	29.7	6.14	24.7	4.08	0.20	256	2.36	0.32	1.01
24.3	23.3	4.50	21.7	3.62	0.23	188	4.32	0.36	0.76
29.1	20.6	7.16	29.6	3.29	0.21	190	6.12	0.33	1.30
30.5	18.2	5.68	28.3	2.97	0.23	286	5.90	0.30	1.16
33.4	16.2	7.81	24.4	2.93	0.20	245	8.83	0.33	1.27
35.0	15.6	6.11	32.1	5.25	0.22	267	7.48	0.25	1.43
40.3	12.1	6.93	24.3	4.17	0.48	259	3.44	0.28	1.07
42.6	11.9	5.15	24.5	3.82	0.23	252	6.38	0.35	0.94
46.5	10.0	5.54	23.5	3.94	0.19	224	10.73	0.25	1.37
48.9	9.6	5.83	23.8	4.75	0.24	220	5.25	0.30	1.84
50.0	18.0	5.95	25.4	2.67	0.24	277	5.73	0.39	1.58

Table 2. (**a**) Concentrations of amino acids (all in μM) in plasma samples of the patient during (time in h) the RTR. (**b**) Concentrations of amino acids (all in μM) in urine samples of the patient during (time in h) RTR. (**c**) Concentrations of amino acids (all in μM) in effluent samples of the patient during (time in h) RTR.

(a)

Time	Ala	Thr	Gly	Val	Ser	Sar	Leu	Asp	Gln	Met	Orn	Phe	Tyr	Lys	Arg	hArg	Trp
5.5	*149*	*53*	*82*	*141*	*52*	*1.12*	*143*	*32*	*247*	*35*	*18*	*36*	*31*	*96*	*17*	*1.12*	*5.7*
7.2	281	106	168	296	90	1.98	322	70	662	67	38	82	66	203	37	2.1	9.9
9.0	217	91	163	231	80	1.45	276	63	560	57	39	75	55	163	25	1.52	13.5
10.7	197	88	173	191	85	1.41	249	69	533	57	30	72	50	162	29	1.48	16.9
11.3	190	87	167	178	75	1.32	243	63	512	55	29	72	49	160	30	1.35	16.5
12.6	194	93	183	185	87	1.36	243	69	534	56	32	77	50	180	34	1.28	13.2
15.9	190	107	197	192	117	1.1	259	66	478	54	36	88	57	205	36	1.12	16.3
30.8	280	152	277	303	116	1.72	359	92	610	62	77	113	92	220	30	0.65	28.0
35.0	268	116	222	240	128	1.3	263	78	496	53	56	98	68	173	29	0.48	27.4
40.3	223	102	184	224	98	1.28	254	57	419	47	62	96	62	169	25	0.40	31.9
48.8	240	121	190	298	92	1.23	330	72	420	50	56	95	64	174	31	0.36	24.3
53.3	301	102	228	271	110	1.34	246	80	483	54	54	99	55	174	28	0.38	29.0
57.0	263	84	202	234	97	1.23	199	70	433	49	50	88	46	143	18	0.36	27.5
62.0	211	73	189	206	86	1.09	170	67	399	47	42	92	42	137	22	0.36	25.8
63.0	178	67	177	190	94	1.01	176	52	373	44	43	87	41	130	22	0.32	19.3
64.7	202	87	187	280	92	1.09	269	69	423	50	52	97	49	160	31	0.35	14.3
66.6	217	101	273	296	175	1.25	301	81	496	55	96	105	58	169	34	0.42	34.3

(b)

Time	Ala	Thr	Gly	Val	Ser	Sar	Leu	Asp	Gln	Met	Orn	Phe	Tyr	Lys	Arg	hArg	Trp
5.5	*175*	*116*	*206*	*95*	*105*	*1.7*	*122*	*81*	*652*	*54.5*	*16.1*	*46.4*	*81*	*224*	*14.9*	*0.27*	*12.9*
7.2	135	155	246	91	112	1.8	107	101	823	63.8	21.0	55.7	82	226	13.9	0.24	20.4
9.0	126	200	309	80	141	1.5	136	134	850	66.6	20.7	61.7	90	252	15.2	0.22	23.8
10.7	284	139	199	227	101	2.0	174	81	762	61.6	24.3	54.2	99	365	14.0	0.52	14.1
11.3	290	150	217	219	108	2.4	182	88	847	66.4	25.5	58.0	108	380	15.9	0.53	15.5
12.6	147	281	506	74	206	2.0	234	250	953	69.2	23.4	88.9	102	282	30.5	0.23	25.1
15.9	179	397	745	94	302	2.5	332	553	1202	83.1	37.6	125.9	135	421	46.8	0.27	35.2
30.8	320	524	985	132	420	4.2	530	946	947	77.5	64.0	198.9	208	480	85.6	0.22	78.6
35.0	258	283	659	129	279	3.3	376	631	745	62.6	38.0	136.5	150	293	57.2	0.18	43.9
40.3	361	233	740	172	315	5.0	507	761	928	65.7	39.4	185.0	179	248	87.5	0.19	57.8
46.5	515	194	854	137	293	8.0	539	939	932	63.1	65.2	176.8	169	235	66.2	0.2	71.4
48.8	432	165	724	113	248	5.6	338	820	784	51.3	46.7	135.1	135	167	41.8	0.13	66.6
50.8	277	152	500	84	206	3.1	204	579	572	43.4	31.3	77.5	91	143	38.8	0.1	44.0
53.3	223	67	405	26	134	2.5	63	421	374	34.8	20.1	32.0	50	35	9.3	0.08	24.7
57.0	237	96	469	43	165	2.4	81	412	444	39.9	15.5	35.6	53	56	11.4	0.08	17.9
62.0	148	77	429	35	142	2.9	84	312	425	37.3	14.7	37.0	48	70	12.2	0.07	22.5
63.0	137	82	437	36	149	2.8	91	264	421	39.6	13.3	39.2	48	75	14.6	0.07	15.8
64.7	118	69	407	31	127	3.0	78	164	427	40.1	14.0	39.0	46	81	12.4	0.07	23.3
66.6	107	93	439	34	158	3.1	102	199	479	44.5	20.0	40.6	55	118	13.6	0.09	27.7

(c)

Time	Ala	Thr	Gly	Val	Ser	Sar	Leu	Asp	Gln	Met	Orn	Phe	Tyr	Lys	Arg	hArg	Trp
5.0	*71*	*17*	*28*	*66*	*11.8*	*0.58*	*55*	*9.2*	*104*	*15.3*	*4.7*	*14.1*	*13.3*	*31*	*7.4*	*0.59*	*2.1*
8.8	203	77	115	238	43.7	2.68	242	40.2	541	38.9	21.3	67.0	58.4	138	38.5	1.71	10.4
11.0	140	64	111	166	35.5	1.37	161	35.1	432	35.2	16.2	56.6	40.8	103	28.5	1.36	6.5
12.0	125	60	109	137	34.5	1.45	139	33.2	421	33.7	15.0	52.7	38.3	108	27.0	1.20	6.8
13.0	135	72	135	153	40.4	1.45	166	41.9	482	36.8	18.1	63.5	42.8	133	33.0	1.21	7.7
15.3	156	88	157	160	51.5	2.02	196	49.2	486	39.0	22.1	71.4	50.5	148	43.0	1.22	10.0
17.6	145	90	152	154	53.0	1.35	192	47.8	426	35.8	21.0	72.0	50.4	148	43.9	0.98	9.7
19.5	181	106	158	179	60.6	1.19	223	52.4	395	34.3	25.4	79.8	60.5	163	50.7	0.84	11.4
20.8	158	125	143	191	65.9	1.58	240	57.0	418	35.1	26.9	83.8	70.8	181	54.3	0.80	12.3
24.3	207	129	170	204	68.3	1.25	249	58.2	375	34.4	28.5	84.4	76.7	175	60.3	0.70	13.2
29.1	205	121	165	210	61.9	1.75	240	52.9	371	34.6	33.2	83.5	77.4	141	46.8	0.64	14.9
30.5	182	123	168	220	62.4	1.88	259	52.4	369	35.6	35.7	85.6	73.0	140	48.9	0.58	15.1
33.4	208	112	156	221	58.4	1.91	227	52.2	358	34.9	34.1	84.1	65.7	121	41.3	0.48	13.6
35.0	187	96	140	181	51.1	1.69	180	45.6	317	31.6	28.3	77.8	54.4	107	34.6	0.46	11.8
40.3	153	83	124	177	46.1	1.28	173	36.3	251	28.0	27.8	74.6	46.6	105	32.6	0.33	11.2
42.6	195	107	139	250	51.1	1.64	246	47.3	318	32.8	47.4	91.6	65.0	130	35.3	0.40	14.3
46.5	180	95	128	215	45.1	1.44	204	46.1	291	29.9	41.8	85.1	56.9	109	28.7	0.33	14.5
48.9	157	101	128	223	52.1	1.13	257	48.8	295	33.7	37.6	81.5	51.4	116	40.1	0.36	17.3
50.0	198	122	162	234	63.9	1.66	267	52.9	367	37.9	36.3	89.5	71.5	136	49.0	0.56	14.2

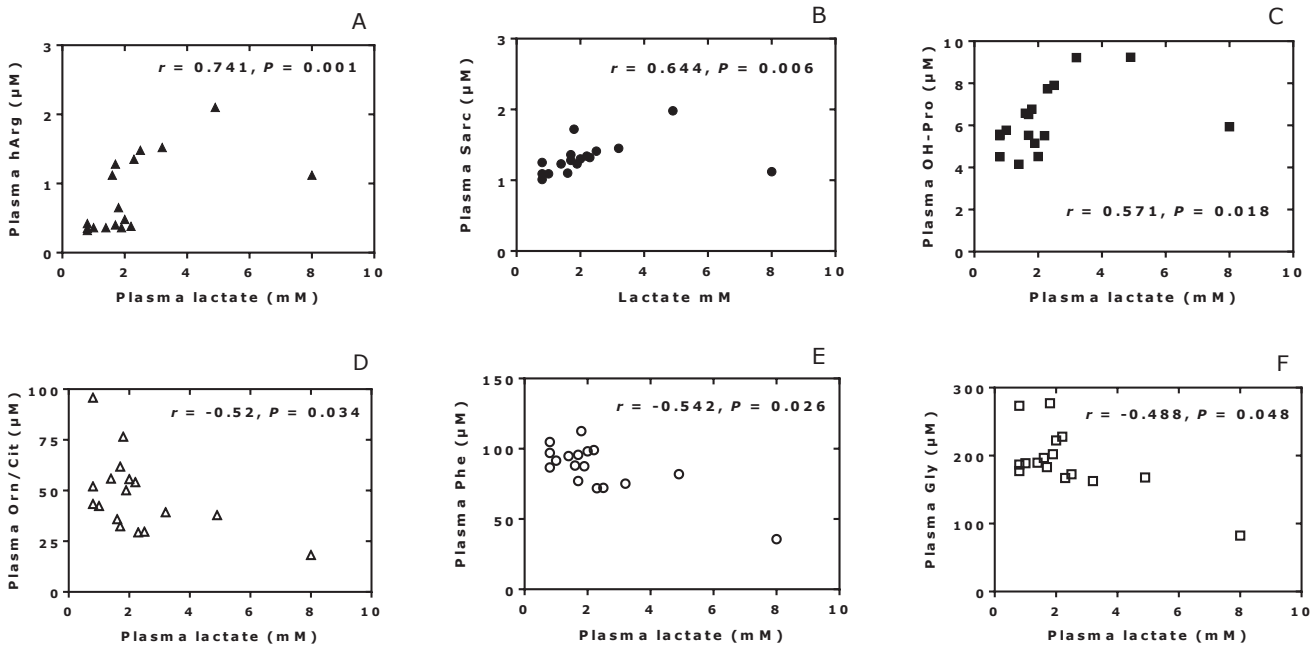


Figure 1. Correlations (after Spearman) between the plasma concentrations of the indicated amino acids and lactate measured in the MALA patient.

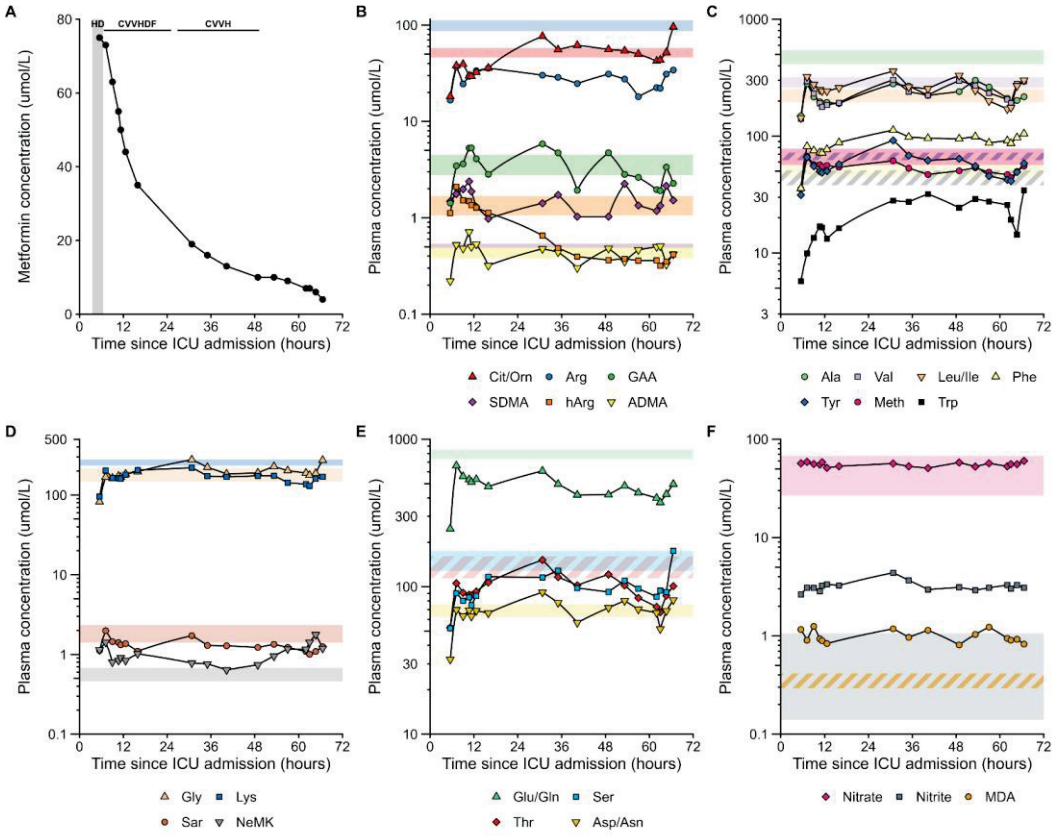


Figure 2. Time course of the plasma concentrations of metformin (**A**), the indicated amino acids (**B**–**E**), and nitrate, nitrite, and malondialdehyde (MDA) (**F**) during the renal replacement treatment (RRT) of the patient in the ICU since admission. HD, hemodialysis; CVVHDF, continuous veno-venous hemodiafiltration; CVVH, continuous veno-venous hemofiltration (CVVH). Shaded areas are reference values (interquartile range) obtained from healthy volunteers.

Table 3. Reported plasma/serum concentrations (range, μM) in healthy humans for the analytes measured in the present study at admission to the ICU (5.5 h) until the end (66 h).

Analyte	Men [34]	Women [33]	MALA Patient 5.5 h–66 h	Fold Change	Refs.
Creatinine	82–101	n.m.	−230	−0.6	[36]
Malondialdehyde	0.31–0.46	n.m.	1.16–0.82	−0.7	[16]
Metformin	n.a.	n.a.	−4	−19.0	n.a.
Nitrate	38–55	n.m.	57–60	+1.0	[14]
Nitrite	1.9–2.6	n.m.	2.64–3.08	+1.2	[14]
Amino acids					
ADMA	0.187–0.534	n.m.	0.220–0.420	+1.9	[30]
Alanine	254–392	203–443	149–217	+1.5	[33]
Arginine	50–90	50–119	17–34	+2.0	[33]
Asparagine	48–94	33–59	32–81	+2.5	[33]
Citrulline	34–48	18–42		+2.3	[33]
Glutamine	449–654	414–669 12–57	247–496	+2.0	[33]
Glycine	147–248	149–397	82.0–273	+3.3	[33]
Guanidinoacetate	1.77–4.57	n.m.	1.42–2.28	+0.9	none
Homoarginine	0.66–1.74	n.m.	1.12–0.42	−2.7	[32]
Hydroxyproline	5.8–10.9	n.m.	5.94–5.58	−0.9	none
Leucine	155–254	74–125 35–66	143–301	+2.1	[33]
Lysine	110–171	115–223	96–169	+1.8	[33]
Methionine	41–59	17–30	35–55	+1.6	[33]
Ornithine	see Cit	25–68	18–96	+5.3	[33]
Phenylalanine	39–69	42–66	36–105	+2.9	[33]
Proline	118–230	70–188	68–86	+1.3	[33]
Sarcosine	1.3–2.6	n.m.	1.12–1.25	+1.1	[33]
SDMA	n.m.	n.m.	1.48–1.52	+1.4	[30]
Serine	106–210	80–157	52–175	+3.4	[33]
Threonine	105–162	68–169	53–101	+1.9	[33]
Tryptophan	6.3–20.4	41–68	5.7–34.3	+6.0	[33]
Tyrosine	36–64	40–74	31–58	+1.9	[33]
Valine	218–286	138–243	141–296	+2.1	[33]
N^{ε}MK	n.m.	n.m.	1.14–1.19	+1.04	[27]

n.a., not applicable; n.m., not measured.

In general, the plasma concentrations of the analyzed amino acids were in the lower range of reference intervals. The concentrations of nitrate, nitrite, and MDA measured in plasma and urine were within normal ranges. These observations suggest rather unaltered amino acid, NO homeostasis, and oxidative stress. The results of the study are discussed in detail as follows below for plasma, urine, and effluent (dialysate).

At admission, the plasma Arg concentration was lower compared to healthy humans (Tables 2 and 3). The plasma concentration of the Arg metabolite ADMA was also lower than in healthy adults. The SDMA plasma concentration was higher, probably due to de-

creased urinary excretion of this Arg metabolite, which is eliminated primarily unchanged by glomerular filtration. The plasma concentration of guanidinoacetate (GAA), an Arg metabolite from the arginine:glycine amidinotransferase (AGAT) pathway and the precursor of creatine, remained within normal ranges. The plasma concentration of hArg, another Arg metabolite from the AGAT pathway, was normal at ICU admission but decreased over time. The plasma concentrations of N^{ε}-methyl lysine (N^{ε}MK), a PTM metabolite of lysine (Lys) residues in proteins, were considerably higher than in healthy subjects, indicating a higher monomethylation extent of Lys in the MALA patient. At admission, the plasma concentrations of nitrate, nitrite, and MDA were within normal ranges (Tables 1 and 3). Thus, NO synthesis and oxidative stress were not elevated in the MALA patient and did not change with renal replacement treatment.

Except for hydroxy-proline (−0.9-fold) and homoarginine (−2.7-fold), at the end of the renal replacement treatment, the plasma amino acid concentrations were up to 6-fold higher compared to those at admission to the ICU (Table 3). The highest increase was observed for tryptophan (6-fold).

We tested for potential correlations between the plasma concentrations of lactate and other analytes. The plasma lactate concentration values correlated positively with the plasma concentrations of homoarginine (hArg; $r = 0.741$, $p = 0.0007$), sarcosine (Sar; $r = 0.644$, $p = 0.005$), and hydroxy-proline (OH-Pro; $r = 0.5707$, $p = 0.0184$), yet not of proline [13] (Figure 1). Lactate has been shown to inhibit proline oxidase activity [35]. The correlation was negative for phenylalanine (Phe; $r = -0.521$, $p = 0.025$), ornithine (Orn; $r = -0.520$, $p = 0.032$), and glycine (Gly; $r = -0.488$, $p = 0.047$) (Figure 1). The plasma lactate concentrations did not correlate with the plasma concentrations of nitrite, nitrate, or MDA. These associations could result from effects of lactate of enzyme activities involved in the metabolism of amino acids [35], but this remains to be investigated in other cases of MALA. Lack of correlation between plasma concentrations of nitrite, nitrate, or MDA and lactate was also observed in healthy young men [34].

The urinary excretion rate of ADMA was lower than in healthy adults. The excretion rate of the ADMA metabolite DMA was higher than in healthy adults. This observation suggests increased metabolism of ADMA to DMA, presumably due to elevated activity of dimethylarginine dimethylaminohydrolase (DDAH) that hydrolyses ADMA to DMA and citrulline.

The tubular reabsorption values of most amino acids (Figure 3A–E) and of nitrite and nitrate (Figure 3F) were low and increased within the first hours of extracorporeal treatment to reach normal values. The tubular reabsorption values of GAA and Asn/Asp differed from those of the other amino acids. The negative tubular reabsorption values seen for GAA (Figure 3A) and Asn/Asp (Figure 3D) are indicative of renal secretion of these amino acids. During ICU admission, urinary Lys and N^{ε}MK excretion decreased temporarily (Figure 3E), suggesting improved tubular reabsorption over time. The low tubular reabsorption values of nitrate and nitrite within the first hours of treatment indicate altered renal management of these NO metabolites in the MALA patient.

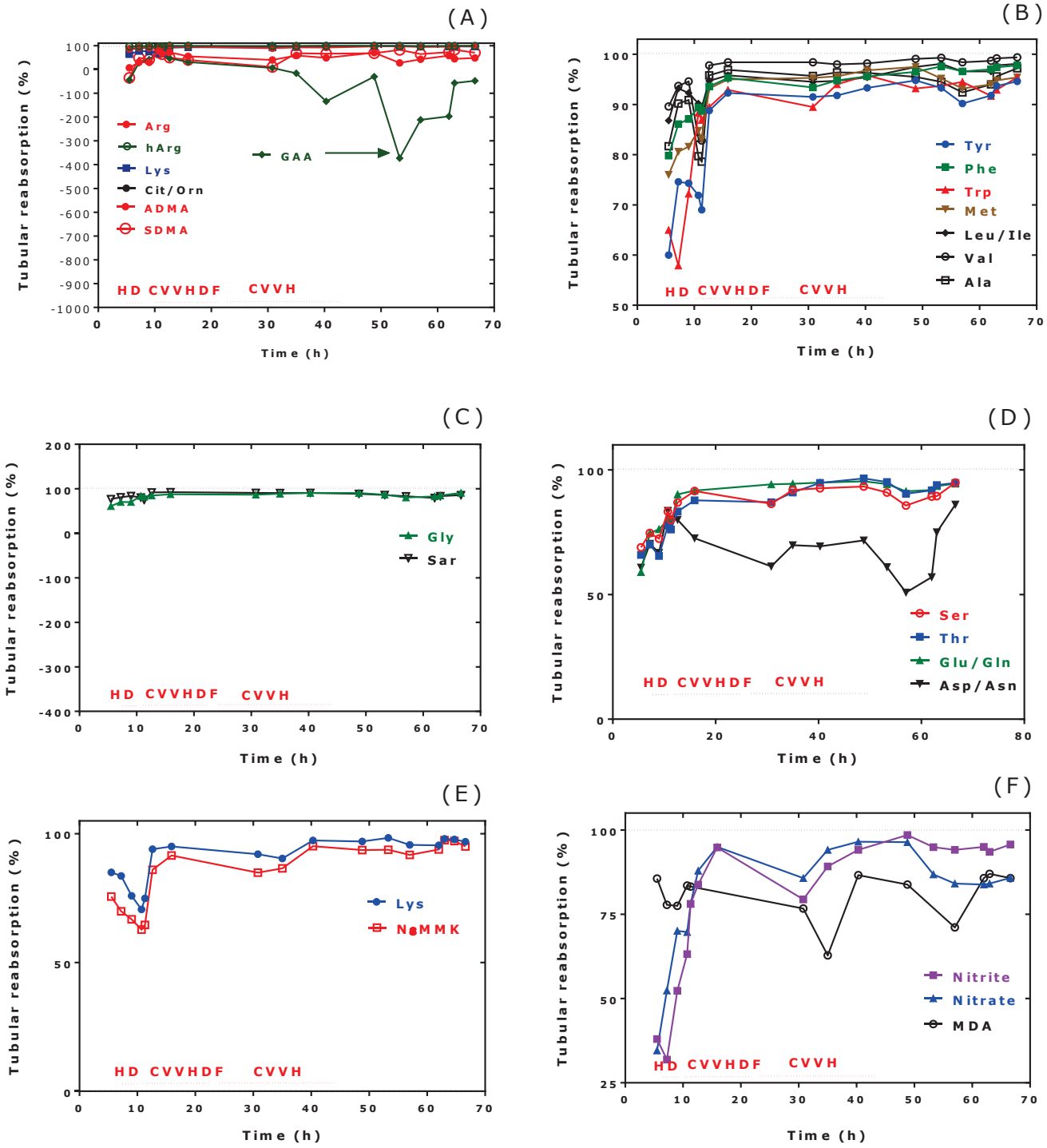


Figure 3. Time course of the calculated tubular reabsorption rates of the indicated amino acids, nitrate, nitrite, and malondialdehyde (MDA) during the renal replacement treatment (RRT) of the patient in the ICU since admission. HD, hemodialysis; CVVHDF, continuous veno-venous hemodiafiltration; CVVH, continuous veno-venous hemofiltration (CVVH).

4. Conclusions

Stable-isotope dilution GC-MS allows quantitative analysis of structurally different physiological inorganic (nitrite, nitrate), organic hydrophilic (amino acids and metabolites), and lipophilic (MDA) substances, as well as drugs (metformin) in complex biological samples such as plasma and urine. Our present and previous [13] study suggest that metformin-intoxication is not associated with greatly altered amino acid homeostasis,

except for an elevated PTM of proline by prolyl-hydroxylation. This PTM seems to be specific for the MALA patient since other PTM metabolites, including those of Arg (i.e., ADMA, SDMA) and Lys (i.e., N^{ε}MK), were not elevated at admission and did not change remarkably during the renal replacement treatment. That the plasma MDA concentration was not elevated in the MALA patient at admission and did not change during the renal replacement therapy suggests that oxidative stress is not associated with MALA. Extracorporeal renal replacement therapy is efficient in MALA, both with respect to metformin elimination and normalization of the renal management of solutes. In this case report, we have analyzed a single MALA patient. This is a study limitation. Confirmation of the observations in this patient is warranted by analyzing plasma, urine, and dialysate samples from additional metformin-intoxicated patients.

Author Contributions: R.A.P., data collection, methodology, analysis, writing; S.J.L.B., analysis, writing; M.W.N., methodology, analysis, writing; D.J.T., methodology, validation, writing, resources; D.T., methodology, validation, writing, resources, supervision. All authors have read and agreed to the published version of the manuscript.

Funding: This research received no external funding.

Institutional Review Board Statement: Ethical approval was given by the institutional review board Medisch Ethische Toetsingscommissie Universitair Medisch Centrum Groningen (METc UMCG) (code 2014-552, approved on 13 January 2015).

Informed Consent Statement: Written informed consent was obtained from the patient admitted with MALA to the ICU to collect residual material and for the publication of this case report according to the CARE guidelines.

Data Availability Statement: Data are available on request.

Acknowledgments: We thank Bibiana Beckmann for technical and administrative support.

Conflicts of Interest: The authors declare no conflicts of interest.

References

1. Davies, M.J.; Aroda, V.R.; Collins, B.S.; Gabbay, R.A.; Green, J.; Maruthur, N.M.; Rosas, S.E.; Del Prato, S.; Mathieu, C.; Mingrone, G.; et al. Management of Hyperglycemia in Type 2 Diabetes, 2022. A Consensus Report by the American Diabetes Association (ADA) and the European Association for the Study of Diabetes (EASD). *Diabetes Care* **2022**, *45*, 2753–2786. [CrossRef] [PubMed]
2. Graham, G.G.; Punt, J.; Arora, M.; Day, R.O.; Doogue, M.P.; Duong, J.K.; Furlong, T.J.; Greenfield, J.R.; Greenup, L.C.; Kirkpatrick, C.M.; et al. Clinical pharmacokinetics of metformin. *Clin. Pharmacokinet.* **2011**, *50*, 81–98. [CrossRef] [PubMed]
3. Lalau, J.D.; Kajbaf, F.; Protti, A.; Christensen, M.M.; De Broe, M.E.; Wiernsperger, N. Metformin-associated lactic acidosis (MALA): Moving towards a new paradigm. *Diabetes Obes. Metab.* **2017**, *19*, 1502–1512. [CrossRef] [PubMed]
4. Protti, A.; Russo, R.; Tagliabue, P.; Vecchio, S.; Singer, M.; Rudiger, A.; Foti, G.; Rossi, A.; Mistraletti, G.; Gattinoni, L. Oxygen consumption is depressed in patients with lactic acidosis due to biguanide intoxication. *Crit. Care* **2010**, *14*, R22. [CrossRef] [PubMed]
5. Takiyama, Y.; Harumi, T.; Watanabe, J.; Fujita, Y.; Honjo, J.; Shimizu, N.; Makino, Y.; Haneda, M. Tubular injury in a rat model of type 2 diabetes is prevented by metformin: A possible role of HIF-1α expression and oxygen metabolism. *Diabetes* **2011**, *60*, 981–992. [CrossRef] [PubMed]
6. Neal, A.; Rountree, A.M.; Philips, C.W.; Kavanagh, T.J.; Williams, D.P.; Newham, P.; Khalil, G.; Cook, D.L.; Sweet, I.R. Quantification of Low-Level Drug Effects Using Real-Time, in vitro Measurement of Oxygen Consumption Rate. *Toxicol. Sci.* **2015**, *148*, 594–602. [CrossRef] [PubMed]
7. Andreis, D.T.; Mallat, J.; Tettamanti, M.; Chiarla, C.; Giovannini, I.; Gatti, S.; Protti, A. Increased ratio of P[v-a]CO2 to C[a-v]O2 without global hypoxia: The case of metformin-induced lactic acidosis. *Respir. Physiol. Neurobiol.* **2021**, *285*, 103586. [CrossRef] [PubMed]
8. Calello, D.P.; Liu, K.D.; Wiegand, T.J.; Roberts, D.M.; Lavergne, V.; Gosselin, S.; Hoffman, R.S.; Nolin, T.D.; Ghannoum, M. Extracorporeal Treatment for Metformin Poisoning: Systematic Review and Recommendations From the Extracorporeal Treatments in Poisoning Workgroup. *Crit. Care Med.* **2015**, *43*, 1716–1730. [CrossRef]
9. Preiss, D.; Rankin, N.; Welsh, P.; Holman, R.R.; Kangas, A.J.; Soininen, P.; Würtz, P.; Ala-Korpela, M.; Sattar, N. Effect of metformin therapy on circulating amino acids in a randomized trial: The CAMERA study. *Diabet. Med.* **2016**, *33*, 1569–1574. [CrossRef]
10. Tsikas, D. Homoarginine in health and disease. *Curr. Opin. Clin. Nutr. Metab. Care* **2023**, *26*, 42–49. [CrossRef]
11. Wu, G. Important roles of dietary taurine, creatine, carnosine, anserine and 4-hydroxyproline in human nutrition and health. *Amino Acids* **2020**, *52*, 329–360. [CrossRef] [PubMed]

12. Wu, Z.; Hou, Y.; Dai, Z.; Hu, C.A.; Wu, G. Metabolism, Nutrition, and Redox Signaling of Hydroxyproline. *Antioxid. Redox Signal* **2019**, *30*, 674–682. [CrossRef] [PubMed]
13. Baskal, S.; Posma, R.A.; Bollenbach, A.; Dieperink, W.; Bakker, S.J.L.; Nijsten, M.W.; Touw, D.J.; Tsikas, D. GC-MS analysis of 4-hydroxyproline: Elevated proline hydroxylation in metformin- associated lactic acidosis and metformin-treated Becker muscular dystrophy patients. *Amino Acids* **2024**, *56*, 21. [CrossRef] [PubMed]
14. Tsikas, D. A critical review and discussion of analytical methods in the L-arginine/nitric oxide area of basic and clinical research. *Anal. Biochem.* **2008**, *379*, 139–163. [CrossRef] [PubMed]
15. Tsikas, D. Urinary Dimethylamine (DMA) and Its Precursor Asymmetric Dimethylarginine (ADMA) in Clinical Medicine, in the Context of Nitric Oxide (NO) and Beyond. *J. Clin. Med.* **2020**, *9*, 1843. [CrossRef] [PubMed]
16. Tsikas, D. Assessment of lipid peroxidation by measuring malondialdehyde (MDA) and relatives in biological samples: Analytical and biological challenges. *Anal. Biochem.* **2017**, *524*, 13–30. [CrossRef] [PubMed]
17. Tsikas, D. Simultaneous Derivatization and Quantification of the Nitric Oxide Metabolites Nitrite and Nitrate in Biological Fluids by Gas Chromatography/Mass Spectrometry. *Anal. Chem.* **2000**, *72*, 4064–4072. [CrossRef] [PubMed]
18. Hanff, E.; Lützow, M.; Kayacelebi, A.A.; Finkel, A.; Maassen, M.; Yanchev, G.R.; Haghikia, A.; Bavendiek, U.; Buck, A.; Lücke, T.; et al. Simultaneous GC-ECNICI-MS Measurement of Nitrite, Nitrate and Creatinine in Human Urine and Plasma in Clinical Settings. *J. Chromatogr. B Anal. Technol. Biomed. Life Sci.* **2017**, *1047*, 207–214. [CrossRef] [PubMed]
19. Hanff, E.; Ruben, S.; Kreuzer, M.; Bollenbach, A.; Kayacelebi, A.A.; Das, A.M.; von Versen-Höynck, F.; von Kaisenberg, C.; Haffner, D.; Ückert, S.; et al. Development and Validation of GC–MS Methods for the Comprehensive Analysis of Amino Acids in Plasma and Urine and Applications to the HELLP Syndrome and Pediatric Kidney Transplantation: Evidence of Altered Methylation, Transamidination, and Arginase Activity. *Amino Acids* **2019**, *51*, 529–547. [PubMed]
20. Baskal, S.; Bollenbach, A.; Mels, C.; Kruger, R.; Tsikas, D. Development, validation of a GC-MS method for the simultaneous measurement of amino acids, their PTM metabolites and AGEs in human urine, and application to the bi-ethnic ASOS study with special emphasis to lysine. *Amino Acids* **2022**, *54*, 615–641. [CrossRef]
21. Baskal, S.; Bollenbach, A.; Henzi, B.; Hafner, P.; Fischer, D.; Tsikas, D. Stable-Isotope Dilution GC-MS Measurement of Metformin in Human Serum and Urine after Derivatization with Pentafluoropropionic Anhydride and Its Application in Becker Muscular Dystrophy Patients Administered with Metformin, L-Citrulline, or Their Combination. *Molecules* **2022**, *27*, 3850. [CrossRef] [PubMed]
22. Kayacelebi, A.A.; Beckmann, B.; Gutzki, F.M.; Jordan, J.; Tsikas, D. GC-MS and GC-MS/MS measurement of the cardiovascular risk factor homoarginine in biological samples. *Amino Acids* **2014**, *46*, 2205–2217. [CrossRef] [PubMed]
23. Tsikas, D.; Thum, T.; Becker, T.; Pham, V.V.; Chobanyan, K.; Mitschke, A.; Beckmann, B.; Gutzki, F.M.; Bauersachs, J.; Stichtenoth, D.O. Accurate quantification of dimethylamine (DMA) in human urine by gas chromatography-mass spectrometry as pentafluorobenzamide derivative: Evaluation of the relationship between DMA and its precursor asymmetric dimethylarginine (ADMA) in health and disease. *J. Chromatogr. B Anal. Technol. Biomed. Life Sci.* **2007**, *851*, 229–239. [CrossRef] [PubMed]
24. Tsikas, D.; Wolf, A.; Mitschke, A.; Gutzki, F.M.; Will, W.; Bader, M. GC-MS determination of creatinine in human biological fluids as pentafluorobenzyl derivative in clinical studies and biomonitoring: Inter-laboratory comparison in urine with Jaffé, HPLC and enzymatic assays. *J. Chromatogr. B Anal. Technol. Biomed. Life Sci.* **2010**, *878*, 2582–2592. [CrossRef] [PubMed]
25. Kajbaf, F.; De Broe, M.E.; Lalau, J.D. Therapeutic Concentrations of Metformin: A Systematic Review. *Clin. Pharmacokinet.* **2016**, *55*, 439–459. [CrossRef] [PubMed]
26. Nichol, A.; Bailey, M.; Egi, M.; Pettila, V.; French, C.; Stachowski, E.; Reade, M.C.; Cooper, D.J.; Bellomo, R. Dynamic lactate indices as predictors of outcome in critically ill patients. *Crit. Care* **2011**, *15*, R242. [CrossRef] [PubMed]
27. Löwer, R.; Lange, H.W.; Hempel, K. Diagnostic meaning of the urinary output of Nepsilon-methylated lysines. Investigation of healthy individuals and patients with malignant diseases, myopathies or renal failure. *Clin. Chim. Acta* **1975**, *58*, 155–164. [CrossRef] [PubMed]
28. Nijveldt, R.J.; Van Leeuwen, P.A.; Van Guldener, C.; Stehouwer, C.D.; Rauwerda, J.A.; Teerlink, T. Net renal extraction of asymmetrical (ADMA) and symmetrical (SDMA) dimethylarginine in fasting humans. *Nephrol. Dial. Transplant.* **2002**, *17*, 1999–2002. [CrossRef] [PubMed]
29. Bjørnestad, E.Ø.; Dhar, I.; Svingen, G.F.T.; Pedersen, E.R.; Svenningsson, M.M.; Tell, G.S.; Ueland, P.M.; Ørn, S.; Sulo, G.; Laaksonen, R.; et al. Trimethyllysine predicts all-cause and cardiovascular mortality in community-dwelling adults and patients with coronary heart disease. *Eur. Heart J. Open* **2021**, *1*, oeab007. [CrossRef]
30. Schwedhelm, E.; Xanthakis, V.; Maas, R.; Sullivan, L.M.; Schulze, F.; Riederer, U.; Benndorf, R.A.; Böger, R.H.; Vasan, R.S. Asymmetric dimethylarginine reference intervals determined with liquid chromatography-tandem mass spectrometry: Results from the Framingham offspring cohort. *Clin. Chem.* **2009**, *55*, 1539–1545. [CrossRef]
31. Schwedhelm, E.; Xanthakis, V.; Maas, R.; Sullivan, L.M.; Atzler, D.; Lüneburg, N.; Glazer, N.L.; Riederer, U.; Vasan, R.S.; Böger, R.H. Plasma symmetric dimethylarginine reference limits from the Framingham offspring cohort. *Clin. Chem. Lab. Med.* **2011**, *49*, 1907–1910. [CrossRef]
32. Atzler, D.; Appelbaum, S.; Cordts, K.; Ojeda, F.M.; Wild, P.S.; Münzel, T.; Blankenberg, S.; Böger, R.H.; Blettner, M.; Beutel, M.E.; et al. Reference intervals of plasma homoarginine from the German Gutenberg Health Study. *Clin. Chem. Lab. Med.* **2016**, *54*, 1231–1237. [CrossRef] [PubMed]

33. Yamamoto, H.; Kondo, K.; Tanaka, T.; Muramatsu, T.; Yoshida, H.; Imaizumi, A.; Nagao, K.; Noguchi, Y.; Miyano, H. Reference intervals for plasma-free amino acid in a Japanese population. *Ann. Clin. Biochem.* **2016**, *53 Pt 3*, 357–364. [CrossRef] [PubMed]
34. Tsikas, D.; Maassen, N.; Thorns, A.; Finkel, A.; Lützow, M.; Röhrig, M.A.; Blau, L.S.; Dimina, L.; Mariotti, F.; Beckmann, B.; et al. Short-Term Supplementation of Sodium Nitrate vs. Sodium Chloride Increases Homoarginine Synthesis in Young Men Independent of Exercise. *Int. J. Mol. Sci.* **2022**, *23*, 10649. [CrossRef] [PubMed]
35. Kowalof, E.M.; Phang, J.M.; Granger, A.S.; Downing, S.J. Regulation of proline oxidase activity by lactate. *Proc. Natl. Acad. Sci. USA* **1977**, *74*, 5368–5371. [CrossRef]
36. Lewis, S.L.; Bucher, L.; Heitkemper, M.M.; Harding, M.M.; Kwong, J.; Roberts, D. *Medical-Surgical Nursing: Assessment and Management of Clinical Problems*, 10th ed.; Elsevier Health Sciences: St. Louis, MO, USA, 2016; p. 1025, ISBN 978-0-323-37143-8.
37. Zhloba, A.A.; Subbotina, T.F. Homoarginine test for evaluation of metabolic renal dysfunction. *Klin. Lab. Diagn.* **2021**, *66*, 709–717. [CrossRef]

Disclaimer/Publisher's Note: The statements, opinions and data contained in all publications are solely those of the individual author(s) and contributor(s) and not of MDPI and/or the editor(s). MDPI and/or the editor(s) disclaim responsibility for any injury to people or property resulting from any ideas, methods, instructions or products referred to in the content.

molecules

MDPI

Article

Clinical Evaluation Based on a New Approach to Improve the Accuracy of 4β-Hydroxycholesterol Measurement as a Biomarker of CYP3A4 Activity

Yuki Taya [1,2], Mari Mizunaga [2], Shunsuke Nakao [2], Mirinthorn Jutanom [1], Naoki Shimizu [1], Yukihiro Nomura [2] and Kiyotaka Nakagawa [1,*]

[1] Laboratory of Food Function Analysis, Graduate School of Agricultural Science, Tohoku University, Sendai 980-8572, Miyagi, Japan
[2] Drug Metabolism and Pharmacokinetics Research Laboratories, Central Pharmaceutical Research Institute, Japan Tobacco Inc., Takatsuki 569-1125, Osaka, Japan
* Correspondence: kiyotaka.nakagawa.c1@tohoku.ac.jp; Fax: +81-22-757-4417

Abstract: This study examines 4β-Hydroxycholesterol (4β-HC), which is considered to be a potential marker for the CYP3A4 induction of new chemical entities (NCEs) in drug development. To ensure the use of 4β-HC as a practical biomarker, it is necessary to accurately measure 4β-HC and demonstrate that CYP3A4 induction can be appropriately assessed, even for weak inducers. In clinical trials of NCEs, plasma is often collected with various anticoagulants, in some cases, the plasma is acidified, then stored for an extended period. In this study, we examined the effects of these manipulations on the measurement of 4β-HC, and based on the results, we optimized the plasma collection and storage protocols. We also found that a cholesterol oxidation product is formed when plasma is stored, and by monitoring the compound, we were able to identify when plasma was stored inappropriately. After evaluating the above, clinical drug–drug interaction (DDI) studies were conducted using two NCEs (novel retinoid-related orphan receptor γ antagonists). The weak CYP3A4 induction by the NCEs (which were determined based on a slight decline in the systemic exposure of a probe substrate (midazolam)), was detected by the significant increase in 4β-HC levels (more specifically, 4β-HC/total cholesterol ratios). Our new approach, based on monitoring a cholesterol oxidation product to identify plasma that is stored inappropriately, allowed for the accurate measurement of 4β-HC, and thus, it enabled the evaluation of weak CYP3A4 inducers in clinical studies without using a probe substrate.

Keywords: biomarkers; cholesterol oxidation; cytochrome P450 CYP3A4 inducers; drug–drug interaction study; 4β-hydroxycholesterol; mass spectrometry

1. Introduction

Cytochrome P450 family 3 subfamily A member 4 (CYP3A4) plays a role in the metabolism (oxidation) of cholesterol to 4β-hydroxycholesterol (4β-HC, Figure 1A) [1,2]. In support of this, many clinical studies have reported that the administration of CYP3A4 inducers (e.g., rifampicin, a strong inducer of CYP3A4) increases the concentration of 4β-HC (or 4β-HC/total cholesterol ratio (4β-HC/TC ratio)) in human plasma [3–7]; thus, 4β-HC is considered a potential marker for assessing the risk concerning whether a new chemical entity (NCE) induces CYP3A4 [8]. Although several clinical studies have assessed the above possibility using strong inducers of CYP3A4 (e.g., rifampicin) [3–7], further clinical studies, with various CYP3A4 inducers (especially weak inducers), are required.

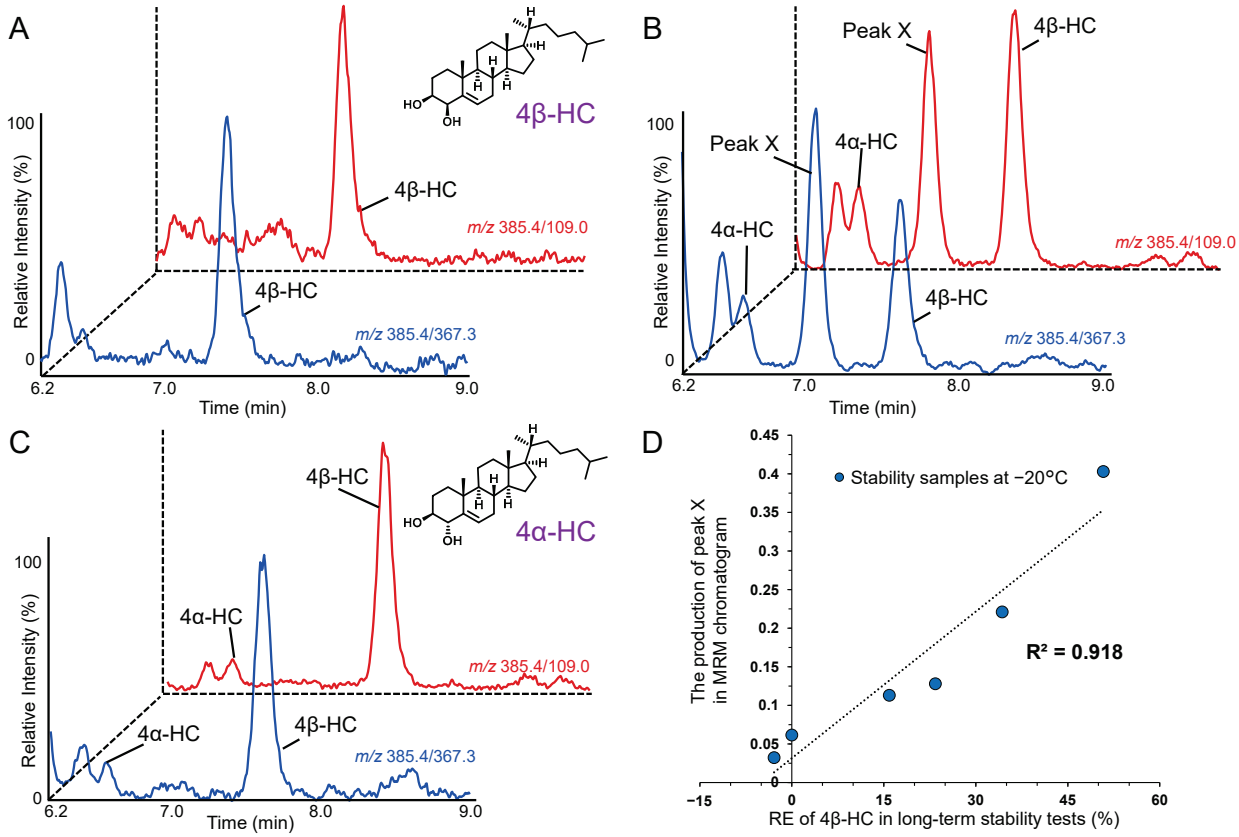


Figure 1. Typical MRM chromatograms analyzing plasma that was obtained with K2-EDTA, then analyzed without storage (**A**), or analyzed after 13 months of storage in the dark at −20 °C (**B**) or −80 °C (**C**). Each plasma sample was saponified, extracted with hexane, and analyzed with LC-MS/MS in the MRM mode. Extended MRM chromatograms between the retention times of 6.2–9.0 min are shown. Other details are described in the Methods section. Identification of 4β-HC and 4α-HC was performed by comparing the two markers against commercial standards. The correlation chart between the production of peak X and the relative error (RE) of 4β-HC in the plasma was analyzed during the long-term storage test (**D**). Peak X was corrected in accordance with the internal standard 4β-HC-d7 (i.e., the ratio of the area of peak X to the area of 4β-HC-d7 was calculated). A correlation diagram was created by plotting the peak area ratio of peak X and 4β-HC-d7 after long-term storage at −20 °C on the Y-axis and the RE shown in Table 1B on the X-axis (**D**).

To correctly evaluate the relationships between CYP3A4 inducers and plasma 4β-HC levels, an accurate analysis of 4β-HC in plasma is necessary. Factors that may hinder accurate analysis include plasma collection conditions and storage conditions [9]. From this perspective, the acidification of plasma (obtained using various anticoagulants) is known to provide a stable measurement of NCEs [10,11]. Nevertheless, the effects of anticoagulants (except K2-EDTA) and acidic conditions on the analysis of 4β-HC in plasma have not been properly evaluated [12–15]. In addition, as various factors (e.g., storage conditions and collection conditions) influence the quality of plasma samples [9], knowledge pertaining to indicators of defective plasma samples (i.e., inappropriately stored samples) is also desirable. In this regard, previous studies have proposed that plasma sample quality is likely to be compromised if the plasma concentration of 4α-hydroxycholesterol (4α-HC, Figure 1C), an isomer of 4β-HC, is remarkably higher than that of basal concentrations [16,17]. Other indicators that are more sensitive when detecting defective plasma should enhance the accuracy of 4β-HC quantitation in plasma and enable a more detailed evaluation of the relationships between CYP3A4 inducers and plasma 4β-HC levels.

To this end, we first assessed the stability of 4β-HC in plasma/serum collected with common anticoagulants (e.g., sodium heparin) and acidic solutions. Next, we confirmed that a cholesterol oxidation compound other than 4α-HC was produced during the storage of plasma samples, thus suggesting that the monitoring of the compound allows the detection of plasma samples stored in improper conditions. Based on the above, appropriate plasma collection conditions, and an indicator that can detect defective plasma samples, were investigated. We further evaluated the effect that weak inducers of CYP3A4 have on 4β-HC levels in plasma. More specifically, we conducted clinical drug–drug interaction (DDI) studies using two in-house developed NCEs (JTE-451 and JTE-761 [18], which were both weak inducers of CYP3A4) and midazolam, a probe substrate for CYP3A4 activity [19]. Repeated administration of JTE-451 and JTE-761 slightly decreased the area under the curve (AUC) for midazolam, thus confirming that both JTE-451 and JTE-761 were, indeed, weak CYP3A4 inducers. Additionally, we found that the plasma 4β-HC/TC ratio, rather than the plasma concentration of 4β-HC, demonstrates a strong negative correlation with the AUC of midazolam. These results suggest that 4β-HC/TC ratios could be used as a marker to determine the strength of CYP3A4 induction (even when induced by weak inducers) by rigorously controlling the conditions of the plasma samples.

Table 1. Long-term storage stability test of human plasma, serum, and acidified plasma.

A								B			C	
	Human Plasma			Acidified Human Plasma					Human Plasma			Human Plasma
Storage Conditions Temperature/Period	K2-EDTA	Heparin Sodium	Heparin Lithium	3.2% Sodium Citrate	K2-EDTA Containing Acetic Acid	Heparin Sodium Containing Acetic Acid	Human Serum	Storage Conditions Temperature/Period	K2-EDTA	Heparin Sodium	Storage Conditions Temperature/Period	K2-EDTA
Before storage	27.9	28.3	27.0	23.6	26.6	27.5	28.4	Before storage	32.5	30.0	Before storage	35.2
−20 °C/1 month	25.3 ± 0.6 (−9.3)	26.5 ± 0.6 (−6.4)	28.5 ± 1.8 (5.6)	22.6 ± 1.2 (−4.2)	26.8 ± 1.3 (0.8)	25.9 ± 1.6 (−5.8)	27.8 ± 2.2 (−2.1)	−20 °C/6 months	30.3 ± 2.2 (−6.8)	30.0 ± 1.6 (0.0)	−70 °C/1 month	35.3 ± 0.5 (0.3)
−20 °C/2 months	26.2 ± 2.4 (−6.1)	25.2 ± 2.7 (−11.0)	26.4 ± 0.8 (−2.2)	22.2 ± 1.2 (−5.9)	25.4 ± 2.0 (−4.5)	25.9 ± 1.6 (−5.8)	26.3 ± 0.9 (−7.4)	−20; °C/9, months	37.4 ± 0.2 (* 15.1)	35.8 ± 0.9 (* 19.3)	−70 °C/3 month	33.4 ± 0.5 (−5.1)
−20 °C/6 months	30.9 ± 1.2 (10.8)	29.2 ± 2.4 (3.2)	30.7 ± 1.4 (13.7)	24.9 ± 0.9 (5.5)	31.0 ± 0.7 (* 16.5)	41.2 ± 1.2 (* 49.8)	28.2 ± 3.7 (5.6)	−20 °C/13 months	45.7 ± 0.9 (* 40.6)	41.5 ± 0.5 (* 38.3)	−70 °C/10 month	35.7 ± 1.2 (1.4)
−80 °C/1 month	25.5 ± 1.0 (−8.6)	26.1 ± 0.8 (−7.8)	28.0 ± 0.2 (3.7)	24.2 ± 0.9 (2.5)	26.5 ± 1.0 (−0.4)	26.5 ± 0.5 (−3.6)	29.7 ± 1.0 (4.6)	−80 °C/6 months	29.5 ± 1.2 (−9.2)	29.1 ± 1.1 (−3.0)		
−80 °C/2 months	25.7 ± 1.4 (−7.9)	26.0 ± 0.6 (−8.1)	24.7 ± 0.8 (−8.5)	22.3 ± 0.7 (−5.5)	27.2 ± 0.5 (2.3)	26.2 ± 1.3 (−4.7)	25.7 ± 1.7 (−9.5)	−80; °C/9, months	32.0 ± 1.0 (−1.5)	30.9 ± 1.3 (3.0)		
−80 °C/6 months	29.7 ± 0.6 (6.5)	28.7 ± 1.2 (1.4)	28.3 ± 0.7 (4.8)	24.2 ± 0.8 (2.5)	28.7 ± 0.6 (7.9)	29.4 ± 0.3 (6.9)	29.0 ± 0.4 (2.1)	−80 °C/13 months	33.8 ± 1.4 (4.0)	33.1 ± 1.3 (10.3)		

Plasma or serum was prepared using blood that was collected from six healthy volunteers (three males and three females who did not take the test drug) using various anticoagulants (K2-EDTA, heparin sodium, heparin lithium, or 3.2% sodium citrate) or a serum-separating medium. Each sample was saponified and extracted with hexane immediately after collection. In the extracts, 4β-HC was quantified with LC-MS/MS, as described in the Methods section. The mean 4β-HC concentrations of six volunteers before storage are shown. The 4β-HC concentrations of each sample were similar to those reported in previous studies [2,20]. The plasma (or serum) of the six volunteers were then pooled into one, and the combined plasma was then subjected to the following storage test: storage at −20 °C or −80 °C in the dark for up to 6 months (**A**) or up to 13 months (**B**). K2-EDTA plasma was stored at −70 °C in the dark for up to 10 months, thus mimicking the storage conditions of clinical testing sites (**C**). The 4β-HC concentrations in the samples that were subjected to the storage test were measured in triplicate, and the results are expressed as mean ± standard deviation (SD). The relative error (RE, in parentheses) was calculated via the difference in concentration of 4β-HC before and after storage, and RE was indicated with an asterisk (*) if it exceeded the acceptance criteria of ±15%.

2. Results and Discussion

2.1. Stability of 4β-HC in Plasma/Serum Collected with Various Anticoagulants and Acid Solutions

The ICH M10 guidelines [21] require that plasma NCEs and their metabolites are measured in clinical trials using appropriate protocols. To accurately measure NCEs and metabolites in accordance with these guidelines, plasma collected with various anticoagulants is often stabilized under acidic conditions to prevent artificial (ex vivo) conversions (e.g., metabolites of NCEs, such as acyl glucuronides, lose their glucuronic acid groups when plasma is stored under neutral conditions) during storage [10,11]; however, little is known about the effects of these anticoagulants, or plasma acidification, on the measurement of 4β-HC. Previous reports are limited to examining the stability of 4β-HC in plasma collected with K2-EDTA or in serum [12–15]; thus, we considered it necessary to evaluate the effects of various anticoagulants and plasma acidification on the measurement of 4β-HC under different plasma storage conditions.

Plasma collected during clinical trials is often frozen for long periods of time (several years in the longest case) before being analyzed [22]. Hence, we first examined the stability of 4β-HC during the long-term storage of plasma that was collected with various anticoagulants (i.e., K2-EDTA, heparin sodium, heparin lithium, and 3.2% sodium citrate). When plasma was stored at −20 °C and −80 °C, 4β-HC was stable for up to 6 months after collection with all the anticoagulants evaluated in this study (Table 1A). Moreover, when plasma obtained with K2-EDTA or heparin sodium was stored at −20 °C for more than 9 months, the concentration of 4β-HC significantly increased, presumably due to autoxidation (Table 1B) [14]; therefore, the antioxidative effects of anticoagulants (e.g., chelation of K2-EDTA) may be insufficient to store plasma for prolonged periods. Additionally, the results suggest that the type of anticoagulant has little influence on the accurate measurement of 4β-HC, and the storage of plasma (or serum) at −80 °C is acceptable; however, due to the occasional occurrence of freezer limitations at the clinical testing sites, the plasma samples were stored at −70 °C before being measured [23]. Thus, we further confirmed that 4β-HC was stable enough for long-term storage (up to 10 months) at temperatures under −70 °C with K2-EDTA (Table 1C); this means that the storage of plasma (or serum) at −70 °C is also acceptable. For reference, 4β-HC was stable in plasma stored at 4 °C, or at room temperature, with or without light for 6 h (data not shown), thus suggesting that 4β-HC is stable during sample preparation procedures. Moreover, 4β-HC was also stable for up to five freeze-thaw cycles at −20 °C and −80 °C (data not shown). We anticipate these data to be important for the accurate measurement of plasma 4β-HC concentrations.

Next, the effect of plasma acidification on the concentration of 4β-HC was examined. Plasma was collected using K2-EDTA or heparin sodium as an anticoagulant. Even under acidic conditions, no significant change in the concentration of 4β-HC was observed in plasma stored at −80 °C for up to 6 months (Table 1A); however, acidified plasma was more unstable compared with unacidified plasma that was stored at lower temperatures. For example, 4β-HC clearly increased when acidified heparin sodium plasma was stored at −20 °C for 6 months (Table 1A). Analyzing the mechanisms behind this increase in 4β-HC should a priority for future studies because, to the best of our knowledge, no study has reported the autooxidation of cholesterol under acidic conditions. Overall, the long-term storage of acidified plasma suggests that it is not desirable to store plasma under acidic conditions when aiming to accurately measure 4β-HC (i.e., plasma stored under acidic conditions to measure NCEs should not be used for the measurement of 4β-HC).

Based on the above results, plasma samples that were taken in order to measure 4β-HC in later clinical DDI studies were collected with K2-EDTA, without acidification, and separately from those that were taken to measure NCEs. The collected plasma samples were stored directly in a deep freezer set at −70 °C (clinical testing sites) or −80 °C (analytical laboratories). For shipment, samples were kept frozen at −79 °C using dry ice.

2.2. Indicators to Detect Defective Plasma That Contribute to Improving the Accuracy of 4β-HC Measurements in Plasma

As described above, we identified the protocols of plasma preparation and storage to accurately measure 4β-HC in plasma; however, even under these conditions, the deterioration of plasma due to unpredictable factors (e.g., opening and closing of freezers) is unavoidable [9]. Thus, an indicator that can detect such defective plasma is useful to ensure the quality of the plasma. As mentioned in the introduction, previous studies have noted that the plasma concentration of 4α-HC (an isomer of 4β-HC) increases when plasma is stored, and thus, 4α-HC may be a suitable indicator that can detect defective plasma [16,17]. To confirm this, plasma obtained with K2-EDTA was stored at −20 °C for 13 months and analyzed using LC-MS/MS. As shown in Figure 1, 4α-HC was indeed detected, along with 4β-HC; however, the increase in 4α-HC when the plasma was stored at −20 °C was not significant, and the correlation between the relative error (RE) and the increase in 4β-HC during storage was weak (data not shown). Therefore, we considered it necessary to find another indicator that was more sensitive than 4α-HC for assessing plasma quality.

Under these circumstances, we noticed that peak X, in the chromatogram of stored plasma (Figure 1D), correlated well with the RE relating to the increase in 4β-HC during storage (correlation coefficient of 0.918). Such a high correlation suggested that peak X is an appropriate indicator of defective plasma. As peak X was detected under the same MRM pairs that were used to detect 4β-HC and 4α-HC (e.g., *m*/*z* 385.4/109.0 and *m*/*z* 385.4/367.3), we presumed that peak X was also a cholesterol oxidation product (Figure 1B). To further analyze its structure, peak X was analyzed with LC-HRMS. Peak X (RT 17.6 min) formulates precursor ions at *m*/*z* 385.3461 $[M+H-H_2O]^+$ and *m*/*z* 425.3391 $[M+Na]^+$, which corresponded with $C_{27}H_{45}O$ (Δ−1.0 ppm) and $C_{27}H_{46}O_2Na$ (Δ−1.2 ppm), respectively (Figure 2A). These spectra suggested that peak X was an isomer of cholesterol hydroxide. MS/MS analysis of *m*/*z* 385.4 showed a distinct product ion at *m*/*z* 177.1266, which corresponded with $C_{12}H_{17}O$ (Δ−4.5 ppm) (Figure 2B). This implied that the hydroxyl group was bound to the A or B ring of the steroid backbone. As the retention time of peak X did not match that of commercially available cholesterol hydroxide standards (4β-HC, 4α-HC, 7α-HC, and 7β-HC), nor that of related compounds (5,6α-epoxy cholesterol and 5,6β-epoxy cholesterol), presumably, the hydroxyl group of peak X is attached to the C5 or C6 position (data not shown). Indeed, previous studies have shown that the free radical-mediated oxidation (autoxidation) of cholesterol produces 4α-HC, 4β-HC, 5α-HC, 5β-HC, 6α-HC, 6β-HC, 7α-HC, and 7β-HC [24–26]. Their expected formation pathways have been reported in previous studies [25,26]. Further studies are needed to determine the exact structure of peak X (i.e., whether the hydroxyl group is bound to the C5 or C6 position). Based on these results, in the following DDI studies, we decided to exclude plasma samples in which peak X was detected during analysis.

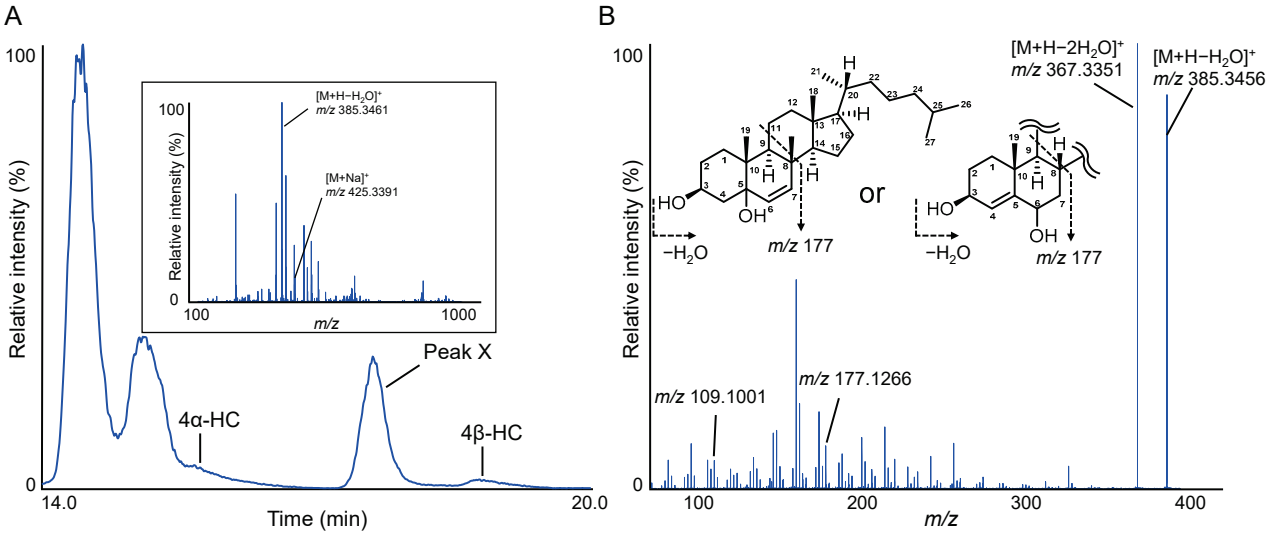


Figure 2. Typical Q1 chromatogram and MS spectrum of peak X (**A**); product ion spectrum of peak X (**B**). An extended Q1 chromatogram between the retention times of 14.0–20.0 min is shown. K2-EDTA plasma collected from healthy volunteers, stored at −20 °C for 13 months in the dark, was analyzed by LC-HRMS. Details of this process are shown in the Methods section. The sample was saponified, extracted with hexane, and analyzed using LC-HRMS. Refer to the Methods section for details regarding the conditions.

2.3. DDI Studies to Evaluate Whether Weak Inducers of CYP3A4 (JTE-451 and JTE-761) Affect Plasma 4β-HC Levels and the AUC of Midazolam

Two DDI studies were conducted under the conditions evaluated above. Using two in-house developed NCEs (JTE-451 and JTE-761 [18], which are weak inducers of CYP3A4) and midazolam (a probe substrate for CYP3A activity [19]), we first evaluated whether the administration of these weak inducers increases plasma 4β-HC concentrations. A significant increase in plasma 4β-HC concentrations were observed only when JTE-451 and JTE-761 were administered at 400 mg BID and 400 mg QD, respectively (Table 2 and Figure 3). Interestingly, 4β-HC/TC ratios were significantly elevated at all dosage levels of JTE-451 and JTE-761 (Table 2 and Figure 3). Similarly, previous studies have reported that 4β-HC/TC ratios fluctuate when CYP3A4 inducers are administered, although no study has been conducted for weak CYP3A4 inducers, to the best of our knowledge [4–7,27]. As cholesterol concentrations influence the generation of 4β-HC [16,28], we believe that 4β-HC/TC ratios are more suitable than 4β-HC concentrations when plasma cholesterol concentrations fluctuate, as was the case in this study (Table 2); however, further clinical studies are needed to demonstrate that the use of 4β-HC/TC ratios are more practical for assessing CYP3A4 induction than 4β-HC concentrations, as there were certain limitations to this study (e.g., no placebo groups were set).

Table 2. Summary of 4β-HC and TC concentrations, 4β-HC/TC ratios, the AUC of midazolam, and the CYP3A4 induction category obtained during the clinical DDI studies.

Parameter		JTE-451 200 mg BID (n = 16 [#])	JTE-451 400 mg BID (n = 18)	JTE-761 400 mg QD (n = 15 [##])
4β-HC concentration (ng/mL)	Before administration	22.7 ± 6.7	21.8 ± 9.5	34.1 ± 9.8
	After administration	25.0 ± 7.3	30.8 ± 13.0	45.6 ± 16.0
	% change (before vs. after)	11.8 ± 22.4	46.1 ± 28.9	33.6 ± 25.7
	Significance (before vs. after)	$p = 0.059$	$p < 0.01$	$p < 0.01$
TC concentration (mg/dL)	Before administration	177.9 ± 35.0	163.5 ± 27.0	181.9 ± 38.3
	After administration	157.6 ± 35.1	141.7 ± 26.5	145.0 ± 27.3
	% change (before vs. after)	−13.3 ± 13.1	−13.4 ± 6.9	−19.7 ± 7.7
4β-HC/TC ratio ($\times 10^5$)	Before administration	1.28 ± 0.42	1.32 ± 0.50	1.93 ± 0.59
	After administration	1.65 ± 0.53	2.16 ± 0.73	3.13 ± 0.84
	% change (before vs. after)	29.3 ± 19.4	68.5 ± 30.6	68.1 ± 37.0
	Significance (before vs. after)	$p < 0.01$	$p < 0.01$	$p < 0.01$
Midazolam AUC (hr × ng/mL)	Before administration	39.2 ± 11.5	39.7 ± 14.9	40.8 ± 16.8
	After administration	36.3 ± 10.5	22.8 ± 7.9	18.9 ± 7.8
	% change (before vs. after)	−7.0 ± 18.8	−40.3 ± 11.7	−49.8 ± 20.9
CYP3A4 induction category		Very weak	Weak	Weak

The AUC of midazolam from time zero to the last quantifiable concentration was calculated from plasma concentrations at 0, 0.5, 0.75, 1, 1.5, 2, 3, 4, 6, 8, 12, 16, and 24 h after administration. Refer to Figure 3 for the calculation of other parameters. All values denote mean ± SD ($p < 0.01$). [#] Two subjects out of eighteen subjects opted out of the clinical study. [##] One subject out of sixteen subjects opted out of the clinical study.

For the assessment of CYP3A4 induction, NCEs were ranked in accordance with the criteria described in the FDA guidance on Clinical Drug Interaction Studies (2020) [29]. NCEs were ranked as strong inducers when the AUC of midazolam decreased by ≥80% upon administration, moderate when the AUC decreased by ≥50% to <80%, and weak when the AUC decreased by ≥20% to <50%. As a result, 400 mg BID of JTE-451 and 400 mg QD of JTE-761 were classified as weak inducers, whereas 200 mg BID of JTE-451 was classified as a very weak inducer (Table 2). As JTE-451 and JTE-761 were confirmed to be weak inducers, we compared the AUC of midazolam with the plasma concentration of 4β-HC (or 4β-HC/TC ratio) after the administration of each NCE. As a result, the increase in 4β-HC/TC ratios, but not the increase in 4β-HC concentrations, significantly correlated with the decrease of AUC in midazolam (Figure 3C). To our knowledge, although previous studies reported a 1.3-fold increase in the 4β-HC/TC ratio after the repeated administration of rifampicin at doses which had a medium inducing effect (10 mg) [4,5], no previous study has demonstrated an increase in plasma 4β-HC concentration or 4β-HC/TC ratio after the administration of a weak inducer in clinical DDI studies. Although the CYP3A4 induction ability of the NCEs used in the present study appears to be weaker than that of 10 mg rifampicin [5], their administration resulted in an increase for the 4β-HC/TC ratios by more than 1.3-fold. This may be attributed to the high precision with which 4β-HC was quantified in this study. These findings suggest that controlling the plasma's sample conditions, and monitoring indicators of defective plasma samples, can provide an accurate assessment of CYP3A4 induction via the measurement of 4β-HC/TC ratios. The results also suggest that plasma 4β-HC/TC ratios may be a more suitable biomarker to assess CYP3A4 induction than 4β-HC concentrations, even for the assessment of weak inducers. It is also of note that plasma 4β-HC concentrations and 4β-HC/TC ratios were increased after the repeated administration of two NCEs, developed in-house, that possess a mechanism of action that is different from rifampicin [30]. Such results enhance the reliability of 4β-HC as a biomarker that can evaluate CYP3A4 induction potential.

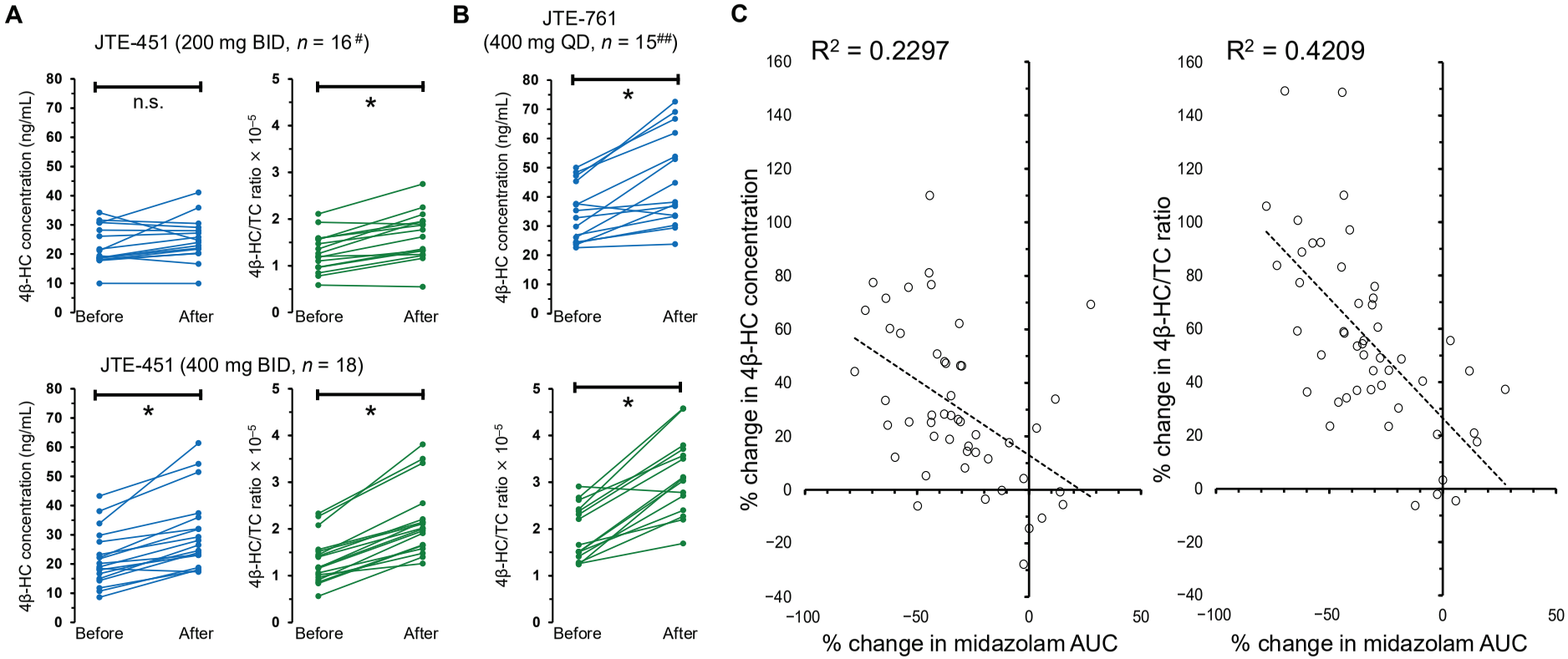


Figure 3. The 4β-HC concentrations and 4β-HC/TC ratios before and after the repeated administration of JTE-451 (**A**) and JTE-761 (**B**). The correlation chart between plasma 4β-HC concentrations or 4β-HC/TC ratios and the AUC of midazolam (**C**). Clinical DDI studies were conducted using weak inducers of CYP3A4 (JTE-451 and JTE-761), and blood collection and plasma sample storage were performed based on the results of 4β-HC stability tests. Midazolam and 4β-HC were measured using plasma, and the total cholesterol was measured using serum. The percentage (%) changes in 4β-HC concentration, 4β-HC/TC ratio, and midazolam AUC demonstrate their differences before and after the administration of NCEs. # Two subjects out of eighteen subjects opted out of the clinical study. ## One subject out of sixteen subjects opted out of the clinical study. * $p < 0.01$, n.s.: not significant.

3. Materials and Methods

3.1. Chemicals and Reagents

The 4β-HC, 4β-hydroxycholesterol-d7 (4β-HC-d7, an internal standard), and other oxysterols were purchased from Avanti Polar Lipids (Alabaster, AL, USA). The purity of the standards was >99%. The 4α-HC was obtained from Toronto Research Chemicals (Toronto, ON, Canada). Butylhydroxytoluene (BHT) was obtained from Sigma-Aldrich (St. Louis, MO, USA), and sodium methoxide was obtained from Tokyo Chemical Industry (Tokyo, Japan). All other chemicals were above the analytical grade.

3.2. Investigation of Plasma Collection Methods, Storage Conditions, and Indicators of Defective Plasma Samples

Blood samples were collected from healthy volunteers (three males and three females) into vacuum collection tubes (Terumo Corporation, Tokyo, Japan) containing either K2-EDTA (P/N VP-DK050K), heparin sodium (P/N VP-H100K), heparin lithium (P/N VP-HL050K), 3.2% sodium citrate (P/N VP-CA050K70), or a serum separating medium (P/N VP-AS109K). The tubes were centrifuged at 4 °C for 10 min at 1710× *g* to separate the plasma (or serum). Equal amounts of plasma (or serum) from each volunteer were pooled and dispensed into polypropylene microtubes. Acidified plasma, prepared by adding 1/10 volume of water/acetic acid (19:1, *v*/*v*) to K2-EDTA plasma or sodium heparin plasma, was also dispensed into tubes.

The sample tubes, each containing 600 µL of plasma or serum, were stored for long or short periods of time under various conditions to mimic actual 4β-HC storage conditions (e.g., the sample storage temperature in clinical testing sites and analytical laboratories, shipping conditions, and conditions during sample preparation procedures). For the long-term stability tests, tubes were stored in the dark at −20 °C or −80 °C for up to 13 months (the duration of stability tests: 1, 2, 6, 9, and 13 months) and at −70 °C for up to 10 months (the duration of stability tests: 1, 3, and 10 months). For the short-term stability tests, tubes were stored for 6 h under three conditions: in the dark (in a refrigerator, 4 °C), under fluorescent light (room temperature), and shading with aluminum foil (room temperature). For the freeze-thaw stability tests, tubes were frozen at −20 °C or −80 °C, thawed at room temperature for about 30 min, and then frozen for up to five cycles. After each test, 4β-HC was extracted from the plasma (or serum) and quantified via liquid chromatography-tandem mass spectrometry (LC-MS/MS), as described below. During LC-MS/MS analysis, we found a compound that was a potential indicator for defective plasma samples. Its structure was analyzed using LC-high-resolution mass spectrometry (LC-HRMS), as described below. Based on the results of these experiments, the optimal conditions for sample collection, storage, and shipping, when mimicking the conditions of 4β-HC storage at clinical testing sites and analytical laboratories, were determined.

3.3. Clinical DDI Studies of NCEs (JTE-451 and JTE-761)

Phase 1, open-label DDI studies of two novel retinoid-related orphan receptor γ antagonists, JTE-451 (AE451-U-19-005) and JTE-761 (AE761-U-19-001) [18], were conducted in 36 and 16 healthy adult male subjects, respectively. Thirty-six subjects were enrolled in two cohorts, wherein subjects received either a 200 or 400 mg twice-daily (BID) dose of JTE-451 (18 subjects per cohort). Sixteen subjects were enrolled in another cohort, wherein subjects received a 400 mg once-daily (QD) dose of JTE-761. All subjects received a single oral dose of 3 mg midazolam either 9 days or 1 day prior to the administration of JTE-451 or JTE-761, respectively. Then, JTE-451 or JTE-761 was administered for 14 consecutive days (days 1 to 14). On day 15, JTE-451 or JTE-761 was co-administered with midazolam. An overview of the dosing schedules of the test compounds are shown in Supplementary Figure S1.

Blood was collected before the administration of JTE-451 or JTE-761, and on the last day of the administration of JTE-451 or JTE-761. Plasma was collected and stored using the optimal method described in Section 2.2. Clinical studies, and experiments with the human samples, as described in Section 2.2, were conducted in accordance with the principles of

the Declaration of Helsinki. The protocols were approved by the Institutional Review Board of IntegReview IRB, Austin, Texas. The studies were also conducted in accordance with the principles of Good Clinical Practice. All subjects provided written informed consent prior to participation in the study.

3.4. LC-MS/MS Analysis of 4β-HC in Plasma and Serum

A 100 μL aliquot of human plasma (or serum) was taken from the stability tests or clinical studies and mixed with 10 μL of 4β-HC-d7 (internal standard, 1 μg/mL in 2-propanol), 50 μL of BHT (antioxidant, 1 mg/mL in ethanol), 350 μL of Tween 80 (1% in phosphate-buffered saline (PBS)), and 1 mL of sodium methoxide (2 mol/L in methanol/ethanol (2:3, v/v)) [20,31]. Each sample was saponified at room temperature for 20 min, mixed with 4 mL of hexane and 500 μL of saturated NaCl solution, and held at room temperature for 15 min. After centrifugation (1710× g for 5 min at 4 °C), the organic layer was collected, dried, and dissolved in 100 μL of formic acid/acetonitrile/water (1:900:100, $v/v/v$). Samples were stored at 4 °C in the autosampler, and a 5 μL aliquot was injected into the LC-MS/MS system.

The LC-MS/MS system consisted of a Nexera X2 HPLC (Shimadzu, Kyoto, Japan) coupled with a Triple Quad 6500 mass spectrometer (AB Sciex, Framingham, MA, USA). An L-column2 ODS (150 mm × 2.1 mm ID, 2 μm, Chemical Evaluation and Research Institute, Tokyo, Japan) was used at 50 °C. A binary gradient consisting of mobile phase A (water/formic acid (1000:1), v/v) and B (acetonitrile/formic acid (1000:1), v/v) was employed under the following profile: 0–9.0 min, B 90%; 9.0–9.1 min, B 90–95%; 9.1–12 min, B 95%; 12.0–12.1 min, B 95–90%; 12.1–14.0 min, B 90%. The flow rate was set at 0.5 mL/min. MS/MS detection of the analytes was performed in the multiple reaction monitoring (MRM) mode with positive electrospray ionization. MRM pairs were m/z 385.4/109.0 for 4β-HC and m/z 392.4/109.0 for 4β-HC-d7. The de-clustering potential, collision energy, and collision exit potential were set at 136, 31, and 11 V, respectively. Other MS/MS parameters are described in Supplementary Table S1.

Calibration samples were prepared by spiking 10 μL of 4β-HC (0.05–2.5 μg/mL in 2-propanol) and 10 μL of 4β-HC-d7 (internal standard, 1 μg/mL in 2-propanol) into a surrogate matrix (100 μL of Tween 80 (1% in PBS)). Each sample was extracted using the same procedure as plasma (or serum) and analyzed using LC-MS/MS. A calibration curve for the quantification of 4β-HC in the plasma (or serum) samples was constructed by plotting the peak area ratio of 4β-HC to 4β-HC-d7 against their nominal concentrations (5–250 ng/mL).

3.5. LC-HRMS Analysis of a Potential Indicator to Detect Defective Plasma

The structure of the potential indicator to detect defective plasma, found during the long-term stability test, was analyzed using LC-HRMS. Plasma stored under the long-term storage test conditions (Section 3.4) was extracted, diluted, and subjected to LC-HRMS analysis. The LC-HRMS system consisted of a Nexera X2 HPLC, coupled with a TripleTOF 5600 (AB Sciex). Separation conditions (column, mobile phase, flow rate, and column temperature) for LC-HRMS analysis were the same as for the LC-MS/MS analysis described above. The LC gradient profile was as follows: 0–19.0 min, B 80%; 19.0–19.1 min, B 80–95%; 19.1–22.0 min, B 95%; 22.0–22.1 min, B 95–80%; 22.1–24.0 min, B 80%. HRMS parameters are shown in Supplementary Table S1.

3.6. Other Measurements in Clinical DDI Studies

For the measurement of TC levels, serum samples were collected before the administration of JTE-451 or JTE-761, and on the last day of the administration of JTE-451 or JTE-761, TC levels were measured using a colorimetric analysis kit.

Plasma samples collected from the subjects on midazolam administration dates, as described in Section 2.3, were used to analyze plasma midazolam concentrations. Mida-

zolam was quantified using LC-MS/MS. Contracted research organizations performed these analyses.

3.7. Statistical Methods

A comparison of 4β-HC and 4β-HC/TC ratios before and after the administration of JTE-451 or JTE-761 was analyzed using the paired samples *t*-test. The AUC of midazolam was determined using non-compartmental analysis with Phoenix WinNonlin (version 6.2 or higher, Certara, Inc., Princeton, NJ, USA). The correlation between plasma 4β-HC levels (or 4β-HC/TC ratios) and the AUC of midazolam was assessed using Pearson's correlation coefficient.

Supplementary Materials: The following supporting information can be downloaded at: https://www.mdpi.com/article/10.3390/molecules28041576/s1, Supplementary Figure S1: The dosing schedules of JTE-451 and JTE-761 in clinical DDI studies; Table S1: The parameters of LC-MS/MS and LC-HRMS.

Author Contributions: Conceptualization, Y.T.; methodology, Y.T. and M.M.; validation, Y.T.; formal analysis, Y.T.; investigation, Y.T., M.M. and S.N.; data curation, Y.T.; writing—original draft preparation, Y.T.; writing—review and editing, M.J., N.S. and K.N.; visualization, Y.T., M.J. and K.N.; supervision, K.N.; project administration, Y.N. and K.N. All authors have read and agreed to the published version of the manuscript.

Funding: The clinical DDI studies were funded by Akros Pharma, Inc., Princeton, NJ, USA. Akros Pharma Inc. is a subsidiary of Japan Tobacco Inc.

Institutional Review Board Statement: The protocols concerning blood collection from healthy volunteers (Section 2.2) were approved by the ethics committee of Japan Tobacco Central Pharmaceutical Research Institute (approval numbers: R-82-a). The clinical studies using two NCEs were conducted in accordance with all applicable laws and regulations, including, but not limited to, current Good Clinical Practices. Protocols of all studies were reviewed and approved by the Institutional Review Board of IntegReview IRB, Austin, Texas. The protocol numbers and approved date of JTE-451 and JTE-761 were AE451-U-19-005 (7 June 2019) and AE761-U-19-001 (9 August 2019), respectively.

Informed Consent Statement: Informed consent was obtained from all subjects involved in the storage stability tests of 4β-HC and clinical DDI studies.

Data Availability Statement: Not applicable.

Acknowledgments: We thank Barbara Gerhardt (Clinical Operations, Akros Pharma, Inc., Princeton, NJ, USA), Sudhakar M. Pai, Qingtao (Mike) Huang (Clinical Pharmacology, Akros Pharma, Inc., Princeton, NJ, USA), Shunsuke Fujii (Clinical Development, Pharmaceutical Division, Japan Tobacco Inc., Tokyo, Japan), and Noriko Ninomiya (Clinical Pharmacology, Pharmaceutical Division, Japan Tobacco Inc., Tokyo, Japan) for the support given when measuring 4β-HC in clinical DDI studies. We thank Toshio Taniguchi and Satoru Kobayashi (Drug Metabolism and Pharmacokinetics Re-search Laboratories, Central Pharmaceutical Research Institute, Japan Tobacco Inc., Takatsuki, Osaka, Japan) for their helpful discussions.

Conflicts of Interest: The authors declare no conflict of interest.

Sample Availability: Samples of the compounds are not available from the authors.

References

1. Bodin, K.; Andersson, U.; Rystedt, E.; Ellis, E.; Norlin, M.; Pikuleva, I.; Eggertsen, G.; Björkhem, I.; Diczfalusy, U. Metabolism of 4β-hydroxycholesterol in humans. *J. Biol. Chem.* **2002**, *277*, 31534–31540. [CrossRef]
2. Bodin, K.; Bretillon, L.; Aden, Y.; Bertilsson, L.; Broomé, U.; Einarsson, C.; Diczfalusy, U. Antiepileptic drugs increase plasma levels of 4β-hydroxycholesterolin humans: Evidence for involvement of cytochrome P450 3A4. *J. Biol. Chem.* **2001**, *276*, 38685–38689. [CrossRef]
3. Dutreix, C.; Lorenzo, S.; Wang, Y. Comparison of two endogenous biomarkers of CYP3A4 activity in a drug–drug interaction study between midostaurin and rifampicin. *Eur. J. Clin. Pharmacol.* **2014**, *70*, 915–920. [CrossRef] [PubMed]

4. Björkhem-Bergman, L.; Bäckström, T.; Nylén, H.; Rönquist-Nii, Y.; Bredberg, E.; Andersson, T.B.; Bertilsson, L.; Diczfalusy, U. Quinine compared to 4β-hydroxycholesterol and midazolam as markers for CYP3A induction by rifampicin. *Drug Metab. Pharmacokinet.* **2014**, *29*, 352–355. [CrossRef] [PubMed]
5. Björkhem-Bergman, L.; Bäckström, T.; Nylén, H.; Rönquist-Nii, Y.; Bredberg, E.; Andersson, T.B.; Bertilsson, L.; Diczfalusy, U. Comparison of endogenous 4β-hydroxycholesterol with midazolam as markers for CYP3A4 induction by rifampicin. *Drug Metab. Dispos.* **2013**, *41*, 1488–1493. [CrossRef] [PubMed]
6. Xue, Y.J.; Hoffmann, M.; Tong, Z.; Wu, X.I.; Vallejo, M.; Melo, B.; Ye, Y.; Thomas, M.; Liu, Y.; Weiss, D.; et al. Use of 4β-hydroxycholesterol in animal and human plasma samples as a biomarker for CYP3A induction. *Bioanalysis* **2016**, *8*, 215–228. [CrossRef]
7. Kasichayanula, S.; Boulton, D.W.; Luo, W.L.; Rodrigues, A.D.; Yang, Z.; Goodenough, A.; Lee, M.; Jemal, M.; LaCreta, F. Validation of 4β-hydroxycholesterol and evaluation of other endogenous biomarkers for the assessment of CYP3A activity in healthy subjects. *Br. J. Clin. Pharmacol.* **2014**, *78*, 1122–1134. [CrossRef]
8. Mao, J.; Martin, I.; McLeod, J.; Nolan, G.; van Horn, R.; Vourvahis, M.; Lin, Y.S. Perspective: 4β-hydroxycholesterol as an emerging endogenous biomarker of hepatic CYP3A. *Drug Metab. Rev.* **2017**, *49*, 18–34. [CrossRef]
9. Dakappagari, N.; Zhang, H.; Stephen, L.; Amaravadi, L.; Khan, M.U. Recommendations for clinical biomarker specimen preservation and stability assessments. *Bioanalysis* **2017**, *9*, 643–653. [CrossRef]
10. Jemal, M.; Ouyang, Z.; Xia, Y.Q. Systematic LC-MS/MS bioanalytical method development that incorporates plasma phospholipids risk avoidance, usage of incurred sample and well thought-out chromatography. *Biomed. Chromatogr.* **2010**, *24*, 2–19. [CrossRef]
11. Hilhorst, M.; van Amsterdam, P.; Heinig, K.; Zwanziger, E.; Abbott, R. Stabilization of clinical samples collected for quantitative bioanalysis–a reflection from the European Bioanalysis Forum. *Bioanalysis* **2015**, *7*, 333–343. [CrossRef] [PubMed]
12. Goodenough, A.K.; Onorato, J.M.; Ouyang, Z.; Chang, S.; Rodrigues, A.D.; Kasichayanula, S.; Huang, S.P.; Turley, W.; Burrell, R.; Bifano, M.; et al. Quantification of 4-beta-hydroxycholesterol in human plasma using automated sample preparation and LC-ESI-MS/MS analysis. *Chem. Res. Toxicol.* **2011**, *24*, 1575–1585. [CrossRef] [PubMed]
13. Xu, Y.; Yuan, Y.; Smith, L.; Edom, R.; Weng, N.; Mamidi, R.; Silva, J.; Evans, D.C.; Lim, H.K. LC–ESI-MS/MS quantification of 4β-hydroxycholesterol and cholesterol in plasma samples of limited volume. *J. Pharm. Biomed. Anal.* **2013**, *85*, 145–154. [CrossRef] [PubMed]
14. van de Merbel, N.C.; Bronsema, K.J.; van Hout, M.W.; Nilsson, R.; Sillén, H. A validated liquid chromatography–tandem mass spectrometry method for the quantitative determination of 4β-hydroxycholesterol in human plasma. *J. Pharm. Biomed. Anal.* **2011**, *55*, 1089–1095. [CrossRef]
15. Hasan, M.; Siegmund, W.; Oswald, S. Rapid LC–MS/MS method for the determination of 4-hydroxycholesterol/cholesterol ratio in serum as endogenous biomarker for CYP3A activity in human and foals. *J. Chromatogr. B Analyt. Technol. Biomed. Life Sci.* **2016**, *1033*, 193–199. [CrossRef]
16. Diczfalusy, U.; Nylén, H.; Elander, P.; Bertilsson, L. 4β-hydroxycholesterol, an endogenous marker of CYP3A4/5 activity in humans. *Br. J. Clin. Pharmacol.* **2011**, *71*, 183–189. [CrossRef]
17. Suzuki, Y.; Oda, A.; Negami, J.; Toyama, D.; Tanaka, R.; Ono, H.; Ando, T.; Shin, T.; Mimata, H.; Itoh, H.; et al. Sensitive UHPLC-MS/MS quantification method for 4β-and 4α-hydroxycholesterol in plasma for accurate CYP3A phenotyping. *J. Lipid. Res.* **2022**, *63*, 100184. [CrossRef]
18. Japan Tobacco Inc. Available online: https://www.jt.com/investors/results/S_information/pharmaceuticals/index.html (accessed on 11 December 2022).
19. Fuhr, U.; Jetter, A.; Kirchheiner, J. Appropriate phenotyping procedures for drug metabolizing enzymes and transporters in humans and their simultaneous use in the "cocktail" approach. *Clin. Pharmacol. Ther.* **2007**, *81*, 270–283. [CrossRef]
20. Aubry, A.F.; Dean, B.; Diczfalusy, U.; Goodenough, A.; Iffland, A.; McLeod, J.; Weng, N.; Yang, Z. Recommendations on the development of a bioanalytical assay for 4β-hydroxycholesterol, an emerging endogenous biomarker of CYP3A activity. *AAPS J.* **2016**, *18*, 1056–1066. [CrossRef]
21. The ICH M10 Guideline on Bioanalytical Method Validation and Study Sample Analysis (24 May 2022). Available online: https://database.ich.org/sites/default/files/M10_Guideline_Step4_2022_0524.pdf (accessed on 11 December 2022).
22. van de Merbel, N.; Savoie, N.; Yadav, M.; Ohtsu, Y.; White, J.; Riccio, M.F.; Dong, K.; de Vries, R.; Diancin, J. Stability: Recommendation for best practices and harmonization from the Global Bioanalysis Consortium Harmonization Team. *AAPS J.* **2014**, *16*, 392–399. [CrossRef]
23. Redrup, M.J.; Igarashi, H.; Schaefgen, J.; Lin, J.; Geisler, L.; Ben M'Barek, M.; Ramachandran, S.; Cardoso, T.; Hillewaert, V. Sample management: Recommendation for best practices and harmonization from the global bioanalysis consortium harmonization team. *AAPS J.* **2016**, *18*, 290–293. [CrossRef] [PubMed]
24. Zielinski, Z.A.; Pratt, D.A. Cholesterol autoxidation revisited: Debunking the dogma associated with the most vilified of lipids. *J. Am. Chem. Soc.* **2016**, *138*, 6932–6935. [CrossRef]
25. Zielinski, Z.A.; Pratt, D.A. H-atom abstraction vs addition: Accounting for the diverse product distribution in the autoxidation of cholesterol and its esters. *J. Am. Chem. Soc.* **2019**, *141*, 3037–3051. [CrossRef]
26. Helberg, J.; Pratt, D.A. Autoxidation vs. antioxidants—The fight for forever. *Chem. Soc. Rev.* **2021**, *50*, 7343–7358. [CrossRef] [PubMed]

27. Dong, J.Q.; Gosset, J.R.; Fahmi, O.A.; Lin, Z.; Chabot, J.R.; Terra, S.G.; Le, V.; Chidsey, K.; Nouri, P.; Kim, A.; et al. Examination of the human cytochrome P450 3A4 induction potential of PF-06282999, an irreversible myeloperoxidase inactivator: Integration of preclinical, in silico, and biomarker methodologies in the prediction of the clinical outcome. *Drug Metab. Dispos.* **2017**, *45*, 501–511. [CrossRef] [PubMed]
28. Yang, Z.; Rodrigues, A.D. Does the long plasma half-life of 4β-hydroxycholesterol impact its utility as a cytochrome P450 3A (CYP3A) metric? *J. Clin. Pharmacol.* **2010**, *50*, 1330–1338. [CrossRef]
29. The FDA Guideline on Clinical Drug Interaction Studies—Cytochrome P450 Enzyme- and Transporter-Mediated Drug Interactions Guidance for Industry (January 2020). Available online: https://www.fda.gov/media/134581/download (accessed on 11 December 2022).
30. Umezawa, H.; Mizuno, S.; Yamazaki, H.; Nitta, K. Inhibition of DNA-dependent RNA synthesis by rifamycins. *J. Antibiot.* **1968**, *21*, 234–236. [CrossRef]
31. Sugimoto, H.; Kakehi, M.; Satomi, Y.; Kamiguchi, H.; Jinno, F. Method development for the determination of 24S-hydroxycholesterol in human plasma without derivatization by high-performance liquid chromatography with tandem mass spectrometry in atmospheric pressure chemical ionization mode. *J. Sep. Sci.* **2015**, *38*, 3516–3524. [CrossRef]

Disclaimer/Publisher's Note: The statements, opinions and data contained in all publications are solely those of the individual author(s) and contributor(s) and not of MDPI and/or the editor(s). MDPI and/or the editor(s) disclaim responsibility for any injury to people or property resulting from any ideas, methods, instructions or products referred to in the content.

molecules

MDPI

Review

Current Role and Potential of Triple Quadrupole Mass Spectrometry in Biomedical Research and Clinical Applications

Andreas Tsakalof [1,*], Alexey A. Sysoev [2], Kira V. Vyatkina [3,4,5], Alexander A. Eganov [3], Nikolay N. Eroshchenko [3], Alexey N. Kiryushin [3], Alexey Yu. Adamov [2], Elena Yu. Danilova [3,6] and Alexander E. Nosyrev [3,*]

1 Laboratory of Biochemistry, School of Medicine, University of Thessaly, Biopolis, 41111 Larissa, Greece
2 Laboratory of Applied Ion Physics and Mass Spectrometry, National Research Nuclear University MEPhI (Moscow Engineering Physics Institute), 115409 Moscow, Russia; aasysoyev@mephi.ru (A.A.S.); ayadamov@mephi.ru (A.Y.A.)
3 Biomedical Science and Technology Park, I.M. Sechenov First Moscow State Medical University, 119991 Moscow, Russia; vyatkina_k_v@staff.sechenov.ru (K.V.V.); eganov_a_a@staff.sechenov.ru (A.A.E.); eroshchenko_n_n@staff.sechenov.ru (N.N.E.); kiryushin_a_n@staff.sechenov.ru (A.N.K.); danilova_e_yu_1@staff.sechenov.ru (E.Y.D.)
4 Institute of Translational Biomedicine, Saint Petersburg State University, 199034 St. Petersburg, Russia
5 Department of Software Engineering and Computer Applications, Saint Petersburg Electrotechnical University "LETI", 197376 St. Petersburg, Russia
6 Department of Analytic Chemistry, Faculty of Chemistry, Lomonosov Moscow State University, 119991 Moscow, Russia
* Correspondence: atsakal@med.uth.gr (A.T.); nosyrev_a_e@staff.sechenov.ru (A.E.N.)

Abstract: Mass-spectrometry-based assays nowadays play an essential role in biomedical research and clinical applications. There are different types of commercial mass spectrometers on the market today, and triple quadrupole (QqQ) is one of the time-honored systems. Here, we overview the main areas of QqQ applications in biomedicine and assess the current level, evolution, and trends in the use of QqQ in these areas. Relevant data were extracted from the Scopus database using the specified terms and Boolean operators defined for each field of the QqQ application. We also discuss the recent advances in QqQ and QqQ-based analytical platforms, which promote the clinical application of these systems, and explain the indicated substantial increase in triple quadrupole use in biomedicine. The number of biomedical studies utilizing QqQ increased 2–3 times this decade. Triple quadrupole is most intensively used in the field of endocrine research and testing. On the contrary, the relative rate of immunoassay utilization—a major competitor of chromatography–mass spectrometry—decreased in this area as well as its use within Therapeutic drug monitoring (TDM) and forensic toxicology. Nowadays, the applications of high-resolution accurate mass (HRAM) mass spectrometers in the investigated areas represent only a small fraction of the total amount of research using mass spectrometry; however, their application substantially increased during the last decade in the untargeted search for new biomarkers.

Keywords: mass spectrometry; clinical applications; triple quadrupole; biomedical research; tandem mass spectrometry

1. Introduction

Modern chromatography–mass spectrometry has made a significant contribution to the currently observed progress in bio-medical research and applications; in particular, it has brought a revolution in mass-spectrometry-based disease diagnosis, preventive screening, early disease detection, and the development of personalized/precision medicine [1–5]. Moreover, chromatography–mass spectrometry is the main instrumental platform for the emerging "omics" technologies (proteomics, metabolomics, lipidomics, etc.), which are nowadays reaching the initial translational phase from basic research to routine clinical applications. There are various types of commercial mass spectrometers on the market

today, and selecting an optimal instrument for a particular task is rarely a straightforward consideration. The selection criteria can differ significantly depending on whether the instrument is intended for routine measurements or basic research. In this review, we focus on the current role and potential of the triple quadrupole mass analyzer. The first triple quadrupole mass spectrometer (QqQ) was presented by Christie G. Enke and Richard A. Yost in the late 1970s [6], and our review outlines that it is nowadays the main mass spectrometer used in biomedical research and clinical applications. There is little doubt that this type of instrument will hold this position in the future due to its relatively low cost and variety of modes of operation that make it possible to develop methods with superior specificity and sensitivity. Triple quadrupole mass spectrometers are produced by leading manufacturers of mass spectrometers who are constantly working on improving the features and merits of these devices (Supplementary Table S1). Nowadays, QqQ instruments are used in various application fields, as outlined in Figure 1; however, the extent of their use in each of the identified areas varies. In this review, we aimed to assess the current state of the art and demonstrate the evolution and trends of QqQ use in these areas. We also discussed recent advances in chromatography–QqQ that reflect these trends and are driving wider adoption of this analytical platform in biomedical research and clinical laboratories.

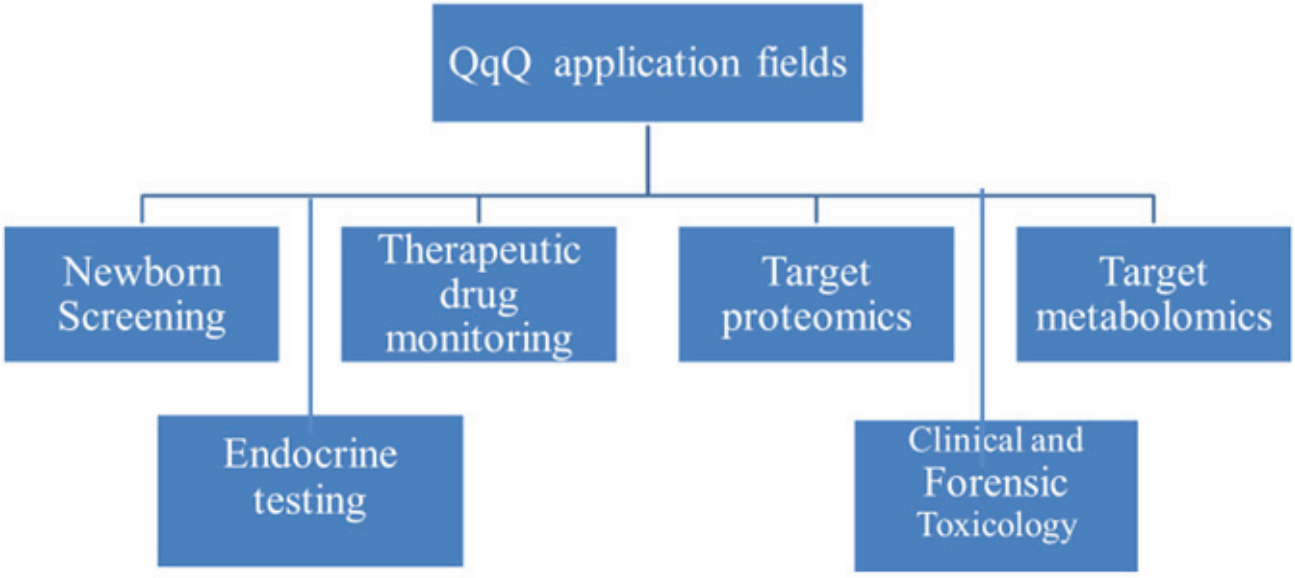


Figure 1. Main application areas of triple quadrupole in biomedicine.

2. Methods of Data Acquisition

Relevant data were extracted from the Scopus database using specified terms and Boolean operators defined for each field and indicated in the corresponding section. The search was limited to "articles" and excluded other document types, e.g., reviews, book chapters, conference papers, and editorials. The specified terms were searched for in the article's title, abstract, and keywords. The triple quadrupole mass analyzer is also often referred to as tandem mass spectrometry or MS/MS, and these terms were united by the Boolean operator "OR". To assess the dynamics of the QqQ utilization rates, the search was conducted independently for two decades: 2004–2014 and 2014–2024. The applications of other tandem configurations, such as Q-TOF and hybrid Orbitrap, were also searched for separately to evaluate their impact on the investigated areas. The extent of use of immunoassay, a major competitor of chromatography–mass spectrometry, was also evaluated.

3. Results and Discussion: Current Status and Trends in the Use of Triple Quadrupole in Clinical Applications and Biomedical Research

3.1. Newborn Screening

Newborn screening (NBS) involves a set of clinical tests of biological samples from newborns for the early, pre-symptomatic detection of congenital abnormalities critical to the child's health. Early diagnosis makes it possible to take preventive measures to preserve child health and reduce child mortality and morbidity [7,8]. Conclusions are drawn based on specific metabolic biomarkers of these abnormalities [8,9]. All developed countries and many developing countries have implemented NBS programs for mandatory testing of infants for a number of congenital diseases, and this number is steadily increasing [10,11]. Thus, starting in 2023, a program of expanded newborn screening is included in the commitments of neonatal services in the Russian Federation, and the testing of newborns has grown from 5 to 36 congenital diseases [12]. The feasibility of such expansion can be largely attributed to the introduction of LC-MS/MS to NBS laboratories in the 1990s [13]. Nowadays, liquid chromatography coupled to a triple quadrupole mass analyzer is the main instrumental platform for routine measurements and research in NBS programs. Thus, a Scopus search using the terms and Boolean operators indicated in Table 1 reveals that in the last decade (2014–2024) at least 84% (924 out of 1098) of studies involved in newborn screening utilized mass spectrometry in their research. In particular, 823 out of those 924 papers explicitly mention tandem mass spectrometry or triple quadrupole. Only a few studies (seven) reported the use of other tandem configurations such as Q-TOF or hybrid Orbitrap MS. This preference for the triple quadrupole mass analyzer is due to the relatively low price of these instruments and, at the same time, their superior specificity and sensitivity in target analysis achieved by two consecutive mass filtering stages, (Section 4.2) despite the low resolution of the single quadrupole mass analyzer. The number of studies in newborn/neonatal screening significantly increased compared to the previous decade (2004–2014, Table 1). Immunoassays, the main alternative to the mass spectrometry approach to quantify different compounds, were also used at the rate of about 15–17% of all the studies in the previous two decades (Table 1).

Table 1. Terms, Boolean operators, and limitations (years, document type) used for the evaluation of QqQ application rate in NBS screening and research.

Terms and Boolean Operators	Retrieved Documents	
	2014–2024	2004–2014
	Number of Publications	
(TITLE-ABS-KEY ({neonatal screening}) OR TITLE-ABS-KEY ({newborn screening}) AND TITLE-ABS-KEY ({mass spectrometry})) AND (LIMIT-TO (DOCTYPE, "ar"))	924	587
(TITLE-ABS-KEY ({newborn screening}) OR TITLE-ABS-KEY ({neonatal screening}) AND TITLE-ABS-KEY ({tandem mass spectrometry}) OR TITLE-ABS-KEY ({triple quadrupole}) OR TITLE-ABS-KEY (ms/ms)) AND (LIMIT-TO (DOCTYPE, "ar"))	823	562
(TITLE-ABS-KEY ({newborn screening}) OR TITLE-ABS-KEY ({neonatal screening}) AND TITLE-ABS-KEY ({Q-TOF})) AND (LIMIT-TO (DOCTYPE, "ar"))	1	0
(TITLE-ABS-KEY ({newborn screening}) OR TITLE-ABS-KEY ({neonatal screening}) AND TITLE-ABS-KEY ({Orbitrap})) AND (LIMIT-TO (DOCTYPE, "ar"))	6	2
(TITLE-ABS-KEY ({newborn screening}) OR TITLE-ABS-KEY ({neonatal screening}) AND TITLE-ABS-KEY ({immunoassay})) AND PUBYEAR > 2003 AND PUBYEAR < 2015 AND (LIMIT-TO (DOCTYPE, "ar"))	167	92

3.2. Endocrine Testing

Endocrine testing focuses on detecting endocrine disorders and relies significantly on measuring hormone levels in biological samples. Endocrine disorders comprise a large list of diseases (>30) that have a negative impact on human well-being as well as a considerable economic burden on society [14]. However, if detected, most of these disorders are treatable and some are easily treated, e.g., thyroid dysfunctions. Accurate quantification of hormones is crucial for the proper diagnosis of disease, and recognizing the importance of these measurements, the 1977 Nobel Prize in Physiology or Medicine was awarded to Rosalyn C. Yalow for the development of the radioimmunoassay (RIA) for precise and specific measurements of the concentrations of peptide hormones and many other biologically significant substances in blood and other body fluids [15]. In the late 1980s, radioactive labels were replaced with chemiluminescent labels and, nowadays, direct chemiluminescent immunoassays (CLIA) are the most frequently used immunoassays for the measurement of hormones [16]. However, immunoassays, along with their advantages, have several significant disadvantages (Section 4), among which the most significant is the inadequate specificity of these tests due to the cross-reactivity of antibodies [17]. This can lead to a large number of false positives, irreproducible results, and overestimated concentrations. On the contrary, mass spectrometry offers superior specificity and more accurate and reliable results. Moreover, in contrast to immunoassays, MS is a multi-component method that allows for multiple steroid detection and steroid profiling for the complex evaluation of steroidogenesis in the organism [18,19]. Given these advantages, endocrine testing shifts strongly nowadays to mass-spectrometry-based assays [20]. Thus, according to the United Kingdom National External Quality Assessment Service (UK NEQAS) steroid hormone proficiency testing scheme, the number of participants using LC-MS/MS increased from 3% to 18% from 2011 to 2019 [20]. This trend was also clearly demonstrated by the recommendation from the editors of the *Journal of Clinical Endocrinology and Metabolism* to avoid using immunoassays and instead use MS for the measurement of sex steroids [21]. The LC–tandem MS (triple quadrupole) is also identified as the reference procedure measurement (RPM) in Clinical Standardization Programs organized by the Centers for Disease Control and Prevention (CDC) [22]. A reference procedure (also known as a reference method) is a measurement method that has been officially defined as the gold standard for a specific analysis. It demonstrates appropriate trueness (accuracy) and precision (reproducibility) for its intended use. The critical advantage of mass-spectrometry-based methods is the ability to profile steroids by simultaneous multiple steroid quantification in a single analysis. Thus, entire metabolic pathways of steroidogenesis can be investigated, and the coverage of endocrine diseases can be expanded in the field [23]. A trend can be observed for developing new methods that cover the increased part of the whole steroidome—a comprehensive collection of steroids present in a biological system [24]. For example, a method based on GC–triple quadrupole MS for the determination of a hundred endogenous steroids in human serum was recently presented [25]. Endocrine research is the most intensive and intensively developing area of application of hybrid mass spectrometry, represented by a large number of publications that have more than doubled over the previous decade (14,968 vs. 6625 studies, Table 2). Mass spectrometry is now used in most endocrine studies, but immunoassays are also popular, apparently because of their ease of implementation; however, the proportion of immunoassays has declined from about 36% in the previous decade to 29% in the current decade. It can be concluded from the data retrieved (Table 2) that the extent of QqQ use (mostly referred to as tandem mass spectrometry) in endocrine research nowadays is notable and has also significantly increased compared to the previous decade. The prevalence of QqQ use is obviously much higher than indicated in Table 2 due to the following reasons: First, in many publications, authors do not specify the type of mass analyzer used in search sections such as the article's title, abstract, and keywords. Second, only a few studies focusing on endocrine research used high-resolution Q-TOF and Orbitrap (Table 2).

Table 2. Terms, Boolean operators, and limitations (years, document type) used for the evaluation of QqQ application rate in endocrine testing and research.

Terms and Boolean Operators	Retrieved Documents	
	2014–2024	2004–2014
	Number of Publications	
((TITLE-ABS-KEY ({hormone) OR TITLE-ABS-KEY ({steroid}) OR TITLE-ABS-KEY ({endocrine}) AND TITLE-ABS-KEY ({mass spectrometry})) AND (LIMIT-TO (DOCTYPE, "ar"))	14,968	6625
(TITLE-ABS-KEY ({hormone}) OR TITLE-ABS-KEY ({steroid}) OR TITLE-ABS-KEY ({endocrine}) AND TITLE-ABS-KEY ({tandem mass spectrometry}) OR TITLE-ABS-KEY ({triple quadrupole}) OR TITLE-ABS-KEY ({ms/ms}) AND (LIMIT-TO (DOCTYPE, "ar"))	5193	2391
(TITLE-ABS-KEY ({hormone}) OR TITLE-ABS-KEY ({steroid}) OR TITLE-ABS-KEY ({endocrine}) AND TITLE-ABS-KEY (q-tof)) AND PUBYEAR > 2003 AND (LIMIT-TO (DOCTYPE, "ar"))	204	40
(TITLE-ABS-KEY ({hormone}) OR TITLE-ABS-KEY ({steroid}) OR TITLE-ABS-KEY ({endocrine}) AND TITLE-ABS-KEY (orbitrap)) AND (LIMIT-TO (DOCTYPE, "ar"))	243	48
(TITLE-ABS-KEY ({hormone}) OR TITLE-ABS-KEY ({steroid}) OR TITLE-ABS-KEY ({endocrine}) AND TITLE-ABS-KEY (immunoassay)) AND (LIMIT-TO (DOCTYPE "ar"))	6121	3746

3.3. Therapeutic Drug Monitoring (TDM)

Therapeutic drug monitoring (TDM) specializes in measuring circulating drug levels and is an important component of the concept of personalized/precision medicine [26]. Due to human genetic polymorphism, drug–drug interactions (when multiple drugs are administered), and drug–disease interactions, high variability in the pharmacokinetics of drugs may be observed and, therefore, the dosing regimen of drugs should be personalized for the most effective treatment and/or prevention of drugs' toxic effects. This is particularly important for drugs with a low therapeutic index (small difference between the minimum effective concentration and the minimum toxic concentration in the blood), for example, a variety of antiviral drugs, antibiotics, antiepileptics, psychotropics, and immunosuppressive agents [27,28]. Currently, mass-spectrometry-based methods dominate in TDM, and their applications have increased significantly over the last ten years (Table 3). During the last decade, 2014–2024, about 1492 studies used mass spectrometry for TDM, of which 1235 indicated the use of triple quadrupole, referred to as triple quadrupole or tandem mass spectrometry. Only a few studies used Q-TOF or Orbitrap MS. Thus, it can be concluded from the retrieved data that triple quadrupole is the main analyzer used nowadays for TDM as only a few applications of another tandem MS, viz., Q-TOF or Orbitrap, were retrieved (Table 3).

This area of mass spectrometry application will expand as the incorporation of precision medicine into clinical practice has been identified as a priority of national and international health policy [29,30]. The European Commission recognizes the importance of personalized medicine and has established the European Partnership for Personalized Medicine. This partnership aims to promote all areas and disciplines of precision medicine, facilitate innovation, and integrate it into health systems for continuous improvement [31,32].

Table 3. Terms, Boolean operators, and limitations (years, document type) used for the evaluation of QqQ application rate in TDM.

Terms and Boolean Operators	Retrieved Documents	
	2014–2024	2004–2014
	Number of Publications	
(TITLE-ABS-KEY ({therapeutic drug monitoring}) AND TITLE-ABS-KEY ({mass spectrometry})) AND (LIMIT-TO (DOCTYPE, "ar"))	1492	486
(TITLE-ABS-KEY ({therapeutic drug monitoring}) AND TITLE-ABS-KEY ({tandem mass spectrometry}) OR TITLE-ABS-KEY ({triple quadrupole}) OR TITLE-ABS-KEY (ms/ms)) AND (LIMIT-TO (DOCTYPE, "ar"))	1235	439
(TITLE-ABS-KEY ({therapeutic drug monitoring}) AND TITLE-ABS-KEY (q-tof)) AND (LIMIT-TO (DOCTYPE, "ar"))	3	-
(TITLE-ABS-KEY ({therapeutic drug monitoring}) AND TITLE-ABS-KEY (rbitrap)) AND (LIMIT-TO (DOCTYPE "ar"))	18	1
(TITLE-ABS-KEY ({therapeutic drug monitoring}) AND TITLE-ABS-KEY (immunoassay)) AND (LIMIT-TO (DOCTYPE, "ar"))	356	214

3.4. Clinical and Forensic Toxicology

Clinical and forensic toxicology are two main fields of analytical toxicology that use common analytical techniques to detect, identify, and quantify xenobiotics that cause poisoning or fatal intoxication. In the case of clinical toxicology, the acquired data assist in the diagnosis and treatment of poisoning, while in the case of forensic toxicology, the results assist in the medical–legal investigation of death (postmortem forensic toxicology), abnormal human behavior (human performance forensic toxicology), or use of illicit substances (forensic drug testing). Forensic toxicology data are used as evidence in legal proceedings and special demands are made on their quality. Therefore, during the last two decades, mass spectrometry has replaced less specific identification techniques in forensic toxicology, and strict criteria for accepting mass spectrometry data and quality control in Forensic Toxicology Laboratories have been established [33]. Chromatography–mass spectrometry has a high identification power in conformity with the "identification point" system that has been developed for rating and comparing different identification techniques [34]. Non-mass-spectrometric techniques, e.g., colorimetric tests, immunoassays, and chromatography coupled with non-MS detectors (NPD, ECD, and fluorescence), have low identification power and cannot achieve point scores—defined as the lowest score for unambiguous compound identification. They can be used for screening and should be confirmed by a verification method [34,35]. The verification method enables the unequivocal identification and, if necessary, quantification of the compound. Hyphenated mass spectrometry is a method of choice for confirmation. Until recently, xenobiotic detection and identification workflow comprised rapid screening by immunoassay and subsequent confirmation of positive results by LC- or GC-MS [36]; however, the recent significant simplification and acceleration of chromatography–mass spectrometry analysis (see Section 6) allows for screening and identification to be performed solely by this method, which has sufficient identification power. The identification point system drives laboratories to use chromatography–mass spectrometry as the most powerful instrumentation platform for the identification of xenobiotics. The number of publications in the field of forensic toxicology performed with the use of mass spectrometry techniques doubled in comparison with the previous decade (Table 4). The number of studies that directly indicated the use of the triple quadrupole also doubled. Only a relatively small percentage of published studies indicated the use of HRAM Q-TOF and Orbitrap (Table 4). However, the application of HRAM mass spectrometry will increase for the detection and identification of newly synthesized

illicit New Psychoactive Substances (NPS) [37]. These substances are introduced into the market yearly in large diversity and quantities [38], and targeted analytical approaches are unsuitable for their detection and identification.

Table 4. Terms, Boolean operators, and limitations (years, document type) used to evaluate mass spectrometry and QqQ application rate in forensic toxicology.

Terms and Boolean Operators	Retrieved Documents	
	2014–2024	2004–2014
	Number of Publications	
(TITLE-ABS-KEY ({forensic toxicology}) AND TITLE-ABS-KEY ({mass spectrometry})) AND (LIMIT-TO (DOCTYPE, "ar"))	1474	860
(TITLE-ABS-KEY ({forensic toxicology}) AND TITLE-ABS-KEY ({tandem mass spectrometry}) OR TITLE-ABS-KEY ({triple quadrupole}) OR TITLE-ABS-KEY (ms/ms)) AND (LIMIT-TO (DOCTYPE, "ar"))	1268	689
(TITLE-ABS-KEY ({forensic toxicology}) AND TITLE-ABS-KEY ({orbitrap})) AND (LIMIT-TO (DOCTYPE, "ar"))	35	6
(TITLE-ABS-KEY ({forensic toxicology}) AND TITLE-ABS-KEY ({Q-TOF})) AND (LIMIT-TO (DOCTYPE, "ar"))	14	5
(TITLE-ABS-KEY ({forensic toxicology}) AND TITLE-ABS-KEY ({immunoassay})) AND (LIMIT-TO (DOCTYPE, "ar"))	86	73

Unlike forensic toxicology, in clinical toxicology, the turnaround time (TAT, or results waiting time) is an important criterion for the method's clinical utility for diagnosis and treatment of poisoning [39]. In particular, for an antidote administration, the poison must be identified shortly after the patient is admitted to the hospital. Thus, in case of acetaminophen poisoning, the administration of antidote N-acetylcysteine is effective within 8–12 h of drug ingestion. In the case of acetaminophen and some other toxins, the treatment depends on their concentration in the biological sample [40,41]. Rapid point-of-care (POC) or laboratory tests are most suitable to offer the desired information, and nowadays, immunoassays and chemical tests are dominant methods due to the rapid TAT [42]. In combination with observed patient symptoms, the patient's history, and circumstantial evidence (e.g., empty drug containers), these tests provide sufficient information to guide the patient's treatment. Immunoassays continue to evolve, providing enhanced sensitivity and multiplexing capabilities for the rapid detection of multiple drugs in a single test and they will obviously continue to be applied in emergency toxicology. Hyphenated MS assays have a slow turnaround time and, thus, for the time being, cannot contribute significantly to decisions for patient treatment in the emergency department. This can explain the relatively small number of publications retrieved with the terms {clinical toxicology} and {mass spectrometry} (Table 5). However, the analytical advantages of mass spectrometry have stimulated the development of new MS-based technologies to meet the main requirements of clinical toxicology—rapid TAT, high sample throughput, and availability at the point of care. An example of a system with high throughput and analysis speed is the RapidFire365-MS/MS online solid-phase extraction mass spectrometry system from Agilent Technologies Inc. [43]. In this technology, the ultra-fast RapidFire 365 automated solid-phase extraction system is directly integrated with the triple quadrupole mass spectrometer without the use of LC. With RapidFire365-MS/MS, the sample analysis time is usually <10–15 s. With the use of this technology, 18,000 urine samples were screened for 14 synthetic cannabinoids and synthetic cathinones within 4 weeks with a total instrument time of 55 h [44]. These samples were previously analyzed by traditional LC-MS/MS within 3 months and the total instrument time was 2850 h.

Table 5. Terms, Boolean operators, limitations (years, document type) used for the evaluation of mass spectrometry and QqQ application rate in clinical toxicology.

Terms and Boolean Operators	Retrieved Documents	
	2014–2024	2004–2014
	Number of Publications	
(TITLE-ABS-KEY ({clinical toxicology}) AND TITLE-ABS-KEY ({mass spectrometry})) AND (LIMIT-TO (DOCTYPE, "ar"))	141	80
(TITLE-ABS-KEY ({clinical toxicology}) AND TITLE-ABS-KEY ({tandem mass spectrometry}) OR TITLE-ABS-KEY ({triple quadrupole}) AND TITLE-ABS-KEY (ms/ms)) AND (LIMIT-TO (DOCTYPE, "ar"))	112	69
(TITLE-ABS-KEY ({clinical toxicology}) AND TITLE-ABS-KEY ({orbitrap})) AND (LIMIT-TO (DOCTYPE, "ar"))	6	1
(TITLE-ABS-KEY ({clinical toxicology}) AND TITLE-ABS-KEY ({Q-TOF})) AND (LIMIT-TO (DOCTYPE, "ar"))	3	0
(TITLE-ABS-KEY ({clinical toxicology}) AND TITLE-ABS-KEY ({immunoassay})) AND (IMIT-TO (DOCTYPE, "ar"))	17	9

3.5. Targeted Metabolomics and Proteomics

Metabolomics is a relatively new field of research that evaluates the performance of various biochemical reactions/processes in living organisms by tracking the metabolites and the end or intermediate products of these reactions. Alterations in metabolites' levels or profiles testify to abnormalities in the relevant biochemical processes caused by pathophysiologic reasons. Identification of these alterations has proved to be a useful tool clinically for disease screening and diagnosis as well as for the monitoring of therapeutic outcomes [45]. Metabolomics is also increasingly used for clarifying disease biochemical backgrounds (pathophysiology) and using this knowledge for the definition of optimal drug targets and the development of new drugs [46]. While genomics gives information about what can happen in the organism, metabolomics indicates what is currently happening, the metabolic phenotype of the organism. Nowadays, two approaches are implemented in metabolomics: untargeted and targeted. Target metabolomics measures predetermined target metabolites and compares them to established reference levels for clinical decision-making. In contrast, untargeted metabolomics aims to discover new metabolite biomarkers of disease by analyzing in an unbiased screening mode all ions produced in the ion source and detecting chromatographic peaks without information about the corresponding compound's nature. By multi-step data treatment and analysis from compared population groups, e.g., patients and controls, putative metabolites-biomarkers are identified and, subsequently, their structures are elucidated (Figure 2) [47,48]. However, processing the large amounts of data acquired is time-consuming and does not fit the demand for quick analysis and high throughput in clinical laboratories. Thus, nowadays, these two approaches have complementary roles with untargeted metabolomics used for biomarker discovery and targeted metabolomics for their implication in clinical practice within clinical laboratories (Figure 2). High-resolution accurate mass (HRAM) mass spectrometers offer more powerful capabilities for unveiling unknown compounds' structures. Orbitrap and TOF-based systems are the most widely used HRAM mass spectrometers for untargeted metabolomics, while triple quadrupole-based systems, GC-MS/MS, or LC-MS/MS are the most popular for targeted metabolomics.

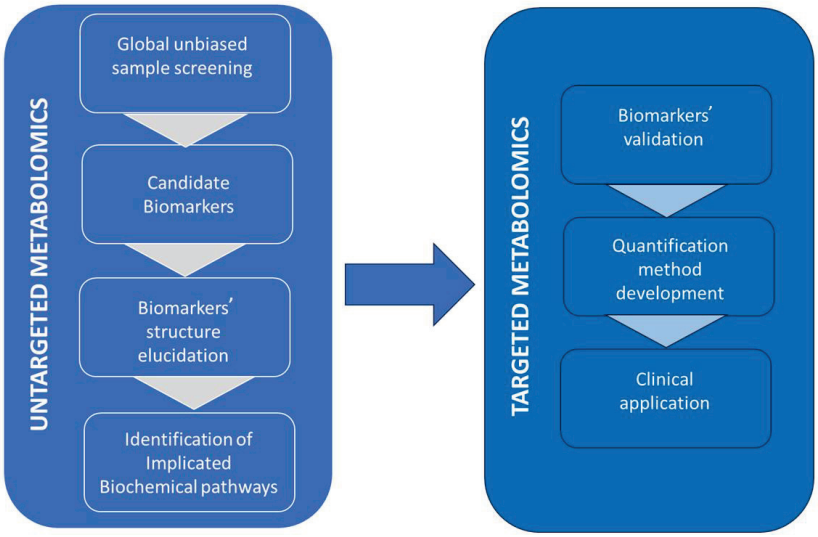


Figure 2. Complimentary role of untargeted and targeted metabolomics in biomedical research. Biomarkers (e.g., of disease) are discovered by untargeted metabolomics and then implicated in clinical practice with the use of targeted metabolomics.

The term "metabolome" was first introduced in 1998 [49]; however, GC-MS protocols for investigating key metabolic pathways such as the tricarboxylic acid (TCA) cycle, glycolysis, and the pentose phosphate pathway were developed substantially earlier [50,51]. Our search retrieved rather few (75) research articles on targeted metabolomics with the use of mass spectrometry for the 2004–2014 decade (Table 6). This research was tremendously intensified during the last decade, 2014–2024, with 1177 publications on the same topic. From these publications, 947 clarified that tandem mass spectrometry was used.

Table 6. Terms, Boolean operators, limitations (years, document type) used for the evaluation of mass spectrometry and QqQ application rate in targeted metabolomics.

Terms and Boolean Operators	Retrieved Documents	
	2014–2024	2004–2014
	Number of Publications	
(TITLE-ABS-KEY ({targeted metabolomics}) AND TITLE-ABS-KEY ({mass spectrometry}) AND NOT TITLE-ABS-KEY ({non-targeted metabolomics) OR TITLE-ABS-KEY ({untargeted metabolomics}) AND (LIMIT-TO (DOCTYPE, "ar"))	1177	75
(TITLE-ABS-KEY ({targeted metabolomics}) AND TITLE-ABS-KEY ({tandem mass spectrometry}) OR TITLE-ABS-KEY ({triple quadrupole}) OR TITLE-ABS-KEY (ms/ms) AND NOT TITLE-ABS-KEY ({non-targeted metabolomics}) AND NOT TITLE-ABS-KEY ({untargeted metabolomics})) AND (LIMIT-TO (DOCTYPE, "ar"))	947	65
(TITLE-ABS-KEY ({targeted metabolomics}) AND TITLE-ABS-KEY ({orbitrap}) AND NOT TITLE-ABS-KEY ({non-targeted metabolomics}) AND NOT TITLE-ABS-KEY ({untargeted metabolomics})) AND (LIMIT-TO (DOCTYPE, "ar"))	29	0
(TITLE-ABS-KEY ({targeted metabolomics}) AND TITLE-ABS-KEY ({Q-TOF}) AND NOT TITLE-ABS-KEY ({non-targeted metabolomics}) AND NOT TITLE-ABS-KEY ({untargeted metabolomics})) AND (LIMIT-TO (DOCTYPE, "ar"))	20	0
(TITLE-ABS-KEY ({targeted metabolomics}) AND TITLE-ABS-KEY ({immunoassay})) AND (LIMIT-TO (DOCTYPE, "ar"))	11	0

Another relatively new field of triple quadrupole MS application is expression proteomics, which studies the quantitative and qualitative expression of proteins [52]. The concept of the proteome was introduced in 1995 and characterizes the "total protein complement able to be encoded by a given genome" [53]. Today, the study of the proteome (proteomics) plays an important role in biomedicine in the fields of disease diagnosis and drug research and development. The use of triple quadrupole MS in MRM mode is very popular for the quantification of targeted proteins and identification of proteins' post-translational modifications [54]. Targeted MRM-MS proteomics is a reproducible, accurate, and multiplex method for quantifying protein biomarkers that provide information on the biological status of the organism. The high multiplexing power of QqQ MS is one of the main advantages over enzyme-linked immunosorbent assays (ELISAs) that have been the dominant technique for measuring the absolute abundance of protein in complex mixtures but only one protein at a time [55]. Thus, for example, 136 urinary proteins were precisely quantified by LC/MRM-MS on a triple quadrupole mass spectrometer [56]. Also of note is the wide range of concentrations of quantified proteins from 8.6 μg/mL to 25 pg/mL (over five orders of magnitude). The triple quadrupole MS dominates in the field of targeted proteomics and its application has tripled in comparison with the previous decade (Table 7).

Table 7. Terms, Boolean operators, and limitations (years, document type) used to evaluate mass spectrometry and QqQ application rate in targeted proteomics.

Terms and Boolean Operators	Retrieved Documents	
	2014–2024	2004–2014
	Number of Publications	
(TITLE-ABS-KEY ({targeted proteomics}) AND TITLE-ABS-KEY ({mass spectrometry}) AND NOT TITLE-ABS-KEY ({non-targeted proteomics}) AND NOT TITLE-ABS-KEY ({untargeted proteomics})) AND (LIMIT-TO (DOCTYPE, "ar"))	626	205
(TITLE-ABS-KEY ({targeted proteomics}) AND TITLE-ABS-KEY ({tandem mass spectrometry}) OR TITLE-ABS-KEY ({triple quadrupole}) OR TITLE-ABS-KEY (ms/ms) AND NOT TITLE-ABS-KEY ({non-targeted proteomics}) AND NOT TITLE-ABS-KEY ({untargeted proteomics})) AND (LIMIT-TO (DOCTYPE, "ar"))	404	126
(TITLE-ABS-KEY ({targeted proteomics}) AND TITLE-ABS-KEY ({Orbitrap}) AND NOT TITLE-ABS-KEY ({non-targeted proteomics}) AND NOT TITLE-ABS-KEY ({untargeted proteomics})) AND (LIMIT-TO (DOCTYPE, "ar"))	39	9
(TITLE-ABS-KEY ({targeted proteomics}) AND TITLE-ABS-KEY ({Q-TOF}) AND NOT TITLE-ABS-KEY ({non-targeted proteomics}) AND NOT TITLE-ABS-KEY ({untargeted proteomics})) AND (LIMIT-TO (DOCTYPE, "ar"))	2	0
(TITLE-ABS-KEY ({targeted proteomics}) AND TITLE-ABS-KEY ({immunoassay}) AND NOT TITLE-ABS-KEY ({non-targeted proteomics}) AND NOT TITLE-ABS-KEY ({untargeted proteomics})) AND (LIMIT-TO (DOCTYPE, "ar"))	24	14

4. Recent Advances in Triple Quadrupole Mass Analyzer Technology and QqQ-Based Methodologies

From the above analysis, we can conclude that immunoassays remain the main competitors of QqQ-based methods. The former has several advantages (Table 8), which at the same time are the main disadvantages when implementing MS-based methods in biomedical applications. However, in recent years, new developments have largely eliminated these disadvantages and facilitated the application of MS-based methods. These

developments make chromatography–mass spectrometry more accessible and increase the speed of analysis.

Table 8. Advantages and disadvantages of immunoassays and MS-based assays.

	Advantages	Disadvantages
Immunoassays	Low limit of detection (LOD) Low equipment cost Simplicity of implementation Unspecialized staff (low staff cost) High throughput rate	High reagents' costs Ethical issues (animal use in antibody production) Specificity problems One component assay Kit–level variations
Mass Spectrometry	Highly specific Low limit of detection (LOD) Multi-component (multiplexing) analysis Low reagents' costs	Challenging method development and implementation Specialized staff (high staff cost) High equipment cost (initial investment) Labor sample pre-treatment step Low throughput rate

4.1. Making the Chromatography–Mass Spectrometry More Accessible—Automatization of Method Development and Application

Developing the LC-MS or GC-MS method is a complex and time-consuming process requiring an analyst with a high level of knowledge and experience. Automatization of the method's development, optimization, and measurement quality control/quality assurance intend to address the drawbacks of the challenging method development and implementation and the need for specialized staff. Software for automatic chromatographic method development and optimization has been created and commercialized [57–59]. Software to help automate the development of targeted triple quadrupole methods has also been introduced to the market [60]. This software can optimize MRM's specific parameters and ion source parameters in a fully automated or semi-automated fashion [60]. Another important feature is the automatic system troubleshooting, which provides timely notification of maintenance needs. All these software developments simplify the use of LC-MS and GC-MS instrumentation and make their application in biomedical research more attractive. Method development can be significantly simplified using LC-MS/MS complete kits supplied by specialized providers (e.g., Chromsystems™ (Gräfelfing, Germany), Recipe™ (Vaughan, ON, USA), and Waters™ (Milford, MA, USA)). These kits include all the reagents and materials to transfer the method developed by the provider to the laboratory applying the method: analytical columns, mobile phases, controls, and calibrators. LC-MS/MS kits for TDM, newborn screening, steroids, and amino acid analyses are available on the market.

4.2. Increasing the Throughput Rate by Reducing the Analysis Time

The latest developments both in chromatography and mass spectrometry have increased the throughput rated of LC-MS and GC-MS. The shift from HPLC to UHPLC (or UPLC) started in 2004 and led to a significant increase in chromatographic resolution and a reduction in separation time [61]. To couple mass spectrometry with the UHPLC data, the acquisition rate by mass spectrometry was increased to fit the reduction in chromatographic peak width from more than 10 s (HPLC) to 1–2 s (UHPLC), and sufficient data points (at least 10) were collected to ensure an excellent chromatographic peak shape and, finally, excellent quantitation. For the full-scan mode, this was achieved by a considerable increase in scan speed from ~650 Da/s in 1970 to ~10,000 in 2012 [62] and up to 30,000 Da/s nowadays (depending on the model, Supplementary Table S1). Concerning Multiple Reaction Monitoring (MRM, Figure 3), one of the most widely used MS modes today, the implementation

of algorithms for scheduling MRM according to the elution time of the components of interest significantly increased the number of transitions to be monitored concurrently (up to 500 transitions per second) and, thus, the number of analytes that can be quantified in a single run. Moreover, this scheduling removes the requirement for baseline chromatographic resolution and enables the quantification of co-eluting compounds (Figure 4). Thus, by the application of scheduled MRM, 151 pesticides were quantified by UHPLC-QqQ-MS/MS in 12 min [63]. Different vendors have developed these algorithms and have different trademarks; AB SCIEX (Framingham, MA, USA) calls this approach Scheduled MRM™, Agilent (Santa Clara, CA, USA) named it Dynamic MRM, while Thermo (Waltham, MA, USA) calls it "timed-SRM" but they all work in basically the same way.

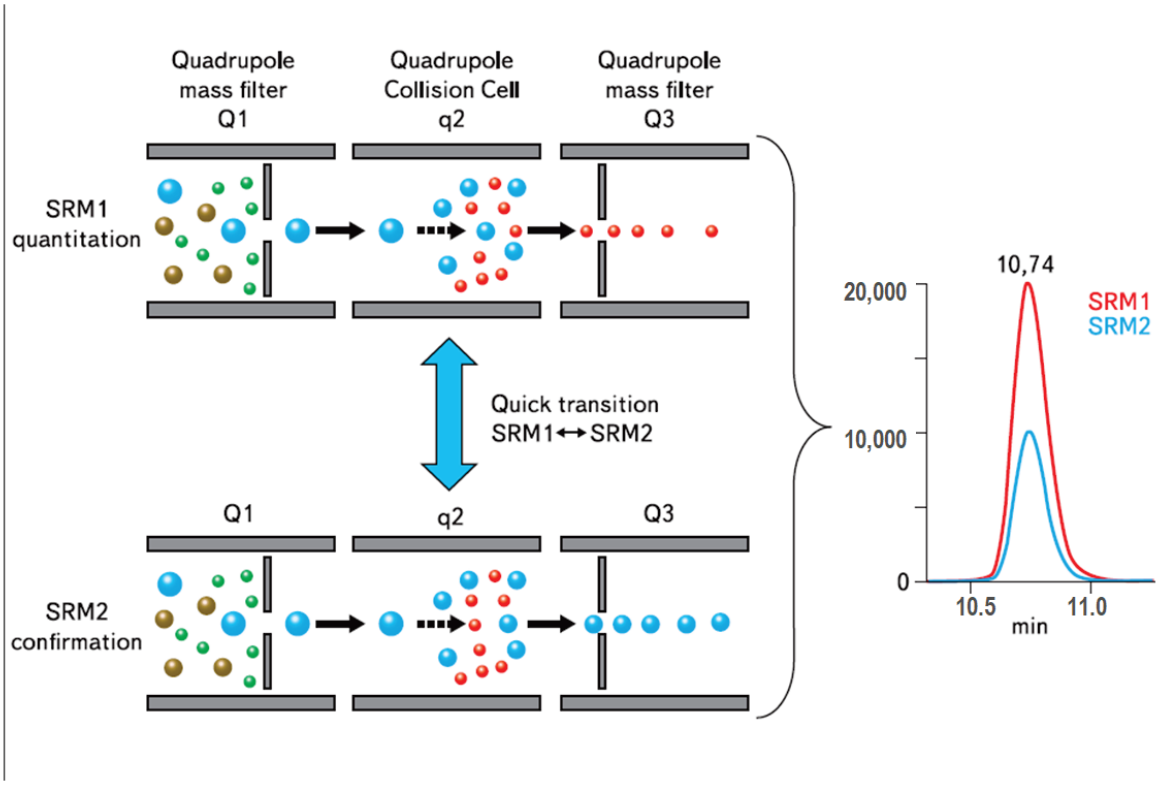


Figure 3. Operation of triple quadrupole MS in Multiple Reaction Monitoring (MRM) mode. Q1, Q2, and Q3 are constituent parts of triple quadrupole MS. In MRM mode Q1 and Q3 represent two mass filters for precursor and product ion selection, while Q2 (collision cell) creates fragment ions via collisionally induced dissociation (CID). The first mass filter Q1 selects the desired precursor ion with defined m/z *from the ions produced by the compound fragmentation in the ion so*urce. However, due to the low resolution of a quadrupole mass filter, the ions within $m/z \pm 1$ from other co-eluting compounds/contaminants can also pass Q1 filter (where ± 1 is the typical resolution of quadrupole mass filter, nowadays much improved (Supplementary Table S1)). After passing Q1, the ions are fragmented in Q2. Q3 selects only product ions specific to the desired precursor ion. There is very little probability that other ions within $m/z \pm 1$ have the same product ions and these two levels of mass selection ensure high selectivity of QqQ. Due to high selectivity, background noise is minimized, resulting in a higher signal-to-noise ratio and increased sensitivity. The transition from precursor ion to product ion is a fragmentation reaction. Morden QqQ mass spectrometer can monitor about 500 fragmentation reactions per second (Supplementary Table S1). Usually, two to four transitions are monitored using one product ion for quantitation (quantifier or target ion) and the other product ions (qualifier ion/ions) for confirmation of the analyte's identity. The ratio of the intensities of the quantifier and qualifier ions must be within the tolerance limits.

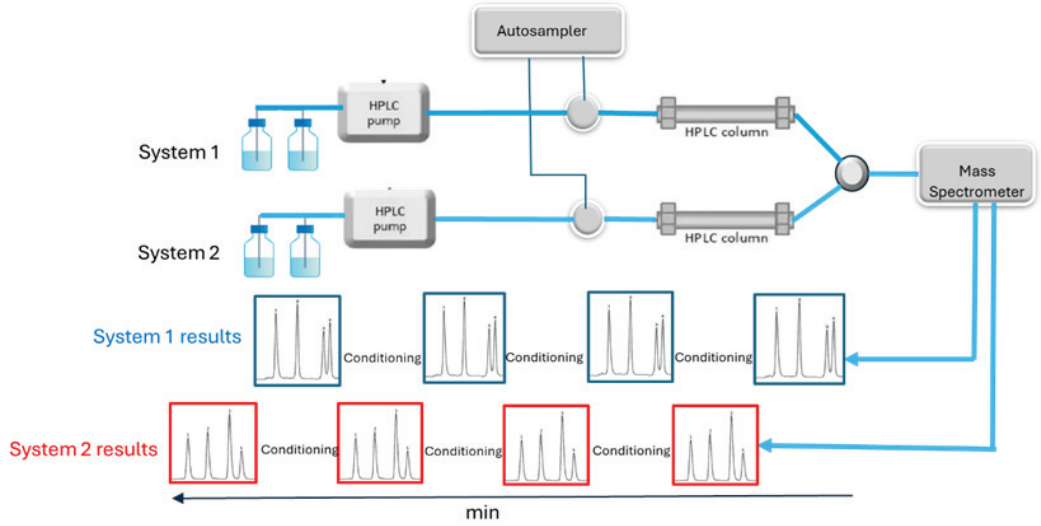


Figure 4. LC–multiplexing (duplexing) by connecting the two independent LC systems to one mass spectrometer in alternating mode (blue arrows). Each system is connected to the mass spectrometer in turn and only when the target components are eluting (dark-blue frames). Meanwhile, column conditioning and preparation for sample introduction are performed in the second system (red frames). Two different applications can be run in parallel (increased flexibility) or the same application on two LC systems (increased throughput).

A significant increase in sample throughput rate was also achieved in the above-mentioned RapidFire™-MS/MS system with an automated online solid-phase extraction directly integrated with the triple quadrupole MS [43]. This direct integration was made possible by advances in mass spectrometry, enabling the quantification of co-eluting compounds.

Sample preparation or sample pre-treatment has been the most time-consuming and error-prone step in sample analysis, which is mainly responsible for the low throughput of GC-MS- and LC-MS-based methods. This bottleneck was addressed by the development of automated (robotic) sample preparation systems and online with column-switching sample treatment techniques [64–67]. With the successful introduction of automation, the cost of analysis falls and the acquired data quality improves. Many instrumental solutions for automated sample preparation are currently available on the market, which are reviewed in detail in other publications [68,69].

5. Future Perspectives: The Transformation of LC-MS/MS to a Fully Automated Clinical Analyzer

The complete automation of the analysis by integrating most steps in one device is the key to implementing LC-MS/MS into routine clinical settings. In the last decade, such efforts were made to reduce the operator's involvement in the process and, thus, make this high-performance technology available to less-trained staff, accelerate the analysis, and increase its throughput [70]. A milestone of these efforts is the all-in-one Cascadion™ SM Clinical Analyzer (Thermo Fisher Scientific, Vantaa, Finland) launched in 2018 [71]. This analyzer comprises a fully automated sample preparation compartment, two parallel LC channels, and triple quadrupole MS equipped with an electrospray ionization interface. Triple quadrupole MS was selected as the most suitable technology for targeted quantitative analysis, mainly implemented in clinical laboratories and referred to in the above sections. Two separate chromatographic channels with multiplexing capability (Figure 4) ensure up to 25 samples/h (serum or plasma) throughput or two different assays to run parallel into a single MS [72,73].

6. Conclusions

The observed progress in biomedical research and applications is directly related to the increasing use of mass spectrometry, and QqQ is the primary mass analyzer, the "workhorse", used in the previous two decades. The number of biomedical studies utilizing QqQ has seen a 2–3-fold increase in the current decade compared to the previous. The triple quadrupole is most intensively used in the field of endocrine research and testing, it dominates in newborn screening and therapeutic drug monitoring, and is utilized in the emerging fields of target metabolomics and proteomics. Recent advances in chromatography–QqQ MS significantly reduced analysis time and increased the throughput of analysis. Automating or simplifying the crucial steps in LC-MS/MS method development and application reduced the demand for highly educated specialists to implement this technique and made it more attractive and available for routine clinical applications. Indeed, according to the data from different quality assurance programs, the number of laboratories using an LC-MS platform for routine applications increased, e.g., in endocrine testing from 3% to 18% from 2011 to 2019 and in 25-hydroxyvitamin D measurements from 0 in 2004 to 17% in 2017 and 21% in 2021 [74,75]. On, the contrary, the relative rate of immunoassay utilization—a major competitor of chromatography–mass spectrometry—decreased in endocrine research and as well as in therapeutic drug monitoring (TDM) and forensic toxicology.

Thus, taking into account the constant work of the main manufacturers to improve triple quadrupole figures of merit as well as the observed expansion of its use in biomedicine, it can be expected that triple quadrupole mass spectrometry will continue to hold a significant share in biomedical research and will be more extendedly used in routine clinical applications.

Supplementary Materials: The following supporting information can be downloaded at: https://www.mdpi.com/article/10.3390/molecules29235808/s1, Table S1: Specification of some modern mass analysers.

Author Contributions: Conceptualization, A.T., A.E.N. and A.A.S.; Investigation N.N.E., A.A.E., A.N.K., E.Y.D. and K.V.V.; Resources—K.V.V. and A.A.S.; Data curation—A.Y.A., A.A.S. and K.V.V.; Writing—original draft preparation N.N.E., A.A.E., A.N.K., E.Y.D., A.T. and K.V.V.; Writing—review and editing, A.T., N.N.E., A.A.E., E.Y.D., K.V.V. and A.A.S.; Supervision, A.T., A.E.N. and A.A.S. Project administration, A.E.N., A.T. and A.Y.A. Funding acquisition, A.E.N., K.V.V. and A.A.S. All authors have read and agreed to the published version of the manuscript.

Funding: The authors gratefully acknowledge the financial support from the Ministry of Science and Higher Education of the Russian Federation in the framework of Agreements No. 075-02-2022-1674 and No. 075-03-2023-097.

Data Availability Statement: No new data were created or analyzed in this study.

Conflicts of Interest: The authors declare no conflicts of interest. The funders had no role in the design of the study; in the collection, analyses, or interpretation of data; in the writing of the manuscript; or in the decision to publish the results.

References

1. Chace, D.H. Mass spectrometry-based diagnostics: The upcoming revolution in disease detection has already arrived. *Clin. Chem.* **2003**, *49*, 1227–1228. [CrossRef] [PubMed]
2. Bravo-Veyrat, S.; Hopfgartner, G. Mass spectrometry based high-throughput bioanalysis of low molecular weight compounds: Are we ready to support personalized medicine? *Anal. Bioanal. Chem.* **2022**, *414*, 181–192. [CrossRef] [PubMed]
3. Hristova, J.; Svinarov, D. Enhancing precision medicine through clinical mass spectrometry platform. *Biotechnol. Biotechnol. Equip.* **2022**, *36*, 106–116. [CrossRef]
4. Gelb, M.H.; Basheeruddin, K.; Burlina, A.; Chen, H.J.; Chien, Y.H.; Dizikes, G.; Dorley, C.; Giugliani, R.; Hietala, A.; Hong, X.; et al. Liquid Chromatography–Tandem Mass Spectrometry in Newborn Screening Laboratories. *Int. J. Neonatal Screen.* **2022**, *8*, 62. [CrossRef] [PubMed]
5. Rankin-Turner, S.; Heaney, L.M. Mass spectrometry in the clinical laboratory. A short journey through the contribution to the scientific literature by CCLM. *Clin. Chem. Lab. Med.* **2023**, *61*, 873–879. [CrossRef]

6. Yost, R.A.; Enke, C.G. Selected ion fragmentation with a tandem quadrupole mass spectrometer. *J. Am. Chem. Soc.* **1978**, *100*, 2274–2275. [CrossRef]
7. Voronin, S.V.; Voronina, V.G.; Zakharova, E.Y.; Egorova, S.V.; Bruenok, E.V.; Chausova, P.A.; Zinchenko, R.; Kutsev, S.I. Experience of newborn screening for 37 hereditary metabolic diseases by tandem mass spectrometry in Primorsky Region, Russia. *Med. Genet.* **2022**, *21*, 51–55. [CrossRef]
8. Berry, S.A. Newborn Screening. *Clin. Perinatol.* **2015**, *42*, 441–453. [CrossRef]
9. Yoon, H.R. Screening newborns for metabolic disorders based on targeted metabolomics using tandem mass spectrometry. *Ann. Pediatr. Endocrinol. Metab.* **2015**, *20*, 119–124. [CrossRef]
10. Therrell, B.L.; Padilla, C.D.; Loeber, J.G.; Kneisser, I.; Saadallah, A.; Borrajo, G.J.C.; Adams, J. Current status of newborn screening worldwide: 2015. *Semin. Perinatol.* **2015**, *39*, 171–187. [CrossRef]
11. Therrell, B.L.; Padilla, C.D.; Borrajo, G.J.C.; Khneisser, I.; Schielen, P.; Knight-Madden, J.; Malherbe, H.L.; Kase, M. Current Status of Newborn Bloodspot Screening Worldwide 2024: A Comprehensive Review of Recent Activities (2020–2023). *Int. J. Neonatal. Screen* **2024**, *10*, 38. [CrossRef]
12. Voronin, S.V.; Kutsev, S.I. Neonatal screening for hereditary diseases in Russia: Yesterday, today, and tomorrow. *Neonatology* **2022**, *10*, 34–39. [CrossRef]
13. Chace, D.H.; DiPerna, J.C.; Naylor, E.W. Laboratory integration and utilization of tandem mass spectrometry in neonatal screening: A model for clinical mass spectrometry in the next millennium. *Acta Paediatr. Suppl.* **1999**, *88*, 45–47. [CrossRef] [PubMed]
14. Crafa, A.; Calogero, A.E.; Cannarella, R.; Mongioi', L.M.; Condorelli, R.A.; Greco, E.A.; Aversa, A.; La Vignera, S. The Burden of Hormonal Disorders: A Worldwide Overview with a Particular Look in Italy. *Front. Endocrinol.* **2021**, *12*, 694325. [CrossRef] [PubMed]
15. Kahn, C.R.; Roth, J. Rosalyn Sussman Yalow (1921–2011). *Proc. Natl. Acad. Sci. USA* **2012**, *109*, 669–670. [CrossRef]
16. Casals, G.; Costa, R.F.; Rull, E.U.; Escobar-Morreale, H.F.; Argente, J.; Sesmilo, G.; Biagetti, B. Recommendations for the measurement of sexual steroids in clinical practice. A position statement of SEQCML/SEEN/SEEP. *Adv. Lab. Med.* **2023**, *4*, 52–60. [CrossRef]
17. Taylor, A.E.; Keevil, B.; Huhtaniemi, I.T. Mass spectrometry and immunoassay: How to measure steroid hormones today and tomorrow. *Eur. J. Endocrinol.* **2015**, *173*, D1–D12. [CrossRef]
18. Andrew, R.; Homer, N.Z.M. Mass spectrometry: Future opportunities for profiling and imaging steroids and steroid metabolites. *Curr. Opin. Endocr. Metab. Res.* **2020**, *15*, 71–78. [CrossRef]
19. Wang, Z.; Wang, H.; Peng, Y.; Chen, F.; Zhao, L.; Li, X.; Qin, J.; Li, Q.; Wang, B.; Pan, B.; et al. A liquid chromatography-tandem mass spectrometry (LC-MS/MS)-based assay to profile 20 plasma steroids in endocrine disorders. *Clin. Chem. Lab. Med. (CCLM)* **2020**, *58*, 1477–1487. [CrossRef]
20. Seger, C.; Salzmann, L. After another decade: LC–MS/MS became routine in clinical diagnostics. *Clin. Biochem.* **2020**, *82*, 2–11. [CrossRef]
21. Handelsman, D.J.; Wartofsky, L. Requirement for mass spectrometry sex steroid assays in the Journal of Clinical Endocrinology and Metabolism. *J. Clin. Endocrinol. Metab.* **2013**, *98*, 3971–3973. [CrossRef] [PubMed]
22. Vesper, H.W.; Botelho, J.C.; Shacklady, C.; Smith, A.; Myers, G.L. CDC project on standardizing steroid hormone measurements. *Steroids* **2008**, *73*, 1286–1292. [CrossRef] [PubMed]
23. Yuan, T. A review on analysis of steroid profile in different biological matrices. *Microchem. J.* **2022**, *172*, 106897. [CrossRef]
24. Olesti, E.; Boccard, J.; Visconti, G.; González-Ruiz, V.; Rudaz, S. From a single steroid to the steroidome: Trends and analytical challenges. *J. Steroid Biochem. Mol. Biol.* **2021**, *206*, 105797. [CrossRef]
25. Hill, M.; Hána, V.; Velíková, M.; Pařízek, A.; Kolátorová, L.; Vítků, J.; Škodová, T.; Šimková, M.; Šimják, P.; Kancheva, R.; et al. A method for determination of one hundred endogenous steroids in human serum by gas chromatography-tandem mass spectrometry. *Physiol. Res.* **2019**, *68*, 179–207. [CrossRef]
26. Delpierre, C.; Lefèvre, T. Precision and personalized medicine: What their current definition says and silences about the model of health they promote. Implication for the development of personalized health. *Front. Sociol.* **2023**, *8*, 1112159. [CrossRef]
27. Decosterd, L.A.; Widmer, N.; André, P.; Aouri, M.; Buclin, T. The emerging role of multiplex tandem mass spectrometry analysis for therapeutic drug monitoring and personalized medicine. *TrAC-Trends Anal. Chem.* **2016**, *84*, 5–13. [CrossRef]
28. Drugbank. Available online: https://go.drugbank.com/categories/DBCAT003972 (accessed on 6 March 2024).
29. Gavan, S.P.; Thompson, A.J.; Payne, K. The economic case for precision medicine. *Expert. Rev. Precis. Med. Drug Dev.* **2018**, *3*, 1–9. [CrossRef]
30. Collins, F.S.; Varmus, H. A new initiative on precision medicine. *N. Engl. J. Med.* **2015**, *372*, 793–795. [CrossRef]
31. European Commission. Council conclusions on personalised medicine for patients. *Off. J. Eur. Union* **2015**, *451*, 1–26.
32. Beccia, F.; Hoxhaj, I.; Castagna, C.; Strohäker, T.; Cadeddu, C.; Ricciardi, W.; Boccia, S. An overview of Personalized Medicine landscape and policies in the European Union. *Eur. J. Public. Health* **2022**, *32*, 844–851. [CrossRef] [PubMed]
33. *Standard for Mass Spectral Analysis in Forensic Toxicology*, 1st ed.; American Academy of Forensic Sciences (AAFS): Colorado Springs, CO, USA, 2023; Available online: https://www.aafs.org/sites/default/files/media/documents/098_Std_e1.pdf (accessed on 1 March 2024).

34. *Standard for Identification Criteria in Forensic Toxicology*, 1st ed.; American Academy of Forensic Sciences (AAFS): Colorado Springs, CO, USA, 2022; Available online: https://www.aafs.org/asb-standard/standard-identification-criteria-forensic-toxicology (accessed on 3 September 2024).
35. *2002/657/EC*; Commission Decision of 12 August 2002 Implementing Council Directive 96/23/EC Concerning the Performance of Analytical Methods and the Interpretation of Results (Text with EEA Relevance) (Notified Under Document Number C(2002) 3044). European Commission: Brussels, Belgium, 2002; pp. 8–36.
36. Busardò, F.P.; Pacifici, R.; Pichini, S. Mass spectrometry vs. immunoassay in clinical and forensic toxicology: Qui modus in rebus est? *Clin. Chem. Lab. Med.* **2017**, *55*, e236–e237. [CrossRef] [PubMed]
37. Mohr, A.L.A.; Logan, B.K.; Fogarty, M.F.; Krotulski, A.J.; Papsun, D.M.; Kacinko, S.L.; Huestis, M.A.; Ropero-Miller, J.D. Reports of Adverse Events Associated with Use of Novel Psychoactive Substances, 2017–2020: A Review. *J. Anal. Toxicol.* **2022**, *46*, e116–e185. [CrossRef] [PubMed]
38. European Drug Report 2023: Trends and Developments; European Monitoring Centre for Drugs and Drug Addiction. 2023. Available online: https://d9www.euda.europa.eu/publications/european-drug-report/2023_en#level-9-section7 (accessed on 1 March 2024).
39. Kaushik, N.; Khangulov, V.S.; O'hara, M.; Arnaout, R. Reduction in laboratory turnaround time decreases emergency room length of stay. *Open Access Emerg. Med.* **2018**, *10*, 37–45. [CrossRef]
40. Archer, J.R.H.; Wood, D.M.; Dargan, P.I. How to use toxicology screening tests. *Arch. Dis. Child.-Educ. Amp; Pract. Ed.* **2012**, *97*, 194–199. [CrossRef]
41. Vale, A.; Bradberry, S. Assessment and diagnosis of the poisoned patient. *Medicine* **2016**, *44*, 82–86. [CrossRef]
42. Wiencek, J.R.; Colby, J.M.; Nichols, J.H. Chapter Five-Rapid Assessment of Drugs of Abuse. In *Advances in Clinical Chemistry*; Makowski, G.S., Ed.; Elsevier: Amsterdam, The Netherlands, 2017; Volume 80, pp. 193–225.
43. Jannetto, P.J.; Langman, L.J. High-throughput online solid-phase extraction tandem mass spectrometry: Is it right for your clinical laboratory? *Clin. Biochem.* **2016**, *49*, 1032–1034. [CrossRef]
44. Neifeld, J.R.; Regester, L.E.; Holler, J.M.; Vorce, S.P.; Magluilo, J., Jr.; Ramos, G.; Bosy, T.Z. Ultrafast Screening of Synthetic Cannabinoids and Synthetic Cathinones in Urine by RapidFire-Tandem Mass Spectrometry. *J. Anal. Toxicol.* **2016**, *40*, 379–387. [CrossRef]
45. Odom, J.D.; Sutton, V.R. Metabolomics in Clinical Practice: Improving Diagnosis and Informing Management. *Clin. Chem.* **2021**, *67*, 1606–1617. [CrossRef]
46. Wishart, D.S. Emerging applications of metabolomics in drug discovery and precision medicine. *Nat. Rev. Drug Discov.* **2016**, *15*, 473–484. [CrossRef]
47. Alonso, A.; Marsal, S.; Julià, A. Analytical Methods in Untargeted Metabolomics: State of the Art in 2015. *Front. Bioeng. Biotechnol.* **2015**, *3*, 23. [CrossRef] [PubMed]
48. Di Minno, A.; Gelzo, M.; Stornaiuolo, M.; Ruoppolo, M.; Castaldo, G. The evolving landscape of untargeted metabolomics. *Nutr. Metab. Cardiovasc. Dis.* **2021**, *31*, 1645–1652. [CrossRef] [PubMed]
49. Alseekh, S.; Fernie, A.R. Metabolomics 20 years on: What have we learned and what hurdles remain? *Plant J. Cell Mol. Biol.* **2018**, *94*, 933–942. [CrossRef] [PubMed]
50. Rey-Stolle, F.; Dudzik, D.; Gonzalez-Riano, C.; Fernandez-Garcia, M.; Alonso-Herranz, V.; Rojo, D.; Barbas, C.; Garcia, A. Low and high resolution gas chromatography-mass spectrometry for untargeted metabolomics: A tutorial. *Anal. Chim. Acta* **2022**, *1210*, 339043. [CrossRef]
51. Fiehn, O. Metabolomics by Gas Chromatography–Mass Spectrometry: Combined Targeted and Untargeted Profiling. *Curr. Protoc. Mol. Biol.* **2016**, *114*, 30.4.1–30.4.32. [CrossRef]
52. Al-Amrani, S.; Al-Jabri, Z.; Al-Zaabi, A.; Alshekaili, J.; Al-Khabori, M. Proteomics: Concepts and applications in human medicine. *World J. Biol. Chem.* **2021**, *12*, 57–69. [CrossRef]
53. Wasinger, V.C.; Cordwell, S.J.; Cerpa-Poljak, A.; Yan, J.X.; Gooley, A.A.; Wilkins, M.R.; Duncan, M.W.; Harris, R.; Williams, K.L.; Humphery-Smith, I. Progress with gene-product mapping of the Mollicutes: Mycoplasma genitalium. *Electrophoresis* **1995**, *16*, 1090–1094. [CrossRef]
54. Elschenbroich, S.; Kislinger, T. Targeted proteomics by selected reaction monitoring mass spectrometry: Applications to systems biology and biomarker discovery. *Mol. BioSystems* **2011**, *7*, 292–303. [CrossRef]
55. Van Gool, A.; Corrales, F.; Čolović, M.; Krstić, D.; Oliver-Martos, B.; Martínez-Cáceres, E.; Jakasa, I.; Gajski, G.; Brun, V.; Kyriacou, K.; et al. Analytical techniques for multiplex analysis of protein biomarkers. *Expert. Rev. Proteom.* **2020**, *17*, 257–273. [CrossRef]
56. Percy, A.J.; Yang, J.; Hardie, D.B.; Chambers, A.G.; Tamura-Wells, J.; Borchers, C.H. Precise quantitation of 136 urinary proteins by LC/MRM-MS using stable isotope labeled peptides as internal standards for biomarker discovery and/or verification studies. *Methods* **2015**, *81*, 24–33. [CrossRef]
57. Bos, T.S.; Boelrijk, J.; Molenaar, S.R.A.; van 't Veer, B.; Niezen, L.E.; van Herwerden, D.; Samanipour, S.; Stoll, D.R.; Forré, P.; Ensing, B.; et al. Chemometric Strategies for Fully Automated Interpretive Method Development in Liquid Chromatography. *Anal. Chem.* **2022**, *94*, 16060–16068. [CrossRef] [PubMed]
58. Galushko, S.V.; Shishkina, I.; Urtans, E.; Rotkaja, O. ChromSword®: Software for Method Development in Liquid Chromatography. In *Software-Assisted Method Development in High Performance Liquid Chromatography*; World Scientific Publishing Co. Pte. Ltd.: Singapore, 2019; pp. 53–94.

59. MoInjr, I.; Rieger, H.J.; Kormsny, R. Modeling of HPLC Methods Using QbD Principles in HPLC. *Adv. Chromatogr.* **2017**, *53*, 331–350. [PubMed]
60. Fan, A.; He, V.J.; Pyke, J.; Lopez, E.; Aurand, S.; Wu, L.; Batoon, P.M. *Advances in Mass Spectrometry Instrument Intelligence*; Separation Science: Ashford, UK, 2022; Available online: https://www.sepscience.com/advances-in-mass-spectrometry-instrument-intelligence/ (accessed on 1 March 2024).
61. Fekete, S.; Schappler, J.; Veuthey, J.-L.; Guillarme, D. Current and future trends in UHPLC. *TrAC Trends Anal. Chem.* **2014**, *63*, 2–13. [CrossRef]
62. Rodriguez-Aller, M.; Gurny, R.; Veuthey, J.L.; Guillarme, D. Coupling ultra high-pressure liquid chromatography with mass spectrometry: Constraints and possible applications. *J. Chromatogr. A* **2013**, *1292*, 2–18. [CrossRef]
63. Wang, J.; Chow, W.; Cheung, W. Application of a Tandem Mass Spectrometer and Core–Shell Particle Column for the Determination of 151 Pesticides in Grains. *J. Agric. Food Chem.* **2011**, *59*, 8589–8608. [CrossRef]
64. Dugheri, S.; Mucci, N.; Cappelli, G.; Trevisani, L.; Bonari, A.; Bucaletti, E.; Squillaci, D.; Arcangeli, G. Advanced Solid-Phase Microextraction Techniques and Related Automation: A Review of Commercially Available Technologies. *J. Anal. Methods Chem.* **2022**, *2022*, 8690569. [CrossRef]
65. Kataoka, H. Sample preparation for liquid chromatography. In *Liquid Chromatography: Applications*, 2nd ed.; Elsevier: Amsterdam, The Netherlands, 2017; Volume 2, pp. 1–37.
66. Palaiogiannis, D.; Bekou, E.; Pazaitou-Panayiotou, K.; Samanidou, V.; Tsakalof, A. On-line SPE sample treatment as a tool for method automatization and detection limits reduction: Quantification of 25-hydroxyvitamin D3/D2. *J. Chromatogr. B Analyt. Technol. Biomed. Life Sci.* **2017**, *1043*, 219–227. [CrossRef]
67. Vargas Medina, D.A.; Maciel, E.V.S.; Lanças, F.M. Modern automated sample preparation for the determination of organic compounds: A review on robotic and on-flow systems. *TrAC Trends Anal. Chem.* **2023**, *166*, 117171. [CrossRef]
68. Maciel, E.V.S.; Vargas Medina, D.A.; Borsatto, J.V.B.; Lanças, F.M. Towards a universal automated and miniaturized sample preparation approach. *Sustain. Chem. Pharm.* **2021**, *21*, 100427. [CrossRef]
69. More, D.; Khan, N.; Tekade, R.K.; Sengupta, P. An update on current trend in sample preparation automation in bioanalysis: Strategies, challenges and future direction. *Crit. Rev. Anal. Chem.* **2024**, 1–25. [CrossRef]
70. Zhang, Y.V.; Rockwood, A. Impact of automation on mass spectrometry. *Clin. Chim. Acta* **2015**, *450*, 298–303. [CrossRef] [PubMed]
71. ThermoScientific. Fully Automated, Random Access Analyzer for In Vitro Diagnostic Use. Available online: https://www.thermofisher.com/diagnostic-education/dam/clinical-mass-spectrometry/global/resources/library/assets/D15952-08-Cascadion-SM-Clinical-Analyzer-TechSpecs-EN.pdf (accessed on 16 February 2024).
72. Junger, S.; Hoene, M.; Shipkova, M.; Danzl, G.; Schöberl, C.; Peter, A.; Lehmann, R.; Wieland, E.; Braitmaier, H. Automated LC-MS/MS: Ready for the clinical routine Laboratory? *J. Mass. Spectrom. Adv. Clin. Lab.* **2023**, *30*, 1–9. [CrossRef] [PubMed]
73. Benton, S.C.; Tetteh, G.K.; Needham, S.J.; Mücke, J.; Sheppard, L.; Alderson, S.; Ruppen, C.; Curti, M.; Redondo, M.; Milan, A.M. Evaluation of the 25-hydroxy vitamin D assay on a fully automated liquid chromatography-mass spectrometry system, the Thermo Scientific Cascadion SM Clinical Analyzer with the Cascadion 25-hydroxy vitamin D assay in a routine clinical laboratory. *Clin. Chem. Lab. Med.* **2020**, *58*, 1010–1017. [CrossRef] [PubMed]
74. Carter, G.D.; Berry, J.; Durazo-Arvizu, R.; Gunter, E.; Jones, G.; Jones, J.; Makin, H.L.J.; Pattni, P.; Sempos, C.T.; Twomey, P.; et al. Hydroxyvitamin D assays: An historical perspective from DEQAS. *J. Steroid Biochem. Mol. Biol.* **2017**, *177*, 30–35. [CrossRef]
75. Briggs, L.E.; Whitewood, J.K.; Williams, E.L. Analytical variation concerning total 25-hydroxyvitamin D measurement, where are we now? A DEQAS review of current assay performance. *J. Steroid Biochem. Mol. Biol.* **2023**, *231*, 106328. [CrossRef]

Disclaimer/Publisher's Note: The statements, opinions and data contained in all publications are solely those of the individual author(s) and contributor(s) and not of MDPI and/or the editor(s). MDPI and/or the editor(s) disclaim responsibility for any injury to people or property resulting from any ideas, methods, instructions or products referred to in the content.

molecules

MDPI

Article

Development of a Highly Sensitive Hybrid LC/MS Assay for the Quantitative Measurement of CTLA-4 in Human T Cells

Dong Wei [1], Kristin L. Horton [1], John Chen [2], Linlin Dong [1], Susan Chen [1], Kojo Abdul-Hadi [1], Ting Ting Zhang [1], Cierra N. Casson [1], Michael Shaw [1], Tsubasa Shiraishi [1], Brandon Wilkinson [1], Chengjie Ji [2] and Mark G. Qian [1,*]

[1] Takeda Pharmaceutical Company International Co., 35 Landsdowne Street, Cambridge, MA 02139, USA
[2] NovaBioAssays LLC, 52 Dragon Ct, Suite 3B, Woburn, MA 01801, USA
* Correspondence: mark.qian@takeda.com

Abstract: Cytotoxic T-lymphocyte-associated protein 4 (CTLA-4) is a check point protein expressed on the surface of T cells and plays a central role in regulating the immune response. In recent years, CTLA-4 has become a popular target for cancer immunotherapy in which blocking CTLA-4 can restore T-cell function and enhance the immune response against cancer. Currently, there are many CTLA-4 inhibitors in a variety of modalities, including cell therapies, which are being developed in both preclinical and clinical stages to further harness the potential of the target for the treatment of certain types of cancer. In drug discovery research, measuring the level of CTLA-4 in T cells is important for drug discovery and development because it provides key information for quantitative assessment of the pharmacodynamics, efficacy, and safety of the CTLA-4-based therapies. However, to our best knowledge, there is still no report of a sensitive, specific, accurate, and reliable assay for CTLA-4 measurement. In this work, an LC/MS-based method was developed to measure CTLA-4 in human T cells. The assay demonstrated high specificity with an LLOQ of 5 copies of CTLA-4 per cell when using 2.5 million T cells for analysis. As shown in the work, the assay was successfully used to measure CTLA-4 levels in subtype T-cell samples from individual healthy subjects. The assay could be applied in supporting the studies of CTLA-4-based cancer therapies.

Keywords: T-lymphocyte-associated protein 4 (CTLA-4); human T cells; LC/MS; quantification

1. Introduction

The adapted immune response of T cells is determined by T-cell antigen-receptor (TCR) signaling, as well as the co-stimulatory and co-inhibitory molecules such as CD28 and cytotoxic T-lymphocyte-associated protein 4 (CTLA-4). The carefully regulated dual CD28/CTLA-4 mechanisms ensure that the anti-pathogen and anti-tumor immune effects are carried out without autoimmune responses and collateral damage to normal tissues [1]. The expression of CTLA-4 has been demonstrated in lymphoid and myeloid cells as well as tumor cells. It was proposed that the blockage mechanism of CTLA-4 could be used in cancer treatments. The remarkable clinical results of ipilimumab, a CTLA-4 blocker, and its subsequent approval for the treatment of melanoma, opened a new era in immune-oncology [2–4]. While the checkpoint blockers that include anti-CTLA-4 and anti-programmed cell death protein-1/ligand-1 (PD1/PDL1) have demonstrated unprecedented efficacy in treating a number of cancers such as non-small cell lung cancer, melanoma, and urothelial carcinoma, the response rate remains unsatisfactory [2]. In contrast to CD28, the biology of CTLA-4, as well as the mechanism of action of anti-CTLA4 therapies, is not fully understood. While CD28 is constitutively expressed in all T cells, CTLA-4 is constitutively expressed only in regulatory T cells. Its level is low or not detectable in naïve, resting T cells but can be measured in induced T cells, as well as CD4 and CD8 T cells in cancer [5]. In addition, it was found that most CTLA-4 resides in the cytoplasmic vesicles, which could be trafficked to the plasma membrane upon activation.

The expression of CTLA-4 in cells has been evaluated by qPCR at mRNA levels, as well as by flow cytometry, Western blot, and immunohistochemistry including quantitative digital image analysis [5,6]. While these methodologies have been used extensively in the research of CTLA-4, they possess some inherent limitations including but not limited to insufficient sensitivity, semi-quantification, and/or the inability to differentiate and measure the intracellular proteins. Thus, a more sophisticated quantitative assay for CTLA-4 in human immune cells is needed which, if available, will enable better understanding of CTLA-4 biology, including the protein's baseline expression, turnover, and mechanism of T-cell activation. Equally important though, is the reliable measurement of CTLA-4 levels which would allow for a detailed quantitative pharmacological and toxicological assessment of the target in cancer immunotherapies. For example, the measured level can be used to determine the threshold of CTLA4 copies and/or the ratio of CD28 to CTLA4 required for the activation of CD8+ cytotoxic T cells for subsequent tumor killings. In addition, knowledge of the CTLA-4 level in diverse biological matrices and settings may also facilitate immune oncology drug discovery, including the understanding of target engagement, patient selection and stratification, prognostic and predicative assessment of drug responses. For these important reasons, we developed a quantitative method to measure the CTLA-4 level in human T cells using the hybrid liquid chromatography–mass spectrometry (LC/MS) technology.

In recent years, the LC/MS-based methodology, in particular when coupled with immunoprecipitation, has been widely used for the analysis of a broad spectrum of protein therapeutics as well as biomarkers [7–9]. For example, a hybrid LC/MS method has been developed to measure PD-1 and PD-L2 in human tumor samples using a proteomics approach as well as a hybrid LC/MS method [10–12].

In this paper, we describe the development of a highly specific and sensitive hybrid LC/MS assay that quantitatively measures the CTLA-4 level in human immune cells with a low detection limit of five copies per cell. The method was used to assess the CTLA-4 level from various T- and B cells isolated from human blood samples. As shown in the paper, the method could potentially be used as a tool for the study of CTLA-4 biology and the measurement of CTLA-4 biomarkers in patient blood samples.

2. Results and Discussion

2.1. Assay Design

Based on previous publications, the CTLA-4 protein is localized in the intracellular compartments as well as on the plasma membrane. Our assay is thus designed to allow for extraction and quantitative measurement of the total CTLA-4 level from the cell samples. There are two approaches in the immune extraction of the proteins from biological samples in the hybrid LC/MS methodologies shown in Figure 1. In the first approach, the target protein of interest is selectively captured by an antibody conjugated on magnetic beads. The captured protein is then enzymatically digested on or off beads into peptides. One or more unique peptides from the protein digest, from those with the highest mass-spectrometric response and the lowest interference from matrices, are typically chosen as surrogates to measure the protein abundance in the samples.

The second approach is termed Stable-Isotope Standards and Capture by Anti-Peptide Antibodies (SISCAPA), in which the total protein is extracted from the samples and enzymatically digested into peptides. An antibody against a targeted surrogate peptide is conjugated onto magnetic beads or packed in a column and is used to selectively extract the target surrogate peptide for analysis by LC/MS.

Since CTLA-4 is a cross-membrane protein with hydrophobic domains which may lead to loss due to aggregation and/or non-specific absorption onto vial surfaces, the second approach with the anti-peptide antibody is thus believed to be superior and was therefore used for the work described subsequently in the report. In our study, the total protein from the cell samples was dissolved directly in 8 M urea, denatured, alkylated, and

digested into peptides. This approach minimized the loss of the CTLA-4 analyte during the sample–preparation process and thereby maximized its recovery.

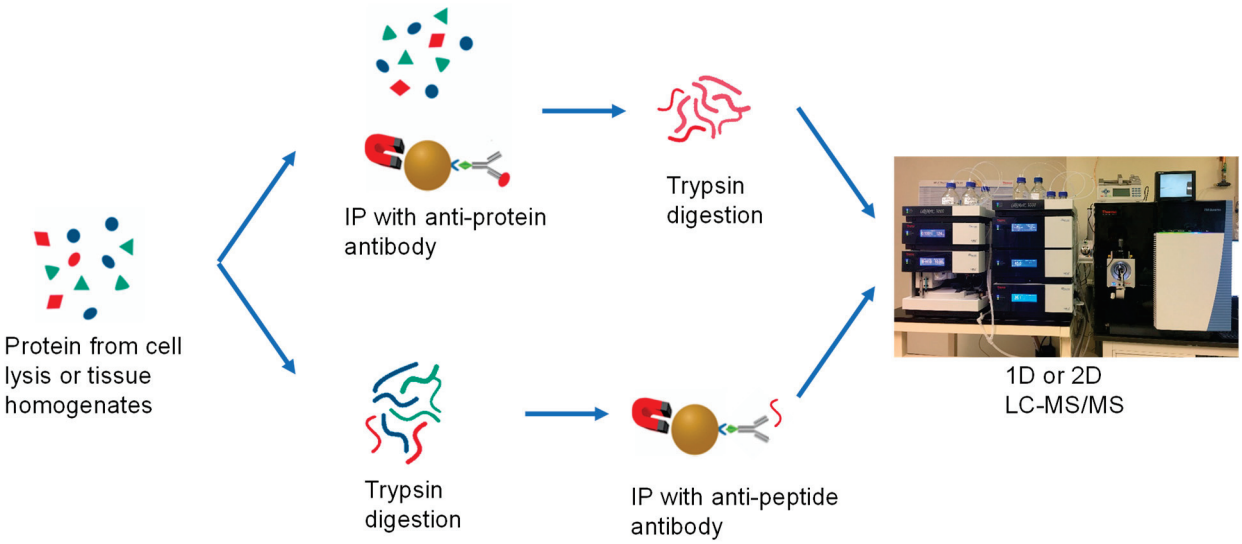


Figure 1. Two typical workflows for immunoprecipitation of the proteins from biological samples.

The assay was designed to measure the CTLA-4 protein in human T cells, which are typically isolated from human whole-blood samples and thus are inherently of limited sample quantities especially for cancer patients. To achieve the best sensitivity for such samples, a 2D nano-LC/MS system was employed. The extracted samples were first injected into a trap cartridge to enrich the analyte. Then, the analyte was eluted into a nano-LC column running at a nano flow prior to MS detection.

2.2. Selection of the Reference Standard and Surrogate Peptide

Human CTLA-4 is a homodimer membrane protein that includes an extracellular domain (ECD 36–161, UniProt P16410), a hydrophobic transmembrane section (162–182), and a cytoplasmic domain (183–223). For practical reasons, recombinant proteins that include the extracellular binding domain (36–161) were used as the reference material for method development and preparation of spiked standard/QC samples.

One of the key steps in developing a hybrid LC/MS assay is to choose a surrogate peptide that could render the optimal sensitivity, specificity, and minimal interference from biological matrices. In the hybrid method that uses an anti-peptide antibody to selectively extract the analyte (SISCAPA), the surrogate peptide is used for dual purposes: as the target antigen to generate polyclonal antibodies for immunocapture, and as the surrogate analyte for the target protein in LC/MS quantitation. Therefore, the surrogate peptide selected should have a high immunogenic potential after anchoring to a carrier protein for inducing polyclonal antibodies in rabbits. In our method development, the recombinant CTLA-4 was digested and tuned on the Thermo triple–quadrupole mass spectrometer. The most sensitive transition obtained was from peptide GIASFV[C]EYASPGK, a y8+ ion at m/z 911.4 from the doubly charged parent ion at m/z 743.3. Furthermore, the peptide was chosen as the surrogate peptide for its additional favorable attributes: (1) a unique peptide based on protein blast in human–protein databases; (2) a relative long peptide which was hypothesized to be favorable in polyclonal antibody generation.

2.3. Assay Performance

A recombinant CTLA-4 protein with Fc was used as the reference material and spiked into a surrogate matrix (0.1% BSA in PBS) to prepare standard curves. A representative calibration curve and related selected extracted ion chromatograms are shown in Figure 2. The linearity of the standard curve was $R^2 = 0.9921$. The accuracy of the back-calculated

standard samples was within ±20% of nominal concentrations. The dynamic range of the assay was 0.1 to 6.4 ng/mL with the lower limit of quantification (LLOQ) at 0.1 ng/mL. (Table 1).

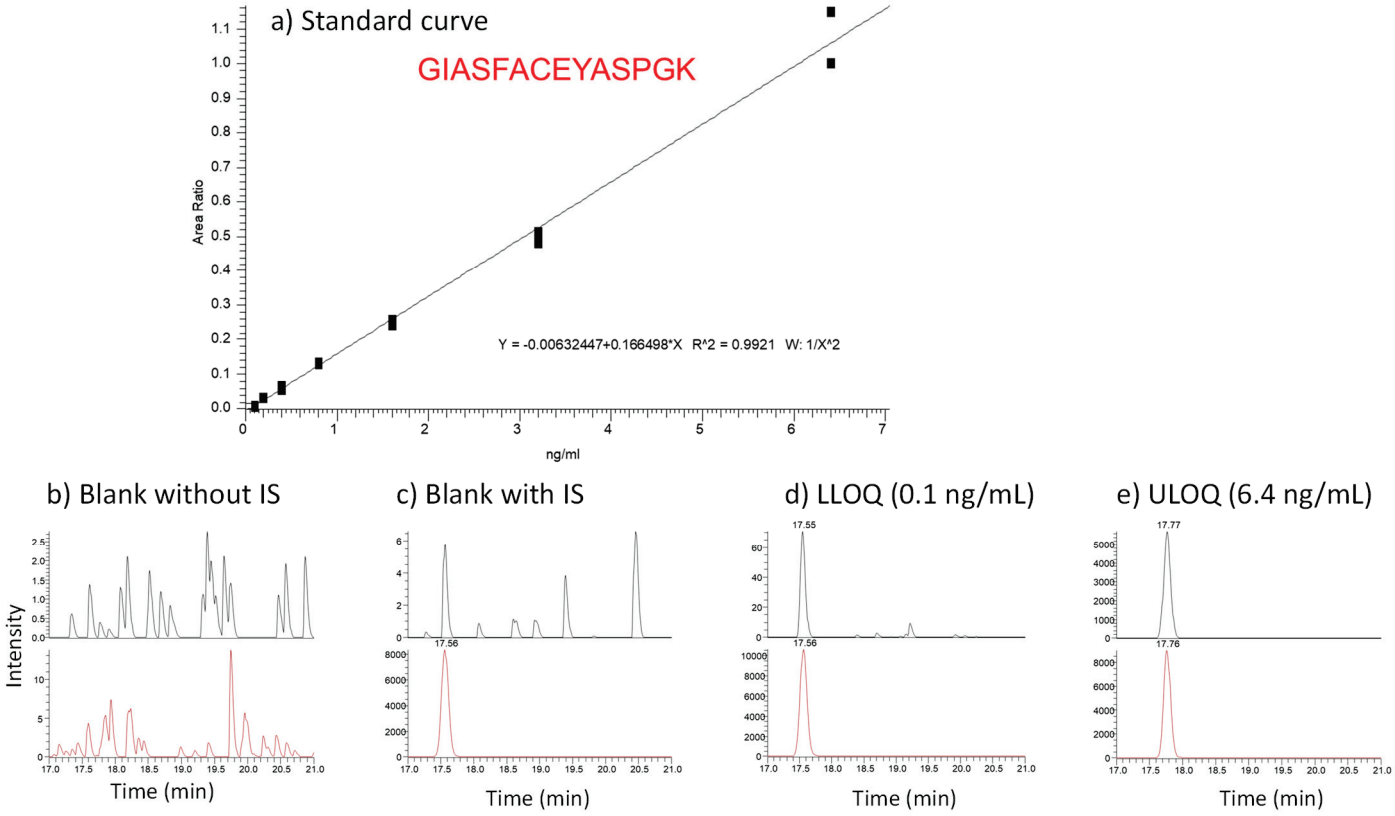


Figure 2. The standard curve and representative LC-MRM MS chromatograms.

Table 1. A Representative Standard Curve of Total CTLA-4 Assay.

Sample Type	Nominal CTLA-4 Conc. (ng/mL)	Back Calculated Conc. (ng/mL)	%Diff
Std1-1	0.1	0.07	−30% *
Std1-2	0.1	0.092	−8%
Std2-1	0.2	0.23	15%
Std2-2	0.2	0.131	−34% *
Std3-1	0.4	0.379	−5%
Std3-2	0.4	0.427	7%
Std4-1	0.8	0.84	5%
Std4-2	0.8	0.815	2%
Std5-1	1.6	1.581	−1%
Std5-2	1.6	1.489	−7%
Std6-1	3.2	3.122	−2%
Std6-2	3.2	2.94	−8%
Std7-1	6.4	6.954	9%
Std7-2	6.4	6.059	−5%

* Excluded from regression.

The assay also showed high specificity. In the chromatogram of the blank samples in the surrogate matrix, no interference peaks were found (Figure 2). Among all the samples tested, the CTLA-4 level in the CD19+ B cell samples was below the LLOQ (Figure 3).

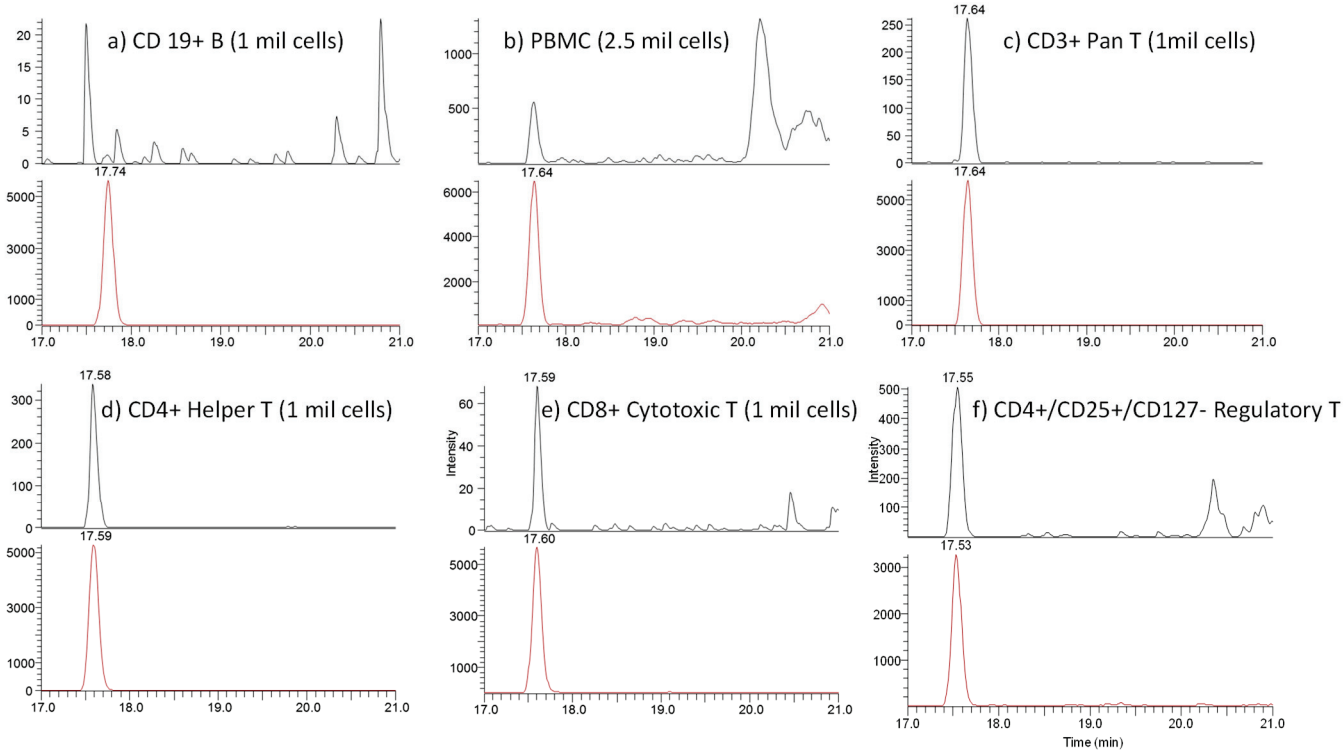


Figure 3. The representative LC-MRM MS Chromatograms for cell samples with analyte (**top**) and IS (**bottom**).

To determine the total percentage recovery of the reference standard spiked in human cell samples compared to that spiked in the surrogate matrix (0.1% BSA in PBS), a recovery experiment was carried out by spiking the reference standard at 0.400 ng/mL into B-cell and pan T-cell samples (0.5 million cells for each). The samples were measured using a standard curve in a surrogate matrix. The recovery was found to be 106% in spiked B-cell samples, which have no measurable level of endogenous CTLA-4. The recovery was slightly higher in the spiked pan T-cell samples (140%), which however included a measurable level of endogenous CTLA-4 at 0.253 ng/mL in the 0.5-million-cell sample. Since the endogenous CTLA-4 protein was different from the spiked reference standard, determining the true recovery of the analyte during the extraction and tryptic digestion was not feasible. However, the data demonstrated a comparable recovery of the CTLA-4 reference protein spiked in a surrogate matrix versus that spiked in B- and T-cell samples (Table 2).

To determine the parallelism of the assay method for the T-cell samples, the same batch of CD3+ pan T cells was used to prepare samples at 0.2, 0.5 and 1 million cells per well. The samples were measured against a standard curve. The measured CTLA-4 levels from cell counts in the range of 0.2 to 1 million cells per well showed acceptable parallelism results with %CV at 11.4%. (Table 2)

Table 2. Spiked Recovery and Parallelism of the CTLA4 Assay.

Sample Type	Cell Number (Million)	Nominal Conc. (ng/mL)	Back Calculated Conc. (ng/mL)	%Diff	
Std 1		0.1	0.081	−19%	
Std 2		0.2	0.199	0%	
Std 3		0.4	0.477	19%	
Std 4		0.8	0.822	3%	
Std 5		1.6	1.60	0%	
Std 6		3.2	3.12	−3%	
		Spike Conc. (ng/mL)	**Measured Conc. (ng/mL)**	**Accuracy (%)**	**Response Factor**
Human B Cell	0.5	0	0.068 (BLPQ)	N/A	
Human B Cell	0.5	0.800	0.920	106	
Human T Cell	0.2	0	0.118	N/A	0.591
Human T Cell	0.5	0	0.253	N/A	0.506
Human T Cell	1.0	0	0.635	N/A	0.635
Human T Cell	0.5	0	1.474	140	
CV of Response Factors		0.8			11%

2.4. Measurement of Human Blood Cell Samples

Human cells from multiple donors were purchased from commercial sources and measured for the CTLA-4 levels. The representative extracted ion chromatograms from the samples are shown in Figure 2 and the results are listed in Table 3. The copy number of CTLA-4 protein per cell was calculated based on the measured total CTLA-4 concentration in pg/mL using the following equation with the assumption that each endogenous CTLA-4 protein is a homodimer with two copies of the surrogate peptide which is the same as the reference standard.

$$[CTLA-4]\left(\frac{copy}{cell}\right) = \frac{[CTLA-4]\left(\frac{pg}{mL}\right) \times [Final\ Sample\ Volume](mL) \times 6.022 \times 10^{23}}{[Number\ of\ Cells\ in\ Sample] \times 10^{12}\left(\frac{pg}{g}\right) \times 115{,}000(MW\ of\ CTLA-4\ Standard)} \quad (1)$$

It was found that the CD4+/CD25+/CD127-regulatory T cells showed the highest CTLA-4 levels, averaging between 349 and 1132 copies per cell in the samples from two donors. In the CD19+ B cell samples, the CTLA-4 level proved to be below the LLOQ (equivalent to < five copies per cell). The levels of CTLA-4 from other cell types were: PMBC 46–98 copies per cell; CD3+ pan T 67–112 copies per cell; CD4+ Helper T 27–77 copies per cell; and CD8+ cytotoxic T <12.5–19 copies per cell. The results are consistent with previous reports. It should be pointed out that since regulatory T cells have significantly higher levels of CTLA-4 compared with other type of cells, they could elevate the CTLA-4 level of the cell samples that contain them, such as PBMCs and CD3+ Pan T cells. This seemed to be the case as the CTLA-4 levels of these two types of cell showed higher copies per cell vs. the CD4+ helper T and CD8+ cytotoxic T cells. The result of the study also indicates that the purity of the cell samples is important since a small impurity of regulatory T cells could artificially elevate the overall measured CTLA-4 level in other types of cell samples, such as the helper T and cytotoxic T samples. The purity of most of the cells was > 90%. Among the different T-cell types, the CD8+ cytotoxic T cells demonstrated the lowest CTLA-4 level and the three samples measured were with results close to the LLOQ of 12.5 copies per cell.

Table 3. Measured Total CTLA-4 Concentration in Human T, B, and Cultured Jurkat Cells.

Cell Samples	Lots	Purity (Viability)	Gender	Age	Measured CTLA-4 (Copy per Cell)
CD19+ B	14034019	>90% (>95%)	M	29	<5
	16039855	N/A (>95%)	M	23	46
PBMC	20062721	N/A (>95%)	F	51	98
	20062803	N/A (>95%)	F	43	46
	20061999	>90% (>95%)	M	39	67
CD3+ Pan T	20063759	>90% (>95%)	M	54	112
	16038257	>90% (>95%)	M	29	97
	20063853	>90% (>95%)	M	58	77
CD4+ Helper T	20064018	>90% (>95%)	M	38	27
	21067658	>90% (>95%)	M	27	56
	18048894	>90% (>95%)	M	52	19
CD8+ Cytotoxic T	18048997	>90% (>95%)	F	39	13
	19057442	>90% (>95%)	M	23	<12.5
CD4+/CD25+/CD127-Regulatory T	20062260	>80% (>95%)	M	47	1132
	20063080	>80% (>95%)	M	42	349
CTLA-4 Expressing Jurkat T cell					23,000

PD1/PD-L1 and CTLA-4 represented the two central classes of targets in immune oncology that demonstrated promising efficacies after inhibition. PD-L1 was found elevated on the cell surface of certain tumors such as non-small cell lung cancer. PD-L1 immunohistochemistry (ICH) assays were approved by the FDA as a companion diagnosis for risk/benefit predictions [13]. LC/MS assays were also developed to quantitatively measure PD1/PD-L2 in tumor tissues [10–12].

The expression of CTLA-4 was reported to be predominantly in T cells, as well as other blood cells and tumor cells. The research into CTLA-4 biology has been focused on its function in T cells, especially the immune suppression of regulatory T cells [14]. Quantitative imaging analysis by CTLA-4 immunohistochemistry (ICH) was used to measure the CTLA-4 expression of the tumor-infiltrating lymphocytes [5]. Previous studies have shown that CTLA-4 is predominantly and constitutively expressed in T_{Reg} cells [15], and the CTLA-4 expression is higher in CD4+ T cells than in CD8+ T cells from healthy subjects [16]. In this work, an LC/MS method was developed and used to quantitatively measure the total of CTLA-4 in subtypes of T cells from healthy subjects. The results showed that the CTLA-4 levels in human T cells are T_{Reg} >> CD4+ T > CD8+ T, which are consistent with the abovementioned publications. The results also demonstrated significant variations (two-three-fold) among subjects in each T-cell subtype. The LC/MS assay demonstrated the feasibility of quantitatively measuring CTLA-4 in fewer than one million subtype T cells, thus enabling its potential application as a companion diagnosis together with liquid biopsy in immunotherapy development. There have been other publications that reported the measured soluble CTLA-4 levels in biological fluids. However, the identities of the analytes were subject to debate [17,18]. The LC/MS assay developed herein has the potential to measure soluble CTLA-4 ECD in biological fluid and tissue samples with high specificity and less ambiguity.

3. Materials and Methods

3.1. Chemicals and Reagents

Recombinant human CTLA-4 extracellular domain (ECD) protein with a His-tag was manufactured at Wuxi Biologics (Shanghai, China). Recombinant human CTLA-4 Fc Chimera Avi-tag Protein (Biotin-labeled) was obtained from R&D Systems (Minneapolis, MN, USA). The surrogate tryptic peptide of CTLA-4 H2N-GIASFVC(CAM)EYASPGKˆ-OH (Cys modified by iodoacetamide with a carbamidomethyl group) and its stable isotope-labeled internal standard H2N-GIASFVC(CAM)EYASPGKˆ-OH (K +8 Da) were purchased from Thermo Scientific (Waltham, MA, USA). The Sulfo ChromaLink Biotin was obtained from Trilink Biotech (San Diego, CA, USA). The Dynabeads™ MyOne™ Streptavidin T1 was purchased from Thermo Fisher (Chicago, IL, USA). Acetonitrile, water, and formic acid (FA) were of HPLC grade or higher. A mass spectrometry grade Trypsin/Lys-C Rapid Digestion kit was purchased from Promega (Madison, WI, USA). The Tris buffer (0.1 M, pH 7.5), 1X PBS buffer (pH 7.4), PBST1 (PBS with 0.01% Tween 20), PBST5 (PBS with 0.05% Tween 20), 10 M urea, 100 mM DTT in 1 M pH 7.5 Tris-HCl, 240 mM iodoacetamide (IAA) in 100 mM pH 7.5 Tris-HCl, 3 M sodium acetate (pH 5.2), 4% BSA-PBST, 0.05% CHAPS in 1X PBS, 25 mM HCl in water, were prepared in-house.

3.2. Cell Samples

Human blood cells (B, CD4+ and CD8+ T, regulatory T) were purchased from Hemacare (Los Angeles, CA, USA) and stored at −80 °C until use. The cell count number was provided by the vendor. The Jurkat T-cell line stably expressing human CTLA-4 and an IL2-Luciferase reporter was purchased from Promega (Cat# CS186903, Madison, MI, USA) and cultured in the following media: Gibco RPMI 1640 90% (Thermo Fisher Scientific, Waltham, MA, USA); HyClone FBS 10% (Fisher Scientific, Hampton, NH, USA); MEM non-essential amino acids 1X; sodium pyruvate 100 mM 1X; hygromycin B 200 ug/mL (Thermo Fisher Scientific); and Promega G418 (Fisher Scientific). The cells were maintained in a culture medium between 2×10^5 and 2×10^6 cells/mL. Cells were passaged by diluting with a fresh culture medium to a seeding density of 4×10^5 cell/mL (2-day passage) or 2–3 $\times 10^5$ cells/mL (3-day passage). The cells were counted with a Cellometer (Nexcelom, Lawrence, MA, USA), washed with PBS (×2), centrifuged, and the harvested pellet was stored at −80 °C until use.

Human T and B cells in 1 mL CryoStor freezing media were purchased from Hemacare, with each vial containing 25 million Cryo-PBMCs, 10 million CD3+ Pan T cells, 25 million PB Cryo-CD4 cells, 10 million PB Cryo-CD8 cells, 10 million PB Cryo-B cells, or 1 million PB Cryo-CD127D T_{Reg} cells.

3.3. Generation of Anti-Peptide Polyclonal Antibody

An anti-peptide polyclonal antibody was generated at BBI Solutions (Portland, ME, USA). The peptide was extended by a Cys at the n-terminal and conjugated with keyhole limpet hemocyanin (KLH). A total of 3 rabbits were used for immunization and antisera collections. The primary immunization was administered with 250 μg of the antigen with Complete Freund's adjuvant. Subsequent boosts consisted of 125 μg of the antigen with Incomplete Freund's adjuvant every 3 weeks. The rabbits were bled and tested for titers. The purifications were carried out 2.5 and 4 months after the initial challenges. The polyclonal antibody was purified with Protein A and peptide antigen-affinity chromatography.

3.4. Preparation of Calibration Standard and Internal Standard

Calibration standards at 0.1, 0.2, 0.4, 0.8, 1.6, 3.2, and 6.4 ng/mL were prepared in 0.1% BSA in PBS solution (surrogate matrix) by dilution from a stock solution of recombinant human CTLA-4 Fc chimera Avi-tag protein at 1.5 mg/mL. The internal standard solution of 1 nM in 5% acetonitrile in water was prepared by diluting the stable labeled internal standard stock solution that was prepared by dissolving the peptide powder in 5% acetonitrile in water.

3.5. Sample Processing

Cell sample denaturation and homogenization: A volume of 0.1 mL of cell mixtures was aliquoted into a vial containing 98 mg of urea which led to the final mixture volume of about 0.2 mL with the urea concentration at 8 M, adequate for protein denaturing. The suspended cells were then homogenized using an ultrasonics processor with a tip probe (Zhengzhou TCH Instrument Co., Zhengzhou, China), followed by mixing with 20 μL of 1 nM internal standard solution.

Calibration standards denaturation: An aliquot of 25 μL of each calibration standard was transferred to a 96-well Thermo Kingfisher plate containing 28 mg urea per sample well and mixed with 20 μL of 1 nM internal standard solution.

Tryptic digestion: Each of the denatured cell samples and the calibration standards was mixed with 10 μL of 50 mM DTT in 1 M pH 7.5 Tris-HCl. The plate was then incubated with shaking at 550 rpm at 37 °C for 1 h. An aliquot of 10 μL of 120 mM IAA in 100 mM pH 7.5 Tris-HCl was added to each well and the samples were incubated in the dark with shaking at 550 rpm at room temperature for 30 min, then under light for 20 min. Each sample was mixed with 500 μL of 100 mM pH 7.5 Tris-HCl and 50 μL of 0.1 μg/μL of Trypsin/LysC in 100 mM pH 7.5 Tris-HCl. The samples were then digested overnight by incubating with shaking at 550 rpm at 37 °C. To adjust the pH, 20 μL 3 M sodium acetate (pH 5.2) was added to each well after digestion.

Immunoaffinity enrichment: The anti-peptide antibody was biotinylated with the Sulfo ChromaLink Biotin following the vendor's protocol. An aliquot of 20 μL of 0.075 mg/mL of biotinylated anti-peptide antibody was added to each well containing the digested sample. The plate was incubated at 8 °C with shaking at 850 rpm for 90 min. Each sample was then mixed with 10 μL Streptavidin T1 Dynabeads and incubated at 25 °C for 1 h at 950 rpm, and then placed onto a Kingfisher system. All samples were subjected to duplicate washes with 0.05% CHAPS in 1X PBS (400 μL), a single wash with 0.017% CHAPS in 1X PBS (400 μL) prior to eluting with 150 μL of 25 mM HCl. The eluted peptides were injected for LC-MS analysis.

3.6. Liquid Chromatography and Mass Spectrometry

A Thermo Ultimate 3000 UHPLC system and Ultimate 3000 RSLC nano system (Waltham, MA, USA) interfaced to a Thermo TSQ Quantiva triple-quadrupole mass spectrometer with an EasySpray nano source (Waltham, MA, USA) were used for peptide quantitation. A total of 100 μL of immunoaffinity-enriched peptide eluates from each sample was injected onto a C18 PepMap trap column (0.3 mm × 5 mm, 5 μm, 300 Å, Thermo Fisher) with 0.5% TFA in water at the flow rate of 0.2 mL/min for 3 min. Subsequently, the peptides eluted from the C18 trap column were separated using a PepMap^{TM} C18 Column (3 μm, 100 Å, 75 μm × 15 cm, Thermo Fisher) running at 60 °C. Mobile phases A and B were 0.1% FA in water, and acetonitrile containing 0.1% FA, respectively, and the total flow was 0.6 μL/min.

The nano-LC gradient employed was as follows: maintained at 3% B for 6 min for loading; then ramped to 11% B in one minute; continued to ramp to 19% B in 15 min; and then held at 80% B for 2 min. The mass spectrometer was operated at an MRM positive ionization mode, and the transitions at 743.3 > 911.4 and 747.3 > 919.4 were used for the analyte and corresponding internal standard, respectively.

The LC/MS data were acquired and processed using Thermo Xcaliber software 4.0. Linear calibration curves were established based on the peak area ratio (analyte/IS) vs. concentration using 1/X weighting to enable the assay optimization as well as quantification of unknowns.

4. Conclusions

A highly sensitive and specific hybrid LC/MS assay has been developed and applied to quantitatively measure CTLA-4 levels in human blood cells. The assay is sensitive enough to measure as low as 5 copies of CTLA-4 per cell using 2.5 million cells per sample,

or 12.5 copies per cell using 1 million cells per sample. The measurement was believed to be reliable based on the surrogate spiked CTLA-4 recovery assessment in relevant cell matrices. The novel method provided a practical quantitative method for the total of CTLA-4 level in human T cells, which could be widely applicable in studying CTLA-4 as an important drug target for developing immunotherapies for cancer treatment.

Author Contributions: Conceptualization, D.W., C.J. and M.G.Q.; Methodology, D.W., J.C., L.D. and C.J.; Formal analysis, K.L.H. and J.C. ; Investigation, M.G.Q.; Resources, K.L.H., K.A.-H., T.T.Z., M.S., T.S. and B.W.; Data curation, L.D. and S.C.; Writing—original draft, D.W., J.C., C.J. and M.G.Q.; Writing—review & editing, D.W., K.L.H., J.C., L.D., S.C., K.A.-H., T.T.Z., C.N.C., M.S., T.S., B.W., C.J. and M.G.Q.; Supervision, M.G.Q. All authors have read and agreed to the published version of the manuscript.

Funding: This research received no external funding.

Institutional Review Board Statement: Not applicable.

Informed Consent Statement: Not applicable.

Data Availability Statement: The data presented in this study are available up on request.

Conflicts of Interest: The authors declare no conflict of interest.

Sample Availability: Samples in the study are not available from the authors.

References

1. Chambers, C.A.; Kuhns, M.S.; Egen, J.G.; Allison, J.P. CTLA-4-Mediated Inhibition in Regulation of T Cell Responses: Mechanisms and Manipulation in Tumor Immunotherapy. *Annu. Rev. Immunol.* **2001**, *19*, 565–594. [CrossRef]
2. Seidel, J.A.; Otsuka, A.; Kabashima, K. Anti-PD-1 and Anti-CTLA-4 Therapies in Cancer: Mechanisms of Action, Efficacy, and Limitations. *Front. Oncol.* **2018**, *8*, 86. [CrossRef] [PubMed]
3. Hodi, F.S.; Mihm, M.C.; Soiffer, R.J.; Haluska, F.G.; Butler, M.; Seiden, M.V.; Davis, T.; Henry-Spires, R.; MacRae, S.; Willman, A.; et al. Biologic activity of cytotoxic T lymphocyte-associated antigen 4 antibody blockade in previously vaccinated metastatic melanoma and ovarian carcinoma patients. *Proc. Natl. Acad. Sci. USA* **2003**, *100*, 4712–4717. [CrossRef] [PubMed]
4. Phan, G.Q.; Yang, J.C.; Sherry, R.M.; Hwu, P.; Topalian, S.L.; Schwartzentruber, D.J.; Restifo, N.P.; Haworth, L.R.; Seipp, C.A.; Freezer, L.J.; et al. Cancer regression and autoimmunity induced by cytotoxic T lymphocyte-associated antigen 4 blockade in patients with metastatic melanoma. *Proc. Natl. Acad. Sci. USA* **2003**, *100*, 8372–8377. [CrossRef] [PubMed]
5. Brown, C.; Sekhavati, F.; Cardenes, R.; Windmueller, C.; Dacosta, K.; Rodriguez-Canales, J.; Steele, K.E. CTLA-4 Immunohistochemistry and Quantitative Image Analysis for Profiling of Human Cancers. *J. Histochem. Cytochem.* **2019**, *67*, 901–918. [CrossRef] [PubMed]
6. Miller, R.E.; Fayen, J.D.; Mohammad, S.F.; Stein, K.; Kadereit, S.; Woods, K.D.; Sramkoski, R.M.; Jacobberger, J.W.; Templeton, D.; Shurin, S.B.; et al. Reduced CTLA-4 protein and messenger RNA expression in umbilical cord blood T lymphocytes. *Exp. Hematol.* **2002**, *30*, 738–744. [CrossRef] [PubMed]
7. Neubert, H.; Shuford, C.M.; Olah, T.V.; Garofolo, F.; Schultz, G.A.; Jones, B.R.; Amaravadi, L.; Laterza, O.F.; Xu, K.; Ackermann, B.L. Protein Biomarker Quantification by Immunoaffinity Liquid Chromatography–Tandem Mass Spectrometry: Current State and Future Vision. *Clin. Chem.* **2020**, *66*, 282–301. [CrossRef] [PubMed]
8. Neubert, H.; Xu, K. New opportunities with quantification of protein therapeutics by LC–MS. *Bioanalysis* **2018**, *10*, 971–973. [CrossRef] [PubMed]
9. Sugimoto, H.; Wei, D.; Dong, L.; Ghosh, D.; Chen, S.; Qian, M.G. Perspectives on potentiating immunocapture-LC–MS for the bioanalysis of biotherapeutics and biomarkers. *Bioanalysis* **2018**, *10*, 1679–1690. [CrossRef] [PubMed]
10. Morales-Betanzos, C.A.; Lee, H.; Gonzalez Ericsson, P.I.; Balko, J.M.; Johnson, D.B.; Zimmerman, L.J.; Liebler, D.C. Quantitative Mass Spectrometry Analysis of PD-L1 Protein Expression, N-glycosylation and Expression Stoichiometry with PD-1 and PD-L2 in Human Melanoma. *Mol. Cell. Proteom.* **2017**, *16*, 1705–1717. [CrossRef] [PubMed]
11. Zhang, Q.; Salzler, R.; Dore, A.; Yang, J.; Ma, D.; Olson, W.C.; Liu, Y. Multiplex Immuno-Liquid Chromatography–Mass Spectrometry–Parallel Reaction Monitoring (LC–MS–PRM) Quantitation of CD8A, CD4, LAG3, PD1, PD-L1, and PD-L2 in Frozen Human Tissues. *J. Proteome Res.* **2018**, *17*, 3932–3940. [CrossRef] [PubMed]
12. Zhu, Y.; Zalaznick, J.; Sleczka, B.; Parrish, K.; Yang, Z.; Olah, T.; Shipkova, P. Immunoaffinity microflow liquid chromatography/tandem mass spectrometry for the quantitation of PD1 and PD-L1 in human tumor tissues. *Rapid Commun. Mass Spectrom.* **2020**, *34*, e8896. [CrossRef] [PubMed]
13. Liu, D.; Wang, S.; Bindeman, W. Clinical applications of PD-L1 bioassays for cancer immunotherapy. *J. Hematol. Oncol.* **2017**, *10*, 110. [CrossRef] [PubMed]

14. Oyewole-Said, D.; Konduri, V.; Vazquez-Perez, J.; Weldon, S.A.; Levitt, J.M.; Decker, W.K. Beyond T-Cells: Functional Characterization of CTLA-4 Expression in Immune and Non-Immune Cell Types. *Front. Immunol.* **2020**, *11*, 608024. [CrossRef] [PubMed]
15. Rowshanravan, B.; Halliday, N.; Sansom, D.M. CTLA-4: A moving target in immunotherapy. *Blood* **2018**, *131*, 58–67. [CrossRef] [PubMed]
16. Chan, D.V.; Gibson, H.M.; Aufiero, B.M.; Wilson, A.J.; Hafner, M.S.; Mi, Q.S.; Wong, H.K. Differential CTLA-4 expression in human CD4+ versus CD8+ T cells is associated with increased NFAT1 and inhibition of CD4+ proliferation. *Genes Immun.* **2014**, *15*, 25–32. [CrossRef] [PubMed]
17. Esposito, L.; Hunter, K.M.D.; Clark, J.; Rainbow, D.B.; Stevens, H.; Denesha, J.; Duley, S.; Dawson, S.; Coleman, G.; Nutland, S.; et al. Investigation of Soluble and Transmembrane CTLA-4 Isoforms in Serum and Microvesicles. *J. Immunol.* **2014**, *193*, 889–900. [CrossRef] [PubMed]
18. Sato, S.; Fujimoto, M.; Hasegawa, M.; Komura, K.; Yanaba, K.; Hayakawa, I.; Matsushita, T.; Takehara, K. Serum soluble CTLA-4 levels are increased in diffuse cutaneous systemic sclerosis. *Rheumatology* **2004**, *43*, 1261–1266. [CrossRef] [PubMed]

Disclaimer/Publisher's Note: The statements, opinions and data contained in all publications are solely those of the individual author(s) and contributor(s) and not of MDPI and/or the editor(s). MDPI and/or the editor(s) disclaim responsibility for any injury to people or property resulting from any ideas, methods, instructions or products referred to in the content.

MDPI AG
Grosspeteranlage 5
4052 Basel
Switzerland
Tel.: +41 61 683 77 34

MDPI Books Editorial Office
E-mail: books@mdpi.com
www.mdpi.com/books



Disclaimer/Publisher's Note: The title and front matter of this reprint are at the discretion of the Topic Editors. The publisher is not responsible for their content or any associated concerns. The statements, opinions and data contained in all individual articles are solely those of the individual Editors and contributors and not of MDPI. MDPI disclaims responsibility for any injury to people or property resulting from any ideas, methods, instructions or products referred to in the content.





Academic Open
Access Publishing

mdpi.com

ISBN 978-3-7258-7776-8